Search for CP violation in four-body fully charged b-baryon decays with the LHCb spectrometer

Jan Mickelle Maratas

Numéro d'ordre : 2613 PCCF T 1508
EDSF : 836

UNIVERSITÉ BLAISE PASCAL
(U.F.R. Sciences, Technologies et Santé)

ÉCOLE DOCTORALE DES SCIENCES FONDAMENTALES

THÈSE

présentée pour obtenir le grade de

DOCTEUR D'UNIVERSITÉ
(SPÉCIALITÉ PHYSIQUE DES PARTICULES)

par

Jan Mickelle V. MARATAS

SEARCH FOR *CP* VIOLATION IN FOUR-BODY FULLY CHARGED *b*-BARYON DECAYS WITH THE LHCB SPECTROMETER

Thèse soutenue le 6 novembre 2015 devant la commission d'examen :

Président :	M.	Alain	FALVARD
Rapporteurs :	M.	Tim	GERSHON
	M.	Vincenzo	VAGNONI
Examinateurs :	M.	Yuval	GROSSMAN
	M.	Régis	LEFÈVRE
Directeur de thèse :	M.	Stéphane	MONTEIL

Abstract

This thesis presents the search for *CP* violation in four-body fully-charged charmless weak decays of Λ_b^0 and Ξ_b^0 baryons. The events are gathered and reconstructed using the LHCb spectrometer installed at the Large Hadron Collider (LHC) of CERN at Geneva, Switzerland. Although the assumed aim of this study is to unravel new sources of *CP* violation, the first necessary step consists in observing *CP* violation in baryon decays, which has not yet been observed by previous experiments. A total of seven charmless decay modes were looked at for the search, particularly the Λ_b^0 $(\Xi_b^0) \to ph^-h'^+h''^-$ decay modes, where h, h' and h'' can either be a π or a K. Since these decay modes are also not yet observed prior to this thesis, we conducted a search on the same seven final decay modes of Λ_b^0 and Ξ_b^0. This thesis presents also the calibration and ageing study on the Pre-shower (PS) sub-detector of LHCb. Minimum ionizing particles were used to accomplish the task. Presented as well in this thesis is the branching fraction limit calculation of $B_s^0 \to K_S^0 K^+ K^-$ using a modified Feldman-Cousins inference.

Keywords:
LHCb, CKM matrix, direct *CP* violation, *b*-flavoured baryons, Flavour Physics, Pre-shower

Résumé

Cette thèse d'Université présente une recherche de brisure de la symétrie *CP* dans les désintégrations à quatre corps électriquement chargés des baryons beaux Λ_b^0 et Ξ_b^0. L'analyse utilise les données enregistrées par l'expérience LHCb installée auprès du grand collisionneur de hadrons (LHC), sis au CERN à Genève (Suisse). Le but ultime de ce travail est de mettre à jour une nouvelle source de brisure de la symétrie *CP*. La première étape dans cette quête consiste toutefois à observer pour la première fois une brisure de symétrie dans les désintégrations de baryon. Sept désintégrations ont été recherchées dans ce travail de thèse. Six d'entre elles, explicitement $\Lambda_b^0 \to p\pi^+\pi^-\pi^-$, $\Lambda_b^0 \to pK^-\pi^+\pi^-$, $\Xi_b^0 \to pK^-\pi^+\pi^-$, $\Lambda_b^0 \to pK^-K^+\pi^-$, $\Xi_b^0 \to pK^-\pi^+K^-$ et $\Lambda_b^0 \to pK^-K^+K^-$ ont été observées pour la première fois et leurs asymétries *CP*, intégrées sur l'espace des phases des désintégrations d'intérêt, ont été mesurées. Aucun signe de brisure de symétrie *CP* n'a été observé. Ce travail de thèse comprend également les études de calibration du détecteur PreShower de LHCb au moyen de particules au minimum d'ionisation. Un travail portant sur le calcul de la limite sur le rapport d'embranchement du mode de désintégration $B_s^0 \to K_S^0 K^+ K^-$ au moyen d'un inférence de Feldman-Cousins modifiée, complète le matériel scientifique rassemblé dans ce manuscrit de thèse.

Mots clés:
LHCb, baryons beaux, brisure de la symétrie *CP*, Pre-shower

Acknowledgements

Perhaps, the best part in writing a thesis manuscript is the pleasure of acknowledging the efforts of the many people whose names may not appear in the cover, but whose support, friendship and understanding were undeniably crucial to the completion of the thesis. In a span of three years, several individuals helped me along the way and in the following paragraphs, I would like to invoke my privilege to publicly express my heartfelt appreciation and deepest gratitude to everyone.

I would like to start thanking the members of the Thesis Panel Committee. I could not have finished this thesis without the help of my supervisor, Stéphane Monteil, who guided me during the entire course of the PhD program. His insights and inputs were the best I could ever ask for. I would also like to thank Tim Gershon, Vincenzo Vagnoni, Yuval Grossman, Régis Lefèvre and Alain Falvard for reviewing the thesis content and the manuscript, as well as for the constructive inquiries during the defense.

The other members of the LPC-Clermont LHCb group, particularly Marc Grabalosa, Olivier Deschamps, Eric Cogneras, Valentin Niess, Marouen Baalouch, Ibrahim El-Rifaî, Mostapha Hoballah, Guilio Gazzoni, Mohamad Kozeiha and Maxime Vernet, also has helped me a lot. I am thankful to them for helping me pull through the whole program and for patiently answering my queries knowing that I did not have a solid background in HEP. Marouen has always been a good friend and always there to extend his help whenever I needed one. I will surely miss the small talks we had during coffee breaks.

I would also like to express my gratitude to the CNRS and the Auvergne region administrations for funding my doctorate program, as well the Physics department of MSU-IIT for allowing me to further my professional career.

And of course, I am thankful to my very supportive wife Lucilyn Maratas, who even accompanied me in France for one-and-a-half year just to help me adapt to the changes. Inspiring me even more to finish is our little girl Malaya who was made and born while I was pursuing the PhD program.

Lastly, I would like to apologize to everyone who helped but I was unable to note here. My mind might be forgetful these days, but my heart remembers it all.

Introduction

Once postulated to be an exact symmetry of nature is now an experimentally-established fact that *CP*-symmetry is slightly violated in decays involving weak interaction. First observed in the decays of neutral kaons [1], *CP*-violation is also observed in the B system as seen by BaBar [2–4] and Belle [5–7] experiments, and recently by the LHCb collaboration [8, 9]. The Standard Model (SM) of particle physics can explain this phenomenon as a consequence of quark-mixing of at least three generations as explained in the Kobayashi-Maskawa (KM) mechanism [10]. With 3 generations of quarks, the KM mechanism predicts one phase that governs all *CP*-violation phenomena. With several decay modes to look at, tremendous progress was done in the last 15 years to redundantly-constrain the KM predictions and so far found no evidence of significant deviation from it [11, 12]. This achievement is a pillar of the SM. Search for *CP*-asymmetries with *b*eauty baryons (or *b*-baryons) however have received lesser attention up to now. In the SM, the weak phase governing the *CP* violation in the K and B systems drives also the *CP* violation in *b*-baryons. Although the assumed aim of the work defended in this thesis is to unravel new sources of *CP* violation, the very first necessary step consists in observing a *CP*-violating phenomenon in baryon decays.

Some few attempts have been done to search for direct *CP* asymmetries involving *b*-baryons [13–15] and so far found to be consistent with no asymmetry. The LHCb experiment operated at center-of-mass energies above the threshold for *b*-baryon production, and hence has an excellent potential to further improve the understanding of *b*-baryons.

In this thesis, *CP*-asymmetries are searched for in the charmless fully-charged four-body weak decays of two neutral *b*-flavoured baryons, namely Λ_b^0 and Ξ_b^0, using the Run I data of LHCb experiment corresponding to an integrated luminousity of 3.0 fb^{-1}. Few promising modes to observe direct *CP* violation in *b*-baryons are in the charmless decays to multibody, where the decays can proceed simultaneously through $b \to u$ tree transition or Flavour Changing Neutral Current penguin loop transitions $b \to s$ and $b \to d$. It is also worth noting that the seven decay modes studied in this analysis are yet unobserved and hence, the establishment of these decays is implicit in the analysis. The interference pattern of four-body decays is expected to be rich of structures, in particular in the low two-body baryon resonances ($\Lambda^{*0}(1520)$, $N^{*0}(1520)$, Δ series). Difference in strong phases between two competing amplitudes might enhance the weak-induced asymmetries.

In Chapter 1, the basic theory describing the Standard Model of particle physics is discussed, which includes how the KM mechanism explains the *CP*-violation phenomena. Chapter 2 is dedicated to the LHCb detector, with an emphasis on the tracking detectors of utmost importance for the physics analyses discussed here. Chapter 3 discusses the details of the Pre-shower subdetector. My work on the ageing and calibration of the Pre-shower is also included in this Chapter.

Prior to this analysis, I was involved in the search and measurement of $B^0_{d,s} \to K^0_S h^+ h'^-$ (h,h'=π,K) relative branching fractions at LHCb [16], particularly in the search for $B^0_s \to K^0_S K^+ K^-$ decay mode. In Chapter 4, I will present my contribution on this analysis and specifically a discussion on the setting of the limit of the relative branching fraction of

$B_s^0 \to K_S^0 K^+ K^-$.

The main topic of this thesis, which is the search for *CP*-asymmetries in charmless decays of beautiful neutral baryons, is discussed in Chapters 5 and 6. This covers from data selection up to the summary of the results. The *CP*-asymmetry observables are measured in 3 different phase space cuts, namely (1) integrated throughout the full phase space of the decay, (2) in the low-invariant mass region of the quasi-resonant decay, particularly with an excited baryon mass less than 2 GeV/c^2, and (3) within the phase space region of the quasi-2-body decays involving an excited baryon resonance less than 2 GeV/c^2 and an associated mesonic resonance of typical mass below 1.6 GeV/c^2. A section is also dedicated on establishing the signal decays. Chapter 7 summarizes the results of the whole thesis and discusses potential for further studies.

An exploratory work was also conducted to assess the possibility of reconstructing the invariant mass of parent particle without explicitly reconstructing one of its final daughter particles – a technique dubbed "partial reconstruction". In LHCb, this is possible in some decays due to the excellent vertexing of the production and decay vertices. A discussion on this work is presented in Appendix B.

Contents

Chapter 1

Theoretical context

Contents

1.1 Introduction

The Standard Model (SM) of particle physics has been very successful in explaining the interactions of fundamental particles. This provides a very elegant theoretical framework in describing experimental results with high precision. In this Chapter, the theoretical underpinning of the SM is introduced and how the SM describes the interactions of fundamental particles is given.

Section 1.2 introduces the list of fundamental particles of the SM and how this gauge theory describes the interactions. Since one of the main focuses of the LHCb experiment and the main topic of this thesis is on the *CP*-violation in the quark sector, a discussion on the quark mixing and CKM matrix is written in Section 1.5. This is followed by a section (Section 1.6) about the *CP*-violation and the classification of its three possible manifestations. Finally, dedicated section is assigned for the discussion on the review of b-baryons and on the decay channels studied in this thesis.

1.2 The Standard Model

The Standard Model (SM) of particle physics is a renormalizable quantum field theory constructed under the principle of local gauge invariance. It describes the interactions based on the symmetry group $SU(3)_C \otimes SU(2)_L \otimes U(1)_Y$, where the strong interaction is governed by symmetry group of color rotations $SU(3)_C$ and the electroweak interaction by the $SU(2)_L \otimes U(1)_Y$ symmetry group. In this model, the dynamics of the particles and their interactions is described using a Lagrangian $\mathcal{L}_{\text{SM}}$. Being a gauge theory, the SM Lagrangian is

invariant under continuous local transformations. The discussion in this Section starts with the fundamental particles and fundamental forces of the SM, and ends with a discussion on the Lagrangian of the SM and how the spinor fields are represented.

1.2.1 The fundamental particles

The fundamental particles of the SM are believed to have no further internal structure and serves as the building blocks of other composite particles. There are two distinct types of particles in the SM, namely fermions and bosons. Fermionic-type particles, which have half-integer spins, obey Fermi-Dirac statistics, while bosonic-type particles, having integer spins, obey Bose-Einstein statistics.

There are 12 fermions, composed of six quarks and six leptons, considered as fundamental particles in the SM. The quarks are further classified according their third weak isospin projection T_3 into up-type quarks (u, c, t), down-type quarks (d, s, b), while the leptons are classified as charged-leptons (e, μ, τ) and the neutrinos (ν_e, ν_μ, ν_τ). The fermions can be arranged as three generations, as shown in Table 1.1, where each generation has the same quantum number as the other generations except that they have different masses. The generations are arranged with increasing masses of the fermions, that is the third and second generations have fermion masses higher that the second and first generations, respectively.

Although not shown in Table 1.1, each quark can actually have three possible distinct color quantum number, conventionally dubbed "red", "green" and "blue". Also not shown in the Table is that each quark has an anti-particle, having the same fundamental properties as the quark except that the quantum charges are opposite and can take for instance three possible color charges "anti-red", "anti-green" or "anti-blue".

Table 1.1: The fundamental fermions of the Standard Model written as doublets and arranged by generation.

Charge	I	II	III	
$\begin{pmatrix} +\frac{2}{3} \\ -\frac{1}{3} \end{pmatrix}$	$\overbrace{\begin{pmatrix} u \\ d \end{pmatrix}}$	$\overbrace{\begin{pmatrix} c \\ s \end{pmatrix}}$	$\overbrace{\begin{pmatrix} t \\ b \end{pmatrix}}$	Quarks
$\begin{pmatrix} +1 \\ 0 \end{pmatrix}$	$\begin{pmatrix} e \\ \nu_e \end{pmatrix}$	$\begin{pmatrix} \mu \\ \nu_\mu \end{pmatrix}$	$\begin{pmatrix} \tau \\ \nu_\tau \end{pmatrix}$	Leptons

Mediating the interaction of the fermions are the gauge bosons of the SM. The four types of gauge bosons of the SM are the photon (γ), the gluons (g), the $W^\pm$ and the Z^0. Table 1.2 lists the fundamental bosons of the SM. The photon mediates the electromagnetic interaction, while the gluon is the mediating boson of the strong force. Weak force is mediated via massive charged bosons $W^\pm$ and massive neutral boson Z^0. The photon couples only to charged particles and hence does not couple to neutrinos, neither on the other neutral gauge bosons including itself. The quarks, carrying a colour charge, can also interact via their couplings to the gluons, while the leptons, which has no colour charge, do not interact via strong force. Lastly, the weak force interacts to all fermions and hence the only interaction that the neutrinos participate. The gravitational force, negligible at the energies we are interested in this thesis, does not belong so far to this quantum field theory framework and will not be discussed further.

Table 1.2: The fundamental bosons of the Standard Model. Shown as well are their respective electric charges, masses, spins, and interactions being mediated. Note that the properties are as the SM predicted, except for the masses where the experimental value is quoted when the SM prediction is nonzero.

Boson	Electric charge	Mass (in GeV/c^2)	Spin	Interaction mediated
γ	0	massless	1	Electromagnetic
$W^{\pm}$	± 1	80.385±0.015 [17]	1	Weak charged current
Z^0	0	91.1876±0.0021 [17]	1	Weak neutral current
g	0	massless	1	Strong
H^0	0	125.09 ± 0.21(stat) ± 0.11(syst) [18]	0 [19, 20]	Mass generation

Also shown in Table 1.2 is the Higgs boson particle [21–26]. A narrow bosonic state has been recently discovered by ATLAS [27] and CMS [28] experiments and is so far consistent with the fundamental scalar of the SM. Unlike the other fundamental bosons of the SM, the Higgs boson is a scalar boson (spin 0) and is not a mediator of any of the fundamental forces. It undergoes however elementary interactions with both fermions and bosons as discussed later in this chapter.

1.2.2 The fundamental forces in the SM

As mentioned in the previous subsection, the fermions interact with each other via different types of forces, namely electromagnetic interaction, weak interaction and strong interaction. The electromagnetic interaction, described by the theory of Quantum Electrodynamics (QED), occurs only among charged particles via the exchange of photon, implying that neutrinos (as well as Z^0 bosons) does not interact with other particles via electromagnetic force. Since a photon does not carry an electric charge, it does not couple to other photons, in contrast to gluons which can couple to other gluons as well.

The weak force is mediated by either the massive charged boson $W^{\pm}$ or the massive neutral boson Z^0. The theory describing the weak interaction is combined together with the electromagnetic interaction, to become the electroweak theory (EWT). The EWT was first proposed by S. Glashow [29], S. Weinberg [30] and A. Salam [31] based on the $SU(2)_L \otimes U(1)_Y$ symmetry group. Fermions can change their flavour by emitting a charged $W^{\pm}$ boson. In the SM, this is the only tree level transition that changes the flavour, and in particular the generation of quarks. Hence, there is no Flavour Changing Neutral Current (FCNC) in tree-level transitions in the SM. Neither the neutral current Z^0 can change the flavour of fermions in tree-level transitions as explained by the Glashow-Iliopoulos-Maiani (GIM) mechanism [32]. Since neutrinos has no electric charge and colour charge, they do not interact via electromagnetic force nor via strong force, leaving only the weak interaction. Moreover, since only left-handed leptons, represented as doublets in the $SU(2)_L$, are involved in the weak interaction, the right-handed neutrinos then become sterile, should they actually exist.

The strong interaction, which is responsible, in a residual way, of the binding (and confinement) of quarks to form hadrons, is mediated by gluons. The theory involved in the strong interaction is called Quantum ChromoDynamics (QCD), based on the $SU(3)_C$ symmetry group. There are actually eight different gluons, corresponding to the eight generators of the $SU(3)_C$ symmetry group. The quarks come as a colour triplet, while the leptons are singlets of $SU(3)_C$. In analogy to QED, quarks carry "colour" charges. However, unlike

in QED, the gluons can interact also with other gluons. Quark confinement, *i.e.* the fact that quarks can not be isolated singularly, can be explained by the colour interaction. As a quark-antiquark pair separate, the gluon field strength between them does not diminish, regardless of their distance. At some point of the separation, it becomes more energetically favourable to spontaneously pop-in a new quark-antiquark pair from the vacuum than to extend the separation.

1.2.3 Standard Model Lagrangian

The SM of particle physics describes the laws of Nature based on Quantum Field Theory (QFT). In QFT, this leads to formulating the Lagrangian of Nature. The most compact full Lagrangian $\mathcal{L}_{\text{SM}}$ of the SM consists of four parts, as written in Equation 1.1,

$$\mathcal{L}_{\text{SM}} = \mathcal{L}_{\text{Gauge}} + \mathcal{L}_{\text{Kinetic}} + \mathcal{L}_{\text{Higgs}} + \mathcal{L}_{\text{Yukawa}}, \tag{1.1}$$

where $\mathcal{L}_{\text{Gauge}}$ is the kinetic term of the gauge fields, $\mathcal{L}_{\text{Kinetic}}$ is the kinetic term describing the dynamics of the spinor Dirac ψ, $\mathcal{L}_{\text{Higgs}}$ describes the Higgs scalar field and its potential, and $\mathcal{L}_{\text{Yukawa}}$ describes the interaction between the Higgs field and the fermions (so called Yukawa couplings). The kinetic term of the fermion fields is given by,

$$\mathcal{L}_{\text{Kinetic}} = i\overline{\psi}(D^{\mu}\gamma_{\mu})\psi \tag{1.2}$$

where the spinor fields ψ ($\overline{\psi} = \psi^{\dagger}\gamma^{0}$, γ^{0} as one of the Dirac gamma matrices in chiral basis) contains the three fermion generations, consisting of the following five representations :

$$Q^{I}_{Li}(3,2,+1/3),\quad u^{I}_{Ri}(3,1,+4/3),\quad d^{I}_{Ri}(3,1,-2/3),\quad L^{I}_{Li}(1,2,-1),\quad l^{I}_{Ri}(1,1,-2)\ . \tag{1.3}$$

This notation tells that quarks are triplets in the $SU(3)_C$ color rotation, while the leptons are singlets in $SU(3)_C$. The left-hand component of the spinor ψ is a doublet in the $SU(2)_L$ rotation, while the right-hand component is a singlet. The last quantum number inside the parentheses specifies its weak hypercharge Y of the $U(1)_Y$, which is equal to 2(Q- T_3), where Q is the electric charge and T_3 is third component of the weak isospin. In example, the notation $Q^{I}_{Li}(3,2,+1/3)$ means that this is a triplet in $SU(3)_C$, a left-handed doublet in $SU(2)_L$ and with a hypercharge $Y = 1/3$. The subscript i stands for the three generations, while the superscript I signifies that this is written in the interaction basis. Hence, the explicit forms of the representations in Equation 1.3 are,

$$Q^{I}_{Li}(3,2,+1/3) = \overbrace{\begin{pmatrix} u^I_r,\ u^I_g,\ u^I_b \\ d^I_r,\ d^I_g,\ d^I_b \end{pmatrix}_L}^{1^{\text{st}}\text{ generation}}, \quad \overbrace{\begin{pmatrix} c^I_r,\ c^I_g,\ c^I_b \\ s^I_r,\ s^I_g,\ s^I_b \end{pmatrix}_L}^{2^{\text{nd}}\text{ generation}}, \quad \overbrace{\begin{pmatrix} t^I_r,\ t^I_g,\ t^I_b \\ b^I_r,\ b^I_g,\ b^I_b \end{pmatrix}_L}^{3^{\text{rd}}\text{ generation}}, \tag{1.4}$$

$$L^{I}_{Li}(1,2,-1) = \begin{pmatrix} {\nu_e}^I \\ e^I \end{pmatrix}_L, \quad \begin{pmatrix} {\nu_\mu}^I \\ \mu^I \end{pmatrix}_L, \quad \begin{pmatrix} {\nu_\tau}^I \\ \tau^I \end{pmatrix}_L, \tag{1.5}$$

$$u^{I}_{Ri}(3,1,+4/3) = \left(u^I_r,\ u^I_g,\ u^I_b \right)_R, \quad \left(c^I_r,\ c^I_g,\ c^I_b \right)_R, \quad \left(t^I_r,\ t^I_g,\ t^I_b \right)_R, \tag{1.6}$$

$$d^{I}_{Ri}(3,1,-2/3) = \left(d^I_r,\ u^I_g,\ d^I_b \right)_R, \quad \left(s^I_r,\ c^I_g,\ s^I_b \right)_R, \quad \left(b^I_r,\ t^I_g,\ b^I_b \right)_R, \tag{1.7}$$

$$l^{I}_{Ri}(1,1,-2) = \left(e^I \right)_R, \quad \left(\mu^I \right)_R, \quad \left(\tau^I \right)_R, \tag{1.8}$$

where the subscripts r, g, and b are the three color quantum numbers; u, c and t are the up-type quarks; and d, s and b are the down-type quarks.

The covariant derivative D^{μ} in Equation 1.2 is a replacement of the ordinary derivative in order to maintain the gauge invariance. This is written in four terms as,

$$D^{\mu} = \partial^{\mu} + ig_s G^{\mu}_a L_a + igW^{\mu}_b T_b + ig'B^{\mu}Y\ , \tag{1.9}$$

where the first term is the ordinary derivative, L_a are the generators of the $SU(3)_C$ group (the 3×3 Gell-Mann matrices: $\frac{1}{2}\lambda_a$ for triplets and 0 for singlets) and T_b are $SU(2)_L$ generators (the 2×2 Pauli matrices: $\frac{1}{2}\sigma_b$ for doublets and 0 for singlets). G_a^μ are the eight gluons fields, W_b^μ are the three weak interaction bosons and B^μ is the hypercharge boson.

The Higgs scalar field ϕ and its potential $V(\phi^\dagger\phi)$ is added to the Lagrangian of the SM in order for the bosons of the weak interaction to acquire mass via the spontaneous symmetry breaking mechanism, also known as the Brout-Englert-Higgs (BEH) mechanism [21–23].

The $\mathcal{L}_{\text{Higgs}}$ term has the form,

$$\mathcal{L}_{\text{Higgs}} = (D^\mu\phi)^\dagger(D^\mu\phi) + \mu^2\phi^\dagger\phi - \lambda(\phi^\dagger\phi)^2 \ , \tag{1.10}$$

where the Higgs complex scalar field is an isodoublet,

$$\phi(x) = \begin{pmatrix} \phi^+ \\ \phi^0 \end{pmatrix} \ . \tag{1.11}$$

The development of the covariant derivative product in the kinetic term of Equation 1.10 can describe the coupling of the Higgs to the gauge fields. The couplings of the Higgs field to the fermion fields on the contrary are not manifested in the Higgs Lagrangian and hence they are added by hand. These couplings, known as Yukawa couplings, are written as follows,

$$-\mathcal{L}_{\text{Yukawa}} = Y_{ij}\overline{\psi_{Li}}\phi\psi_{Rj} + (\text{hermitian conjugate}) \tag{1.12}$$

$$= Y^u_{ij}\overline{Q^I_{Li}}\tilde{\phi}u^I_{Rj} + Y^d_{ij}\overline{Q^I_{Li}}\phi d^I_{Rj} + Y^l_{ij}\overline{L^I_{Li}}\phi l^I_{Rj} + (\text{hermitian conjugate}) \tag{1.13}$$

where,

$$\tilde{\phi}(x) = i\sigma_2\phi^* = \begin{pmatrix} \overline{\phi}^0 \\ -\phi^- \end{pmatrix} \ . \tag{1.14}$$

The arbitrary complex matrices Y^d_{ij}, Y^u_{ij} and Y^l_{ij} operate in the flavour space, with different couplings between different generations, and hence quark mixing. Once the Higgs field acquires a non-zero vacuum expectation value, the mass of the fermions are then generated. More discussion on the quark mixing and mass generation will be presented in Section 1.5.

1.3 Weak interactions in the flavour sector

This thesis is closely connected to the weak interactions in the flavour sector. As such, this particular section is dedicated to the EWT of the SM. As already mentioned in the previous Section, $SU(2)_L \otimes U(1)_Y$ is the symmetry group describing the electroweak interaction. The discusion will start with the discrete symmetries of the SM that are closely-related to flavour physics.

1.3.1 Discrete symmetries of the SM

There are two discrete symmetries of the SM that are closely related to flavour physics, which are the charge conjugation C and space inversion (or parity operation) P. The discrete C symmetry postulates that Nature should be the same if particles are replaced with anti-particles, *i.e.* by changing the internal quantum numbers like the electromagnetic charge. On the other hand, the P symmetry postulates that it should be the same if the space coordinates are inverted, which cause the spacetime coordinate $x^\mu \mapsto x_\mu$.

A third discrete symmetry of interest in understanding the laws of Nature is the time reversal T, where it states that physics laws should be the same whether going forward or backward in time (*i.e.* which causes $x^\mu \mapsto -x_\mu$). There is a strong reason for the combined CPT operation to be a symmetry of Nature, as any Lorentz invariant local field theory must have the combined CPT symmetry. The effect that fundamental particles and their antiparticles have the same masses and widths can be explained as a consequence of the CPT invariance.

It has been experimentally observed that although C, P and the combined CP are exact symmetries of the electromagnetic and strong interactions, the weak interaction maximally violates the C and P operation individually and slightly violates the combined CP symmetry.

1.3.2 The $SU(2)_L \otimes U(1)_Y$ theory

As discussed earlier, the EWT based on $SU(2)_L \otimes U(1)_Y$ symmetry group, pioneered by the combined efforts of S. Glashow [29], S. Weinberg [30] and A. Salam [31], is successful in making a unified theory of weak and electromagnetic interactions. Since it was already observed in experiments that only the left-handed fermions and right-handed antifermions participate in charged current mediated weak decays, the *chirality* is directly embedded into the theory, implying that left-handed and right-handed components of the spinor field interact differently with the weak interaction.

The Dirac spinor field ψ in Equation 1.2 can actually be decomposed into left-handed and right-handed chiral components, that is,

$$\psi = \psi_L + \psi_R \tag{1.15}$$
$$\overline{\psi} = \overline{\psi}_L + \overline{\psi}_R \tag{1.16}$$

where,

$$\psi_L = \frac{1}{2}(1-\gamma^5)\psi \quad \text{and} \quad \psi_R = \frac{1}{2}(1+\gamma^5)\psi \tag{1.17}$$
$$\overline{\psi}_L = \overline{\psi}\frac{1}{2}(1+\gamma^5) \quad \text{and} \quad \overline{\psi}_R = \overline{\psi}\frac{1}{2}(1-\gamma^5)\ . \tag{1.18}$$

The projection operators $P_L = \frac{1}{2}(1-\gamma^5)$ and $P_R = \frac{1}{2}(1+\gamma^5)$ are constructed using the fifth Dirac gamma matrix, $\gamma^5 = i\gamma^0\gamma^1\gamma^2\gamma^3$. If these chirality-decomposed Dirac spinors are inserted to the kinetic term of the SM Lagrangian in Equation 1.9, it becomes obvious that the left-handed and right-handed spinor field components interact separately, hence it is possible to treat left- and right-handed components as separate fields in the EWT. Since the two components can be treated separately, they can have different couplings to the gauge fields. The chirality-separated representations of the fermion fields in the SM is listed in Equation 1.3, where left-handed components of the fermions are doublets of $SU(2)_L$ and the right-handed components are singlets.

Deducing from Equation 1.9, the Lagrangian of the weak current interaction (dropping the term involving the strong interaction for simplicity) between the fermions are written as,

$$\mathcal{L}_{\text{Kinetic,Weak}}(Q^I_{Li}) = i\overline{Q^I_{Li}}(\partial^\mu + \frac{i}{2}gW^\mu_b\sigma_b + \frac{i}{6}g'B^\mu)\gamma_\mu Q^I_{Li} \tag{1.19}$$

$$\mathcal{L}_{\text{Kinetic,Weak}}(L^I_{Li}) = i\overline{L^I_{Li}}(\partial^\mu + \frac{i}{2}gW^\mu_b\sigma_b - \frac{i}{2}g'B^\mu)\gamma_\mu L^I_{Li} \tag{1.20}$$

$$\mathcal{L}_{\text{Kinetic,Weak}}(u^I_{Ri}) = i\overline{u^I_{Ri}}(\partial^\mu + \frac{2}{3}ig'B^\mu)\gamma_\mu u^I_{Ri} \tag{1.21}$$

$$\mathcal{L}_{\text{Kinetic,Weak}}(d^I_{Ri}) = i\overline{d^I_{Ri}}(\partial^\mu - \frac{i}{3}g'B^\mu)\gamma_\mu d^I_{Ri} \tag{1.22}$$

$$\mathcal{L}_{\text{Kinetic,Weak}}(l^I_{Ri}) = i\overline{l^I_{Ri}}(\partial^\mu - ig'B^\mu)\gamma_\mu l^I_{Ri}\ , \tag{1.23}$$

where the right-handed components of the fermion fields, being singlets of $SU(2)_L$, do not couple to the weak interaction bosons W^μ_b, but can couple to the hypercharge boson B^μ. The interaction gauge bosons W^μ and B^μ are not however the physical massive charged $W^\pm$ and massive neutral Z^0 bosons. To identify the physical bosons of the weak interaction, the product $W^\mu_b\sigma_b$ is expanded as,

$$W^\mu_b\sigma_b = W^\mu_1\begin{pmatrix}0 & 1\\ 1 & 0\end{pmatrix} + W^\mu_2\begin{pmatrix}0 & -i\\ i & 0\end{pmatrix} + W^\mu_3\begin{pmatrix}1 & 0\\ 0 & -1\end{pmatrix} \tag{1.24}$$

$$W^\mu_b\sigma_b = \begin{pmatrix}W^\mu_3 & W^\mu_1 - iW^\mu_2\\ W^\mu_1 + iW^\mu_2 & -W^\mu_3\end{pmatrix}\ , \tag{1.25}$$

where the physical charged weak bosons are identified as off-diagonal elements ($W^\pm = W^\mu_1 \pm iW^\mu_2$). This will become apparent as physical bosons as they will acquire mass once the Higgs field acquires a nonzero vacuum expectation value, which is discussed in Section 1.4. The diagonal element W^μ_3, however, is not the physical Z^0 boson since W^μ_3 acts only on the left-handed components. The physical neutral boson Z^0 (Z^μ) and the photon (A^μ) are identified from the mixing of the two neutral interaction bosons W^μ_3 and B^μ, particularly,

$$Z^\mu = \cos\theta_w W^\mu_3 - \sin\theta_w B^\mu \tag{1.26}$$

$$A^\mu = \sin\theta_w W^\mu_3 + \cos\theta_w B^\mu\ , \tag{1.27}$$

where θ_w is the electroweak mixing angle known as the Weinberg angle. The Z^μ boson will acquire mass once the symmetry is spontaneously broken, while the A^μ remains massless. Expressing the bosons W^μ_3 and B^μ in terms of Z^μ and A^μ and identifying the factors in front of A^μ as electromagnetic coupling constant α_{em}, the three coupling constants g, g' and α_{em} can be linked as follows,

$$g\sin\theta_w = g'\cos\theta_w = \alpha_{em}, \tag{1.28}$$

thus determining just two parameters will fix the three couplings.

1.4 Spontaneous symmetry breaking

In the SM Lagrangian, explicitly adding a mass term breaks the local gauge invariance. As soon as mass terms for the gauge bosons are explicitly added, *e.g.* $-\frac{1}{2}M^2_W W_\mu W^\mu$, the local $SU(2)_L \otimes U(1)_Y$ gauge invariance is violated, which is,

$$-\frac{1}{2}M^2_W W_\mu W^\mu \mapsto -\frac{1}{2}M^2_W(W_\mu - \frac{1}{g}\partial_\mu\alpha - \alpha W_\mu)\ (W^\mu - \frac{1}{g}\partial^\mu\alpha - \alpha W^\mu) \neq -\frac{1}{2}M^2_W W_\mu W^\mu$$

where $\alpha = \alpha(x^\mu)$ are the transformation parameters. The same can be said for the explicit addition of a mass term for a fermion, *i.e.* $-m\overline{\psi}\psi = -m(\overline{\psi}_L + \overline{\psi}_R)(\psi_L + \psi_R) = -m(\overline{\psi}_L\psi_R + \overline{\psi}_R\psi_L)$.

Since weak isospin symmetry transformation acts differently for left-handed and right-handed components, the mass term will break the gauge invariance of the theory. Clearly, in order to keep the local gauge invariance, the gauge bosons and the fermions have to remain massless. However, it is known experimentally that the weak gauge bosons and most if not all fermions are massive. There is a need for a mechanism that allows the generation of masses without breaking the local gauge invariance of $SU(2)_L \otimes U(1)_Y$. This is realized via the *spontaneous symmetry breaking* mechanism, a.k.a. BEH mechanism in particle physics.

The BEH mechanism keeps the Lagrangian invariant under symmetry transformations, but not the expectation value of the vacuum. Needing to generate three masses of the weak gauge bosons, while keeping the photon massless, the Higgs field is constructed as a complex $SU(2)$ doublet with four degrees of freedom,

$$\phi = \begin{pmatrix} \phi^+ \\ \phi^0 \end{pmatrix} = \begin{pmatrix} \phi_1 + i\phi_2 \\ \phi_3 + i\phi_4 \end{pmatrix} \tag{1.29}$$

where ϕ_i are 4 real scalar fields. The Higgs potential described in Equation 1.10 has degenerate minima at $-\mu^2/2\lambda$ when $\mu^2 < 0$ (and $\lambda > 0$ to bound the potential from below). The symmetry is spontaneously broken once one of the degenerate minima is chosen. Since the electric charge has to be conserved, *i.e.* preserve $U(1)_{\text{em}}$ symmetry, the nonzero expectation value has to be in the neutral direction, hence the convenient choice of setting $\phi_1 = \phi_2 = \phi_4 = 0$. With this choice, the neutral component ϕ_3 develops a nonzero vacuum expectation value given by,

$$\langle 0|\phi|0\rangle = \frac{1}{\sqrt{2}}\begin{pmatrix} 0 \\ v \end{pmatrix}, \quad \text{with} \quad v = \left(-\frac{\mu^2}{\lambda}\right)^{1/2} . \tag{1.30}$$

A new scalar field $H(x)$, with $\langle 0|H(x)|0\rangle = 0$, is introduced in order to investigate the situation in the vicinity of the minimum of the potential. Expanding the kinetic term of the Higgs Lagrangian term in Equation 1.10,

$$(D^\mu\phi)^\dagger(D^\mu\phi) = \frac{g^2v^2}{8}(W^+)(W^-) + \frac{v^2}{8}(gW_3^\mu - g'B^\mu)^2 + \dots . \tag{1.31}$$

The first term is identified as the mass term of the charged weak bosons, and the second term is a mixture of the two neutral interaction bosons W_3^μ and B^μ. The truncated terms include couplings of the Higgs field to the weak interaction bosons. After moving to the physical boson eigenstates Z^μ and A^μ, one identifies the mass of the Z^0 boson from the term $\frac{1}{2}M_Z^2 Z_\mu Z^\mu$ and correctly found no mass term involving the photon (A^μ). Along with the other predictions of the BEH mechanism of breaking the symmetry, it predicts that the masses of the physical bosons $W^\pm$ and Z^0 are related via the electroweak mixing angle, as well as the $SU(2)_L$ and $U(1)_Y$ gauge couplings, given by,

$$M_W = \frac{gv}{2} \qquad \text{and} \qquad M_Z = \frac{1}{2}v\sqrt{g^2 + g'^2} \tag{1.32}$$

$$\sin\theta_w = \frac{g'}{\sqrt{g^2 + g'^2}} \qquad \text{and} \qquad \cos\theta_w = \frac{g}{\sqrt{g^2 + g'^2}} \tag{1.33}$$

hence,

$$M_Z = \frac{M_W}{\cos\theta_w} . \tag{1.34}$$

1.5 The CKM matrix

Although the couplings of the gauge fields to the Higgs field and the mass generation of the physical weak bosons follow from the covariant derivative in the kinetic term of the Higgs Lagrangian, the interaction of the Higgs field and the fermions and eventually fermion mass generation has to be added by hand. The arrangement of the complex scalar Higgs field in Equation 1.29 as an $SU(2)$ doublet allows the construction of an $SU(2)_L \otimes U(1)_Y$ invariant interaction of the Higgs field with the fermions via the so-called Yukawa couplings. The mathematical formulation of the said coupling was written in Equation 1.13 of Section 1.2.

Since this thesis is closely connected to the *CP* violation involving the mixing of quarks, the Yukawa couplings of the quark fields with the Higgs are explicitly spelled out for clarity purposes as,

$$Y^d_{ij}\overline{Q^I_{Li}}\phi d^I_{Rj} = Y^d_{ij}\overline{(u\ d)^I_{Li}}\begin{pmatrix}\phi^+\\ \phi^0\end{pmatrix} d^I_{Rj} \tag{1.35}$$

$$= \begin{pmatrix} Y_{11}\overline{(u\ d)^I_L}\begin{pmatrix}\phi^+\\ \phi^0\end{pmatrix} & Y_{12}\overline{(u\ d)^I_L}\begin{pmatrix}\phi^+\\ \phi^0\end{pmatrix} & Y_{13}\overline{(u\ d)^I_L}\begin{pmatrix}\phi^+\\ \phi^0\end{pmatrix} \\ Y_{21}\overline{(c\ s)^I_L}\begin{pmatrix}\phi^+\\ \phi^0\end{pmatrix} & Y_{22}\overline{(c\ s)^I_L}\begin{pmatrix}\phi^+\\ \phi^0\end{pmatrix} & Y_{23}\overline{(c\ s)^I_L}\begin{pmatrix}\phi^+\\ \phi^0\end{pmatrix} \\ Y_{31}\overline{(t\ b)^I_L}\begin{pmatrix}\phi^+\\ \phi^0\end{pmatrix} & Y_{32}\overline{(t\ b)^I_L}\begin{pmatrix}\phi^+\\ \phi^0\end{pmatrix} & Y_{33}\overline{(t\ b)^I_L}\begin{pmatrix}\phi^+\\ \phi^0\end{pmatrix} \end{pmatrix} \cdot \begin{pmatrix} d^I_R \\ s^I_R \\ b^I_R \end{pmatrix} . \tag{1.36}$$

Once the symmetry is spontaneously broken as described in Section 1.4, the quarks (fermions in general, except neutrinos in the "standard" SM) acquire a term that is identifiable as the mass term, *e.g.*,

$$-\mathcal{L}_{\text{Yukawa}}(\text{Quarks}) = Y^d_{ij}\overline{d^I_{Li}}\frac{v}{\sqrt{2}}d^I_{Rj} + Y^u_{ij}\overline{u^I_{Li}}\frac{v}{\sqrt{2}}u^I_{Rj} + (\text{h.c.}) + (\text{interaction terms}) \tag{1.37}$$

$$= M^d_{ij}\overline{d^I_{Li}}d^I_{Rj} + M^u_{ij}\overline{u^I_{Li}}u^I_{Rj} + (\text{h.c.}) + (\text{interaction terms})\ , \tag{1.38}$$

where the truncated interaction terms of the form $\sim q\bar{q}H(x)$ describe the interaction of the Higgs field with the fermion fields. In order to identify the physical particle content, which are the mass eigenstates, it is necessary to diagonalize the two matrices M^d_{ij} and M^u_{ij} by applying unitary transformations as

$$M^u_{ij,\text{diag.}} = V^u_L M^u_{ij} V^{u\dagger}_R = \begin{pmatrix} m_u & 0 & 0 \\ 0 & m_c & 0 \\ 0 & 0 & m_t \end{pmatrix} \tag{1.39}$$

$$M^d_{ij,\text{diag.}} = V^d_L M^d_{ij} V^{d\dagger}_R = \begin{pmatrix} m_d & 0 & 0 \\ 0 & m_s & 0 \\ 0 & 0 & m_b \end{pmatrix} . \tag{1.40}$$

Knowing that the matrices V are unitary, *e.g.* $V^{u\dagger}_L V^u_L = \mathbb{I}_{3\times3}$, the Yukawa Lagrangian in Equation 1.38 can be rewritten as follows,

$$-\mathcal{L}_{\text{Yukawa}}(\text{Quarks}) = \overline{d^I_{Li}}V^{d\dagger}_L V^d_L M^d_{ij} V^{d\dagger}_R V^d_R d^I_{Rj} + \overline{u^I_{Li}}V^{u\dagger}_L V^u_L M^u_{ij} V^{u\dagger}_R V^u_R u^I_{Rj} + (\text{h.c.}) + \dots$$

$$= \overline{d_{Li}}M^d_{ij,\text{diag.}}d_{Rj} + \overline{u_{Li}}M^u_{ij,\text{diag.}}u^I_{Rj} + (\text{h.c.}) + \dots \tag{1.41}$$

where the quark mass eigenstates u and d are linear combinations of the weak eigenstates u^I and d^I given by,

$$u_{Li} = (V_L^u)_{ij} u_{Lj}^I \quad \text{and} \quad u_{Ri} = (V_R^u)_{ij} u_{Rj}^I \tag{1.42}$$
$$d_{Li} = (V_L^d)_{ij} d_{Lj}^I \quad \text{and} \quad d_{Ri} = (V_R^d)_{ij} d_{Rj}^I \ . \tag{1.43}$$

The second term in the kinetic Lagrangian of the weak interaction of left-handed quarks in Equation 1.19 and the expansion of the matrix product $W_b^\mu \sigma_b$ shown in Equation 1.25, expressed now in terms of the mass eigenstates become,

$$\begin{aligned} \mathcal{L}_{\text{Kinetic,Weak,CC}}(Q_{Li}^I) &= \frac{ig}{\sqrt{2}} \overline{u_{Li}^I} \gamma_\mu W^{-\mu} d_{Li}^I + \frac{ig}{\sqrt{2}} \overline{d_{Li}^I} \gamma_\mu W^{+\mu} u_{Li}^I + \dots \\ &= \frac{ig}{\sqrt{2}} \overline{u_{Li}} \left(V_L^u V_L^{d\dagger} \right)_{ij} \gamma_\mu W^{-\mu} d_{Li} + \frac{ig}{\sqrt{2}} \overline{d_{Li}} \left(V_L^d V_L^{u\dagger} \right)_{ij} \gamma_\mu W^{+\mu} u_{Li} + \dots \end{aligned} \tag{1.44}$$

where it appears that in the charged current interaction there is a mixing of quarks between generations. The quark mixing matrix given in Equation 1.45 is known as the Cabbibo-Kobayashi-Maskawa (CKM) matrix [10, 33],

$$V_{\text{CKM}} = (V_L^u V_L^{d\dagger})_{ij} = \begin{pmatrix} V_{ud} & V_{us} & V_{ub} \\ V_{cd} & V_{cs} & V_{cb} \\ V_{td} & V_{ts} & V_{tb} \end{pmatrix} , \tag{1.45}$$

where it is conventionally-adopted that the weak and interaction quark eigenstates are chosen to be the same for up-type quarks, while the down-type quarks are rotated from interaction basis to mass basis as,

$$Q_{Li}^I = \begin{pmatrix} u^I \\ d^I \end{pmatrix}_{Li} = V_L^{u\dagger} \begin{pmatrix} u \\ \left(V_L^u V_L^{d\dagger} \right) d \end{pmatrix}_{Li} . \tag{1.46}$$

1.6 *CP* symmetry violation in the SM

After the experiment by C.S. Wu and colleagues in 1956 [34] and the subsequent experiment by L.M. Lederman and colleagues [35], it became an experimental fact that charge conjugation C and parity operation (space inversion) P are maximally-violated in decays involving weak interaction. The results of the experiments can be explained if neutrinos has only one chirality (or at least only one chirality participates in the weak interaction), *i.e.* there are only left-handed neutrinos and only right-handed antineutrinos. Thereafter, experimental observations made clear that only left-handed fermions (or right-handed antifermions) chiralities participate in the weak interaction and that the interaction strength appears to be universal.

Few years after the observation of the individually violated C and P symmetries, J.W. Cronin, V.L. Fitch and colleagues observed that the combined CP is as well violated, but only slightly, in the weak decay of neutral kaons [1]. This result triggered theoretical works out of which a remarkable achievement is the Kobayashi-Maskawa paradigm. Few explanations and descriptions of the phenomenology of the matrix will be given in the following as well as a state of the art on the subject. We will conclude this section by specifying the three phenomenological types of CP violation, putting emphasis on the one type searched for in this thesis.

1.6.1 Parameterisations of the CKM matrix

As a product of unitary matrices, the CKM matrix described in the Section 1.5 is itself unitary. Being dimensioned to the number of quark generations n, it comprises n^2 complex elements, and hence can be described with $2n^2$ real parameters. The unitarity of the matrix provides $n^2 - n(n-1)/2$ independent unitarity relations, n of them being real (involving the line or column unitarity). Thus, n^2 parameters can be determined from the unitarity properties of the matrix. On top of that, there are $2n$ arbitrary phases related to each quark field. They can be redefined up to a single global phase, hence $(2n-1)$ phases are fixed.

The number of independent parameters of the CKM matrix describing n generations of quarks amounts to $n(n-2)+1$ parameters, out of which $(n(n-3)+2)/2$ are phases, changing sign under the *CP* transformation. Henceforth, the KM paradigm for 3 generations of quarks brings three real independent parameters and one *CP*-violating phase. We take note that two generations would not bring any, while four generations are bringing 3 *CP*-violating phases.

Among the possible parameterisations of $V_{\rm CKM}$, we focus here on the two most frequent in the literature. The standard parameterisation adopted by the Particle Data Group [17] uses three rotation angles θ_{12}, θ_{23} and θ_{13} and one phase denoted δ. It reads:

$$V_{\rm CKM} = \mathcal{R}_{23}(\theta_{23}, 0) \otimes \mathcal{R}_{13}(\theta_{13}, \delta_{13}) \otimes \mathcal{R}_{12}(\theta_{12}, 0) \ , \tag{1.47}$$

and can be expanded as:

$$V_{\rm CKM} = \begin{pmatrix} c_{12}c_{13} & s_{12}c_{13} & s_{13}e^{-i\delta_{13}} \\ -s_{12}c_{23} - c_{12}s_{23}s_{13}e^{i\delta_{13}} & c_{12}c_{23} - s_{12}s_{13}s_{23}e^{i\delta_{13}} & s_{23}c_{13} \\ s_{12}s_{23} - c_{12}c_{23}s_{13}e^{i\delta_{13}} & -c_{12}s_{23} - s_{12}c_{23}s_{13}e^{i\delta_{13}} & c_{23}c_{13} \end{pmatrix} \tag{1.48}$$

where $c_{ij} = \cos\theta_{\rm ij}$, $s_{ij} = \sin\theta_{\rm ij}$ with $i, j = 1, 2, 3$.

An alternative parameterisation, named after Altomari-Wolfenstein [36], uses the observed experimental hierarchy between the mixing angles. The four independent parameters are denoted λ, A, ρ and η, where the parameter λ controls the hierarchy of the transition probability in between generations quarks. It reads:

$$s_{12} = \lambda \ , \tag{1.49}$$

$$s_{23} = A\lambda^2 \ , \tag{1.50}$$

$$s_{13}e^{-i\delta} = A\lambda^3(\rho - i\eta) \ . \tag{1.51}$$

This definition [37] ensures unitarity of the matrix at any order in λ expansion. For illustration, the development at order $\mathcal{O}(\lambda^4)$ is:

$$V_{\rm CKM} = \begin{pmatrix} 1 - \lambda^2/2 - 1/8\lambda^4 & \lambda & A\lambda^3(\rho - i\eta) \\ -\lambda & 1 - \lambda^2/2 - 1/8\lambda^4(1 + 4A^2) & A\lambda^2 \\ A\lambda^3(1 - \rho - i\eta) & -A\lambda^2 + A\lambda^4(1 - 2(\rho + i\eta))/2 & 1 - A^2\lambda^4/2 \end{pmatrix} + \mathcal{O}(\lambda^5) \ . \tag{1.52}$$

1.6.2 Jarlskog invariant

The relevant physics quantities to describe the matrix must be independent of the phase choice conventions. The quadrilinear products are one such examples of them. The Jarlskog invariant [38] for instance can be defined as:

$$J \sum_{\sigma\gamma=1}^{3} \epsilon_{\mu\nu\sigma}\epsilon_{\alpha\beta\gamma} = {\rm Im}(V_{\mu\alpha}V_{\nu\beta}V^*_{\mu\beta}V^*_{\nu\alpha}) \ , \tag{1.53}$$

where the ϵ's are the anti-symmetric Levi-Civita tensors. There is *CP* violation if $J \neq 0$. Following Wolfenstein parameterisation and anticipating the next section, $J = A^2\lambda^6\eta(1 - \lambda^2/2) \simeq 10^{-5}$. This small magnitude is a consequence of the strong hierarchy between the matrix elements and tells how elusive *CP* violation phenomena can be. One should not wrongly conclude that all *CP* asymmetries are small.

1.6.3 Unitarity triangles

Off-diagonal unitarity equations V_{CKM} ($\sum_i V_{ij}V_{ik}^* = \delta_{jk}$) with $j \neq k$ are triangles in the complex plane. The area $\mathcal{A}$ of any triangle one can form is proportional to the Jarlskog invariant[a] $\mathcal{A} = \frac{1}{2}|J|$. Let us focus on the two following unitarity relations involving the b quark:

$$\frac{V_{ud}V_{ub}^*}{V_{cd}V_{cb}^*} + \frac{V_{cd}V_{cb}^*}{V_{cd}V_{cb}^*} + \frac{V_{td}V_{tb}^*}{V_{cd}V_{cb}^*} = 0 \ , \tag{1.54}$$

$$\frac{V_{td}V_{ud}^*}{V_{cd}V_{cb}^*} + \frac{V_{ts}V_{us}^*}{V_{cd}V_{cb}^*} + \frac{V_{tb}V_{ub}^*}{V_{cd}V_{cb}^*} = 0 \ . \tag{1.55}$$

Using the Wolfenstein parameterisation, we note that the sides of the triangles are of same length $\mathcal{O}(1)$. Large *CP*-violating asymmetries can hence be expected. In contrast, the triangles involving s or c quarks are squashed. This unique feature related to the b-quark makes the *CP*-violation studies in b-hadrons decays or mixing attractive.

Figure 1.1 displays the unitarity triangle defined in Equation 1.54, where both sides and angles are shown. Eventually, the apex of the triangle is defined, phase-convention independent, by its coordinates in the complex plane:

$$\bar{\rho} + i\bar{\eta} = -\left(\frac{V_{ud}V_{ub}^*}{V_{cd}V_{cb}^*}\right) . \tag{1.56}$$

where A, λ, $\bar{\rho}$ and $\bar{\eta}$ are the four free SM parameters, which can be constrained redundantly by flavour observables.

1.6.4 Phenomenology of *CP* violation asymmetries

There are so far three ways for *CP* symmetry violation to manifest in Nature, namely (1) direct *CP* violation; (2) *CP* violation in the mixing (referred to as indirect *CP* violation); and (3) *CP* violation in the decays with and without mixing. In order to understand the different manisfestations of *CP* violation, We start by defining the decay amplitude of a process as,

$$A_f = \langle f|\mathbf{H}|B\rangle, \qquad \overline{A}_f = \langle f|\mathbf{H}|\overline{B}\rangle, \tag{1.57}$$

$$A_{\overline{f}} = \langle \overline{f}|\mathbf{H}|B\rangle, \qquad \overline{A}_{\overline{f}} = \langle \overline{f}|\mathbf{H}|\overline{B}\rangle, \tag{1.58}$$

where $\mathbf{H}$ is the weak Hamiltonian, f is the final state, B is the initial meson state, and $\overline{B}$ and $\overline{f}$ are the *CP* conjugate states of B and f, respectively. Both B and $\overline{B}$ have definite flavour content. The *CP* operation transforms the states into their *CP* conjugates with an arbitrary and unphysical phase $\epsilon_{\{B,f\}}$, hence,

$$CP|B\rangle = e^{i\epsilon_B}|\overline{B}\rangle, \qquad CP|f\rangle = e^{i\epsilon_f}|\overline{f}\rangle, \tag{1.59}$$

$$CP|\overline{B}\rangle = e^{-i\epsilon_B}|B\rangle, \qquad CP|\overline{f}\rangle = e^{-i\epsilon_f}|f\rangle \ . \tag{1.60}$$

[a] A change of phase-convention results in a rotation of the triangle in the complex plane leaving the area invariant.

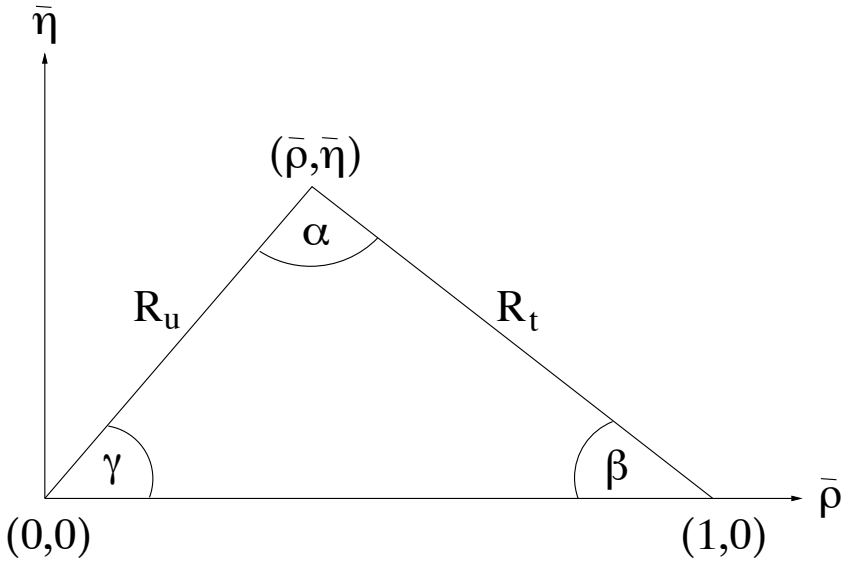

Figure 1.1: Unitarity triangle involving b quark transitions. The real axis is defined such that $\mathrm{Im}(V_{cd}V_{cb}^*) = 0$ and lengths are normalized to $|V_{cd}V_{cb}^*|$.

If B_q^0 and $\overline{B}_q^0$ are neutral meson states, they can mix via box diagrams. It evolves with time-dependent coefficients $a(t)$ and $b(t)$ governing the relative weights of the B_q^0 and $\overline{B}_q^0$ in the state. As such, at any time t, the B_q meson is a superposition of states given by,

$$|B_q(t)\rangle = a(t)|B_q^0\rangle + b(t)|\overline{B}_q^0\rangle + \Sigma_i c_i(t) f_i \ , \tag{1.61}$$

where $c_i(t)$ is time-dependent coefficient of the allowed final state f_i. If the time-range is much larger than the typical strong interaction scale, the Weisskopf-Wigner approximation simplifies the evolution of the mixing terms to,

$$|B_q(t)\rangle = a(t)|B_q^0\rangle + b(t)|\overline{B}_q^0\rangle \ , \tag{1.62}$$

with $|a(t)|^2 + |b(t)|^2 = 1$. The time-evolution of the mixing can be described by a 2×2 effective Hamiltonian matrix, where the diagonal terms represent flavour-conserving transitions and the off-diagonal terms represent flavour-changing currents (or the mixing term). This Hamiltonian matrix is not Hermitian, as otherwise it would not describe the oscillation and the B_q^0 would not decay, but can be written as a sum of two Hermitian matrices, given by,

$$\mathbf{H} = \mathbf{M} - \frac{i}{2}\mathbf{\Gamma}. \tag{1.63}$$

The mass matrix $\mathbf{M}$ represents the dispersive transitions ("off-shell" transitions), while the decay matrix $\mathbf{\Gamma}$ represents the absorptive parts ("on-shell" transitions). As a consequence of *CPT* invariance, which we assume to hold true here and throughout this thesis, $M_{11} = M_{22}$ and $\Gamma_{11} = \Gamma_{22}$. Since the matrices are Hermitian, then $M_{21} = M_{12}^*$ and $\Gamma_{21} = \Gamma_{12}^*$. The time evolution of the B_q meson mixing is described by the Schrödinger equation,

$$i\frac{d}{dt}\begin{pmatrix} a(t) \\ b(t) \end{pmatrix} = \mathbf{H}\begin{pmatrix} a(t) \\ b(t) \end{pmatrix} = \begin{pmatrix} M & M_{12} \\ M_{12}^* & M \end{pmatrix}\begin{pmatrix} a(t) \\ b(t) \end{pmatrix} - \frac{i}{2}\begin{pmatrix} \Gamma & \Gamma_{12} \\ \Gamma_{12}^* & \Gamma \end{pmatrix}\begin{pmatrix} a(t) \\ b(t) \end{pmatrix} \ . \tag{1.64}$$

There are two solutions for Equation 1.64, with eigenstates of definite masses $M_{H,L}$ and widths $\Gamma_{H,L}$. One mass eigenstate[b] is heavy and the other is light, hence the subscripts H

[b] In the case of neutral K meson, the eigenstates are more distinct in their lifetimes, than in their masses, hence named K_{S}^0 and K_{L}^0.

and L. These mass eigenstates $B_{H,L}$ and the eigenvalues $\lambda_{H,L}$ are,

$$|B_{H,L}\rangle = \frac{p|B_q^0\rangle \pm q|\overline{B}_q^0\rangle}{\sqrt{|p|^2+|q|^2}} \ , \tag{1.65}$$

$$\lambda_{H,L} = M + i\frac{\Gamma}{2} \pm \sqrt{(M_{12}^* + i\frac{\Gamma_{12}^*}{2})(M_{12} + i\frac{\Gamma_{12}}{2})} \ , \tag{1.66}$$

where,

$$\frac{q}{p} = \sqrt{\frac{M_{12}^* - (i/2)\Gamma_{12}^*}{M_{12} - (i/2)\Gamma_{12}}} \ . \tag{1.67}$$

Direct *CP* violation

The *CP* violation in the decay implies a difference between the partial width of two conjugate decays, namely $\Gamma(B \to f) \neq \Gamma(\overline{B} \to \overline{f})$. It is often referred to as direct *CP* violation in the literature as it originates directly at the amplitude level of the considered decay. Such an asymmetry requires at least two amplitudes with different weak phases to interfere. The first observation of *CP* violation in the decays of particles was brought in 2001 for kaon decays [39] and 2004 for B meson decays [4]. It is worth noticing that non-vanishing *CP* asymmetries have been measured for B^0, B^+ and B_s^0 mesons [9].

The direct *CP* asymmetry mathematically reads,

$$\mathcal{A}^{CP} = \frac{\Gamma(\overline{B}_q^0 \to \overline{f}) - \Gamma(B_q^0 \to f)}{\Gamma(\overline{B}_q^0 \to \overline{f}) + \Gamma(B_q^0 \to f)} = \frac{|\overline{A}(\overline{B}_q^0 \to \overline{f})|^2 - |A(B_q^0 \to f)|^2}{|\overline{A}(\overline{B}_q^0 \to \overline{f})|^2 + |A(B_q^0 \to f)|^2} \ . \tag{1.68}$$

Considering at least two contributing amplitudes to the decay, *e.g.* Tree and Penguin diagrams shown in Figure 1.3 of Section 1.7, then,

$$A = |A_1|e^{i\delta_1}e^{i\phi_1} + |A_2|e^{i\delta_2}e^{i\phi_2} \ , \tag{1.69}$$

$$\overline{A} = |A_1|e^{i\delta_1}e^{-i\phi_1} + |A_2|e^{i\delta_2}e^{-i\phi_2} \ , \tag{1.70}$$

where $|A_1|$ and $|A_2|$ are the magnitudes of the two contributing amplitudes, while δ's and ϕ's are its associated unphysical strong and weak phases, respectively. The physical measurable reaction rates are proportional to $|A|^2$, as such, the direct $\mathcal{A}^{CP}$ defined in Equation 1.68 reads,

$$\mathcal{A}^{CP} = \frac{2|A_1||A_2|\sin(\delta_1-\delta_2)\sin(\phi_1-\phi_2)}{|A_1|^2+|A_2|^2+2|A_1||A_2|\cos(\delta_1-\delta_2)\cos(\phi_1-\phi_2)} \ . \tag{1.71}$$

Henceforth, the nonvanishing direct *CP* asymmetry arises due to the interference between two weak amplitudes, that requires weak phase difference $\phi_1 - \phi_2$ and strong phase difference $\delta_1 - \delta_2$. The neutral baryons studied in this thesis, as quantum distinguishable states, can not mix. The only way to observe a *CP*-violating phenomenon left is through direct *CP* violation.

Indirect *CP* violation

The *CP* violation in the mixing (referred to as indirect *CP* violation) of neutral mesons was first observed in [1] as mentioned earlier. It means that the probability of the mixing $K^0\overline{K^0}$ is not equivalent to the conjugate $\overline{K^0}K^0$. The counterpart in the neutral beautiful mesons B^0 and B_s^0 has not yet been observed. This occurs when $|q/p| \neq 1$ (See Equation 1.67).

CP violation in the decays with and without mixing

A third class of *CP* violation phenomena comes from the interference between the mixing and the decay amplitudes, each bringing different weak phases. Choosing the B^0 meson for the sake of illustration, the mixing-induced *CP* asymmetry implies $\Gamma(B^0 \to f) \neq \Gamma(B^0 \to \overline{B}^0 \to f)$, where the final state f is a *CP* eigenstate. The first observation of a mixing-induced *CP* asymmetry was brought in 2001 [2, 5] through the time-dependent asymmetry of the decay mode $B^0 \to J/\psi K^0_S$. Many other final states measurements followed and are gathered here [40]. A first evidence for mixing-induced *CP* asymmetry in B^0_s decays was brought recently by the LHCb experiment [41].

We define a parameter λ_f, which is,

$$\lambda_f = \frac{q}{p}\frac{\overline{A}_f}{A_f} \,, \tag{1.72}$$

where q/p is defined in Equation 1.67, and A_f and $\overline{A}_f$ are the amplitudes of a B^0 and $\overline{B}^0$ decaying to the same final *CP* eigenstate f. Even in the case where direct and indirect *CP* violation are vanishing, an interference phase between the mixing and the decay can lead to $\mathcal{I}(\lambda_f) \neq 0$. This form of *CP* violation can be observed using the time-dependent *CP* asymmetry of neutral B^0 meson decays into a *CP* eigenstate f,

$$\mathcal{A}^{CP}(t) = \frac{\Gamma_{B^0\to f}(t) - \Gamma_{\overline{B}^0\to f}(t)}{\Gamma_{B^0\to f}(t) + \Gamma_{\overline{B}^0\to f}(t)} \tag{1.73}$$

$$= \frac{(|\lambda_f|^2 - 1)\cos(\Delta M t) + 2\mathcal{I}(\lambda_f)\sin(\Delta M t)}{(|\lambda_f|^2 + 1)\cosh(\frac{\Delta\Gamma}{2}t) - 2\mathcal{R}(\lambda_f)\sinh(\frac{\Delta\Gamma}{2}t)} \tag{1.74}$$

$$= \frac{\mathcal{A}^{\rm dir}\cos(\Delta M t) + \mathcal{A}^{\rm mix}\sin(\Delta M t)}{\cosh(\frac{\Delta\Gamma}{2}t) - \mathcal{A}^{\Delta\Gamma}\sinh(\frac{\Delta\Gamma}{2}t)} \,, \tag{1.75}$$

where,

$$\mathcal{A}^{\rm dir} = \frac{|\lambda_f|^2 - 1}{|\lambda_f|^2 + 1} \,, \qquad \mathcal{A}^{\rm mix} = \frac{2\mathcal{I}(\lambda_f)}{|\lambda_f|^2 + 1} \,, \qquad \mathcal{A}^{\Delta\Gamma} = -\frac{2\mathcal{R}(\lambda_f)}{|\lambda_f|^2 + 1} \,. \tag{1.76}$$

These three asymmetries satisfies the condition $|\mathcal{A}^{\rm dir}|^2 + |\mathcal{A}^{\rm mix}|^2 + |\mathcal{A}^{\Delta\Gamma}|^2 = 1$.

1.6.5 CKM matrix and New Physics: state of the art

Many observables can be used to (over-)constrain the unitarity triangle. The interested reader can go to the reference [42] to check for the detailed description of them. Let us just state here that only the observables for which a good control of the attached theoretical uncertainties is achieved are eventually considered. They mainly comprise the measurements of the sides of the triangle on one hand, *i.e.* the magnitudes of the matrix elements $|V_{ub}|$, $|V_{cb}|$ and $|V_{td}|$ achieved by measurements of the semileptonic branching fractions of b-baryons for the two former and the oscillation frequency of $B^0_s\overline{B}^0_s$ mixing for the latter and the angle measurements on the other hand through phase difference observables in b quark transitions, in mixing and/or decay.

Figure 1.2 displays a superimposition of the experimental constraints, provided with exclusion region at 95% C.L., under the SM hypothesis. A unique region in the complex plane is selected which means that this comprehensive set of data so far can be described with the KM paradigm of the SM.

The single *CP*-violation phase of the SM being enough to accommodate all the *CP*-violating observables (and consistently the *CP*-conserving observables) and it is likely that,

given the current precision, the KM phase is the dominant source of *CP* violation in beautiful and strange meson systems studied at both the *B*-factories and LHC experiments. Still, the precision achieved so far leaves room for sub-dominant *CP*-violating phases beyond the SM. In particular, *CP* violation has not been observed to date in baryon decays and this constitutes a new territory to be explored.

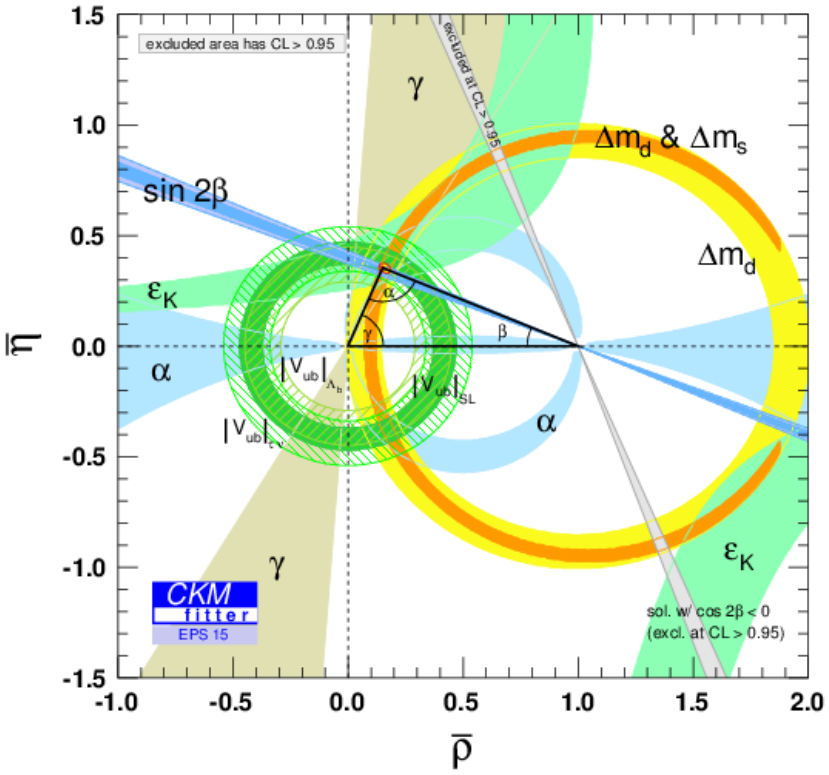

Figure 1.2: Individual constraints on the $(\bar{\rho};\bar{\eta})$ coordinates displayed with 95% C.L. exclusion. The region of the apex not excluded at 95 % C.L. by the global fit is shown as a yellow area.

1.7 Quick overview of Λ_b^0 and Ξ_b^0 charmless decays to four-body

Bottom baryons have received some attention starting on the first observation of the lowest-lying state Λ_b^0 by UA1 experiment in 1991 [43]. Several heavier ground states of *b*-baryons have been discovered since then, which includes Σ_b, Ξ_b^0, Ξ_b^- and Ω_b^-. Recently, LHCb has observed two more baryonic resonances Ξ_b' and Ξ_b^{*-} [44], having spin-parity configuration of $J^P = (1/2)^+$ and $J^P = (3/2)^+$, respectively.

Two weakly-decaying neutral *b*-baryons are the focus of the main analysis presented in this thesis, namely the lowest-lying ground states Λ_b^0 and Ξ_b^0. The Λ_b^0 is a resonance of the *udb* quarks, while the Ξ_b^0 (first observed by CDF [45]) can be described as an *usb* state in the quark model. Recent precise measurements on the mass and lifetime of Λ_b^0 were conducted by LHCb [46, 47], as well as on mass and lifetime of Ξ_b^0 [48]. In terms of *CP* violation measurements, only few attempts have been made so far. The CDF experiment has published recently their measurement on the direct $\mathcal{A}^{CP}$ of $\Lambda_b^0 \to p\pi^-$ and $\Lambda_b^0 \to pK^-$

and found these to be compatible with no asymmetry [13]. The LHCb collaboration as well has measured the direct $\mathcal{A}^{CP}$ of charmless[c] decay of Λ_b^0 into $pK_S^0\pi^-$ and found this as well to be consistent with zero [14]. Even more recently, LHCb found the $\Delta\mathcal{A}^{CP}$ of $\Lambda_b^0 \to J/\psi p\pi^-$ and $\Lambda_b^0 \to J/\psi pK^-$ to be compatible with CP symmetry at 2.2σ level [15]. Hence, CP violation has not yet been observed in the baryon decays.

The main analysis of this thesis focuses on the charmless four-body fully charged decays of Λ_b^0 and Ξ_b^0, where aside from non-resonant components the decays can proceed through baryonic resonances, *i.e.* Λ^{*0}, N^{*0} and Δ series. In addition, mesonic resonances can also occur (*i.e.* $\pi\pi$, $K\pi$ and $K\,K$). Consequently, the interference pattern is expected to be rich of resonance structures. Most of the four-body decays of Λ_b^0 and Ξ_b^0 proceed simultaneously through $b\to u$ transition or $b\to d$ and $b\to s$ FCNC, as shown in Figures 1.3 and 1.4.

The direct $\mathcal{A}^{CP}$ observable can be enhanced by the presence of significant phase differences from strong resonances of at least two competing amplitudes. The rich resonance structure in the low two-body invariant mass of these decays could provide these.

The ensemble of diagrams given in Figures 1.3 and 1.4 are some straightforward illustrations at the quark level of the possible anticipated richness of the interference patterns that can be reached in these modes.

[c] Charmless decays of b-hadrons refer to decays involving $b\to u$ tree transition or flavour-changing neutral current $b\to d$ or $b\to s$ penguin loop transitions.

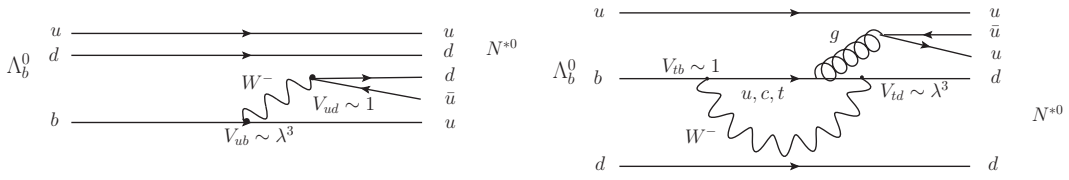

(a) Tree and penguin loop contributions of the $\Lambda_b^0 \to p\pi^-\pi^+\pi^-$ decays proceeding through an N^{*0} resonance.

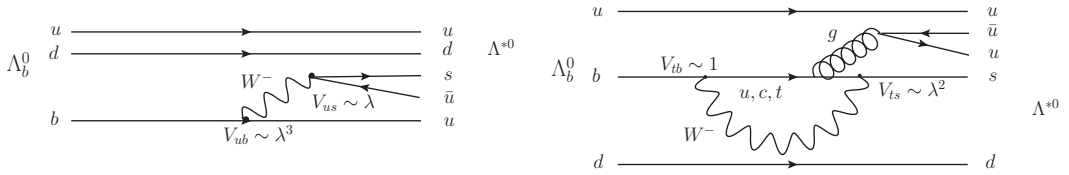

(b) Tree and penguin loop contributions of the $\Lambda_b^0 \to pK^-\pi^+\pi^-$ decays proceeding through a Λ^{*0} resonance.

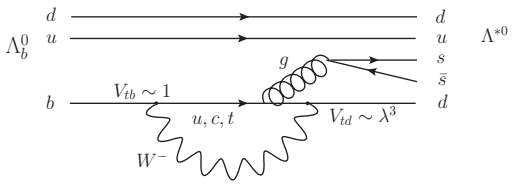

(c) Penguin loop contribution of the $\Lambda_b^0 \to pK^-K^+\pi^-$ decays proceeding through a Λ^{*0} resonance.

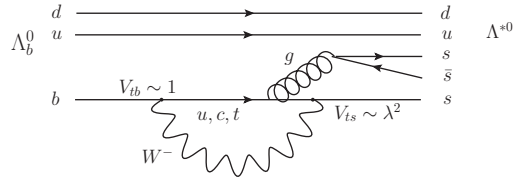

(d) Penguin loop contribution of the $\Lambda_b^0 \to pK^-K^+K^-$ decays proceeding through a Λ^{*0} resonance.

Figure 1.3: Feynman diagrams of the fully charged four-body decay modes of Λ_b^0 studied in this analysis proceeding through N^{*0} or Λ^{*0}. The N^{*0} resonance eventually decays to $p\pi$, while Λ^{*0} decays to pK. The $\Lambda_b^0 \to pK^-\pi^+\pi^-$ and $\Lambda_b^0 \to pK^-K^+\pi^-$ decays proceeding through N^{*0} resonance are not shown. Note that the $\Lambda_b^0 \to pK^-K^+\pi^-$ and $\Lambda_b^0 \to pK^-K^+K^-$ decays can also proceed through $b \to u$ tree transition but then require an $s\bar{s}$ pair to pop-in from the vacuum.

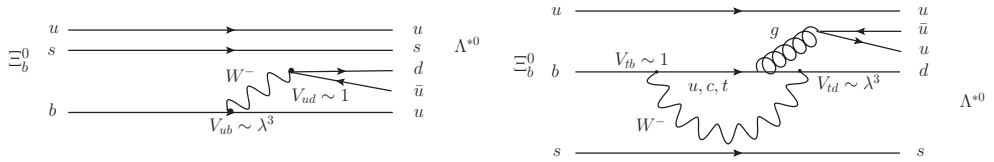

(a) Tree and penguin loop contributions of the $\Xi_b^0 \to pK^-\pi^+\pi^-$ decays proceeding through a Λ^{*0} resonance.

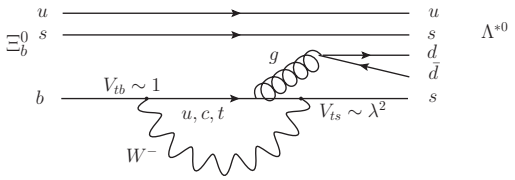

(b) Penguin loop contributions of the $\Xi_b^0 \to pK^-\pi^+K^-$ decays proceeding through a Λ^{*0} resonance.

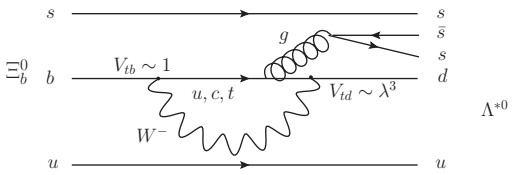

(c) Penguin loop contribution of the $\Xi_b^0 \to pK^-K^+K^-$ decays proceeding through a Λ^{*0} resonance.

Figure 1.4: Feynman diagrams of the fully-charged four-body decay modes of Ξ_b^0 studied in this analysis proceeding through N^{*0} or Λ^{*0}. The N^{*0} resonance eventually decays to $p\pi$, while Λ^{*0} decays to pK. The $\Xi_b^0 \to pK^-\pi^+\pi^-$ decay proceeding through N^{*0} resonance is not shown. Note that the $\Xi_b^0 \to pK^-\pi^+K^-$ and $\Xi_b^0 \to pK^-K^+K^-$ decays can also proceed through $b \to u$ tree transition but then require an $s\bar{s}$ pair to pop-in from the vacuum.

Chapter 2

The LHC and the LHCb experiment

Contents

2.1 Introduction

The analyses presented in this thesis used the data collected during the Run I data taking of the Large Hadron Collider *b*eauty (LHCb) experiment at the Large Hadron Collider (LHC) of CERN. As such, this Chapter presents the overview of the LHC machine and the LHCb detector.

2.2 The LHC machine

The Large Hadron Collider (LHC) machine, owned and managed by the European Organization for Nuclear Research (CERN), is an underground two-ring superconducting hadron accelerator and collider [49, 50]. It is located under the French-Swiss border, just outside Geneva. Using the same 26.7 km long underground tunnel previously housing the Large Electron Positron (LEP) collider, the LHC accelerates and then smashes two proton beams circulating in opposite directions. Up to date, the LHC machine is the highest energy accelerator ever built.

The first beam circulation took place on the 10th of September 2008, but an unfortunate technical accident occured in one of the superconducting magnetic poles resulting to damages in the infrastructure. Stable beams were back in the LHC on the 20th of November 2009, and thus the new era of high energy physics collider researches and measurements commenced. The LHC delivered stable proton beams, which are intended for physics measurements, on years 2011 and 2012 with a short scheduled technical stop at the end of 2011 up to the first quarter of 2012. The center-of-mass energy during the 2011 data taking campaign was 7 TeV, while it was 8 TeV for the 2012 campagn. The LHC is also capable of accelerating and colliding lead ions (Pb). In early 2013, the LHC delivered proton-Pb and Pb-Pb collisions. After a two-year scheduled long shutdown, the LHC again delivered stable proton beams starting on the 3rd of June 2015, at a center-of-mass energy of 13 TeV.

2.2.1 Accelerator overview

The LHC is a cold machine circulating proton beams in opposite directions up to high energies before colliding them in four different interaction points. Shown in Figure 2.1 is a schematic diagram of the accelerator chain. The protons are first accelerated in the linear accelerator (LINAC 2) system to an energy of 50 MeV. The proton beams are then circulated in the Proton Synchroton (PS), accelerated to 26 GeV and transferred to the Super Proton Synchrotron (SPS). The SPS further accelerates the beams up to 450 GeV before they are injected into the main ring. The 26.7 km main ring will then accelerate the beams up to the planned nominal energy. Finally, the beams are collided in four different interaction points where different particle detectors are present. A more detailed presentation of the beam delivery scheme can be found in Refs. [49–51].

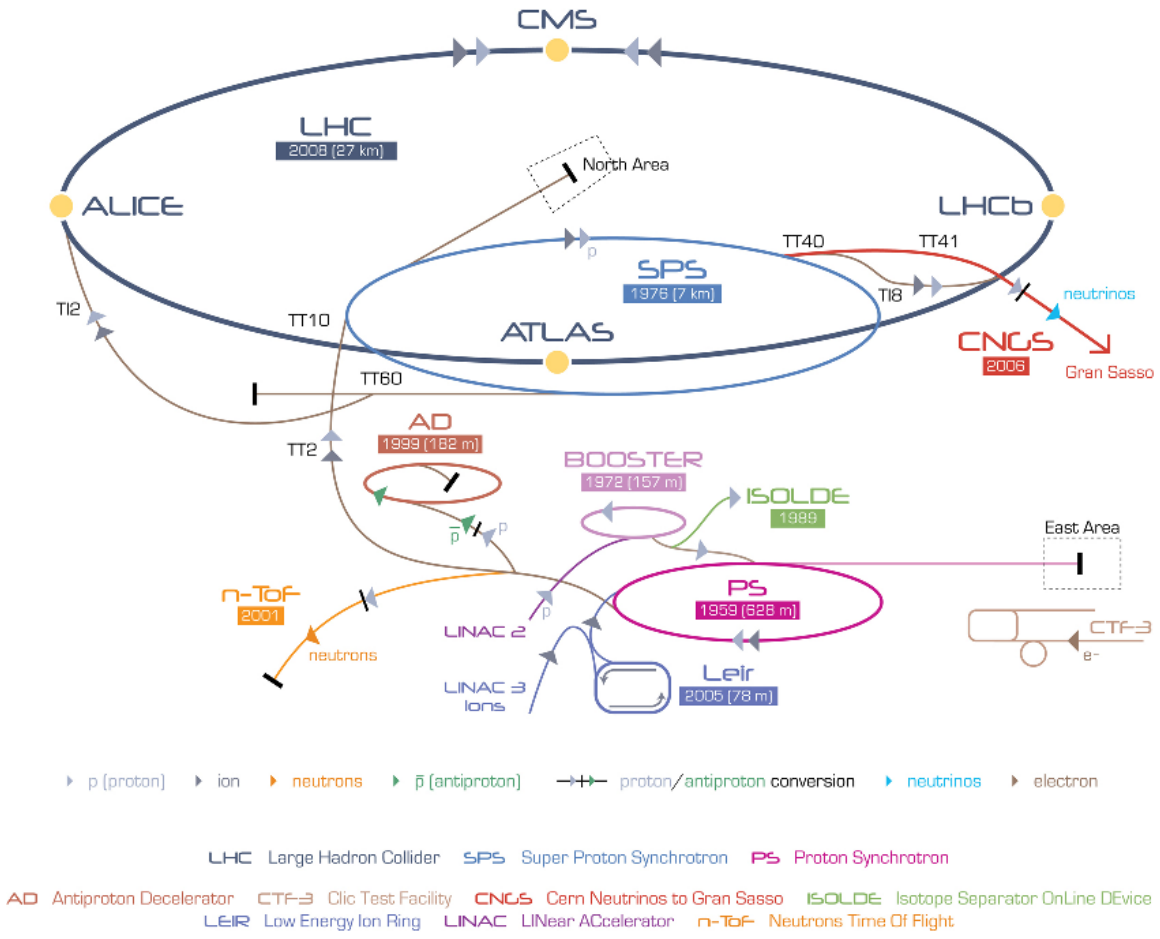

Figure 2.1: Schematic representation of the accelerator systems at CERN [52]. Shown also are the four main experiments at LHC.

The LHC is designed to operate at 14 TeV center-of-mass energy, but due to the technical accident in 2008, the decision to operate at center-of-mass energies at around half of its original design was opted for the Run I data taking. The beams in the LHC main ring are deflected using superconducting magnets in cryostats cooled with superfluid helium in order to keep the magnets below 2 K. A total of 1232 dipole magnets maintain the beams in the accelerator pipe, together with 392 quadrupole magnets to focus the beams. The acceleration is provided by 16 radiofrequency cavities.

2.2.2 LHC experiments

There are several experiments placed at different points of the LHC. The four main experiments are A ToroidaL LHC Apparatus (ATLAS), Compact Muon Solenoid (CMS), Large Hadron Collider *b*eauty (LHCb) and A Large Ion Collider Experiment (ALICE). The ATLAS [53–55], CMS [56, 57] and ALICE [58–60] experiments use 4π detectors, while LHCb [61, 62] uses a forward spectrometer, with a coverage of 2 to 5 in pseudorapidity angle. Further details of the LHCb detector will be discussed in Section 2.3. These four main detectors are placed at different collision points of the LHC as shown in Figure 2.1.

The ATLAS and CMS collaborations both observed the long-sought Higgs boson in 2012 [27, 28]. Moreover, their objective is to search for new physics by directly observing new particles predicted by theories extending the SM, including supersymmetric particles. The ALICE experiment seeks to explore and understand the quark-gluon plasma. The LHCb experiment specializes in investigating the slight differences between matter and anti-matter by studying b-flavoured hadrons and charmed hadrons, and indirect searches for new physics through measurements on rare decays.

Finally, there are also smaller experiments conducted at the LHC. These are the TOTal Elastic and diffractive cross-section Measurement (TOTEM), the Large Hadron Collider forward (LHCf) and the Monopole & Exotic Detector At the LHC (MoEDAL) experiments. The TOTEM experiment [63–65], which measures precisely the total cross-section of proton-proton collisions at the LHC, has spread several detectors across almost half a kilometer around the CMS interaction point. It is designed to measure the protons as they emerge from collisions at small angles, in a region not accessible by other experiments. Two detectors, which sits along the LHC beam and placed 140 m from either side of the ATLAS collision point, compose the LHCf experiment [66–68]. The LHCf is intended to study the neutral-particle production cross-sections in the very forward region, with the objective of understanding the development of cosmic rays. Lastly, the MoEDAL experiment [69–71], in complementary with the main LHC detectors, aims to search for exotic particles, particularly magnetic monopoles (or dyons) and other highly ionizing stable massive particles.

2.2.3 Luminosity

In HEP experiments, aside from the requirement of having a high energy collision, there is also a need to produce large enough samples of different decays for analysis, which can be achieved by increasing the luminosity of the collider machine. The luminosity of a collider machine defines the number of interactions in a certain time over the interaction cross section. In the LHC, this is given by [49],

$$\mathcal{L} = \frac{N_1 N_2 k_b f \gamma F}{4\pi\beta^* \epsilon} \ , \tag{2.1}$$

where N_i is the number of protons in each proton bunch, k_b is the number of colliding bunches, f is the revolution frequency, γ is the relativistic factor, β^* is the value of the betatron function at the interaction point, ϵ is the emittance and F accounts for the reduction due to the crossing angle of the beams.

Each experiment has its own luminosity requirement in accordance to their physics interest. The ATLAS and CMS collaborations opted for higher luminosities in order to search for heavy particles with expectedly low cross-section production. In contrast, the LHCb experiment chose a lower luminosity in order to limit the number of proton-proton vertices as a requirement for precise measurements. Shown in Figure 2.2 is how the probability of the number of interactions scale with luminosity. Practically, the lower luminosity at

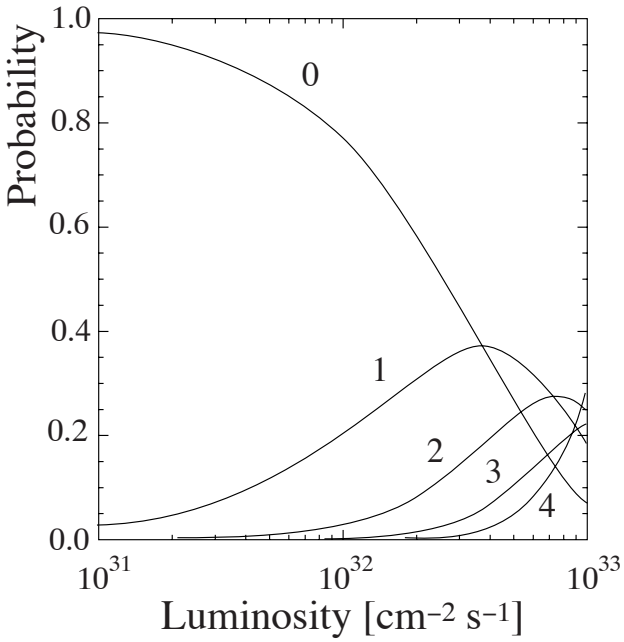

Figure 2.2: Probability of number of interaction per bunch crossing as a function of the luminosity.

the LHCb collision point was achieved by refocusing the proton beams and hence changing how the beams overlap at the interaction point – a technique called *beam levelling*. In this way, ATLAS and CMS kept the high luminosity configuration, while LHCb decided to have a lower luminosity of $2\times10^{32}\,\mathrm{cm}^{-2}\mathrm{s}^{-1}$. For the design luminosity of the experiment, the expected number of proton-proton interaction per bunch would have been a typical 0.5. However, as can be seen in Figure 2.3, LHCb received an average luminosity above the design specification reaching up to an average visible interaction per bunch (μ_{vis}) of ∼2.5 [72].

2.2.4 $b\bar{b}$ pair production

The dominant mechanism of $b\bar{b}$ pair production in the LHC proton-proton collisions is gluon-gluon fusion. Shown in Figure 2.4 are typical gluon-gluon interactions producing $b\bar{b}$ pair. The $b\bar{b}$ pairs are mostly going either in the forward or backward directions. Figure 2.5 shows the polar angle distribution of the $b\bar{b}$ pairs as simulated using PYTHIA for $p-p$ collisions at a center-of-mass energy of 8 TeV. It also shows the angular distribution in terms of pseudorapidities. This angular distribution leads to the design of the LHCb spectrometer to be a single-arm forward spectrometer[a].

The direct production of $b\bar{b}$ pairs at the LHC occurs mostly entirely via QCD processes that do not discriminate between b and $\bar{b}$ quarks. However, some weak interaction processes are also present which are not flavour-conserving and distinct for b and $\bar{b}$ quarks [73, 74], resulting to an asymmetry referred to in the following as production asymmetry.

2.3 The LHCb experiment and LHCb detector

One of the four main experiments at the LHC is the LHCb experiment. This experiment specializes in studying the differences of matter and anti-matter by looking mainly at the decay processes of b-flavoured hadrons or charmed hadrons. In addition, it also measures

[a]Definition of forward and backward direction is a matter of adopted convention.

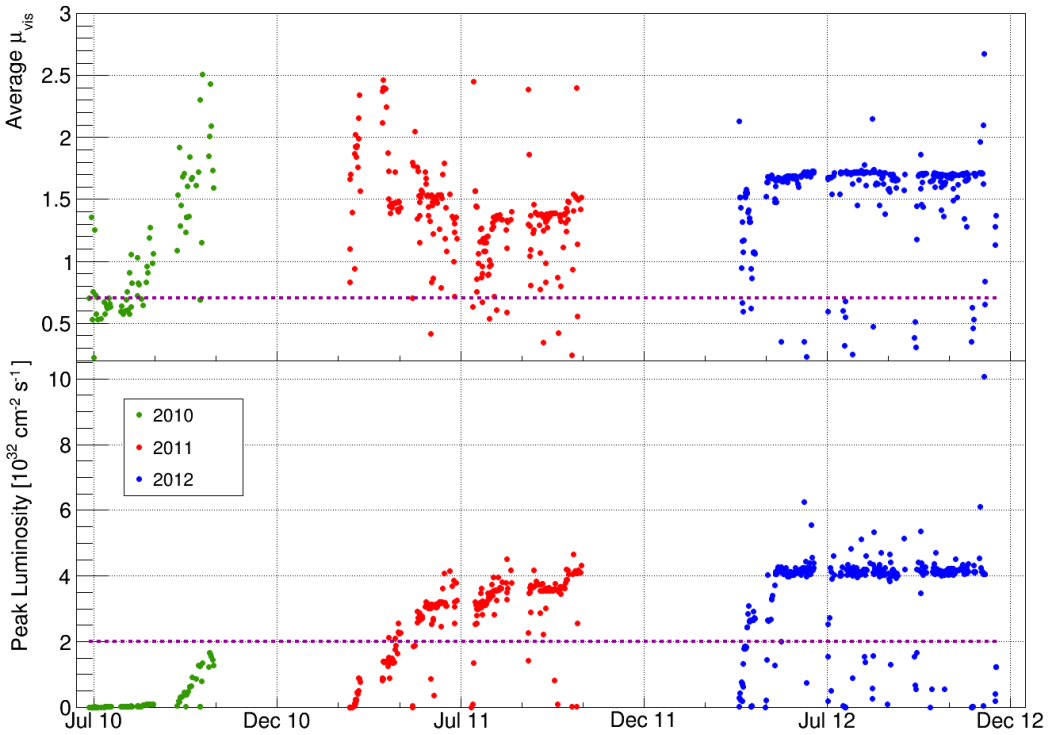

Figure 2.3: (Top) Average number of visible interactions per bunch crossing and (bottom) instantaneous luminosity at the LHCb interaction point during the 2010-2012 running period. The dotted lines show the design values.

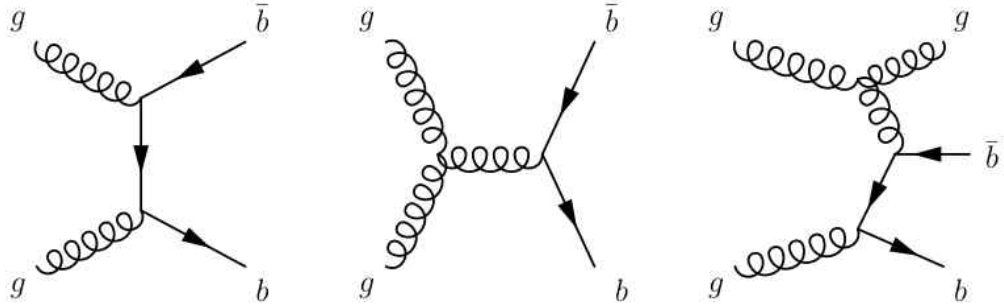

Figure 2.4: Examples of Feynman diagrams of typical gluon-gluon interactions that produces $b\bar{b}$ pair at the LHC.

observables of rare decays, which are indirect probes for new physics, *e.g.* the recent analysis of $B^0 \to \mu^+\mu^-$ and $B_s^0 \to \mu^+\mu^-$ decays [75] (combined with the data collected by CMS).

The data used in the analyses presented in this thesis are gathered using the LHCb detector. Hence, I discuss in this Section the LHCb detector and its sub-components. I will first briefly present the different subdetectors in Section 2.3.1 in a sequence naturally traversed by a particle produced at the interaction point.

2.3.1 Overview

Eventually, the main goal of LHCb is to search indirectly for a new physics evidence by looking for effects of new particles in processes that are precisely predicted in the SM. The CKM matrix, which contains one *CP*-violating phase, describes the mixing of the quarks in

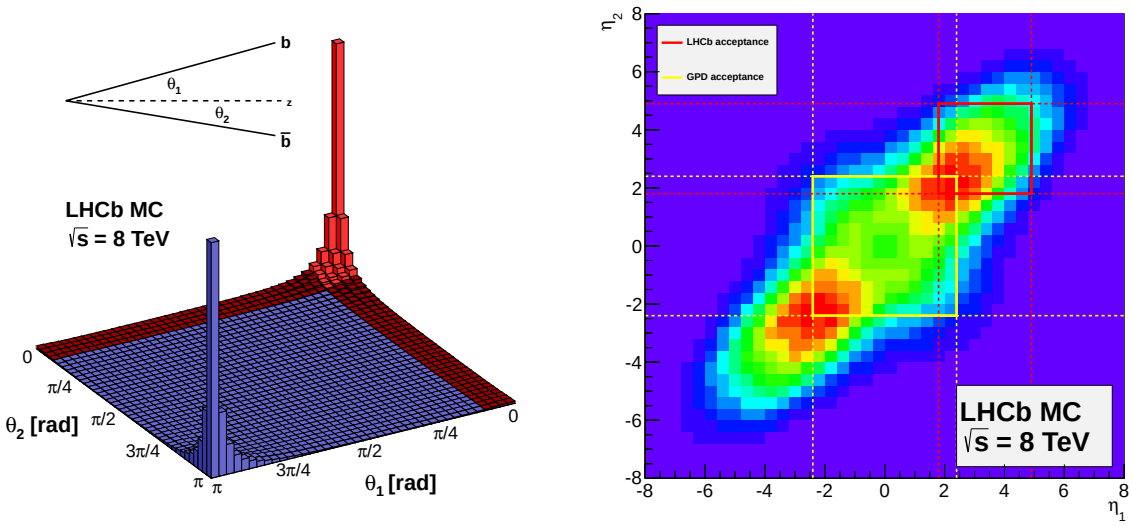

Figure 2.5: (Left) Polar angle distribution of the $b\bar{b}$ pairs produced at the LHC collisions as simulated using PYTHIA for $p-p$ collisions at 8 TeV center-of-mass energy. (Right) The same MC-simulated $b\bar{b}$ production fractions expressed in terms pseudorapidities. The LHCb acceptance is bounded by the red lines, while the typical General Purpose Detector (GPD) acceptance is bounded by the yellow lines.

the SM. New sources of *CP* violation beyond the SM are needed since the *CP* violation in the weak interactions of the SM, although closely linked to the matter-antimatter asymmetry of the universe [76], can not fully account the asymmetry by several orders of magnitude. Several models extending the SM predict contributions that can change the expectation values of the *CP*-violating phases or on the branching fractions of rare decays. Henceforth, large data sample is needed in order to conduct precise measurements of many different decay modes and thus examine the deviations, if there are any. A large statistics of $b\bar{b}$ pairs are produced at the LHC during collisions. As such, the LHCb collaboration exploited these events in order to study precisely the physics observables involving b-flavoured hadrons or charmed hadrons.

The LHCb detector is a single-arm forward spectrometer covering the angular range of 10 mrad to 300 mrad in the bending plane[b] and 10 mrad to 250 mrad vertically. In terms of pseudorapidity η, the coverage along the vertical direction is from 2 to 5. With this angular coverage, it is expected that about 27% of b or $\bar{b}$ quarks are produced inside the LHCb acceptance. A schematic diagram of the LHCb detector is shown in Figure 2.6. The detector is divided into two identical halves: left and right sides, but more commonly called C side (the cryogenics side) and A side (the cavern access side). The two sides can be moved horizontally, which allows access for maintenance. The LHCb detector is located at the Interaction Point number 8 of the LHC, which was previously occupied by the DELPHI detector during the LEP times.

Following the natural flow of a physics event, I will briefly discuss the subcomponents of the LHCb detector. The LHC proton beams come from two opposite sides and then made to collide at the interaction (or collision) point, which is located inside the Vertex Locator (VELO). Production of $b\bar{b}$ pairs occurs at the interaction point, where they create production vertex (or vertices) when they hadronize to long-lived mesons or baryons before flying along the positive z-axis direction. Typically, the b-flavoured hadron decays inside

[b] The bending plane refers to the horizontal plane, which is perpendicular to the magnetic field.

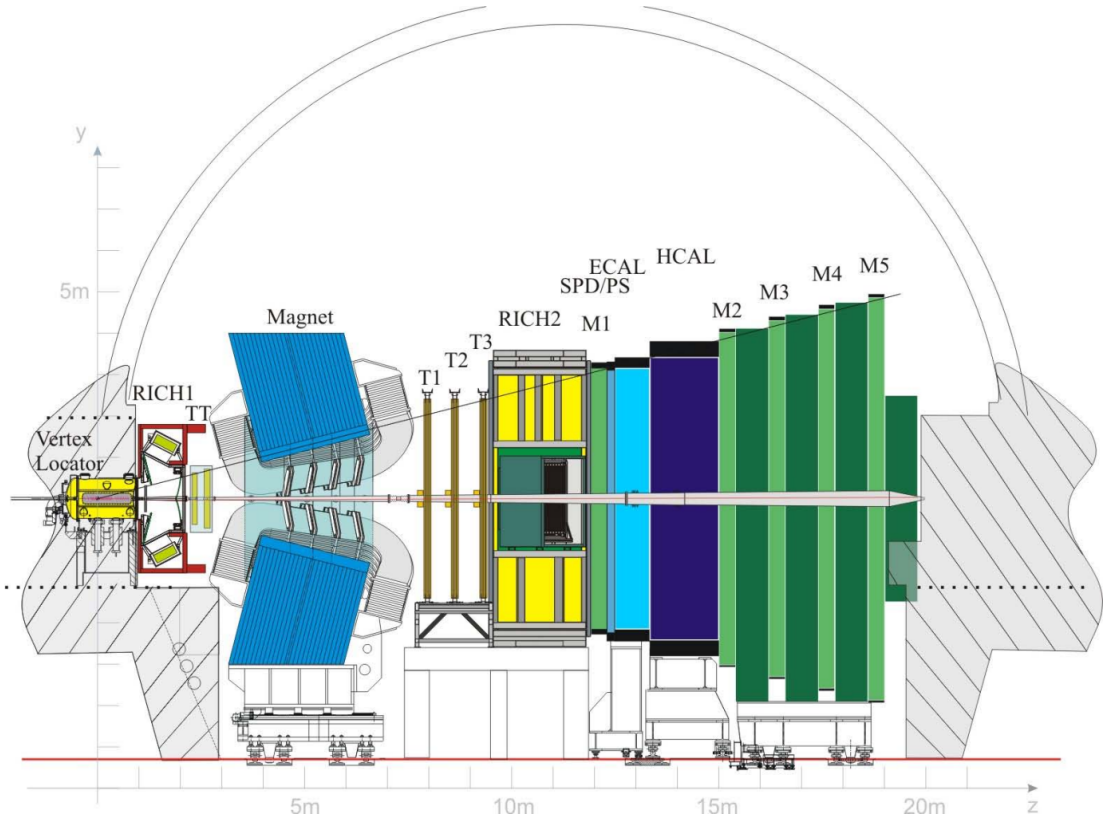

Figure 2.6: Schematic diagram of the vertical cross-section of the LHCb detector showing its subcomponents.

the VELO, creating the decay vertex[c], into several charged or neutral daughter particles. As the name suggests, the main purpose of the VELO is to locate these vertices, starting by the production vertices. The daughter particles then traverse the detector either fully or partially. First, the particle passes the first Ring Imaging Cherenkov detector (RICH1), where it produces Cherenkov radiation useful for particle identification, and then passes the TT (Tracker Turicensis) stations. The magnet, located just after the TT stations, bends the track trajectory allowing one to measure the momentum of the tracks as well as their electric charges. After the magnet, the tracks traverse three more tracking stations named T1, T2, and T3, before passing the second RICH detector (RICH2). One muon station (labelled M1) is placed just before the calorimeter (CALO) system. The CALO system, which is composed of several subdetectors each with its own purpose, provides energy and position of the particles, in addition to triggering electrons, photons and hadrons and aiding the particle identification process. From nearest to farthest from the interaction, the CALO subdetectors are the Silicon Pad Detector (SPD), the Preshower detector (PS), the Electromagnetic Calorimeter (ECAL) and the Hadronic Calorimeter (HCAL). Finally, if the tracks are muons, they likely leave traces in four more muon stations located after the CALO system.

In the next Subsections, a more detailed description of each subdetector will be presented. In presenting these subdetectors, they are gathered together in systems, *i.e.* vertexing and tracking system, particle identification system, calorimeter system and muon system.

[c]The decay vertex is sometimes referred to as secondary vertex, while the production vertex is sometimes called primary vertex.

2.3.2 Vertexing and tracking system

The vertexing and the tracking system provides mostly the topological variables of the decay. In a typical event with a long-lived b-flavoured hadron, two vertices are present in the vertex locator, corresponding to its production and decay vertices. The tracks of the daughter particles are then traced using the different tracking stations and some hits in the VELO if available.

Vertex locator

The VELO [77], which is a silicon tracker, is the closest detector to the interaction point, since it is primarily aimed for reconstructing the position of the production and decay vertices. The VELO is designed to be retractable, and thus is open when beams are still unstable, and closed when physics data taking is to be conducted. In a closed position, the first active strip of the VELO is only 8.2 mm from the beams, which is within LHC's beam aperture during beam injection phase, and thus has to be retracted out to 30 mm before having stable beams. Shown in Figure 2.7 is a sketch of the VELO, showing that it is made of several detector modules arranged along the z-axis. Notice also that the modules are closer near the interaction point.

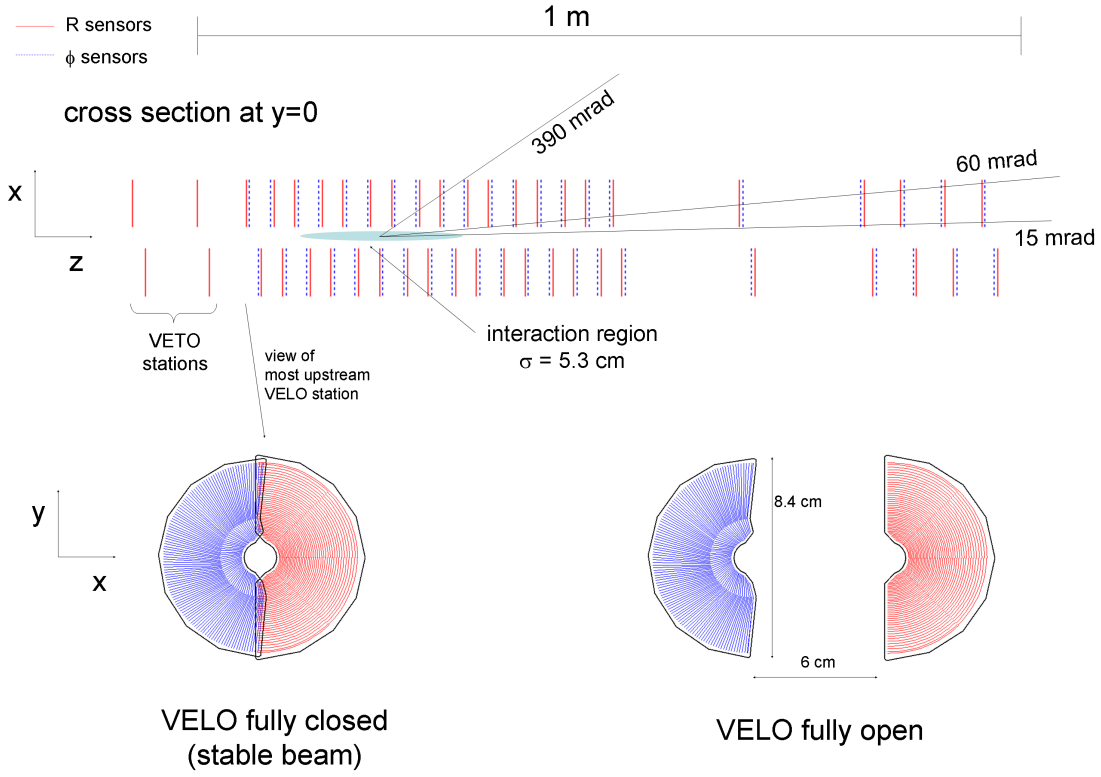

Figure 2.7: (Top) Sketch of the (x,z) cross-section of the VELO showing the arrangement of the sensors along the z-axis. Shown also is a single sensor in (bottom-left) fully-closed and (bottom-right) fully-open positions.

As depicted in Figure 2.7, there are a total of 42 semicircular detector modules (not counting the VETO stations), having 21 on each side. Each module is positioned perpendicular to the beam pipe and has two types of sensors, namely R-sensor and ϕ-sensor, placed

back-to-back. The R-type sensors, designed to measure the charge energy deposition's radial position, has silicon strips arranged radially from the beam axis; while the ϕ-type sensors, designed to measure the azimuthal coordinate, has silicon strips arranged as semicircles co-centered from the beam axis. Shown in Figure 2.8(left) is a sketch of the two sensor types. Each sensor has a total of 2048 silicon strips. In order to shield the electronics of the VELO from the radiations produced by the circulating proton beams, a ~300 μm thick aluminum foil, called RF foil, is placed between the sensors and the beam vacuum. Its shape can be seen in Figure 2.8(right), where it shows that the shape flows around the sensor planes.

A charged particle track produced in the VELO region has to traverse at least 3 sensor modules to be reconstructed as a track. This is one of the requirements of a "VELO"-, "Upstream"- or "Long"-type track[d]. Even tracks with high transverse momentum (p_{T}) typically traverse 3 or more sensor modules due to the close z spacing of the modules near the interaction point. In case of low p_{T} tracks, the sensor modules at the furthest right-end of the VELO are also placed close together in order to maximize the number of traversed sensors.

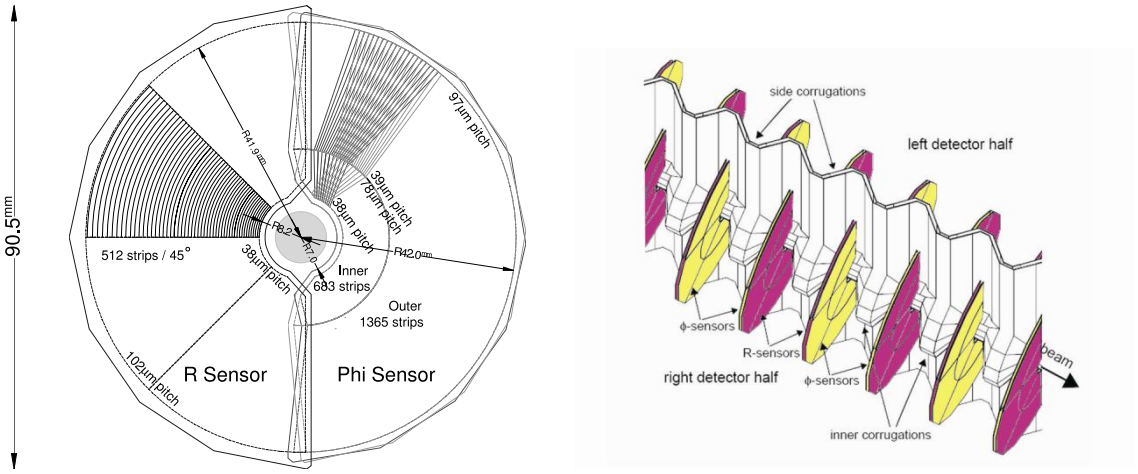

Figure 2.8: (Left) A sketch showing the arrangement of the silicon strips for each sensor type. (Right) The VELO detector in closed position, showing as well the RF foil that protects the two sides of the VELO.

The overall performance of the VELO detector is presented in Refs. [78, 79]. It has been found that at the end of the LHC Run I, 0.6% of the strips are inefficient and 0.02% are noisy. These numbers are effectively identical to those at the start of operations in 2010. The primary vertices are reconstructed by collecting several reconstructed tracks in the VELO that points to the same location. The average spatial resolution of reconstructed primary vertex (PV) improves as a function of the number of associated tracks (N). Figure 2.9(left) shows how the resolution along the z-axis (σ_z) improves with N during the 2012 campaign. A typical PV has 25 associated tracks and hence a typical σ_z of ~90 μm, and a typical resolution perpendicular to the z-axis of ~13 μm [79]. The impact parameter, which is defined as the closest approach of a track to the PV, is widely used in online (trigger) and offline signal selections. Shown in Figure 2.9(right) is how the impact parameter resolution varies with the $1/p_{\mathrm{T}}$ of the track. This demonstrates the good performance of the VELO.

With such good performance, we investigated the feasibility of reconstructing a decay with one missing particle in the final state. The excellent vertexing could provide constraints, together other kinematical constraints, that would allow a reconstruction of the b-flavoured hadron. The findings of this study are discussed in Appendix B.

[d] Different type of tracks are discussed in Section 2.12.

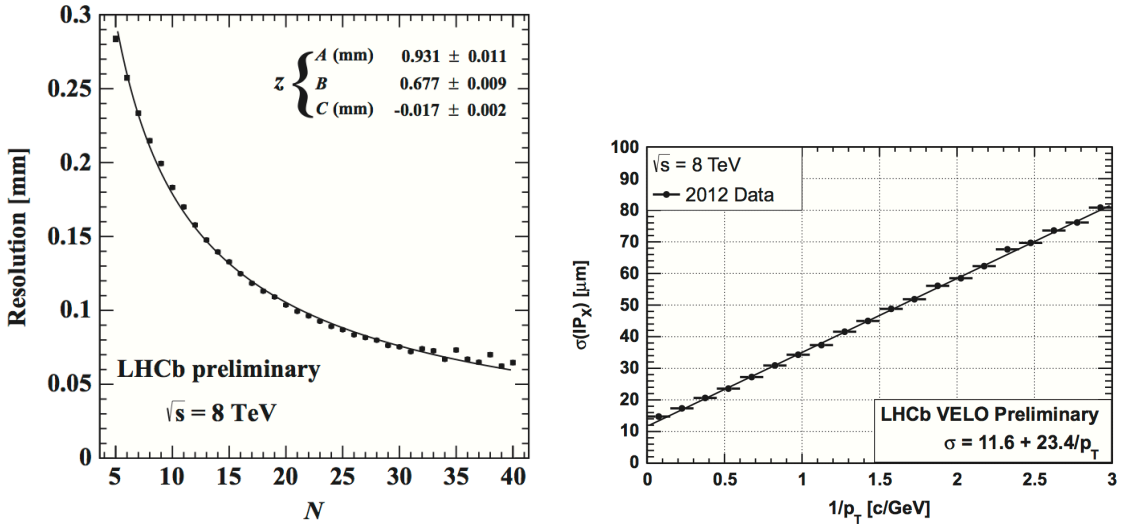

Figure 2.9: (Left) Spatial resolution of reconstructed PV along the z-axis as a function of the number of associated tracks during the 2012 data taking campaign. The data points have been fitted with a function: $\sigma_z = A/N^B + C$. (Right) Impact parameter resolution along the x-axis versus the $1/p_{\mathrm{T}}$ of the tracks during the 2012 campaign. Effectively the same impact parameter resolution is observed along the y-axis.

Magnet

LHCb has a warm dipole magnet designed to deliver an integrated field of 4 Tm [80]. Shown in Figure 2.10(left) is a sketch of the magnet. Figure 2.10(right) maps the field strength along the z-axis. from the interaction point. The field strength goes up to 1 T. The momentum of charged particles is measured by analyzing the bending of trajectories by this field. The polarity of the magnetic field is regularly reversed, collecting about the same data for each polarity and allowing the study of detector asymmetries. The magnet is water cooled, its two coils are made of pure aluminum (weighting a total of 50 tons) and the yoke, weighting 1500 tons, is made from plates of laminated carbon steel.

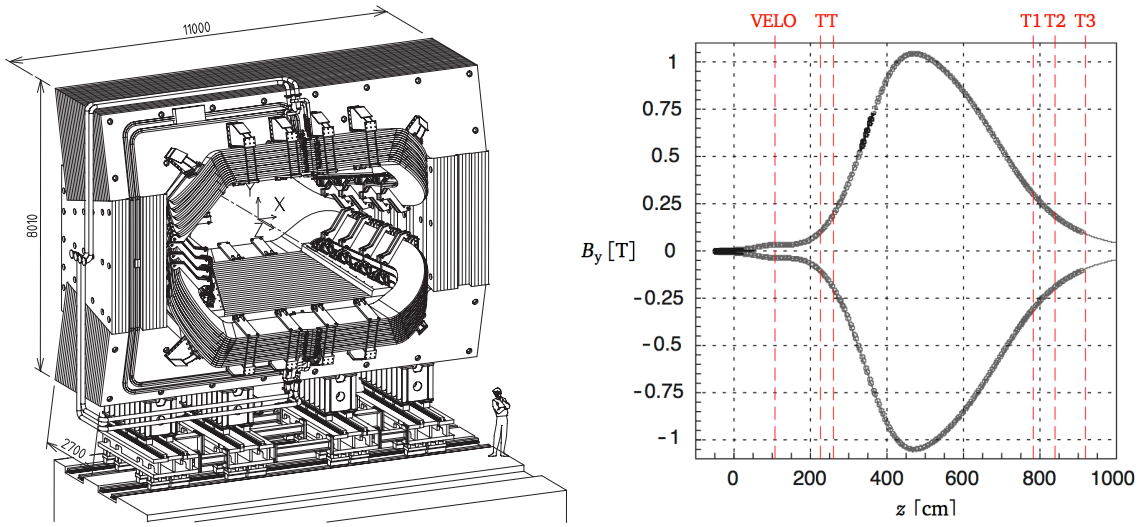

Figure 2.10: (Left) A sketch of the LHCb magnet depicting its dimensions in units of mm. The two coils are conical saddle shaped and are placed mirror symmetric to one another (see also Figure 2.6). (Right) The magnetic field strength along the z-axis.

Silicon trackers

Aside from the VELO detector, there are two more sections that contributes in the tracking system. These are the Silicon Tracker (ST) and the Outer Tracker (OT). The OT is discussed in Section 2.3.2. The ST is further divided into two seprate detectors, namely the Tracker Turicensis (TT) and the Inner Tracker (IT) [81]. A schematic diagram of the layout of the ST and OT stations is shown in Figure 2.11(left). The TT station, which covers the whole LHCb angular acceptance is located just before the magnet, while the IT stations are located after the magnets. The three IT stations, together with the OT stations, are named as T1, T2 and T3 stations, with T1 neareast to the collision point and T3 being farthest.

ST stations use silicon microstrip sensors having a pitch size of about 200 μm. Each ST station has four detection layers. The strips in the first and last layers are arranged vertically, while the second and third layers are rotated by an angle of $+5°$ and -5°, respectively. See for example Figure 2.11(right) for the schematic diagram of the third TT detection layer. The number of readout strips used in the TT is 143360, while 129024 strips are used in the IT. This corresponds to an overall active area of 8.4 m^2 and 4.0 m^2 for TT and IT stations, respectively.

The TT stations, covering the overall LHCb acceptance angle, has a height of about 130 cm and width of about 150 cm. On the other hand, the IT stations are 120 cm wide and 40 cm tall, but shaped like a cross located near the beam pipe (see Figure 2.11(left)).

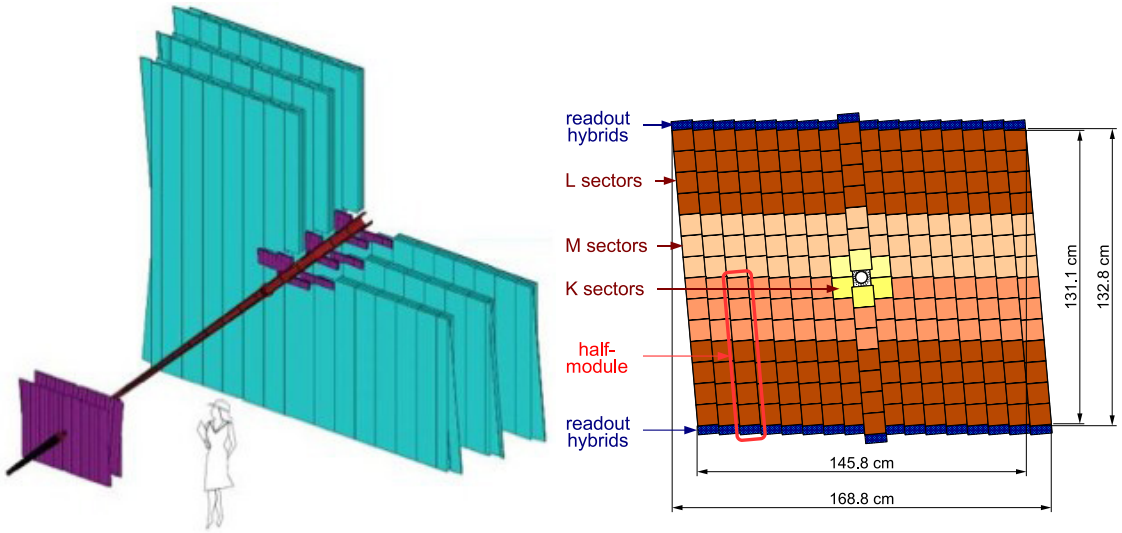

Figure 2.11: (Left) Schematic diagram of the layout of the Silicon Trackers (ST) and the Outer Trackers (OT) of LHCb, where other detector components are removed for clarity. Stations colored in purple are the ST stations, while those colored in cyan are the OT stations. (Right) A sketch of the third TT detection layer.

Outer tracker

The Outer Tracker (OT) is a gaseous straw tube detector [82,83] covering an area of about 5×6 m^2 with a total of 12 double layers of straw tubes. It is located in the outer part of the T1, T2 and T3 stations, as shown in Figure 2.11(left). It is designed to allow both tracking and measurement of track momentum over a large acceptance angle not covered by the IT. Staggered layers of drift tubes compose each module of OT, where each tube is filled with a mixture of 70% Argon, 28.5% CO_2 and 1.5% O_2. Like in the case of ST stations, each OT

station consists of four layers, where the first and last layers are oriented vertically, while the second and third layers are tilted by -5° and +5° with respect to the vertical, respectively.

Track types

There are five reconstructed track types defined in LHCb depending on which tracking stations were used to reconstruct the track. These are shown in Figure 2.12. The "VELO" tracks refer to reconstructed tracks which only VELO hits are associated with it. The "Upstream" tracks have hits in the VELO, as well as in the TT stations. The two most common used track types in LHCb analyses are the "Long" tracks and the "Downstream" tracks. As depicted in Figure 2.12, Downstream tracks have hits in the TT stations and in the T stations. The Long tracks refer to tracks reconstructed with hits information from the VELO, the TT and the T stations. Lastly, the "T" tracks has associated hits only in the T stations.

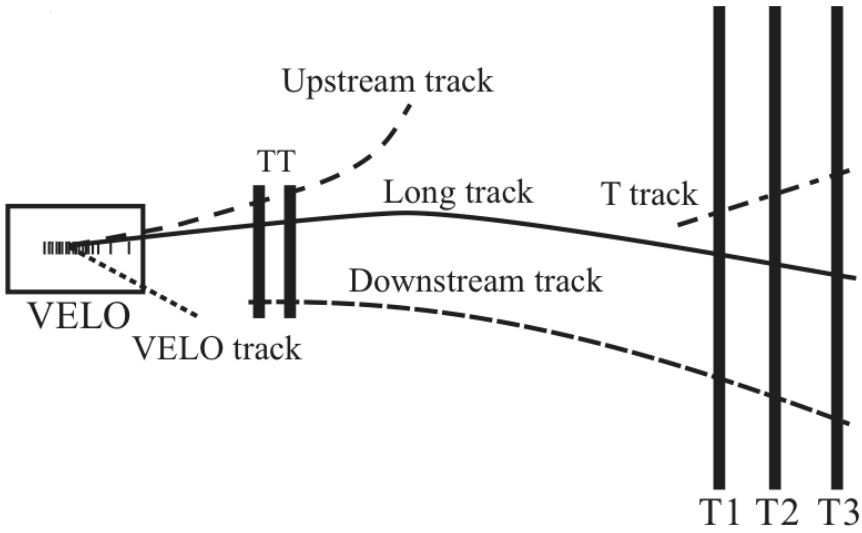

Figure 2.12: Different types of reconstructed track defined in LHCb.

2.3.3 Particle identification system: RICHes

Particle identification system (PID) is required for any flavour physics experiment and is of utmost importance for the searches presented in this document.

Since the momentum spectrum of the charged tracks issued from proton collisions (and subsequent b-hadron decays) is harder at small polar angles, it has been chosen to have two RICH (Ring Imager Cherenkov) detectors in order to get an efficient PID over the full momentum range relevant for physics. The RICH1 (upstream detector before the magnet) is made of aerogel and C_4F_{10} radiators to handle the low momentum charged particles in the range ~1-60 GeV/c. The RICH2 (downstream detector after the magnet) covers the high momentum range from ~15 GeV/c up to and beyond 100 GeV/c using CF_4 as radiator. Figure 2.13 shows the Cherenkov angle as a function of the momentum for the different radiators. Conversely, the acceptances of each detector are different: RICH1 is covering the full LHCb acceptance from ±25 mrad to ±300 mrad horizontally and ±250 mrad vertically, while RICH2 has a limited angular acceptance of ~ ±15 mrad to ±120 mrad horizontally and ±100 mrad vertically. The latter corresponds to the region where the high momentum particles are mostly distributed.

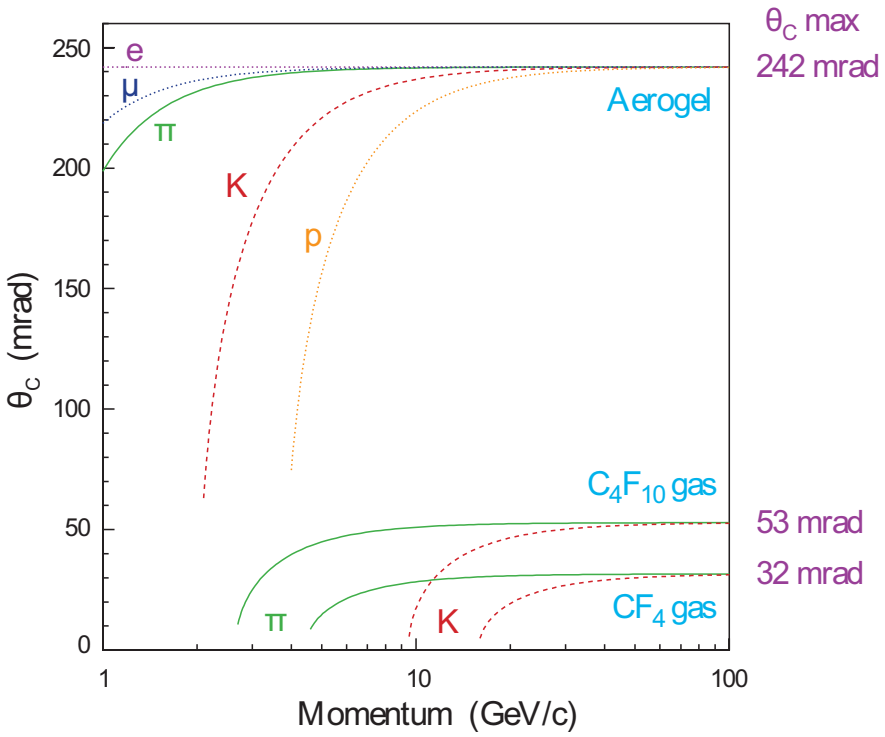

Figure 2.13: Cherenkov angle versus particle momentum given for the different RICHes radiators.

Both RICH1 and RICH2 detectors are using a combination of spherical and flat mirrors to reflect the image out of the spectrometer acceptance. The Cherenkov light is eventually read by Hybrid Photo Detectors. Figure 2.14 shows the layout of these two detectors (radiators, mirrors, HPDs and acceptance).

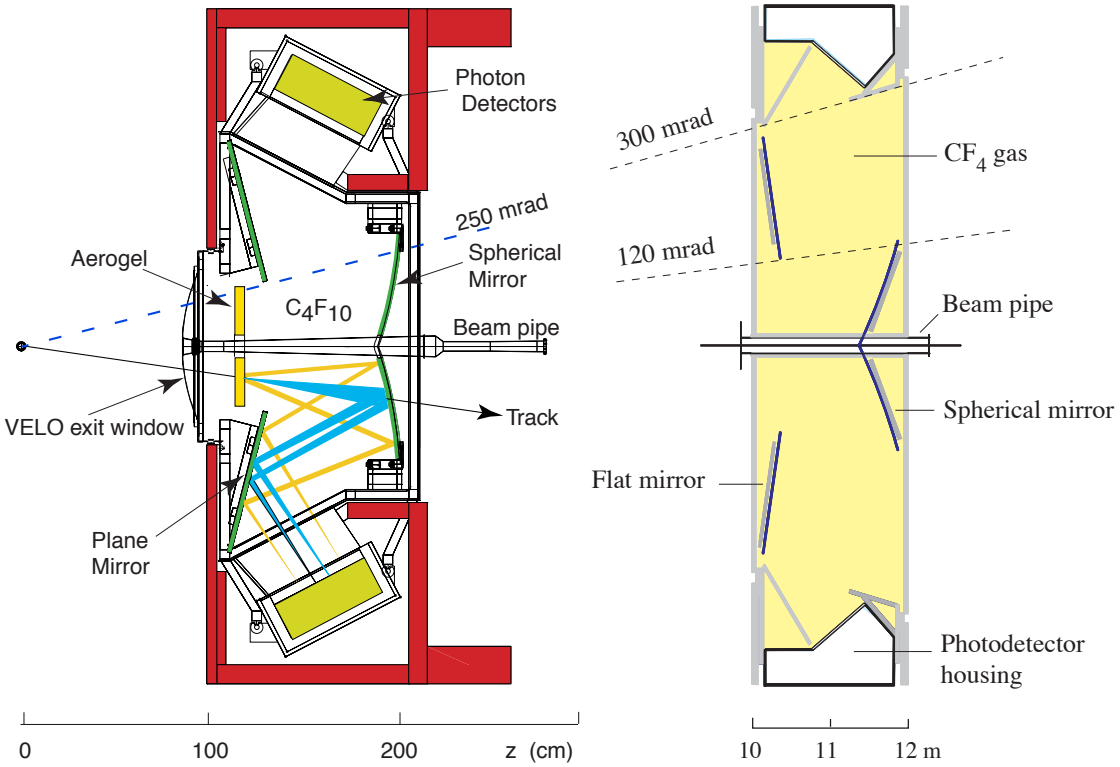

Figure 2.14: Artist view of the RICH1 and RICH2 layouts.

The performance of the PID requirements applied to the search of neutral b-baryon decays

will be discussed in Section 5.6.

2.3.4 Calorimeter system

The calorimeter system of the LHCb spectrometer [84] is, in first place, used to select high transverse energy hadron, electron, photon and π^0 candidates for the first level of trigger of the experiment (L0). It provides as well the identification of electrons and photons and the measurement of their energies and positions. These are used in turn for flavour tagging information, studies of radiative decays or *CP* violation studies in measurements of final states with π^0 to cite some of them.

The fast identification of an electromagnetic object in a high hadronic multiplicity environment requires a longitudinal segmentation of its shower. This is realized by a preshower detector[e] (a lead converter sheet upstream a plane of scintillating detectors, denoted PS) followed by the main section of the electromagnetic calorimeter (ECAL). The choice of the lead thickness (2.5 radiation lengths, X_0) of the PS results from a compromise between trigger performance and ultimate energy resolution [85]. In addition, a Scintillator Pad Detector (SPD) plane is set upstream the PS in order to tag at the L0 trigger the charged or neutral nature of the particle initiating the electromagnetic shower.

The ECAL thickness was chosen to be $25X_0$ [86] such that the showers from high energy photons are in average contained in the detector, ensuring a satisfactory energy resolution. The HCAL instead is mostly used at the L0 trigger and its thickness is set to 5.6 interaction lengths [87] due to space limitations.

The four sub-detectors mentioned above have a variable lateral segmentation (displayed in Figure 2.15) in order to cope with the hit density variation over the calorimeter surface. Three different sections of elementary cells have been chosen for the ECAL. The SPD and PS detectors are accordingly segmented, with elementary cell sizes defined such that the SPD/PS/ ECAL system is projective. In reason of the dimensions of the hadronic showers, the HCAL is only segmented into two zones with larger cell sizes.

The active calorimeter detector elements are scintillating materials. ECAL is designed with a sampling scintillator/lead structure readout by plastic wavelength shifting (WLS) fibres (Shashlik calorimeter). This choice is adapted to LHCb requirements in terms of modest energy resolution, fast time response and radiation resistance. The HCAL follows the same conservative design [84], being a sampling device made from iron as absorber and scintillating tiles as active material, read out by WLS fibres. For these two sub-detectors, the light of an elementary cell is read out by a photomultiplier tube. The next chapter of this thesis will provide a detailed description of the SPD and PS sub-detectors.

2.3.5 Muon system

The muon system, aimed at both triggering on and identifying muons, is a key element of the LHCb spectrometer. Muons are however not used in the analyses presented in this thesis. The description of the detector will hence be rapid. The muon system provides in first place high-p_T candidates for the L0 trigger decision. It comprises five rectangular stations (M1-M5) installed along the beam axis. The first station (M1) is placed in front of the calorimeters. The high charged tracks multiplicity at this position in the innermost part of the detector made necessary the use of triple-GEM (Gas Electron Multiplier) chambers. The outermost part active detectors are Multi Wire Porportionnal Chambers (MWPC). The very same MWP chambers equip the last four stations, placed after the calorimetric system

[e] Details on the Pre-shower detector is discussed in Chapter 3.

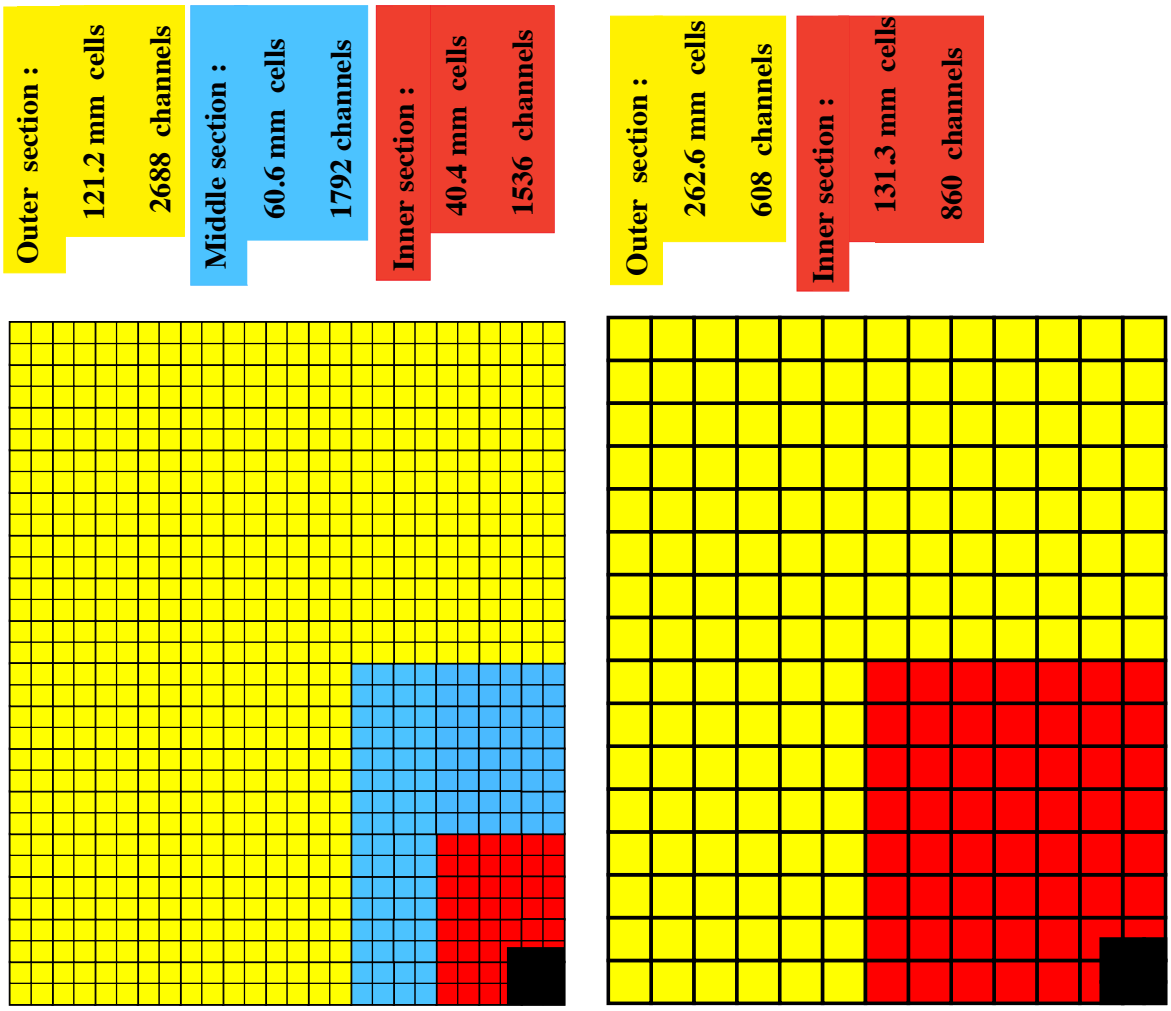

Figure 2.15: (Left) SPD/PS and ECAL and (rigth) HCAL lateral segmentations (one quarter of the detector front face is represented).

and interleaved with 80 cm thick iron absorbers aimed at stopping hadrons. Figure 2.16 displays the muon system layout [88]. The geometry of the five stations is projective. Each detector is split into rectangular logical pads (grouping of anode wires depending on the chamber) whose dimensions define the x, y resolution of the hit reconstruction.

2.3.6 Triggering scheme

Not all collision events are eventually saved for further analysis. Only about 1% of the visible proton-proton interactions results in the production of a $b\bar{b}$ pair, and only about 20% of these are within the LHCb angular acceptance. There is also a technical limit on the amount of data that can be written into storage in a given time. The available bandwidth of writing in LHCb is about 3 kHz (reached higher values in recent operation), while LHCb designed luminosity corresponds to a rate of collision events with at least one visible interaction at a level of 10 MHz. As such, an efficient online selection of interesting events has to cope up with the disproportion between the available writing rate and the LHCb operational frequency. This is achieved by a multi-stage trigger system.

There are two main stages in the LHCb triggering process [89,90]. The first stage, called level 0 (L0) trigger, is implemented in the hardware, while the second stage is the software-based High Level Trigger (HLT). The flow of the triggering scheme is summarized in Figure

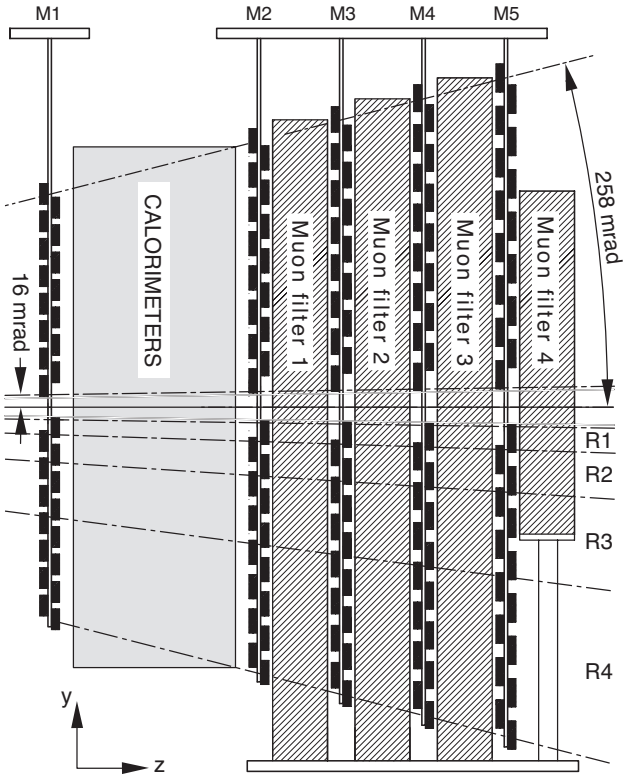

Figure 2.16: Layout of the muon system (vertical cross-section).

2.17.

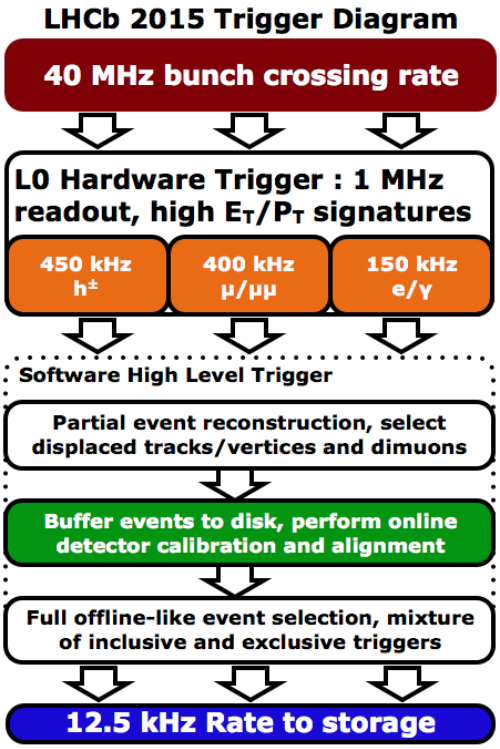

Figure 2.17: Flowchart of the LHCb triggering scheme.

The bunch crossing frequency of the LHC is 40 MHz. The L0 trigger works in sync with this and is designed to reduce the rate to 1 MHz, which is the maximum frequency at which

the detector can be read. The L0 trigger is consists of the pile-up, calorimeter and muon subsytems. Although eventually it has not been used, the pile-up subsystem distinguishes the multiplicity of visible interactions in each bunch crossing. The presence of large tranverse momentum track is one of the signatures of B meson decay. As such, the data from the muon detectors are analyzed in order to trigger on large momentum muon candidates. Data delivered by the calorimeter system are also analyzed to trigger on large transverse energy hadron, electron or photon candidates. If any of the alley passes the threshold cut, the event is passed to the HLT for further screening.

For timing reasons, the HLT is split into two stages, which are the HLT1 and HLT2 stages [91]. In the HLT1 stage, the process performs a fast tracking searching for a very good quality track with a high transverse momentum and high impact parameter with respect to any reconstructed primary vertex. Eventually, the aim of HLT1 is to reduce the rate by a factor of around 20. Events passing the HLT1 selection are processed by the HLT2, which performs a full reconstruction close to the offline reconstruction. For the analyses presented in this document, we are making use of the HLT2 inclusive trigger based on topological selection of a 2 to 4 tracks displaced vertex. Events that passed the full trigger chain are eventually saved to storage. Further offline selection cuts are to be applied depending on the strategy and needs of the analysts.

2.3.7 Stripping lines

The number of events saved in the LHCb data storage is enormous and requires further offline selection cuts in order to remove events which are not of interest. The stripping line is the first offline selection that is applied by the analysts in accordance to its physics interest. During stripping campaigns, the common particle reconstruction is done centrally and each analyst, subject to availability of bandwidth, submits its own selection requirements known as *Stripping line*. Stripping lines for somewhat similar physics programme are grouped together into *Streams*. One example of a stripping line selection is presented in Section 5.4.

Chapter 3

Pre-shower detector studies

Contents

3.1 Introduction

During the Run I data taking campaign of the LHC, the LHCb spectrometer has recorded an integrated luminosity of 1 fb^{-1} for 2011 and 2 fb^{-1} for the 2012 data taking. With such amount of data, the different sub-detector components could wear-and-tear throughout the data taking period, resulting to ageing.

In this chapter, the ageing and calibration of the Pre-Shower (PS) subdetector, which the LHCb-Clermont group is responsible for, is studied. There are two main sources of ageing for the PS detector: the decrease of transparency of the scintillating material and the permanent decrease of the gain of the photomultiplier channel. Both are correctible to some extent through a recalibration of the detector which will be as well addressed in this chapter.

The discussion will start with an overview of the PS sub-detector, specifically on its structure, in addition to what was presented in Section 2.3.4. The front-end electronics and its implications for the calibration and ageing studies, are also reviewed. Finally, due to difference in center-of-mass energy for 2011 and 2012, the results are presented in different sections for the two data taking periods.

3.2 Pre-shower detector characteristics and definitions

The Pre-Shower (PS) detector is one of the four sub-detectors of the calorimeter system of the LHCb spectrometer. The three other subdetectors are the Scintillating Pad Detector

(SPD), the Electromagnetic Calorimeter (ECAL), and the Hadronic Calorimeter (HCAL). Although each of these subdetectors has its own purpose, they work in unity to trigger on electrons, photons and hadrons. On an offline event analysis, they also provide the energy and position of neutral particles and help in the identification of particles. Tracks coming from the interaction point will traverse first the SPD, followed by the PS detector, and then the ECAL and HCAL.

Inserted in between the SPD and PS detector is a 15 mm thick lead, corresponding to $2.5X_0$. This lead will increase the probability of photons and electrons to interact with the material, thereby start the electromagnetic shower. The PS detector is used to differentiate charged pions from electromagnetic showers, providing the information for the L0 trigger decision, where no other part of the LHCb detector can be used to distinguish those two types of particles.

The PS detector is divided into two sides, namely A and C sides. Furthermore, each side is divided into three regions, namely Inner (I), Middle (M) and Outer (O) region. A schematic diagram of the PS detector showing the sides and regions is shown in Figure 3.1.

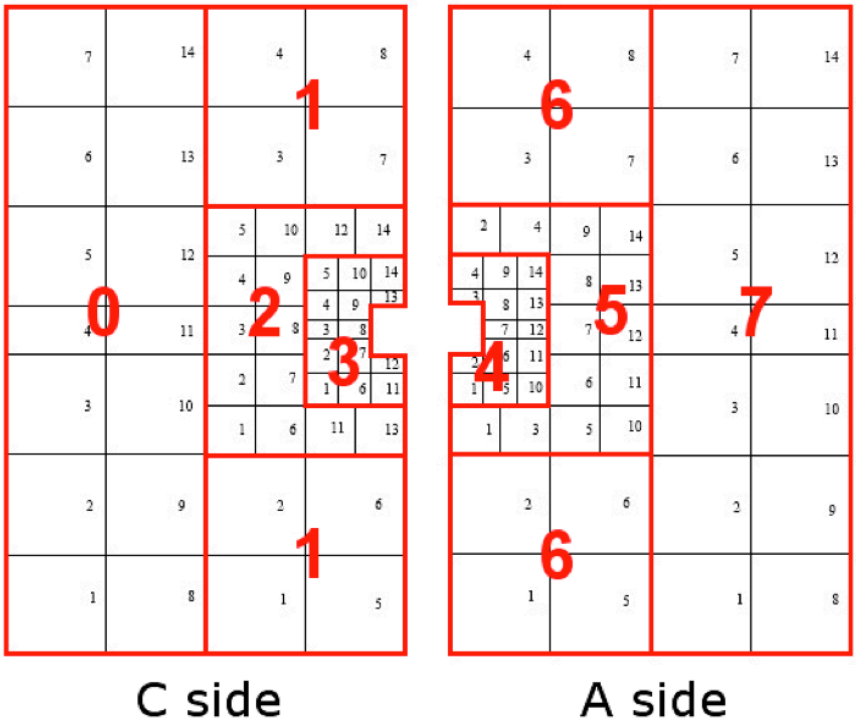

Figure 3.1: Schematic diagram of the PS detector showing the sides, regions, crate numbering and front-end-board numbering per crate. A detailed summary can be found in Table 3.2.

3.2.1 The Pre-shower detector overview

The basic unit of the PS detector is a square scintillating polysterene cell. A sketch and an actual photo of one cell is shown in Figure 3.2. There are three different cell sizes depending on the region. The cell size is smaller for cells near the beam pipe, to account for the high track multiplicity in that region, and larger in the outermost region, leading to a size ratio of 1:1.5:3. A total of 6016 cells composes the whole PS detector. Reported in Table 3.1 are the cell dimensions for the different PS regions. The thickness of all the scintillators is 15.0 mm. We take note that the cell size is larger than the cuboid scintillator size. For each cell, a WLS fiber is inserted into a 3.5 circle-shaped loop. This choice is the result of the

optimization reported in [92]. As shown in Figure 3.2, both ends of the WLS fiber exit the scintillator. These two ends are attached to two clear fibers, which are then finally connected to the same pixel of a photomultiplier.

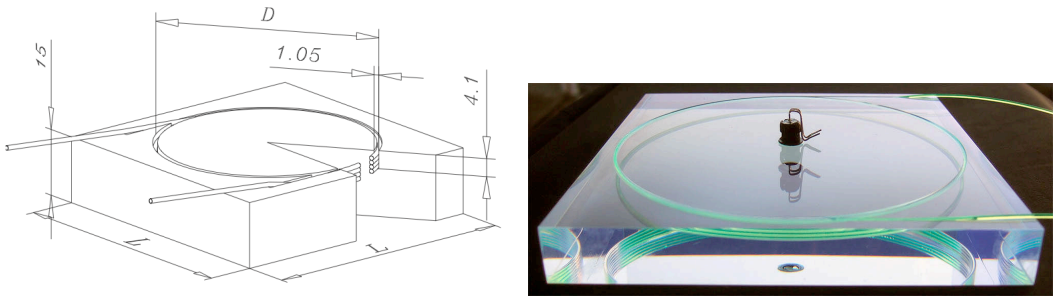

Figure 3.2: (Left) Sketch of one scintillator cell and (right) an actual photo of a cell. The diameter D of the WLS fibre groove is equal to 37 mm, 56 mm and 100 mm for cells in the Inner, Middle and Outer regions, respectively.

Table 3.1: PS cell dimensions.

Region	Cell size (mm × mm)	Scintillator size (mm × mm)	No. of cells
Inner	39.84 × 39.84	39.5 × 39.5	1536
Middle	59.76 × 59.76	59.4 × 59.4	1792
Outer	119.5 × 119.5	119.1 × 119.1	2688

The cells are then organized by modules. Depending on the PS region, the full-modules have 144, 64 and 16 cells for the Inner, Middle and Outer regions, respectively. In the Inner region, the cells are arranged in 12 rows by 12 columns for full-modules, and in 12 rows by 6 columns for half-modules. The same can be said for the Middle and Outer regions, where the cells in the full-modules are arranged in 8 rows × 8 columns and 4 rows × 4 columns, respectively. Schematic diagrams of typical modules in the Inner and Outer regions are shown in Figure 3.3, showing as well the fiber routing. The electronic boards reading the modules (see next Subsection) are grouped together to per crate basis. There are 8 crates in total. The crate (numbered 0 to 7) and front-end-board numbering per crate are shown in Figure 3.1. The number of full front-end-boards (64 channels) and half front-end-boards (32 channels) are summarized in Table 3.2.

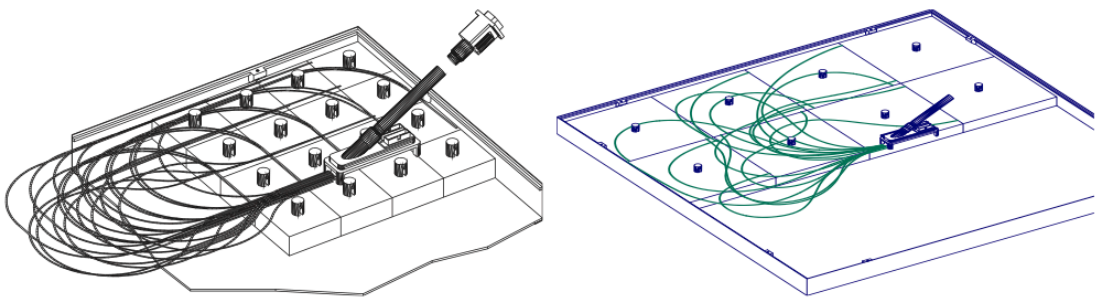

Figure 3.3: Schematic diagrams of the cell arrangement inside a module in the (left) Inner region and (right) Outer region. Note that the two diagrams do not scale.

Structurally, the modules are built together into supermodules to create a large column of 7.7 m in height, which is the entire PS detector height, and about 96 cm in width. These

are then mounted to a support plate. Eight supermodules composed the PS detector, 4 supermodules on each side.

Table 3.2: Summary of number of full and half front-end boards per region and per crate.

Side	Region	Crate no.	No. of full-boards	No. of half-boards
C	Outer	PRS 0	12	2
		PRS 1	8	0
	Middle	PRS 2	14	0
	Inner	PRS 3	10	4
A	Inner	PRS 4	10	4
	Middle	PRS 5	14	0
	Outer	PRS 6	8	0
		PRS 7	12	2

3.2.2 Pre-shower electronics overview

The design of the electronics of the PS detector is more complicated, if not equally complex, than its structural design. Hence, we refer to [92] for the complete details of it. Presented in this section, however, are the elements we believe sufficient to understand its implications for the calibration.

As mentioned in Section 3.2.1, the two ends of the fiber exiting from the scintillator cells are attached to the same pixel of a multi-anode photomultiplier (Ma-PMT). Each Ma-PMT has a single photo-cathode. Behind this photo-cathode are focusing electrodes that guide the photo-electrons to one of the 64 anodes (pixels). Schematic diagrams of a Ma-PMT[a] used in the PS detector is shown in Figure 3.4.

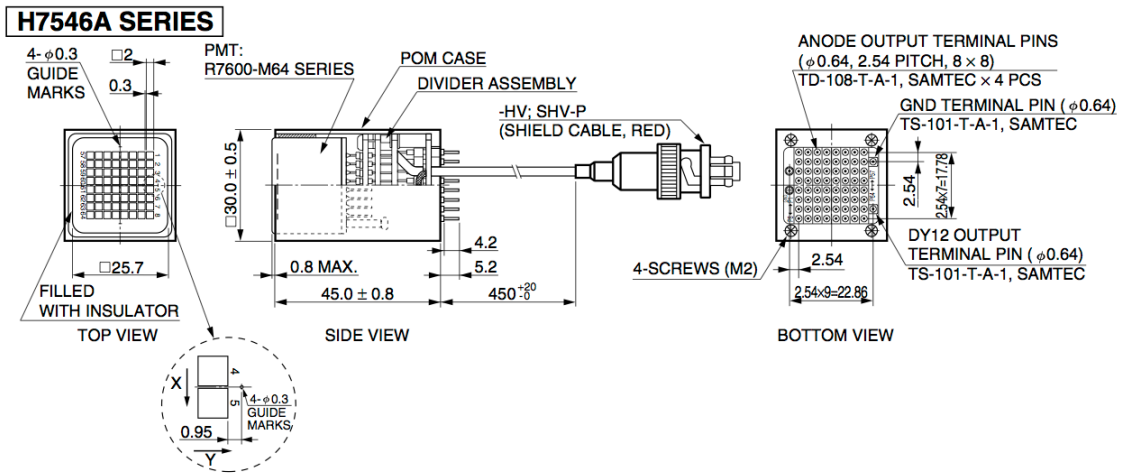

Figure 3.4: Schematic diagram of the Ma-PMT used in the PS detector. One pixel of this Ma-PMT has an area of 2×2 mm^2. Each pixel is separated by a distance of 0.3 mm.

The electronic signals produced by the Ma-PMT of the PS detector are received by the very-front-end (VFE) boards. Driven by two-fold detector task, namely input to L0 trigger decision and ECAL electromagnetic energy measurement correction, the lower energy threshold to select an electromagnetic cluster is envisaged to be 0.1 times the energy deposit

[a]The photomultipliers are manufactured by the Hamamatsu company. An 8-stages amplification Ma-PMT was chosen among the available technologies at that time.

of a MIP, with a precision of 5%. While the upper energy threshold is driven by the decision of wanting to correct the ECAL electromagnetic energy measurement yielding up to 100 MIPs energy deposit. This lead to the decision of using a 10-bit coding of the PS energy information to be delivered to the front-end (FE) board. The typical signal response of a scintillating cell being read out by the Ma-PMT lasts more than 25 ns, where 85% (on average and observed to be un-erratic) of the signal is received within the 25 ns window[b]. Part of the solution adopted cope with this technological challenge is by having two interleaved fast integrators, where one integrator is receiving the signal for 25 ns, while the other integrator is being in digital reset mode. This lead to a design of two parallel paths on the VFE board, one path corresponding to one parity of the bunch crossing number. Anticipating the notation we will use in later discussions, two bunch parities are defined, namely "Even" bunch crossings and "Odd" bunch crossings. A direct consequence of having two paths is the possible different output, due to difference in the amplification between the paths, for the same input.

The PS analog signals coming from the VFE boards are received by the front-end (FE) boards, together with the binary data coming from the SPD. Among other several functions, the FE electronics also provide synchronization signal to the VFE electronics. Upon receiving the 64 analog PS data, the analog block of the VFE electronics, which is consist of 10-bit 40 MHz differential analog-to-digital converter (ADC), digitizes the data. A total of 8 identical asics, each processing 8 PS and 8 SPD channels, composes the processing block. Every 25 ns, the FE board applies corrections to the digitized data corresponding to three factors. These are the pedestal correction, the gain adjustment and then the spill-over correction. These are further discussed in the next Section. After these corrections are applied, a transcoding of the 10-bit data to an 8-bit floating format is done in order to save resources. For each channel, a trigger bit is produced by comparing the post-correction data to an *a priori* given threshold.

3.2.3 The online corrections to the raw data

As briefly mentioned in the previous Section, two corrections and one adjustment are applied, just after the digitization of the PS signal from the VFE boards. These corrections/adjustment are done prior to transcoding the data to an 8-bit format.

Pedestal corrrection

The first correction applied is the pedestal correction, which aims at subtracting the VFE constant integrated noise over 25 ns for each channel. In a given channel, this offset is constant with a typical stochastic variation of 1 ADC count. The VFE asics have been selected in order that the maximal correction can be coded on 8 bits. The offsets are measured regularly on an online calibration stream which allows to make offline fine adjustment corrections to the PS calibration procedure. With a total of 6016 PS channels, each having two offset corrections due to different VFE paths (corresponding to two bunch crossing parity), 12032 pedestal corrections have to be coded.

Gain correction

After the pedestal correction, an adjustment is applied to the digital data, whose purpose is to uniformize the response of the channels in the FE board (64 channels or 32 channels of

[b] The bunch spacing of LHC is 25 ns.

the same Ma-PMT). Global multiple effects, such as differences in Ma-PMT channels and electronic amplification, are expected to be corrected via this method. Two gain factors[c] G, one for each bunch crossing parity, are supplied for each channel. The method involves adding a fraction (and no subtraction) to the yet ungained value. The gain factor is given by,

$$G = 1 + \epsilon, \qquad 0 \leq \epsilon \leq 1, \tag{3.1}$$

where ϵ is an unsigned 8-bit number. Denoting the yet ungained data and the gained data as D_r and D_g, respectively, the relation between the two is given by,

$$D_g = D_r + \epsilon D_r, \tag{3.2}$$

where it is now apparent that $D_r \leq D_g \leq 2D_r$. Since the ϵ is small, there was no need to preserve all the 10 bits precision of the raw data in the ϵD_r term, hence an 8×9 multiplier has been chosen leading to a maximum error of 1 LSB on the gained data D_g. This translates to a precision of better than 1% at full scale.

During the first few LHC runs in 2011, these factors were determined and has been used since then all throughout the Run I campaign. A detailed determination of these gains is presented in this document [93]. It was found that after the gain correction the response of the PS channels is calibrated to a precision of 10%. This calibration technique has been revisited in this study to determine whether or not the calibration has significantly changed during the 2011 and 2012 campaign periods.

Spill-over correction

As stated in Section 3.2.2, the typical signal response of the scintillating cell lasts more than the 25 ns bunch spacing. About 85% of the energy is delivered within this 25 ns window, and the remaining 15% leaks to the next time window[d]. As such, a correction has to be applied on the current data with respect to the immediate previous data. Denoting the current data as D_n and the immediate previous as D_{n-1}, it is possible to correct for this *spill-over effect* statistically, using this relation,

$$D_n = D_n - \alpha D_{n-1}, \tag{3.3}$$

where the α's for each cell/channel has been measured during test beam periods. Electronically, α is coded using an unsigned 8-bit value yielding an accuracy of 1/512 LSB. If $D_n \gg D_{n-1}$, the correction is considered as an underflow and the value is set to 0.

Transcoding the data

The 10-bit corrected gained data is almost ready for transmission and processing. A transcoding procedure is however needed since the readout from the board is expected to be in an 8-bit format. A transcoding algorithm, summarized in Table 3.3, has been adopted to minimize the loss of precision. We take note that for values less than 128 ADC counts, there is no loss in precision. The PS was designed to work at 10 ADC counts for the most probable value of the MIP energy loss distribution.

[c] One gain factor G may be used per channel, but since there might be small effects coming from the difference between the VFE paths, two gain factors are (and will be) assigned in the end.

[d] The leak is smaller for the smaller scintillating cells since the WLS fibers are shorter and hence the signal time dispersion is smaller.

Table 3.3: Transcoding of the digitized data from 10-bit format (d_{10}) to 8-bit format (d_8).

	$d_{10} \leq 128$	$128 < d_{10} \leq 256$	$256 < d_{10} \leq 512$	$512 < d_{10}$
d_8	d_{10}	$128 + \frac{d_{10}-128}{2}$	$192 + \frac{d_{10}-256}{8}$	$224 + \frac{d_{10}-512}{16}$

In the Tell1 board, the transcoded 8-bit data has to be transcoded back to the original 10-bit format, this is where the absolute precision is lost. The reversed transcoding algorithm is summarized in Table 3.4.

Table 3.4: Reverse transcoding of the 8-bit data format (d_8) in the Tell1 board back to 10-bit data format (d'_{10}).

	$d_8 \leq 128$	$128 < d_8 \leq 192$	$192 < d_8 \leq 224$	$224 < d_8$
d'_{10}	d_8	$2 \cdot d_8 - 128$	$8 \cdot d_8 - 1280$	$16 \cdot d_8 - 3072$

3.3 Pre-shower calibration method

The method used to calibrate the PS detector proceeds in two steps. The first step involves per board channel by channel intercalibration. The channels[e] in each board are calibrated using the gaining technique discussed in Section 3.2.3. The second step is to calibrate the full PS detector by adjusting the applied voltage on the Ma-PMT of each board. These steps are presented in the next Sections, but a discussion on the MIPs and track reconstruction comes first.

3.3.1 Some words about Minimum Ionizing Particles (MIP) and other reminders

Particles with minimum energy loss rate in a thin scintillator are called Minimum Ionizing Particles (MIPs). For practical purposes, these are particles moving with relativistic velocity that ionizes the traversed medium resulting in an energy deposition. The calibration method used in this analysis involve MIPs.

If the main purpose of the PS is to help in triggering on electromagnetic objects, it can also detect the energy deposit coming from charged particles, hadrons or muons. The dynamics of the electronic read-out has been defined such that it can measure the small energy loss coming from these ionizing particles. For the sake of further discussion, let us recall the general expression of the kinetic energy loss due to Bethe and Bloch:

$$-\left\langle \frac{dE}{dx} \right\rangle = Kz^2 \frac{Z}{A} \frac{1}{\beta^2} \left[\frac{1}{2} \ln \frac{2m_e c^2 \beta^2 \gamma^2 T_{\max}}{I^2} - \beta^2 - \frac{\delta(\beta\gamma)}{2} \right], \tag{3.4}$$

which describes the mean rate of energy loss by moderately relativistic ($0.1 \lesssim \beta\gamma \lesssim 1000$) charged particles. In the Equation 3.4, K is a constant equal to $4\pi N_A r_e^2 m_e c^2$, where N_A is the Avogadro's number, r_e is the classical electron radius, m_e is the electron mass. The other terms in Equation 3.4 are: Z – the atomic number of the absorber, A – the atomic

[e]The channels refer to the individual scintillator cells, together with its corresponding fibers and VFE paths.

mass, T_{max} – the maximum kinetic energy which can be imparted to a free electron in a single collision, I – the mean excitation energy, $\delta(\beta\gamma)$ – the density correction, β and γ – the kinetic parameters of the particle, and z – the charge of the particle. In the given range of $\beta\gamma$ (1-100) the accuracy of the law is better than few percent. Outside this range it starts to fail, for low $\beta\gamma$ additional corrections from the electron structure of the material have to be applied, while above the upper limit radiative effects start to play important role.

The ionizing particles (dominantly pions) used in the calibration process and ageing studies lie in a moderate range of $\beta\gamma$. This allows to consider an average minimum ionizing particle, which is momentum-independent and exhibits the same properties for all pre-shower cells [93]. The most probable value (MPV) of the energy loss distribution of these average MIPs will be used as the estimator of the energy deposits response of a detector cell.

A MIP crosses a cell of the detector and losses a fraction of its energy in the scintillating material. Light is emitted proportionally to the deposit in the scintillator and captured by the WLS fibers. The light is then collected and amplified by the photomultiplier, and the outcome is an electric signal, processed by electronics. An output from the electronics, represented by a number, interpreted as an energy measured in a given calorimeter cell is an outcome of all parts of the described process, and each part of it has an impact on the final result. First, the energy deposited by a particle of a given energy which crosses a thin scintillator with a certain angle can be described by a Landau distribution. The most probable value of the Landau distribution depends not only on the $\beta\gamma$ of the particle, but also on a length of a path of the particle inside the scintillator. The scintillation and the light collection efficiency are the next processes which modify the outcome of the measurement. The photomultiplier photostatistics adds up a fluctuation. The last part is the noise produced in the electronics. The digital output signal of the energy deposited by MIPs is not a simple distribution, but a convolution of multiple distributions described above. A complete description of this physics is beyond the scope of this document. For the purpose of the detector calibration, the convolution of the Landau distribution with a gaussian function accounting for the material and electronics effects (dE/dx dependency on $\beta\gamma$, scintillation and light collection efficiency, tubes photostatistics, stochastic variation of electronic offsets), is enough. After proper correction of a different track lengths of particles passing a cell from various angles is taken into account, the target is a 10% absolute calibration.

3.3.2 Charged tracks reconstruction

In order to build a sample of MIPs, offline reconstructed data are used corresponding to the inclusive muon stripped data of LHCb. It is expected that this sample provides enough charged tracks statistics to perform the calibration. Very mild cuts to select charged tracks are employed. In order to have a good purity of the MIP sample inside PS cells (*i.e* no electromagnetic contamination), a cut on the closest electromagnetic cluster from the extrapolation of the track in the calorimeter is applied. Three more cuts are also applied in order to avoid too busy environment, which are the maximum number of channels with tracks passing through it should be at most 300, the maximum number of reconstructed vertices in the event is 2, and only the channels with only one track passing through it are considered.

3.3.3 Corrections to the raw energy deposit in the PS

As mentioned earlier, a couple of corrections are required in order to have most realistic energy deposit in the cell: the track length in the cell varying with the charged particle

trajectory (the entrance angle in the detector) and the pedestal variation. They are described in details in Ref. [93] and we are only highlighting here their important features.

Track length correction

The MIPs are crossing the detector with different angles. As such, their paths inside cells are different and must be corrected for. Figure 3.5 illustrates the passage of a charged particle in a scintillating cell in order to define the geometric coordinates of the problem.

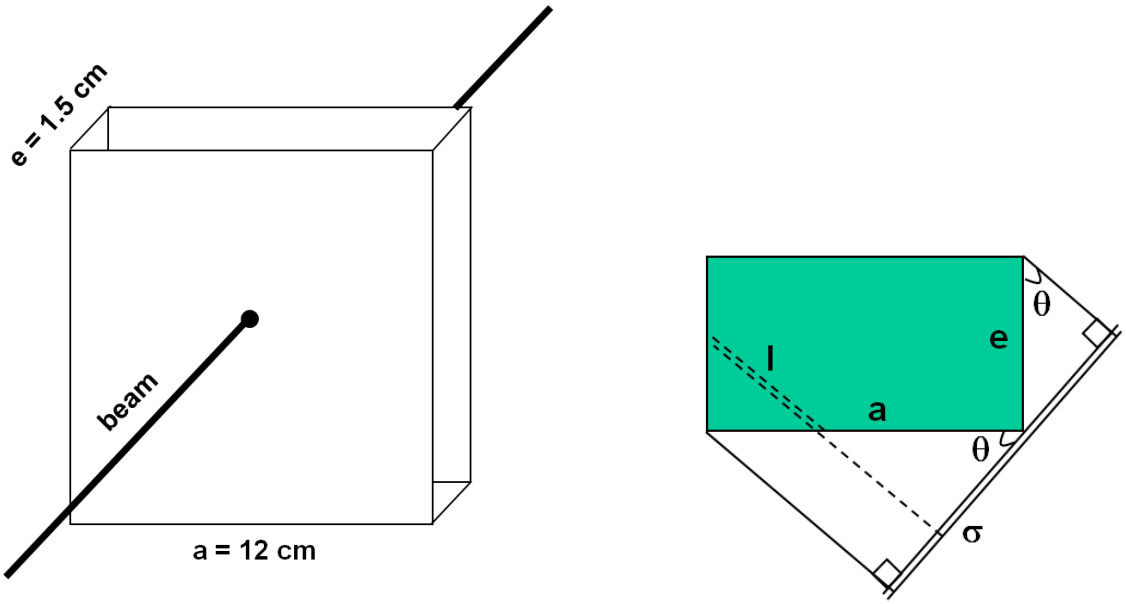

Figure 3.5: PS cell geometry isometric view (left) and top view (right) together with the definition of the main variables used in the track length correction.

The cross section σ of a cell for a track with given cylindrical coordinates angles θ and ϕ can be written as,

$$\sigma = a(a\cos(\theta) + e\sin(\theta)(\sin(\phi) + \cos(\phi))), \tag{3.5}$$

where a and e are the cell front plane length and the cell depth respectively. The volume V of the cell being defined as,

$$V = a^2 e, \quad V = \sigma \langle l \rangle ,$$

where the average track length $\langle l \rangle$ for the angles θ and ϕ is determined to be,

$$\langle l \rangle = \frac{ae}{a\cos(\theta) + e\sin(\theta)(\sin(\phi) + \cos(\phi))}. \tag{3.6}$$

The track length correction to the measured ADC value $ADC_{measured}$ is eventually set to be,

$$\overline{ADC} = ADC_{measured}\frac{e}{\langle l \rangle} \tag{3.7}$$

Residual pedestal corrections

As mentioned earlier, the electronics offsets are corrected in the FE electronics, up to the stochastic fluctuations of the VFE integrators. However, the experimental conditions change between the time the pedestal measurements are made and set into the electronics and the actual measurement can induce a drift from the measured values[f]. Though the absolute variation is observed to be modest (a typical ADC count), it is a non negligible fraction of the MIP MPV value. The residual pedestals are measured continuously in the online monitoring system. For a given period of data taking, the typical observed drifts, when applicable, are taken into account as a further correction of the measured charge for each cell.

3.3.4 Numeric gains derivation

The gathering of new numeric gains first proceeds through degaining the saved raw data in LHCb. A track-length correction is then applied, and then a modelling of the resulting ADC distribution is done. The MPV values are obtained for each channel and are eventually used for the assignment of new numetic gains.

Charge distribution degaining

For a given dataset, two charge collection distributions are built per channel with one distribution for "Even" bunch crossings and another one for "Odd" bunch crossings (hereafter referred simply as Even Bx and Odd Bx). The information saved in the LHCb stripped data are already with applied gains, using the numeric gains set at the start of 2011 data taking period. A typical distribution of ADC counts for MIPs in a single channel is shown in Figure 3.6(left). Notice the empty bins in the distribution. These empty bins, which sometimes can be two consecutive bins, are due to the gaining procedure, which electronically operates on integers. Knowing however that there is a one-to-one correspondence between the gained ADC values and the pre-gained ADC values, we can recover the distribution of the pre-gained ADC counts by a degaining method. The degaining is simply a reverse process of the gaining proceduce, but a special care is taken in order to reproduce the electronic implementation of the method. A typical distribution of the degained ADC counts can be seen in Figure 3.6(right). Track length correction, as described in Section 3.3.3, is applied to the degained ADC values.

ADC distribution modelling

Once track-length corrected, the ADC counts distribution per channel is now ready for modelling. The model used to describe the distribution is a convolution of a Landau function and a Gaussian function. The Landau distribution [94] simply represents the energy loss of MIPs in a thin scintillator. Its corresponding most probable value (MPV), denoted μ_{L}, characterizes the scintillating channel and its related electronics. In a perfectly calibrated detector, the MPVs are the same for all cells. The Landau width σ_{L} is a characteristic of the material being used. However, there are various effects which can cause the energy deposits to fluctuate. Main contributors to this fluctuation are the variable photomultiplier photostatistics and the uncertainties in the track length correction.

This fluctuation is modelled by a Gaussian function $G(x; \mu_{\mathrm{G}} = 0, \sigma_{\mathrm{G}})$, where the value of σ_{G} describes the effect. Since the Gaussian function can cause the distribution to allow

[f] Power cycling of crates is the usual culprit for these changes.

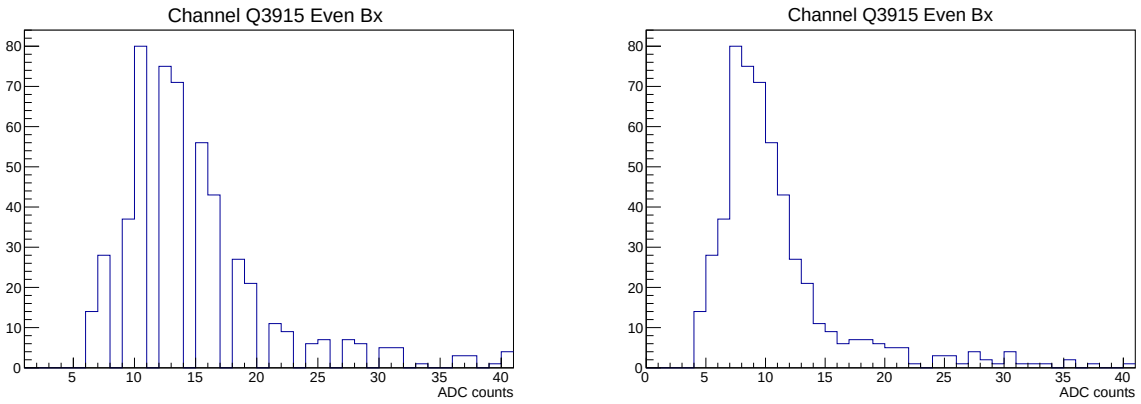

Figure 3.6: Typical ADC counts distribution of MIPs in a single channel (left) before the degaining method and (right) after degaining it.

negative values of ADC counts, it is not a good PDF when it comes to low values of ADC counts. However, since the MIP MPV position is typically in the range 7-10 ADC counts, with a resolution of ∼2 ADC, the effect is negligible for the purpose of the calibration. In the PMT reading, the statistical fluctuation of the collected charge Q is hypothesized to be directly proportional to the number of photoelectrons arriving at the first dynode. On average, the number of photoelectrons in the smallest cell is ∼25 for MIPs, implying a statistical fluctuation of 20%. Since we are measuring a charge collection of about 10 ADC for MIPs, we expect that the charge Q has a statistical fluctuation of 2 ADC counts. We therefore further constrained the value of σ_{G} by a Gaussian function of mean $\mu_C = 2$ and width of $\sigma_{\mathrm{C}} = 0.6$, where σ_{C} takes into account in the case where one of the two clear fibers is broken. The total fit model PDF is given by,

$$P(x;\mu_{\mathrm{L}},\sigma_{\mathrm{L}},\sigma_{\mathrm{G}},\sigma_{\mathrm{C}}) = \mathcal{N}\cdot[(L(x;\mu_{\mathrm{L}},\sigma_{\mathrm{L}})\otimes G_{\mathrm{G}}(x;0,\sigma_{\mathrm{G}}))]\cdot G_{\mathrm{C}}(\sigma_{\mathrm{G}};\mu_{\mathrm{C}}=2,\sigma_{\mathrm{C}})\ , \tag{3.8}$$

where $\mathcal{N}$ is the normalization of the whole PDF, G_{G} is the Gaussian function convoluting the Landau function L and the G_{C} is the gaussian constraint applied on σ_{G}. Typical fit results can be seen in Figure 3.7. The Landau MPV values are then gathered to be used for the re-calibration of the PS detector. New numeric gains are therefore collected for each channel, with one numeric gain for even bunch crossings and one for the odd bunch crossings.

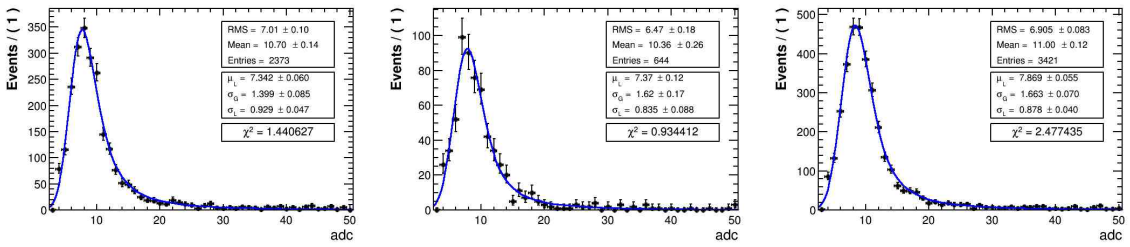

Figure 3.7: Typical fit results of the degained and track-length corrected ADC distribution. A total of 12032 of such ADC distributions is fitted with the Landau⊗Gauss model.

Residual pedestal subtraction

Prior to calculation of new numeric gains, residual pedestal subtraction is applied to the degained and track-length corrected MPV values for each channel. As mentioned in Section

3.2.3, pedestals are already corrected in the FE electronics. A drift on these values, resulting to residual pedestals, however can happen during the actual measurement. Although this is typically at the order of 1 ADC, this is not negligible for an MPV of MIPs set at around 10 ADC. Two residual pedestal measurements for each channel, one for each bunch crossing parity, are continuously measured in the online monitoring system of the LHCb detector.

Calculation of new numeric gains

The re-calibration of the PS detector involves multiplying each of the gathered MPV value by a new numeric gain factor. The objective is to uniformize the response of one board, *i.e.* intercalibrating the channels in each board. The final board-to-board calibration is done by adjusting the high voltage settings, which will be discussed in Section 3.3.5. The gain factor, as described in Section 3.2.3, is a positive number ranging from 1 to 2. With this limited range, there are channels that might be outside the adjustable range[g]. As such, a target gained ADC value is chosen, which maximizes the number of channels to be within the adjustable range. MPV values below the adjustable range are assigned with a gain factor of 2, while those above the range are assigned with a gain factor of 1.

The procedure of finding the best targeted ADC value requires to sort the MPVs of all the channels such that they are indexed in a decreasing value of MPV, *i.e.*,

$$\forall(i,j;i>j):\mu_i \leq \mu_j \ , \tag{3.9}$$

where i,j are indices of two subsequent sorted channels and μ_i, μ_j are their corresponding MPV values. One channel is chosen such that its MPV is the targeted reference MPV value, *i.e.* the assigned gain factor in this channel is 1. Among all the channels in the board, the reference channel k is chosen in a way that maximizes the number of channels which have μ_l within the range $[\mu_k/2,\ \mu_k]$. The assignment of gain factors follow, the gain factor g_l of channel l being equal to,

$$g_l = \begin{cases} 1 & \text{if } \mu_l \geq \mu_k \\ \frac{\mu_k}{\mu_l} & \text{if } \frac{\mu_k}{2} < \mu_l < \mu_k \\ 2 & \text{if } \mu_l \leq \frac{\mu_k}{2} \ . \end{cases} \tag{3.10}$$

Electronically, these factors are implemented as an 8-bit information. Hence, numeric gains are coded as 0 for a gain factor of 1; 255 for a gain factor of 2; and within 0 - 255 for gain factors in between 1 - 2.

3.3.5 HV settings

The second step of the calibration involves adjusting the high voltage settings of the multi-anode photomultipliers (Ma-PMT) in order to calibrate all the boards, consequently calibrating the whole PS detector. Each board, containing 64 or 32 channels, is connected to a single Ma-PMT. Once the (new) numeric gains are applied onto each channel, the average gained MPV per board is calculated. These average values represent the MPV of the board.

In general, the response of each channel in terms of ADC counts can be written as,

$$R_{\text{ch}} = G_{\text{ch}} \cdot \alpha_{\text{ch}} \cdot V^{\beta} \ , \tag{3.11}$$

where G_{ch} is the gain factor applied in the electronics, α_{ch} is the parameter characterizing the channel response prior to gain corrections, V is the applied voltage to the Ma-PMT

[g]Adjustable range refers to the MPV values that can be multiplied by a factor within 1 - 2 that results to the targeted value.

and β is the high voltage scaling factor. The scaling factor β has been measured using a LED calibration system and its derivation is discussed in Ref. [93]. Denoting the variables of the new HV settings with primed variables and the previous HV settings with unprimed variables, the ratio of the required new response R'_{ch} to the old response R_{ch} is given by,

$$\frac{R'_{\mathrm{ch}}}{R_{\mathrm{ch}}} = \frac{G'_{\mathrm{ch}}}{G_{\mathrm{ch}}} \left(\frac{V'}{V}\right)^{\beta} . \tag{3.12}$$

The new applied voltage to re-intercalibrate the boards, is therefore,

$$V' = V \left(\frac{\langle R'_{\mathrm{ch}} \rangle}{\langle R_{\mathrm{ch}} \rangle} \cdot \frac{G_{\mathrm{ch}}}{G'_{\mathrm{ch}}}\right)^{\frac{1}{\beta}} . \tag{3.13}$$

Equation 3.13 is used whenever a new set of voltage settings is required.

3.4 Calibration results for 2011

In order to investigate the calibration of 2011, about 100 pb^{-1} of data collected during the end of 2011 data taking is used[h]. Particularly, the data correspond to the inclusive muon stripped data of LHCb processed during the Stripping20(r1) campaign. It was checked that with this amount of data, enough number of tracks are available in the outermost cells to provide ADC distribution of MIPs.

For each channel, the ADC distribution of MIPs are gathered, degained, corrected for track-length and modelled as discussed in the previous Sections. Shown in Figures 3.8 and 3.9 are the fit results and the track occupancy of each channel displayed as a 2D map. As shown in the first column of Figure 3.8, there are more tracks passing the channels near the beam pipe than in the outermost channels of each region of the PS detector. This results to larger statistical uncertainties of the Landau function parameters in the corners of each region as can be seen in the third column of Figure 3.8, as well as in the second column of Figure 3.9.

For illustration purposes, one dimensional histogram projections of the MIP MPVs, corrected for residual pedestals, are shown in Figures 3.10 and 3.11 (separated by regions of the PS detector). The distributions are fitted with a Gaussian function to determine the mean of the distribution and its corresponding spread. As shown in the inset of the plots, the typical mean is 7, with a typical width of 1 ADC. The spread of the MPV values in each region is well-described by the normal distribution, as one would expect for correctly degained and pedestal-corrected MPV values. Up to corrections of systematic uncertainties of the degaining method, these distributions correspond to the actual ungained MPV distributions during the actual data taking. Expectedly, the precision after the gaining method meets the objective of typical 10% precision.

The absolute calibration of the PS detector during the end of the 2011 data taking campaign is checked by multiplying the degained and pedestal corrected MPV values shown in Figures 3.10 and 3.11 by the old numeric gains set in the electronics during the said period. This can be seen in Figures 3.12 and 3.13. As shown in the Figures, the widths of the distributions is typically less than 1 ADC with mean of the distributions at around 10 ADC, implying the 10% absolute calibration. Note that these MPVs are not readily extractable from the raw data due to the empty bins as discussed in Section 3.3.4 and hence the need to degain the values first, extract the Landau MPVs from the fit model and then applying the old gain factors.

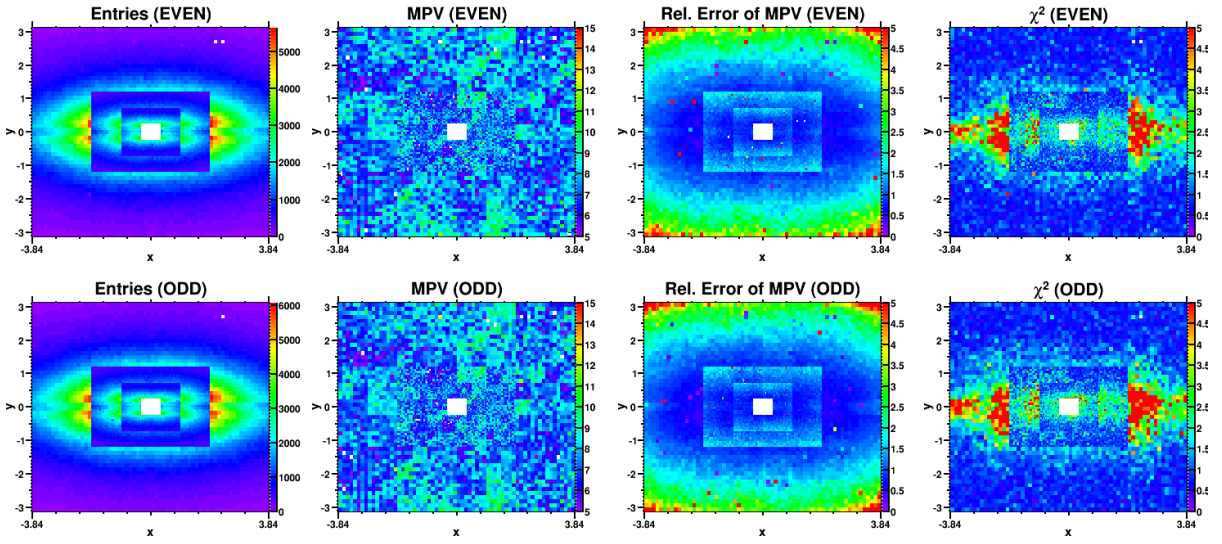

Figure 3.8: Two-dimensional maps of the (from left to right) track occupancy, Landau μ, relative uncertainty of the Landau μ and the χ^2 of the fit for each channel with 2011 data. Plots in the upper row are for the data corresponding to Even Bx, while plots in the lower row are for the Odd Bx data.

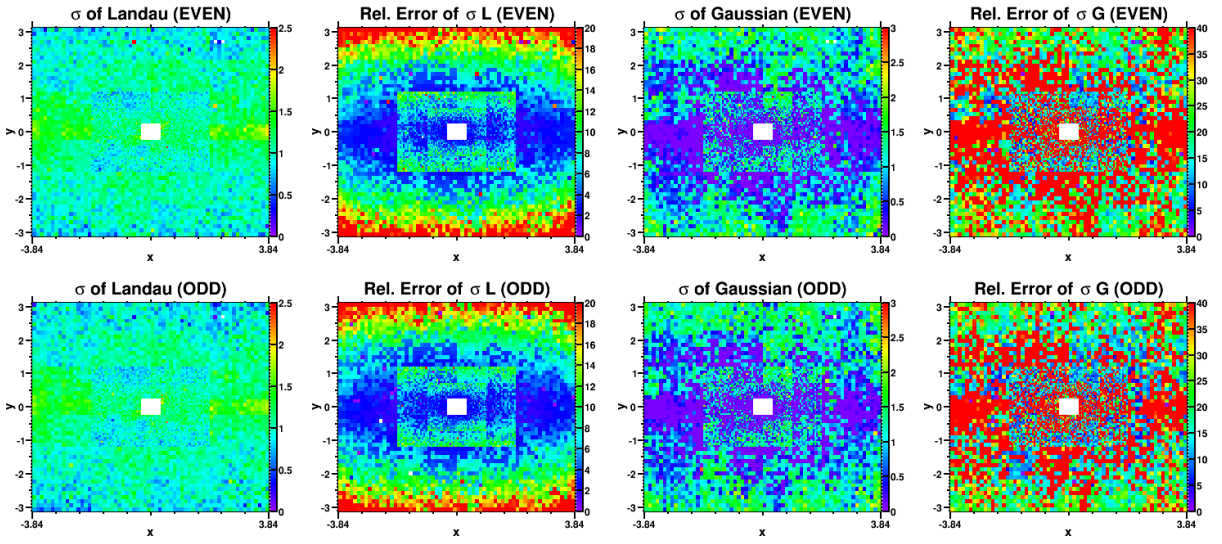

Figure 3.9: Two-dimensional maps of the (from left to right) Landau σ_{L}, relative uncertainty of σ_{L}, the Gaussian σ_{G} and the relative uncertainty of σ_{G} for each channel with 2011 data. Plots in the upper row are for the data corresponding to Even Bx, while plots in the lower row are for the Odd Bx data.

Furthermore, a new set of numeric gains are derived using the gathered degained and pedestal-corrected MPV values. The calculation of the new numeric gains follows the procedure described in Section 3.3.4. The new numeric gains are compared with the old gains to further assess *a posteriori* the PS calibration status during the end of 2011 data taking. The correlation plots, separated by PS region and bunch crossing parity, of the new gains versus the old gains are shown in Figures 3.14 and 3.15. The correlations, which are included as inset in each plot, ranges from 70% to 85%. With this level of correlation, together with

[h] These data correspond to LHC fill numbers 2210 to 2267 and LHCb run numbers 103391 to 104414 that occurred from 14 October 2011 to 30 October 2011.

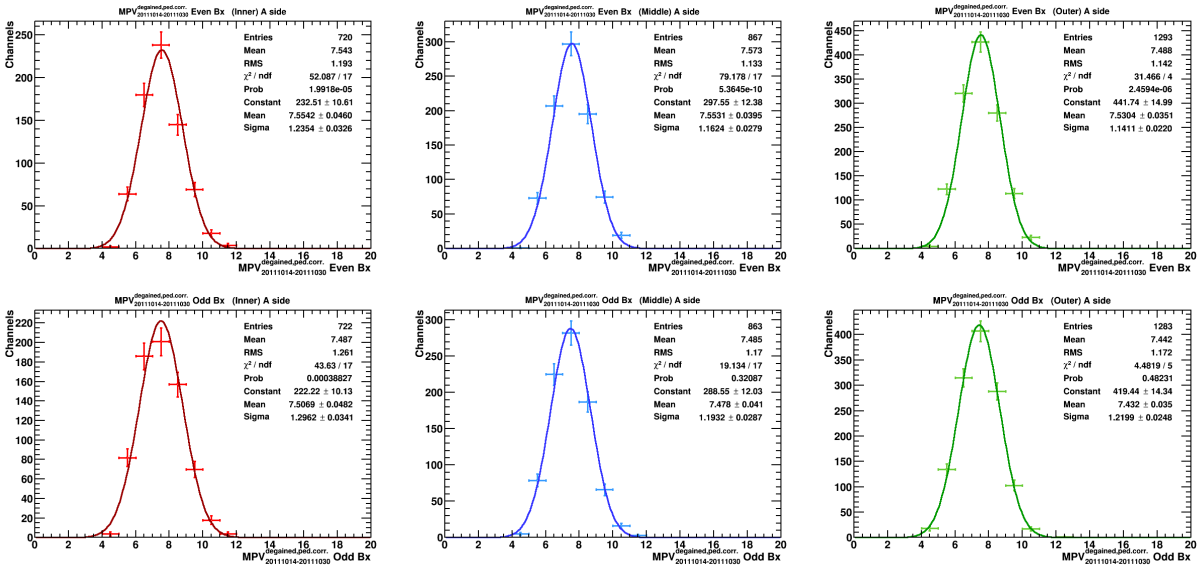

Figure 3.10: Distributions of the degained and pedestal corrected MIP MPVs fitted with a Gaussian function for (from left to right) the channels in the Inner, Middle and Outer regions of the A side of the PS detector with 2011 data. Plots in the upper column correspond to Even Bx parity, while plots in the lower column correspond to Odd Bx parity.

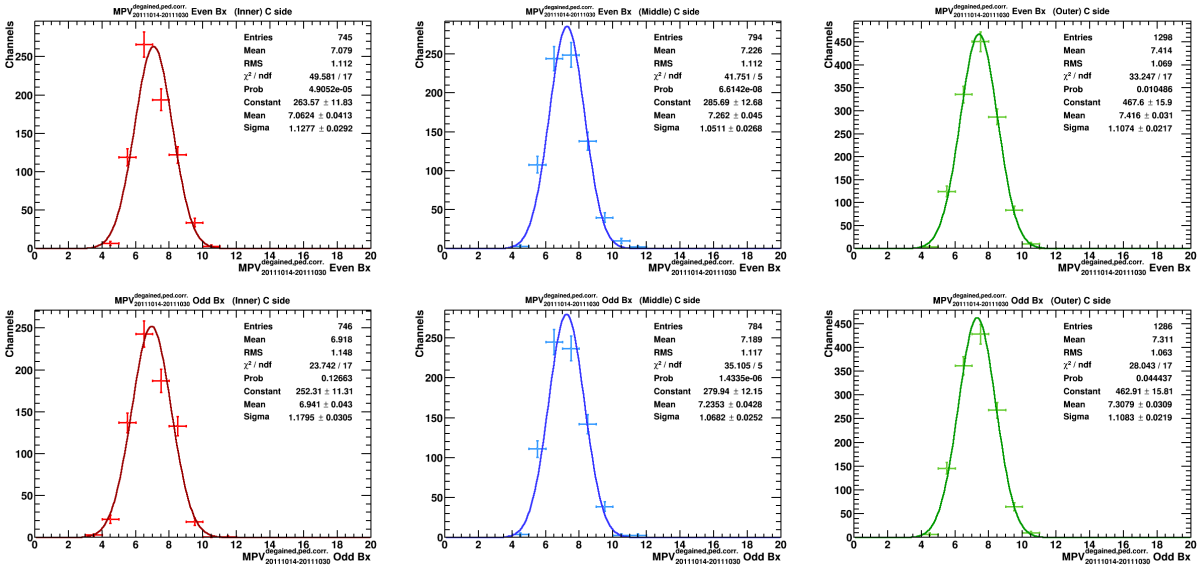

Figure 3.11: Distributions of the degained and pedestal corrected MIP MPVs fitted with a Gaussian function for (from left to right) the channels in the Inner, Middle and Outer regions of the C side of the PS detector with 2011 data. Plots in the upper column correspond to Even Bx parity, while plots in the lower column correspond to Odd Bx parity.

the derivation of absolute precision of 10% shown in Figures 3.12 and 3.13, it is verified *a posteriori* that there was no need for new set of calibration numbers for the start of 2012 data taking period.

3.5 Ageing results for 2011

The LHCb spectrometer has collected an integrated luminosity of 1 fb^{-1} during the 2011 data taking. Such amount of data could result to ageing of the detector that might require

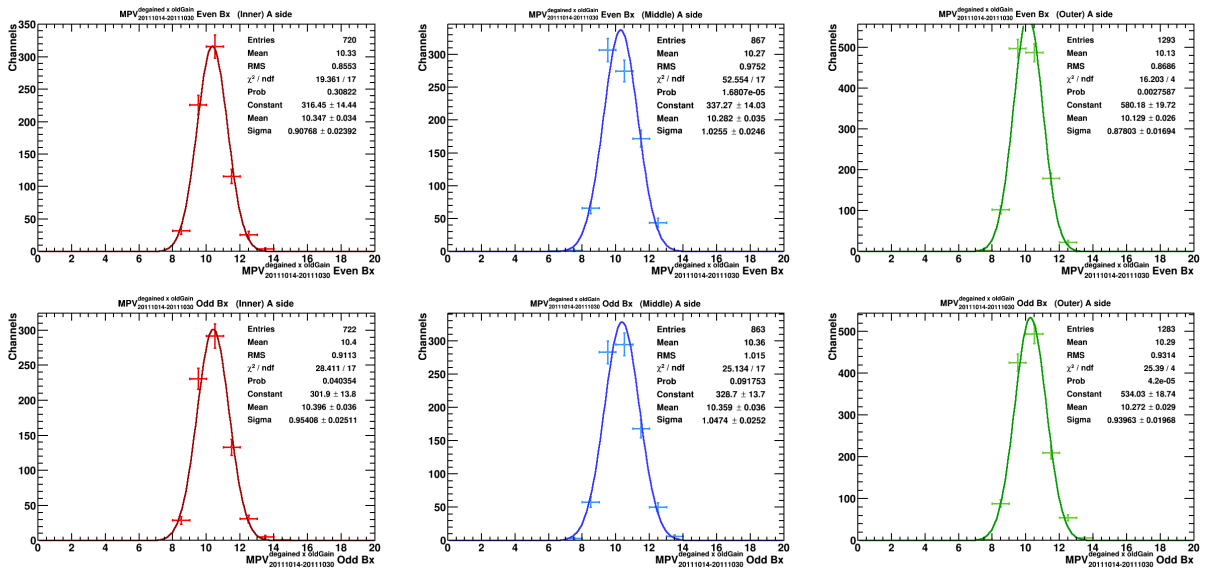

Figure 3.12: Distributions of the degained MIP MPVs multiplied by the old gain factors fitted with a Gaussian function for (from left to right) the channels in the Inner, Middle and Outer regions of the A side of the PS detector with 2011 data. Plots in the upper column correspond to Even Bx parity, while plots in the lower column correspond to Odd Bx parity.

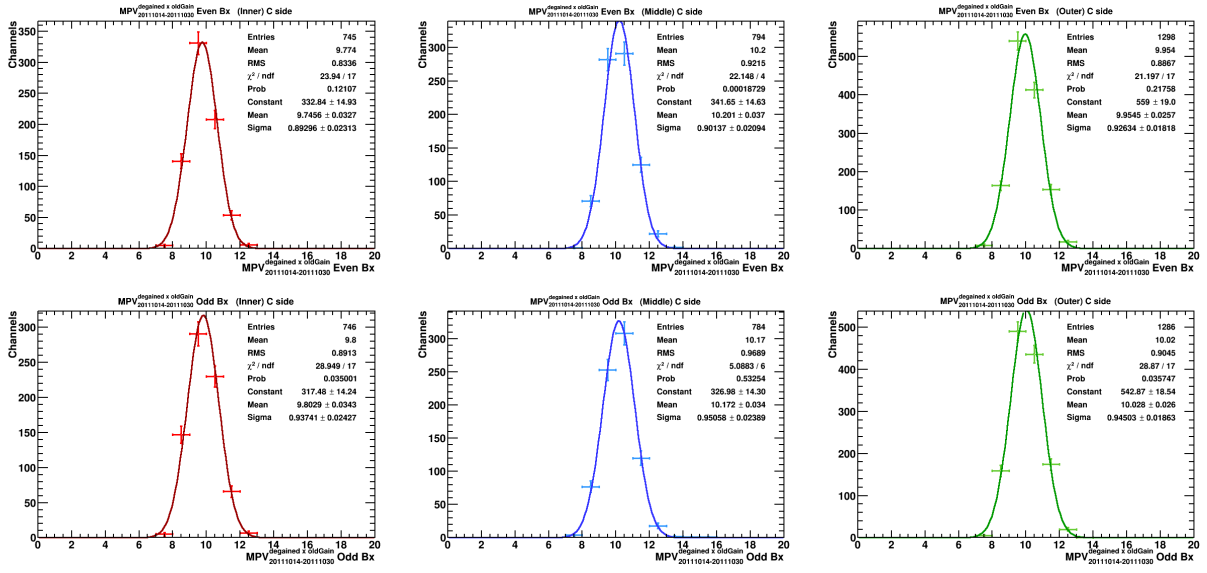

Figure 3.13: Distributions of the degained MIP MPVs multiplied by the old gain factors fitted with a Gaussian function for (from left to right) the channels in the Inner, Middle and Outer regions of the C side of the PS detector with 2011 data. Plots in the upper column correspond to Even Bx parity, while plots in the lower column correspond to Odd Bx parity.

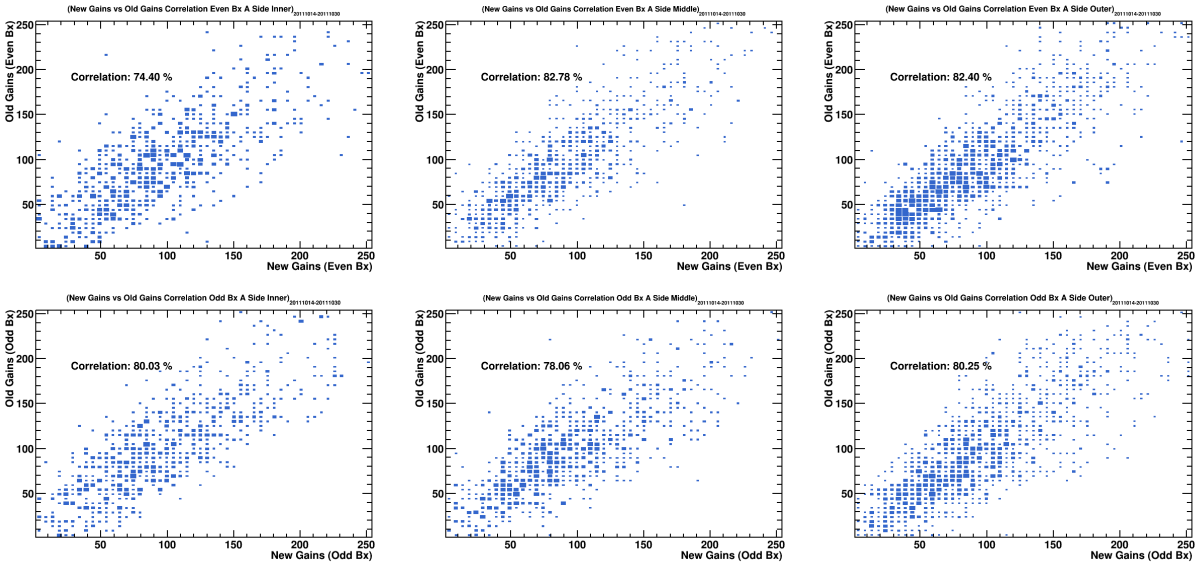

Figure 3.14: Correlation plots of new numeric gains versus old numeric gains for (from left-to-right) the channels in the Inner, Middle and Outer regions of the A side of the PS detector with 2011 data. Plots in the upper column correspond to Even Bx parity, while plots in the lower column correspond to Odd Bx parity.

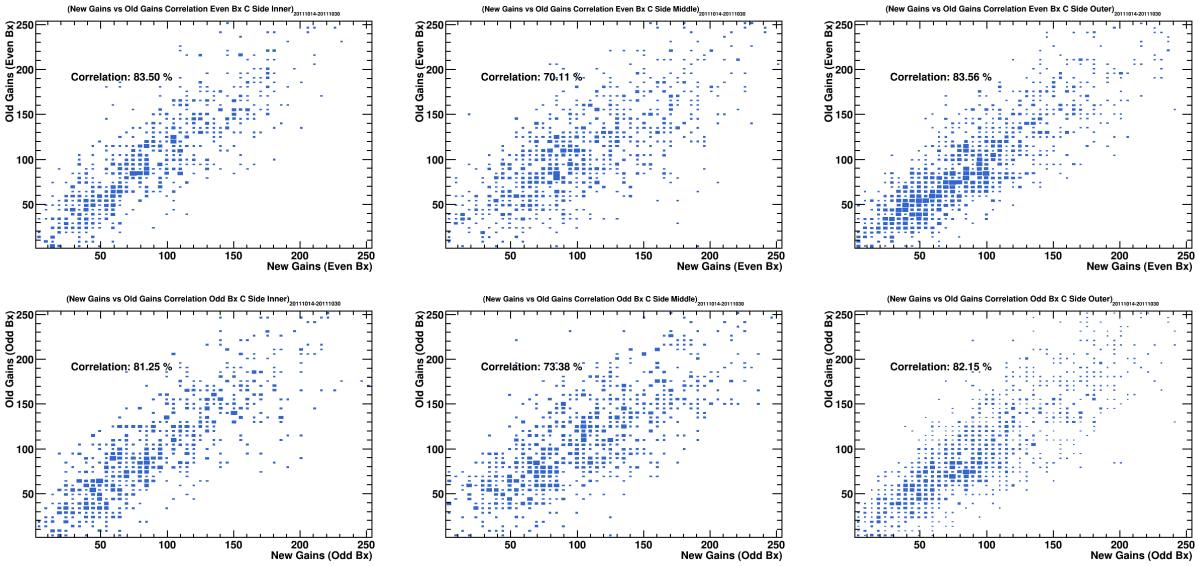

Figure 3.15: Correlation plots of new numeric gains versus old numeric gains for (from left-to-right) the channels in the Inner, Middle and Outer regions of the C side of the PS detector with 2011 data. Plots in the upper column correspond to Even Bx parity, while plots in the lower column correspond to Odd Bx parity.

corrective actions. In particular, the ageing could come from the decrease of transparency of the scintillating material and the permanent decrease of the gain of the photomultipliers. We studied the ageing effect by checking how the average MPVs of MIPs in each PS region has changed throughout the data taking period. As such, the LHCb 2011 data is divided into several samples.

3.5.1 Splitting 2011 data in periods of $\int \mathcal{L} \approx 100\,\mathrm{pb}^{-1}$

The calibration with MIPs requires large statistics samples as far as the least occupied cells are concerned. It has been chosen to sample the data per unit of 100 pb^{-1}, trying to mitigate the minimal statistics together with consistent and continuous detector operation characteristics within each sample, *i.e.* splitting the data avoiding technical stops within each sample. Summarized in Table 3.5 is the splitting of the 2011 data in approximately 100 pb^{-1} in each period. Listed as well in the table are the corresponding LHC fill numbers, LHCb run numbers and dates. A typical track occupancy in each channel can be seen in the first column of Figure 3.8 in the previous Section[i], where expectedly the occupancy is less at the corners of each region of the PS.

Table 3.5: The splitting of 2011 data.

Period	Fill Numbers [start – end]	Run Numbers [start – end]	Dates [start – end]	$\int \mathcal{L}$ (pb^{-1})
P1	1617 – 1756	87219 – 90763	Mar, 14th – May, 3rd	81.5
P2	1782 – 1844	91556 – 92929	May, 15th – Jun, 3rd	105.6
P3	1845 – 1867	92939 – 93522	Jun, 4th – Jun, 13th	98.3
P4	1868 – 1901	93550 – 94386	Jun, 14th – Jun, 28th	103.8
P5	1944 – 1996	95929 – 97587	Jul, 14th – Jul, 31st	100.8
P6	1997 – 2009	97761 – 98232	Aug, 2nd – Aug, 8th	110.6
P7	2010 – 2040	98269 – 100256	Aug, 9th – Aug, 22nd	89.0
P8	2083 – 2129	101373 – 102092	Sep, 7th – Sep, 20th	100.0
P9	2135 – 2177	102139 – 102772	Sep, 21st – Oct, 2nd	108.1
P10	2178 – 2208	102788 – 103379	Oct, 3rd – Oct, 13th	104.2
P11	2210 – 2267	103391 – 104414	Oct, 14th – Oct, 30th	106.5

3.5.2 Ageing plots for 2011

In each period listed in Table 3.5, ADC distribution of MIPs are gathered and then degained, corrected for track-length and finally modelled with Landau⊗Gauss function. The MPVs of the Landau function are averaged either by Front-End Board (FEB) or by PS region. The decreasing trend of the averaged MPVs per PS region are shown in Figures 3.16 and 3.17. We take note however the increase of the average MPVs on the A side of the PS at the end of 2011. This effect is likely coming from a decrease of the residual pedestals in the corresponding period. Defining an ageing parameter which is the relative decrease of the averaged MPV at the start of 2011 and the lowest averaged MPV among the samples, we observed a typical maximal 10% ageing.

[i] This is the same as sample P11 in Table 3.5.

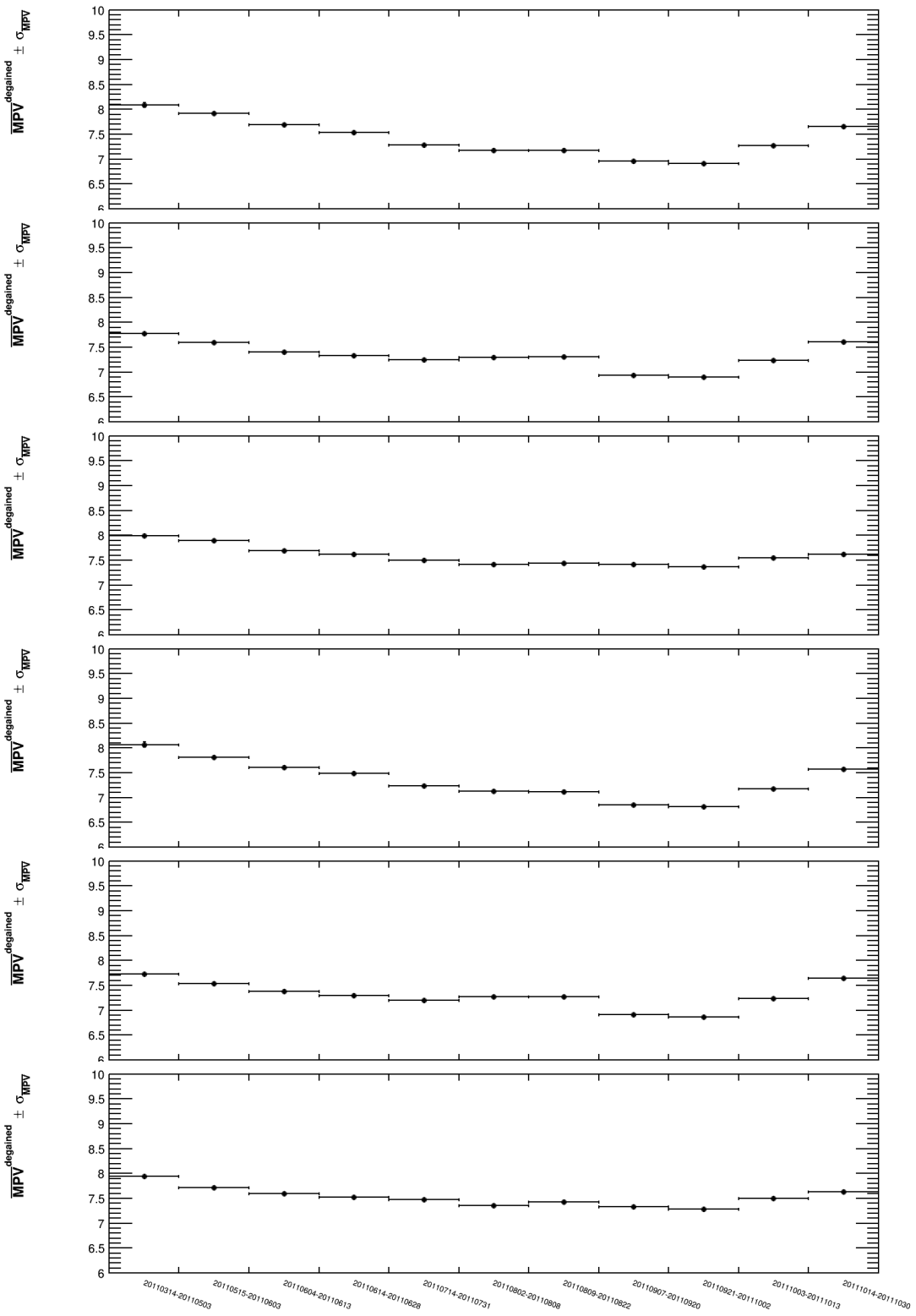

Figure 3.16: The degained MPVs with 2011 data, averaged per PS region, as a function of increasing period for (from top to bottom) the channels in the Inner, Middle and Outer regions of the A side of the PS detector, where the three uppermost plots correspond to the Even Bx and the lowermost plots correspond to Odd Bx.

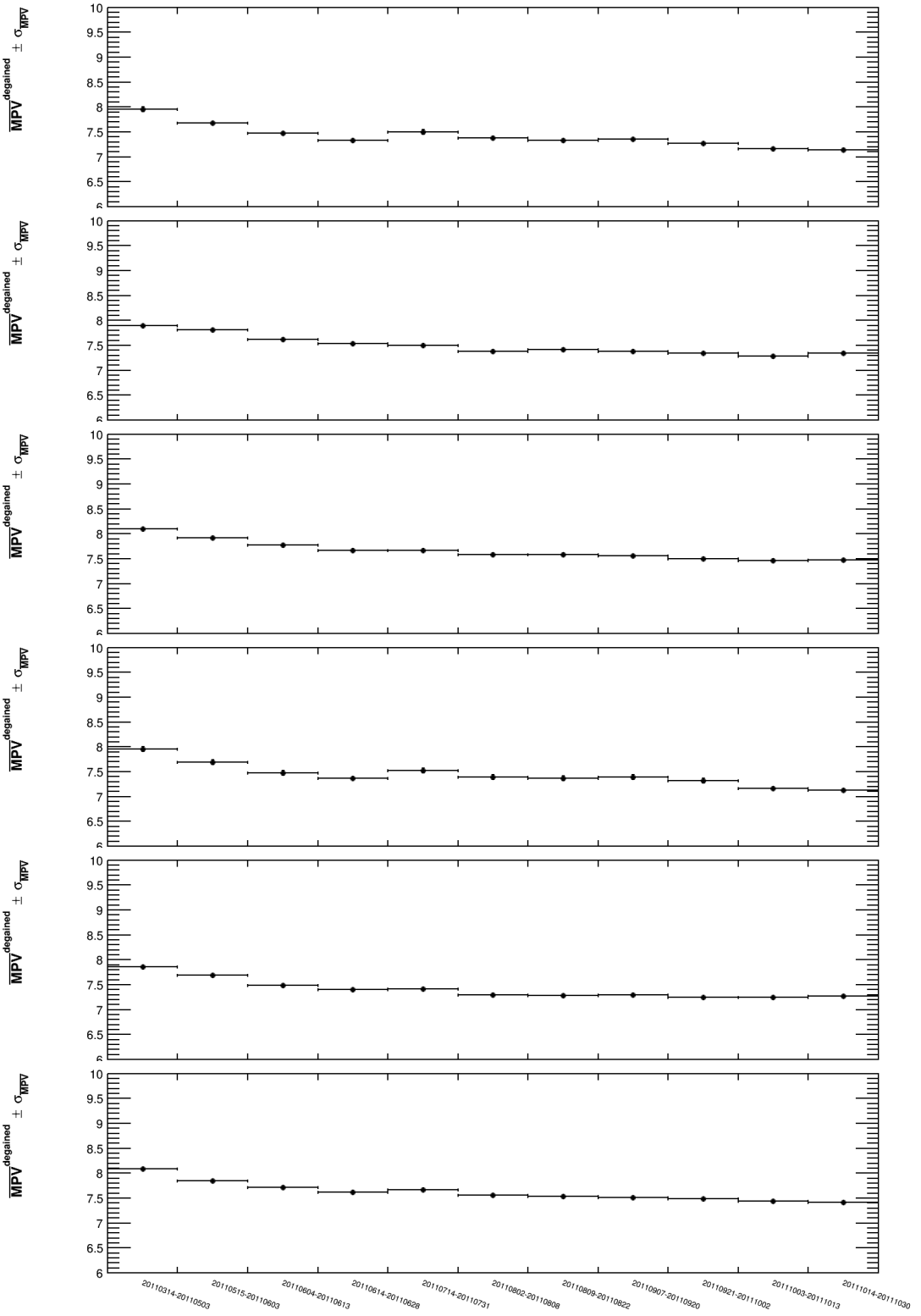

Figure 3.17: The degained MPVs with 2011 data, averaged per PS region, as a function of increasing period for (from top to bottom) the channels in the Inner, Middle and Outer regions of the C side of the PS detector, where the three uppermost plots correspond to the Even Bx and the lowermost plots correspond to Odd Bx.

3.6 Calibration results for 2012

Using the same procedure as discussed in Section 3.4, about 200 pb^{-1} of LHCb inclusive muon stripped data[j] at the end of 2012 data taking are used to investigate the PS calibration status. We increased the integrated luminosity to ~200 pb^{-1} in order to have enough statistics at the outermost corners of the PS detector. The ADC distributions of MIPs for each channel are gathered, separately for Even Bx and Odd Bx parities. A series of corrections, which includes the degaining the ADC values, correcting for track-length, modelling the resulting distribution with Landau⊗Gauss PDF and correcting for residual pedestals, leads to the distributions shown in Figures 3.18 and 3.19. Expectedly, the MPV values behave as a normal distribution, with typical mean value of 7-8 ADC and width of 1.2 ADC (shown as insets in the plots).

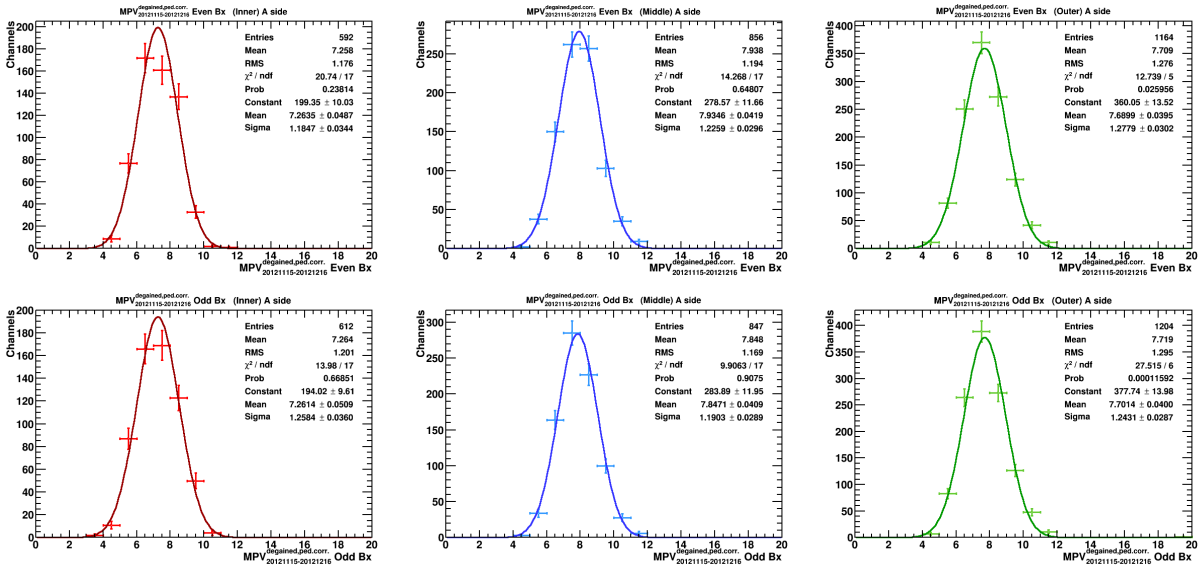

Figure 3.18: Distributions of the degained and pedestal corrected MIP MPVs fitted with a Gaussian function for (from left to right) the channels in the Inner, Middle and Outer regions of the A side of the PS detector, with 2012 data. Plots in the upper column correspond to Even Bx parity, while plots in the lower column correspond to Odd Bx parity.

The degained and pedestal corrected MPV values are multiplied back with the old gain factors in order to determine the absolute calibration of the PS at the end of the 2012 data taking. The resulting distributions, separated by PS regions, can be seen in Figures 3.20 and 3.21, showing a typical mean value of 10 ADC counts but a spread of 1.2 ADC counts. The absolute precision at the end of 2012 is therefore slightly degraded. It meets however the physics requirement of the energy correction.

Following the procedure described in Section 3.3.4, a new set of numeric gains are derived using the collection of degained and pedestal-corrected MPV values. Correlation plots between the newly-derived numeric gains and the old numeric gains are shown in Figures 3.22 and 3.23. Typically, the correlation is in the range of 60% to 75%. This is lower than the correlations between the end of 2011 and old numeric gains as presented in Section 3.4. A new set of numeric gains are therefore desirable for the start of 2015 data taking. However, the LHC Run II is starting after a long shutdown of about two years. Recovery of the tubes

[j] This data corresponds to LHC fill numbers 3287 to 3453 and LHC run numbers 132309 to 134455 that occured from 15 November 2012 to 16 December 2012.

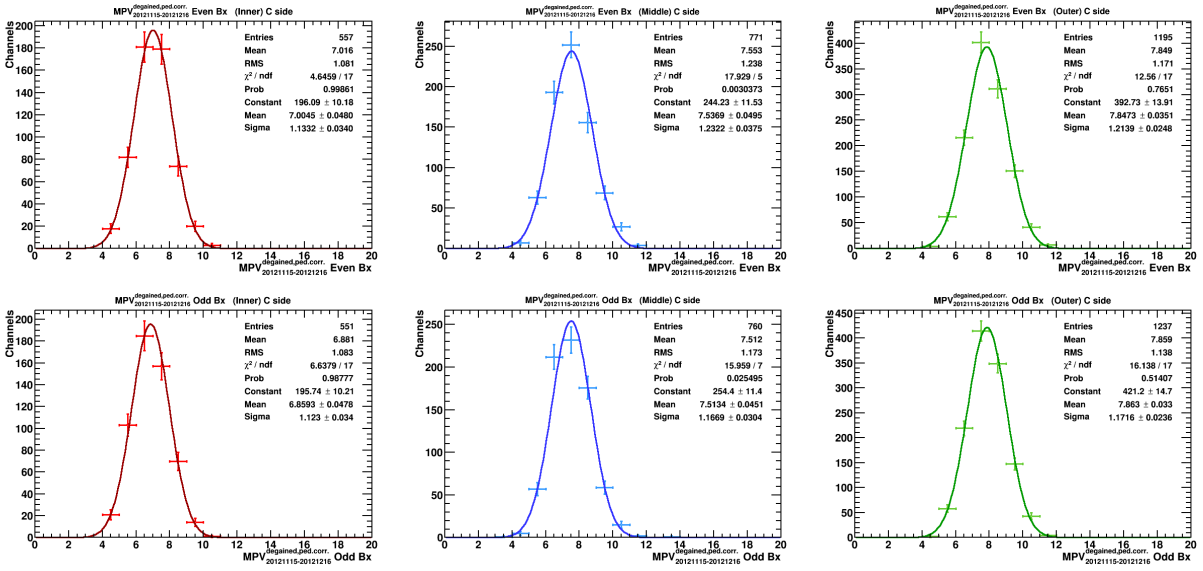

Figure 3.19: Distributions of the degained and pedestal corrected MIP MPVs fitted with a Gaussian function for (from left to right) the channels in the Inner, Middle and Outer regions of the C side of the PS detector, with 2012 data. Plots in the upper column correspond to Even Bx parity, while plots in the lower column correspond to Odd Bx parity.

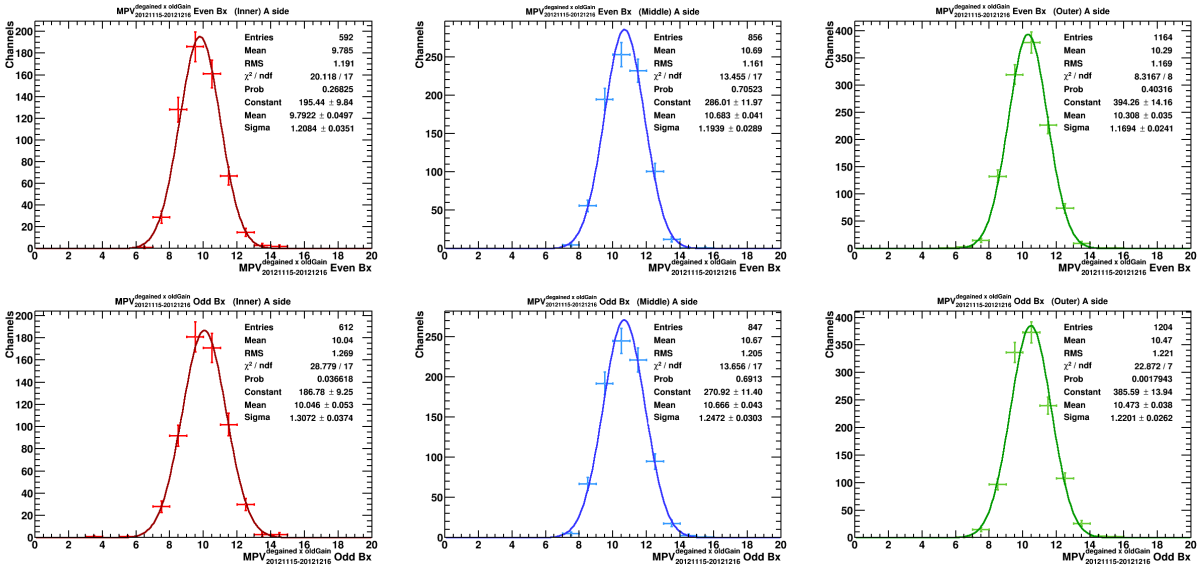

Figure 3.20: Distributions of the degained MIP MPVs multiplied by the old gain factors fitted with a Gaussian function for (from left to right) the channels in the Inner, Middle and Outer regions of the A side of the PS detector, with 2012 data. Plots in the upper column correspond to Even Bx parity, while plots in the lower column correspond to Odd Bx parity.

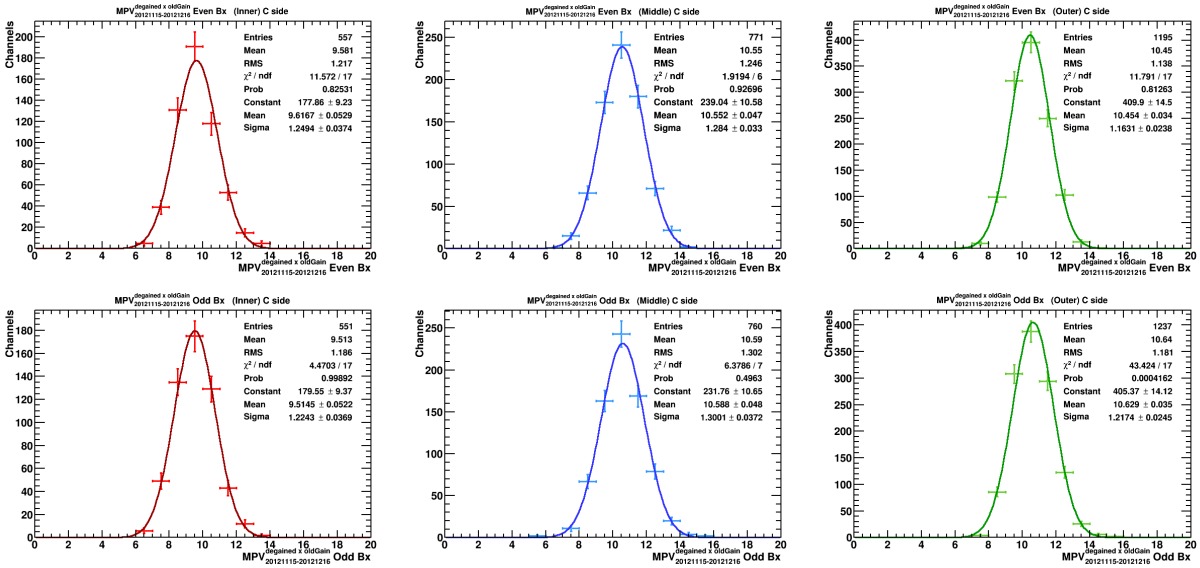

Figure 3.21: Distributions of the degained MIP MPVs multiplied by the old gain factors fitted with a Gaussian function for (from left to right) the channels in the Inner, Middle and Outer regions of the C side of the PS detector, with 2012 data. Plots in the upper column correspond to Even Bx parity, while plots in the lower column correspond to Odd Bx parity.

in particular and possible changes in experimental conditions in general make mandatory to perform a new re-calibration of the PS with the early 2015 data.

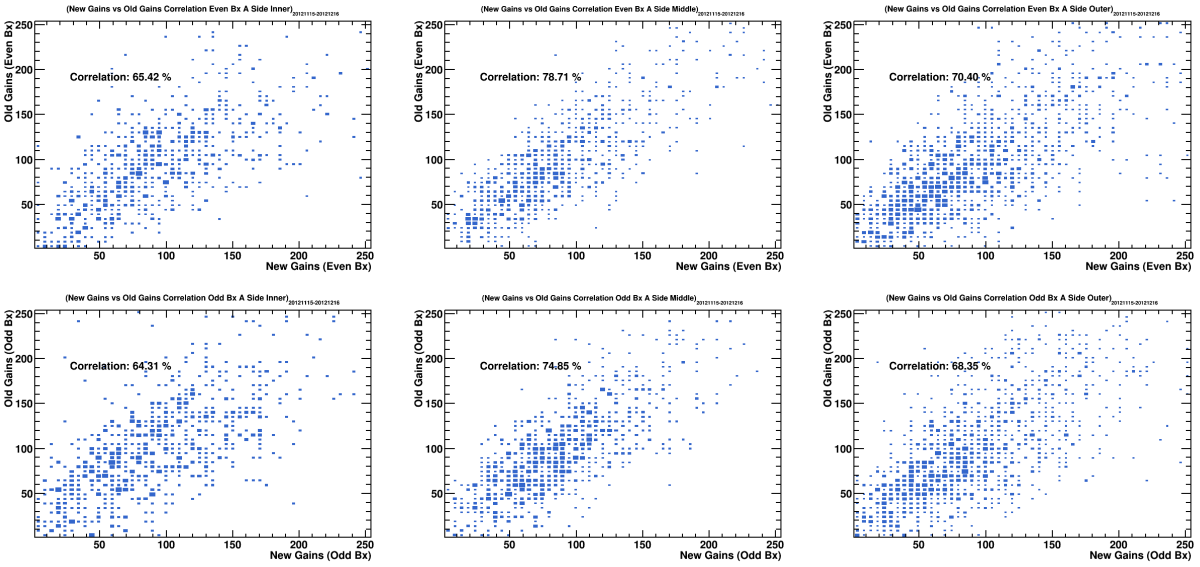

Figure 3.22: Correlation plots of new numeric gains versus old numeric gains for (from left-to-right) the channels in the Inner, Middle and Outer regions of the A side of the PS detector, with 2012 data. Plots in the upper column correspond to Even Bx parity, while plots in the lower column correspond to Odd Bx parity.

3.7 Ageing results for 2012

A total of about 2 fb^{-1} integrated luminosity has been collected by the LHCb spectrometer for the 2012 data taking campaign. Aside from a factor of 2 increase in received integrated

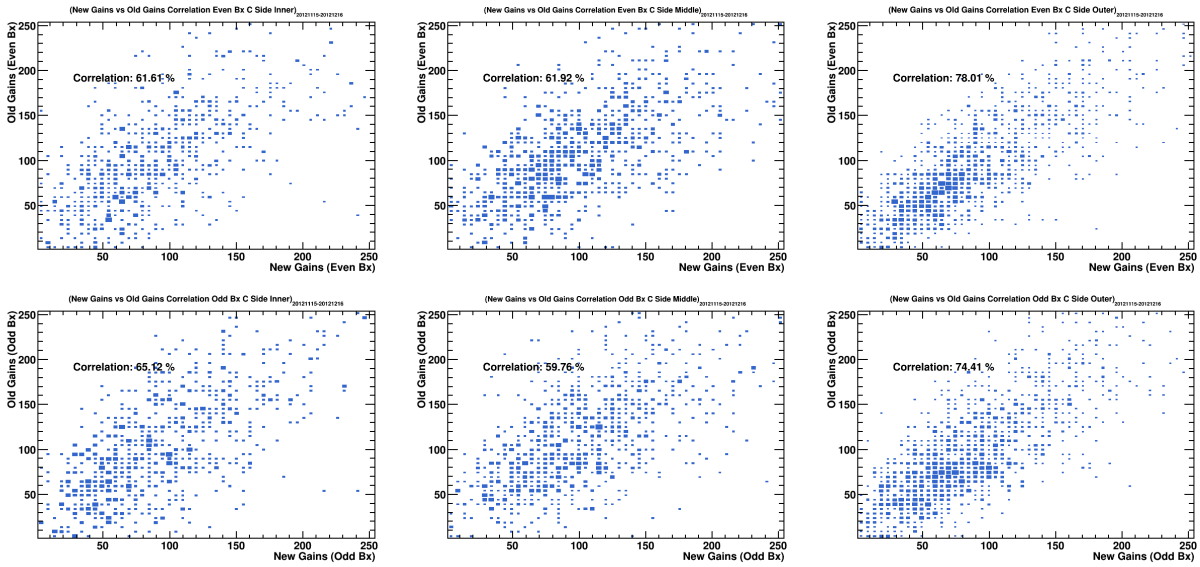

Figure 3.23: Correlation plots of new numeric gains versus old numeric gains for (from left-to-right) the channels in the Inner, Middle and Outer regions of the C side of the PS detector, with 2012 data. Plots in the upper column correspond to Even Bx parity, while plots in the lower column correspond to Odd Bx parity.

luminosity, the center-of-mass energy of the collision has also been increased from 7 TeV in 2011 to 8 TeV in 2012. This results to a busier environment and significantly more tracks traversing the PS detector. Using the same strategy as presented in Section 3.5, we studied the ageing of the PS detector by looking at the change in the average MPVs of MIPs in each PS region as a function of the data taking periods.

3.7.1 Splitting 2012 data in periods of $\int \mathcal{L} \approx 200\,\mathrm{pb}^{-1}$

The 2012 data of LHCb is divided into 8 samples, with about 200 pb^{-1} in each sample. It has been checked that with this splitting, enough number of tracks passed trough the outermost channels in order to make a fit of the MIPs ADC distribution. Technical stops are also avoided such that the same continuous detector operation characteristics occurred in each period. Table 3.6 lists the splitting of 2012 data, as well as its corresponding LHC fill number, LHCb run numbers and dates. Note that there are two periods explicitly not included here, which are the first ∼200 fb^{-1} of 2012 and another ∼200 fb^{-1} during the period of 7 October 2012 to 28 October 2012. In between each of these two periods, an accidental exchange of applied gains occurred in the electronics (perhaps due to mis-aligned time synchronization) and hence spoils a fraction of the data.

3.7.2 Ageing plots for 2012

In the same way as used in Section 3.5, the ADC response distributions of MIPs are gathered and degained, corrected for track-length and then modelled by a Landau⊗Guass PDF. This is done for each period defined in Table 3.6. The MPVs of the fitted Landau function are averaged by PS region (or by Front-End Board). In general, the averaged MPVs per PS region decreases with data taking period as can be seen in Figures 3.24 and 3.25, except for the dramatic changes in the Middle region of the A side during the last two periods. Again, this effect is likely related to an unidentified variation of the residual pedestals. A typical

Table 3.6: The splitting of 2012 data.

Period	Fill Numbers [start – end]	Run Numbers [start – end]	Dates [start – end]	$\int \mathcal{L}$ (pb^{-1})
P1	2644 – 2692	115834 – 117277	May, 19th – Jun, 4th	201.6
P2	2698 – 2736	117473 – 118792	Jun, 5th – Jun, 17th	218.5
P3	2795 – 2884	119956 – 124019	Jul, 2nd – Jul, 27th	215.0
P4	2886 – 2978	124054 – 125818	Jul, 28th – Aug, 16th	209.8
P5	2980 – 3019	125864 – 126940	Aug, 17th – Sep, 1st	197.7
P6	3020 – 3134	126972 – 129905	Sep, 2nd – Oct, 6th	209.2
P7	3236 – 3286	131093 – 132284	Oct, 29th – Nov, 14th	206.7
P8	3287 – 3453	132309 – 134455	Nov, 15th – Dec, 16th	190.3

10% ageing, defined as the relative decrease of the averaged MPV at the start of 2012 and the lowest averaged MPV among the samples, is observed.

3.8 Conclusion

This section gathered the results of an instrumental work conducted on the calibration and ageing study of the Pre-shower detector. The calibration of the PS proceeds with the study of the response of the detector cells to the passage of selected MIPs produced in proton-proton collisions. The calibration method initially developed in [93] has been strengthened as far as the electronics corrections and the fit model are concerned. It has been applied to check the stability of the detector during the Run I data taking period, in particular to measure the probable ageing of both the scintillating materials and the photomultipliers. A typical maximal ageing of 10 % was eventually observed. This level of ageing does not require any corrective action so far.

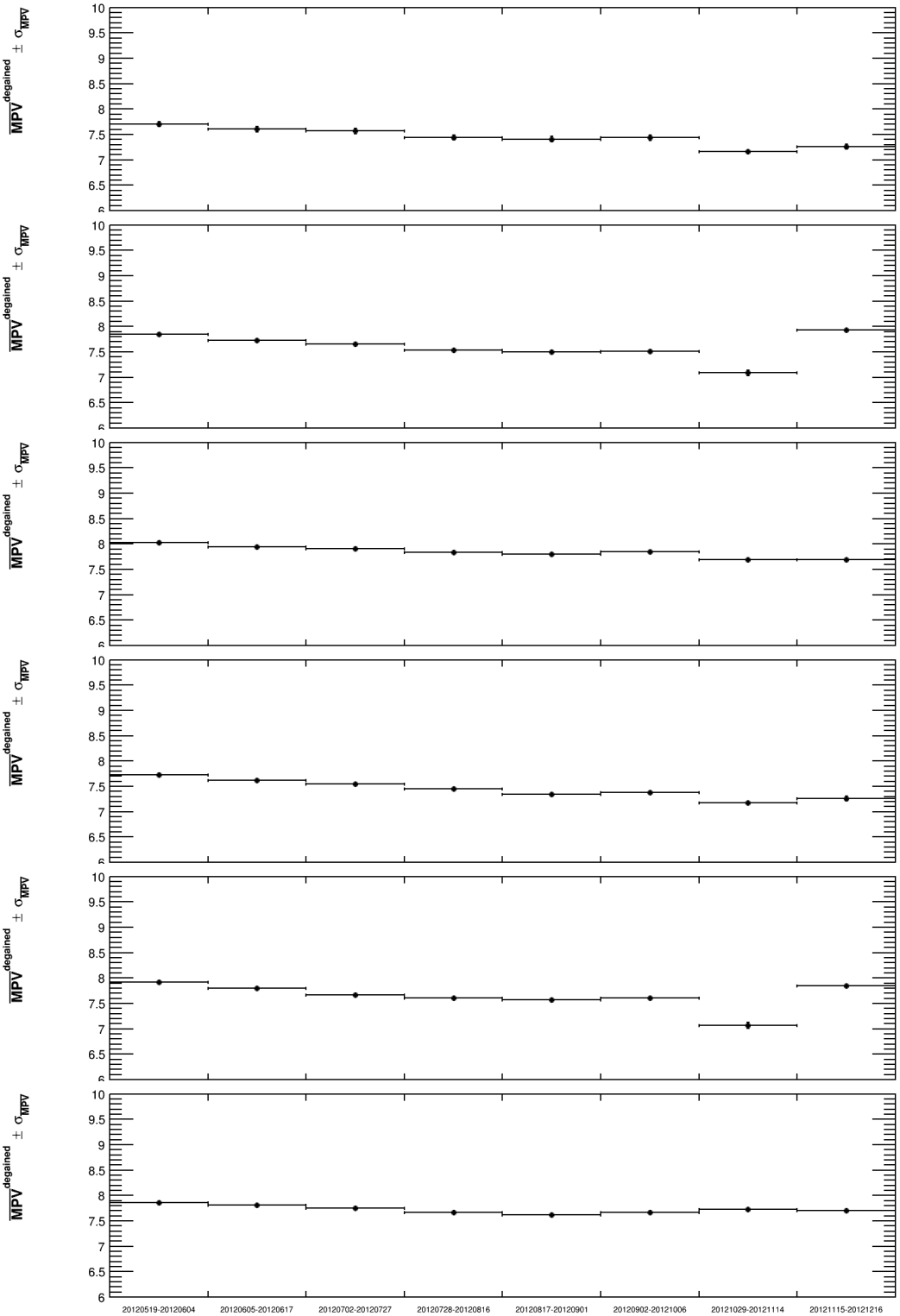

Figure 3.24: The degained MPVs with 2012 data, averaged per PS region, as a function of increasing period for (from top to bottom) the channels in the Inner, Middle and Outer regions of the A side of the PS detector, where the three uppermost plots correspond to the Even Bx and the lowermost plots correspond to Odd Bx.

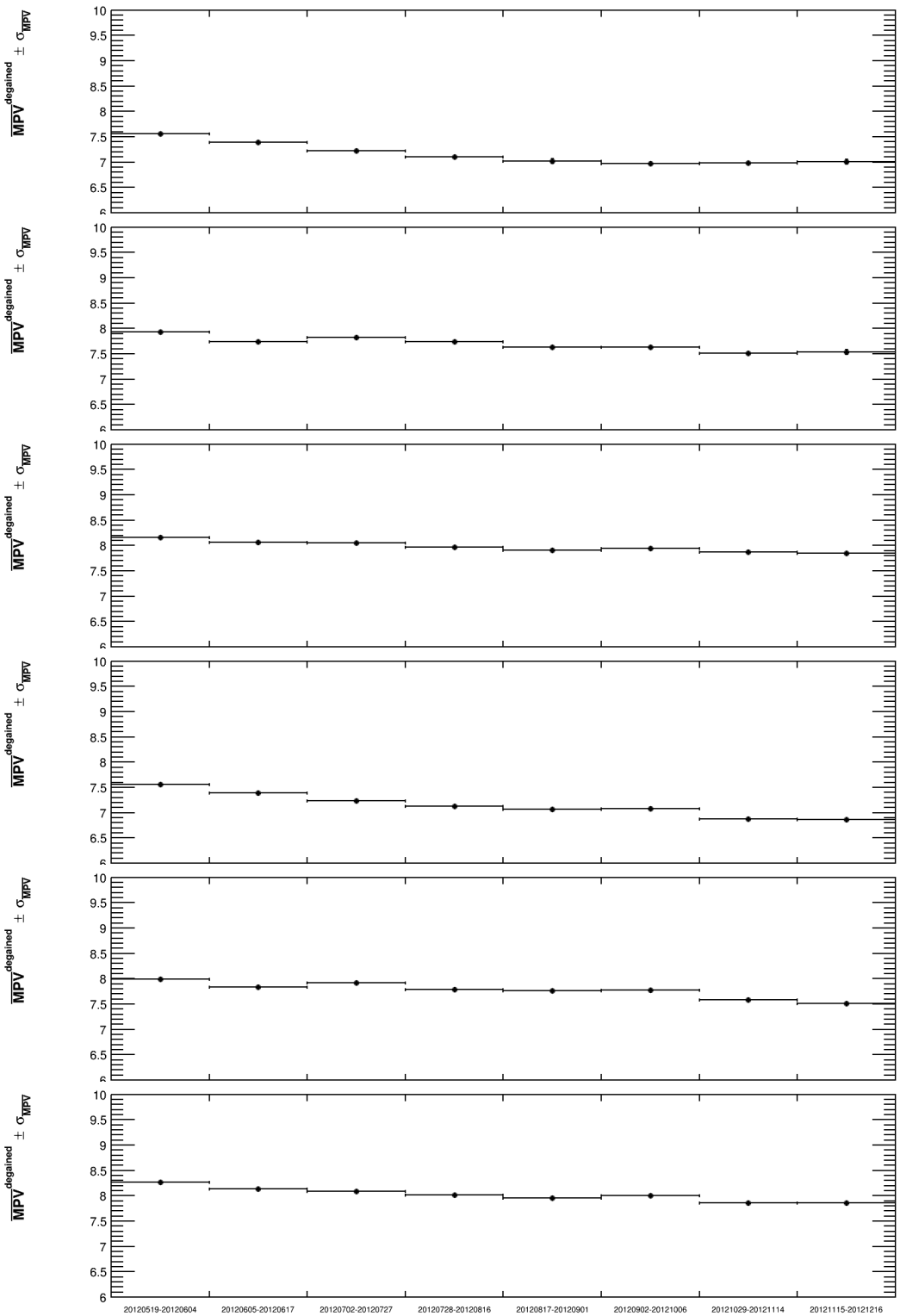

Figure 3.25: The degained MPVs with 2012 data, averaged per PS region, as a function of increasing period for (from top to bottom) the channels in the Inner, Middle and Outer regions of the C side of the PS detector, where the three uppermost plots correspond to the Even Bx and the lowermost plots correspond to Odd Bx.

Chapter 4

Branching fraction limit determination of $B_s^0 \to K_S^0 K^+ K^-$

Contents

4.1 Introduction

In the introduction of the theoretical context of this thesis, we took note that the *CP*-violating phase emerging from the Cabibbo-Kobayashi-Maskawa paradigm is enough to describe all *CP*-violating observables measured so far in particle systems [42]. The existence of new sources of *CP* violation in addition to that predicted by the CKM matrix is made necessary to account for the baryonic asymmetry in the Universe [95] and an appealing approach to it consists in searching for new sources of *CP* violation in the decay-time distribution of neutral B meson decays to *CP*-eigenstates hadronic final states mediated by a $b \to s$ loop amplitude (so-called penguin amplitude). Many measurements have been performed by the Babar and Belle experiments in that respect, such as B^0 decays to ϕK_S^0 or $\eta' K_S^0$ to cite only the most sensitive. Gathering all of these studies, the latest results [40] provide a consistent picture with the SM predictions, demanding an improved precision to increase the sensitivity to new *CP*-violating phases.

The final states $B^0 \to K_S^0 \pi^+ \pi^-$ and $B^0 \to K_S^0 K^+ K^-$ allow for the measurement of the weak phase of B^0-$\overline{B}^0$ mixing in $b \to q\bar{q}s$ transitions, which can be obtained, for example, by a time-dependent analysis of the three-body Dalitz plane. The comparison of the weak phase extractions in $b \to q\bar{q}s$ and $b \to c\bar{c}s$ transitions can be a measure of New Physics (NP) contributions in the $\Delta F = 1$ $b \to s$ decay, under the assumption that the $b \to c\bar{c}s$ transition is dominated by Standard Model processes. Similarly, the final states $B_s^0 \to K_S^0 \pi^+ \pi^-$ and $B_s^0 \to K_S^0 K^+ K^-$ would offer a window to measure NP contributions in the $\Delta F = 1$ $b \to s$ decay in comparing the weak phase of B_s^0-$\overline{B}_s^0$ mixing determinations in $b \to q\bar{q}s$ and $b \to c\bar{c}s$ transitions. A more promising mode in that respect given the current reconstructed statistics could be the decay $B_s^0 \to K_S^0 K^{\pm} \pi^{\mp}$. The first Dalitz analysis of it is ongoing. On a similar note, the Dalitz plane analysis of the decays $B_s^0 \to K_S^0 K^+ K^-$ and $B_s^0 \to K_S^0 \pi^+ \pi^-$ are

necessary inputs in various methods to determine the CKM phase γ in charmless transitions [96–100].

The first step towards these physics goals is to establish the signals with the LHCb spectrometer and measure their branching fractions. The aim of the updated study is to improve the sensitivity on the unobserved $K^0_S h^+ h^-$ modes of the previous analysis [101] and to improve the significance of the measured ones. Furthermore, we aim also to quantify the branching fractions of the observed modes relative to the mode $B^0 \to K^0_S \pi^+ \pi^-$ which has been precisely measured at the B-factories [102, 103]. Table 4.1 summarizes the current experimental knowledge of the branching fractions of these modes at the moment of this work.

Table 4.1: State of the art of the experimental results for branching fractions of $B^0_{d,s} \to K^0_S h^\pm h'^\mp$ modes [40] prior to this work.

Decay Mode	Branching Fraction (10^{-6})			
	BaBar	Belle	LHCb	World Average
$B^0 \to K^0 \pi^+ \pi^-$	50.2 ± 2.3	47.5 ± 4.4		49.6 ± 2.0
$B^0 \to K^0 K^\pm \pi^\mp$	6.4 ± 1.2	< 18	5.8 ± 2.0	6.4 ± 1.2
$B^0 \to K^0 K^+ K^-$	23.8 ± 2.6	28.3 ± 5.2	26.3 ± 5.1	24.7 ± 2.3
$B^0_s \to K^0 \pi^+ \pi^-$	–	–	11.9 ± 5.5	–
$B^0_s \to K^0 K^\pm \pi^\mp$	–	–	97 ± 21	–
$B^0_s \to K^0 K^+ K^-$	–	–	4.2 ± 2.6	–

It is beyond the scope of this manuscript to present the full analysis and I refer the interested reader to the publication [16]. Instead, I will focus on my specific contribution to this paper. The decay modes $B^0_s \to K^0_S \pi^+ \pi^-$ and $B^0_s \to K^0_S K^+ K^-$ were not observed prior to this study. The decay mode $B^0_s \to K^0_S \pi^+ \pi^-$ has been observed for the first time in this search while the measured number of $B^0_s \to K^0_S K^+ K^-$ decays was not significant. Namely, the fit results for $B^0_s \to K^0_S K^+ K^-$ was only 6±4 for Down-Down (DD) K^0_S reconstruction category[a] and 3±3 for Long-Long (LL), as reported in Ref. [16]. A naive estimate of the significance results in about 2 standard deviations and hence a limit has to be set instead of a branching fraction measurement. A frequentist approach has been designed to determine this limit. The method and the results we obtained are discussed in this Chapter.

4.2 Using Feldman-Cousins "cut-and-count" strategy

The usual procedure of quoting a one-sided or two-sided limit is to employ the "cut-and-count" strategy of Feldman-Cousins inference as presented in Ref. [104]. In this procedure, the probability density function of observing a quantity n given μ is a Poisson distribution:

$$P(n|\mu) = (\mu + b)^n \exp(-(\mu + b))/n! \tag{4.1}$$

where n is the sum of signal and background events, μ is the unknown mean of the signal distribution (a Poisson distribution) which we want to infer, and b is the known mean of the background distribution (also a Poisson distribution). We construct an interval,

$$\int_{\mu_1}^{\mu_2} P(\mu_t|n_0) d\mu_t = \alpha \tag{4.2}$$

[a] See Section 2.3.2 for discussion on Downstream and Long tracks.

where μ_1 is the lower limit, μ_2 is the upper limit, $P(\mu_t|n_0)$ is the probability density of finding the true value μ_t given that the observed events is n_0, and α is the desired confidence level (C.L.).

Using the fit function (total PDF) used in the search for $B^0_{(s)} \to K^0_S K^+ K^-$ and counting naively the yield in the range -2σ to +2σ of the nominal B^0_s mass, we got $n_0 = 21$ and $b = 15$ for DD, while $n_0 = 10$ and $b = 7$ for LL. Targetting a 90% C.L., this gives us a two-sided limit on true value μ_t ([0.383, 14.996]) in the case of DD, and an upper limit (≤ 9.501) on μ_t in the case of LL. Converting these limits on μ_t to branching ratio of $B^0_s \to K^0_S K^+ K^-$ to the normalization decay mode $B^0 \to K^0_S \pi^+ \pi^-$ using,

$$\mathcal{B}_{\mathrm{KK}/\pi\pi} = \left(\frac{\epsilon_{\pi\pi}}{\epsilon_{\mathrm{KK}}}\right)\left(\frac{N_{\mathrm{KK}}}{N_{\pi\pi}}\right)\left(\frac{1}{f_s/f_d}\right) \tag{4.3}$$

we got the following limits on the $\mathcal{BF}_{\mathrm{KK}/\pi\pi}$,

$$\frac{\mathcal{B}(B^0_s \to K^0_S K^+ K^-)}{\mathcal{B}(B^0 \to K^0_S \pi^+ \pi^-)}_{\mathrm{Down-Down}} \quad \epsilon \ [0.004, 0.159] \quad @\ 90\%\ \mathrm{C.L.} \tag{4.4}$$

$$\frac{\mathcal{B}(B^0_s \to K^0_S K^+ K^-)}{\mathcal{B}(B^0 \to K^0_S \pi^+ \pi^-)}_{\mathrm{Long-Long}} \quad \leq \ 0.132 \quad @\ 90\%\ \mathrm{C.L.} \tag{4.5}$$

4.3 This limit calculation

Instead of using the Poisson law as probability density function in a usual cut-and-count experiment as described in the previous subsection, we instead use a Gaussian probability density function. This will allow us to consider the total uncertainty as the quadratic sum of the systematic and statistical uncertainties and take benefit of the fit result. The procedure for constructing the confidence belt is summarized below:

- Using pure toy studies, 100 toys are generated for each $N_{\mathrm{gen}} \ \epsilon \ \{0, 5, 10, 15\}$ both for Down-Down and Long-Long. For each toy, we plot the number of fitted events N_{fit} and found out that N_{fit} is normally distributed. The same is also true for the σ of the fitted events, where σ is the error of the fit of each toy and not the standard deviation of the Gaussian distribution of N_{fit}.

- The N_{fit} for each value of N_{gen} is then fitted with a Gaussian function (See sample plot shown in Figure 4.1). The mean of Gaussian distribution, $\overline{N_{\mathrm{fit}}}$, versus N_{gen} can be well-described by a linear function both for DD and LL, as shown in Figure 4.2(top), and hence we use it here. The line functions are given by,

$$\overline{N_{\mathrm{fit}}} = (0.347^{+0.314}_{-0.314}) + (0.935^{+0.044}_{-0.044}) \times N_{\mathrm{gen}} \qquad \text{for DD} \tag{4.6}$$

$$\overline{N_{\mathrm{fit}}} = (-0.403^{+0.262}_{-0.262}) + (1.036^{+0.033}_{-0.033}) \times N_{\mathrm{gen}} \qquad \text{for LL} \tag{4.7}$$

  Small biases can be observed for both DD and LL at $N_{\mathrm{gen}} = 0$.

- The error σ for each N_{fit} is also normally distributed. We fit it with a Gaussian function and plot the square of the mean of the Gaussian distribution, $\overline{\sigma}^2$, versus N_{gen}. These can be parametrized by a linear function as shown in Figure 4.2(bottom). The line functions are given by,

$$\overline{\sigma}^2 = (9.555^{+0.403}_{-0.403}) + (1.073^{+0.051}_{-0.051}) \times N_{\mathrm{gen}} \qquad \text{for DD} \tag{4.8}$$

$$\overline{\sigma}^2 = (3.946^{+0.355}_{-0.355}) + \quad (1.089^{+0.039}_{-0.039}) \times N_{\text{gen}} \qquad \text{for LL} \tag{4.9}$$

The error σ described here is considered as the statistical error, hereafter referred as σ_{stat}.

- We also consider the systematic uncertainties in our construction of the confidence belt. These systematics uncertainties come from the selection efficiency of $B_s^0 \to K_S^0 K^+ K^-$ (ϵ_{KK}), selection efficiency of $B^0 \to K_S^0 \pi^+ \pi^-$ ($\epsilon_{\pi\pi}$), the number of observed $B^0 \to K_S^0 \pi^+ \pi^-$ events ($N_{\pi\pi}$), and the uncertainty from hadronization fraction f_s/f_d. These are the quantities used to derive the expected signal yield N_{gen} for a given relative branching fraction $\mathcal{B}_{\text{KK}/\pi\pi}$,

$$N_{\text{gen}} = (\mathcal{B}_{\text{KK}/\pi\pi}) \frac{\epsilon_{\text{KK}}}{\epsilon_{\pi\pi}} (N_{\pi\pi})(f_s/f_d) \tag{4.10}$$

  As such, the systematic uncertainty is given by,

$$\sigma^2_{\text{sys}} = \sigma^2_{N_{\text{gen}}} = \left(\frac{\sigma^2_{\epsilon_{\text{KK}}}}{\epsilon^2_{\text{KK}}} + \frac{\sigma^2_{\epsilon_{\pi\pi}}}{\epsilon^2_{\pi\pi}} + \frac{\sigma^2_{N_{\pi\pi}}}{N^2_{\pi\pi}} + \frac{\sigma^2_{f_{sd}}}{f^2_{sd}} \right) N^2_{\text{gen}} \tag{4.11}$$

- A Gaussian PDF is then constructed for each hypothesized $\mathcal{B}_{\text{KK}/\pi\pi}$ with mean $\overline{N_{\text{fit}}}$ calculated from Equations 4.6 for DD (4.7 for LL) and 4.10. The standard deviation, σ_{tot}, of the Gaussian PDF is the quadratic sum of the statistical and systematic uncertainties. Take note that σ_{tot} increases with $\mathcal{B}_{\text{KK}/\pi\pi}$ since σ_{sys} and σ_{stat} are linear functions of N_{gen}, and N_{gen} is proportional to $\mathcal{B}_{\text{KK}/\pi\pi}$. At $\mathcal{B}_{\text{KK}/\pi\pi} = 0$ however, the remaining uncertainty is due to the constant part of the statistical uncertainty as given in Equation 4.8 for DD (or Equation 4.9 for LL).

For each value of hypothesized relative branching fraction, we construct a 90% confidence interval. This confidence interval is constructed by choosing which interval of the Gaussian PDF shall be included[b]. Using the ranking procedure of Feldman & Cousins [104], the Gaussian PDF is divided into several small intervals and each interval has a corresponding rank, given by,

$$R(x) = \frac{P(x|\mu, \sigma)}{P(x|\mu_{best}, \sigma)} \ . \tag{4.12}$$

The μ_{best} is chosen to be the best physically allowed mean. This means that μ_{best} is equal to x when x is non-negative, and 0 otherwise, resulting to the following equations,

$$R(x) = \begin{cases} e^{-(x-\mu)^2/2\sigma^2} & \text{if } x \geq 0 \\ e^{(2x\mu - \mu^2)/2\sigma^2} & \text{if } x < 0 \end{cases}$$

Starting from the highest ranked interval, the probability for each small interval given by $P(x + dx|\mu, \sigma)$ is added until the 90% requirement is reached.

4.3.1 Down-Down

The 90% confidence belt for the Down-Down category is shown in Figure 4.3. The observed number of $B_s^0 \to K_S^0 K^+ K^-$ events for the Down-Down category is 6±4, resulting to a two-sided limit $0.003 \leq \mathcal{B}_{\text{KK}/\pi\pi} \leq 0.066$ @ 90% confidence level.

[b] In Neyman's ordering procedure, the 90% confidence interval of a Gaussian PDF is the range $[\mu - 1.64\sigma, \mu + 1.64\sigma]$. In this study, we use the Feldman-Cousins ordering principle as this procedure avoids the concept of "flip-floping".

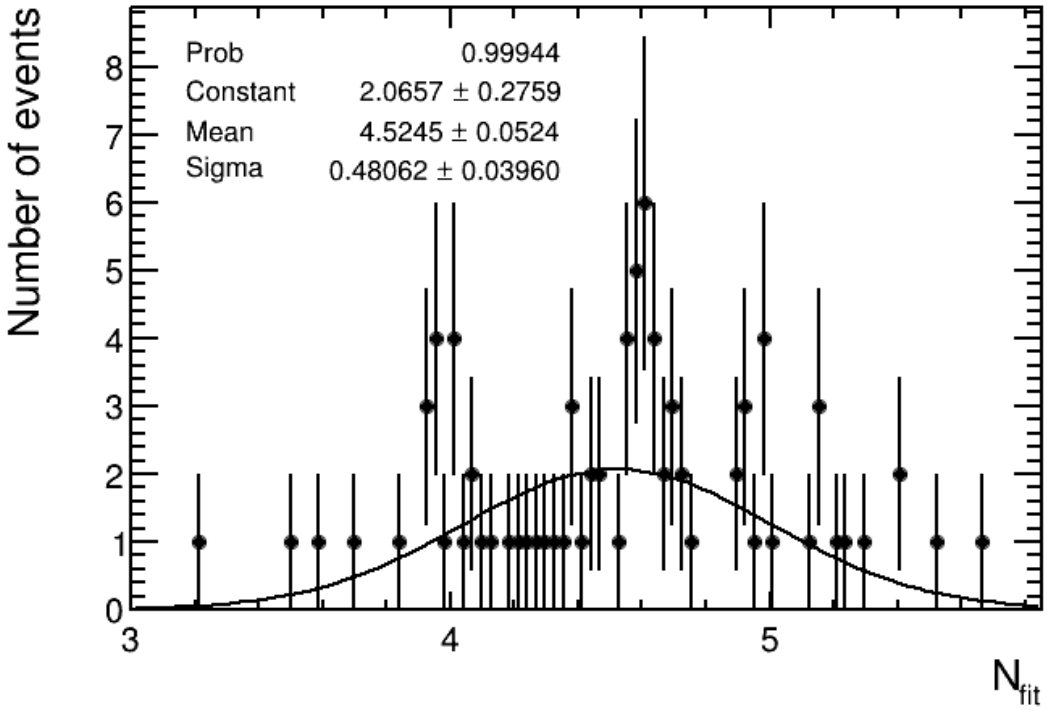

Figure 4.1: Distribution of N_{fit} fitted with a Gaussian function. This sample histogram is for LL with N_{gen} set to 5.

4.3.2 Long-Long

The 90% confidence belt for the Long-Long category is shown in Figure 4.4. The observed number of $B_s^0 \to K_S^0 K^+ K^-$ events for the Long-Long category is 3±3, resulting to a one-sided limit $\mathcal{B}_{KK/\pi\pi} \leq 0.130$ @ 90% confidence level.

4.3.3 Down-Down and Long-Long Combined

The two Gaussian probability density functions from Down-Down and Long-Long are then combined to make a final 90% confidence belt and confidence interval. The combined probability density function is the product of the two Gaussian PDF, which is also a Gaussian PDF whose mean μ and standard deviation σ are given by Equations 4.13 and 4.14.

$$\mu = \frac{\sigma_{\text{LL}}^2 \mu_{\text{DD}} + \sigma_{\text{DD}}^2 \mu_{\text{LL}}}{\sigma_{\text{DD}}^2 + \sigma_{\text{LL}}^2} \tag{4.13}$$

$$\sigma = \sqrt{\frac{\sigma_{\text{DD}}^2 \sigma_{\text{LL}}^2}{\sigma_{\text{DD}}^2 + \sigma_{\text{LL}}^2}} \tag{4.14}$$

Since the number of observed $B_s^0 \to K_S^0 K^+ K^-$ events is 6±4 for the case of Down-Down and 3±3 for the Long-Long category, the weighted observed events is equal to 4.08 as calculated from Equation 4.13. This results to a two-sided limit $0.008 \leq \mathcal{B}_{\text{KK}/\pi\pi} \leq 0.068$ @ 90% confidence level as shown in Figure 4.5.

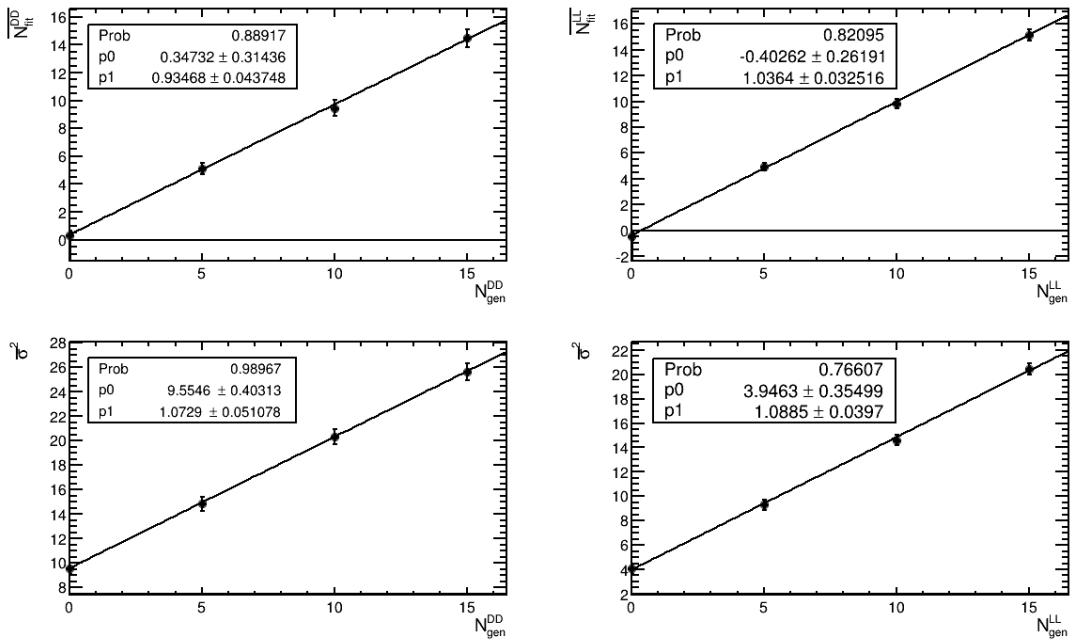

Figure 4.2: Top: $\overline{N_{\text{fit}}}$ as a function of N_{gen} fitted with a linear function for DD (left) and LL (right). Bottom: $\overline{\sigma}^2$ as a function of N_{gen} fitted with a linear function for DD (left) and LL (right).

4.4 Summary of results

Using a modified Feldman-Cousins inference on quoting one-sided or two-sided limits, we have calculated the limits on the relative branching ratio of $B_s^0 \to K_S^0 K^+ K^-$ with respect to the normalization mode $B^0 \to K_S^0 \pi^+ \pi^-$. We have chosen to quote a 90% C.L. The branching ratio limits are calculated separately for events involving K_S^0 decaying into Downstream tracks and events decaying into Long tracks. Eventually, the two results are combined into one measurement, taking only once the uncertainty of fs/fd in the calculation. The combined results is,

$$\frac{\mathcal{B}(B_s^0 \to K_S^0 K^+ K^-)}{\mathcal{B}(B^0 \to K_S^0 \pi^+ \pi^-)}_{\text{Combined}} \in [0.008, 0.068] \quad @\ 90\%\ \text{C.L.} \tag{4.15}$$

Finally, using the best knowledge on the branching fraction of $B^0 \to K_S^0 \pi^+ \pi^-$ ($(4.96 \pm 0.20) \times 10^{-5}$ [105, 106]) at the time this analysis was done, the limit on the branching fraction of $B_s^0 \to K_S^0 K^+ K^-$ is therefore,

$$\mathcal{B}(B_s^0 \to K_S^0 K^+ K^-) \in [0.2, 3.4] \times 10^{-6} \quad @\ 90\%\ \text{C.L.}\ . \tag{4.16}$$

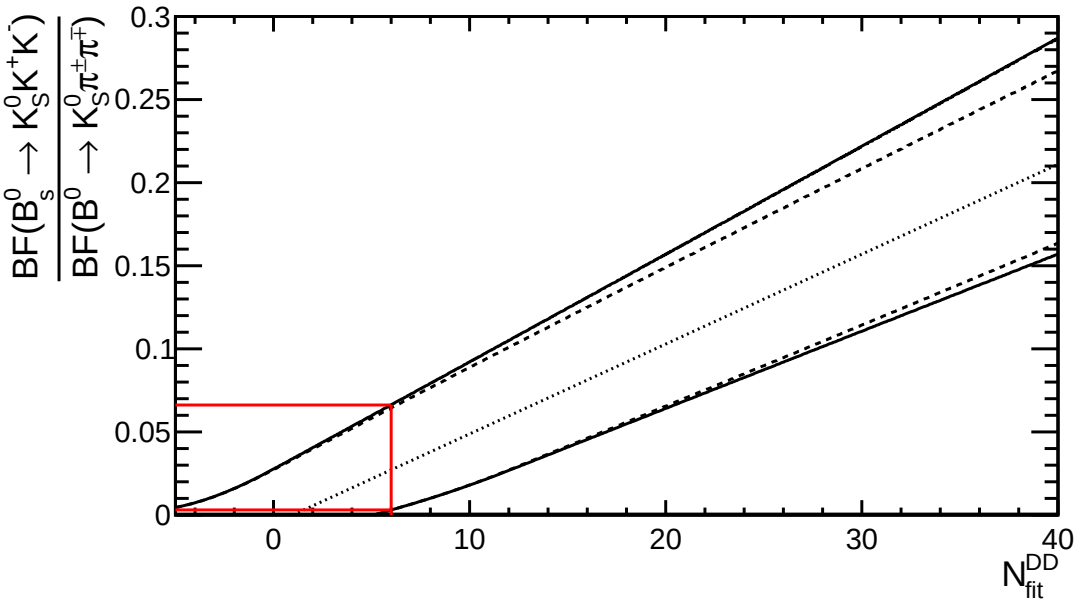

Figure 4.3: 90% confidence belt for the Down-Down category. The dotted line corresponds to the mean of the Gaussian distribution, the dashed line corresponds to the upper and lower limit for statistical uncertainty only, while the solid line corresponds to the upper and lower limit for combined statistical and systematic uncertainties. The red lines correspond to the observed $N_{\mathrm{KK}}^{\mathrm{DD}}$ and the upper and lower limits.

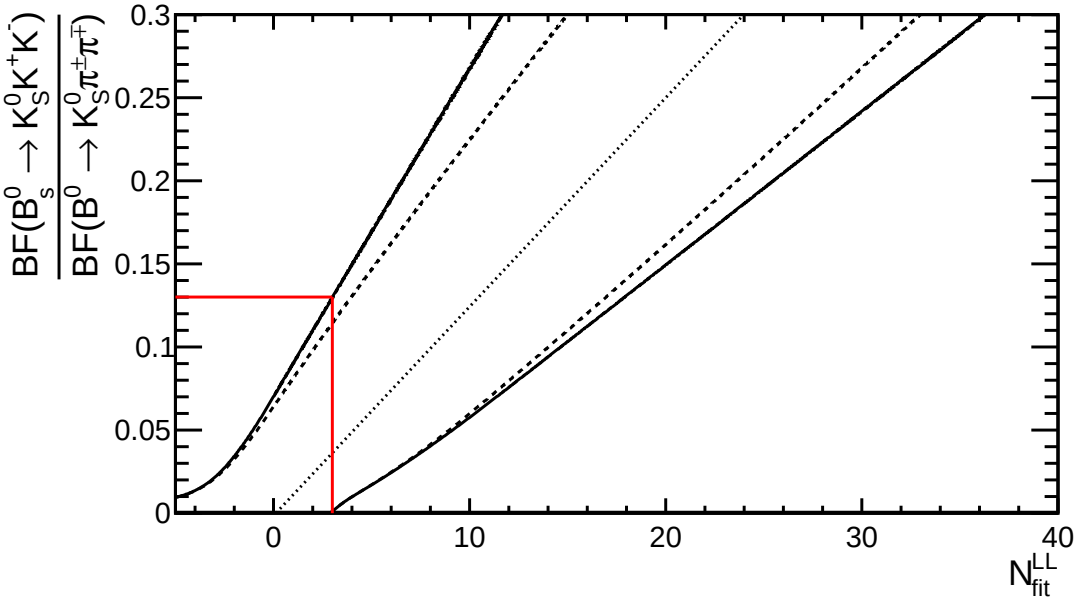

Figure 4.4: 90% confidence belt for the Long-Long category. The dotted line corresponds to the mean of the Gaussian distribution, the dashed line corresponds to the upper and lower limit for statistical uncertainty only, while the solid line corresponds to the upper and lower limit for combined statistical and systematic uncertainties. The red lines correspond to the observed $N_{\mathrm{KK}}^{\mathrm{LL}}$ and the upper limit.

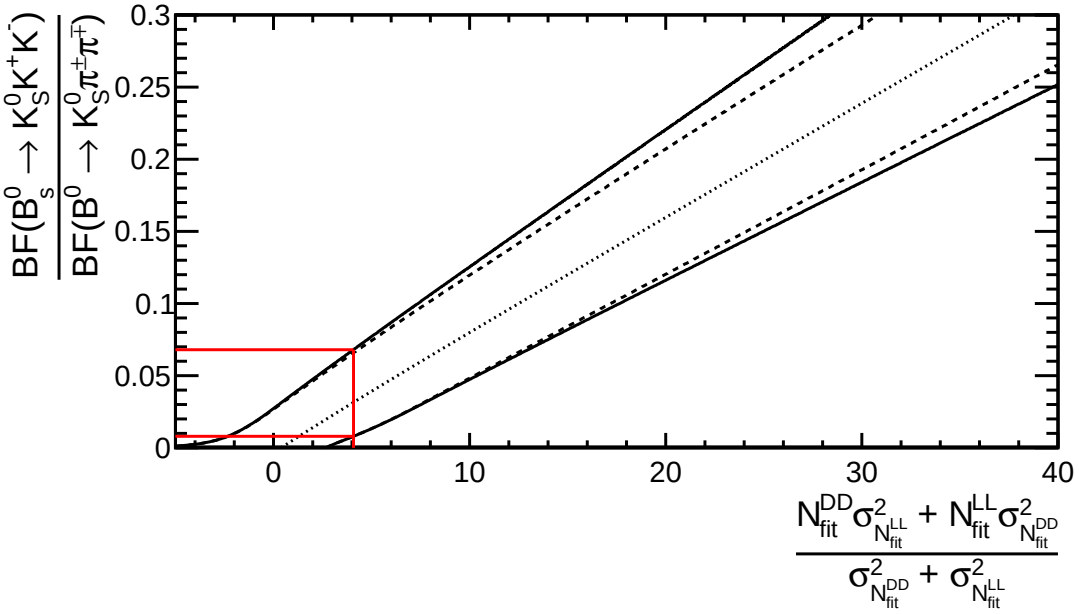

Figure 4.5: The 90% confidence belt for the combination of Down-Down and Long-Long categories. The dotted line corresponds to the mean of the Gaussian distribution, the dashed line corresponds to the upper and lower limit for statistical uncertainty only, while the solid line corresponds to the upper and lower limit for combined statistical and systematic uncertainties. The red lines correspond to the observed N_{KK} and the lower and upper limits.

Chapter 5

Search for CP aymmetries in the charmless 4-body decays of Λ_b^0 and Ξ_b^0

Contents

5.1 Introduction

The measurements of CP violation phenomena receive so far a consistent interpretation within the SM paradigm. CP asymmetries $\mathcal{A}^{CP}$ have been observed in the K and B mesons decays and in the latter case, large asymmetries are measured in several laboratories (2-body and 3-body decays). The control of the hadronic parameters for most of these observables is however not satisfactory and prevents an electroweak interpretation.

The b-flavoured baryons however remain largely unexplored. Recently, the CDF experiment published their measurement of the direct $\mathcal{A}^{CP}$ in the decay of $\Lambda_b^0 \to p\pi^-$ and $\Lambda_b^0 \to pK^-$ and found these to be compatible with no asymmetry [13][a]. The latest published result of the LHCb collaboration on the phase-space integrated direct $\mathcal{A}^{CP}$ of charmless decay of $\Lambda_b^0 \to pK_S^0\pi^-$ using $\int \mathcal{L} = 1\,\text{fb}^{-1}$ of data also showed to be consistent with zero [14]. More recently, LHCb published the $\Delta\mathcal{A}^{CP}$ of $\Lambda_b^0 \to J/\psi\, p\pi^-$ and $\Lambda_b^0 \to J/\psi\, pK^-$ and found it to be compatible with CP symmetry at 2.2σ level [15]. Therefore, the CP violation in

[a] LHCb is also measuring the direct $\mathcal{A}^{CP}$ of these decay modes in an as-yet unpublished results.

baryons remains unobserved up to date. Few promising modes to observe direct CP violation in b-baryons are in the charmless decays to multibody, where the decays can proceed simultaneously through $b\to u$ tree transition or Flavour Changing Neutral Current penguin loop transitions $b\to s$ and $b\to d$. The BaBar and Belle experiments operated at center-of-mass energies below the threshold for b-baryon production. Since LHCb operated at center-of-mass energies above the threshold for b baryon production, it has excellent potential to further improve the understanding of b-baryons.

In multibody decays of b-baryons, the interference pattern is expected to be rich of resonance structures, in particular in the low mass two-body baryon resonances (Λ^{*0}, N^{*0} and Δ series). This is in addition to the structures in the two-body non-baryonic resonances (*i.e.* $\pi\pi$, $K\pi$ and K^+K^- invariant mass spectra). Consequently, the weak interaction induced asymmetries might receive significant enhancement from the phase differences coming from these strong resonances.

In fully-charged decays, the Λ_b^0 or Ξ_b^0 is self-tagged by the presence of either the proton or anti-proton, providing a direct information on the flavour of the Λ_b^0 or Ξ_b^0. We will assume in this analysis that the baryon number is conserved in the decays of interest. A simple counting experiment can measure the direct $\mathcal{A}^{CP}$ up to corrections of instrumental and productions asymmetries. In LHCb, this amounts to correction on the K^+/K^-, π^+/π^- and $p/\overline{p}$ detection asymmetries and b-baryon/$\overline{b}$-baryon production asymmetry. Although the K^+/K^- and π^+/π^- detection asymmetries were both measured in LHCb to percent level [107], the production asymmetry of $b(\overline{b})$-baryons and $p/\overline{p}$ detection asymmetry, two inputs needed for the extraction of $\mathcal{A}^{CP}$ from $\mathcal{A}^{\rm raw}$, remain unmeasured. There are at least two ways to overcome these experimental hurdles. One method is by measuring T-odd observables which is expected to cancel the production and detection asymmetries[b]. The other method is by taking the difference of $\mathcal{A}^{\rm raw}$ of the charmless decay mode to the $\mathcal{A}^{\rm raw}$ of a control mode, where the control mode has the same unpaired final tracks[c] as the charmless decay mode but the decay proceeds through a different quark transition. If the $\Delta\mathcal{A}^{\rm raw}$ is small enough, the production and detection asymmetries cancel, while for large values of $\Delta\mathcal{A}^{\rm raw}$, the production and detection asymmetries are again needed to extract the $\mathcal{A}^{CP}$ if one wishes to do so[d]. Let us note that in the case of a vanishing CP asymmetry, the cancellation of production and detection asymmetries is exact.

In this analysis, we aim to measure the $\Delta\mathcal{A}^{\rm raw}$ of both Λ_b^0 and Ξ_b^0 (hereafter referred collectively as X_b^0) charmlessly decaying to fully-charged four-body final states with respect to charmed decays having the same unpaired final tracks, as summarized in Table 5.1. Specifically, the decays[e] are $\Lambda_b^0\to p\pi^-\pi^+\pi^-$, $\Lambda_b^0\to pK^-\pi^+\pi^-$, $\Lambda_b^0\to pK^-K^+\pi^-$, $\Lambda_b^0\to pK^-K^+K^-$, $\Xi_b^0\to pK^-\pi^+\pi^-$, $\Xi_b^0\to pK^-\pi^+K^-$, $\Xi_b^0\to pK^-K^+K^-$. All of these charmless decay modes of X_b^0 are yet unobserved. The control mode for each charmless decay, as listed in Table 5.1, is chosen in a way that they have the same set of unpaired tracks, except for the $\Xi_b^0\to pK^-\pi^+K^-$ and $\Xi_b^0\to pK^-K^+K^-$ decay modes. Corrections for K^+/K^- and π^+/π^- detection asymmetries are then necessary. The $\mathcal{A}^{CP}$s of the control modes are expected to be consistent with no asymmetry as they proceed solely through a tree level diagram. Two of the decay modes studied in this analysis are of particular interest for direct $\mathcal{A}^{CP}$ measurement due to the same order of the tree (T) and penguin (P) contributions to the decay, which are the $\Lambda_b^0\to p\pi^-\pi^+\pi^-$ and $\Xi_b^0\to pK^-\pi^+\pi^-$. Both the tree and gluonic

[b] LHCb has an on-going analysis on the T-odd observables on the same decay modes studied in this analysis.

[c] Unpaired tracks are the particle tracks which has no charge conjugate present on the final decay. In example, in the decay $\Lambda_b^0\to pK^-\pi^+\pi^-$, the p and K are unpaired tracks while π^+ and π^- are pairs.

[d] This is discussed further in Appendix A.1.

[e] Charge conjugation is implied throughout in this analysis, unless categorically stated otherwise.

penguin loop contributions are of $\mathcal{O}(\lambda^3)$ as shown in the Feynman diagrams in Figure 5.1, where the udd or uds quarks combinations can hadronize in the excited states N^{*0} or Λ^{*0} before decaying to $p\pi$ or pK final states. Nonetheless, large asymmetries can still be seen as well in places where $\mathcal{O}(\lambda^2)$ penguin and $\mathcal{O}(\lambda^4)$ tree diagrams as observed in the fully-charged three-body B decays. Finally, the $\Delta\mathcal{A}^{\text{raw}}$ is calculated for three phase space regions, i.e., (1) integrated throughout the phase space, (2) with m_{ph} (h being a π or K) less than 2 GeV/c^2, and (3) with m_{ph} less than 2 GeV/c^2 and $m_{h'h''}$ (h' & h'' the two other tracks) less than $\sim$1.65 GeV/c^2.

Table 5.1: The four-body fully-charged charmless decays of X_b^0 studied in this analysis and its corresponding charmed decays as control modes.

Charmless decay	Quark transition	Charmed decay	Quark transition
$\Lambda_b^0 \to p\pi^-\pi^+\pi^-$	$b\to u\bar{u}d$ (T + P)	$\Lambda_b^0 \to (\Lambda_c^+ \to p\pi^-\pi^+)\pi^-$	$b\to c\bar{u}d$ (T)
$\Lambda_b^0 \to pK^-\pi^+\pi^-$	$b\to u\bar{u}s$ (T + P)	$\Lambda_b^0 \to (\Lambda_c^+ \to pK^-\pi^+)\pi^-$	$b\to c\bar{u}d$ (T)
$\Lambda_b^0 \to pK^-K^+\pi^-$	$b\to d\bar{s}s$ (T + P)	$\Lambda_b^0 \to (\Lambda_c^+ \to p\pi^-\pi^+)\pi^-$	$b\to c\bar{u}d$ (T)
$\Lambda_b^0 \to pK^-K^+K^-$	$b\to s\bar{s}s$ (T + P)	$\Lambda_b^0 \to (\Lambda_c^+ \to pK^-\pi^+)\pi^-$	$b\to c\bar{u}d$ (T)
$\Xi_b^0 \to pK^-\pi^+\pi^-$	$b\to u\bar{u}d$ (T + P)	$\Xi_b^0 \to (\Xi_c^+ \to pK^-\pi^+)\pi^-$	$b\to c\bar{u}d$ (T)
$\Xi_b^0 \to pK^-\pi^+K^-$	$b\to s\bar{d}d$ / $b\to u\bar{u}s$ (P / T)	$\Xi_b^0 \to (\Xi_c^+ \to pK^-\pi^+)\pi^-$	$b\to c\bar{u}d$ (T)
$\Xi_b^0 \to pK^-K^+K^-$	$b\to d\bar{s}s$ (P)	$\Xi_b^0 \to (\Xi_c^+ \to pK^-\pi^+)\pi^-$	$b\to c\bar{u}d$ (T)

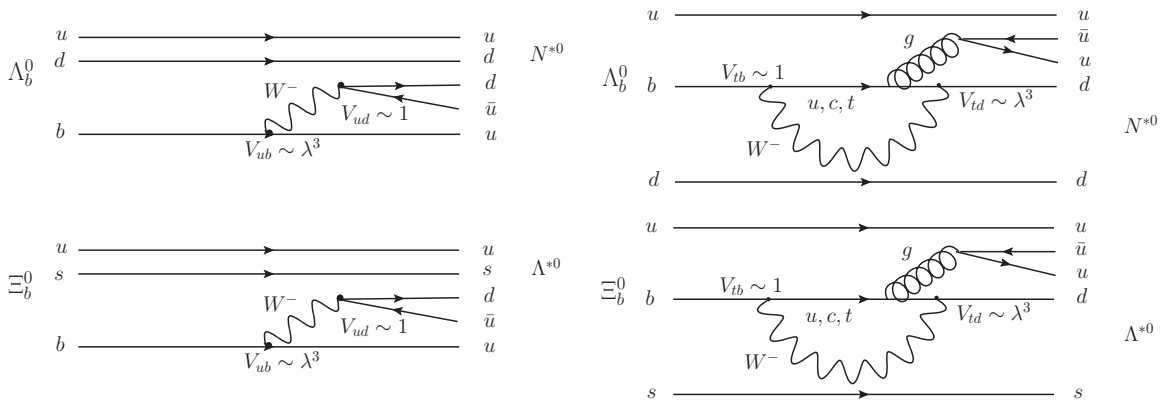

Figure 5.1: Tree and gluonic penguin loop diagrams of $\Lambda_b^0 \to p\pi^-\pi^+\pi^-$ (top) and $\Xi_b^0 \to pK^-\pi^+\pi^-$ (bottom).

5.2 Data and Monte Carlo samples

The results described in this analysis are obtained using the full Run I data collected by LHCb at the LHC at a center-of-mass energy of $\sqrt{s} = 7$ TeV for the 2011 campaign and $\sqrt{s} = 8$ TeV for the 2012 campaign. The 2011 data corresponds to an integrated luminosity of $\int \mathcal{L} = 1\,\text{fb}^{-1}$, while the 2012 data corresponds to $\int \mathcal{L} = 2\,\text{fb}^{-1}$. The reconstruction of the events are obtained using Reco14 for both year campaign. The data are stripped during the Stripping21 campaign using Stripping21r1 for the 2011 data and Stripping21 for the 2012 data, both using the StrippingXb2phhhLine.

Monte Carlo (MC) generated samples are produced using Gauss with Sim08 configuration. They are used to study the behaviour of the signal and background events (both signal cross-feeds and B meson decays, in order to model the invariant mass lineshapes of

signals, signal cross-feeds and backgrounds. The simulation conditions have a pile-up factor of $\nu = 2.0$ for 2011 and $\nu = 2.5$ for 2012 in order to resemble the data taking conditions. The trigger conditions are also different for 2011 and 2012, and hence the MC samples are simulated using TCKs (Trigger Configuration Key) that are representative of the two data taking periods, which are 0x40760037 and 0x409f0045, respectively. The number of MC events produced for each decay mode (signal and background) and year is summarized in Table 5.2. About 50% of these events are produced with MagDown detector configuration, and the other 50% are produced with MagUp detector configuration.

As far as signal events are concerned, we have chosen to simulate a mixture of non resonant (phase space) and quasi-2-body decays involving either an N^{*0} or Λ^{*0} baryon associated with a low-mass meson. The typical ratio Phase Space to Resonances is 1:2. For the case of $B^0_{d,s}$ to 4-body decays, MC simulated events are generated with specific quasi 2-body intermediate states. These are large fractions, but since measurements of inclusive branching fractions in the PDG are only limits, no firm statement can be made about their dominance.

Table 5.2: Number of generated signal and background MC events used in this analysis.

Decay mode	Event type	Year	Yield	Resonances included (in %)
$\Lambda_b^0 \to p\pi^-\pi^+\pi^-$	15204010	2011 (2012)	1033876 (2025489)	PHSP [0.35] + N^{*0} $\{\rho^0, f_2\}$ [0.65]
$\Lambda_b^0 \to pK^-\pi^+\pi^-$	15204011	2011 (2012)	1046073 (2017682)	PHSP [0.30] + Λ^{*0} $\{\rho^0, f_2, K^{*0}, K\pi$ $\}$ [0.70]
$\Lambda_b^0 \to pK^-K^+\pi^-$	15204012	2011 (2012)	1025976 (2011991)	PHSP [0.35] + Λ^{*0} $\{K^{*0}, K\pi$ $\}$ [0.65]
$\Lambda_b^0 \to pK^-K^+K^-$	15204013	2011 (2012)	1032138 (2019736)	PHSP [0.35] + Λ^{*0} $\{\phi^0, f_2'\}$ [0.65]
$\Xi_b^0 \to pK^-\pi^+\pi^-$	16204040	2011 (2012)	1021760 (2037415)	PHSP [0.30] + Λ^{*0} $\{\rho^0, f_2, K^{*0}, K\pi$ $\}$ [0.70]
$\Xi_b^0 \to pK^-\pi^+K^-$	16204041	2011 (2012)	1001562 (2024475)	PHSP [0.35] + Λ^{*0} $\{K^{*0}, K\pi$ $\}$ [0.65]
$\Xi_b^0 \to pK^-K^+K^-$	16204042	2011 (2012)	1051785 (2067281)	PHSP [0.35] + Λ^{*0} $\{\phi^0, f_2'\}$ [0.65]
$\Lambda_b^0 \to (\Lambda_c^+ \to pK\pi)\pi$	15264011	2012	1011237	$\Lambda_b^0 \to (\Lambda_c^+ \to pK^-\pi^+)\pi^-$ [1.00]
$\Lambda_b^0 \to (\Lambda_c^+ \to pK\pi)K$	15364011	2012	538205	$\Lambda_b^0 \to (\Lambda_c^+ \to pK^-\pi^+)K^-$ [1.00]
$B^0 \to \pi^+\pi^-\pi^+\pi^-$	11104061	2011 (2012)	1557242 (3005995)	$B^0 \to \rho^0(\pi^+\pi^-)\rho^0(\pi^+\pi^-)$ [1.00]
$B^0 \to K^+\pi^-\pi^+\pi^-$	11104041	2011 (2012)	2048997 (4021486)	$B^0 \to K^{*0}(K^+\pi^-)\rho^0(\pi^+\pi^-)$ [1.00]
$B^0 \to K^+K^-K^+\pi^-$	11104020	2011 (2012)	2043494 (4017984)	$B^0 \to \phi^0(K^+K^-)K^{*0}(K^+\pi^-)$ [1.00]
$B_s^0 \to K^+\pi^-\pi^+K^-$	13104001	2011 (2012)	1014357 (2037039)	$B_s^0 \to K^{*0}(K^+\pi^-)\overline{K}^{*0}(\pi^+K^-)$ [1.00]
$B_s^0 \to K^+K^-K^+K^-$	13104013	2011 (2012)	1035749 (1025247)	$B_s^0 \to \phi^0(K^+K^-)\phi^0(K^+K^-)$ [1.00]

A cut on the $p_{\rm T} > 400$ MeV of each daughter track is included in the generation of the $B_s^0 \to \phi^0(K^+K^-)\phi^0(K^+K^-)$ MC sample.

5.3 Trigger

Events that are triggered by either the L0Hadron TOS (Triggered-On-Signal) or L0Global TIS (Triggered-Independent-of-Signal) are collected in the first stage of the trigger sequence. These events are then required to pass the Hlt1TrackAllL0 TOS requirements. Finally, events passing either of the six Hlt2Topo[2,3,4]Body{BBDT,Simple} TOS decisions are recorded for further stripping and selection for the 2011 data. The rationale behind the use of the Simple topological Hlt2 algorithm is the addition of events in the corners of the Phase Space of the decays. However, sometime in 2012, the Hlt2Topo[2,3,4]BodySimple has been turned off and hence for 2012 data we only require the events to pass either of the three Hlt2Topo[2,3,4]BodyBBDT TOS. Trigger requirements were not included in the stripping in order to study their impact on the selection of the signals. They are hence included as offline selection cuts on the raw stripping output.

5.4 Stripping

None of the stripping lines pre-existing for the selection of the signals of interest were satisfactory to study their *CP*-violating asymmetries. As underlined in the motivations of this work, the richness of these charmless 4-body baryon decays final states lies in the interference patterns of quasi 2-body amplitudes contributing to the decay. Those amplitudes involve resonances often at threshold, *e.g* $\Lambda^{*0}(1520)$, which in turn produce in the final state hadrons with low momentum. A dedicated stripping line has then been designed for this analysis to maximize the selection of the signal events.

During the Stripping21 campaign, the stripping line called StrippingXb2phhhLine was added to the BHADRON.MDST stream. The stripping line was designed in a way to preserve the low two-body invariant mass region, specifically the ph invariant mass where the $\Lambda^{*0}(1520)$ and $N^{*0}(1520)$ are expected to be present. As such, only a loose kinematical cut is applied on the daughter tracks and no kinematical cut on the two-body pairs is applied.

We are aiming at an inclusive stripping selection of all relevant charmless and charmed decay modes. The proton tracks come from the StdLooseANNProtons standard particle container, while the three other tracks come from the StdNoPIDsPions container. Since those three tracks can either be pions or kaons, no particle identification (PID) is applied on them, while a loose ProbNNp cut is applied on the proton in order to reduce the retention rate to an acceptable level. The actual PID selection for the final states of interest is then left to the analysts with the minimal affordable bias.

Moreover, in order to avoid border effects in the invariant mass of X_b^0 candidate, the minimum 4-body invariant mass is calculated using the $pKKK$ mass hypotheses, while the maximum is calculated using the $p\pi\pi\pi$ mass hypotheses.

Using the available RelatedInfoTools, two isolation variables (smallest $\Delta\chi^2_{\text{vtx}}$ and p_{T} asymmetry in a given cone angle[f]) are saved as well for each X_b^0 candidate. These variables are used in the training of a multivariate discriminant, discussed later in this analysis. Let us mention here that this specific line among others was used for the commissioning of the RelatedInfoTools for this Stripping version.

The summary of the stripping line selection cuts is presented in Table 5.3. A comment is in order as far the vertexing and pointing variables are concerned. All topological variables used in this analysis are of significance type to retain the best reconstructed candidates irrespective of the absolute vertex observable value. The requirement on the minimal p_{T} of the daughters has been tuned in order to cope with the allowed retention rate. The obtained value is low enough to preserve the signal efficiency of the quasi 2-body decays at threshold for the intermediate resonances.

5.5 Background studies

The structure of the background of the charmless 4-body fully-charged decays of Λ_b^0 and Ξ_b^0 is rich. There are at least five main categories of backgrounds identified that appears in the mass distribution of the real data candidates. These are (1) the peaking backgrounds coming from charmed decays and charmless but charming decays (we are referring here to the tree level $b \to u$ quark transition followed by $W \to \bar{c}s$), (2) the partially reconstructed backgrounds, (3) the cross-feeds from other signal modes, (4) the physics backgrounds coming from 4-body decays of B^0 or B_s^0, and (5) the random combinatorial of one or several tracks unrelated to the decay of the interest.

[f] These variables are discussed further in Section 5.6.4.

Table 5.3: Cuts applied in the stripping line StrippingXb2phhhLine selecting the candidate events.

Variable definition	Selection requirements
Cuts on daughter tracks (p,π)	
Daughter tracks' momentum	$p > 1500.$ MeV/c
Daughter tracks' tranverse momentum	$p_{\rm T} > 250.$ MeV/c
Daughter tracks' χ^2 over degrees of freedom	Trk. $\chi^2/{\rm ndf} < 3.0$
Daughter tracks' minimum impact parameter χ^2 to any PV	Min. $\chi^2_{\rm IP} > 16.0$
Daughter tracks' probability of being a ghost track	Prob$ghost < 0.40$
Proton track's probability of being a proton	ProbNN$p > 0.05$
Combination cuts (before vertex fit)	
Mass of the X_b^0 candidate with $pKKK$ tracks hypothesis	$m_{pKKK} > 5195.$ MeV/c^2
Mass of the X_b^0 candidate with $p\pi\pi\pi$ tracks hypothesis	$m_{p\pi\pi\pi} < 6405.$ MeV/c^2
X_b^0 candidate's tranverse momentum	$p_{\rm T} > 1500.$ MeV/c
Sum of the daughter tracks' tranverse momentum	$\Sigma_{\rm daug.}p_{\rm T} > 3500.$ MeV/c
Distance of closest approach χ^2 of any two daughters	$\chi^2_{\rm DOCA} < 20.$
Combination cuts (after vertex fit)	
X_b^0 candidate's vertex χ^2	$\chi^2_{\rm vtx} < 20.$
X_b^0 candidate's flight distance χ^2 w.r.t. best PV	$\chi^2_{\rm FD} > 50.$
X_b^0 candidate's impact parameter χ^2 w.r.t. best PV	$\chi^2_{\rm IP} < 16.$
Cosine of the X_b^0 candidate pointing angle	$\cos(\theta_{\rm DIRA}) > 0.9999$

5.5.1 Peaking backgrounds

Fully-reconstructed charmed and charming decays if not properly removed can appear as peaking background. Since the final state of these decays is the same as the charmless modes, they can not be removed via PID optimization and neither on using MVA-based cuts without relying on the small topological and kinematical difference. The unique way to reduce them without losing a significant amount of signal events is to properly veto them by cutting on the mass of a given intermediate state. The intermediate states explicitly vetoed in this analysis are Λ_c^+, Ξ_c^+, D^+, D_s^+, D^0, χ_{c0} and J/ψ. The reconstructed mass of Λ_c^+ is required to be ± 30 MeV/c^2 outside from $m_{\Lambda_c^+} = 2283.$ MeV/c^2, where it is adjusted about 3 MeV/c^2 to the left w.r.t. the PDG value in order to take into account the asymmetry of the distribution as seen in the data, while Ξ_c^+, D^+, D_s^+ and D^0 are required to be ± 30 MeV/c^2 outside from the PDG values. A wider mass window of ± 50 MeV/c^2 from the PDG value is required for vetoing χ_{c0} and J/ψ. The list of final state decays considered for these charmed resonances can be found in Section 5.6.5, where all relevant daughter combination is considered in the mass reconstruction. Furthermore, these mass veto cuts are applied as a global cut, *e.g.* 3 tracks are reconstructed as $pK\pi$ in order to veto Λ_c^+, regardless of the spectrum. In this way, the candidate is vetoed in all spectra. Let us notice that the vetoed charmed decay modes involving a Λ_c^+ and Ξ_c^+ are used in turn as control channels for the detection efficiencies and production asymmetries.

5.5.2 Partially reconstructed backgrounds

The 5-body decays of Λ_b^0 and/or Ξ_b^0 with one particle missing can still be a significant amount of background events populating the left side of reconstructed invariant mass distribution.

The dominant contributor of the partially-reconstructed backgrounds are the events with a missing π^0. Actually, the partially reconstructed backgrounds with a missing charged pion in the final state are reduced by the isolation variable denoted smallest $\Delta\chi^2_{\text{vtx}}$, which is searching for a better vertex with an additional charged track to the 4-tracks vertex. The mass threshold considered when modelling this background is therefore the π^0 mass.

Although not included in the nominal fit, Partially-reconstructed backgrounds with a missing γ is also possible through the decay $\Lambda_b^0 \to pK^-(\eta' \to \pi^+\pi^-\gamma)$. This will give partially-reconstructed backgrounds closer to the signal peak than the decays with missing π^0. A systematic uncertainty will be assign to this and this is presented in the list of systematics in Section 5.11.

5.5.3 Cross-feeds or reflections

Seven charmless decay modes are explicitly searched in this analysis as listed in Table 5.1 in Section 5.1. The PID selection is chosen in a way that a candidate can appear only in one spectrum and not on the other spectra (mutually exclusive selection) in order that a simultaneous fit of all the relevant spectra can be possible. More detailed discussion on the strategy can be found in Section 5.6.2. After optimizing the PID selection to reduce the cross-feeds in each spectrum, a significant number of true signal events may still appear as a cross-feed in other spectrum. The dominant cross-feeds are signal events from other spectra with only one particle misidentified, and hence peaks not very far from the signal peak. Henceforth, an accurate handling on the yields and shapes of these background contributions must be achieved. This is realized by constraining in the simultaneous fit their relative yields to the data-driven misidentification probabilities. The procedure is described in details in Section 5.8.

5.5.4 $B \to$ 4-body physics backgrounds

Four-body decays coming from B^0 or B_s^0 with a misidentified K or π as a proton can appear in the invariant mass distribution. Given that the hadronization fraction of b quark to B^0 is significantly higher the the hadronization fraction of b quark to neutral baryons Λ_b^0 and Ξ_b^0, they are expected to dominate the mass distribution if not properly reduced. The hadronization fraction of b quark to B_s^0, although smaller than the hadronization fraction of b quark to Λ_b^0, can also populate significantly if not handled. Since this background can exhibit significant CP asymmetries, their accurate handling is mandatory and certainly constitutes a challenge of this analysis. Five possible dominant B physics backgrounds are envisioned, which includes $B^0 \to \pi^+\pi^-\pi^+\pi^-$, $B^0 \to K^+\pi^-\pi^+\pi^-$, $B^0 \to K^+K^-K^+\pi^-$, $B_s^0 \to K^+\pi^-\pi^+K^-$ and $B_s^0 \to K^+K^-K^+K^-$. Since they have the same final state particles, except for the proton, as the signal modes, they can not be significantly reduced by the $\text{PID}_{K\pi}$ selection without reducing as well the signal events. Neither MVA-based cuts can reduce them since they are relatively topologically and kinematically the same as the signal events. However, a tight PID cut (ProbNNp) on the proton particle can significantly reduce these B physics events, while retaining signal events with an acceptable efficiency. A dedicated study of the right-hand side-band (RHSB) of the invariant mass distributions for each spectra has been undergone and is reported in Section 5.7.

5.5.5 Combinatorial background

Aside from the physical backgrounds described above, there are also combinatorial backgrounds coming solely from the random combination of one or several tracks unrelated to

the signal decay. The topology and kinematics[g] of these background events are different enough from the signal events that they can be reduced by a univariate or multivariate-based cuts. It is important to emphasize that the understanding of the different above-mentioned sources of background (not straightforwardly reducible) benefits from the largest as possible suppression of the combinatorial background. This is in particular true for the dominant B physics. Therefore, a special care has been brought to the design of the tool to fight against the combinatorial background. As will be discussed further in Section 5.6.4, a BDT-based MVA is trained using variables with weak linear correlations (but in principle nonlinearly correlated) or with different correlations for background and signal events in order to reduce these backgrounds.

5.6 Selection

The X_b^0 candidates saved after stripping still contain significant amount of background events. In order to reduce these backgrounds while keeping the signal events, further offline selection cuts are applied. In this section, the several components of the offline selection are described together with its corresponding strategy. The design and presentation of the selection steps we are proposing have the following logic: the PID cuts have been optimized first with the objective of mastering the signal cross-feeds and B physics. This allowed to select a rather pure combinatorial background sample on the data which was used to train a multivariate discriminative tool. In turn, this combinatorics killer selection was applied to the data sample in order to master the B physics yields to feed the simultaneous fit with data-driven constraints. The optimization on the cut values are also presented. At the end of this section, a subsection is dedicated to the signal efficiency given by each stage of the selection. The very first step presented in this section consists in a preselection in line with the tupling strategy.

5.6.1 Offline selection

Some further offline selection cuts, trigger requirements and fiducial cuts are applied to the stripped data prior to particle identification (PID) optimization and multivariate (MVA) selection.

In the stripping selection, the candidate events are reconstructed as $\Lambda_b^0 \to p\pi^-\pi^+\pi^-$, although no PID requirement is applied on the three pions. However, in the final tupling of the data, each candidate is reconstructed using the appropriate mass hypotheses of the daughter particles corresponding to the different possible final states. These final states are namely $p\pi\pi\pi$, $pK\pi\pi$, $pKK\pi$, $pK\pi K$ and $pKKK$. For each set of mass hypotheses, a refit on the decay tree using the DecayTreeFitter tool is done in order to properly recalculate the kinematics of the decay. More importantly, the mass of X_b^0 candidate is now properly defined for each final state. A mass range cut on the X_b^0 mass is then required to be in the range 5340 MeV/c^2 to 6400 MeV/c^2.

A selection rule was also applied as early as in the tupling level to decide which track is the kaon in the case of $X_b^0 \to pK^-\pi^+\pi^-$ and $X_b^0 \to pK^-K^+\pi^-$ spectra. In these spectra (labelled $X_b^0 \to h_1h_2h_3h_4$ for discussion purposes), the true K^- particle out of the stripping selection may end up either in the h_2 location or in the h_4 location since there was no PID

[g] Discussed later in this analysis is the BDT strategy to reduce these combinatorics. No kinematical variables are used in the BDT to avoid the BDT cutting events in the low two-body invariant mass, where the $\Lambda^{*0}(1520)$ and $N^{*0}(1520)$ are expected to appear.

applied on $h_{\{2,3,4\}}$, with a certain probability[h]. The product of h_2 ProbNNπ and h_2 (1 - ProbNNK) is compared to the product of h_4 ProbNNπ and (h_4 1 - ProbNNK). Whichever has the larger value is chosen as the π and the other as the K. This selection rule is irrelevant for the other spectra since both h_2 and h_4 are either both pions (in the case if of $X_b^0 \to p\pi^-\pi^+\pi^-$) or both kaons.

Since the PID information given by the RICH detectors might no longer be reliable outside some momentum range and pseudo-rapidity, fiducial cuts are also applied on each of the final tracks. The momentum range of the track is required to be within the range 3 GeV/$c < p <$ 100 GeV/c and the pseudo-rapidity angle of the track is required to be within $1.5 < \eta < 5$.

5.6.2 K/π PID selection optimization

The optimization of the PID selection in this study is driven by two objectives. The first objective is to optimally reject the signal cross-feeds within the $\pm 3\sigma$ of the nominal mass of the signal mode. The second objective is to ensure that we have mutually exclusive events present in each spectrum, and hence avoiding the complicated statistical treatment of errors given by the simultaneous fit when dealing with non-mutually exclusive spectra. This can be done by ensuring that there is no overlapping regions in the particle identification (PID) selection of kaons and pions.

There are two possible neural network based variables that can be used to select pions and kaons. These are the ProbNNπ and ProbNNK, where pions can be selected as those particles having ProbNNπ larger than some cut value and the kaons are the particles with ProbNNK larger than some cut value. However, this does not guarantee that the same particle will not be selected as both a pion and a kaon, and hence may appear as a signal in one spectrum and as a cross-feed in the other spectra. In a simultaneous fit of all the spectra, the resulting uncertainties of measured quantities would have to be corrected for the statistical correlations. In order to avoid this complication, the pions and kaons are chosen in a way that they are mutually exclusive, and henceforth implying mutually exclusive spectra.

In the ProbNNK-vs-ProbNNπ plane, most of the kaons populate at the (0,1) location, while the pions populate at the (1,0) location. This is illustrated in Figure 5.2 using MC-matched pions and kaons from MC-generated $\Lambda_b^0 \to pK^-\pi^+\pi^-$ events. In this analysis, a circular cut centered at (1,0) is chosen in order to differentiate pions from kaons. Particles inside the circular envelope (those inside the radius of $\sqrt{a_\pi^{\text{cut}}}$) are considered pions, while the rest are considered kaons. In principle, the kaon cut a_K^{cut} can be larger than a_π^{cut}, but the a_K^{cut} is restricted not to be less than a_π^{cut} in order to ensure non-overlapping regions of kaons and pions. Anticipating the results of the optimization, it was eventually found that the best cuts are identical for both a_π^{cut} and a_K^{cut}. We however chose to present them separately since their best values are not aligned by definition.

The particle identification (PID) variables defined in Equation 5.1 and Equation 5.2 are used to select kaons and pions. As a short-hand notation, from hereon we refer PID$_K$ and PID$_\pi$ as the variables defined in Equation 5.1 and Equation 5.2, respectively. Anticipating the results of the optimization, we found the same optimal cut values for kaons and pions, and hence we collectively refer them in the later part of this analysis as PID$_{K\pi}$. Mathematically,

[h]Probability of landing in h_2 or h_4 is not 50%-50% because of p_{T} sequencing in StdNoPIDsPions track container.

the PID cuts are given by,

$$\mathrm{PID}_K : ((h\_\mathrm{ProbNN}\pi - 1.0)^2 + h\_\mathrm{ProbNN}K^2) > a_K^{\mathrm{cut}} \tag{5.1}$$
$$\mathrm{PID}_\pi : ((h\_\mathrm{ProbNN}\pi - 1.0)^2 + h\_\mathrm{ProbNN}K^2) < a_\pi^{\mathrm{cut}} \ , \tag{5.2}$$

where h can be a kaon or a pion depending on which spectrum it is applied.

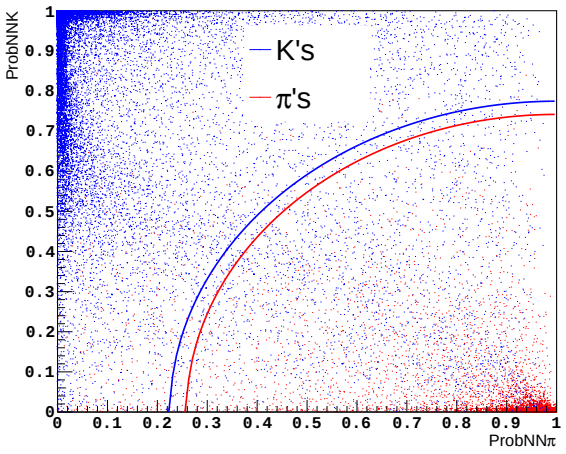

Figure 5.2: Illustration of the distribution of kaons and pions in the ProbNNK-vs-ProbNNπ plane using MC-matched kaons and pions from MC-generated $\Lambda_b^0 \to pK^-\pi^+\pi^-$ events.

The ProbNN variables of kaons and pions from real data are not well described by the MC-calculated ProbNN variables. To correct this discrepancy, a set of PID (mis)identification efficiency maps for each a_π^{cut} and a_K^{cut} cut values is prepared in bins of momentum p and pseudo-rapidity angle η, knowing that the PID (mis)identification efficiency depends on the kinematics of the particles. The binning scheme used in producing the efficiency maps[i] for each year and each particle type is summarized in Table 5.4.

A MC-generated event is then used to calculate the kinematics of the tracks, which are in turn used to calculate the efficiency of an event to pass a certain a_π^{cut} and/or a_K^{cut} cut values taking into account correlations. These event-by-event efficiencies are then averaged to calculate the probability of a certain decay mode to pass the $\mathrm{PID}_{K\pi}$ cut values. The PIDCalibTool implements this strategy, which uses real data kaons and pions coming from D^0's where the D^0's come from the decay of $D^{*+} \to (D^0 \to \pi^+K^-)\pi^+$.

Since the branching fractions of the signal modes are not yet measured and that the hadronization fraction of b quark to heavy baryons in LHCb is dependent on the momentum and pseudo-rapidity angle of the baryon, there is no direct approximation of the possible yield of events of both signal and cross-feeds. A modified Figure of Merit (FoM) is then defined that does not depend on the approximated yields but rather on the relative efficiencies of the signal mode and the cross-feeds. This FoM is given by,

$$\mathrm{FoM}(\mathrm{PID}_{\mathrm{cut}}) = \frac{\epsilon_{\mathrm{Sig.}}^{\mathrm{PID}}}{\sqrt{\epsilon_{\mathrm{Sig.}}^{\mathrm{PID}} + \Sigma\alpha_{\mathrm{CF}}\epsilon_{\mathrm{CF}}^{\mathrm{PID}}}} \ , \tag{5.3}$$

where $\epsilon_{\mathrm{Sig.}}^{\mathrm{PID}}$ and $\epsilon_{\mathrm{CF}}^{\mathrm{PID}}$ are the efficiencies as a function of PID cut of signal and cross-feeds, respectively. A scaling factor α_{CF} relative to the signal is multplied to each of the cross-feed

[i]The $\mathrm{PID}_{K\pi}$ efficiency maps for he optimal a_π^{cut} and a_K^{cut} are shown in Appendix A.2.

Table 5.4: The binning scheme used to produce the $\text{PID}_{K\pi}$ (mis)identification efficiency maps.

Particle type (year)	p binning boundaries (in GeV/c^2)	η binning boundaries
K's (2011)	{3000; 9300; 15600; 18515; 28325; 40097; 59717; 100000}	{1.5; 2.4975; 2.7075; 3.0575; 3.3725; 3.7225; 4.0025; 5.0}
K's (2012)	{3000; 9300; 15600; 16553; 26363; 38135; 57755; 100000}	{1.5; 2.4625; 2.6725; 2.9875; 3.3025; 3.6525; 3.8975; 5.0}
π's (2011)	{3000; 9300; 15600; 16553; 24401; 36173; 55793; 100000}	{1.5; 2.4625; 2.7075; 3.0225; 3.3375; 3.6875; 3.9675; 5.0}
π's (2012)	{3000; 9300; 14591; 15600; 24401; 34211; 53831; 100000}	{1.5; 2.4275; 2.6375; 2.9525; 3.2675; 3.6175; 3.8975; 5.0}

efficiencies, which reflects the approximate ratio of signal-to-crossfeed before any PID cut. This α_{CF} factor is calculated using the equation,

$$\alpha_{\text{CF}} = \frac{\mathcal{B}_{\text{Sig.}}\epsilon^{\text{Sel.}}_{\text{Sig.}}\epsilon^{\text{Mwindow}}_{\text{Sig.}}}{\mathcal{B}_{\text{CF}}\epsilon^{\text{Sel.}}_{\text{CF}}\epsilon^{\text{Mwindow}}_{\text{CF}}} f_{s,d} f_{s\to u} \tag{5.4}$$

where $\mathcal{B}_{\text{X}}$, $\epsilon^{\text{Sel.}}_{\text{X}}$, $\epsilon^{\text{Mwindow}}_{\text{X}}$ are the branching fractions, selection efficiencies and the mass window cut efficiencies of signal and crossfeeds. The selection efficiencies include acceptance, trigger, track reconstruction, stripping and offline fiducial cuts efficiencies. The mass window cut efficiencies are the efficiencies of signal and cross-feeds requiring that the reconstructed mass be within the $\pm 3\sigma$ from the nominal mass of the baryon. All of these efficiencies are calculated from the MC generated events. The $f_{s,d}$ is the ratio of the hadronization fraction of b quark to Ξ_b^0 and of b quark to Λ_b^0, which is equal to 1 if both signal and cross-feed come from Λ_b^0 or both from Ξ_b^0 and equal to 0.256 (3.906) if cross-feed comes from Ξ_b^0 (Λ_b^0) and signal comes from Λ_b^0 (Ξ_b^0). This $f_{s,d} = f_{\Xi_b^0}/f_{\Lambda_b^0}$ is approximated to be equal to $f_{B_s^0}/f_{B^0}$ [108]. When the signal and cross-feed do not come from the same heavy baryon type, an additional factor $f_{s\to u}$ is multiplied to the scaling factor α_{CF}, in order to take into account the fraction of events of Ξ_b^0 decaying to $\Lambda_b^0\pi^0$ (hence contributing to Λ_b^0). The fraction of Ξ_b^0 decaying to $\Lambda_b^0\pi^0$ is guesstimated to be 0.025. Hence the $f_{s\to u}$ factor is equal to 1 if both signal and cross-feed come from Λ_b^0 or both from Ξ_b^0, and equal to 0.975 (1.025) if cross-feed comes from Ξ_b^0 (Λ_b^0) and signal comes from Λ_b^0 (Ξ_b^0).

The FoM defined in Equation 5.3 requires ratios of branching fractions and ratio of hadronization fractions as inputs, rather than absolute values in the case of Punzi FoM or the standard significance $S/\sqrt{S+B}$. As mentioned above, there is no measurement yet on the branching fraction of the signal decay modes. An educated guess however can be made by considering that the ratios of branching fractions of the $B^+ \to 3$ body fully-charged decays as good approximates of the ratios of branching fractions of the signal modes studied in this analysis. These $B^+ \to 3$ body decays exhibit the same quark transition, and hence the same CKM elements as for the signal modes are assumed. Summarized in Table 5.5 are the $B^+ \to 3$ body fully-charged decays which are used to approximate the branching fractions of our signal modes.

There are five FoMs to optimize corresponding to the five spectra studied in this analysis[j], each having its own optimal cut values of a_π^{cut} and a_K^{cut}. For the reason of ensuring mutually-

[j]The same $\text{PID}_{K\pi}$ cut is to be optimized for $\Lambda_b^0 \to pK^-\pi^+\pi^-$ and $\Xi_b^0 \to pK^-\pi^+\pi^-$, since they belong to the same spectrum. The same can be said for $\Lambda_b^0 \to pK^-K^+K^-$ and $\Xi_b^0 \to pK^-K^+K^-$. For these two

Table 5.5: The four-body fully-charged charmless decays of X_b^0 studied in this analysis and its corresponding $B^+ \to 3$ body fully-charged decays that are used to approximate the branching fractions of signal modes.

Charmless decay	$B^+ \to 3$ body decay	Branching fraction [17]
$\Lambda_b^0 \to p\pi^-\pi^+\pi^-$	$B^+ \to \pi^+\pi^-\pi^+$	$(1.52 \pm 0.14) \times 10^{-5}$
$\Lambda_b^0 \to pK^-\pi^+\pi^-$	$B^+ \to K^+\pi^-\pi^+$	$(5.10 \pm 0.29) \times 10^{-5}$
$\Lambda_b^0 \to pK^-K^+\pi^-$	$B^+ \to K^+K^-\pi^+$	$(5.0 \pm 0.7) \times 10^{-6}$
$\Lambda_b^0 \to pK^-K^+K^-$	$B^+ \to K^+K^-K^+$	$(3.40 \pm 0.14) \times 10^{-5}$
$\Xi_b^0 \to pK^-\pi^+\pi^-$	$B^+ \to \pi^+\pi^-\pi^+$	$(1.52 \pm 0.14) \times 10^{-5}$
$\Xi_b^0 \to pK^-\pi^+K^-$	$B^+ \to K^+\pi^-\pi^+$	$(5.10 \pm 0.29) \times 10^{-5}$
$\Xi_b^0 \to pK^-K^+K^-$	$B^+ \to K^+K^-\pi^+$	$(5.0 \pm 0.7) \times 10^{-6}$

exclusive spectra, one PID$_{K\pi}$ optimization is chosen as the baseline. The mode which is considered for this is the $\Xi_b^0 \to pK\pi\pi$ decay following the rationale that this is one of the interesting modes where both tree and penguin loop contributions are of order $\mathcal{O}(\lambda^3)$ and can both proceed through the resonant particles N^{*0} and Λ^{*0}. In order to build mutually-exclusive spectra, it must be required that the a_π^{cut} cut (a_K^{cut} cut) is less (more) than the optimal a_π^{cut} (a_K^{cut}) cuts for the baseline mode. It happens that this condition is never realized for our choice of baseline mode (it can however happen for other choices of baseline mode and other choices of FoM). The very same cuts are then eventually applied to all spectra.

The optimal PID$_{K\pi}$ cuts for each mode are summarized in Table 5.6. The optimal PID$_{K\pi}$ a_π^{cut} and a_K^{cut} cuts for the baseline mode are 0.55 and 0.55, as shown in Figure 5.3. The FoMs of other modes can be found in Appendix A.4. The other modes did not statisfy the condition stated above and hence their PID$_{K\pi}$ cut is chosen to be the same as the PID$_{K\pi}$ of the baseline mode, i.e., ($a_\pi^{\text{cut}} = 0.55$, $a_K^{\text{cut}} = 0.55$).

Table 5.6: The list of optimal PID$_{K\pi}$ a_π^{cut} and a_K^{cut} cuts.

Signal mode	2011 optimal PID$_{K\pi}$ cuts (a_π^{cut}, a_K^{cut})		2012 optimal PID$_{K\pi}$ cuts (a_π^{cut}, a_K^{cut})	
	MagDown	MagUp	MagDown	MagUp
$\Xi_b^0 \to pK^-\pi^+\pi^-$	**(0.55, 0.55)**	**(0.55, 0.55)**	**(0.55, 0.55)**	**(0.55, 0.55)**
$\Lambda_b^0 \to p\pi^-\pi^+\pi^-$	(1.00, 1.00)	(1.00, 1.00)	(1.00, 1.00)	(1.00, 1.00)
$\Lambda_b^0 \to pK^-K^+\pi^-$	(0.15, 0.15)	(0.15, 0.15)	(0.20, 0.20)	(0.20, 0.20)
$\Xi_b^0 \to pK^-\pi^+K^-$	(0.35, 0.35)	(0.35, 0.35)	(0.35, 0.35)	(0.35, 0.35)
$\Xi_b^0 \to pK^-K^+K^-$	(0.30, 0.30)	(0.30, 0.30)	(0.30, 0.30)	(0.30, 0.30)

The signal and cross-feed efficiencies for this optimal PID$_{K\pi}$ cut values are summarized in Table A.1 (using 2011 calibration samples) and Table A.2 (using 2012 calibration samples) of Appendix A.5. Shown in Figure A.9 in Appendix A.5 are illustrations of how the expected relative distribution changes before and after applying the PID$_{K\pi}$ cut, where the relative distributions are calculated using the α_{CF} and the PID (mis)identification efficiencies $\epsilon_{\text{Sig.}}$ and ϵ_{CF}.

spectra, the optimization is performed on the yields of the Ξ_b^0 decays since they are suffering from a worse signal-to-noise ratio, the latter being mostly cross-feeds from Λ_b^0 signal decays.

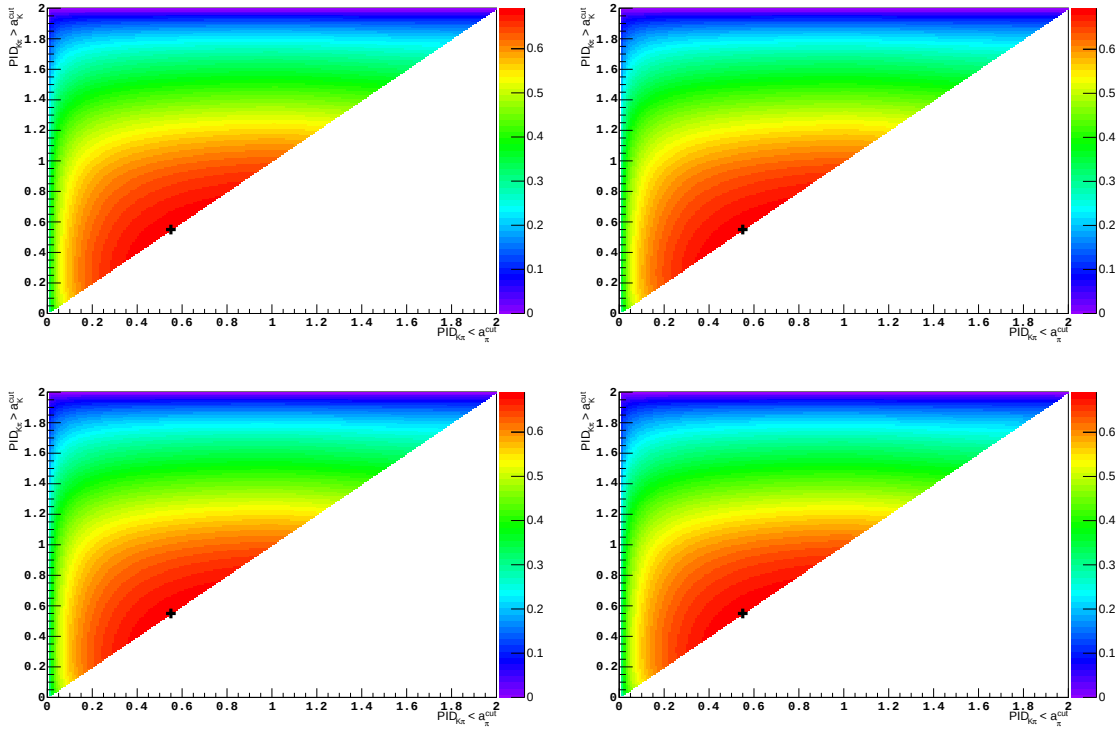

Figure 5.3: Figure of merits of $\text{PID}_{K\pi}$ optimization of $\Xi_b^0 \to pK^-\pi^+\pi^-$ for [top-left] 2011 MagDown, [top-right] 2011 MagUp, [bottom-left] 2012 MagDown and [bottom-right] 2012 MagUp.

5.6.3 Proton PID cut

Common to all the signal modes, both in the charmless and control channels, is the presence of the proton track. Hence, the efficiencies of signal and cross-feeds are basically the same, up to the difference in kinematics, for each ProbNNp cut value. As underlined in Section 5.5, a cut on PID (ProbNNp) is however necessary to reduce and/or reject the physics backgrounds coming from the 4-body decays of $B^0_{d,s}$. When a pion or a kaon from these decays is mis-identified as a proton, the event can appear in the invariant mass distribution of $phhh$ as a background and potentially yield a CP asymmetry. The inclusive branching fractions of most of the $B^0_{d,s}$ decays to fully-charged 4-body are yet unmeasured but their experimental upper limits, when they exist, are typically of order $\mathcal{O}(10^{-4})$. Moreover, the hadronization fraction of b quark to B^0 is larger than the hadronization fraction to Λ_b^0 and Ξ_b^0. Alhtough the hadronization fraction of b quark to B_s^0 is smaller than its hadronization fraction to Λ_b^0, it can still populate the spectra significantly if not properly reduced. Hence, to reduce these B physics backgrounds, an arbitrary ProbNN$p > 0.50$ PID cut is applied on the proton track. This is guesstimated to remove significant amount of these backgrounds while keeping most of our signal events. The distributions of these background events and its modelling are discussed in Section 5.8.3.

For the same reason stated in Section 5.6.2 that the ProbNN variables are not well-described in MC, a PID re-weighting is needed to properly calculate the (mis)identification efficiency[k]. To do this, PID (mis)identification efficiency maps for the PID_p cut are prepared in bins of momentum p and pseudo-rapidity angle η since the (mis)identification efficiency depends on the kinematics of the particles. The binning scheme in producing the efficiency maps for each year for the proton tracks is summarized in Table 5.7, while the K's and π's

[k] These numbers are inputs of the Gaussianly-constrained cross-feed yields in the fit as will be detailed in Section 5.8.2.

are the same as in Table 5.4. Proton tracks coming from real data inclusive Λ_c^+ decays are used to produce the identification efficiency map of proton using the PIDCalibTool. The 2D efficiency maps can be found at Appendix A.3. The signal efficiencies of the combined $\text{PID}_{K\pi}$ and PID_p cuts are gathered in Tables 5.13 and 5.14 of Section 5.6.7. They are found to be ∼45% for the two modes with three K's in the final state and ∼60% for the $\Lambda_b^0 \to p\pi\pi\pi$ mode.

Table 5.7: The binning scheme used to produce the ProbNN$p > 0.50$ identification efficiency maps.

Particle type (year)	p binning boundaries (in GeV/c^2)	η binning boundaries
p's (2011)	{3000; 9300; 15600; 18515; 28325; 40097; 59717; 100000}	{1.5; 2.4975; 2.7075; 3.0575; 3.3725; 3.7225; 4.0025; 5.0}
p's (2012)	{3000; 9300; 15600; 16553; 26363; 38135; 57755; 100000}	{1.5; 2.4625; 2.6725; 2.9875; 3.3025; 3.6525; 3.8975; 5.0}

5.6.4 MVA selection optimization

Taking advantage of nonlinearly correlated discriminating variables, an MVA-based discriminant is used in order to combine the discriminating variables into one final discriminant. Using the TMVA toolkit [109], a boosted decistion tree (BDT) discriminant, using AdaBoost boosting algorithm, has been chosen to maximize the signal separation from the combinatorial background. In order to train the BDT, signal events are taken from $\Lambda_b^0 \to p\pi\pi\pi$ MC-generated events, while combinatorial background events are taken from the right-hand sideband (RHSB) of real data events in the $X_b^0 \to p\pi\pi\pi$ spectrum. RHSB events are defined as the events with 4-body invariant mass in the range $5840. < m_{p\pi\pi\pi} < 6400.$ MeV/c^2. The choice of this spectrum is dictated at first by the absence of signal cross-feeds in the RHSB, which is a unique feature among the five experimental spectra of interest. Specifically, the misidentification of a kaon as a pion results in a shift to the left of the nominal mass of Λ_b^0 and/or Ξ_b^0 in the $X_b^0 \to p\pi\pi\pi$ spectrum.

Aiming at selecting the most relevant sample of combinatorial background to fight against, the trigger requirements, the fiducial cuts, the optimal $\text{PID}_{K\pi}$ cuts and a ProbNN$p > 0.50$ on the proton are applied prior to training the BDTs. However, B^0 physics backgrounds still populate the RHSB even at a ProbNN$p > 0.50$ cut on the proton particle. In order to further cleanup the RHSB from the dominant $B^0 \to K\pi\pi\pi$ physics backgrounds a mass veto cut[l] is applied on the background events. The mass of the proton particle is swapped with the mass of a kaon and events within the ±50 MeV/c^2 from the nominal B^0 mass are removed ($m_{\text{B}^0} = 5279.\,\text{MeV}/c^2$). As will be discussed in the Section 5.7, a significant physics background of this spectrum is coming from the decays $B^0 \to \pi\pi\pi\pi$. However, this contamination was found small enough in the RHSB such that no further specific mass veto cut was needed to select the background training sample.

In order to use maximally the RHSB statistics for the training of the multivariate discriminant, two BDTs (hereafter referred as BDT_1 and BDT_2) for each year[m] are trained

[l]This mass veto cut is not applied in the final analysis. The purpose here is only to purify the background events to be composed only of combinatorial in the training of the BDT.

[m]The center-of-mass energy of the collisions during the 2011 data taking campaign was 7 TeV, while it was 8 TeV during the 2012 data taking campaign. Hence, separate BDTs are trained for the 2011 and 2012 data.

by randomly dividing the RHSB events and the MC-generated events into two subsamples. For completeness, the random numbers are calculated using the algorithm ((134*evtNum + runNum) % 531241)/531241.0, where the evtNum and runNum are the event number and run number of the candidate, respectively. The resulting random number r assigned to each candidate ranges from 0 to 1, where RHSB events having $r \geq 0.50$ are used to train BDT_1, and the rest are used to train BDT_2. The events are then crossed-over in the testing of the BDT response for overtraining and calculating the efficiencies for a given BDT cut. When cutting the BDT in the real data events, RHSB events that were used in training BDT_1 are selected using BDT_2, and vice versa. In this way, the full Run I data can be used in the analysis without introducing bias. The real data events not used in the training of the two BDTs are also cut either using BDT_1 or BDT_2 in the same random selection algorithm as was used for the RHSB events.

We have considered ten discriminating variables for the training of the two BDTs. These are the topological and pointing variables of the candidate baryon X_b^0: η, χ^2_{FD}, χ^2_{IP}, χ^2_{vtx}, $\cos(\theta_{\mathrm{DIRA}})$; the two isolation variables : smallest $\Delta\chi^2_{\mathrm{vtx}}$ and p_{T} asymmetry in a cone around the direction of the candidate X_b^0; the sum of the χ^2_{IP} of the final daughter particles $\sum\chi^2_{\mathrm{IP}}$ (h_i); the maximum of the qualities of the tracks of the final particles Max.(χ^2/ndf (trk. h_i)); and the p_{T} of the candidate baryon X_b^0. These variables are gathered and defined in Table 5.8.

As for the stripping line construction, the design of this selection is governed by the physics we want to measure. No kinematical variable of the daughter particles is used in the BDT design in order to avoid possible biased cutting of signal events proceeding through the low two-body invariant mass resonances N^{*0}, Λ^{*0} and/or Δ series. Conversely, it is required to make a comprehensive use of the signal decay topology. X_b^0 candidate vertex properties as well as pointing quantities, all expressed in terms of significance observables, are hence simultaneously used. The selection is completed by two *isolation* variables: the smallest $\Delta\chi^2_{\mathrm{vtx}}$ is meant to select exactly four tracks vertices while the p_{T} asymmetry measures the cleanliness of the event in the region of interest (along the momentum of the X_b^0 candidate). Eventually, it was observed that the combinatorial background can be made from a well-defined vertex of three tracks complemented with an additional track of poor reconstruction quality. The variable defined maximum of the (χ^2/ndf (trk. h_i)) aims at rejecting this specific source of background.

Some of the variables (expressed as the square of the significance) have very large ranges. Their logarithm is taken instead in the BDT design. The *importance* of a variable is defined as how many times the variable (expressed in %) is used to separate background and signal in the forest of trees. Hence, the importance does not necessarily select the intrinsic discriminating power but accounts for the correlations the variable has with the ensemble of discriminative variables. The importances of the set of variables in the BDT design are listed in Table 5.9 and the distributions of the variables are shown in Figure 5.4, superimposing RHSB background events and MC-generated signal events[n]. The least important variables has been used in the BDT more than 5% of the time, with the highest ranking variable being used roughly 20% of the time. The importances are given here for illustration of the individual power of the discriminative variables within the BDT. It was not used to provide a selection rule of them.

Shown in Figure 5.5 is the correlation map of the variables used to train the BDT_1 for 2011. Most of the variables have weak linear correlations. Although the linear correlations are high for some pairs of variables, the correlations are not the same for signal and background events. Aside from that, for the same pair of variables, the correlations of these

[n] The counterpart distributions for the other BDT are shown in Appendix A.6.

Table 5.8: List of variables used in the BDT design.

Variable	Description
η (X_b^0)	The pseudo-rapidity angle of the reconstructed X_b^0 candidate.
$p_{\rm T}$ (X_b^0)	The transverse momentum of the reconstructed X_b^0 candidate.
$\chi^2_{\rm FD}$ (X_b^0)	The consistency that the X_b^0 candidate is detached from the primary vertex.
$\chi^2_{\rm IP}$ (X_b^0)	The quality of the impact parameter of the reconstructed X_b^0 candidate.
$\chi^2_{\rm vtx}$ (X_b^0)	The quality of the secondary vertex of the reconstructed X_b^0 candidate.
$\cos(\theta_{\rm DIRA})$ (X_b^0)	The cosine of the subtended angle between the reconstructed momentum of the X_b^0 candidate and the line connecting the primary vertex to the secondary vertex.
Smallest $\Delta\chi^2_{\rm vtx}$ (X_b^0)	The difference of the vertex quality of the reconstructed X_b^0 candidate when added an extra most compatible track.
Asym. $p_{\rm T}$ (X_b^0)	This variables is defined as the asymmetry of the $p_{\rm T}$ of the reconstructed X_b^0 candidate when considering the $p_{\rm T}$ of the other tracks in the event that are within a given angle from the direction of the X_b^0 candidate. In this analysis, the cone angle used is 1.7°. Mathematically, this is defined as ($p_{\rm T}{}^{X_b^0}$ - $p_{\rm T}{}^{\rm inAngle}$) / ($p_{\rm T}{}^{X_b^0}$ + $p_{\rm T}{}^{\rm inAngle}$), where $p_{\rm T}{}^{\rm inAngle}$ is the vector sum of the $p_{\rm T}$'s of all tracks inside the 1.7° cone angle.
$\sum\chi^2_{\rm IP}$ (h_i's)	The consistency that the tracks are detached from the primary vertex.
Largest $\chi^2_{\rm trk.}$/ndf (of h_i's)	The largest track quality divided by number of degrees of freedom among the four daughter tracks.

variables to the other variables are not the same for signal and background events.

Figure 5.6 indicates that there is no obvious sign of overtraining, as also indicated by the Kolmogorov-Smirnov tests. In order to check whether the X_b^0 invariant mass is not learned by the BDT, we gathered in Table 5.10 the correlation of X_b^0 invariant mass and the BDT using MC signal events. Summarized in Table 5.11 are the signal efficiencies for a given BDT cut that gives a background selection efficiency (or rejection efficiency) of 1% (99%), 10% (90%) and 30% (70%). Fisher and gradient-boosted BDT have been compared with the AdaBoost-boosted BDT. Shown in Figure 5.7 are the background-rejection efficiency versus signal selection efficiency curves (ROC-curve) for 2011 $\rm BDT_1$ and 2012 $\rm BDT_2$. The ROC-curve integral of Fisher (both 0.983 for 2011 and 0.973 & 0.977 for 2012) is expectedly smaller than the AdaBoost-boosted BDT, indicating that the non-linear correlations between variables are at work in the discriminative power of the BDT. The ROC-curve integral of gradient-boosted BDT (0.989 & 0.988 for 2011 and 0.986 & 0.985 for 2012) is very similar to the AdaBoost-boosted BDT (0.988 & 0.988 for 2011 and 0.985 & 0.984 for 2012). For the sake of consistency with former analyses that we developed, the AdaBoost-boosted BDT is decided to be used in this analysis.

The same BDT machinery is applied to all spectra. Optimal BDT cut for each spectrum is then calculated. Since all the signal regions are blind, it has been chosen to use the Punzi

Table 5.9: The importance of the variables in the BDT design.

Variable	Variable importance (in %)			
	2011		2012	
	BDT_1	BDT_2	BDT_1	BDT_2
log(Smallest $\Delta\chi^2_{\text{vtx}}$) ($X_b^0$)	17.67	17.90	17.02	14.60
η (X_b^0)	11.52	11.54	11.91	12.49
1.0 - log(cos(θ_{DIRA})) (X_b^0)	10.90	11.97	10.29	10.52
p_{T} (X_b^0)	10.88	11.34	9.457	10.78
log(χ^2_{FD}) (X_b^0)	9.093	10.94	9.332	7.962
log(χ^2_{IP}) (X_b^0)	8.612	7.854	8.380	10.12
Asym. p_{T} (X_b^0)	8.338	7.368	7.973	8.910
log(χ^2_{vtx}) (X_b^0)	8.157	6.737	9.025	9.385
Largest log($\chi^2_{\text{trk.}}$/ndf) (of h_i's)	7.567	7.922	7.916	7.816
log($\sum\chi^2_{\text{IP}}$) (h_i's)	7.268	6.419	8.699	7.410

Table 5.10: Correlation of the BDT values and the X_b^0 invariant mass calculated using MC-generated signal events.

Signal decay mode	Correlations (in %)	
	2011	2012
$\Lambda_b^0 \to p\pi\pi\pi$	-0.93 ± 0.93	0.26 ± 0.69
$\Lambda_b^0 \to pK\pi\pi$	0.04 ± 0.95	-0.17 ± 0.71
$\Lambda_b^0 \to pKK\pi$	-0.79 ± 1.01	-0.32 ± 0.74
$\Lambda_b^0 \to pKKK$	-1.34 ± 0.99	-0.27 ± 0.72
$\Xi_b^0 \to pK\pi\pi$	-0.62 ± 0.93	-1.93 ± 0.68
$\Xi_b^0 \to pK\pi K$	-0.89 ± 0.96	-0.69 ± 0.71
$\Xi_b^0 \to pKKK$	0.15 ± 0.93	-0.90 ± 0.68

Figure of Merit [110] as the estimator for the optimization. Mathematically, it reads:

$$\text{FoM}(\text{BDT}_{\text{cut}}) = \frac{\epsilon^{\text{BDT}}_{\text{Sig.}}}{\frac{a}{2} + \sqrt{\text{B}^{\text{SigReg.}}_{\text{Comb.}}}}, \tag{5.5}$$

where $\epsilon^{\text{BDT}}_{\text{Sig.}}$ is the signal efficiency for a given BDT cut, a is the number of sigmas corresponding to the desired significance of the limit, and $\text{B}^{\text{SigReg.}}_{\text{Comb.}}$ is the expected number of combinatorial backgrounds under the signal peak for a given BDT cut. In this analysis, $a = 2$ is chosen.

The signal efficiency $\epsilon^{\text{BDT}}_{\text{Sig.}}$ at each BDT cut is calculated from the MC-generated events, while the number of combinatorial backgrounds under the signal peak is approximated using the RHSB region. Before any BDT cut, real data events in the RHSB (5840 MeV/c^2 < m_{phhh} < 6400 MeV/c^2) region are fitted with an exponential function. This exponential function is then projected to the signal mass region, which is within $\pm 3\sigma$ from the nominal mass of Λ_b^0 or Ξ_b^0 (*i.e.*, [5575 MeV/c^2, 5665 MeV/c^2] for Λ_b^0 and [5743 MeV/c^2, 5833 MeV/c^2] for Ξ_b^0).

The extrapolated number of combinatorial backgrounds under the signal peak before any BDT cut is estimated using the projected exponential function. A word of caution is in order here. Since there must be a contamination of B physics backgrounds in the RHSB region, the approximation of the combinatorial shape and level using RHSB events must be slightly

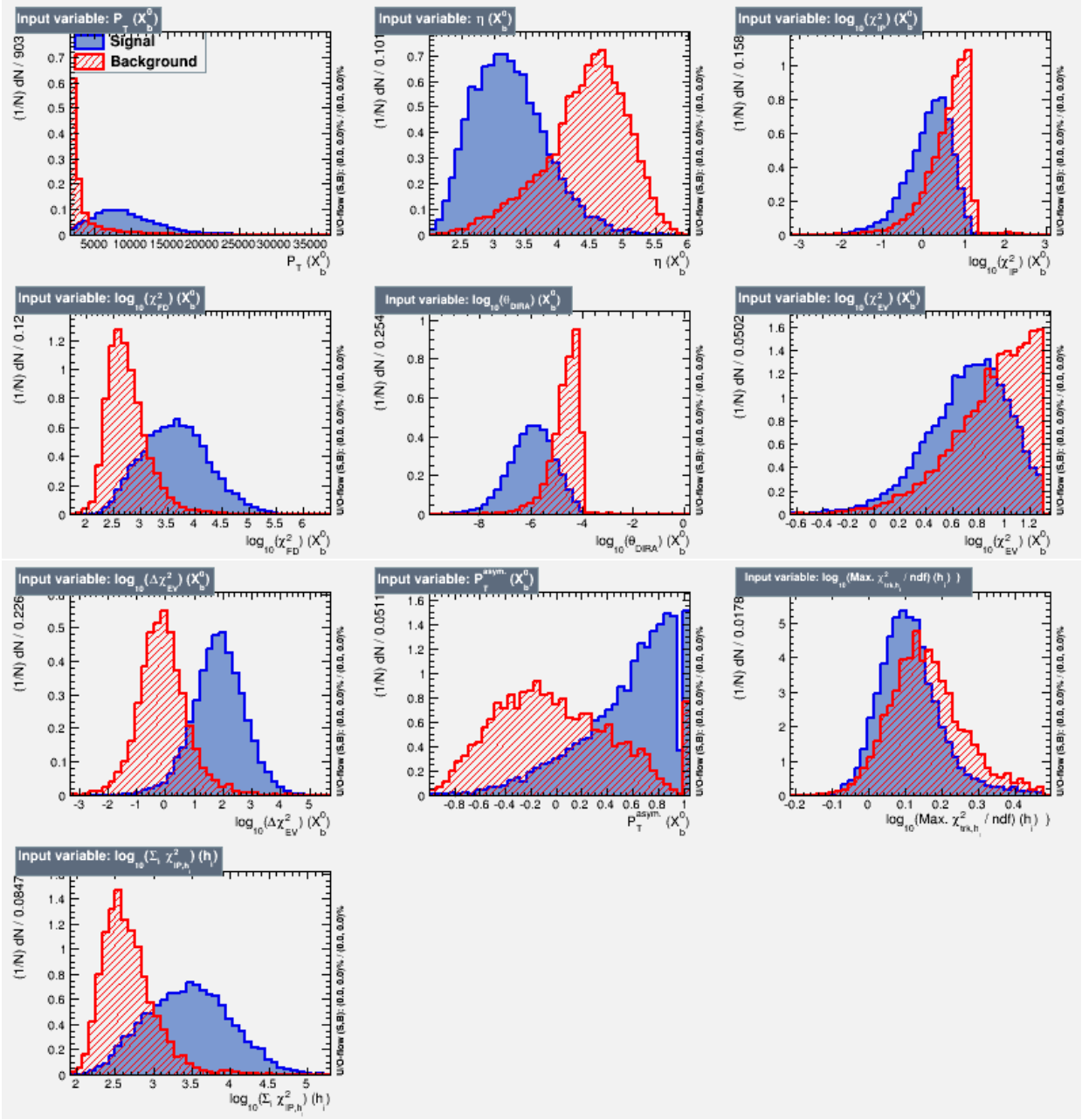

Figure 5.4: Distribution of variables used in the training of BDT_1 for 2011, superimposing RHSB background events (in Red) and MC-generated signal events (in Blue).

overestimated. For the subsequent BDT cuts, the number of combinatorics under the signal peak linearly scales with the number of combinatorics in the RHSB, i.e., knowing that the shape of the combinatorial is not significantly changing[o]. Hence, this is calculated by,

$$\mathrm{B}^{\mathrm{SigReg.}}_{\mathrm{Comb.}}(\mathrm{BDT}_{\mathrm{cut}}) = r \cdot \mathrm{B}^{\mathrm{RHSB}}_{\mathrm{Comb.}}, \tag{5.6}$$

where r is the scaling factor equal to $(\mathrm{B}^{\mathrm{SigReg.}}_{\mathrm{Comb.}})/(\mathrm{B}^{\mathrm{RHSB}}_{\mathrm{Comb.}})$ calculated with no BDT cut.

The Figures of Merit for all the modes are displayed in Figure 5.8. In the case of $X_b^0 \to pK\pi\pi$ and $X_b^0 \to pKKK$ spectra where both Λ_b^0 and Ξ_b^0 signals are present, the Ξ_b^0 signals are chosen to be optimized. The optimal BDT cuts are lying in a range [0.2 - 0.4]

[o]We have verified that the combinatorics slope measured (up to the moment it cannot be measured anymore because of too few events) is consistent with the reference one within uncorrelated statistical uncertainty.

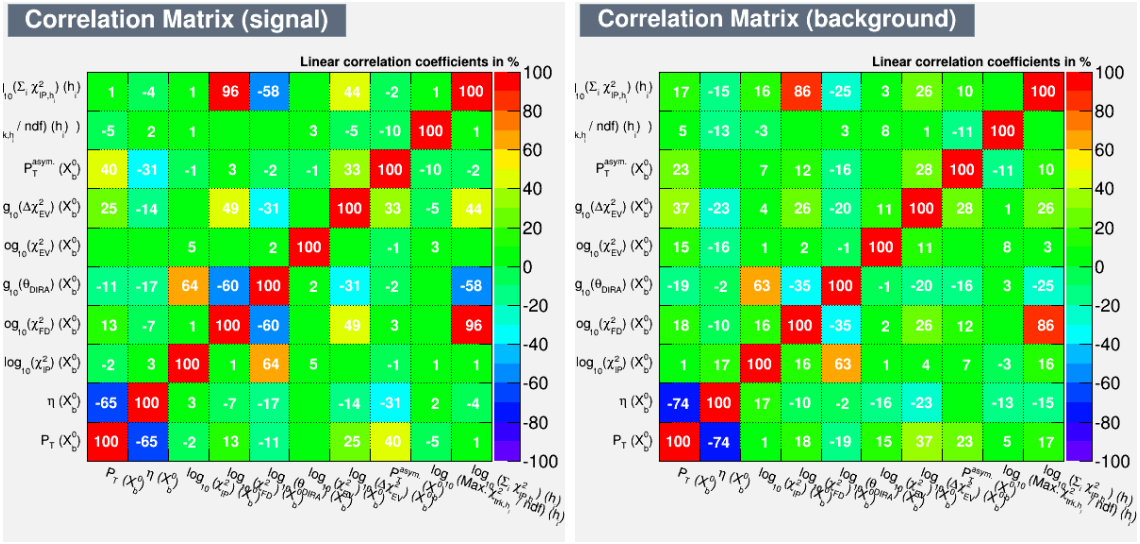

Figure 5.5: Linear correlation of variables used in the training of BDT_1 for 2011 for (left) signal events and (right) background events. See Appendix A.7 for the other BDTs.

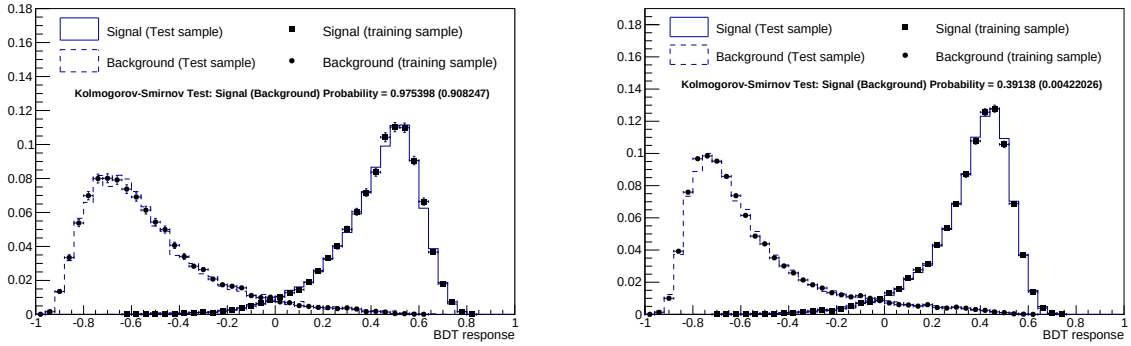

Figure 5.6: BDT response for (left) combined 2011 BDTs and (right) combined 2012 BDTs.

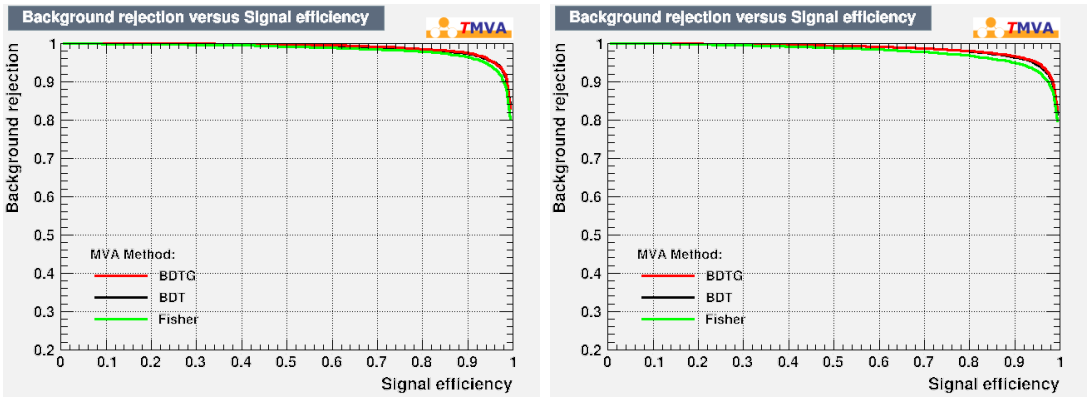

Figure 5.7: ROC-curve for [left] 2011 BDT_1 and [right] 2012 BDT_1.

for all spectra. Dictated by a sake of simplicity of bookkeeping, a unique BDT cut value of 0.30 is chosen for all the charmless spectra.

Table 5.11: Signal selection efficiencies for BDT cuts with corresponding background selection efficiencies of 1%, 10% and 30%.

BDT Classifier	Year	ROC-integral	Signal efficiencies (for a given background efficiency)		
			$\epsilon_{\text{Comb.}} = 1\%$	$\epsilon_{\text{Comb.}} = 10\%$	$\epsilon_{\text{Comb.}} = 30\%$
BDT_1	2011	0.988	76.0%	98.8%	100%
BDT_2	2011	0.988	77.7%	98.6%	100%
BDT_1	2012	0.985	63.4%	98.4%	100%
BDT_2	2012	0.984	64.0%	98.2%	100%

5.6.5 Charm veto cuts

Charmed and charmonia resonances mass veto cuts are applied to remove the Λ_b^0 and Ξ_b^0 decaying to the same final state as the interest modes but proceeding via a charm resonance. The veto cuts are applied globally to all the spectra, that is, candidates vetoed in one spectrum does not appear in the other spectra. Vetoed charmed and charmonia resonances include Λ_c^+, Ξ_c^+, D^+, D_s^+, D^0, χ_{c0} and J/ψ, where the invariant mass of these resonances is calculated by simply adding vectorially the four-vector momenta of the tracks without a refit on the decay tree. The mass window cut applied is ± 30 MeV/c^2 from the nominal mass of the resonance, except for the χ_{c0} and J/ψ where the mass window cut is ± 50 MeV/c^2. Note that the nominal mass of Λ_c^+ is adjusted to the left of the PDG value by about 3 MeV/c^2 in order to take into account the asymmetry of the Λ_c^+ mass distributions as can be seen in Figure 5.9. Aside from the mass veto cuts, two tracks of opposite charge are required not to be muons by cutting on the isMuon variable. Furthermore, in order to remove possible backgrounds coming from semi-leptonic decays of X_b^0, where the muon most likely carries large momentum, an isMuon cut is applied to the track having the highest p_{T}. The list of charm veto cuts is gathered in Table 5.12. For labelling purposes, we arranged the four charged tracks in each spectrum in this sequence: $(ph^-h^+h^-)$ or $(\overline{p}h^+h^-h^+)$. Hence, the proton is labelled as h_1, and the remaining h's are labelled h_2, h_3 and h_4 in a charge arrangement defined in the previous sentence. For example, the notation $h_ih_jh_k\_p\pi\pi$ means the reconstructed invariant mass of the combination, where h_i is assigned with the mass of the proton, while h_j and h_k are assigned with the mass of the pion.

5.6.6 Selection strategy for control modes

The single requirement of a weakly interacting charmed resonance is enough to reconstruct with a high purity the control channels out of the stripping events. No PID selection optimization nor BDT selection optimization is done for the control modes. The same set of $\text{PID}_{K\pi}$ and PID_p cuts are however applied on the control modes in order to avoid possible difference of production asymmetry and detection asymmetries when the PID cuts are not the same for charmless modes and control modes. A lower BDT cut of $>$ -0.10 is chosen. Events whose invariant mass is within $\pm$ 30 MeV/c^2 from the nominal mass of the charmed resonances Ξ_c^+ and Λ_c^+ ($m_{\Lambda_c^+} = 2283.0$ MeV/c^2, $m_{\Lambda_c^+}$ adjusted to take into account the asymmetry of the distribution) are considered to belong to the control modes. This mass window cut is the reverse veto cut applied in the charmless modes, again ensuring that we have statistically independent events for the simultaneous fit. The invariant mass distributions of the Λ_c^+ and Ξ_c^+ are shown in Figures 5.9.

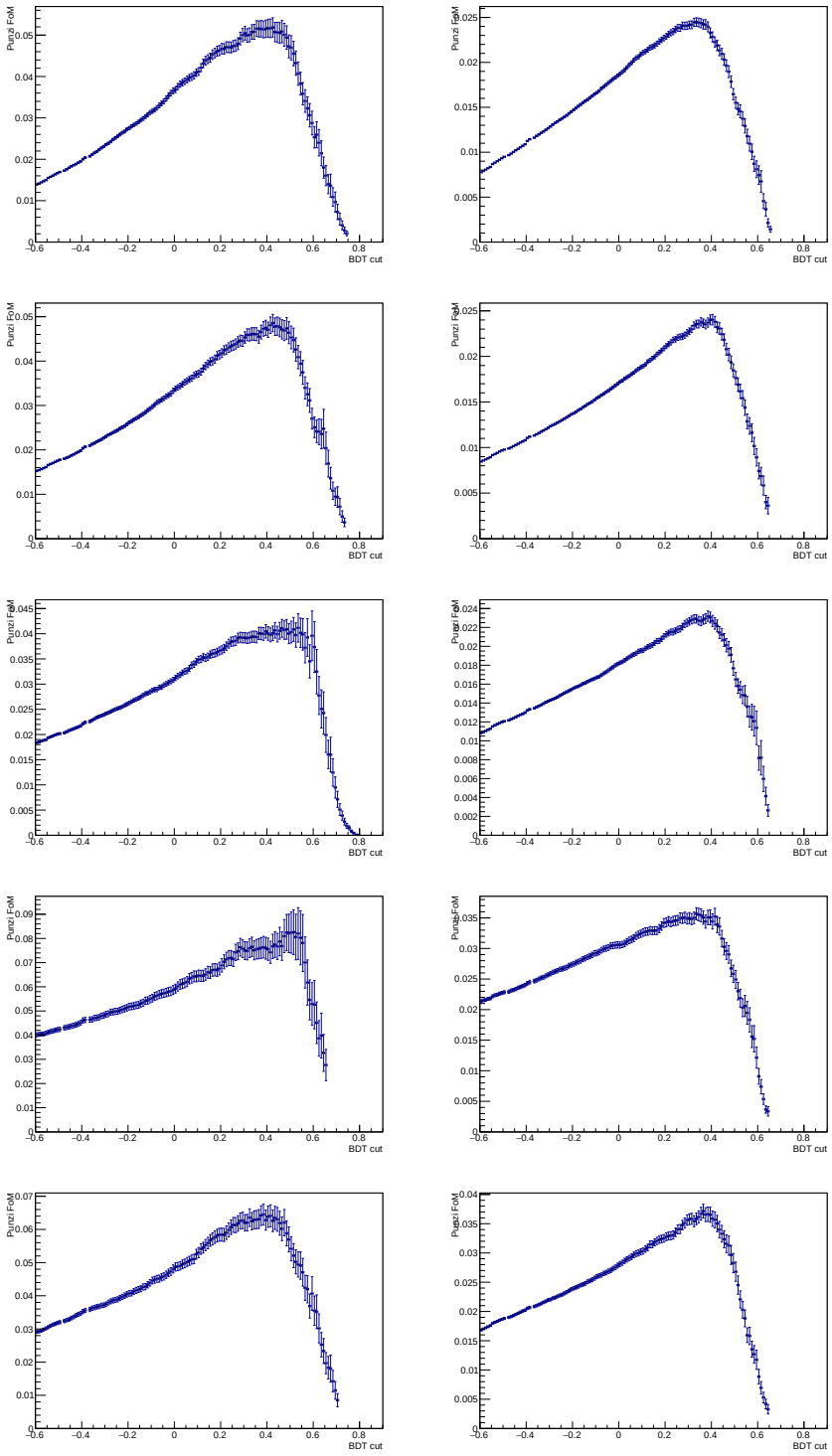

Figure 5.8: Punzi figures of merit for BDT cut optimization for the spectra (from top to bottom) $X_b^0 \to p\pi\pi\pi$, $X_b^0 \to pK\pi\pi$, $X_b^0 \to pKK\pi$, $X_b^0 \to pKKK$ and $X_b^0 \to pK\pi K$. Figures on the left column are for the 2011 data and figures on the right column are for the 2012 data.

5.6.7 Efficiencies

Summarized in Tables 5.13 (for 2011) and 5.14 (for 2012) are the signal efficiencies calculated for each selection step. Each efficiency is calculated with respect to the immediate previous selection step, except for the row labelled "From reco. to isMuon" where this is the efficiency from the reconstruction up to isMuon cuts. The last rows with header "MagDown and MagUp

Table 5.12: List of charm veto cuts applied on the data.

Charmed resonance	Decay	Cut applied (mass in units of MeV/c^2)
Λ_c^+	$\Lambda_c^+ \to p\pi^-\pi^+$	$\lvert 2283.00 - h_1h_2h_3\_p\pi\pi\rvert > 30.$ and $\lvert 2283.00 - h_1h_4h_3\_p\pi\pi\rvert > 30.$
	$\Lambda_c^+ \to pK^-\pi^+$	$\lvert 2283.00 - h_1h_2h_3\_pK\pi\rvert > 30.$ and $\lvert 2283.00 - h_1h_4h_3\_pK\pi\rvert > 30.$
	$\Lambda_c^+ \to pK^-K^+$	$\lvert 2283.00 - h_1h_2h_3\_pKK\rvert > 30.$ and $\lvert 2283.00 - h_1h_4h_3\_pKK\rvert > 30.$
Ξ_c^+	$\Xi_c^+ \to pK^-\pi^+$	$\lvert 2467.80 - h_1h_2h_3\_pK\pi\rvert > 30.$ and $\lvert 2467.80 - h_1h_4h_3\_pK\pi\rvert > 30.$
$\overset{(-)}{D^0}$	$\overset{(-)}{D^0} \to \pi^-\pi^+$	$\lvert 1864.84 - h_2h_3\_\pi\pi\rvert > 30.$ and $\lvert 1864.84 - h_4h_3\_\pi\pi\rvert > 30.$
	$\overset{(-)}{D^0} \to K^-K^+$	$\lvert 1864.84 - h_2h_3\_KK\rvert > 30.$ and $\lvert 1864.84 - h_4h_3\_KK\rvert > 30.$
	$D^0 \to \pi^+K^-$	$\lvert 1864.84 - h_2h_3\_K\pi\rvert > 30.$ and $\lvert 1864.84 - h_4h_3\_K\pi\rvert > 30.$
	$\overline{D}^0 \to \pi^-K^+$	$\lvert 1864.84 - h_2h_3\_\pi K\rvert > 30.$ and $\lvert 1864.84 - h_4h_3\_\pi K\rvert > 30.$
D^+	$D^+ \to \pi^+K^-\pi^+$	$\lvert 1869.61 - h_2h_3h_4\_\pi K\pi\rvert > 30.$
D_s^+	$D_s^+ \to K^+K^-\pi^+$	$\lvert 1968.30 - h_2h_3h_4\_KK\pi\rvert > 30.$ and $\lvert 1968.30 - h_2h_3h_4\_\pi KK\rvert > 30.$
	$D_s^+ \to \pi^+\pi^-\pi^+$	$\lvert 1968.30 - h_2h_3h_4\_\pi\pi\pi\rvert > 30.$
J/ψ	$J/\psi \to \pi^+\pi^-$	$\lvert 3096.92 - h_2h_3\_\pi\pi\rvert > 50.$ and $\lvert 3096.92 - h_4h_3\_\pi\pi\rvert > 50.$
	$J/\psi \to K^+K^-$	$\lvert 3096.92 - h_2h_3\_KK\rvert > 50.$ and $\lvert 3096.92 - h_4h_3\_KK\_\mathrm{M}\rvert > 50.$
χ_{c0}	$\chi_{c0} \to \pi^+\pi^-$	$\lvert 3414.75 - h_2h_3\_\pi\pi\rvert > 50.$ and $\lvert 3414.75 - h_4h_3\_\pi\pi\rvert > 50.$
	$\chi_{c0} \to K^+K^-$	$\lvert 3414.75 - h_2h_3\_KK\rvert > 50.$ and $\lvert 3414.75 - h_4h_3\_KK\_\mathrm{M}\rvert > 50.$
$X \to \mu^+\mu^-$	!(h_1_isMuon == 1 && h_2_isMuon == 1) and !(h_3_isMuon == 1 && h_4_isMuon == 1)	
	!(h_2_isMuon == 1 && h_3_isMuon == 1) and !(h_1_isMuon == 1 && h_4_isMuon == 1)	

configuration averaged" are the average efficiencies for MagDown and MagUp configurations.

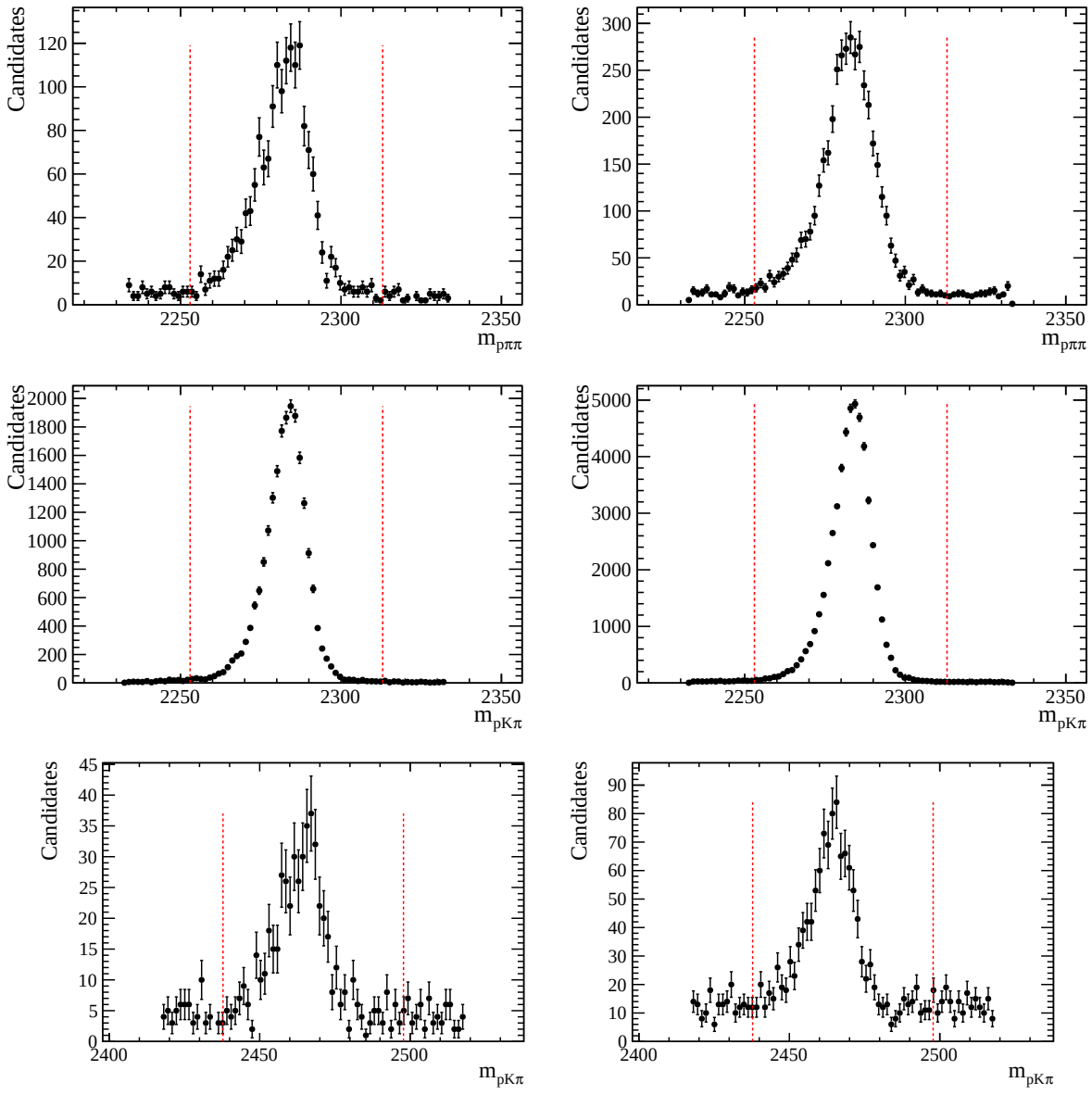

Figure 5.9: Invariant mass distribution of the Λ_c^+ and Ξ_c resonances of the control modes used in this analysis, namely, [top] $\Lambda_b^0 \to (\Lambda_c^+ \to p\pi^-\pi^+)\pi^-$, [middle] $\Lambda_b^0 \to (\Lambda_c^+ \to pK^-\pi^+)\pi^-$ and [bottom] $\Lambda_b^0(\Xi_b^0) \to (\Xi_c^+ \to pK^-\pi^+)\pi^-$ for [left-column] 2011 data and [right-column] 2012 data.

Table 5.13: Summary of signal efficiencies on each applied cut for 2011.

Cut applied	Step by step efficiencies calculated w.r.t. previous cut (in %)						
	$\Lambda_b^0 \to p\pi\pi\pi$	$\Lambda_b^0 \to pK\pi\pi$	$\Lambda_b^0 \to pKK\pi$	$\Lambda_b^0 \to pKKK$	$\Xi_b^0 \to pK\pi\pi$	$\Xi_b^0 \to pK\pi K$	$\Xi_b^0 \to pKKK$
MagDown configuration							
LHCb acceptance cut	16.240±0.042	16.944±0.046	17.707±0.048	18.637±0.051	17.007±0.038	17.646±0.038	18.615±0.038
Reco+Stripping cuts	6.681±0.034	6.430±0.034	6.213±0.034	6.508±0.034	7.024±0.036	6.959±0.036	7.234±0.036
L0 trigger requirement	55.400±0.264	54.100±0.274	53.380±0.279	52.017±0.273	51.889±0.266	51.462±0.268	49.266±0.258
Hlt1 trigger requirement	85.332±0.253	85.891±0.260	85.910±0.267	84.762±0.272	86.558±0.252	86.345±0.256	85.388±0.259
Hlt2 trigger requirement	88.670±0.245	88.705±0.255	88.271±0.266	87.264±0.275	90.844±0.229	90.488±0.236	90.143±0.237
Fiducial cuts	78.786±0.336	81.570±0.332	82.990±0.331	85.196±0.313	80.189±0.332	81.275±0.330	84.253±0.305
BDT cut	76.883±0.390	76.139±0.404	74.357±0.422	72.964±0.424	79.964±0.373	77.786±0.390	75.923±0.390
Charmed veto cuts	68.106±0.492	70.149±0.497	68.949±0.518	75.309±0.482	68.898±0.482	69.410±0.490	74.945±0.453
isMuon cuts	99.379±0.100	99.377±0.102	99.291±0.113	99.004±0.128	99.119±0.117	99.203±0.113	99.006±0.120
From reco. to isMuon	1.148±0.015	1.147±0.015	1.063±0.014	1.160±0.015	1.255±0.016	1.218±0.016	1.302±0.016
PID cuts	59.577±0.292	53.912±0.282	48.857±0.275	44.867±0.253	53.534±0.281	47.627±0.268	44.615±0.244
MagUp configuration							
LHCb acceptance cut	16.129±0.044	17.000±0.044	17.702±0.048	18.709±0.050	17.001±0.038	17.733±0.039	18.663±0.038
Reco+Stripping cuts	6.653±0.035	6.383±0.034	6.215±0.034	6.536±0.034	6.999±0.035	6.946±0.036	7.137±0.035
L0 trigger requirement	55.354±0.271	54.591±0.270	52.978±0.280	52.071±0.271	51.729±0.262	51.268±0.265	48.881±0.257
Hlt1 trigger requirement	84.472±0.266	85.314±0.260	85.964±0.267	84.809±0.270	85.602±0.256	86.476±0.254	85.942±0.255
Hlt2 trigger requirement	88.559±0.254	89.174±0.247	88.446±0.266	87.403±0.271	90.820±0.228	90.679±0.232	90.121±0.236
Fiducial cuts	78.703±0.347	81.818±0.325	83.279±0.330	85.236±0.310	80.153±0.330	81.427±0.326	84.587±0.301
BDT cut	76.488±0.406	77.100±0.391	74.836±0.420	73.506±0.418	79.352±0.374	77.165±0.390	75.842±0.388
Charmed veto cuts	69.237±0.505	68.486±0.493	68.352±0.520	74.969±0.479	68.645±0.481	68.565±0.491	74.422±0.455
isMuon cuts	99.413±0.100	99.145±0.118	99.231±0.118	99.007±0.127	99.107±0.118	99.055±0.123	98.862±0.128
From reco. to isMuon	1.141±0.015	1.135±0.015	1.058±0.014	1.173±0.015	1.218±0.015	1.192±0.015	1.275±0.015
PID cuts	59.066±0.297	53.812±0.274	48.256±0.275	44.653±0.249	53.580±0.275	48.165±0.264	44.385±0.239
MagDown and MagUp configuration averaged							
LHCb acceptance cut	16.184±0.030	16.972±0.032	17.704±0.034	18.673±0.036	17.004±0.027	17.689±0.027	18.639±0.027
Reco+Stripping cuts	6.667±0.025	6.406±0.024	6.214±0.024	6.522±0.024	7.012±0.025	6.953±0.025	7.186±0.025
L0 trigger requirement	55.377±0.189	54.346±0.192	53.179±0.198	52.044±0.193	51.809±0.187	51.365±0.189	49.073±0.182
Hlt1 trigger requirement	84.902±0.183	85.603±0.184	85.937±0.189	84.785±0.192	86.080±0.180	86.411±0.180	85.665±0.182
Hlt2 trigger requirement	88.614±0.176	88.939±0.178	88.358±0.188	87.334±0.193	90.832±0.161	90.584±0.165	90.132±0.167
Fiducial cuts	78.745±0.241	81.694±0.232	83.134±0.233	85.216±0.220	80.171±0.234	81.351±0.232	84.420±0.214
BDT cut	76.686±0.281	76.620±0.281	74.596±0.298	73.235±0.298	79.658±0.264	77.475±0.275	75.882±0.275
Charmed veto cuts	68.672±0.352	69.317±0.350	68.650±0.367	75.139±0.340	68.772±0.340	68.987±0.347	74.684±0.321
isMuon cuts	99.396±0.071	99.261±0.077	99.261±0.082	99.005±0.090	99.113±0.083	99.129±0.084	98.934±0.088
From reco. to isMuon	1.145±0.010	1.141±0.010	1.060±0.010	1.167±0.011	1.237±0.011	1.205±0.011	1.289±0.011
PID cuts	59.322±0.208	53.862±0.197	48.557±0.194	44.760±0.178	53.557±0.197	47.896±0.188	44.500±0.171

Table 5.14: Summary of signal efficiencies on each applied cut for 2012.

Cut applied	Step by step efficiencies calculated w.r.t. previous cut (in %)						
	$\Lambda_b^0 \to p\pi\pi\pi$	$\Lambda_b^0 \to pK\pi\pi$	$\Lambda_b^0 \to pKK\pi$	$\Lambda_b^0 \to pKKK$	$\Xi_b^0 \to pK\pi\pi$	$\Xi_b^0 \to pK\pi K$	$\Xi_b^0 \to pKKK$
MagDown configuration							
LHCb acceptance cut	16.559±0.068	17.381±0.072	17.965±0.075	18.990±0.077	17.330±0.070	18.035±0.072	18.955±0.072
Reco+Stripping cuts	6.032±0.024	5.766±0.023	5.616±0.023	5.853±0.023	6.381±0.024	6.277±0.024	6.569±0.024
L0 trigger requirement	52.360±0.201	51.453±0.207	50.639±0.210	48.868±0.205	48.764±0.195	48.501±0.197	45.660±0.189
Hlt1 trigger requirement	85.890±0.194	86.691±0.196	86.864±0.199	86.488±0.201	86.910±0.188	87.046±0.190	86.845±0.190
Hlt2 trigger requirement	93.273±0.151	92.968±0.158	92.887±0.163	91.932±0.172	94.072±0.141	94.094±0.143	93.223±0.151
Fiducial cuts	76.385±0.265	78.438±0.264	80.464±0.260	82.794±0.248	77.555±0.258	79.293±0.254	82.314±0.238
BDT cut	68.084±0.332	69.550±0.334	65.004±0.349	63.315±0.349	72.028±0.315	68.072±0.328	66.358±0.325
Charmed veto cuts	68.571±0.401	68.973±0.402	68.461±0.422	74.304±0.397	68.623±0.383	67.992±0.397	75.891±0.361
isMuon cuts	99.434±0.078	99.342±0.085	99.241±0.095	98.855±0.112	99.423±0.076	99.082±0.098	99.126±0.090
From reco. to isMuon	0.897±0.009	0.894±0.009	0.815±0.009	0.876±0.009	0.970±0.010	0.907±0.009	0.998±0.010
PID cuts	61.062±0.198	55.741±0.194	50.063±0.191	46.232±0.179	55.439±0.189	49.955±0.185	46.501±0.168
MagUp configuration							
LHCb acceptance cut	16.683±0.071	17.386±0.076	18.015±0.076	19.149±0.080	17.271±0.066	18.000±0.071	18.925±0.072
Reco+Stripping cuts	6.043±0.024	5.850±0.023	5.636±0.023	5.846±0.023	6.406±0.024	6.306±0.024	6.573±0.025
L0 trigger requirement	52.479±0.202	51.113±0.206	50.768±0.210	49.083±0.206	48.463±0.197	48.506±0.199	45.945±0.193
Hlt1 trigger requirement	85.789±0.195	86.465±0.197	86.756±0.200	86.909±0.199	87.121±0.190	87.583±0.189	87.060±0.192
Hlt2 trigger requirement	93.242±0.152	92.786±0.161	92.734±0.165	91.954±0.172	93.922±0.145	93.988±0.145	93.288±0.154
Fiducial cuts	76.419±0.266	78.831±0.263	80.992±0.258	83.776±0.243	77.531±0.261	78.575±0.259	82.480±0.242
BDT cut	68.964±0.331	69.122±0.335	64.124±0.351	63.024±0.348	71.928±0.319	68.290±0.331	67.288±0.328
Charmed veto cuts	68.111±0.402	69.146±0.403	67.736±0.427	75.670±0.389	68.851±0.388	68.085±0.401	74.667±0.371
isMuon cuts	99.531±0.071	99.328±0.086	99.211±0.098	99.087±0.099	99.277±0.086	99.228±0.091	98.889±0.103
From reco. to isMuon	0.906±0.009	0.898±0.009	0.803±0.009	0.908±0.009	0.968±0.010	0.913±0.010	1.005±0.010
PID cuts	60.280±0.198	54.805±0.195	49.472±0.191	45.607±0.175	55.150±0.190	49.031±0.186	45.872±0.172
MagDown and MagUp configuration averaged							
LHCb acceptance cut	16.621±0.049	17.383±0.052	17.990±0.053	19.070±0.055	17.301±0.048	18.018±0.051	18.940±0.051
Reco+Stripping cuts	6.037±0.017	5.808±0.016	5.626±0.016	5.850±0.017	6.393±0.017	6.291±0.017	6.571±0.017
L0 trigger requirement	52.419±0.143	51.283±0.146	50.704±0.149	48.975±0.145	48.613±0.138	48.503±0.140	45.803±0.135
Hlt1 trigger requirement	85.839±0.138	86.578±0.139	86.810±0.141	86.699±0.141	87.016±0.134	87.314±0.134	86.952±0.135
Hlt2 trigger requirement	93.257±0.107	92.877±0.113	92.810±0.116	91.943±0.122	93.997±0.101	94.041±0.102	93.255±0.108
Fiducial cuts	76.402±0.187	78.634±0.186	80.728±0.183	83.285±0.174	77.543±0.183	78.934±0.181	82.397±0.170
BDT cut	68.524±0.235	69.336±0.237	64.564±0.248	63.169±0.246	71.978±0.224	68.181±0.233	66.823±0.231
Charmed veto cuts	68.341±0.284	69.059±0.285	68.098±0.300	74.987±0.278	68.737±0.273	68.038±0.282	75.279±0.259
isMuon cuts	99.483±0.053	99.335±0.060	99.226±0.068	98.971±0.074	99.350±0.057	99.155±0.067	99.008±0.068
From reco. to isMuon	0.902±0.007	0.896±0.007	0.809±0.006	0.892±0.007	0.969±0.007	0.910±0.007	1.001±0.007
PID cuts	60.671±0.140	55.273±0.138	49.768±0.135	45.920±0.125	55.295±0.134	49.493±0.131	46.186±0.120

5.6.8 Multiple candidates

The frequency of finding more than one candidate per event is typically less than 3×10^{-3} as reported in Table 5.15. If the candidates belong to either of the $X_b^0 \to p\pi\pi\pi$, $X_b^0 \to pKKK$ or $X_b^0 \to pK\pi K$ spectra, whichever candidate has a larger ProbNNp value on the proton track is retained, while the others are discarded. If however the candidates have the same proton track (hence the same ProbNNp value), one candidate is chosen randomly to be retained.

For the $X_b^0 \to pK\pi\pi$ and $X_b^0 \to pKK\pi$ spectra, a slightly different selection rule is applied. If two or more candidates has the same proton track, then the ProbNNK values of the h_2s (the first kaon track) are compared. Whichever has the larger value is likely the signal and hence the candidate which is retained. Otherwise, if both proton track and (first) kaon track are the same for two or more candidates, then one candidate is chosen randomly.

Table 5.15: Number of multiple candidates in each spectra.

Spectra	2011 data			2012 data		
	Candidates	Multiple	nCands = 2	Candidates	Multiple	nCands = 2
$X_b^0 \to p\pi\pi\pi$	3604	2	1	8712	2	1
$X_b^0 \to pK\pi\pi$	6207	8	4	13950	8	4
$X_b^0 \to pKK\pi$	1466	0	0	3409	4	2
$X_b^0 \to pKKK$	1067	0	0	2366	0	0
$X_b^0 \to pK\pi K$	866	0	0	1939	0	0
$X_b^0 \to (\Lambda_c^+ \to p\pi\pi)\pi$	1686	0	0	4174	14	7
$X_b^0 \to (\Lambda_c^+ \to pK\pi)\pi$	20652	28	14	51937	70	35
$X_b^0 \to (\Xi_c^+ \to pK\pi)\pi$	540	0	0	1319	6	3

5.7 Study on the RHSB events

In the previously defined right-hand side band (RHSB) of the invariant mass spectra, only combinatorics and B physics events are expected to populate in that region. As will be shown in Section 5.8, the singly mis-identified signal cross-feeds do not have tails long enough to populate significantly in the RHSB region. The B physics shapes however, cover almost the entire invariant mass spectra with tails reaching up to the end of the RHSB. These events are primarily worrisome because their potential contribution to the CP asymmetry observable we want to measure. A further technical difficulty for the invariant mass fit is that the B physics tail shape is almost the same as the combinatorics and cannot be straightforwardly distinguished from the data themselves. An estimate of their number of expected events is also not yet doable since the inclusive branching fractions of these B physics backgrounds are yet unmeasured.

A possible method to estimate the yield of B physics backgrounds can be to reconstruct explicitly the invariant mass of the 4 daughter particles according to the proper set of expected final daughter particles of the B physics background. For example in the $X_b^0 \to p\pi\pi\pi$ spectrum, the p particle is swapped with a K particle hypothesis to estimate the number of $B^0 \to K\pi\pi\pi$ events. In order to avoid any implicit unblinding of the signal events, only the events in the RHSB are used. Figures 5.10 and 5.11 show the RHSB events reconstructed according to a set of mass hypotheses that is presumed to be the dominant B physics background in each spectrum. In the second rows of Figures 5.10 and 5.11, we identify the events just on the left part of the signal peak as $B^0 \to KKK\pi$ events. A doubly-misidentified

$B^0 \to KKK\pi$ as $X_b^0 \to pK\pi\pi$ background shape is included in the fit to data in order to take into account this contribution.

The fit model that we are using has been educated from RHSB samples reconstructed with a milder ProbNNp cut (ProbNN$p > 0.30$) such that all significant sources of B physics events can be identified. Simplified shapes (single Crystal Ball functions) have been considered for all B decays. The dominant contribution of each spectrum is represented with a fixed radiative tail and floating mean and width. The misidentified B decays are also described with a single crystal ball, the CB tail being on the right or the left of the invariant mass distribution according to the nature of the misidentification. It is quite remarkable that the (rather crude) fit models of each spectra resists to the change of ProbNNp cut and gives confidence that the main contributing B decays are actually identified. Few examples of fits with ProbNN$p > 0.30$ are given in Appendix A.9.

The obtained B decay yields from the RHSB are summarized in the fifth and sixth column of Table 5.16, where the yields are obtained separately for candidates with p and $\overline{p}$ from the original spectrum. These yields are then translated as expected full yields for the whole invariant mass spectra by multiplying it by a factor obtained from the MC shapes. Mathematically, the expected full yield $\mathcal{Y}_{\text{full}}$ and its corresponding uncertainty $\sigma_{\mathcal{Y}_{\text{full}}}$ are proportional to the yield $\mathcal{Y}_{\text{RHSB}}$ obtained in the RHSB and its uncertainty $\sigma_{\mathcal{Y}_{\text{RHSB}}}$, respectively. This is given by,

$$\mathcal{Y}_{\text{full}} \pm \sigma_{\mathcal{Y}_{\text{full}}} = f \cdot (\mathcal{Y}_{\text{RHSB}} \pm \sigma_{\mathcal{Y}_{\text{RHSB}}}) \tag{5.7}$$

where f is the ratio of the integrated PDF of the B physics shape for the full invariant mass region and the RHSB region. Columns seven and eight in Table 5.16 summarizes these translated expected full yields for each dominant B physics background in each spectrum. These expectation values are used to Gaussianly-constrained the expected yields of the B physics in the CP asymmetries nominal fit to data.

Table 5.16: The yields of B physics backgrounds from the RHSB of each spectrum.

Spectrum	RHSB cut (in MeV/c^2)	Dominant B	Year	Yields from RHSB		Translated yields	
				w/ p track	w/ $\overline{p}$ track	w/ p track	w/ $\overline{p}$ track
$X_b^0 \to p\pi\pi\pi$	$m_{p\pi\pi\pi} > 5685.$	$B^0 \to K\pi\pi\pi$	2011	46.7 ± 7.6	45.5 ± 7.5	151.2 ± 24.7	147.2 ± 24.4
			2012	187.0 ± 15.2	193.3 ± 15.9	605.2 ± 49.2	625.6 ± 51.6
$X_b^0 \to pK\pi\pi$	$m_{pK\pi\pi} > 5840.$	$B_s^0 \to K\pi\pi K$	2011	14.3 ± 4.2	10.6 ± 3.8	53.3 ± 15.5	39.7 ± 14.3
			2012	74.9 ± 10.3	69.9 ± 9.6	279.8 ± 38.5	260.9 ± 35.6
$X_b^0 \to pKK\pi$	$m_{pKK\pi} > 5840.$	$B^0 \to KKK\pi$	2011	8.9 ± 3.6	9.8 ± 3.8	61.5 ± 24.5	67.3 ± 25.8
			2012	36.0 ± 6.7	35.2 ± 6.8	246.6 ± 46.0	240.9 ± 46.7
$X_b^0 \to pKKK$	$m_{pKKK} > 5840.$	$B_s^0 \to KKKK$	2011	5.3 ± 2.5	6.3 ± 2.7	25.7 ± 11.9	30.6 ± 12.9
			2012	26.3 ± 5.5	32.5 ± 6.2	127.5 ± 26.7	157.9 ± 30.2

The $B^0 \to \pi^+\pi^-\pi^+\pi^-$ is present only in the $X_b^0 \to p\pi\pi\pi$ and not on the other spectra. In general, the yields of the B physics backgrounds are constrained in the spectrum where they are dominant as discussed in this Section. In spectra, where they are not dominant, they are controlled by cross-spectra factors estimated from selection and misidentification efficiencies, as will be discussed in Section 5.8.3. The $B^0 \to \pi^+\pi^-\pi^+\pi^-$ is not the dominant B physics background in the $X_b^0 \to p\pi\pi\pi$ spectrum, neither this is present in other spectra. As such, aside from the Gaussian-constraint on the yields of the dominant B physics background in each spectrum, the ratio r_{RHSB} of $B^0 \to \pi\pi\pi\pi$ yield to $B^0 \to K\pi\pi\pi$ yield in the RHSB of $X_b^0 \to p\pi\pi\pi$ spectrum is also obtained. This ratio of yields is then translated as the ratio of

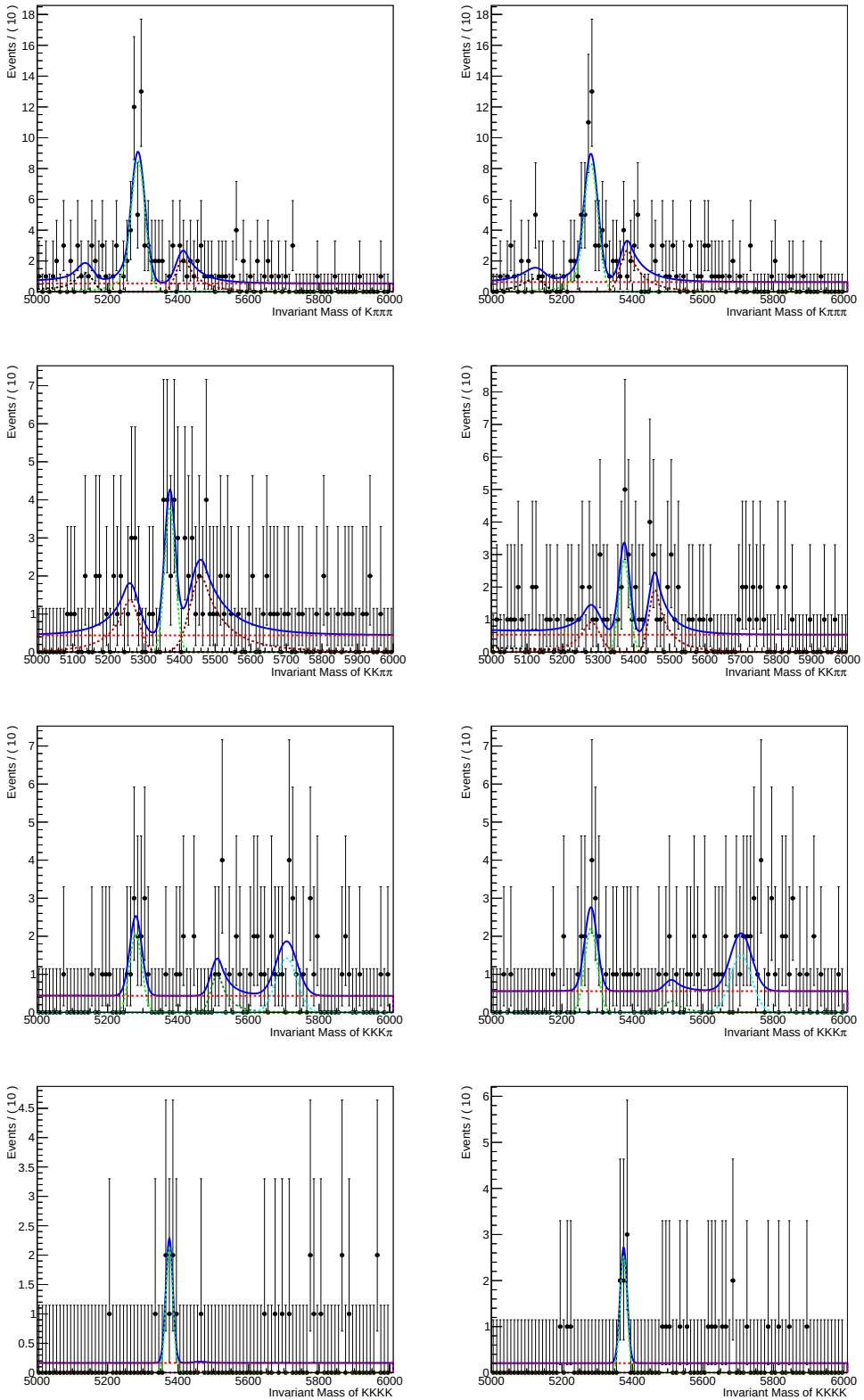

Figure 5.10: Invariant mass spectra of 2011 RHSB events from [from top to bottom] $X_b^0 \to p\pi\pi\pi$ as $B^0 \to K\pi\pi\pi$, $X_b^0 \to pK\pi\pi$ as $B_s^0 \to K\pi\pi K$, $X_b^0 \to pKK\pi$ as $B^0 \to KKK\pi$ and $X_b^0 \to pKKK$ as $B_s^0 \to KKKK$ (left-column) with p and (right-column) $\overline{p}$ separated.

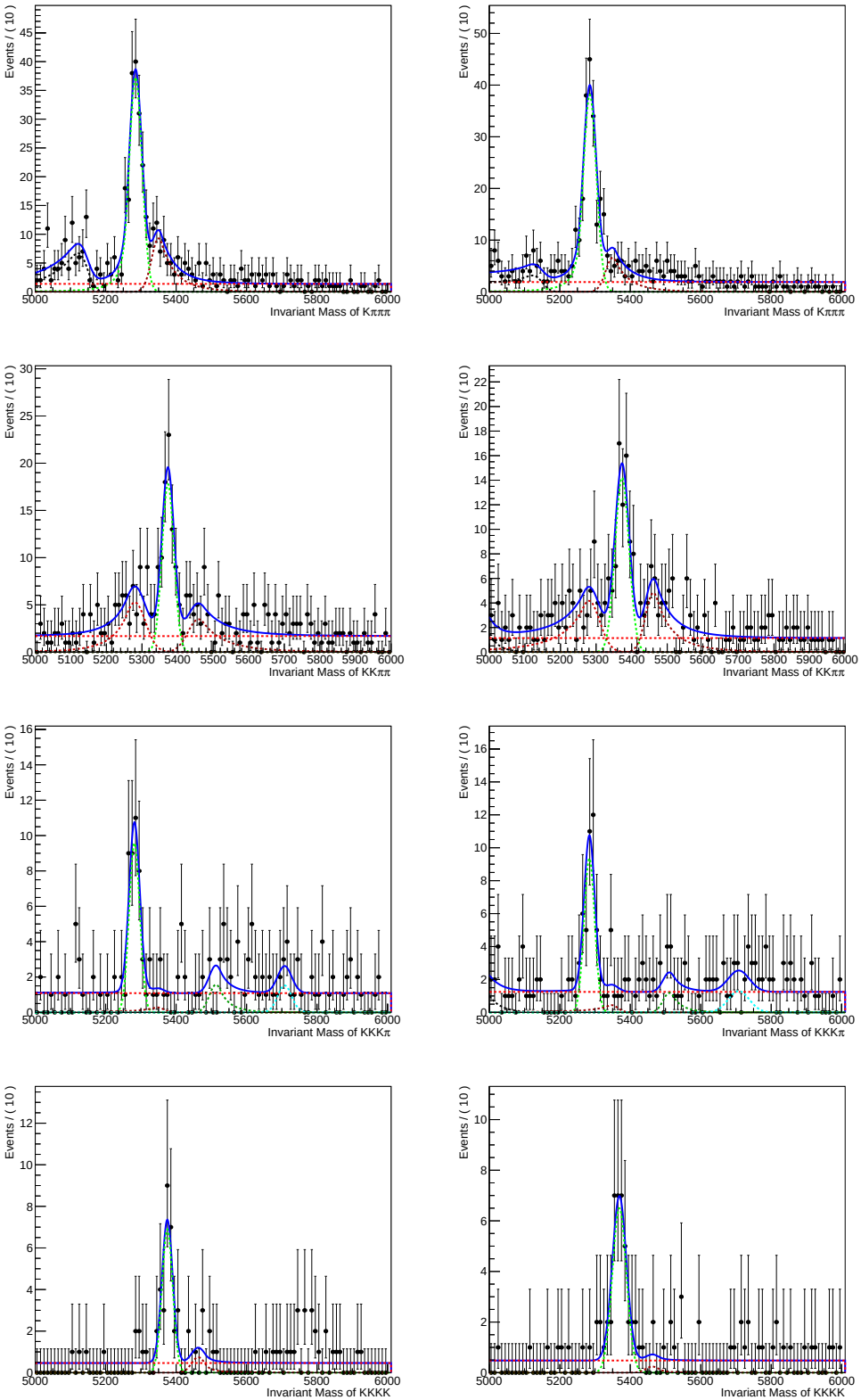

Figure 5.11: Invariant mass spectra of 2012 RHSB events from [from top to bottom] $X_b^0 \to p\pi\pi\pi$ as $B^0 \to K\pi\pi\pi$, $X_b^0 \to pK\pi\pi$ as $B_s^0 \to K\pi\pi K$, $X_b^0 \to pKK\pi$ as $B^0 \to KKK\pi$ and $X_b^0 \to pKKK$ as $B_s^0 \to KKKK$ (left-column) with p and (right-column) $\overline{p}$ separated.

the two backgrounds for the full spectrum. The "full-spectrum" ratio r_{full} is given by:

$$r_{\text{full}} \pm \sigma_{r_{\text{full}}} = (r_{\text{RHSB}} \pm \sigma_{r_{\text{RHSB}}}) \cdot \frac{f_{\text{B}^0\to\text{K}\pi\pi\pi}}{f_{\text{B}^0\to\pi\pi\pi\pi}} , \tag{5.8}$$

where $f_{\text{B}^0\to\text{K}\pi\pi\pi}$ and $f_{\text{B}^0\to\pi\pi\pi\pi}$ are the ratios of the integrated PDFs of $B^0 \to K\pi\pi\pi$ and $B^0 \to \pi\pi\pi\pi$ shapes, respectively, for the full $X_b^0 \to p\pi\pi\pi$ invariant mass region and the RHSB region. The value of ratio r_{RHSB} is calculated using the ratio found in the 2012 data. Figure 5.12 shows the invariant mass distribution of the RHSB events of 2012 $X_b^0 \to p\pi\pi\pi$ real data, combining $\Lambda_b^0/\overline{\Lambda}_b^0$, reconstructed as $B^0 \to K\pi\pi\pi$. The dominant peak is the $B^0 \to K\pi\pi\pi$ peaking at the correct nominal mass of B^0 with a yield of 380.2±22.0, while the shape just on the right of the $B^0 \to K\pi\pi\pi$ peak is identified as the $B^0 \to \pi\pi\pi\pi$ events with a yield of 122.3±16.0. Using Equation 5.8, the "full-spectrum" ratio is calculated to be 27.7% ±3.9%. This ratio parameter is used to Gaussianly-constraint the ratio of the two B physics backgrounds in $X_b^0 \to p\pi\pi\pi$, which is shared by the Λ_b^0 and $\overline{\Lambda}_b^0$ spectra in the fit model. The same constraint is shared with the 2011 $X_b^0 \to p\pi\pi\pi$ spectra.

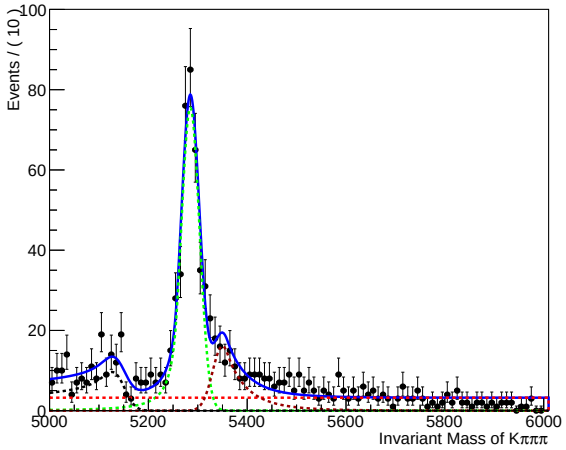

Figure 5.12: Invariant mass spectra of 2012 RHSB events from $X_b^0 \to p\pi\pi\pi$ reconstructed as $B^0 \to K\pi\pi\pi$, where Λ_b^0 and $\overline{\Lambda}_b^0$ events are combined.

5.8 Fit model and strategy

A simultaneous unbinned extended maximum likelihood fit is performed to all the invariant mass spectra, both in the charmless and charmed decays in order to extract the $\mathcal{A}^{\text{raw}}$'s and $\Delta\mathcal{A}^{CP}$'s directly from the fit. A modified version of `V0hhFitter` is used as the simultaneous fitter for this analysis. The nominal fit is composed of the 5 charmless spectra and 2 control spectra, split in b-baryon and $\bar{b}$-baryon, and also split by year. This amounts to a total of 28 separate spectra with several shared and related parameters to be fitted simultaneously. A further splitting of the data in terms of magnet polarity and trigger requirements is performed for the sake of cross-checking the measured $\Delta\mathcal{A}^{CP}$. The models used in this fit is described in the following subsections.

5.8.1 Signal shapes

MC-generated events are used to obtain the signal shapes by fitting the invariant mass distribution with a double Crystal Ball function (DCB) with shared mean μ and shared

width σ. The mathematical description of a Crystal Ball PDF of variable m is given by:

$$P(m;\alpha,n,\mu,\sigma) = \mathcal{N}\cdot\begin{cases}\exp(-(m-\mu)^2/2\sigma^2), & \text{if } (m-\mu)/\sigma > -\alpha \\ (\frac{n}{|\alpha|})^n \exp(-\alpha^2/2)(\frac{n-\alpha^2}{|\alpha|} - \frac{m-\mu}{\sigma})^{-n}, & \text{if } (m-\mu)/\sigma \leq -\alpha\ ,\end{cases} \tag{5.9}$$

where $\mathcal{N}$ is the normalization and m is the invariant mass. The turnover point is denoted (α) and the tail parameter (n) models the radiative tail (for the left tail of signal mass distribution), or the imperfections of the tracking (for the right tail of the mass distribution). Although the two functions in Equation 5.9 are independent of the sign of the parameter α, the sign of α governs on which side of the Crystall Ball (CB) function the tail should appear, where negative α means the tail is on the left side of the CB while positive α means the tail is on the right side. Let us notice that no truth-matching is applied onto the candidates in order to take into account for mismatched and misreconstructed signals in the signal shape. The full selection is applied to the MC events, except for the PID cuts since the ProbNN variables are not well-described by the MC. Since the shape changes with the PID cuts applied, each candidate is weighted by a certain efficiency to pass the PID cuts. The procedure of applying the weights is the same as what was described in Section 5.6.2. All the signal shapes are fitted simultaneously in order to obtain the ratios of the widths, which are used as Gaussianly-constrained parameters in the final PDF to be used to fit the real data.

The 2012 $\Lambda_b^0 \to pK\pi\pi$ is chosen as the reference for these ratios of widths. Summarized in Table 5.17 are the parameters obtained from the fits, which are shown in Figures 5.13 and 5.14. The extracted parameters α_1, α_2/α_2, n_1, n_2/n_1, f_2 are fixed parameters in the nominal fit to the real data. Systematic uncertainties attached to this assumption are estimated by generating pseudo-experiments according to the distributions of the uncertainties on the fixed parameters as found in the fit to simulated MC events.

5.8.2 Crossfeed shapes

There are seven charmless decay modes which are explicitly searched for in this analysis. Significant number of true signal events may still appear as cross-feeds in other spectra. The dominant cross-feeds are those with only one particle misidentified. When a K particle is misidentified as a π particle, the mass distribution of X_b^0 shifts to the left, while it shifts to right if π is misidentified as a K. In both cases, the shift of the most probable value w.r.t. the correct mass is small and hence the singly-misidentified cross-feeds peak near the signal region. To model the shape of these cross-feeds, truth-matched MC signal events are reconstructed with a set of track mass hypotheses for other spectra.

A refit on the decay tree using the DecayTreeFitter tool is done with the appropriate cross-feed mass hypotheses, along the same way it is done on data. The full selection is applied to the events, except for the PID cut, since the ProbNNp variables in the real data are not well-described by MC. For each event, an efficiency weight is applied representing the probability to pass the PID cut. This event-by-event PID weighting is described in Section 5.6.2. The invariant mass distributions shown in Figures 5.15, 5.16 and 5.17 are fitted with a Double Crystal Ball PDF, with shared mean μ but two different widths σ's. The extracted parameters from these fits, which are listed in Table 5.18, are fixed in the final nominal fit to the real data.

It is worth noticing that only the dominant cross-feeds are modelled as the others imply double mis-identification or are coming from Ξ_b^0 decays which are expected to be Cabbibo-suppressed. Specifically, the $\Lambda_b^0 \to pKK\pi$ as cross-feed to $X_b^0 \to pKKK$ spectrum is not included in the fit, as well the $\Xi_b^0 \to pKKK$ cross-feed to $X_b^0 \to pKK\pi$ and $X_b^0 \to$

Table 5.17: Fit parameters obtained in the fit to signal shape.

Year	Fit parameters						
	μ	α_1	α_2/α_1	n_1	n_2/n_1	f_2	σ/σ_{ref}
$\Lambda_b^0 \to p\pi\pi\pi$:							
2011	5620.657±0.221	1.339±0.230	-1.554±0.358	1.799±0.169	1.277±0.220	0.471±0.148	1.052±0.018
2012	5620.734±0.177	0.971±0.300	-2.191±0.721	2.133±0.330	1.230±0.239	0.284±0.103	1.058±0.016
$\Lambda_b^0 \to pK\pi\pi$:							
2011	5620.788±0.204	1.715±0.139	-0.932±0.191	1.528±0.115	2.225±0.424	0.638±0.141	0.997±0.018
2012	5620.947±0.170	1.315±0.242	-1.569±0.347	1.729±0.160	1.453±0.214	0.351±0.114	σ_{ref} =13.995±0.151
$\Lambda_b^0 \to pKK\pi$:							
2011	5621.143±0.222	1.159±0.322	-1.822±0.593	2.142±0.313	1.150±0.270	0.295±0.132	0.962±0.018
2012	5620.975±0.172	1.308±0.237	-1.613±0.333	1.886±0.192	1.260±0.187	0.297±0.099	0.963±0.015
$\Lambda_b^0 \to pKKK$:							
2011	5620.723±0.201	1.297±0.455	-1.555±0.603	1.929±0.343	1.638±0.408	0.198±0.129	0.907±0.016
2012	5621.149±0.154	1.210±0.279	-1.821±0.449	2.168±0.291	1.239±0.234	0.171±0.070	0.902±0.014
$\Xi_b^0 \to pK\pi\pi$:							
2011	5789.404±0.210	0.738±0.450	-2.547±2.201	2.190±0.601	1.480±0.499	0.186±0.101	1.031±0.019
2012	5789.443±0.174	1.529±0.231	-1.301±0.316	1.792±0.131	1.376±0.235	0.528±0.186	1.039±0.016
$\Xi_b^0 \to pK\pi K$:							
2011	5789.480±0.234	1.203±0.413	-1.537±0.647	2.152±0.340	1.340±0.347	0.310±0.178	0.990±0.019
2012	5789.617±0.169	1.054±0.301	-2.148±0.658	2.173±0.286	1.082±0.227	0.226±0.090	0.990±0.015
$\Xi_b^0 \to pKKK$:							
2011	5789.468±0.194	1.855±0.210	-0.984±0.263	1.859±0.169	1.428±0.315	0.581±0.222	0.933±0.016
2012	5789.440±0.153	2.054±0.092	-0.630±0.179	1.888±0.138	2.268±0.651	0.798±0.108	0.929±0.014

$pK\pi K$ spectra, since the fit to data found only few events of them. The estimate on the misidentification of $\Lambda_b^0 \to pKK\pi$ as $X_b^0 \to pKKK$ is at the level of ∼2%, while the estimated misidentification rate of $\Xi_b^0 \to pKKK$ as $X_b^0 \to pKK\pi$ or $X_b^0 \to pK\pi K$ is at the level of ∼8%. Given the level of background in the $X_b^0 \to pKKK$, $X_b^0 \to pKK\pi$ and $X_b^0 \to pK\pi K$ spectra, we think that these are negligible contributions. Note that we expect in the SM the $\Lambda_b^0 \to pKK\pi$ and $\Xi_b^0 \to pKKK$ to be small since they proceed only through $b \to d$ penguin loop diagram.

In the fit to data, the yields of the cross-feeds are Gaussianly-constrained to the corresponding signal yield in its respective spectrum by a relevant misidentification efficiency f. These factors are calculated by taking the ratios of selection efficiencies and PID efficiencies as a cross-feed and as a signal. This is given by:

$$f = \frac{\epsilon_{\text{CF}}^{\text{Sel.}} \cdot \epsilon_{\text{CF}}^{\text{PID}}}{\epsilon_{\text{Sig.}}^{\text{Sel.}} \cdot \epsilon_{\text{Sig.}}^{\text{PID}}} \tag{5.10}$$

where $\epsilon_{\text{CF}}^{\text{PID}}$ and $\epsilon_{\text{Sig.}}^{\text{PID}}$ are the average efficiencies of misidentifying the candidates as cross-feed and identifying as signal, respectively, while the $\epsilon_{\text{CF}}^{\text{Sel.}}$ and $\epsilon_{\text{Sig.}}^{\text{Sel.}}$ are the average efficiencies in selecting the candidates as cross-feed or signal, respectively. The $\epsilon_{\text{CF}}^{\text{Sel.}}$ and $\epsilon_{\text{Sig.}}^{\text{Sel.}}$ includes the BDT selection efficiency and the mass window cut to be within 5340. MeV/c^2 to 6400. MeV/c^2. As expected, these two efficiencies are about the same except for the very small difference in their BDT values because of the slight change in some of the variables due to the refit of the decay tree depending on each spectrum. The uncertainty of these factors is calculated as the quadratic sum of the four efficiencies. These factors are summarized in Table 5.19. Note that some cross-feeds has actually twice the probability since two of its daughter particles can be mis-identified, *e.g.* there are two pions from $\Lambda_b^0 \to p\pi\pi\pi$ that can be mis-identified as a kaon in the $X_b^0 \to pK\pi\pi$ spectrum. This is also the case for

$\Lambda_b^0 \to pKKK$ as $pKK\pi$ and $\Xi_b^0 \to pK\pi K$ as $pK\pi\pi$. These are taken into account in the Gaussian constraints.

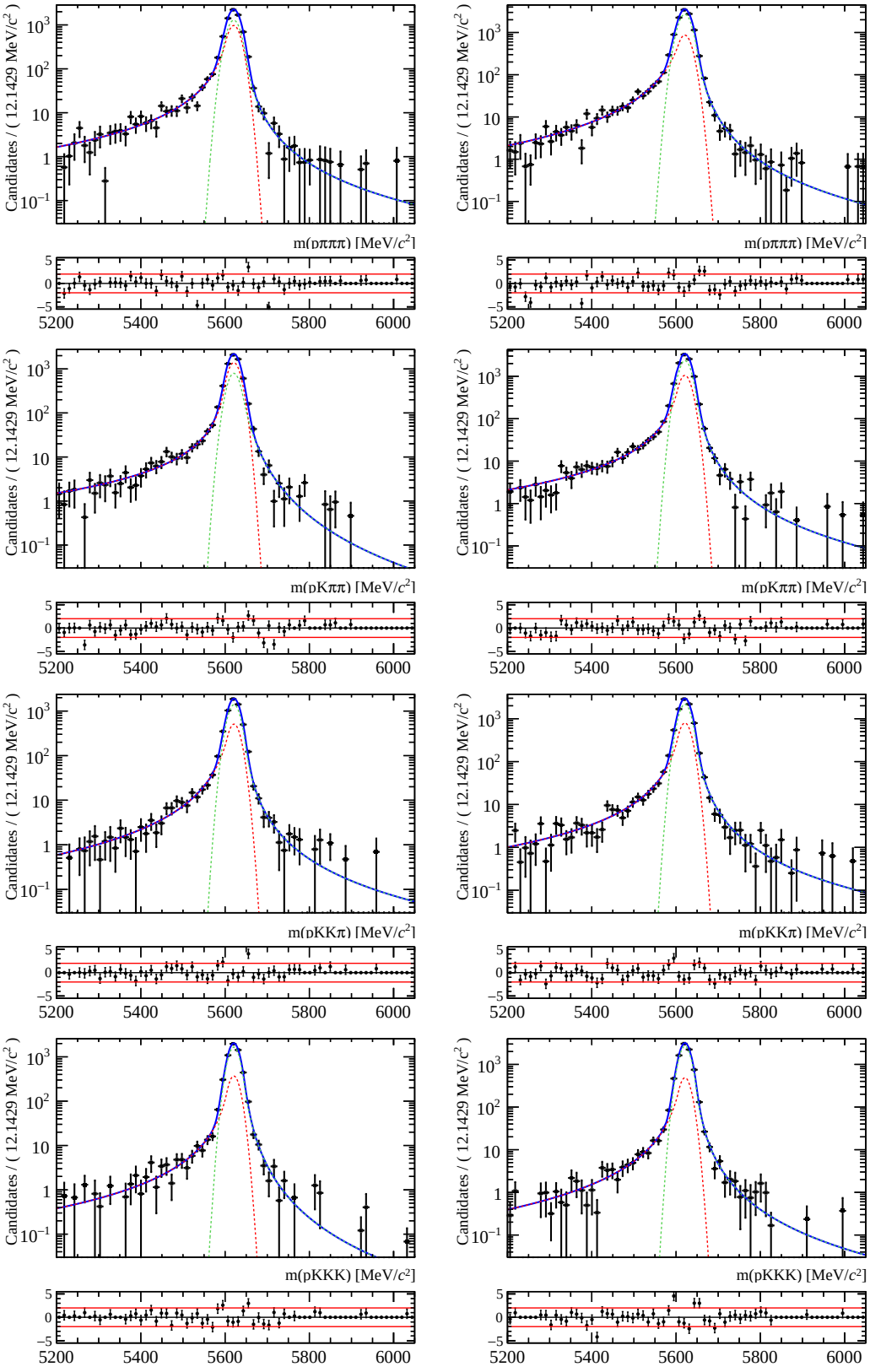

Figure 5.13: Signal invariant mass distribution fitted with DCB PDF for the modes (in order from top to bottom) $\Lambda_b^0 \to p\pi\pi\pi$, $\Lambda_b^0 \to pK\pi\pi$, $\Lambda_b^0 \to pKK\pi$ and $\Lambda_b^0 \to pK^-K^+K^-$ for years (left column) 2011 and (right column) 2012.

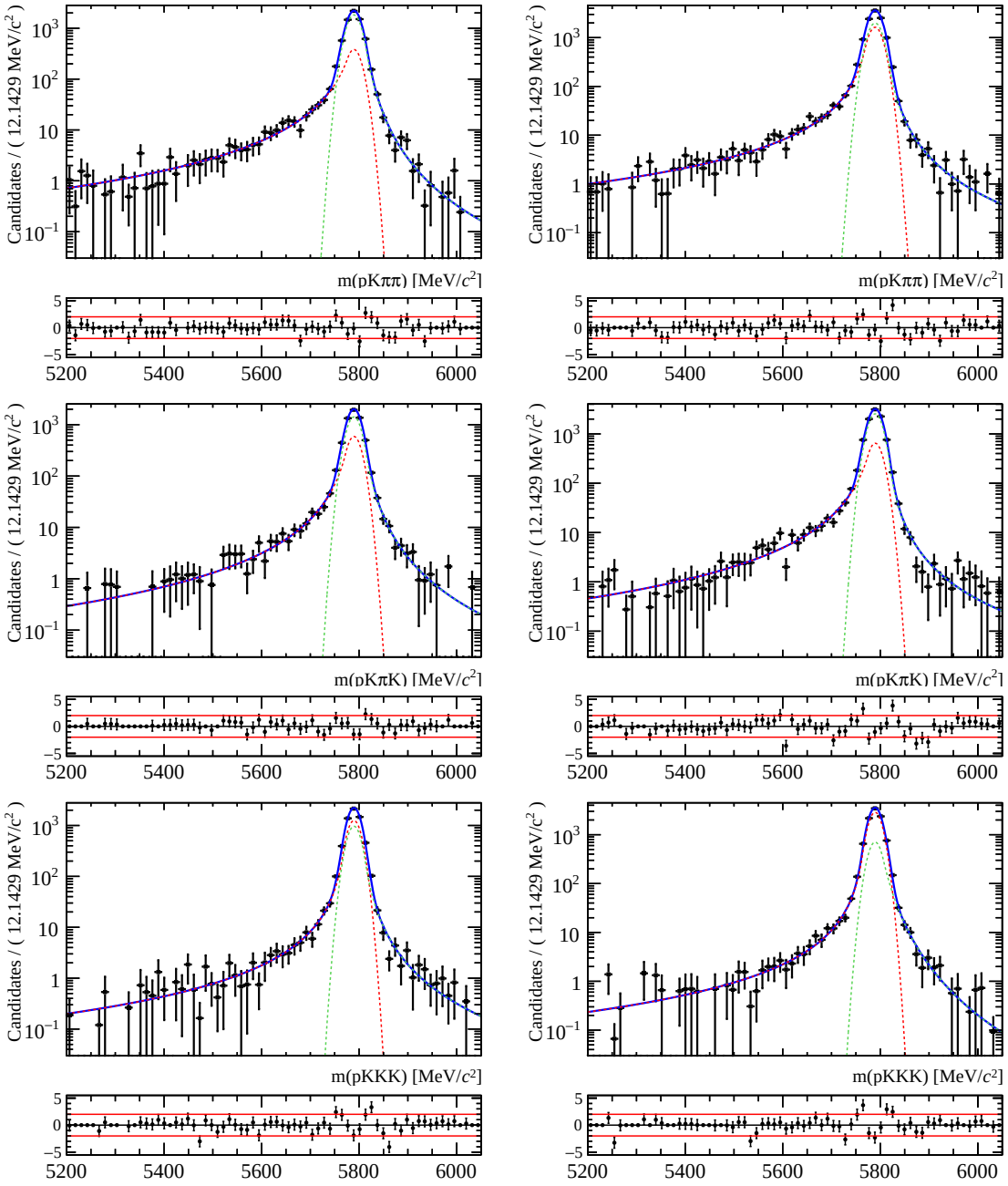

Figure 5.14: Signal invariant mass distribution fitted with DCB PDF for the modes (in order from top to bottom) $\Xi_b^0 \to pK\pi\pi$, $\Xi_b^0 \to pK\pi K$ and $\Xi_b^0 \to pKKK$ for years (left column) 2011 and (right column) 2012.

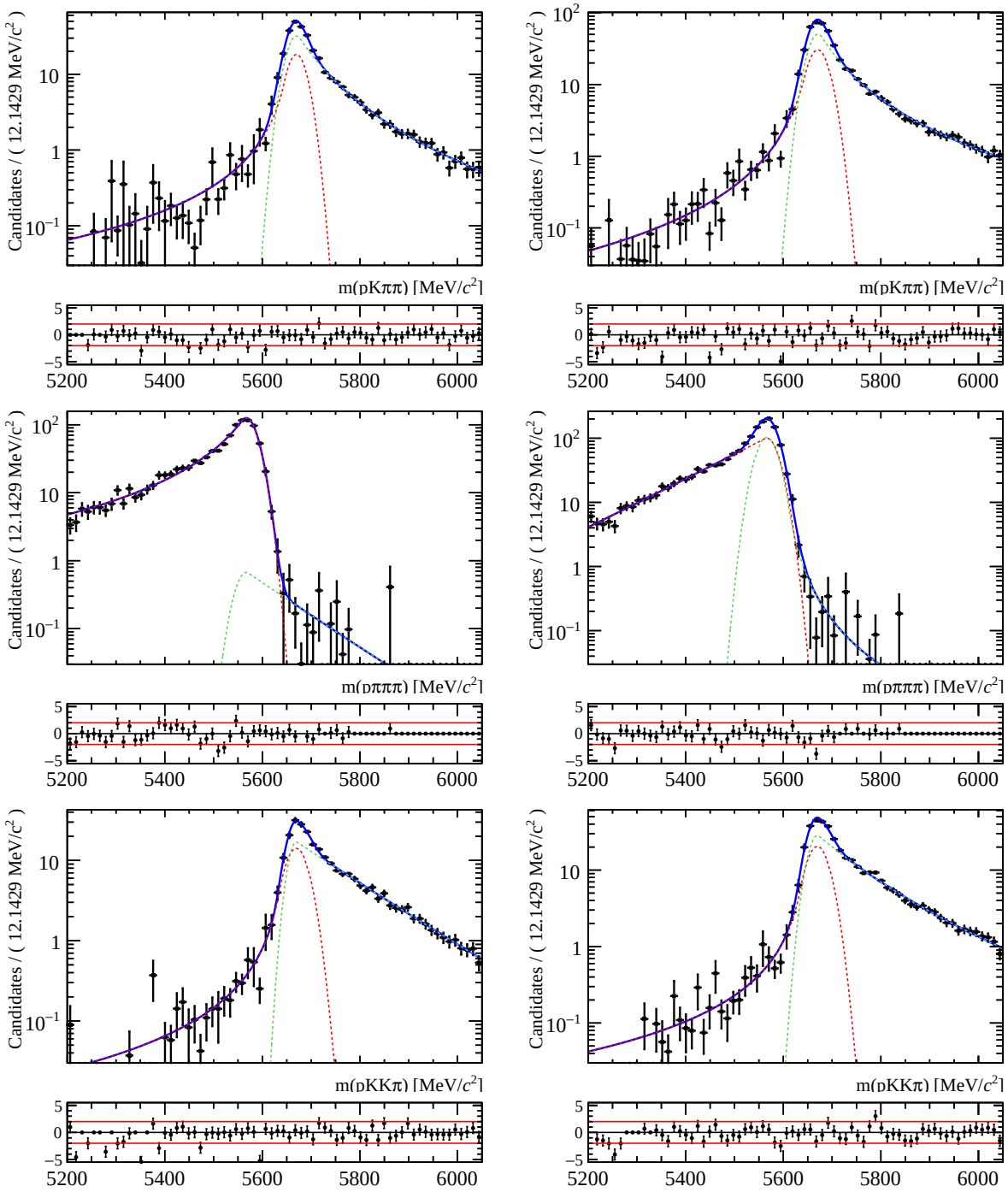

Figure 5.15: Signal cross-feeds invariant mass distributions fitted with DCB PDF for the modes (in order from top to bottom) $\Lambda_b^0 \to p\pi\pi\pi$ as $pK\pi\pi$, $\Lambda_b^0 \to pK\pi\pi$ as $p\pi\pi\pi$, and $\Lambda_b^0 \to pK\pi\pi$ as $pKK\pi$ for years (left column) 2011 and (right column) 2012.

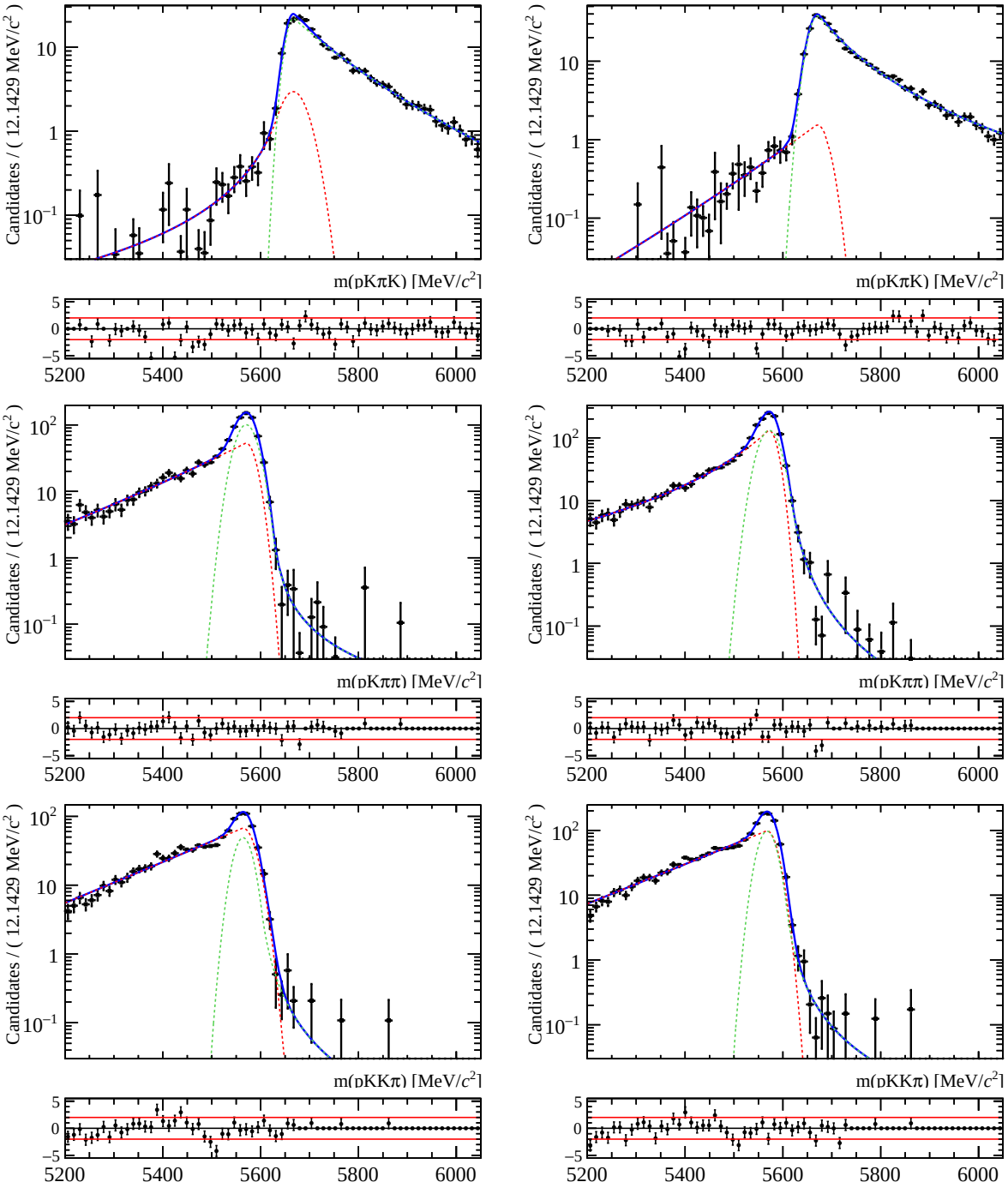

Figure 5.16: Signal cross-feeds invariant mass distributions fitted with DCB PDF for the modes (in order from top to bottom) $\Lambda_b^0 \to pK\pi\pi$ as $pK\pi K$, $\Lambda_b^0 \to pKK\pi$ as $pK\pi\pi$, and $\Lambda_b^0 \to pKKK$ as $pKK\pi$ for years (left column) 2011 and (right column) 2012.

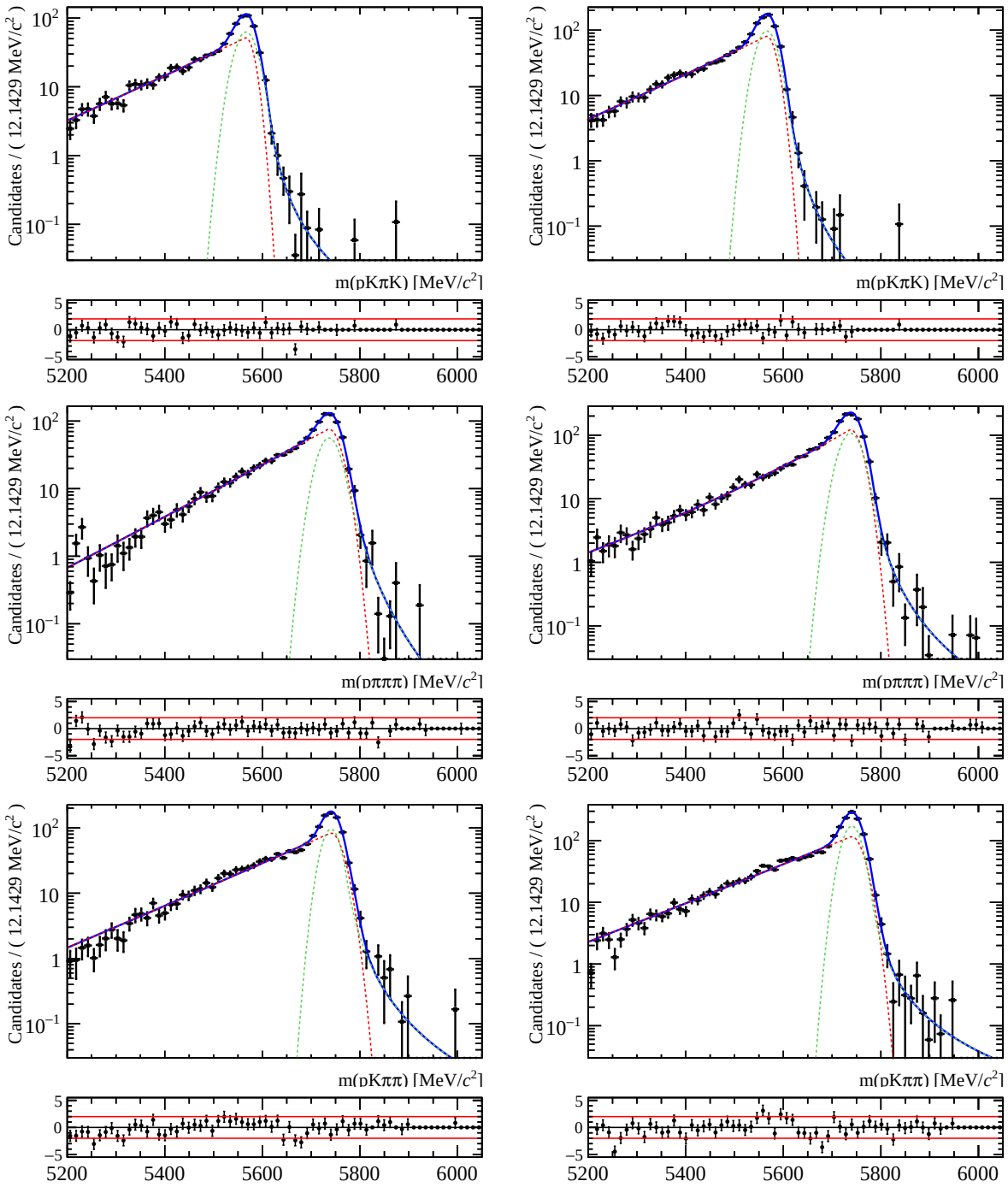

Figure 5.17: Signal cross-feeds invariant mass distributions fitted with DCB PDF for the modes (in order from top to bottom) $\Lambda_b^0 \to pKKK$ as $pK\pi K$, $\Xi_b^0 \to pK\pi\pi$ as $p\pi\pi\pi$, and $\Xi_b^0 \to pK\pi K$ as $pK\pi\pi$ for years (left column) 2011 and (right column) 2012.

Table 5.18: Fit parameters obtained in the fit to crossfeeds shapes. The number of digits is automatically defined to be three in order to ensure in all cases the presence of at least two significant digits.

Cross-feed	Year	Fit parameters							
		α_1	α_2/α_1	n_1	n_2/n_1	σ_1	σ_1/σ_2	μ	f_2
$\Lambda_b^0 \to p\pi\pi\pi$ as $pK\pi\pi$	2011	1.292±0.748	-0.335±0.370	1.615±0.867	1.911±1.967	19.181±6.560	1.016±0.537	5669.871±3.261	0.270±0.223
	2012	1.304±0.828	-0.369±0.496	2.108±1.123	1.199±1.199	20.659±5.042	0.937±0.373	5670.788±2.715	0.291±0.271
$\Lambda_b^0 \to pK\pi\pi$ as $p\pi\pi\pi$	2011	0.452±0.089	-0.502±1.063	1.969±0.440	35.000±26.494	20.524±1.644	0.987±2.935	5566.926±2.492	0.994±0.007
	2012	0.191±0.044	-11.715±2.989	83.792±57.729	0.031±0.189	21.336±3.899	0.945±0.287	5566.096±1.866	0.724±0.052
$\Lambda_b^0 \to pK\pi\pi$ as $pKK\pi$	2011	1.661±0.515	-0.082±0.056	1.627±1.464	28.127±38.586	22.195±4.664	0.668±0.402	5669.541±5.089	0.284±0.098
	2012	1.640±0.559	-0.133±0.122	1.567±0.822	3.514±6.316	21.837±4.645	0.811±0.413	5669.894±4.681	0.270±0.157
$\Lambda_b^0 \to pK\pi\pi$ as $pK\pi K$	2011	1.118±1.411	-0.149±0.255	1.746±2.249	3.604±14.099	27.646±19.970	0.512±0.488	5666.713±7.842	0.092±0.136
	2012	0.217±0.362	-1.422±3.842	22.034±22.673	0.128±0.615	20.684±35.303	0.834±1.224	5670.850±4.780	0.048±0.028
$\Lambda_b^0 \to pKK\pi$ as $pK\pi\pi$	2011	0.148±0.073	-19.065±9.224	14.364±25.616	0.098±0.336	17.563±5.433	1.146±0.416	5570.407±1.987	0.595±0.064
	2012	0.251±0.116	-9.233±4.874	2.847±1.439	0.938±0.709	14.915±2.919	1.341±0.306	5572.017±1.806	0.664±0.094
$\Lambda_b^0 \to pKKK$ as $pKK\pi$	2011	0.150±0.001	-14.789±5.514	105.000±57.260	0.021±0.026	21.479±1.406	0.800±0.124	5564.157±1.717	0.835±0.033
	2012	0.130±0.135	-18.290±5.816	105.000±65.092	0.020±0.020	18.173±4.897	0.944±0.387	5567.665±2.672	0.782±0.033
$\Lambda_b^0 \to pKKK$ as $pK\pi K$	2011	0.117±0.054	-20.650±16.958	65.000±63.936	0.037±0.079	15.113±6.814	1.348±0.685	5566.349±3.194	0.695±0.050
	2012	0.136±0.037	-16.818±6.201	59.997±49.133	0.054±0.085	16.559±4.218	1.154±0.379	5566.142±2.075	0.705±0.042
$\Xi_b^0 \to pK\pi\pi$ as $p\pi\pi\pi$	2011	0.189±0.044	-8.841±3.237	105.000±89.259	0.046±0.087	20.968±4.696	0.998±0.370	5736.637±2.855	0.777±0.049
	2012	0.199±0.057	-10.871±4.234	10.860±9.691	0.275±0.318	19.409±3.571	1.083±0.302	5737.917±2.005	0.737±0.059
$\Xi_b^0 \to pK\pi K$ as $pK\pi\pi$	2011	0.161±0.025	-11.823±3.143	105.000±104.997	0.027±0.025	21.107±3.150	0.824±0.189	5740.656±1.617	0.754±0.032
	2012	0.154±0.023	-15.047±2.655	105.000±104.979	0.020±0.017	20.779±2.940	0.856±0.181	5740.353±1.247	0.705±0.028

Table 5.19: Cross-feed factors. The number of digits is automatically defined to be three in order to ensure in all cases the presence of at least two significant digits.

Crossfeeds	Year	Efficiencies & CF-to-Signal factors (in %)				
		$\epsilon_{\text{CF}}^{\text{PID}}$	$\epsilon_{\text{CF}}^{\text{Sel.}}$	$\epsilon_{\text{Sig.}}^{\text{PID}}$	$\epsilon_{\text{Sig.}}^{\text{Sel.}}$	f
$\Lambda_b^0 \to p\pi\pi\pi$ as $pK\pi\pi$	2011	2.619±0.038	76.798±0.340	59.221±0.241	76.836±0.340	4.419±0.072
	2012	2.677±0.030	68.953±0.284	60.946±0.170	68.690±0.285	4.410±0.058
$\Lambda_b^0 \to pK\pi\pi$ as $p\pi\pi\pi$	2011	8.249±0.091	76.154±0.352	54.038±0.226	76.420±0.340	15.212±0.204
	2012	8.363±0.072	69.102±0.296	55.547±0.165	69.571±0.286	14.954±0.162
$\Lambda_b^0 \to pK\pi\pi$ as $pKK\pi$	2011	2.116±0.030	72.565±0.357	54.038±0.226	76.420±0.340	3.718±0.061
	2012	2.158±0.025	63.943±0.298	55.547±0.165	69.571±0.286	3.571±0.048
$\Lambda_b^0 \to pK\pi\pi$ as $pK\pi K$	2011	1.987±0.026	72.549±0.357	54.038±0.226	76.420±0.340	3.491±0.053
	2012	1.971±0.020	63.922±0.298	55.547±0.165	69.571±0.286	3.260±0.041
$\Lambda_b^0 \to pKK\pi$ as $pK\pi\pi$	2011	8.653±0.096	77.840±0.354	49.035±0.226	74.752±0.360	18.375±0.252
	2012	8.824±0.075	68.707±0.300	50.565±0.169	64.236±0.301	18.665±0.208
$\Lambda_b^0 \to pKKK$ as $pKK\pi$	2011	8.635±0.084	73.163±0.361	45.338±0.208	73.238±0.345	19.027±0.243
	2012	8.729±0.066	63.077±0.299	46.848±0.157	62.986±0.286	18.660±0.196
$\Lambda_b^0 \to pKKK$ as $pK\pi K$	2011	6.915±0.073	73.309±0.355	45.338±0.208	73.238±0.345	15.267±0.204
	2012	6.984±0.058	63.209±0.294	46.848±0.157	62.986±0.286	14.961±0.166
$\Xi_b^0 \to pK\pi\pi$ as $p\pi\pi\pi$	2011	8.357±0.085	79.244±0.323	53.717±0.223	79.319±0.321	15.543±0.193
	2012	8.593±0.068	71.626±0.274	55.747±0.158	71.800±0.271	15.376±0.153
$\Xi_b^0 \to pK\pi K$ as $pK\pi\pi$	2011	10.898±0.098	80.170±0.321	48.249±0.215	77.601±0.333	23.335±0.271
	2012	10.694±0.074	71.829±0.276	50.207±0.159	67.991±0.284	22.502±0.214

5.8.3 B physics shapes

As mentioned in Section 5.5.4, $B_{d,s}^0 \to$ 4-body decays populate the invariant mass spectra of m_{phhh}. Clearly, the dominant $B_{d,s}^0$ physics backgrounds are those with only one π or one K misidentified as a p. The strategy followed in this analysis to reduce these backgrounds, as discussed in Section 5.6.3, is by applying a ProbNN$p > 0.50$ cut on the hypothesized proton track. But even with this chosen PID$_p$ cut, a significant amount of B physics backgrounds survive. Hence, PDFs to model these contributions must be included in the total PDF.

The five dominant B physics backgrounds included in the fit are listed in Table 5.23 of Section 5.8.7. These B physics backgrounds are modelled in each spectrum when only one of its tracks is misidentified as a proton, except for the $B^0 \to KKK\pi$ as cross-feed to $X_b^0 \to pK\pi\pi$ spectrum. Doubly-misidentified $B^0 \to KKK\pi$ events are identified from the RHSB events of the $X_b^0 \to pK\pi\pi$ spectrum as presented in Section 5.7. The shapes of the B physics backgrounds are empirically modelled by a Cruijff function, mathematically given by Equation 5.11. The Cruijff PDF is composed of two Gaussian functions with shared mean μ but two different width σ's and two different tail-correction parameters.

$$P(m;\mu,\sigma_L,\sigma_R,\alpha_L,\alpha_R) = \mathcal{N}\cdot\begin{cases}\exp(-(m-\mu)^2/2(\sigma_L^2+\alpha_L(m-\mu)^2)), & \text{if } m \le \mu\\ \exp(-(m-\mu)^2/2(\sigma_R^2+\alpha_R(m-\mu)^2)), & \text{if } m > \mu\end{cases} \tag{5.11}$$

where μ, σ_L (σ_R) and α_L (α_R) are the turnover point, the width of the left Gaussian (right Gaussian) and the left tail-correction parameter (right tail-correction parameter), respectively. Shown in Figures 5.18, 5.19 and 5.20 are the fits to the MC-generated B physics events passing the full selection and PID-calibrated in the same way as discussed in Section 5.6.2. These MC-generated B physics events proceed through quasi-2-body decays with two

low-mass charmless resonances as listed in Table 5.2. The fit parameters are summarized in Table 5.20.

Table 5.20: Fit parameters obtained in the fit to B physics shapes.

B physics bkg.	Year	Fit parameters σ_L	σ_R	α_L	α_R	μ
$B^0 \to \pi\pi\pi\pi$ as $p\pi\pi\pi$	2011	33.403±41.849	288.239±65.791	0.089±1.273	0.010±1.019	5444.715±43.639
	2012	13.632±21.173	308.616±40.603	0.250±0.280	0.026±0.097	5407.548±15.644
$B^0 \to K\pi\pi\pi$ as $p\pi\pi\pi$	2011	34.587±24.181	159.386±23.525	0.181±0.294	0.162±0.040	5456.590±23.706
	2012	59.549±12.370	196.799±22.671	-0.100±0.324	0.178±0.038	5470.086±18.319
$B^0 \to \pi K\pi\pi$ as $pK\pi\pi$	2011	66.687±47.317	169.693±51.099	0.017±0.315	0.119±0.100	5548.796±51.390
	2012	61.873±38.355	206.453±44.170	-0.012±0.276	0.106±0.085	5531.110±40.908
$B_s^0 \to KK\pi\pi$ as $pK\pi\pi$	2011	80.613±33.946	155.270±37.485	-0.065±0.234	0.185±0.071	5604.441±37.025
	2012	85.911±26.038	198.239±34.341	-0.074±0.142	0.203±0.070	5610.281±27.997
$B_s^0 \to \pi KK\pi$ as $pKK\pi$	2011	28.614±51.989	227.556±107.763	0.148±0.296	0.058±0.272	5579.771±82.041
	2012	38.920±51.689	227.125±135.768	0.111±0.246	0.109±0.207	5590.728±81.095
$B^0 \to KKK\pi$ as $pK\pi\pi$	2011	150.642±86.647	184.891±63.324	0.953±1.490	0.170±0.180	5542.405±152.300
	2012	223.134±62.022	235.021±97.637	-0.100±1.493	0.186±0.224	5567.714±145.657
$B^0 \to KKK\pi$ as $pKK\pi$	2011	46.584±24.459	157.458±23.394	0.047±0.213	0.158±0.038	5489.352±26.079
	2012	60.547±22.617	186.721±21.512	0.001±0.181	0.173±0.036	5511.696±22.375
$B^0 \to KK\pi K$ as $pK\pi K$	2011	45.751±27.695	141.607±27.915	-0.062±0.260	0.161±0.048	5489.213±30.199
	2012	44.629±17.455	182.699±22.579	-0.010±0.163	0.151±0.044	5491.182±20.265
$B^0 \to \pi KKK$ as $pKKK$	2011	55.918±84.500	188.612±89.890	0.008±0.600	0.090±0.192	5540.139±102.421
	2012	71.491±84.761	188.103±81.621	-0.117±0.594	0.146±0.161	5559.523±91.442
$B_s^0 \to KKKK$ as $pKKK$	2011	33.389±11.913	144.256±18.025	0.054±0.080	0.133±0.035	5569.860±17.128
	2012	44.825±14.441	172.124±22.919	0.012±0.101	0.167±0.046	5589.403±18.291

The $B^0 \to K\pi\pi\pi$, $B^0 \to KKK\pi$ and $B_s^0 \to K\pi\pi K$ appear in more than one spectrum, as summarized in last column of Table 5.23. The ratios of yields of these B physics backgrounds from one spectrum to a reference spectrum is Gaussianly-constrained according to the selection efficiency computed from MC and PID mis-identification rate calculated using PIDCalibTool. The reference spectrum for each of these B physics is chosen to be the spectrum where they are expected to be dominant, i.e., $X_b^0 \to p\pi\pi\pi$ for $B^0 \to K\pi\pi\pi$, $X_b^0 \to pK\pi\pi$ for $B_s^0 \to K\pi\pi K$ and $X_b^0 \to pKK\pi$ for $B^0 \to KKK\pi$. The cross-spectra factors are calculated using:

$$f = \frac{\epsilon_{\mathrm{X}}^{\mathrm{Sel.}} \cdot \epsilon_{\mathrm{X}}^{\mathrm{PID}}}{\epsilon_{\mathrm{Ref.}}^{\mathrm{Sel.}} \cdot \epsilon_{\mathrm{Ref.}}^{\mathrm{PID}}}, \tag{5.12}$$

where $\epsilon_{\mathrm{X}}^{\mathrm{PID}}$ and $\epsilon_{\mathrm{Ref.}}^{\mathrm{PID}}$ are the average efficiencies of misidentifying the B physics event as an event in X spectrum and misidentifying as an event in the reference spectrum, respectively, while the $\epsilon_{\mathrm{X}}^{\mathrm{Sel.}}$ and $\epsilon_{\mathrm{Ref.}}^{\mathrm{Sel.}}$ are the average efficiencies of selecting the B physics event as an event in the X spectrum and in the reference spectrum, respectively. The $\epsilon_{\mathrm{X}}^{\mathrm{Sel.}}$ and $\epsilon_{\mathrm{Ref.}}^{\mathrm{Sel.}}$ includes BDT selection and the mass window cut to be within 5340. MeV/c^2 to 6400. MeV/c^2. Table 5.21 summarizes these factors.

5.8.4 Partially-reconstructed background shapes

The partially-reconstructed backgrounds are modelled by an ARGUS function convoluted by a Gaussian resolution. The generalized ARGUS function has three parameters (m_t, c, p) and is given by:

$$P(m; m_t, c, p) = \frac{2^{-p} c^{2(p+1)}}{\Gamma(p+1) - \Gamma(p+1, c^2/2)} \cdot \frac{m}{m_t}(1 - \frac{m^2}{m_t^2})^p \exp\left[-\frac{1}{2}c^2(1 - \frac{m^2}{m_t^2})\right], \tag{5.13}$$

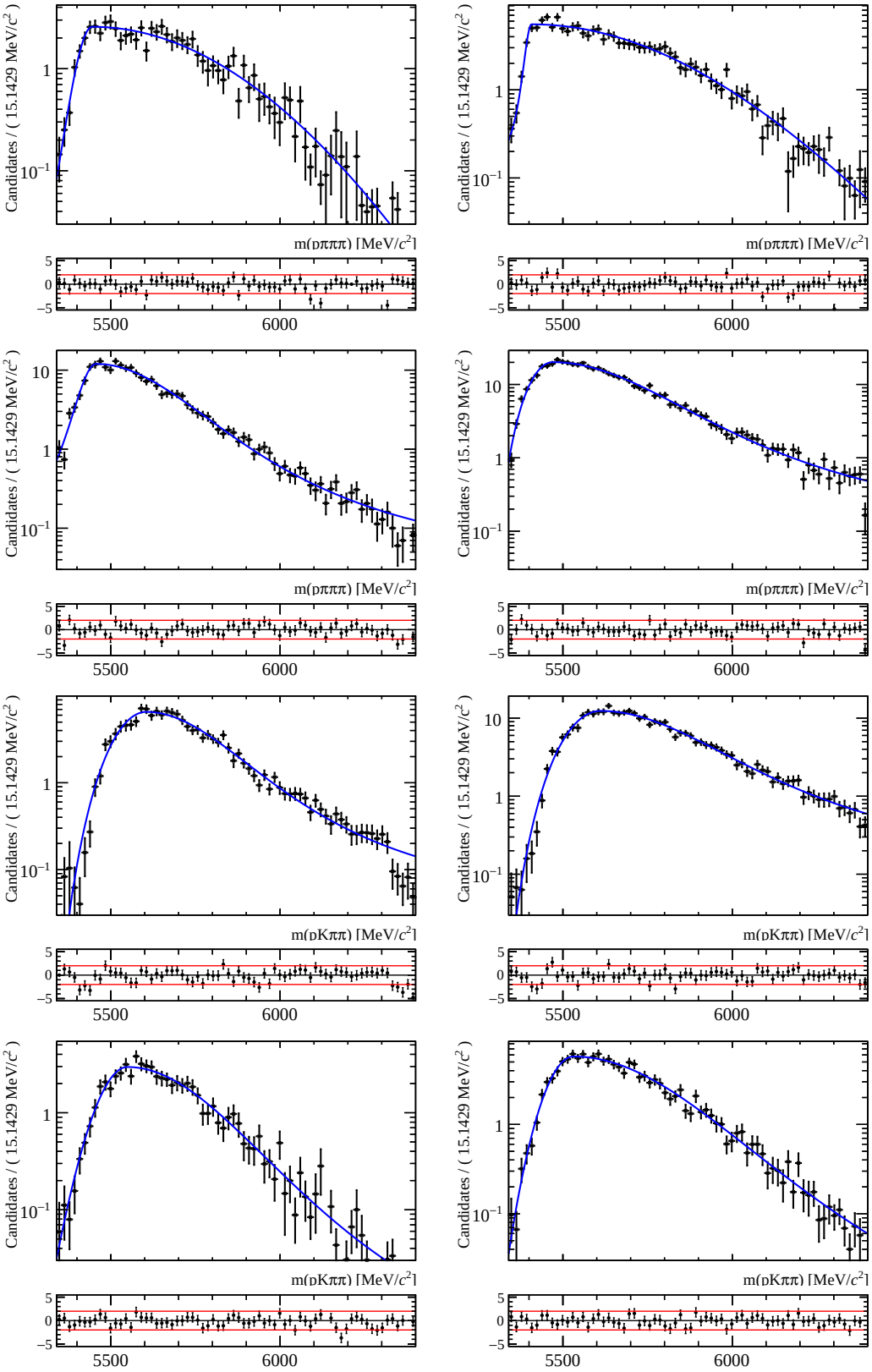

Figure 5.18: B physics backgrounds invariant mass distribution fitted with Cruijff PDF for the modes (in order from top to bottom) $B^0 \to \pi\pi\pi\pi$ as $p\pi\pi\pi$, $B^0 \to K\pi\pi\pi$ as $p\pi\pi\pi$, $B_s^0 \to KK\pi\pi$ as $pK\pi\pi$ and $B^0 \to \pi K\pi\pi$ as $pK\pi\pi$ for years (left column) 2011 and (right column) 2012.

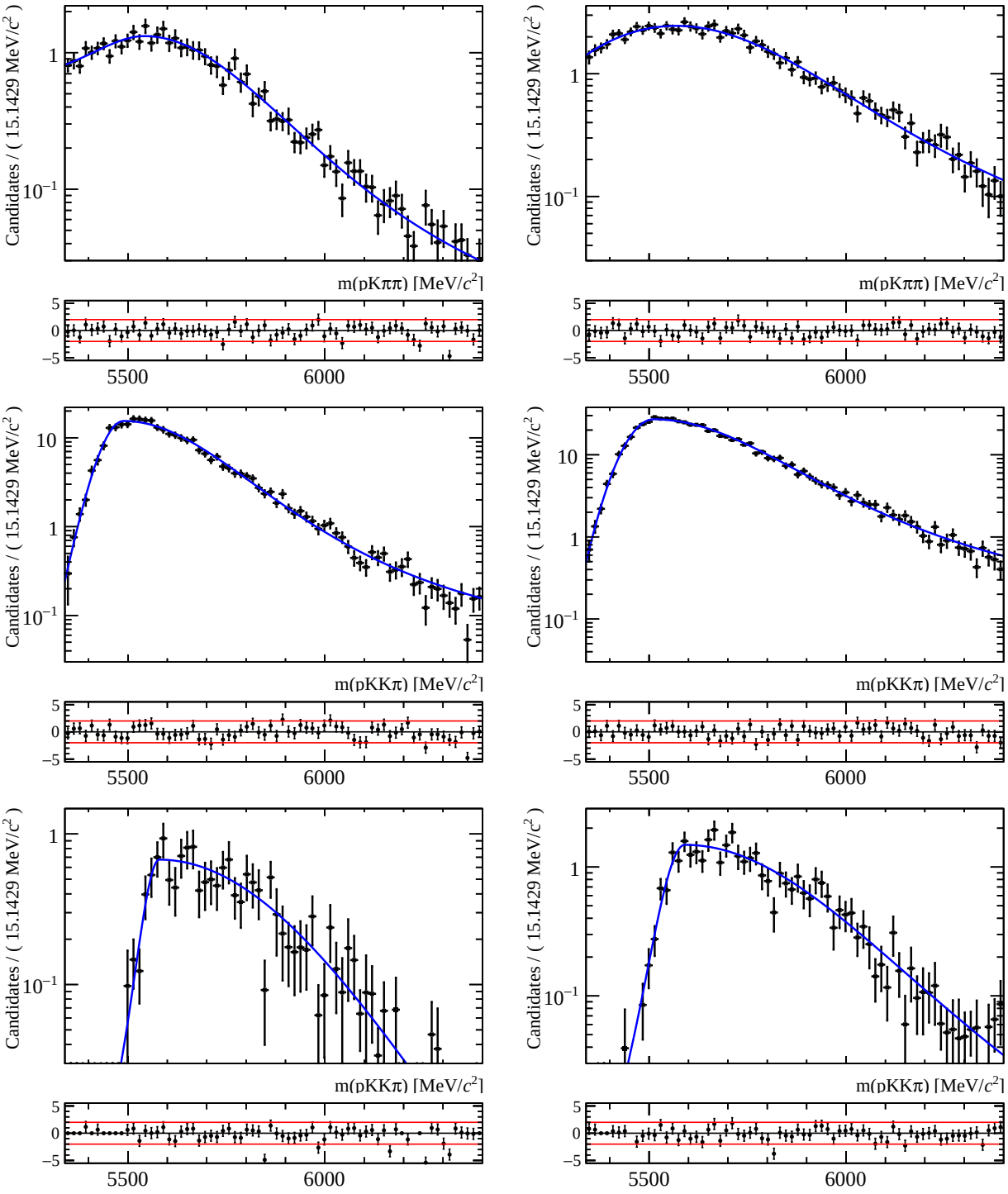

Figure 5.19: B physics backgrounds invariant mass distribution fitted with Cruijff PDF for the modes (in order from top to bottom) $B^0 \to KKK\pi$ as $pK\pi\pi$, $B^0 \to KKK\pi$ as $pKK\pi$ and $B_s^0 \to \pi KK\pi$ as $pKK\pi$ for years (left column) 2011 and (right column) 2012.

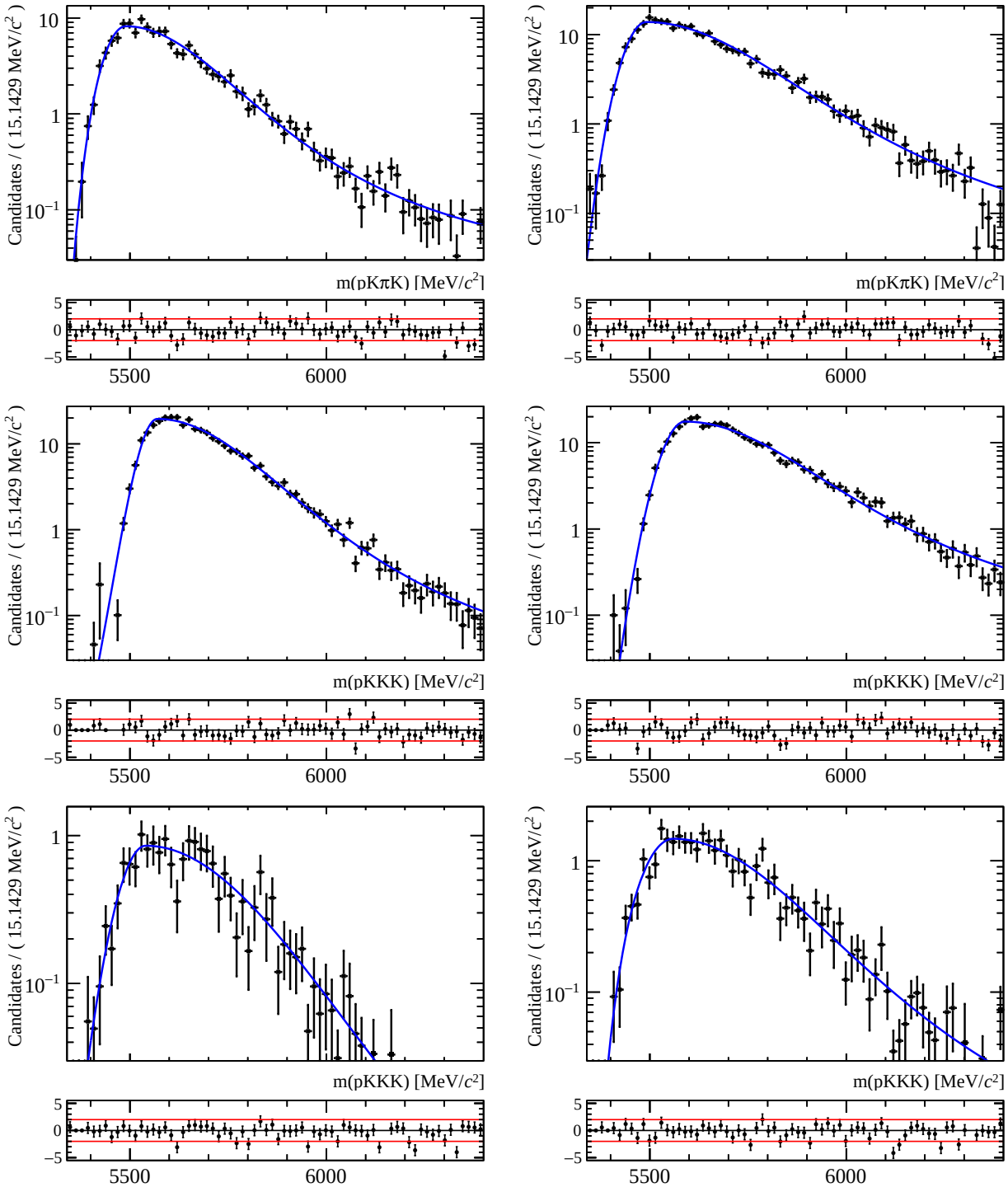

Figure 5.20: B physics backgrounds invariant mass distribution fitted with Cruijff PDF for the modes (in order from top to bottom) $B^0 \to KK\pi K$ as $pK\pi K$, $B_s^0 \to KKKK$ as $pKKK$ and $B^0 \to \pi KKK$ as $pKKK$ for years (left column) 2011 and (right column) 2012.

Table 5.21: B physics cross-spectra factors. The number of digits is automatically defined to be three in order to ensure in all cases the presence of at least two significant digits.

B physics	Efficiencies & X-to-Reference factors (in %)			
	Year	$\epsilon_{\mathrm{X}}^{\mathrm{PID}}$	$\epsilon_{\mathrm{X}}^{\mathrm{Sel.}}$	f
$B^0 \to K\pi\pi\pi$ as $p\pi\pi\pi$	2011	3.521±0.039	$(29.800\pm0.381)\times10^{-2}$	Ref.
	2012	4.431±0.023	$(25.605\pm0.252)\times10^{-2}$	Ref.
$B^0 \to \pi K\pi\pi$ as $pK\pi\pi$	2011	3.464±0.065	$(8.394\pm0.202)\times10^{-2}$	27.710±0.968
	2012	2.963±0.032	$(10.787\pm0.164)\times10^{-2}$	28.173±0.611
$B^0 \to KKK\pi$ as $pKK\pi$	2011	2.962±0.029	$(46.093\pm0.474)\times10^{-2}$	Ref.
	2012	3.763±0.018	$(38.917\pm0.311)\times10^{-2}$	Ref.
$B^0 \to KK\pi K$ as $pK\pi K$	2011	3.091±0.044	$(22.109\pm0.329)\times10^{-2}$	50.056±1.257
	2012	3.841±0.027	$(18.375\pm0.214)\times10^{-2}$	48.197±0.798
$B^0 \to \pi KKK$ as $pKKK$	2011	2.939±0.101	$(2.946\pm0.120)\times10^{-2}$	6.342±0.350
	2012	2.538±0.055	$(3.193\pm0.089)\times10^{-2}$	5.534±0.203
$B^0 \to KKK\pi$ as $pK\pi\pi$	2011	0.402±0.007	$(44.752\pm0.467)\times10^{-2}$	13.171±0.322
	2012	0.513±0.005	$(38.718\pm0.310)\times10^{-2}$	13.576±0.209
$B_s^0 \to KK\pi\pi$ as $pK\pi\pi$	2011	2.947±0.043	$(42.276\pm0.647)\times10^{-2}$	Ref.
	2012	3.892±0.026	$(36.047\pm0.420)\times10^{-2}$	Ref.
$B_s^0 \to \pi KK\pi$ as $pKK\pi$	2011	3.002±0.109	$(4.630\pm0.215)\times10^{-2}$	11.153±0.697
	2012	2.644±0.056	$(5.930\pm0.171)\times10^{-2}$	11.174±0.426

where $\Gamma(n)$ and $\Gamma(n,x)$ are the usual Gamma function and incomplete Gamma function, respectively. The parameter m_t describes the threshold, where if $m > m_t$, the function evaluates to zero. The parameter p controls the curvature of the function and the parameter c controls the falling of the slope.

An ARGUS⊗Gauss PDF is added in each spectrum to model the partially-reconstructed backgrounds with missed π^0 coming from the Λ_b^0 decays. In the $pK\pi\pi$ and $pK\pi K$ spectra, additional ARGUS⊗Gauss shapes are added to model the partially-reconstructed backgrounds coming from the Ξ_b^0 decays. No convoluted ARGUS shape for Ξ_b^0 is added in the $pKKK$ spectrum since this is expected to be small. The parameters of the convoluted ARGUSes are directly determined from fit to data, with some of the parameters shared or expressed in terms of other parameters of the spectra. The convolution of the ARGUSes with a Gaussian function is numerically and computationally demanding. The following items list the physical constraints used in order to help the fit in determining the parameters of the convoluted ARGUSes:

- The slope c and the power p of the ARGUSes are shared among all the charmless spectra, but not shared among years, assuming similar kinematics of the sources.
- The slope c and the power p of the ARGUSes are also shared among charmed spectra. These parameters are also not shared among years.
- Since the main partially-reconstructed backgrounds are $X_b^0 \to 4$ body plus a missing π^0, all the threshold parameters m_t are set to be the difference of the nominal mass of Λ_b^0 (or Ξ_b^0), and the nominal mass of π^0 ($m_{\pi^0}^{\text{PDG}} = 134.9766 \pm 0.0006\,\text{MeV}/c^2$ [17]).
- The resolution of the Gaussian function convoluting the ARGUS function is mainly driven by the detector resolution, and up to first approximation is the same as the resolution of the signal models. The resolutions of the Gaussian functions convoluting the ARGUSes are then set to be the same as the sigma of Λ_b^0 signal shapes (or to Ξ_b^0 in the spectrum $pK\pi K$ where there is no Λ_b^0 signal).
- All the ARGUS⊗Gauss shape parameters are shared by both Λ_b^0 and $\overline{\Lambda}_b^0$ spectra (or Ξ_b^0 and $\overline{\Xi}_b^0$).

5.8.5 Combinatoric shapes

First order Chebychev polynomial of the second kind is used to model the combinatorial background. It has only one parameter c which describes the slope of the line describing the decrease of combinatorial background as a function of the reconstructed invariant mass. In the nominal fit, one slope c per year is shared among all charmless spectra, and one slope c per year is also shared among charmed spectra. An exponential shape is considered to evaluate a systematic uncertainty related to this model choice.

A comment is in order regarding the choice of a polynomial model as the baseline against an exponential shape for the combinatorics. The only valuable information about the combinatorics for most of the modes studied in this analysis lies in the right-hand side-band of the data[p]. The left-handed region of the invariant mass distribution of most of the spectra of interest is populated by the partially reconstructed background and the signal cross-feeds.

[p] It has been mentioned before that there is however a competition in this region with B physics events which forbids the simultaneous determination of these two contributions from the invariant mass data distribution only.

Since the mechanics of the adjustment of an exponential shape requires a leverage on the left-handed part of the invariant mass distribution, it is likely that its fit can absorb overlooked background contributions. These considerations drove us to the choice of the polynomial model for the fit model design with blind signal region.

5.8.6 Charmed decay shapes

Using MC-generated 2012 $\Lambda_b^0 \to (\Lambda_c^+ \to pK^-\pi^+)\pi^-$ events, the reconstructed invariant mass spectra is modelled by a double CB function with shared mean μ and shared width σ. The same selection as applied in charmless spectra, except with a lower BDT cut of -0.10 and reversed Λ_c^+ mass window cuts, is required to the charmed spectra. A PID weight is assigned on an event-by-event basis calculated in the same way as explained in Section 5.6.2. Figure 5.21 displays the fit result to the $pK\pi\pi$ invariant mass and the parameters measured by the fit are summarized in Table 5.22. These parameters, except the mean μ and width σ, are subsequently fixed in the PDF used to fit the real data. Due to lack of MC-generated events for the other charmed decay modes, the same shape is used for $\Lambda_b^0 \to (\Lambda_c^+ \to p\pi^-\pi^+)\pi^-$, $\Lambda_b^0 \to (\Xi_c^+ \to pK^-\pi^+)\pi^-$ and $\Xi_b^0 \to (\Xi_c^+ \to pK^-\pi^+)\pi^-$ (both for 2011 and 2012). All the widths are floated independently, except the widths of $\Lambda_b^0 \to (\Xi_c^+ \to pK\pi)\pi$ and $\Xi_b^0 \to (\Xi_c^+ \to pK\pi)\pi$ where they are shared for each year.

With the large amount of events in the $X_b^0 \to (\Lambda_c^+ \to pK\pi)\pi$ spectrum, the number of $\Lambda_b^0 \to (\Lambda_c^+ \to pK\pi)K$ starts to become a significant cross-feed background. Hence, we added this in the nominal fit model. MC-generated 2012 $\Lambda_b^0 \to (\Lambda_c^+ \to pK^-\pi^+)K^-$ events are used to determine the shape of this cross-feed PDF. A double CB, with shared mean but two different widths, is used to model the invariant mass distribution. Passing the same selection cuts and the same PID reweighting scheme, the fit parameters are gathered in Table 5.22 and the fit result is shown in Figure 5.22. The same shape is also used for the 2011 spectrum. All the parameters of this PDF is fixed in the nominal fit.

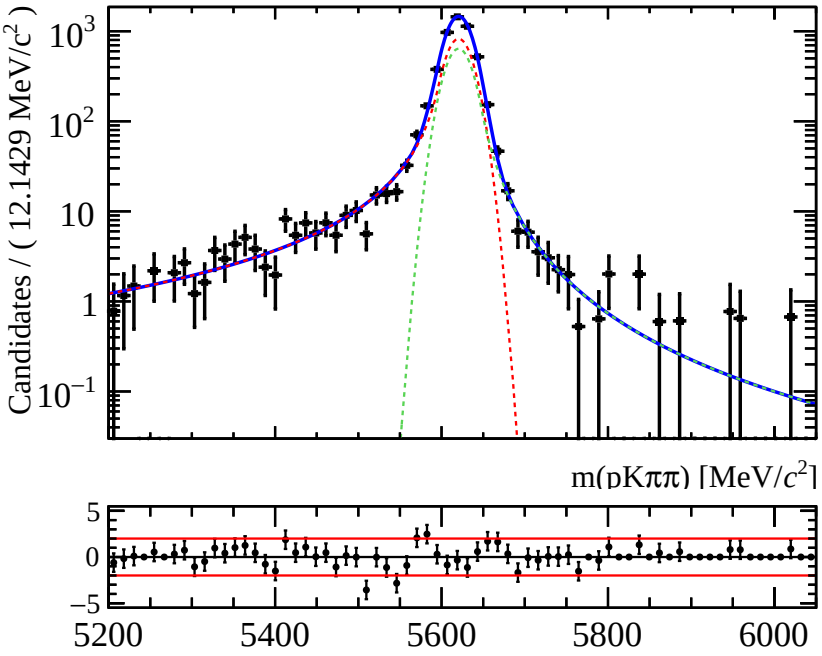

Figure 5.21: MC-generated 2012 $\Lambda_b^0 \to (\Lambda_c^+ \to pK^-\pi^+)\pi^-$ invariant mass distribution fitted with DCB PDF.

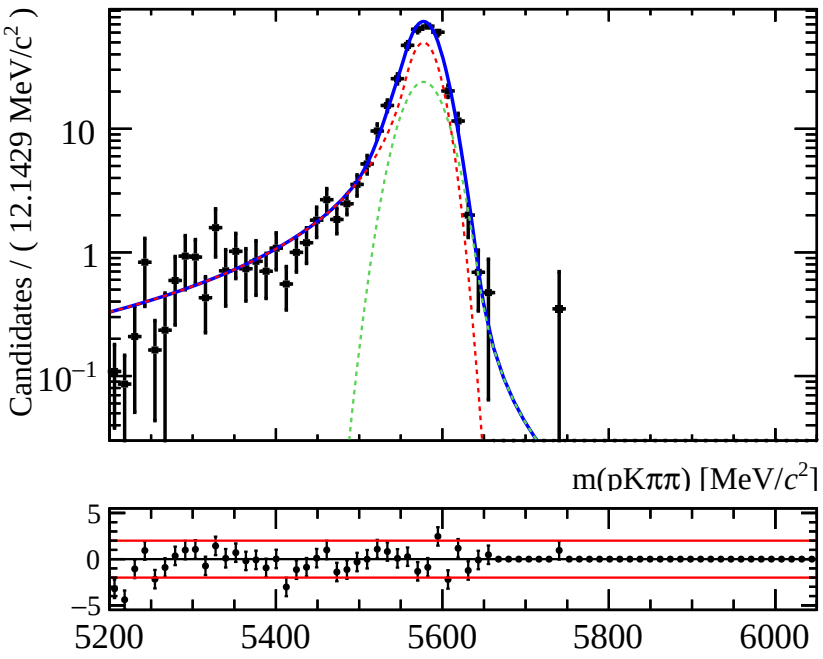

Figure 5.22: MC-generated 2012 $\Lambda_b^0 \to (\Lambda_c^+ \to pK^-\pi^+)K^-$ as $(\Lambda_c^+ \to pK^-\pi^+)\pi^-$ invariant mass distribution fitted with DCB PDF.

Table 5.22: Fit parameters obtained in the fit to $\Lambda_b^0 \to (\Lambda_c^+ \to pK\pi)\pi$ signal shape and $\Lambda_b^0 \to (\Lambda_c^+ \to pK\pi)K$ as $(\Lambda_c^+ \to pK\pi)\pi$ cross-feed shape.

Fit parameters							
α_1	α_2/α_1	n_1	n_2/n_1	f_2	σ_1	σ_2/σ_1	μ
$\Lambda_b^0 \to (\Lambda_c^+ \to pK\pi)\pi$ signal:							
1.536±0.224	-1.125±0.311	1.672±0.169	1.575±0.313	0.579±0.188	15.606±0.281	N/A	5620.547±0.282
$\Lambda_b^0 \to (\Lambda_c^+ \to pK\pi)K$ as $(\Lambda_c^+ \to pK\pi)\pi$ cross-feed:							
1.177±0.389	-2.269±1.175	1.580±0.509	1.225±1.683	0.659±0.294	18.298±2.794	1.338±0.319	5577.394±1.612

5.8.7 The fitter and the simultaneous fit strategy

A modified version of V0hhFitter is used as a tool to simultaneously fit the 28 separate spectra. This fitter was originally developed in Warwick for modes involving a V^0 particle in the final state and hence the name, but can actually be used in any 1-dimensional simultaneous fit. It is used in particular for the analysis of the decays $B^0_{d,s} \to K^0_S hh$'. Some modifications to the original code have been implemented to adapt to the blinding strategy of this analysis.

The implementation of this simultaneous fit was a daunting task. Nonetheless, once implemented, its virtues are invaluable. The philosophy of the simultaneous fit of charmless and charmed signal yields to the corresponding spectra followed a two-fold objective. The information of the charmless spectra (and charmed spectra) are intricated by the presence of signal and background cross-feeds, the common reweighting of the PID, the physical parameters such as the reconstructed baryon masses or the mass threshold of the partially reconstructed backgrounds (to only cite few of them). The simultaneous adjustment of the shared parameters between the signal and control channel modes, as well as the consistent introduction of data-driven constraints to the fit model for all spectra to account for signal cross-feeds or B physics backgrounds, allows to integrate most of the sources of uncertainties

as statistical uncertainty of the fit, and hence minimize the systematic uncertainty budget on the $\mathcal{A}^{\text{raw}}$'s and $\Delta\mathcal{A}^{CP}$'s observables. Conversely, the latter are reduced to the fit model error sources. Eventually, this strategy presents the advantage of a modest bookkeeping of the fit results given the number of spectra under scrutiny in this analysis. The cross-checks of the measurement (magnet polarity and trigger requirements) proceed accordingly in one go.

Some elements of the fit strategies and constraints were already mentioned in the previous Sections and Subsections of this document. They are spelled again here to wrap-up the whole strategy. Table 5.23 gathers the PDFs present in each spectrum. As discussed in Section 5.8.2, only dominant cross-feeds are included in the fit as others involve double mis-identification. Futhermore, $\Lambda_b^0 \to pKK\pi$ as cross-feed to $X_b^0 \to pKKK$ spectrum, and $\Xi_b^0 \to pKKK$ as cross-feed to $X_b^0 \to pKK\pi$ or $X_b^0 \to pK\pi K$ spectra, are not included in the fit since eventually the fit to data found only few events of these cross-feeds. Given the level of estimated mis-identification rates, which are $\sim$2% for $\Lambda_b^0 \to pKK\pi$ as $X_b^0 \to pKKK$ and $\sim$8% for $\Xi_b^0 \to pKKK$ as $X_b^0 \to pKK\pi$ or $X_b^0 \to pK\pi K$, we think that these contributions are negligible. Note that in the SM, the $\Lambda_b^0 \to pKK\pi$ and $\Xi_b^0 \to pKKK$ are expected to proceed only through $b \to d$ penguin loop transition.

For the case of the B physics to 4-body backgrounds, singly misidentified decays (π to p and K to p) are modelled in each spectrum. A doubly-misidentified $B^0 \to K^+K^-K^+\pi^-$ as $X_b^0 \to pK\pi\pi$ is also included in the fit model since $B^0 \to K^+K^-K^+\pi^-$ events have been identified using the RHSB events of $X_b^0 \to pK\pi\pi$ spectrum as discussed in Section 5.7. This background is expected to be the dominant B physics background before any PID cuts are applied and some events still survive in the $X_b^0 \to pK\pi\pi$ spectrum after the PID cuts are applied. Note as well that although $B_s^0 \to K\pi\pi K$ is a background in the $X_b^0 \to pKK\pi$ spectrum, it is triply-misidentified in the $X_b^0 \to pK\pi K$ spectrum since the two kaons should have the same charge.

Table 5.23: List of PDFs in each spectrum.

Spectrum	Signal PDF	Cross-feed PDF	B physics
$X_b^0 \to p\pi\pi\pi$	$\Lambda_b^0 \to p\pi\pi\pi$	$\Lambda_b^0 \to pK\pi\pi$ as $p\pi\pi\pi$ $\Xi_b^0 \to pK\pi\pi$ as $p\pi\pi\pi$	$B^0 \to K\pi\pi\pi$ as $p\pi\pi\pi$ $B^0 \to \pi\pi\pi\pi$ as $p\pi\pi\pi$
$X_b^0 \to pK\pi\pi$	$\Lambda_b^0 \to pK\pi\pi$ $\Xi_b^0 \to pK\pi\pi$	$\Lambda_b^0 \to p\pi\pi\pi$ as $pK\pi\pi$ $\Lambda_b^0 \to pKK\pi$ as $pK\pi\pi$ $\Xi_b^0 \to pK\pi K$ as $pK\pi\pi$	$B_s^0 \to KK\pi\pi$ as $pK\pi\pi$ $B^0 \to \pi K\pi\pi$ as $pK\pi\pi$ $B^0 \to KKK\pi$ as $pK\pi\pi$
$X_b^0 \to pKK\pi$	$\Lambda_b^0 \to pKK\pi$	$\Lambda_b^0 \to pK\pi\pi$ as $pKK\pi$ $\Lambda_b^0 \to pKKK$ as $pKK\pi$	$B^0 \to KKK\pi$ as $pKK\pi$ $B_s^0 \to \pi KK\pi$ as $pKK\pi$
$X_b^0 \to pKKK$	$\Lambda_b^0 \to pKKK$ $\Xi_b^0 \to pKKK$		$B_s^0 \to KKKK$ as $pKKK$ $B^0 \to \pi KKK$ as $pKKK$
$X_b^0 \to pK\pi K$	$\Xi_b^0 \to pK\pi K$	$\Lambda_b^0 \to pKKK$ as $pK\pi K$ $\Lambda_b^0 \to pK\pi\pi$ as $pK\pi K$	$B^0 \to KK\pi K$ as $pK\pi K$
$X_b^0 \to (\Lambda_c^+ \to p\pi\pi)\pi$	$\Lambda_b^0 \to (\Lambda_c^+ \to p\pi\pi)\pi$		
$X_b^0 \to (\Lambda_c^+ \to pK\pi)\pi$	$\Lambda_b^0 \to (\Lambda_c^+ \to pK\pi)\pi$	$\Lambda_b^0 \to (\Lambda_c^+ \to pK\pi)K$ as $(\Lambda_c^+ \to pK\pi)\pi$	
$X_b^0 \to (\Xi_c^+ \to pK\pi)\pi$	$\Lambda_b^0 \to (\Xi_c^+ \to pK\pi)\pi$ $\Xi_b^0 \to (\Xi_c^+ \to pK\pi)\pi$		

∘ Each spectrum has a PDF for the combinatorics modelled by a first order Chebychev function.
∘ Each spectrum has a PDF for partially-reconstructed backgrounds from $\Lambda_b^0 \to$ 4-body + missing π^0 modelled by an ARGUS convoluted by a Gaussian resolution.
∘ Additional convoluted ARGUS⊗Gauss shapes are added in the $X_b^0 \to pK\pi\pi$, $X_b^0 \to pK\pi K$ and $X_b^0 \to (\Xi_c^+ \to pK\pi)\pi$ spectra for partially-reconstructed backgrounds from $\Xi_b^0 \to$ 4-body + missing π^0.

The simultaneous fit strategy is consist of the following:

- The nominal mass of Λ_b^0 and Ξ_b^0 are shared by all spectra, both in charmless and charmed decays.
- The difference of the nominal mass of Λ_b^0 and Ξ_b^0 is Gaussianly-constrained from the PDG value ($m_{\Xi_b^0}$- $m_{\Lambda_b^0}$ = 174.8±2.5).
- The ratio of widths of the charmless signal shapes are Gaussianly-constrained with the values obtained from the fit to MC events. The reference width is the width of $\Lambda_b^0 \to pK\pi\pi$ 2012. These numbers are summarized in the last column of Table 5.17.
- Control modes $\Lambda_b^0 \to (\Lambda_c^+ \to p\pi\pi)\pi$ and $\Lambda_b^0 \to (\Lambda_c^+ \to pK\pi)\pi$ has its own signal width parameters floated in the fit. However, the width of $\Lambda_b^0 \to (\Xi_c^+ \to pK\pi)\pi$ and $\Xi_b^0 \to (\Xi_c^+ \to pK\pi)\pi$ are shared.
- The cross-feeds yields are related to their corresponding signal yields by a factor calculated from the ratio of selection efficiencies and PID (mis)-identification efficiencies as discussed in Section 5.8.2.
- The ratio of yields of B physics backgrounds appearing in more than one spectra is also Gaussianly-constrained in the same way as how the signal cross-feeds yields are constrained. The ratio is calculated from ratios of selection efficiencies and PID efficiencies.
- In addition to the constraints on the ratio of B physics yields, the yield of dominant B physics in each spectrum is Gaussianly-constrained according to their corresponding observed events in the RHSB. This was further discussed in Section 5.7. The ratio of $B^0 \to \pi\pi\pi\pi$ and $B^0 \to K\pi\pi\pi$ in the $X_b^0 \to p\pi\pi\pi$ spetrum is also Gaussianly-constrained.
- One slope c per year is shared among all charmless spectra, and slope c is shared per year also among all charmed spectra.
- The parameters power p and slope s of the convoluted ARGUSes describing the partially-reconstructed backgrounds are shared among all the charmless spectra per year. Another set of shared ARGUS parameters p and s per year is dedicated for the charmed modes. The threshold parameter m_t of the ARGUS shapes is set to be the difference of the nominal mass of Λ_b^0 (or Ξ_b^0 if it comes from $\Xi_b^0 \to$ 5-body) and the nominal mass of π^0. The resolution of the Gaussian function convoluting the ARGUS is set to be the same as the width of the Λ_b^0 signal PDF in the same spectrum (or Ξ_b^0 signal PDF in the $pK\pi K$ spectrum).
- In order to avoid possible bias when the statistics are low, specifically for the signal decays, the signal yields are allowed to go as low as -5% of the total number of events in the spectrum.
- All the shape parameters are shared by the two split spectra Λ_b^0 & $\overline{\Lambda}_b^0$ (or Ξ_b^0 & $\overline{\Xi}_b^0$). The Gaussianly-constrained ratios and factors are also shared by the two split spectra except for the constraint on the yields of dominant B physics backgrounds, which were obtained separately for Λ_b^0 and $\overline{\Lambda}_b^0$ in the RHSB.

The total number of floating parameters in the nominal fit is 203, where 140 are yield parameters and the remaining 63 are shape parameters or ratio parameters. Out of 140 yield parameters, 28 are yield parameters of the charmless signal decays and 16 for charmed/control decays. Although not floating parameters of the fit, the $\mathcal{A}^{CP}$'s and $\Delta\mathcal{A}^{CP}$'s are calculated directly from the fit results using RooFit::RooFormulaVar, which takes into account the correlation of the uncertainties of the fit parameters. The $\mathcal{A}^{CP}$ and $\Delta\mathcal{A}^{CP}$ are given by:

$$\mathcal{A}^{CP} = \frac{\mathcal{N}(X_b^0) - \overline{\mathcal{N}}(\overline{X}_b^0)}{\mathcal{N}(X_b^0) + \overline{\mathcal{N}}(\overline{X}_b^0)} \quad \text{and} \tag{5.14}$$

$$\Delta\mathcal{A}^{CP} = \frac{\mathcal{N}(X_b^0) - \overline{\mathcal{N}}(\overline{X}_b^0)}{\mathcal{N}(X_b^0) + \overline{\mathcal{N}}(\overline{X}_b^0)} - \frac{\mathcal{N}_{\rm C}(X_b^0) - \overline{\mathcal{N}}_{\rm C}(\overline{X}_b^0)}{\mathcal{N}_{\rm C}(X_b^0) + \overline{\mathcal{N}}_{\rm C}(\overline{X}_b^0)}, \tag{5.15}$$

respectively, where $\mathcal{N}_{\rm C}$ and $\overline{\mathcal{N}}_{\rm C}$ in Equation 5.15 are the yields of the control decays.

5.9 Pre-unblinding toy studies

Toy MC studies are conducted to check for possible fit biases on the signal yields. Since all the yields of the charmless modes are blinded, guesstimated values are used instead in the toy study. The signal yields of the charmed modes and backgrounds are set to be the values obtained in the simultaneous fit, as well as the other shape parameters. The fit results are presented in Section 5.10.1. Let us notice that a first attempt has been performed by considering vanishing yields for all signal modes, and no biases were observed.

The generated values for the $\Lambda_b^0 \to pK^-\pi^+\pi^-$ and $\Lambda_b^0 \to p\pi^-\pi^+\pi^-$ are 622 and 386 signal events, respectively, for the 2011 spectra, while 1394 and 892 signal events for the 2012 spectra. These were the yields observed[q] when the $\Lambda_b^0 \to p\pi\pi\pi$ and $\Lambda_b^0 \to pK\pi\pi$ (combined $\Lambda_b^0/\overline{\Lambda}_b^0$) were searched for using the StrippingBetaSQ2B{3,4}piSelectionLine of Stripping20. The rest of charmless Λ_b^0 signals are generated with 100 signal events, and 25 signal events for the Ξ_b^0's. The same generated events are assigned to the $\overline{\Lambda}_b^0$ and $\overline{\Xi}_b^0$ signals. This toy study is however very demanding CPU-wise and hence some simplification to the nominal fit, namely by fixing the ARGUS power and slope in the charmless spectra, have been brought. The correlation of these ARGUS parameters to the signal yields is in the percent level, as summarized in Table A.6 in Appendix A.17. The full CPU-consuming procedure will be be run once the fit model is blessed.

The pull for each MC toy is calculated and gathered, where the pull is defined as,

$$\text{pull}_{\rm g} = \frac{g_{\rm fit} - g_{\rm gen}}{\sigma_{\rm g,fit}}\ , \tag{5.16}$$

where $g_{\rm fit}$ and $g_{\rm gen}$ are the fitted and generated values of the parameter, respectively, while $\sigma_{\rm g,fit}$ is the uncertainty of the parameter obtained by the fit. In an unbiased measurement of the quantity and correctly-estimated uncertainty, the pull distribution results in a unit Gaussian. The pull study of the signal yields can be found in Figures 5.23 and 5.24, where the gaussian means and widths are gathered in Table 5.24. The behaviour of the pulls is Gaussian and no significant biases were observed on the yields, hence on the CP asymmetry observables.

The yield of the dominant B physics background in each spectrum is Gaussianly-constrained according to what is observed in the RHSB events (See Section 5.7 for the details on the

[q] See talk [https://indico.cern.ch/event/368076/].

study of RHSB events). Due to the constraint, the pull distribution is not a unit Gaussian as shown in the Figures in Appendix A.10. The papers [111] and [112] suggest the correct way of calculating the widths of the pulls for constrained parameters of the fit. This will be implemented in a further stage of the analysis if required. No bias is as well observed for these nuisance parameters.

The ensemble of these results provides a satisfactory behaviour of the fit and does not require any corrective action. After unblinding, the uncertainties of the biases as given by the pseudo-experiments using the actual results of the fit will be used however as a systematic uncertainty related to the simultaneous fitter.

Table 5.24: Summary of the Gaussian means and widths of the pull distribution for the charmless and charmed signal yields.

Yield parameter	2011		2012	
	μ	σ	μ	σ
$\mathcal{N}$ (Signal $\Lambda_b^0 \to p\pi\pi\pi$)	-0.017±0.032	0.983±0.023	-0.021±0.033	0.995±0.023
$\overline{\mathcal{N}}$ (Signal $\Lambda_b^0 \to p\pi\pi\pi$)	-0.080±0.034	1.035±0.024	-0.040±0.032	0.969±0.022
$\mathcal{N}$ (Signal $\Lambda_b^0 \to pK\pi\pi$)	-0.053±0.033	1.024±0.024	-0.011±0.032	0.980±0.023
$\overline{\mathcal{N}}$ (Signal $\Lambda_b^0 \to pK\pi\pi$)	0.021±0.033	0.996±0.023	0.008±0.033	1.023±0.024
$\mathcal{N}$ (Signal $\Lambda_b^0 \to pKK\pi$)	-0.039±0.032	0.991±0.023	-0.005±0.033	0.997±0.023
$\overline{\mathcal{N}}$ (Signal $\Lambda_b^0 \to pKK\pi$)	-0.061±0.033	1.015±0.023	-0.022±0.032	0.975±0.023
$\mathcal{N}$ (Signal $\Lambda_b^0 \to pKKK$)	-0.129±0.032	0.987±0.023	0.001±0.032	0.966±0.022
$\overline{\mathcal{N}}$ (Signal $\Lambda_b^0 \to pKKK$)	-0.025±0.033	1.004±0.023	0.044±0.033	1.015±0.023
$\mathcal{N}$ (Signal $\Xi_b^0 \to pK\pi\pi$)	-0.076±0.032	0.981±0.023	-0.084±0.034	1.042±0.024
$\overline{\mathcal{N}}$ (Signal $\Xi_b^0 \to pK\pi\pi$)	-0.030±0.033	1.018±0.024	-0.017±0.032	0.978±0.023
$\mathcal{N}$ (Signal $\Xi_b^0 \to pK\pi K$)	-0.114±0.034	1.030±0.024	-0.047±0.033	1.011±0.023
$\overline{\mathcal{N}}$ (Signal $\Xi_b^0 \to pK\pi K$)	-0.046±0.033	1.000±0.023	-0.103±0.033	1.021±0.024
$\mathcal{N}$ (Signal $\Xi_b^0 \to pKKK$)	-0.067±0.035	1.070±0.025	-0.031±0.032	0.988±0.023
$\overline{\mathcal{N}}$ (Signal $\Xi_b^0 \to pKKK$)	-0.092±0.033	1.000±0.023	-0.048±0.034	1.054±0.024
$\mathcal{N}$ (Signal $\Lambda_b^0 \to (\Lambda_c^+ \to p\pi\pi)\pi$)	0.049±0.032	0.979±0.023	-0.065±0.033	0.997±0.023
$\overline{\mathcal{N}}$ (Signal $\Lambda_b^0 \to (\Lambda_c^+ \to p\pi\pi)\pi$)	-0.070±0.033	1.005±0.023	0.017±0.033	1.003±0.023
$\mathcal{N}$ (Signal $\Lambda_b^0 \to (\Lambda_c^+ \to pK\pi)\pi$)	-0.025±0.032	0.979±0.023	0.050±0.033	1.021±0.024
$\overline{\mathcal{N}}$ (Signal $\Lambda_b^0 \to (\Lambda_c^+ \to pK\pi)\pi$)	-0.019±0.033	1.010±0.023	-0.011±0.033	1.006±0.023
$\mathcal{N}$ (Signal $\Lambda_b^0 \to (\Lambda_c^+ \to pKK)\pi$)	-0.012±0.033	1.007±0.023	0.015±0.033	0.998±0.023
$\overline{\mathcal{N}}$ (Signal $\Lambda_b^0 \to (\Lambda_c^+ \to pKK)\pi$)	-0.007±0.034	1.034±0.024	-0.048±0.032	0.981±0.023

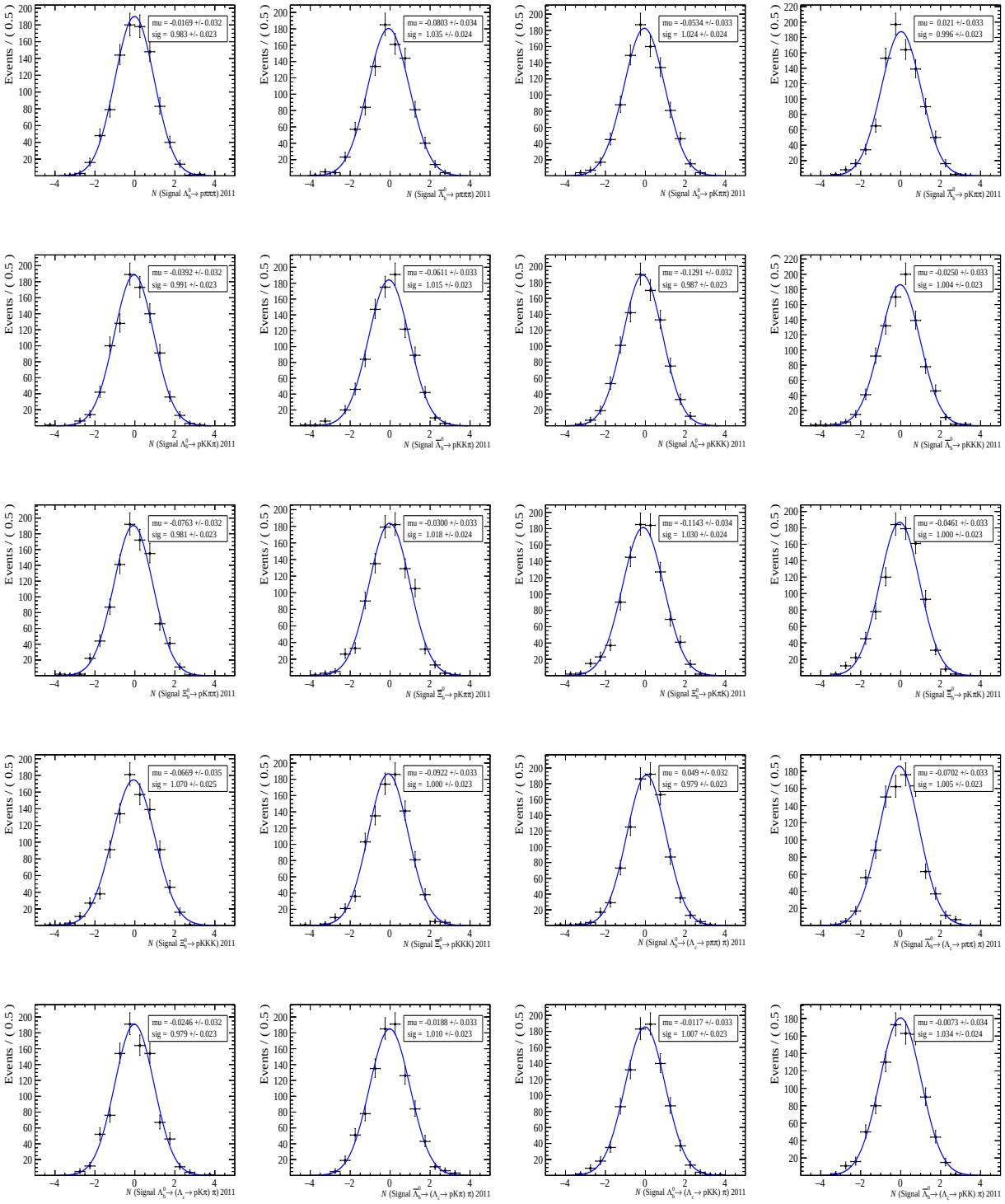

Figure 5.23: Pulls of the 2011 charmless and charmed decay signal yields obtained using about 1000 toys.

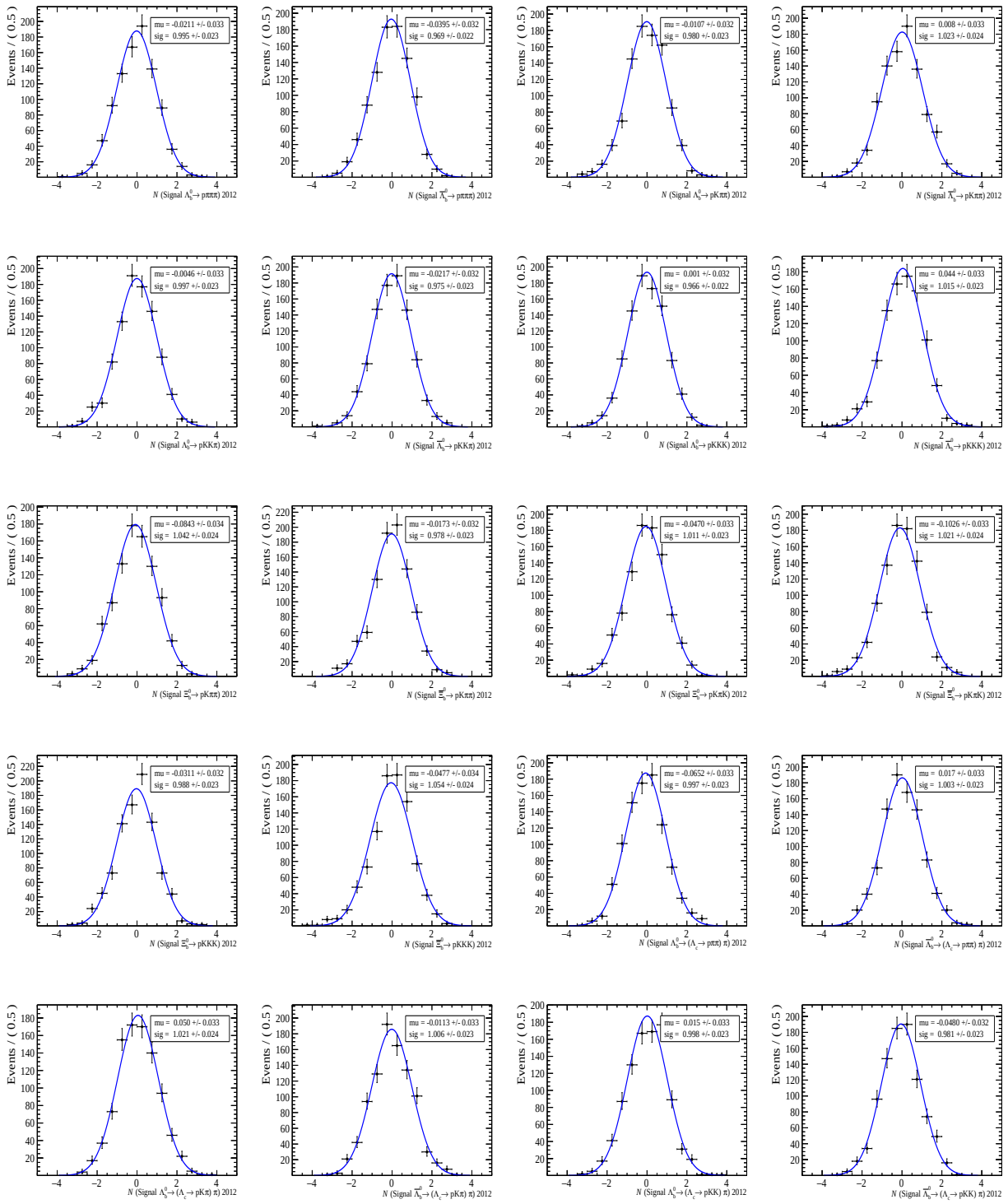

Figure 5.24: Pulls of the 2012 charmless and charmed decay signal yields obtained using about 1000 toys.

5.10 Pre-unblinding fit results

In this Section, we present the fit results and the measurement of CP asymmetry observables in three phase space regions. The first measurement considers the full phase space data, where no invariant mass cut is applied to any of the pair of the daughter particles. The second measurement looks for the CP asymmetries in the low invariant mass of the $p\pi$ or pK, with the objective of scrutinizing the phase space of the decay involving the baryon series Λ^* and N^*. Lastly, CP asymmetries are measured in the low invariant mass of $p\pi$ (or pK) pair and also low invariant mass of the pair of the two other tracks. No such cuts are applied to the control modes in all the measurements. Particularly, the mass cuts on charmless spectra for each measurement are summarized in Table 5.25. For labelling purposes, we arranged the four charged tracks in each spectrum in this sequence: $(ph^-h'^+h''^-)$ or $(\overline{p}h^+h'^-h''^+)$. Hence, the proton is labelled simply as p, and the remaining tracks are labelled h, h' and h'' in a charge arrangement defined in the previous sentence. For example, the notation $m(ph\_p\pi)$ means the reconstructed invariant mass of the combination.

The invariant mass cut on the $p\pi$ or pK pair is set to be less than 2 GeV/c^2, while the invariant mass cut on the two remaining tracks depends on whether it is $\pi\pi$ pair, $K\pi$ pair or KK pair. The choice of these values tries to include several known resonances, in particular, $f_0(1500)$ resonance for $\pi\pi$, the broad scalar $K_0^*(1430)$ resonance for $K\pi$ and the $f_2'(1525)$ resonance for KK. The charmless and charmed decay signal yields are then used to calculate the $\mathcal{A}^{\rm raw}$'s and $\Delta\mathcal{A}^{CP}$'s, with proper propagation of the statistical uncertainties taking into account correlations. Note that the $\Delta\mathcal{A}^{CP}$ of $\Xi_b^0 \to pK\pi K$ and $\Xi_b^0 \to pKKK$ are calculated using the control $\Xi_b^0 \to (\Xi_c^+ \to pK\pi)\pi$, and hence the knowledge of the K^+/K^- and π^+/π^- detection asymmetries correction is necessary for the interpretation of the results in terms of CP violating asymmetries.

Table 5.25: Mass cuts applied in the data in order to search for CP asymmetries in the low invariant mass region of ph and $h'h''$.

Charmless spectrum	Mass cut (in GeV/c^2)
Low invariant mass region of ph:	
$X_b^0 \to p\pi\pi\pi$	$m(ph\_p\pi) < 2$ or $m(ph''\_p\pi) < 2$
$X_b^0 \to pK\pi\pi$	$m(ph\_pK) < 2$ or $m(ph''\_p\pi) < 2$
$X_b^0 \to pKK\pi$	$m(ph\_pK) < 2$ or $m(ph''\_p\pi) < 2$
$X_b^0 \to pK\pi K$	$m(ph\_pK) < 2$ or $m(ph''\_pK) < 2$
$X_b^0 \to pKKK$	$m(ph\_pK) < 2$ or $m(ph''\_pK) < 2$
Low invariant mass region of ph and $h'h''$:	
$X_b^0 \to p\pi\pi\pi$	$(m(ph\_p\pi) < 2$ and $m(h'h''\_\pi\pi) < 1.640)$ or $(m(ph''\_p\pi) < 2$ and $m(h'h\_\pi\pi) < 1.640)$
$X_b^0 \to pK\pi\pi$	$(m(ph\_pK) < 2$ and $m(h'h''\_\pi\pi) < 1.640)$ or $(m(ph''\_p\pi) < 2$ and $m(h'h\_\pi K) < 1.600)$
$X_b^0 \to pKK\pi$	$(m(ph\_pK) < 2$ and $m(h'h''\_K\pi) < 1.600)$ or $(m(ph''\_p\pi) < 2$ and $m(h'h\_KK) < 1.675)$
$X_b^0 \to pK\pi K$	$(m(ph\_pK) < 2$ and $m(h'h''\_\pi K) < 1.600)$ or $(m(ph''\_pK) < 2$ and $m(h'h\_\pi K) < 1.600)$
$X_b^0 \to pKKK$	$(m(ph\_pK) < 2$ and $m(h'h''\_KK) < 1.675)$ or $(m(ph''\_pK) < 2$ and $m(h'h\_KK) < 1.675)$

5.10.1 Full phase space

Figures 5.25, 5.26 and 5.27 display the fit results of the simultaneous fit to the invariant mass spectra using the full phase space 2011 data. Figures 5.28, 5.29 and 5.30 show the fit results for the 2012 data. The fit parameters are summarized in Table 5.26, where it shows which parameters are shared and not shared. The full set of asymmetries observables are summarized in Table 5.27.

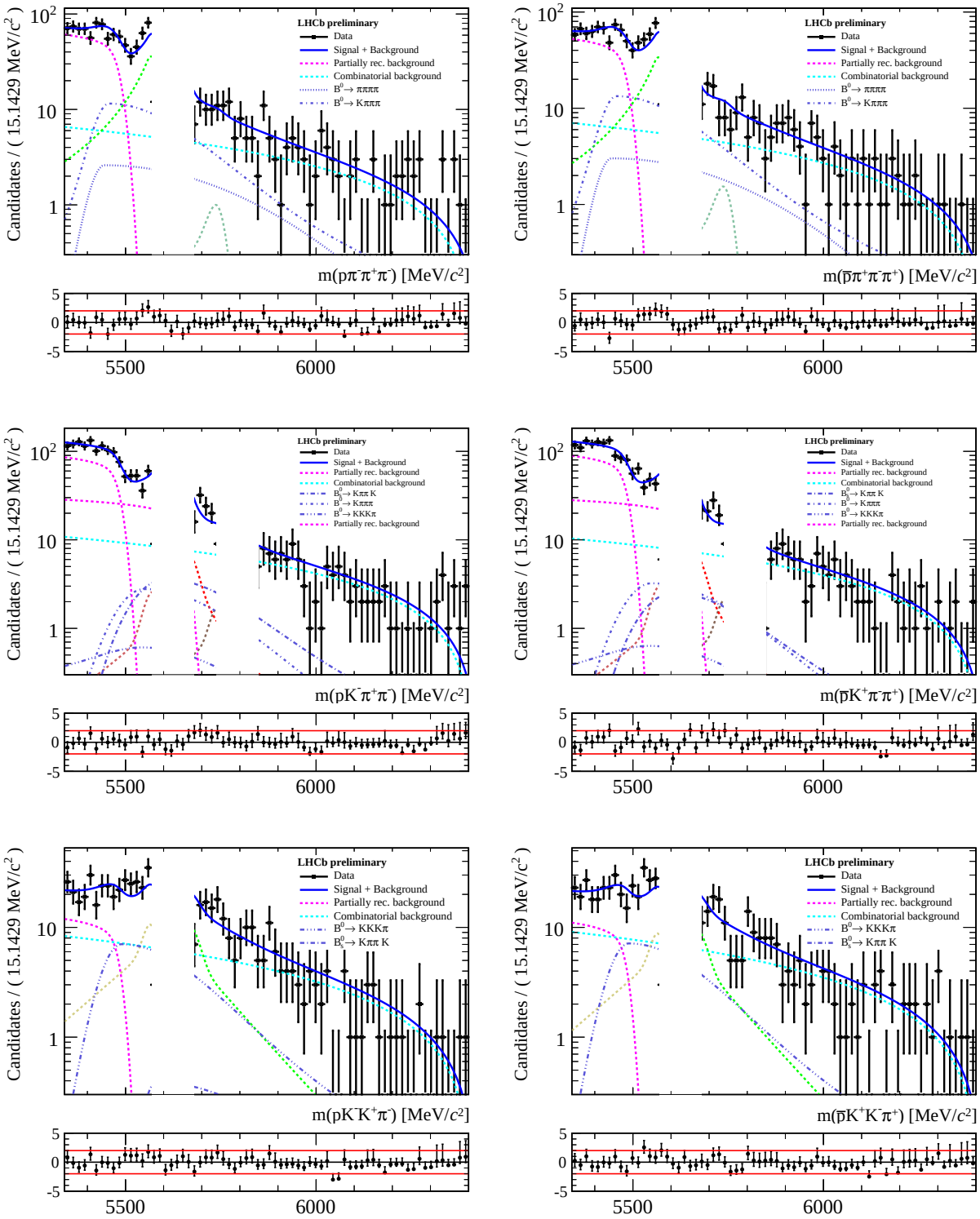

Figure 5.25: Fit results for the [from top to bottom] $X_b^0 \to p\pi\pi\pi$, $X_b^0 \to pK\pi\pi$ and $X_b^0 \to pKK\pi$ spectra using the full phase space data of 2011. Plots in the left-column are for the spectra with X_b^0 and on the right-column for the spectra with $\overline{X}_b^0$.

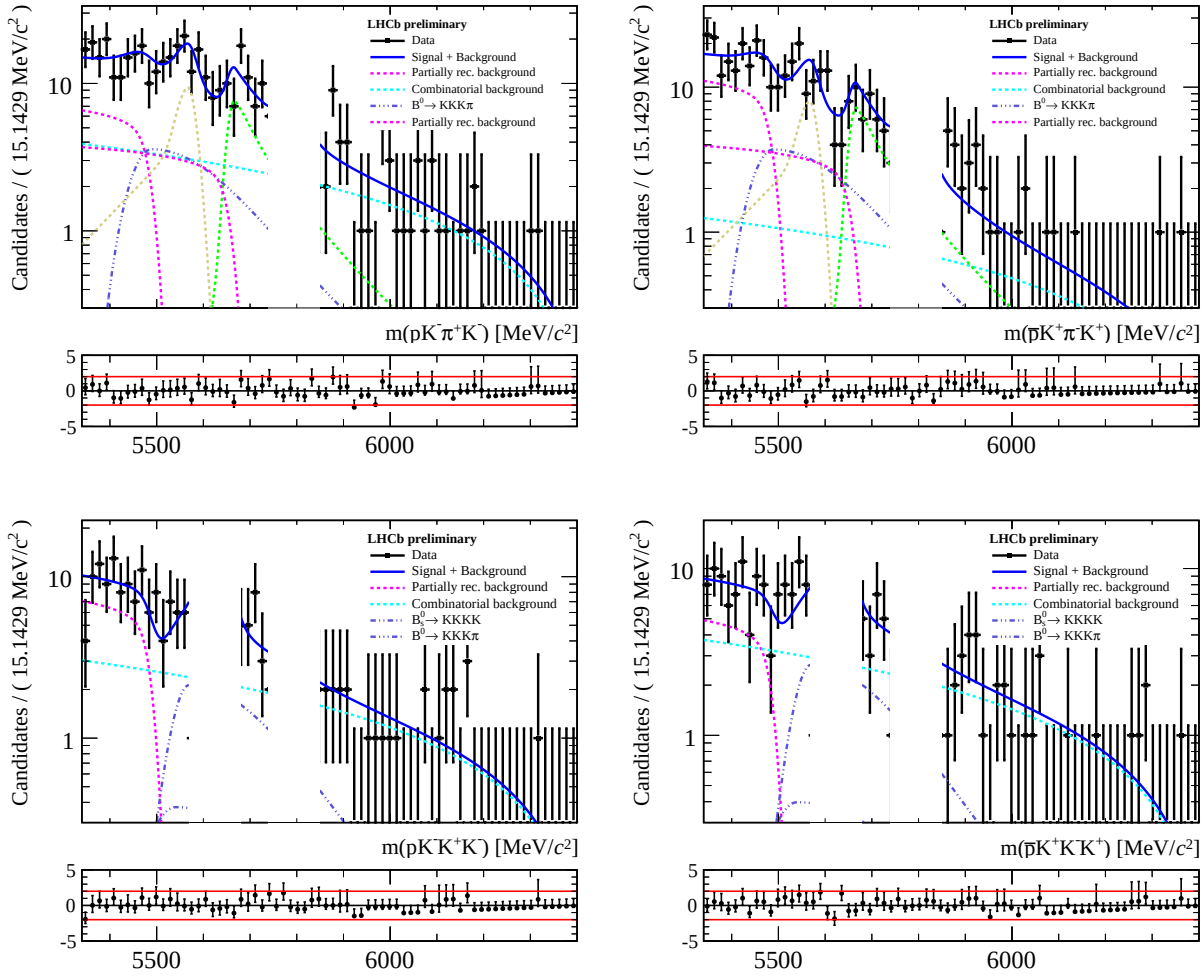

Figure 5.26: Fit results for the [top] $X_b^0 \to pK\pi K$ and [bottom] $X_b^0 \to pKKK$ spectra using the full phase space data of 2011. Plots in the left-column are for the spectra with X_b^0 and on the right-column for the spectra with $\overline{X}_b^0$.

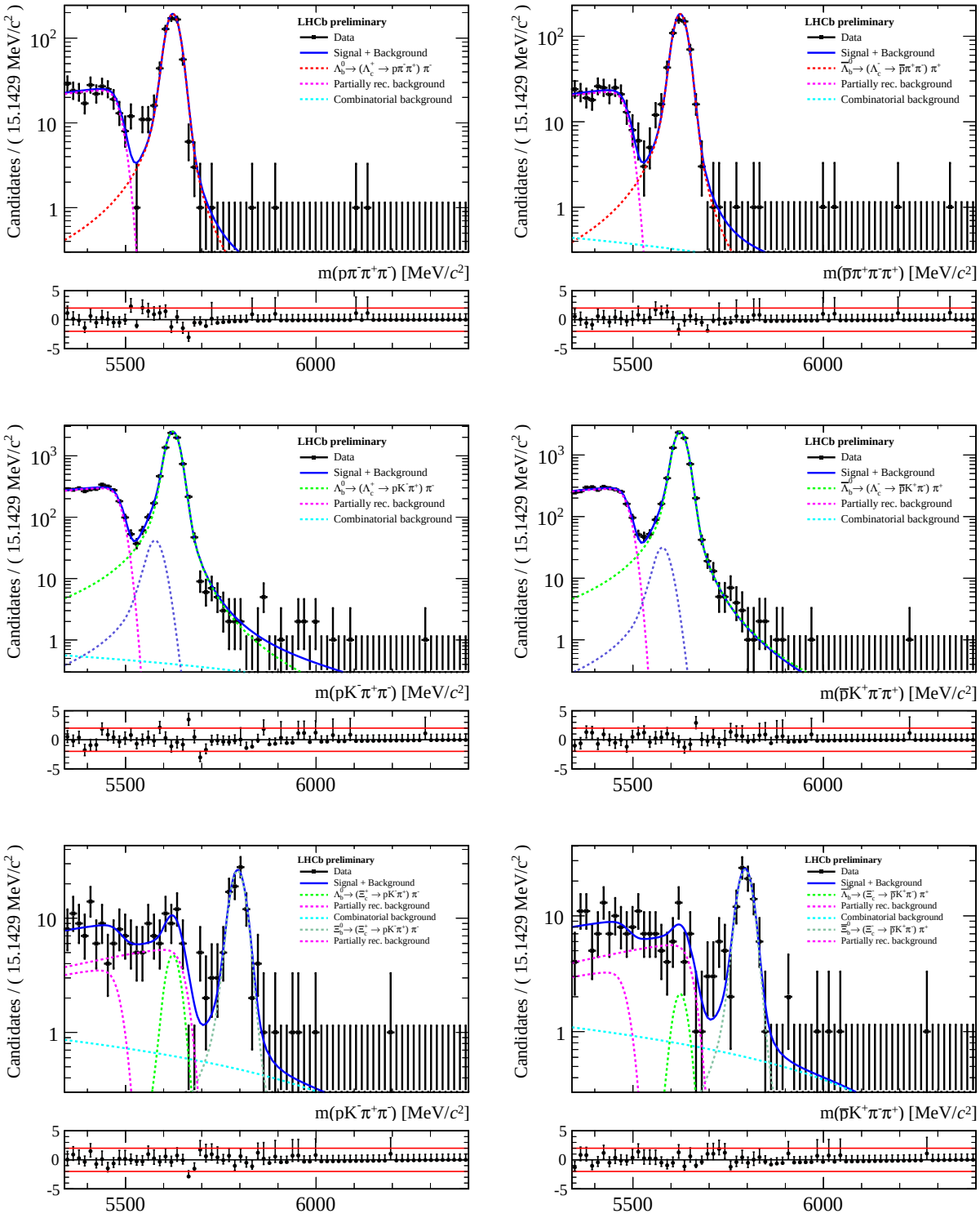

Figure 5.27: Fit results for the [from top to bottom] $X_b^0 \to (\Lambda_c^+ \to p\pi\pi)\pi$, $X_b^0 \to (\Lambda_c^+ \to pK\pi)\pi$ and $X_b^0 \to (\Xi_c^+ \to pK\pi)\pi$ spectra using the full phase space data of 2011. Plots in the left-column are for the spectra with X_b^0 and on the right-column for the spectra with $\overline{X}_b^0$.

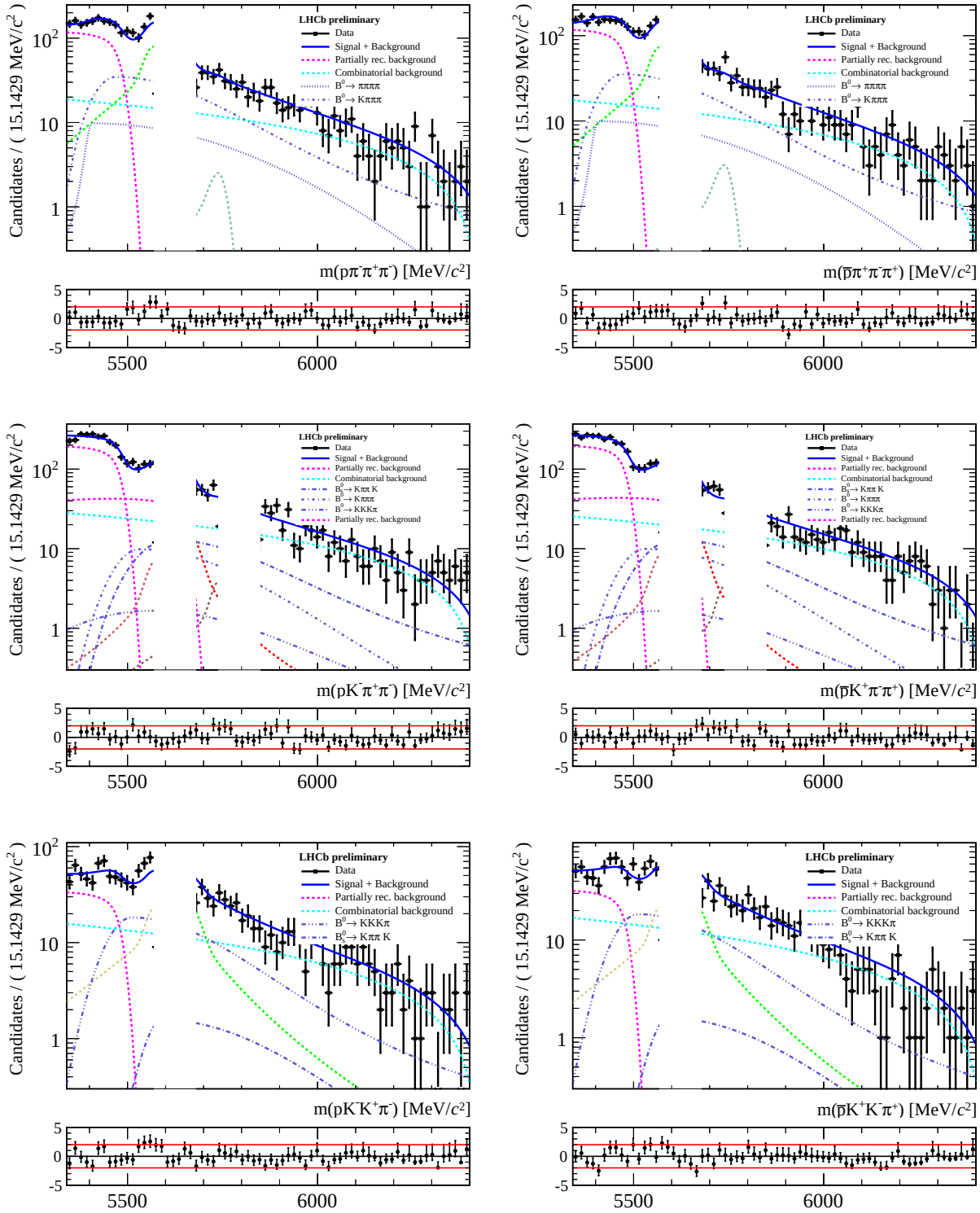

Figure 5.28: Fit results for the [from top to bottom] $X_b^0 \to p\pi\pi\pi$, $X_b^0 \to pK\pi\pi$ and $X_b^0 \to pKK\pi$ spectra using the full phase space data of 2012. Plots in the left-column are for the spectra with X_b^0 and on the right-column for the spectra with $\overline{X}_b^0$.

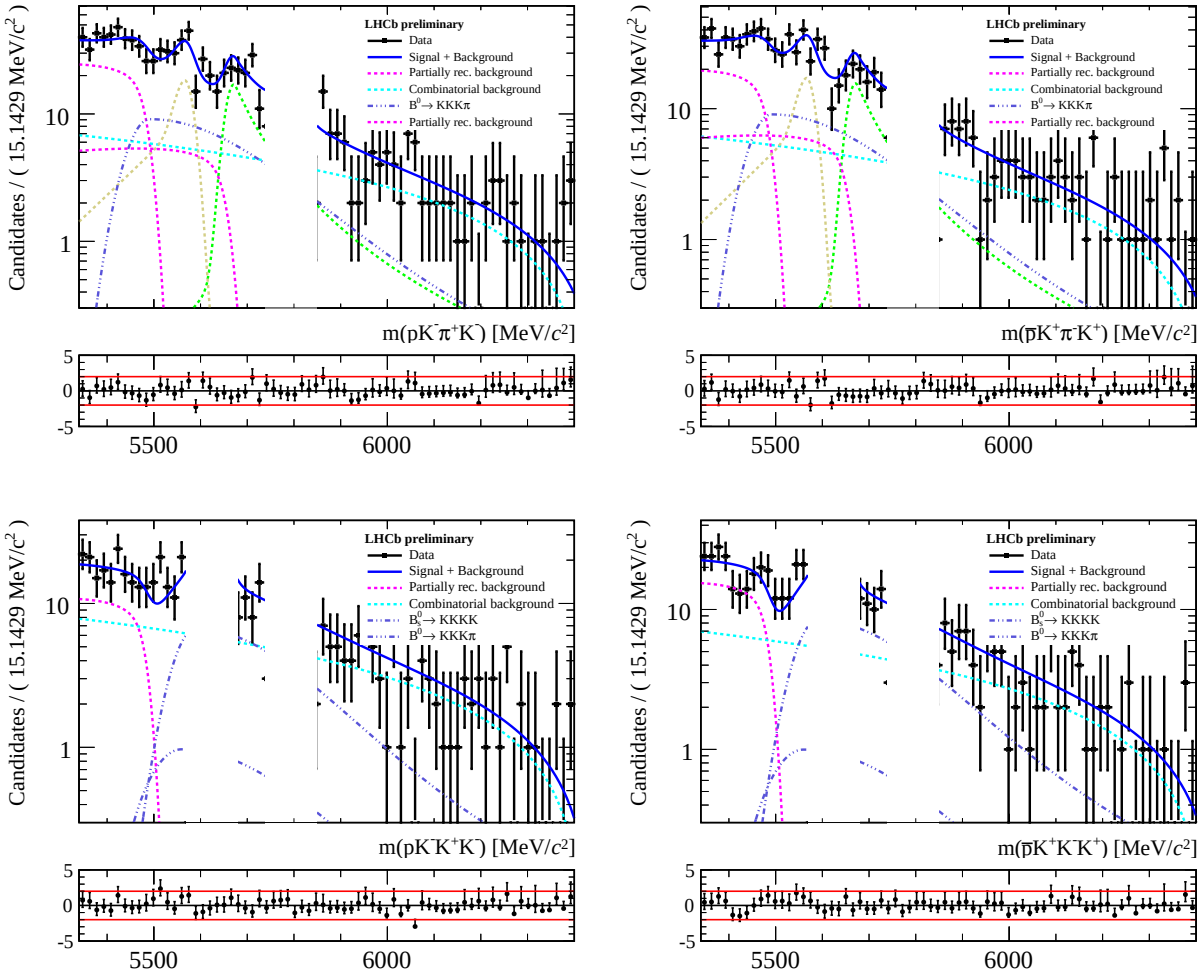

Figure 5.29: Fit results for the [top] $X_b^0 \to pK\pi K$ and [bottom] $X_b^0 \to pKKK$ spectra using the full phase space data of 2012. Plots in the left-column are for the spectra with X_b^0 and on the right-column for the spectra with $\overline{X}_b^0$.

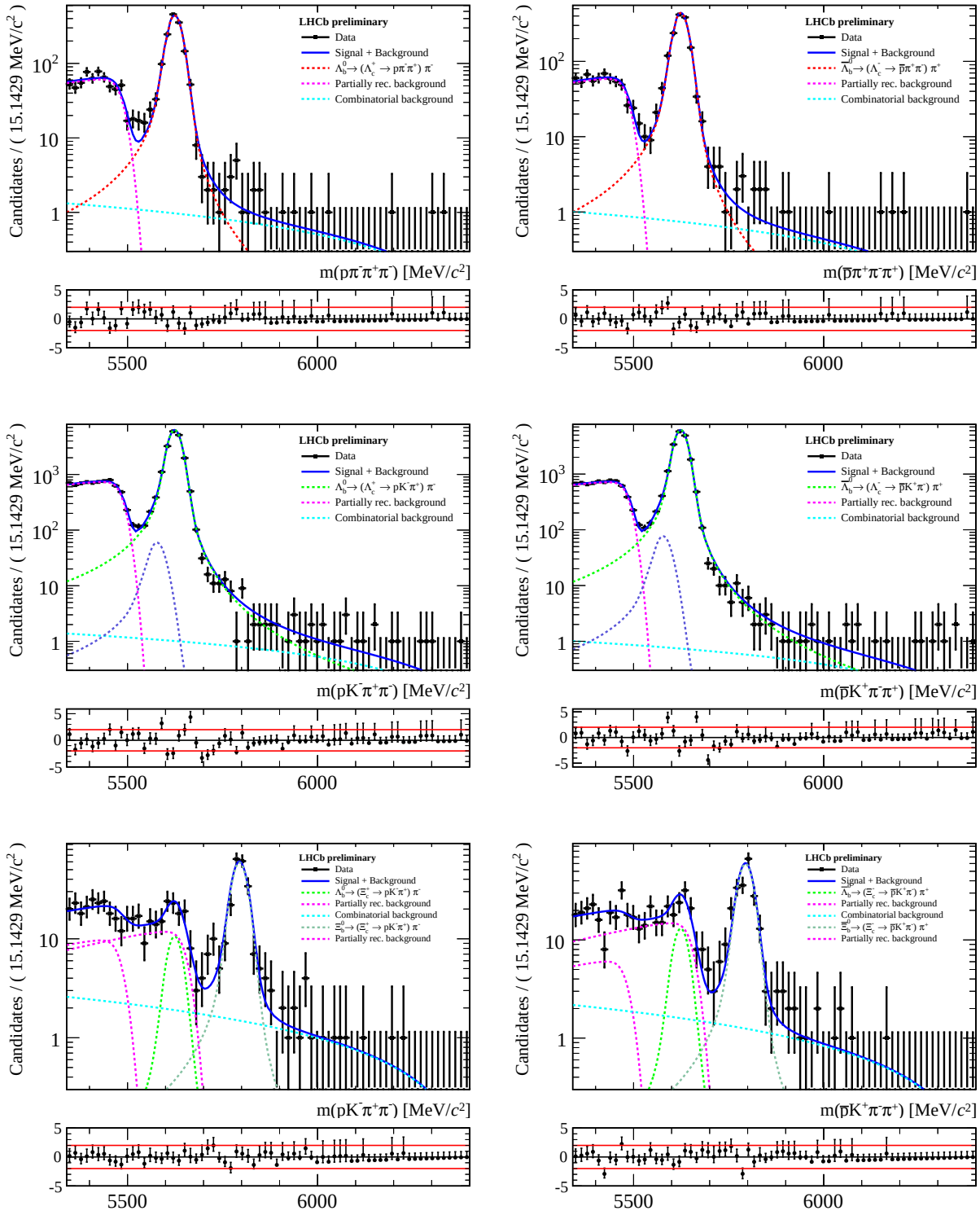

Figure 5.30: Fit results for the [from top to bottom] $X_b^0 \to (\Lambda_c^+ \to p\pi\pi)\pi$, $X_b^0 \to (\Lambda_c^+ \to pK\pi)\pi$ and $X_b^0 \to (\Xi_c^+ \to pK\pi)\pi$ spectra using the full phase space data of 2012. Plots in the left-column are for the spectra with X_b^0 and on the right-column for the spectra with $\overline{X}_b^0$.

Table 5.26: Floating parameters of the simultaneous fit to the full phase space data of 2011 and 2012.

Floating parameter (in Λ_b^0/Ξ_b^0 spectra)	Value	Floating parameter (in $\overline{\Lambda}_b^0/\overline{\Xi}_b^0$ spectra)	Value
Parameters shared 2011 and 2012 :			
μ (Λ_b^0)	5624.054 ± 0.078		
μ (Ξ_b^0) - μ (Λ_b^0)	170.341 ± 0.590		
2012 σ_{core} (Signal $\Lambda_b^0 \to pK\pi\pi$) [ref]	16.804 ± 0.174		
$\mathcal{N}$ ($B^0 \to \pi\pi\pi\pi$ in $p\pi\pi\pi$) / $\mathcal{N}$ ($B^0 \to K\pi\pi\pi$ in $p\pi\pi\pi$)	0.323 ± 0.034		← shared
Parameters for 2011 spectra :			
$\mathcal{N}$ (2011 Signal $\Lambda_b^0 \to p\pi\pi\pi$)	X.XXX ± X.XXX	$\bar{\mathcal{N}}$	X.XXX ± X.XXX
$\mathcal{N}$ (2011 Signal $\Lambda_b^0 \to pK\pi\pi$)	X.XXX ± X.XXX	$\bar{\mathcal{N}}$	X.XXX ± X.XXX
$\mathcal{N}$ (2011 Signal $\Lambda_b^0 \to pKK\pi$)	X.XXX ± X.XXX	$\bar{\mathcal{N}}$	X.XXX ± X.XXX
$\mathcal{N}$ (2011 Signal $\Lambda_b^0 \to pKKK$)	X.XXX ± X.XXX	$\bar{\mathcal{N}}$	X.XXX ± X.XXX
$\mathcal{N}$ (2011 Signal $\Xi_b^0 \to pK\pi K$)	X.XXX ± X.XXX	$\bar{\mathcal{N}}$	X.XXX ± X.XXX
$\mathcal{N}$ (2011 Signal $\Xi_b^0 \to pK\pi\pi$)	X.XXX ± X.XXX	$\bar{\mathcal{N}}$	X.XXX ± X.XXX
$\mathcal{N}$ (2011 Signal $\Xi_b^0 \to pKKK$)	X.XXX ± X.XXX	$\bar{\mathcal{N}}$	X.XXX ± X.XXX
$\mathcal{N}$ (2011 Signal $\Lambda_b^0 \to (\Lambda_c^+ \to p\pi\pi)\pi$)	629.190 ± 25.477	$\bar{\mathcal{N}}$	592.814 ± 24.811
$\mathcal{N}$ (2011 Signal $\Lambda_b^0 \to (\Lambda_c^+ \to pK\pi)\pi$)	7568.744 ± 93.038	$\bar{\mathcal{N}}$	7306.317 ± 91.264
$\mathcal{N}$ (2011 Signal $\Xi_b^0 \to (\Xi_c^+ \to pK\pi)\pi$)	93.308 ± 10.727	$\bar{\mathcal{N}}$	89.849 ± 10.690
$\mathcal{N}$ (2011 Signal $\Lambda_b^0 \to (\Xi_c^+ \to pK\pi)\pi$)	17.037 ± 8.911	$\bar{\mathcal{N}}$	7.568 ± 7.920
$\mathcal{N}$ (2011 Combinatorics in $p\pi\pi\pi$)	225.259 ± 33.667	$\bar{\mathcal{N}}$	240.984 ± 36.135
$\mathcal{N}$ (2011 Combinatorics in $pK\pi\pi$)	384.093 ± 42.410	$\bar{\mathcal{N}}$	365.662 ± 40.948
$\mathcal{N}$ (2011 Combinatorics in $pKK\pi$)	285.931 ± 34.526	$\bar{\mathcal{N}}$	317.927 ± 34.828
$\mathcal{N}$ (2011 Combinatorics in $pKKK$)	109.353 ± 20.629	$\bar{\mathcal{N}}$	131.057 ± 22.159
$\mathcal{N}$ (2011 Combinatorics in $pK\pi K$)	139.505 ± 24.855	$\bar{\mathcal{N}}$	44.728 ± 18.232
$\mathcal{N}$ (2011 Combinatorics in $(\Lambda_c^+ \to p\pi\pi)\pi$)	8.571 ± 5.605	$\bar{\mathcal{N}}$	14.805 ± 6.971
$\mathcal{N}$ (2011 Combinatorics in $(\Lambda_c^+ \to pK\pi)\pi$)	18.852 ± 11.729	$\bar{\mathcal{N}}$	-2.759 ± 9.361
$\mathcal{N}$ (2011 Combinatorics in $(\Xi_c^+ \to pK\pi)\pi$)	28.974 ± 13.184	$\bar{\mathcal{N}}$	36.664 ± 14.216

$\mathcal{N}$ (2011 CF $B^0 \to K\pi\pi\pi$ in $p\pi\pi\pi$)	210.594 ± 22.521	$\bar{\mathcal{N}}$	244.023 ± 23.133
$\mathcal{N}$ (2011 CF $B^0_s \to K\pi\pi K$ in $pK\pi\pi$)	78.713 ± 16.097	$\bar{\mathcal{N}}$	54.423 ± 14.682
$\mathcal{N}$ (2011 CF $B^0 \to KKK\pi$ in $pKK\pi$)	131.056 ± 20.351	$\bar{\mathcal{N}}$	135.857 ± 20.892
$\mathcal{N}$ (2011 CF $B^0_s \to KKKK$ in $pKKK$)	35.733 ± 10.490	$\bar{\mathcal{N}}$	43.245 ± 11.325
$\mathcal{N}$ (2011 PR from $\Lambda^0_b \to$ 5-body in $p\pi\pi\pi$)	489.740 ± 27.746	$\bar{\mathcal{N}}$	421.655 ± 26.684
$\mathcal{N}$ (2011 PR from $\Lambda^0_b \to$ 5-body in $pK\pi\pi$)	711.678 ± 57.955	$\bar{\mathcal{N}}$	737.234 ± 57.797
$\mathcal{N}$ (2011 PR from $\Xi^0_b \to$ 5-body in $pK\pi\pi$)	508.733 ± 72.498	$\bar{\mathcal{N}}$	501.184 ± 71.550
$\mathcal{N}$ (2011 PR from $\Lambda^0_b \to$ 5-body in $pKK\pi$)	95.828 ± 16.747	$\bar{\mathcal{N}}$	90.449 ± 16.708
$\mathcal{N}$ (2011 PR from $\Lambda^0_b \to$ 5-body in $pKKK$)	59.550 ± 11.195	$\bar{\mathcal{N}}$	40.283 ± 10.614
$\mathcal{N}$ (2011 PR from $\Lambda^0_b \to$ 5-body in $pK\pi K$)	55.133 ± 19.205	$\bar{\mathcal{N}}$	92.488 ± 18.892
$\mathcal{N}$ (2011 PR from $\Xi^0_b \to$ 5-body in $pK\pi K$)	66.836 ± 30.633	$\bar{\mathcal{N}}$	70.987 ± 27.337
$\mathcal{N}$ (2011 PR from $\Lambda^0_b \to$ 5-body in $(\Lambda^+_c \to p\pi\pi)\pi$)	229.245 ± 15.721	$\bar{\mathcal{N}}$	211.388 ± 15.192
$\mathcal{N}$ (2011 PR from $\Lambda^0_b \to$ 5-body in $(\Lambda^+_c \to pK\pi)\pi$)	2805.927 ± 54.474	$\bar{\mathcal{N}}$	2661.955 ± 52.967
$\mathcal{N}$ (2011 PR from $\Lambda^0_b \to$ 5-body in $(\Xi^+_c \to pK\pi)\pi$)	33.184 ± 13.544	$\bar{\mathcal{N}}$	30.808 ± 13.749
$\mathcal{N}$ (2011 PR from $\Xi^0_b \to$ 5-body in $(\Xi^+_c \to pK\pi)\pi$)	98.495 ± 20.893	$\bar{\mathcal{N}}$	104.108 ± 21.344
2011 c (Combinatorics in charmless decays)	-0.979 ± 0.018		← shared
2011 c (Combinatorics in charmed decays)	-1.081 ± 0.079		← shared
2011 p (PR from Λ^0_b/Ξ^0_b + 5-body in charmless spectra)	0.196 ± 0.113		← shared
2011 s (PR from Λ^0_b/Ξ^0_b + 5-body in charmless spectra)	0.345 ± 4.379		← shared
2011 p (PR from Λ^0_b + 5-body in $(\Lambda^+_c \to pK\pi)\pi$)	0.092 ± 0.050		← shared
2011 s (PR from Λ^0_b + 5-body in $(\Lambda^+_c \to pK\pi)\pi$)	-5.213 ± 2.643		← shared
$r = (2011\ \sigma_{\text{core}}\ \Lambda^0_b \to p\pi\pi\pi)/(\sigma_{\text{ref}})$	1.054 ± 0.017		← shared
$r = (2011\ \sigma_{\text{core}}\ \Lambda^0_b \to pK\pi\pi)/(\sigma_{\text{ref}})$	1.004 ± 0.014		← shared
$r = (2011\ \sigma_{\text{core}}\ \Lambda^0_b \to pKK\pi)/(\sigma_{\text{ref}})$	0.964 ± 0.018		← shared
$r = (2011\ \sigma_{\text{core}}\ \Lambda^0_b \to pKKK)/(\sigma_{\text{ref}})$	0.909 ± 0.015		← shared
$r = (2011\ \sigma_{\text{core}}\ \Xi^0_b \to pK\pi\pi)/(\sigma_{\text{ref}})$	1.033 ± 0.018		← shared
$r = (2011\ \sigma_{\text{core}}\ \Xi^0_b \to pK\pi K)/(\sigma_{\text{ref}})$	0.990 ± 0.018		← shared
$r = (2011\ \sigma_{\text{core}}\ \Xi^0_b \to pKKK)/(\sigma_{\text{ref}})$	0.935 ± 0.016		← shared
2011 σ_{core} (Signal $\Lambda^0_b \to (\Lambda^+_c \to p\pi\pi)\pi$)	18.285 ± 0.500		← shared

2011 σ_{core} (Signal $\Lambda_b^0 \to (\Lambda_c^+ \to pK\pi)\pi$)	17.159 ± 0.144		← shared
2011 σ_{core} (Signal $\Lambda_b^0 \to (\Xi_c^+ \to pK\pi)\pi$)	20.117 ± 2.022		← shared
f = (2011 $\mathcal{N}$ (CF $\Lambda_b^0 \to p\pi\pi\pi$ in $pK\pi\pi$)/($\mathcal{N}$ (as Signal))	0.049 ± 0.001		← shared
f = (2011 $\mathcal{N}$ (CF $\Lambda_b^0 \to pK\pi\pi$ in $pKK\pi$)/($\mathcal{N}$ (as Signal))	0.043 ± 0.001		← shared
f = (2011 $\mathcal{N}$ (CF $\Lambda_b^0 \to pK\pi\pi$ in $p\pi\pi\pi$)/($\mathcal{N}$ (as Signal))	0.141 ± 0.002		← shared
f = (2011 $\mathcal{N}$ (CF $\Lambda_b^0 \to pK\pi\pi$ in $pK\pi K$)/($\mathcal{N}$ (as Signal))	0.038 ± 0.001		← shared
f = (2011 $\mathcal{N}$ (CF $\Lambda_b^0 \to pKK\pi$ in $pK\pi\pi$)/($\mathcal{N}$ (as Signal))	0.164 ± 0.002		← shared
f = (2011 $\mathcal{N}$ (CF $\Lambda_b^0 \to pKKK$ in $pKK\pi$)/($\mathcal{N}$ (as Signal))	0.174 ± 0.002		← shared
f = (2011 $\mathcal{N}$ (CF $\Lambda_b^0 \to pKKK$ in $pK\pi K$)/($\mathcal{N}$ (as Signal))	0.137 ± 0.002		← shared
f = (2011 $\mathcal{N}$ (CF $\Xi_b^0 \to pK\pi\pi$ in $p\pi\pi\pi$)/($\mathcal{N}$ (as Signal))	0.162 ± 0.002		← shared
f = (2011 $\mathcal{N}$ (CF $\Xi_b^0 \to pK\pi K$ in $pK\pi\pi$)/($\mathcal{N}$ (as Signal))	0.213 ± 0.002		← shared
f = (2011 $\mathcal{N}$ ($B^0 \to K\pi\pi\pi$ in $pK\pi\pi$)/($\mathcal{N}$ (in Ref.))	0.281 ± 0.009		← shared
f = (2011 $\mathcal{N}$ ($B^0 \to KKK\pi$ in $pKKK$)/($\mathcal{N}$ (in Ref.))	0.063 ± 0.003		← shared
f = (2011 $\mathcal{N}$ ($B^0 \to KKK\pi$ in $pK\pi\pi$)/($\mathcal{N}$ (in Ref.))	0.135 ± 0.003		← shared
f = (2011 $\mathcal{N}$ ($B^0 \to KKK\pi$ in $pK\pi K$)/($\mathcal{N}$ (in Ref.))	0.483 ± 0.012		← shared
f = (2011 $\mathcal{N}$ ($B_s^0 \to K\pi\pi K$ in $pKK\pi$)/($\mathcal{N}$ (in Ref.))	0.107 ± 0.006		← shared
Parameters for 2012 spectra :			
$\mathcal{N}$ (2012 Signal $\Lambda_b^0 \to p\pi\pi\pi$)	X.XXX ± X.XXX	$\bar{\mathcal{N}}$	X.XXX ± X.XXX
$\mathcal{N}$ (2012 Signal $\Lambda_b^0 \to pK\pi\pi$)	X.XXX ± X.XXX	$\bar{\mathcal{N}}$	X.XXX ± X.XXX
$\mathcal{N}$ (2012 Signal $\Lambda_b^0 \to pKK\pi$)	X.XXX ± X.XXX	$\bar{\mathcal{N}}$	X.XXX ± X.XXX
$\mathcal{N}$ (2012 Signal $\Lambda_b^0 \to pKKK$)	X.XXX ± X.XXX	$\bar{\mathcal{N}}$	X.XXX ± X.XXX
$\mathcal{N}$ (2012 Signal $\Xi_b^0 \to pK\pi K$)	X.XXX ± X.XXX	$\bar{\mathcal{N}}$	X.XXX ± X.XXX
$\mathcal{N}$ (2012 Signal $\Xi_b^0 \to pK\pi\pi$)	X.XXX ± X.XXX	$\bar{\mathcal{N}}$	X.XXX ± X.XXX
$\mathcal{N}$ (2012 Signal $\Xi_b^0 \to pKKK$)	X.XXX ± X.XXX	$\bar{\mathcal{N}}$	X.XXX ± X.XXX
$\mathcal{N}$ (2012 Signal $\Lambda_b^0 \to (\Lambda_c^+ \to p\pi\pi)\pi$)	1480.755 ± 39.420	$\bar{\mathcal{N}}$	1479.560 ± 39.279
$\mathcal{N}$ (2012 Signal $\Lambda_b^0 \to (\Lambda_c^+ \to pK\pi)\pi$)	19088.916 ± 147.501	$\bar{\mathcal{N}}$	18664.074 ± 146.113
$\mathcal{N}$ (2012 Signal $\Xi_b^0 \to (\Xi_c^+ \to pK\pi)\pi$)	215.106 ± 16.146	$\bar{\mathcal{N}}$	216.414 ± 16.255
$\mathcal{N}$ (2012 Signal $\Lambda_b^0 \to (\Xi_c^+ \to pK\pi)\pi$)	38.398 ± 13.764	$\bar{\mathcal{N}}$	47.388 ± 15.000

$\mathcal{N}$ (2012 Combinatorics in $p\pi\pi\pi$)	662.538 ± 72.601	$\bar{\mathcal{N}}$	620.144 ± 72.965
$\mathcal{N}$ (2012 Combinatorics in $pK\pi\pi$)	1005.179 ± 80.173	$\bar{\mathcal{N}}$	917.127 ± 78.598
$\mathcal{N}$ (2012 Combinatorics in $pKK\pi$)	556.479 ± 57.679	$\bar{\mathcal{N}}$	592.593 ± 59.832
$\mathcal{N}$ (2012 Combinatorics in $pKKK$)	285.775 ± 37.372	$\bar{\mathcal{N}}$	246.223 ± 38.327
$\mathcal{N}$ (2012 Combinatorics in $pK\pi K$)	247.934 ± 36.376	$\bar{\mathcal{N}}$	224.546 ± 34.017
$\mathcal{N}$ (2012 Combinatorics in $(\Lambda_c^+ \to p\pi\pi)\pi$)	46.675 ± 12.674	$\bar{\mathcal{N}}$	35.572 ± 11.224
$\mathcal{N}$ (2012 Combinatorics in $(\Lambda_c^+ \to pK\pi)\pi$)	48.688 ± 16.979	$\bar{\mathcal{N}}$	35.447 ± 15.956
$\mathcal{N}$ (2012 Combinatorics in $(\Xi_c^+ \to pK\pi)\pi$)	91.448 ± 20.289	$\bar{\mathcal{N}}$	76.723 ± 19.965
$\mathcal{N}$ (2012 CF $B^0 \to K\pi\pi\pi$ in $p\pi\pi\pi$)	819.898 ± 46.100	$\bar{\mathcal{N}}$	834.766 ± 47.306
$\mathcal{N}$ (2012 CF $B_s^0 \to K\pi\pi K$ in $pK\pi\pi$)	339.602 ± 37.339	$\bar{\mathcal{N}}$	342.153 ± 36.184
$\mathcal{N}$ (2012 CF $B^0 \to KKK\pi$ in $pKK\pi$)	419.844 ± 40.661	$\bar{\mathcal{N}}$	419.897 ± 41.603
$\mathcal{N}$ (2012 CF $B_s^0 \to KKKK$ in $pKKK$)	138.881 ± 24.179	$\bar{\mathcal{N}}$	168.931 ± 26.155
$\mathcal{N}$ (2012 PR from $\Lambda_b^0 \to$ 5-body in $p\pi\pi\pi$)	970.463 ± 41.923	$\bar{\mathcal{N}}$	975.924 ± 41.704
$\mathcal{N}$ (2012 PR from $\Lambda_b^0 \to$ 5-body in $pK\pi\pi$)	1624.066 ± 76.426	$\bar{\mathcal{N}}$	1659.215 ± 76.892
$\mathcal{N}$ (2012 PR from $\Xi_b^0 \to$ 5-body in $pK\pi\pi$)	826.240 ± 97.983	$\bar{\mathcal{N}}$	854.466 ± 98.334
$\mathcal{N}$ (2012 PR from $\Lambda_b^0 \to$ 5-body in $pKK\pi$)	278.240 ± 25.922	$\bar{\mathcal{N}}$	263.915 ± 26.237
$\mathcal{N}$ (2012 PR from $\Lambda_b^0 \to$ 5-body in $pKKK$)	92.130 ± 16.404	$\bar{\mathcal{N}}$	128.731 ± 17.510
$\mathcal{N}$ (2012 PR from $\Lambda_b^0 \to$ 5-body in $pK\pi K$)	209.760 ± 27.319	$\bar{\mathcal{N}}$	168.907 ± 26.930
$\mathcal{N}$ (2012 PR from $\Xi_b^0 \to$ 5-body in $pK\pi K$)	105.887 ± 41.405	$\bar{\mathcal{N}}$	124.236 ± 41.309
$\mathcal{N}$ (2012 PR from $\Lambda_b^0 \to$ 5-body in $(\Lambda_c^+ \to p\pi\pi)\pi$)	573.579 ± 25.103	$\bar{\mathcal{N}}$	550.877 ± 24.473
$\mathcal{N}$ (2012 PR from $\Lambda_b^0 \to$ 5-body in $(\Lambda_c^+ \to pK\pi)\pi$)	6867.955 ± 85.154	$\bar{\mathcal{N}}$	6676.363 ± 83.922
$\mathcal{N}$ (2012 PR from $\Lambda_b^0 \to$ 5-body in $(\Xi_c^+ \to pK\pi)\pi$)	91.043 ± 20.450	$\bar{\mathcal{N}}$	56.825 ± 21.302
$\mathcal{N}$ (2012 PR from $\Xi_b^0 \to$ 5-body in $(\Xi_c^+ \to pK\pi)\pi$)	214.015 ± 31.574	$\bar{\mathcal{N}}$	268.659 ± 34.412
2012 c (Combinatorics in charmless decays)	-0.958 ± 0.017		← shared
2012 c (Combinatorics in charmed decays)	-0.984 ± 0.057		← shared
2012 p (PR from Λ_b^0/Ξ_b^0 + 5-body in charmless spectra)	0.300 ± 0.083		← shared
2012 s (PR from Λ_b^0/Ξ_b^0 + 5-body in charmless spectra)	-3.892 ± 3.293		← shared
2012 p (PR from Λ_b^0 + 5-body in $(\Lambda_c^+ \to pK\pi)\pi$)	0.120 ± 0.032		← shared
2012 s (PR from Λ_b^0 + 5-body in $(\Lambda_c^+ \to pK\pi)\pi$)	-6.652 ± 1.707		← shared

$r = (2012\ \sigma_{\rm core}\ \Lambda_b^0 \to p\pi\pi\pi)/(\sigma_{\rm ref})$	1.072 ± 0.014	$\leftarrow$ shared
$r = (2012\ \sigma_{\rm core}\ \Lambda_b^0 \to pK\pi\pi)/(\sigma_{\rm ref})$	0.966 ± 0.015	$\leftarrow$ shared
$r = (2012\ \sigma_{\rm core}\ \Lambda_b^0 \to pKK\pi)/(\sigma_{\rm ref})$	0.887 ± 0.012	$\leftarrow$ shared
$r = (2012\ \sigma_{\rm core}\ \Xi_b^0 \to p\pi\pi\pi)/(\sigma_{\rm ref})$	1.043 ± 0.017	$\leftarrow$ shared
$r = (2012\ \sigma_{\rm core}\ \Xi_b^0 \to pK\pi\pi)/(\sigma_{\rm ref})$	0.993 ± 0.015	$\leftarrow$ shared
$r = (2012\ \sigma_{\rm core}\ \Xi_b^0 \to pKK\pi)/(\sigma_{\rm ref})$	0.930 ± 0.014	$\leftarrow$ shared
$2012\ \sigma_{\rm core}$ (Signal $\Lambda_b^0 \to (\Lambda_c^+ \to p\pi\pi)\pi$)	18.930 ± 0.344	$\leftarrow$ shared
$2012\ \sigma_{\rm core}$ (Signal $\Lambda_b^0 \to (\Lambda_c^+ \to pK\pi)\pi$)	16.979 ± 0.090	$\leftarrow$ shared
$2012\ \sigma_{\rm core}$ (Signal $\Lambda_b^0 \to (\Xi_c^+ \to pK\pi)\pi$)	20.427 ± 1.208	$\leftarrow$ shared
$f = (2012\ \mathcal{N}$ (CF $\Lambda_b^0 \to p\pi\pi\pi$ in $pK\pi\pi)/(\ \mathcal{N}$ (as Signal))	0.048 ± 0.001	$\leftarrow$ shared
$f = (2012\ \mathcal{N}$ (CF $\Lambda_b^0 \to pK\pi\pi$ in $pKK\pi)/(\ \mathcal{N}$ (as Signal))	0.043 ± 0.001	$\leftarrow$ shared
$f = (2012\ \mathcal{N}$ (CF $\Lambda_b^0 \to pK\pi\pi$ in $p\pi\pi\pi)/(\ \mathcal{N}$ (as Signal))	0.140 ± 0.001	$\leftarrow$ shared
$f = (2012\ \mathcal{N}$ (CF $\Lambda_b^0 \to pK\pi\pi$ in $pK\pi K)/(\ \mathcal{N}$ (as Signal))	0.037 ± 0.000	$\leftarrow$ shared
$f = (2012\ \mathcal{N}$ (CF $\Lambda_b^0 \to pK\pi\pi$ in $pK\pi\pi)/(\ \mathcal{N}$ (as Signal))	0.159 ± 0.002	$\leftarrow$ shared
$f = (2012\ \mathcal{N}$ (CF $\Lambda_b^0 \to pKK\pi$ in $pKK\pi)/(\ \mathcal{N}$ (as Signal))	0.171 ± 0.002	$\leftarrow$ shared
$f = (2012\ \mathcal{N}$ (CF $\Lambda_b^0 \to pKK\pi$ in $pK\pi K)/(\ \mathcal{N}$ (as Signal))	0.130 ± 0.001	$\leftarrow$ shared
$f = (2012\ \mathcal{N}$ (CF $\Xi_b^0 \to pK\pi\pi$ in $p\pi\pi\pi)/(\ \mathcal{N}$ (as Signal))	0.161 ± 0.002	$\leftarrow$ shared
$f = (2012\ \mathcal{N}$ (CF $\Xi_b^0 \to pK\pi K$ in $pK\pi\pi)/(\ \mathcal{N}$ (as Signal))	0.200 ± 0.002	$\leftarrow$ shared
$f = (2012\ \mathcal{N}$ ($B^0 \to K\pi\pi\pi$ in $pK\pi\pi)/(\ \mathcal{N}$ (in Ref.))	0.286 ± 0.006	$\leftarrow$ shared
$f = (2012\ \mathcal{N}$ ($B^0 \to KKK\pi$ in $pKKK)/(\ \mathcal{N}$ (in Ref.))	0.055 ± 0.002	$\leftarrow$ shared
$f = (2012\ \mathcal{N}$ ($B^0 \to KKK\pi$ in $pK\pi\pi)/(\ \mathcal{N}$ (in Ref.))	0.140 ± 0.002	$\leftarrow$ shared
$f = (2012\ \mathcal{N}$ ($B^0 \to KKK\pi$ in $pK\pi K)/(\ \mathcal{N}$ (in Ref.))	0.466 ± 0.008	$\leftarrow$ shared
$f = (2012\ \mathcal{N}$ ($B_s^0 \to K\pi\pi K$ in $pKK\pi)/(\ \mathcal{N}$ (in Ref.))	0.110 ± 0.004	$\leftarrow$ shared

All signal yields, and hence raw and *CP* asymmetries observables, are blind. Although limited, some comments are however in order concerning the fit results and fit behaviour in general.

- The fit model describes in a satisfactory way all the reconstructed spectra of interest. The likelihood behaviour, studied in Section 5.9 dedicated to the understanding of fit biases thanks to pseudo-experiments, is as well satisfactory.
- All sources of background seem to be identified and adequately modelled. In particular, signal cross-feeds and B physics backgrounds, data-driven constrained, are in place. No sign of an overlooked contribution is observed[r].
- The empirical adjustment of the partially reconstructed background shapes brings a consistent understanding of this component among the spectra.
- The combinatorial backgrounds are found to be present in all the charmless spectra and described with similar shapes.
- Consistent results are obtained between the two years of data taking for the parameters which can be compared.

The raw asymmetries of the control channels are unblinded and can hence be interpreted. The fit results are there as well consistent in between the years and the precision basically scales expectedly with the luminosity. They show asymmetries compatible with zero. These asymmetries embody both the detection asymmetries between charges (π, K and proton) and the b-baryon production asymmetries in addition to a *CP* asymmetry expectedly extremely small in the Standard Model. In line with similar observation in the charmless 2-body decays of the Λ_b^0 baryon, the consistency of the raw asymmetry with a vanishing asymmetry can be seen as an indication of the smallness of the detection and production asymmetry corrections. Eventually, the sensitivities on the $\Delta\mathcal{A}^{CP}$ observables measurements are also provided. The very large uncertainty on the $\Delta\mathcal{A}^{CP}$ observable which is found for the decay mode $\Xi_b^0 \to pKKK$, particularly in the 2012 data, is likely related to a negative yield measurement. This is not a problem per se but indicates that an asymmetry measurement is irrelevant for this channel. We chose however to present this result as it came.

5.10.2 Low invariant mass region of ph

Cutting on the invariant mass of the ph pair requires re-estimation of the gaussian constraints of the B physics yields from the RHSB region of the invariant mass spectra. Using the same fit model and the same strategy as discussed in Section 5.7, we obtained the estimates of the B physics "full-spectrum" yield constraints, as summarized in Table 5.28. The fits can be found in Appendix A.11. However, in the $X_b^0 \to pKKK$ 2011 spectra, estimation of the B physics yields from the RHSB is no longer doable due to lack of events. Hence, in order to estimate these, we scaled the 2012 B physics RHSB yield to the case of 2011 spectra. In example, we denote the scale factor as s and the 2012 estimated RHSB yield as $\mathcal{N}^{2012}_{\text{RHSB}}$, and the scaled 2011 B physics RHSB yield as $\mathcal{N}^{2011}_{\text{RHSB}}$, then the scaling is simply $\mathcal{Y}^{2011}_{\text{RHSB}} \pm \sigma\mathcal{Y}^{2011}_{\text{RHSB}} = s \cdot (\mathcal{Y}^{2012}_{\text{RHSB}} \pm \sigma\mathcal{Y}^{2012}_{\text{RHSB}})$, where the σ's are the corresponding uncertainties. The scaling factor s is obtained from the ratios of 2011 and 2012 RHSB yields of B physics using the full phase space data, which can be found in Table 5.16 in Section 5.7.

[r] An indication of an overlooked background contribution would result in particular in a gaussian constraint far from its central value.

A re-calculation of the cross-feed constraints for the charmless signal modes, as well as the cross-spectra constraints of the B physics backgrounds, was done. However, due to the fact the $X_b^0 \to phh'h''$ MC events are generated with a significant fraction with low invariant mass resonances and that the MC B physics events are generated with low two-body mass resonances, the effect on the factors is small. This might not be the case in the real data. Since we practically apply the same cut for all the spectra ($m_{p\pi}/m_{pK} < 2\,\text{GeV}/c^2$), the re-calculated ratios are still meaningful.

Shown in Figures 5.31 and 5.32 are the fit results of the simultaneous fit to the invariant mass spectra using the 2011 data with $m_{ph} < 2$ GeV/c^2 phase space cut. Figures 5.33 and 5.34 show the fit results for the 2012 data. Since, no further phase space cut is applied to the control spectra, the resulting fits and fit parameters are relatively the same as in Section 5.10.1. Figures A.20 and A.21 shown in Appendix A.13 display the fits of the invariant mass spectra of the control modes. The measured CP observables are summarized in Table 5.29, while the results on the fit parameters are shown in Appendix A.14.

Similar remarks as made for the full phase space fits can be repeated here. In particular, the identification and modelling of the combinatorial background, signal cross-feeds and B physics backgrounds seem satisfactory.

5.10.3 Low invariant mass region of ph and $h'h''$

With the additional cut on the invariant mass of the $h'h''$ pair, a re-calculation of the gaussian constraints of the B physics yields from the RHSB region is necessary. Using the RHSB events of the 2012 spectra, the "full-spectrum" yield constraints on the B physics backgrounds are estimated via the same strategy as discussed in Section 5.7. The fits can be seen in Appendix A.12 and the estimated "full-spectrum" yields are summarized in Table 5.30. However, in the 2011 spectra, estimation of the B physics yields from the RHSB is no longer doable due to lack of events, except for the $X_b^0 \to p\pi\pi\pi$ spectrum. Again, in order to estimate these, we scaled the 2012 B physics RHSB yield to the case of 2011 spectra.

The cross-feed constraints of the charmless signals modes and cross-spectra constraints of the B physics backgrounds are also re-calculated. Since the $X_b^0 \to phh'h''$ MC events are generated with a significant fraction with low invariant mass resonances and that the MC B physics events are generated with low two-body mass resonances, the effect on the factors is negligible, which might not be the case in the real data. However, since we apply relatively the same phase space cut for all the spectra, the re-calculated ratios are still usable.

Figures 5.35 and 5.36 display the fit results of the simultaneous fit to the invariant mass spectra using the 2011 data with $m_{ph} < 2$ GeV/c^2 and $m_{h'h''} < \sim$1.65 GeV/c^2 phase space cuts. Figures 5.37 and 5.38 show the fit results for the 2012 data. Since, no further phase space cut is applied to the control spectra, the resulting fits and fit parameters are relatively the same as in Section 5.10.1. Figures A.22 and A.23 shown in Appendix A.15 show the fits of the invariant mass spectra of the control modes. The measured CP observables are summarized in Table 5.31, while the results on the fit parameters are shown in Appendix A.16.

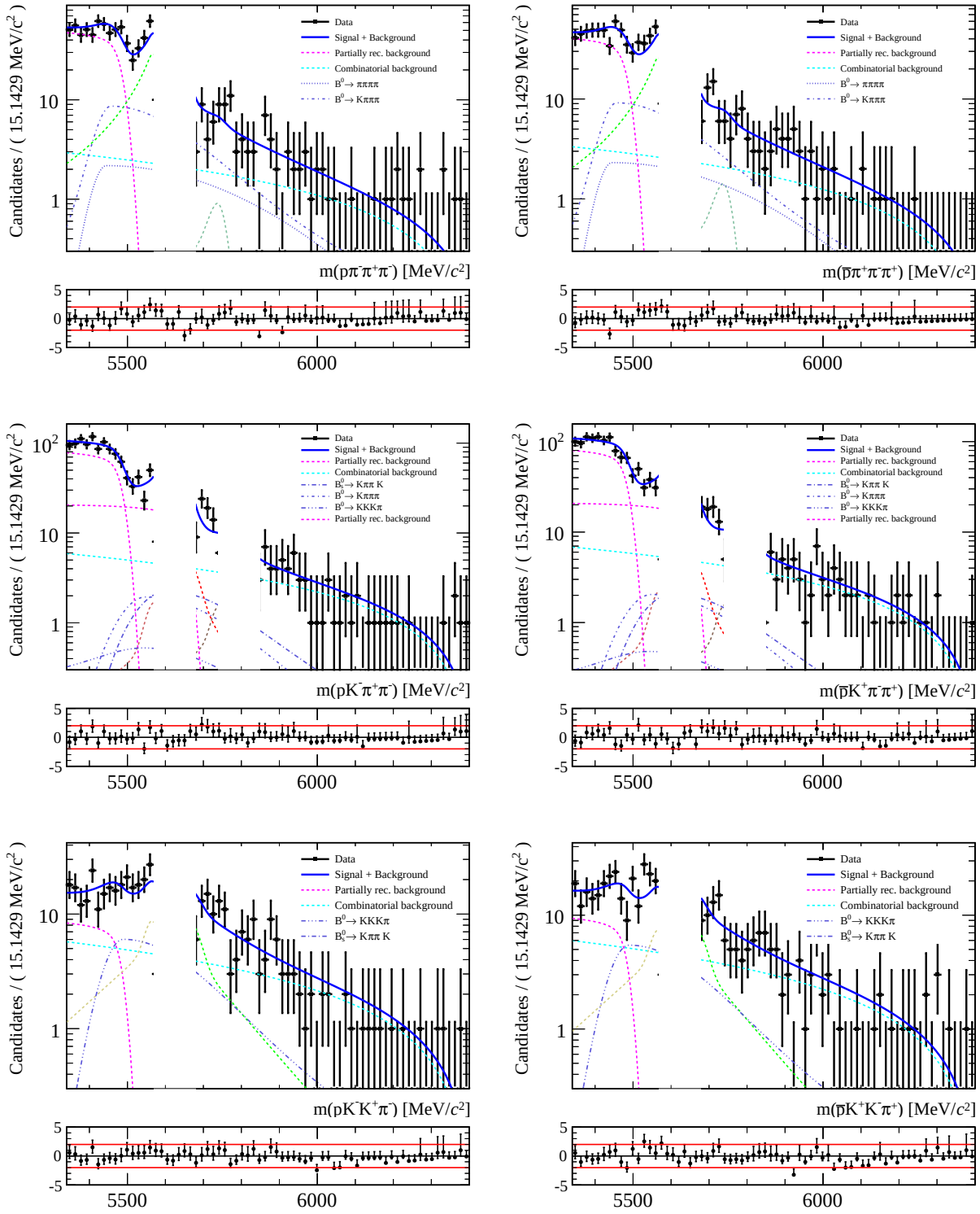

Figure 5.31: Fit results for the [from top to bottom] $X_b^0 \to p\pi\pi\pi$, $X_b^0 \to pK\pi\pi$ and $X_b^0 \to pKK\pi$ spectra using the 2011 data with $m_{ph} < 2$ GeV/c^2 phase space cut. Plots in the left-column are for the spectra with X_b^0 and on the right-column for the spectra with $\overline{X}_b^0$.

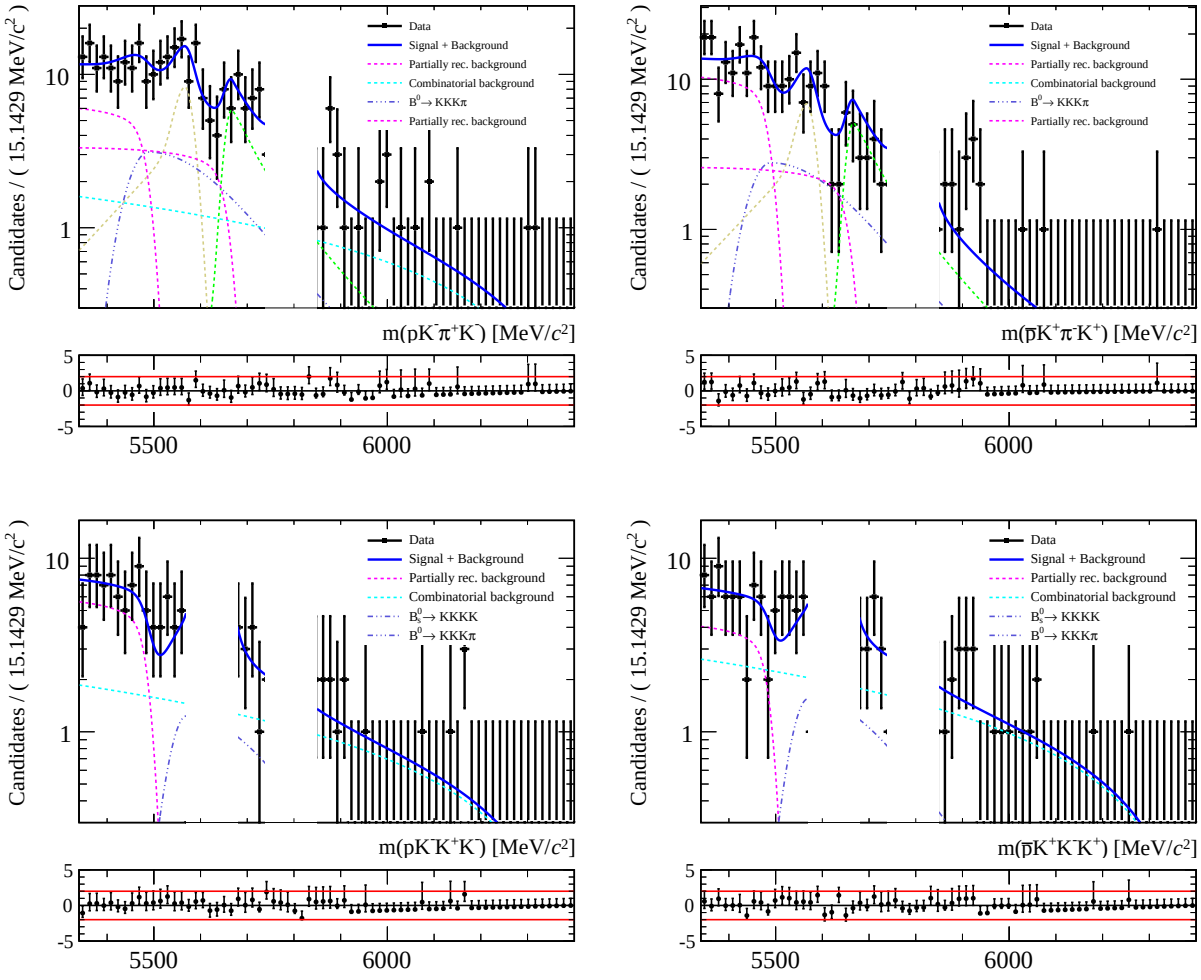

Figure 5.32: Fit results for the [top] $X_b^0 \to pK\pi K$ and [bottom] $X_b^0 \to pKKK$ spectra using the 2011 data with $m_{ph} < 2$ GeV/c^2 phase space cut. Plots in the left-column are for the spectra with X_b^0 and on the right-column for the spectra with $\overline{X}_b^0$.

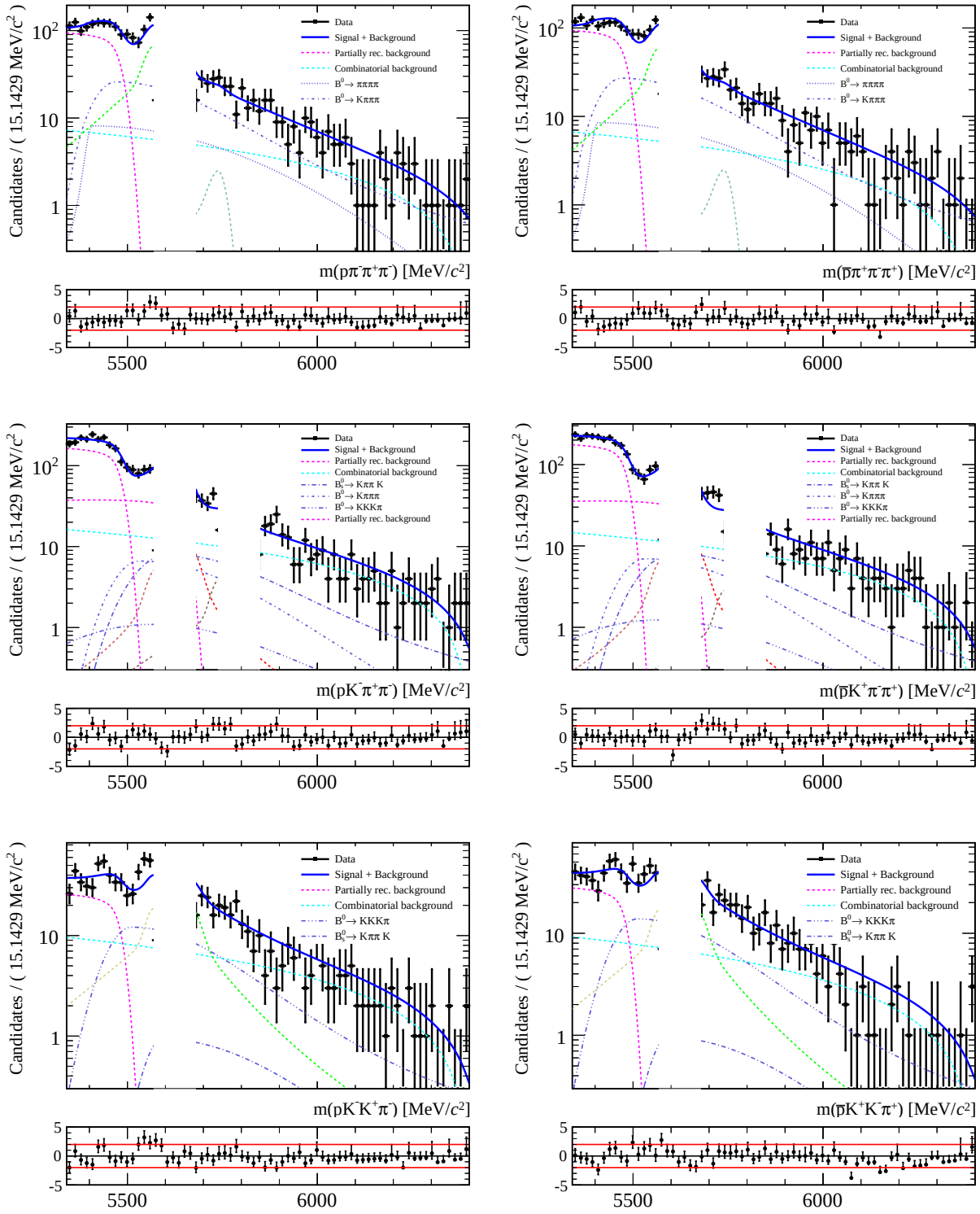

Figure 5.33: Fit results for the [from top to bottom] $X_b^0 \to p\pi\pi\pi$, $X_b^0 \to pK\pi\pi$ and $X_b^0 \to pKK\pi$ spectra using the 2012 data with $m_{ph} < 2$ GeV/c^2 phase space cut. Plots in the left-column are for the spectra with X_b^0 and on the right-column for the spectra with $\overline{X}_b^0$.

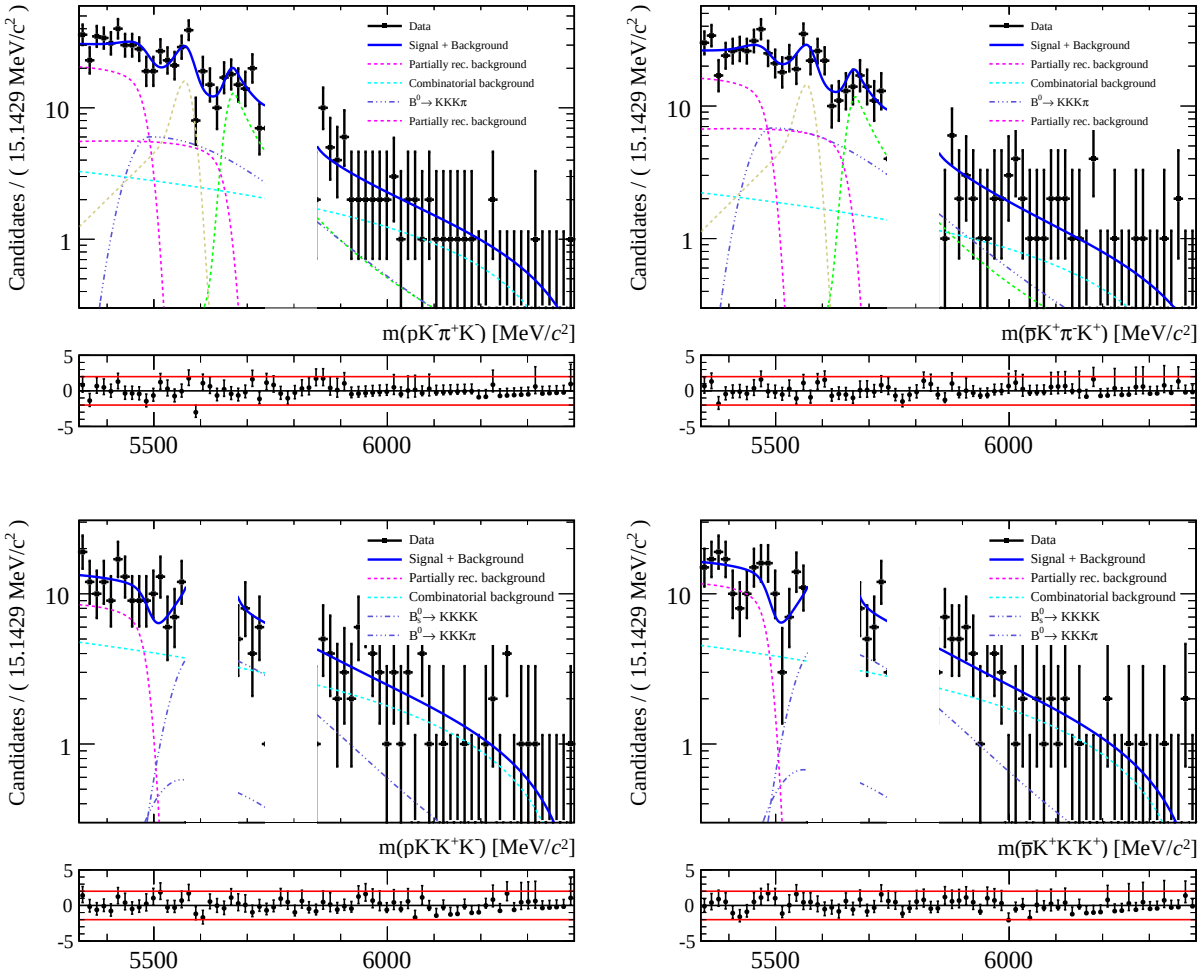

Figure 5.34: Fit results for the [top] $X_b^0 \to pK\pi K$ and [bottom] $X_b^0 \to pKKK$ spectra using the 2012 data with $m_{ph} < 2$ GeV/c^2 phase space cut. Plots in the left-column are for the spectra with X_b^0 and on the right-column for the spectra with $\overline{X}_b^0$.

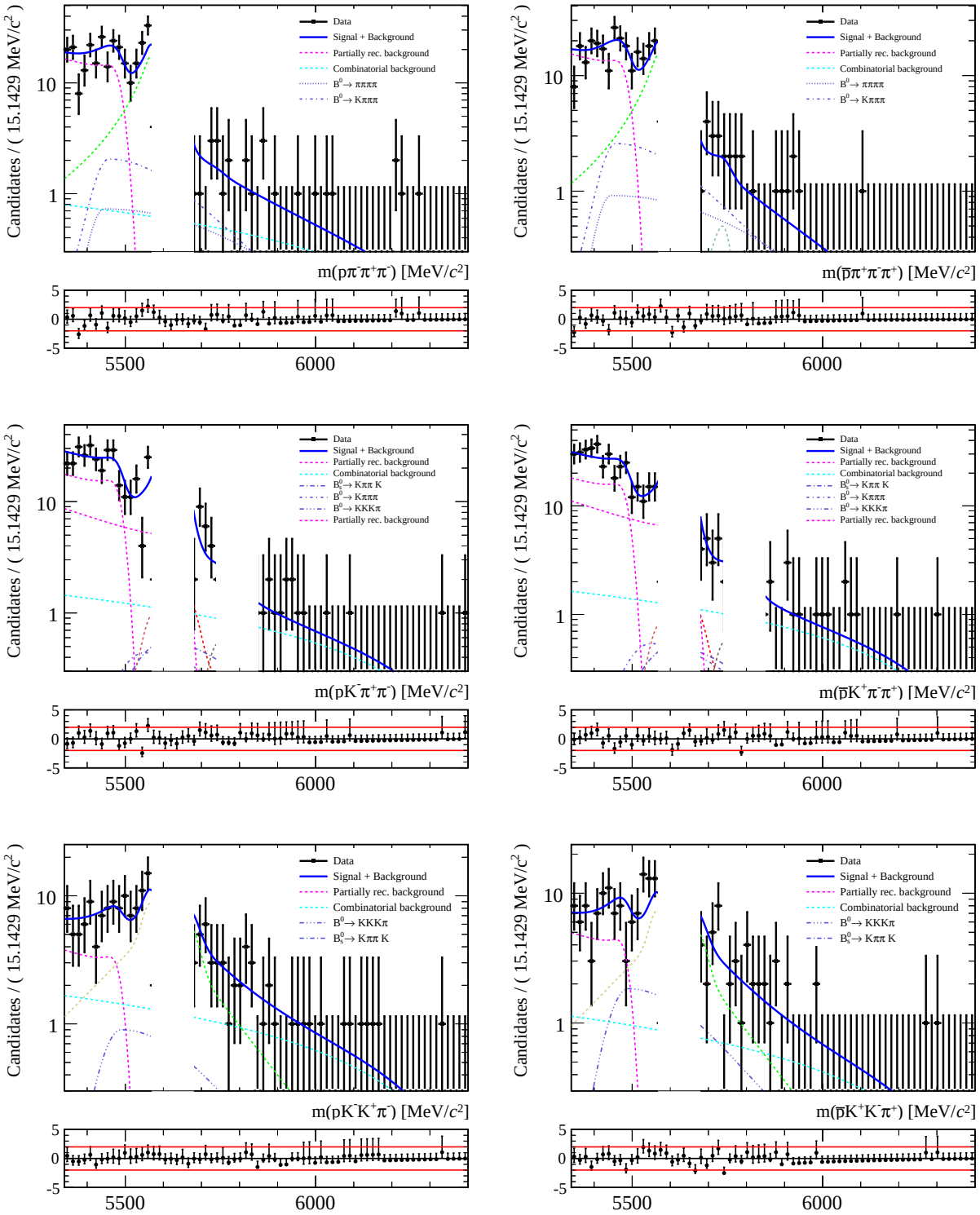

Figure 5.35: Fit results for the [from top to bottom] $X_b^0 \to p\pi\pi\pi$, $X_b^0 \to pK\pi\pi$ and $X_b^0 \to pKK\pi$ spectra using the 2011 data with $m_{ph} < 2$ GeV/c^2 and $m_{h'h''} < \sim$1.65 GeV/c^2 phase space cuts. Plots in the left-column are for the spectra with X_b^0 and on the right-column for the spectra with $\overline{X}_b^0$.

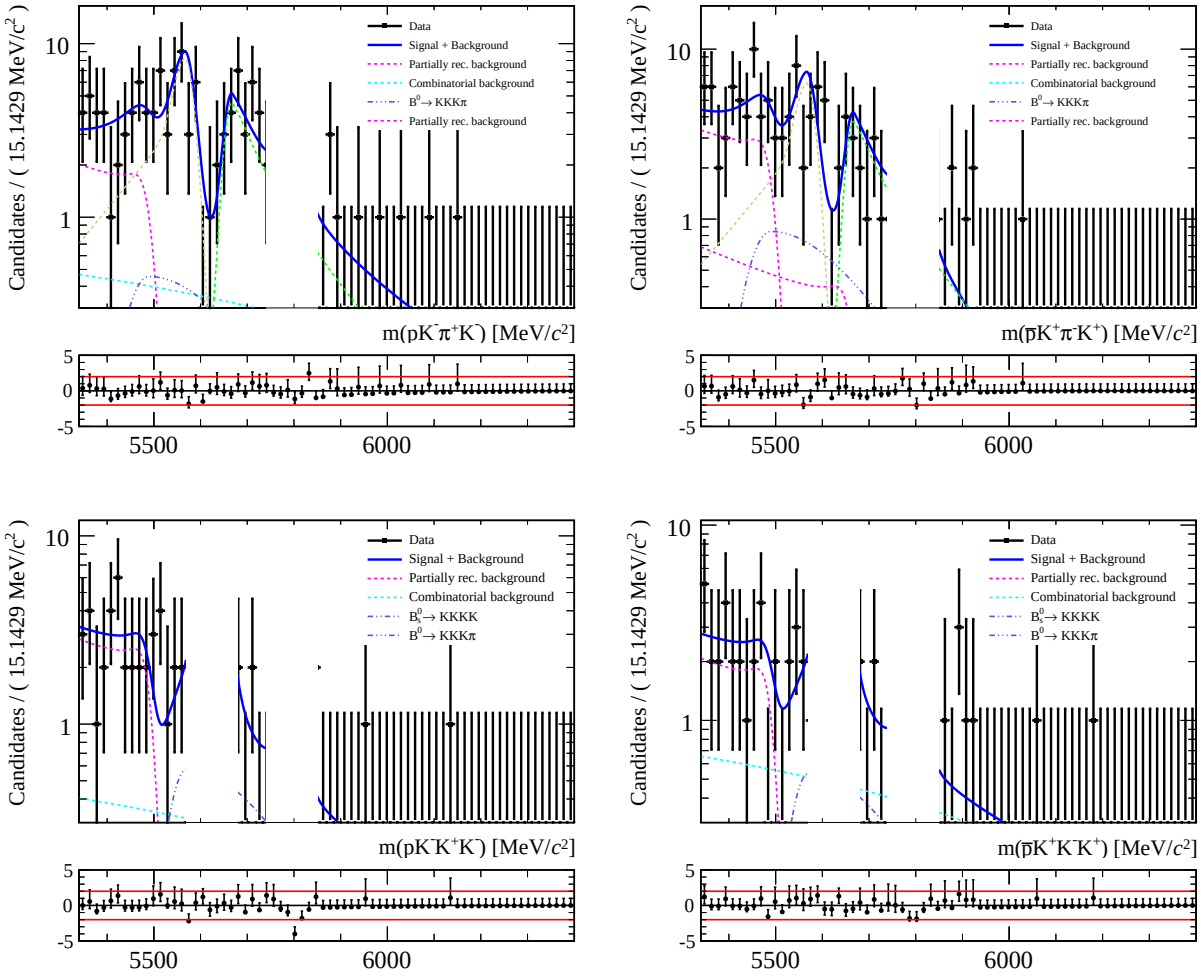

Figure 5.36: Fit results for the [top] $X_b^0 \to pK\pi K$ and [bottom] $X_b^0 \to pKKK$ spectra using the 2011 data with $m_{ph} < 2$ GeV/c^2 and $m_{h'h''} < \sim$1.65 GeV/c^2 phase space cuts. Plots in the left-column are for the spectra with X_b^0 and on the right-column for the spectra with $\overline{X}_b^0$.

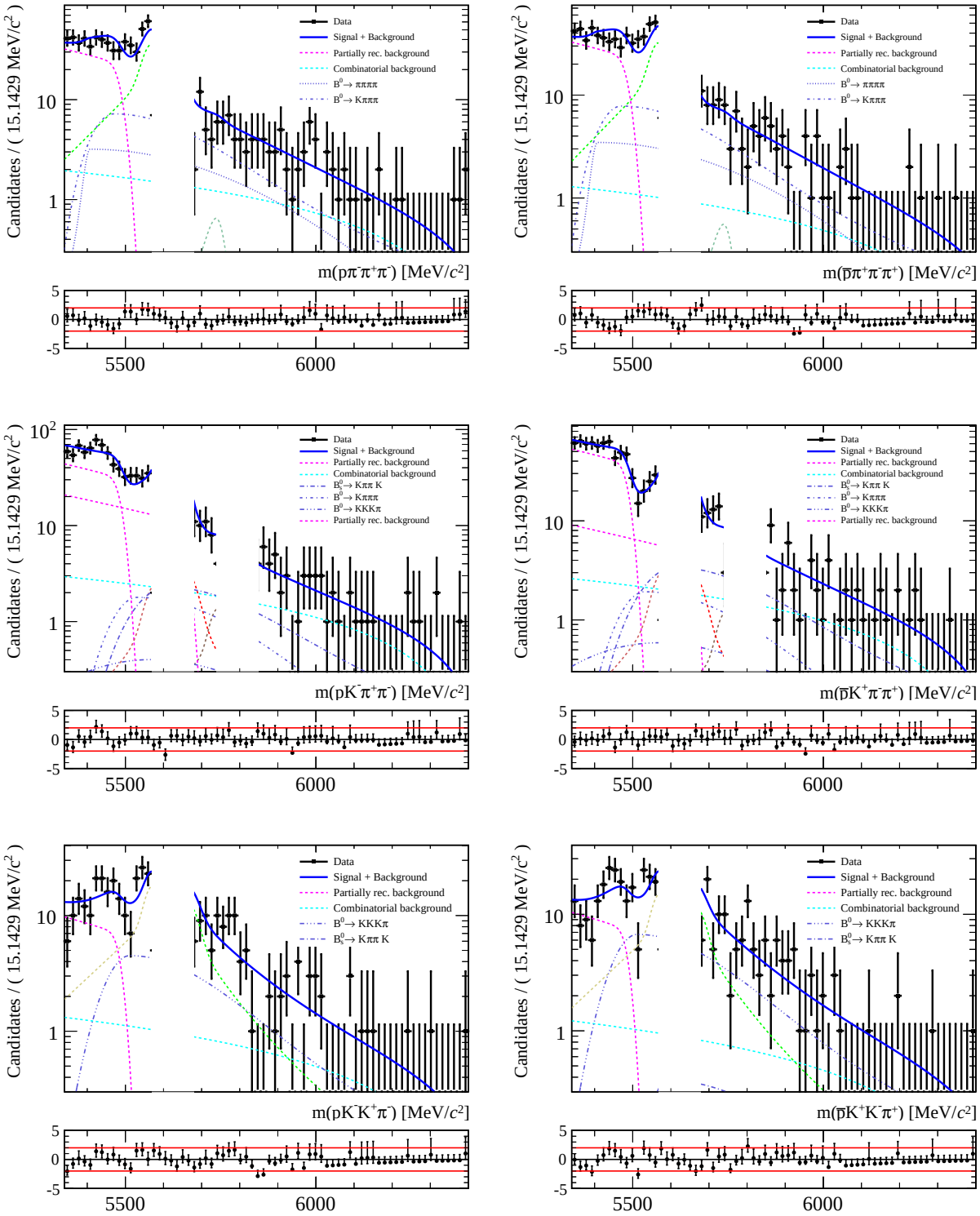

Figure 5.37: Fit results for the [from top to bottom] $X_b^0 \to p\pi\pi\pi$, $X_b^0 \to pK\pi\pi$ and $X_b^0 \to pKK\pi$ spectra using the 2012 data with $m_{ph} < 2$ GeV/c^2 and $m_{h'h''} < \sim 1.65$ GeV/c^2 phase space cuts. Plots in the left-column are for the spectra with X_b^0 and on the right-column for the spectra with $\overline{X}_b^0$.

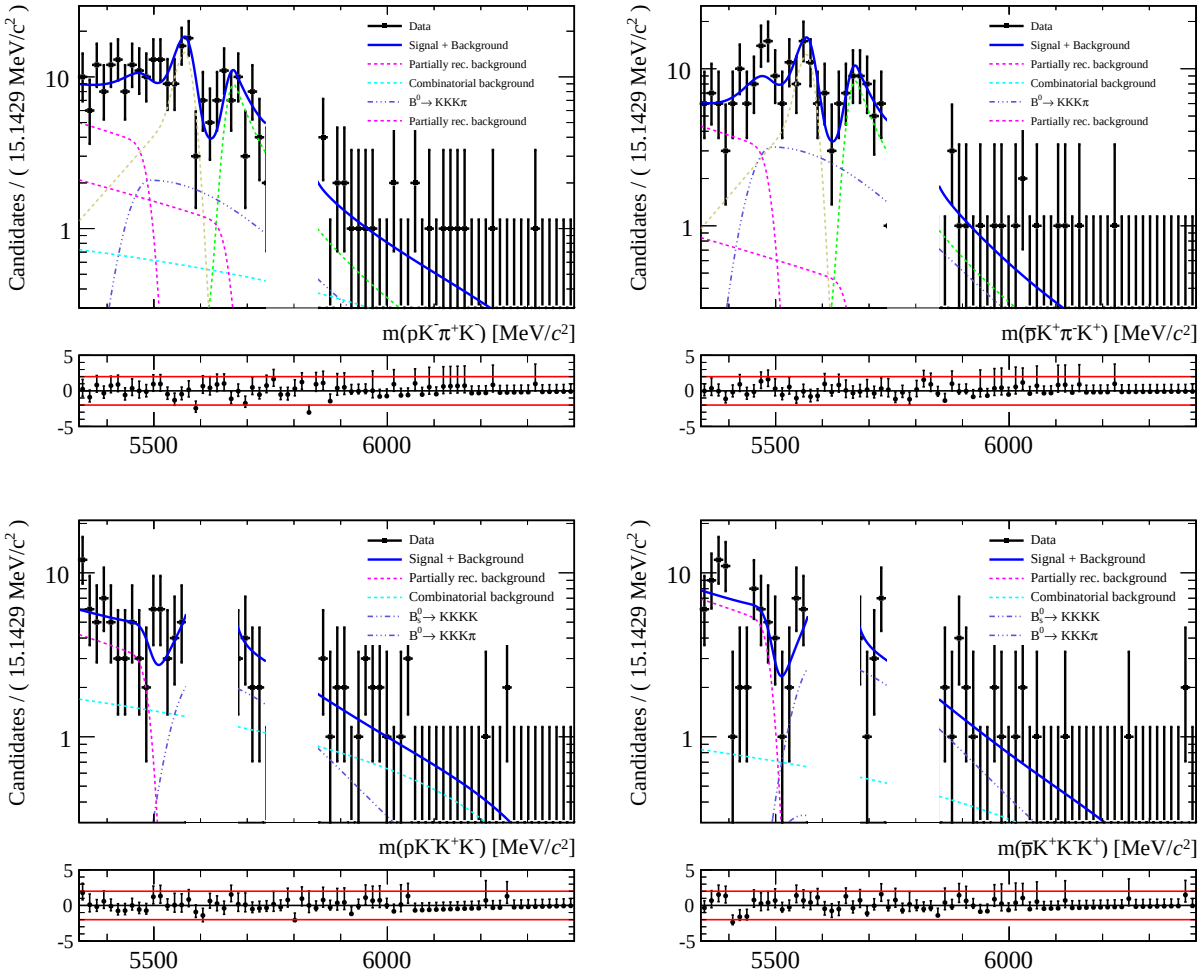

Figure 5.38: Fit results for the [top] $X_b^0 \to pK\pi K$ and [bottom] $X_b^0 \to pKKK$ spectra using the 2012 data with $m_{ph} < 2$ GeV/c^2 and $m_{h'h''} <\sim 1.65$ GeV/c^2 phase space cuts. Plots in the left-column are for the spectra with X_b^0 and on the right-column for the spectra with $\overline{X}_b^0$.

Table 5.27: The *CP* asymmetry observables obtained from the results of the fit to the full phase space data.

CP asymmetry observable	Value
Observables for 2011 spectra:	
$\mathcal{A}^{\text{raw}}$ ($\Lambda_b^0 \to p\pi\pi\pi$)	X.XXX ± X.XXX
$\mathcal{A}^{\text{raw}}$ ($\Lambda_b^0 \to pK\pi\pi$)	X.XXX ± X.XXX
$\mathcal{A}^{\text{raw}}$ ($\Lambda_b^0 \to pKK\pi$)	X.XXX ± X.XXX
$\mathcal{A}^{\text{raw}}$ ($\Lambda_b^0 \to pKKK$)	X.XXX ± X.XXX
$\mathcal{A}^{\text{raw}}$ ($\Xi_b^0 \to pK\pi\pi$)	X.XXX ± X.XXX
$\mathcal{A}^{\text{raw}}$ ($\Xi_b^0 \to pK\pi K$)	X.XXX ± X.XXX
$\mathcal{A}^{\text{raw}}$ ($\Xi_b^0 \to pKKK$)	X.XXX ± X.XXX
$\mathcal{A}^{\text{raw}}$ ($\Lambda_b^0 \to (\Lambda_c^+ \to p\pi\pi)\pi$)	0.030 ± 0.029
$\mathcal{A}^{\text{raw}}$ ($\Lambda_b^0 \to (\Lambda_c^+ \to pK\pi)\pi$)	0.018 ± 0.009
$\mathcal{A}^{\text{raw}}$ ($\Xi_b^0 \to (\Xi_c^+ \to pK\pi)\pi$)	0.019 ± 0.081
$\Delta\mathcal{A}^{CP} = \mathcal{A}^{\text{raw}}$ ($\Lambda_b^0 \to p\pi\pi\pi$) - $\mathcal{A}^{\text{raw}}$ ($\Lambda_b^0 \to (\Lambda_c^+ \to p\pi\pi)\pi$)	X.XXX ± 0.042
$\Delta\mathcal{A}^{CP} = \mathcal{A}^{\text{raw}}$ ($\Lambda_b^0 \to pK\pi\pi$) - $\mathcal{A}^{\text{raw}}$ ($\Lambda_b^0 \to (\Lambda_c^+ \to pK\pi)\pi$)	X.XXX ± 0.022
$\Delta\mathcal{A}^{CP} = \mathcal{A}^{\text{raw}}$ ($\Lambda_b^0 \to pKK\pi$) - $\mathcal{A}^{\text{raw}}$ ($\Lambda_b^0 \to (\Lambda_c^+ \to p\pi\pi)\pi$)	X.XXX ± 0.109
$\Delta\mathcal{A}^{CP} = \mathcal{A}^{\text{raw}}$ ($\Lambda_b^0 \to pKKK$) - $\mathcal{A}^{\text{raw}}$ ($\Lambda_b^0 \to (\Lambda_c^+ \to pK\pi)\pi$)	X.XXX ± 0.040
$\Delta\mathcal{A}^{CP} = \mathcal{A}^{\text{raw}}$ ($\Xi_b^0 \to pK\pi\pi$) - $\mathcal{A}^{\text{raw}}$ ($\Xi_b^0 \to (\Xi_c^+ \to pK\pi)\pi$)	X.XXX ± 0.175
$\Delta\mathcal{A}^{CP} = \mathcal{A}^{\text{raw}}$ ($\Xi_b^0 \to pK\pi K$) - $\mathcal{A}^{\text{raw}}$ ($\Xi_b^0 \to (\Xi_c^+ \to pK\pi)\pi$)	X.XXX ± 0.143
$\Delta\mathcal{A}^{CP} = \mathcal{A}^{\text{raw}}$ ($\Xi_b^0 \to pKKK$) - $\mathcal{A}^{\text{raw}}$ ($\Xi_b^0 \to (\Xi_c^+ \to pK\pi)\pi$)	X.XXX ± 0.821
Observables for 2012 spectra:	
$\mathcal{A}^{\text{raw}}$ ($\Lambda_b^0 \to p\pi\pi\pi$)	X.XXX ± X.XXX
$\mathcal{A}^{\text{raw}}$ ($\Lambda_b^0 \to pK\pi\pi$)	X.XXX ± X.XXX
$\mathcal{A}^{\text{raw}}$ ($\Lambda_b^0 \to pKK\pi$)	X.XXX ± X.XXX
$\mathcal{A}^{\text{raw}}$ ($\Lambda_b^0 \to pKKK$)	X.XXX ± X.XXX
$\mathcal{A}^{\text{raw}}$ ($\Xi_b^0 \to pK\pi\pi$)	X.XXX ± X.XXX
$\mathcal{A}^{\text{raw}}$ ($\Xi_b^0 \to pK\pi K$)	X.XXX ± X.XXX
$\mathcal{A}^{\text{raw}}$ ($\Xi_b^0 \to pKKK$)	X.XXX ± X.XXX
$\mathcal{A}^{\text{raw}}$ ($\Lambda_b^0 \to (\Lambda_c^+ \to p\pi\pi)\pi$)	0.000 ± 0.019
$\mathcal{A}^{\text{raw}}$ ($\Lambda_b^0 \to (\Lambda_c^+ \to pK\pi)\pi$)	0.011 ± 0.005
$\mathcal{A}^{\text{raw}}$ ($\Xi_b^0 \to (\Xi_c^+ \to pK\pi)\pi$)	-0.003 ± 0.052
$\Delta\mathcal{A}^{CP} = \mathcal{A}^{\text{raw}}$ ($\Lambda_b^0 \to p\pi\pi\pi$) - $\mathcal{A}^{\text{raw}}$ ($\Lambda_b^0 \to (\Lambda_c^+ \to p\pi\pi)\pi$)	X.XXX ± 0.029
$\Delta\mathcal{A}^{CP} = \mathcal{A}^{\text{raw}}$ ($\Lambda_b^0 \to pK\pi\pi$) - $\mathcal{A}^{\text{raw}}$ ($\Lambda_b^0 \to (\Lambda_c^+ \to pK\pi)\pi$)	X.XXX ± 0.015
$\Delta\mathcal{A}^{CP} = \mathcal{A}^{\text{raw}}$ ($\Lambda_b^0 \to pKK\pi$) - $\mathcal{A}^{\text{raw}}$ ($\Lambda_b^0 \to (\Lambda_c^+ \to p\pi\pi)\pi$)	X.XXX ± 0.066
$\Delta\mathcal{A}^{CP} = \mathcal{A}^{\text{raw}}$ ($\Lambda_b^0 \to pKKK$) - $\mathcal{A}^{\text{raw}}$ ($\Lambda_b^0 \to (\Lambda_c^+ \to pK\pi)\pi$)	X.XXX ± 0.027
$\Delta\mathcal{A}^{CP} = \mathcal{A}^{\text{raw}}$ ($\Xi_b^0 \to pK\pi\pi$) - $\mathcal{A}^{\text{raw}}$ ($\Xi_b^0 \to (\Xi_c^+ \to pK\pi)\pi$)	X.XXX ± 0.131
$\Delta\mathcal{A}^{CP} = \mathcal{A}^{\text{raw}}$ ($\Xi_b^0 \to pK\pi K$) - $\mathcal{A}^{\text{raw}}$ ($\Xi_b^0 \to (\Xi_c^+ \to pK\pi)\pi$)	X.XXX ± 0.101
$\Delta\mathcal{A}^{CP} = \mathcal{A}^{\text{raw}}$ ($\Xi_b^0 \to pKKK$) - $\mathcal{A}^{\text{raw}}$ ($\Xi_b^0 \to (\Xi_c^+ \to pK\pi)\pi$)	X.XXX ± 1.164

Table 5.28: The yields of B physics backgrounds from the RHSB of each spectrum with $m_{ph} < 2$ GeV/c^2 phase space cut.

Spectrum	RHSB cut (in MeV/c^2)	Dominant B	Year	Yields from RHSB w/ p track	Yields from RHSB w/ $\overline{p}$ track	Translated yields w/ p track	Translated yields w/ $\overline{p}$ track
$X_b^0 \to p\pi\pi\pi$	$m_{p\pi\pi\pi} > 5685.$	$B^0 \to K\pi\pi\pi$	2011	30.5 ± 7.4	25.9 ± 5.6	98.6 ± 23.8	83.9 ± 18.1
			2012	123.4 ± 12.3	140.2 ± 13.0	399.3 ± 39.9	453.7 ± 42.2
$X_b^0 \to pK\pi\pi$	$m_{pK\pi\pi} > 5840.$	$B_s^0 \to K\pi\pi K$	2011	9.5 ± 3.6	8.8 ± 3.4	35.3 ± 13.6	32.9 ± 12.9
			2012	45.4 ± 7.8	37.6 ± 6.8	169.3 ± 29.0	140.3 ± 25.4
$X_b^0 \to pKK\pi$	$m_{pKK\pi} > 5840.$	$B^0 \to KKK\pi$	2011	7.4 ± 3.2	5.8 ± 3.2	50.8 ± 21.8	40.1 ± 21.8
			2012	23.9 ± 5.3	19.8 ± 5.1	164.2 ± 36.5	135.7 ± 34.8
$X_b^0 \to pKKK$	$m_{pKKK} > 5840.$	$B_s^0 \to KKKK$	2011	scaled		57.9 ± 14.7	31.7 ± 9.3
			2012	17.7 ± 4.5	14.6 ± 4.3	85.9 ± 21.8	70.8 ± 20.7

Table 5.29: The *CP* asymmetry observables obtained from the results of the fit to the data with $m_{ph} < 2$ GeV/c^2 phase space cut in the charmless spectra.

CP asymmetry observable	Value
Observables for 2011 spectra:	
$\mathcal{A}^{\rm raw}$ ($\Lambda_b^0 \to p\pi\pi\pi$)	X.XXX ± X.XXX
$\mathcal{A}^{\rm raw}$ ($\Lambda_b^0 \to pK\pi\pi$)	X.XXX ± X.XXX
$\mathcal{A}^{\rm raw}$ ($\Lambda_b^0 \to pKK\pi$)	X.XXX ± X.XXX
$\mathcal{A}^{\rm raw}$ ($\Lambda_b^0 \to pKKK$)	X.XXX ± X.XXX
$\mathcal{A}^{\rm raw}$ ($\Xi_b^0 \to pK\pi\pi$)	X.XXX ± X.XXX
$\mathcal{A}^{\rm raw}$ ($\Xi_b^0 \to pK\pi K$)	X.XXX ± X.XXX
$\mathcal{A}^{\rm raw}$ ($\Xi_b^0 \to pKKK$)	X.XXX ± X.XXX
$\mathcal{A}^{\rm raw}$ ($\Lambda_b^0 \to (\Lambda_c^+ \to p\pi\pi)\pi$)	0.030 ± 0.029
$\mathcal{A}^{\rm raw}$ ($\Lambda_b^0 \to (\Lambda_c^+ \to pK\pi)\pi$)	0.018 ± 0.009
$\mathcal{A}^{\rm raw}$ ($\Xi_b^0 \to (\Xi_c^+ \to pK\pi)\pi$)	0.019 ± 0.081
$\Delta\mathcal{A}^{CP} = \mathcal{A}^{\rm raw}$ ($\Lambda_b^0 \to p\pi\pi\pi$) - $\mathcal{A}^{\rm raw}$ ($\Lambda_b^0 \to (\Lambda_c^+ \to p\pi\pi)\pi$)	X.XXX ± 0.047
$\Delta\mathcal{A}^{CP} = \mathcal{A}^{\rm raw}$ ($\Lambda_b^0 \to pK\pi\pi$) - $\mathcal{A}^{\rm raw}$ ($\Lambda_b^0 \to (\Lambda_c^+ \to pK\pi)\pi$)	X.XXX ± 0.025
$\Delta\mathcal{A}^{CP} = \mathcal{A}^{\rm raw}$ ($\Lambda_b^0 \to pKK\pi$) - $\mathcal{A}^{\rm raw}$ ($\Lambda_b^0 \to (\Lambda_c^+ \to p\pi\pi)\pi$)	X.XXX ± 0.135
$\Delta\mathcal{A}^{CP} = \mathcal{A}^{\rm raw}$ ($\Lambda_b^0 \to pKKK$) - $\mathcal{A}^{\rm raw}$ ($\Lambda_b^0 \to (\Lambda_c^+ \to pK\pi)\pi$)	X.XXX ± 0.043
$\Delta\mathcal{A}^{CP} = \mathcal{A}^{\rm raw}$ ($\Xi_b^0 \to pK\pi\pi$) - $\mathcal{A}^{\rm raw}$ ($\Xi_b^0 \to (\Xi_c^+ \to pK\pi)\pi$)	X.XXX ± 0.173
$\Delta\mathcal{A}^{CP} = \mathcal{A}^{\rm raw}$ ($\Xi_b^0 \to pK\pi K$) - $\mathcal{A}^{\rm raw}$ ($\Xi_b^0 \to (\Xi_c^+ \to pK\pi)\pi$)	X.XXX ± 0.149
$\Delta\mathcal{A}^{CP} = \mathcal{A}^{\rm raw}$ ($\Xi_b^0 \to pKKK$) - $\mathcal{A}^{\rm raw}$ ($\Xi_b^0 \to (\Xi_c^+ \to pK\pi)\pi$)	X.XXX ± 0.146
Observables for 2012 spectra:	
$\mathcal{A}^{\rm raw}$ ($\Lambda_b^0 \to p\pi\pi\pi$)	X.XXX ± X.XXX
$\mathcal{A}^{\rm raw}$ ($\Lambda_b^0 \to pK\pi\pi$)	X.XXX ± X.XXX
$\mathcal{A}^{\rm raw}$ ($\Lambda_b^0 \to pKK\pi$)	X.XXX ± X.XXX
$\mathcal{A}^{\rm raw}$ ($\Lambda_b^0 \to pKKK$)	X.XXX ± X.XXX
$\mathcal{A}^{\rm raw}$ ($\Xi_b^0 \to pK\pi\pi$)	X.XXX ± X.XXX
$\mathcal{A}^{\rm raw}$ ($\Xi_b^0 \to pK\pi K$)	X.XXX ± X.XXX
$\mathcal{A}^{\rm raw}$ ($\Xi_b^0 \to pKKK$)	X.XXX ± X.XXX
$\mathcal{A}^{\rm raw}$ ($\Lambda_b^0 \to (\Lambda_c^+ \to p\pi\pi)\pi$)	0.000 ± 0.019
$\mathcal{A}^{\rm raw}$ ($\Lambda_b^0 \to (\Lambda_c^+ \to pK\pi)\pi$)	0.011 ± 0.005
$\mathcal{A}^{\rm raw}$ ($\Xi_b^0 \to (\Xi_c^+ \to pK\pi)\pi$)	-0.003 ± 0.052
$\Delta\mathcal{A}^{CP} = \mathcal{A}^{\rm raw}$ ($\Lambda_b^0 \to p\pi\pi\pi$) - $\mathcal{A}^{\rm raw}$ ($\Lambda_b^0 \to (\Lambda_c^+ \to p\pi\pi)\pi$)	X.XXX ± 0.032
$\Delta\mathcal{A}^{CP} = \mathcal{A}^{\rm raw}$ ($\Lambda_b^0 \to pK\pi\pi$) - $\mathcal{A}^{\rm raw}$ ($\Lambda_b^0 \to (\Lambda_c^+ \to pK\pi)\pi$)	X.XXX ± 0.017
$\Delta\mathcal{A}^{CP} = \mathcal{A}^{\rm raw}$ ($\Lambda_b^0 \to pKK\pi$) - $\mathcal{A}^{\rm raw}$ ($\Lambda_b^0 \to (\Lambda_c^+ \to p\pi\pi)\pi$)	X.XXX ± 0.077
$\Delta\mathcal{A}^{CP} = \mathcal{A}^{\rm raw}$ ($\Lambda_b^0 \to pKKK$) - $\mathcal{A}^{\rm raw}$ ($\Lambda_b^0 \to (\Lambda_c^+ \to pK\pi)\pi$)	X.XXX ± 0.030
$\Delta\mathcal{A}^{CP} = \mathcal{A}^{\rm raw}$ ($\Xi_b^0 \to pK\pi\pi$) - $\mathcal{A}^{\rm raw}$ ($\Xi_b^0 \to (\Xi_c^+ \to pK\pi)\pi$)	X.XXX ± 0.130
$\Delta\mathcal{A}^{CP} = \mathcal{A}^{\rm raw}$ ($\Xi_b^0 \to pK\pi K$) - $\mathcal{A}^{\rm raw}$ ($\Xi_b^0 \to (\Xi_c^+ \to pK\pi)\pi$)	X.XXX ± 0.099
$\Delta\mathcal{A}^{CP} = \mathcal{A}^{\rm raw}$ ($\Xi_b^0 \to pKKK$) - $\mathcal{A}^{\rm raw}$ ($\Xi_b^0 \to (\Xi_c^+ \to pK\pi)\pi$)	X.XXX ± 5.932

Table 5.30: The yields of B physics backgrounds from the RHSB of each spectrum with $m_{ph} < 2$ GeV/c^2 phase and $m_{h'h''} < \sim$1.65 GeV/c^2 space cuts.

Spectrum	RHSB cut (in MeV/c^2)	Dominant B	Year	Yields from RHSB w/ p track	Yields from RHSB w/ $\overline{p}$ track	Translated yields w/ p track	Translated yields w/ $\overline{p}$ track
$X_b^0 \to p\pi\pi\pi$	$m_{p\pi\pi\pi} > 5685.$	$B^0 \to K\pi\pi\pi$	2011	8.5 ± 3.2	8.0 ± 2.9	27.3 ± 10.3	25.9 ± 9.3
			2012	44.4 ± 7.9	36.1 ± 6.9	143.7 ± 25.6	116.9 ± 22.4
$X_b^0 \to pK\pi\pi$	$m_{pK\pi\pi} > 5840.$	$B_s^0 \to K\pi\pi K$	2011	scaled		8.1 ± 2.4	16.9 ± 4.2
			2012	12.8 ± 3.7	17.8 ± 4.4	47.7 ± 14.1	66.5 ± 16.5
$X_b^0 \to pKK\pi$	$m_{pKK\pi} > 5840.$	$B^0 \to KKK\pi$	2011	scaled		17.3 ± 6.1	31.8 ± 9.6
			2012	9.5 ± 3.4	12.8 ± 3.9	65.3 ± 22.9	87.6 ± 26.5
$X_b^0 \to pKKK$	$m_{pKKK} > 5840.$	$B_s^0 \to KKKK$	2011	scaled		19.1 ± 6.2	13.8 ± 4.5
			2012	10.2 ± 3.2	9.6 ± 3.2	49.5 ± 16.1	46.7 ± 15.3

Table 5.31: The *CP* asymmetry observables obtained from the results of the fit to the data with $m_{ph} < 2$ GeV/c^2 and $m_{h'h''} < \sim 1.65$ GeV/c^2 phase space cuts in the charmless spectra.

CP asymmetry observable	Value
Observables for 2011 spectra:	
$\mathcal{A}^{\rm raw}$ ($\Lambda_b^0 \to p\pi\pi\pi$)	X.XXX ± X.XXX
$\mathcal{A}^{\rm raw}$ ($\Lambda_b^0 \to pK\pi\pi$)	X.XXX ± X.XXX
$\mathcal{A}^{\rm raw}$ ($\Lambda_b^0 \to pKK\pi$)	X.XXX ± X.XXX
$\mathcal{A}^{\rm raw}$ ($\Lambda_b^0 \to pKKK$)	X.XXX ± X.XXX
$\mathcal{A}^{\rm raw}$ ($\Xi_b^0 \to pK\pi\pi$)	X.XXX ± X.XXX
$\mathcal{A}^{\rm raw}$ ($\Xi_b^0 \to pK\pi K$)	X.XXX ± X.XXX
$\mathcal{A}^{\rm raw}$ ($\Xi_b^0 \to pKKK$)	X.XXX ± X.XXX
$\mathcal{A}^{\rm raw}$ ($\Lambda_b^0 \to (\Lambda_c^+ \to p\pi\pi)\pi$)	0.030 ± 0.029
$\mathcal{A}^{\rm raw}$ ($\Lambda_b^0 \to (\Lambda_c^+ \to pK\pi)\pi$)	0.018 ± 0.009
$\mathcal{A}^{\rm raw}$ ($\Xi_b^0 \to (\Xi_c^+ \to pK\pi)\pi$)	0.019 ± 0.081
$\Delta\mathcal{A}^{CP} = \mathcal{A}^{\rm raw}$ ($\Lambda_b^0 \to p\pi\pi\pi$) - $\mathcal{A}^{\rm raw}$ ($\Lambda_b^0 \to (\Lambda_c^+ \to p\pi\pi)\pi$)	X.XXX ± 0.074
$\Delta\mathcal{A}^{CP} = \mathcal{A}^{\rm raw}$ ($\Lambda_b^0 \to pK\pi\pi$) - $\mathcal{A}^{\rm raw}$ ($\Lambda_b^0 \to (\Lambda_c^+ \to pK\pi)\pi$)	X.XXX ± 0.030
$\Delta\mathcal{A}^{CP} = \mathcal{A}^{\rm raw}$ ($\Lambda_b^0 \to pKK\pi$) - $\mathcal{A}^{\rm raw}$ ($\Lambda_b^0 \to (\Lambda_c^+ \to p\pi\pi)\pi$)	X.XXX ± 0.162
$\Delta\mathcal{A}^{CP} = \mathcal{A}^{\rm raw}$ ($\Lambda_b^0 \to pKKK$) - $\mathcal{A}^{\rm raw}$ ($\Lambda_b^0 \to (\Lambda_c^+ \to pK\pi)\pi$)	X.XXX ± 0.047
$\Delta\mathcal{A}^{CP} = \mathcal{A}^{\rm raw}$ ($\Xi_b^0 \to pK\pi\pi$) - $\mathcal{A}^{\rm raw}$ ($\Xi_b^0 \to (\Xi_c^+ \to pK\pi)\pi$)	X.XXX ± 0.266
$\Delta\mathcal{A}^{CP} = \mathcal{A}^{\rm raw}$ ($\Xi_b^0 \to pK\pi K$) - $\mathcal{A}^{\rm raw}$ ($\Xi_b^0 \to (\Xi_c^+ \to pK\pi)\pi$)	X.XXX ± 0.210
$\Delta\mathcal{A}^{CP} = \mathcal{A}^{\rm raw}$ ($\Xi_b^0 \to pKKK$) - $\mathcal{A}^{\rm raw}$ ($\Xi_b^0 \to (\Xi_c^+ \to pK\pi)\pi$)	X.XXX ± 0.083
Observables for 2012 spectra:	
$\mathcal{A}^{\rm raw}$ ($\Lambda_b^0 \to p\pi\pi\pi$)	X.XXX ± X.XXX
$\mathcal{A}^{\rm raw}$ ($\Lambda_b^0 \to pK\pi\pi$)	X.XXX ± X.XXX
$\mathcal{A}^{\rm raw}$ ($\Lambda_b^0 \to pKK\pi$)	X.XXX ± X.XXX
$\mathcal{A}^{\rm raw}$ ($\Lambda_b^0 \to pKKK$)	X.XXX ± X.XXX
$\mathcal{A}^{\rm raw}$ ($\Xi_b^0 \to pK\pi\pi$)	X.XXX ± X.XXX
$\mathcal{A}^{\rm raw}$ ($\Xi_b^0 \to pK\pi K$)	X.XXX ± X.XXX
$\mathcal{A}^{\rm raw}$ ($\Xi_b^0 \to pKKK$)	X.XXX ± X.XXX
$\mathcal{A}^{\rm raw}$ ($\Lambda_b^0 \to (\Lambda_c^+ \to p\pi\pi)\pi$)	0.000 ± 0.019
$\mathcal{A}^{\rm raw}$ ($\Lambda_b^0 \to (\Lambda_c^+ \to pK\pi)\pi$)	0.011 ± 0.005
$\mathcal{A}^{\rm raw}$ ($\Xi_b^0 \to (\Xi_c^+ \to pK\pi)\pi$)	-0.003 ± 0.052
$\Delta\mathcal{A}^{CP} = \mathcal{A}^{\rm raw}$ ($\Lambda_b^0 \to p\pi\pi\pi$) - $\mathcal{A}^{\rm raw}$ ($\Lambda_b^0 \to (\Lambda_c^+ \to p\pi\pi)\pi$)	X.XXX ± 0.051
$\Delta\mathcal{A}^{CP} = \mathcal{A}^{\rm raw}$ ($\Lambda_b^0 \to pK\pi\pi$) - $\mathcal{A}^{\rm raw}$ ($\Lambda_b^0 \to (\Lambda_c^+ \to pK\pi)\pi$)	X.XXX ± 0.020
$\Delta\mathcal{A}^{CP} = \mathcal{A}^{\rm raw}$ ($\Lambda_b^0 \to pKK\pi$) - $\mathcal{A}^{\rm raw}$ ($\Lambda_b^0 \to (\Lambda_c^+ \to p\pi\pi)\pi$)	X.XXX ± 0.096
$\Delta\mathcal{A}^{CP} = \mathcal{A}^{\rm raw}$ ($\Lambda_b^0 \to pKKK$) - $\mathcal{A}^{\rm raw}$ ($\Lambda_b^0 \to (\Lambda_c^+ \to pK\pi)\pi$)	X.XXX ± 0.035
$\Delta\mathcal{A}^{CP} = \mathcal{A}^{\rm raw}$ ($\Xi_b^0 \to pK\pi\pi$) - $\mathcal{A}^{\rm raw}$ ($\Xi_b^0 \to (\Xi_c^+ \to pK\pi)\pi$)	X.XXX ± 0.232
$\Delta\mathcal{A}^{CP} = \mathcal{A}^{\rm raw}$ ($\Xi_b^0 \to pK\pi K$) - $\mathcal{A}^{\rm raw}$ ($\Xi_b^0 \to (\Xi_c^+ \to pK\pi)\pi$)	X.XXX ± 0.132
$\Delta\mathcal{A}^{CP} = \mathcal{A}^{\rm raw}$ ($\Xi_b^0 \to pKKK$) - $\mathcal{A}^{\rm raw}$ ($\Xi_b^0 \to (\Xi_c^+ \to pK\pi)\pi$)	X.XXX ± 8.457

5.11 Systematic uncertainties and cross-checks

Systematic uncertainties will come when the unblinding of the fit results and proton-antiproton spectra will occur. We are rapidly reviewing in this Section the main sources of systematic uncertainties and the methods we have installed for their determinations. We will as well spend few words on the envisaged cross-checks after unblinding.

5.11.1 Systematic uncertainties sources

- The fixed parameters of the signal shapes, signal cross-feed shapes and B physics background shapes modelling as determined from the MC simulated events. The parameters are for instance the tail parameters of the signal DCB model. In most cases, they have been determined by a simultaneous fit of several MC simulated events datasets with a finite number of events and their determination comes with a statistical uncertainty. Pseudo-experiments can be generated by fluctuating the parameters of the MC fit according to the results of the fit and taking into account its covariance matrix. The distribution of the final observables will be used as an estimate of the related systematic uncertainty. The procedure has been successfully commissioned with educated values of the fit results. It is however very demanding CPU-wise and some simplification to the nominal fit, namely by fixing the parameters of the partially reconstructed background shape, have been brought. The full CPU-consuming procedure will be be run once the fit model is blessed.

- The PID systematic corrections: pseudo-experiments will be generated by fluctuating the uncertainties of the parameters of the MC PID re-weighted shapes. The spread of the toy results will be assigned as the related systematics.

- The combinatorics shape: the results of the baseline fit model with a first order Chebychev polynomial will be compared to the ones obtained with an exponential shape. The observed difference of the measured yields will be taken as the systematic uncertainty estimate related to the choice of a polynomial shape for the combinatorics.

- The L0hadron trigger efficiencies for the different charges of L0Hadron TOS pions and kaons: the calorimeter group is providing tables of L0HadronTOS efficiencies with associated upper and lower systematic uncertainties from a selected sample of offline reconstructed $D^0 \to K^-\pi^+$. The efficiencies are determined for both pions and kaons and split by charge. The observed variation in the fit results by changing these efficiencies within their errors (driven by the size of the calibration sample) will be taken as the corresponding systematic uncertainty.

- The tracking efficiency systematic uncertainties: the detection efficiency of X_b^0 and $\overline{X}_b^0$ in the charmless spectra is cancelled, up to corrections of kinematics difference, by the control channels. A second-order correction on the tracking efficiency comes due to the difference of their kinematics. The tracking group is providing tables of efficiencies for kaons and pions with associated upper and lower systematic uncertainties (and split by charge) as a function of momentum. The observed spread of results by varying the track efficiency within errors will be assigned as the corresponding systematic uncertainty. However, no such table yet exists for protons and hence we plan to take the same systematic correction from what we will get from the kaon and pion corrections.

- Partially-reconstucted backgrounds from $\Lambda_b^0 \to pK^-(\eta' \to \pi^+\pi^-\gamma)$: This possible contribution is not modelled in the fit to data. As such, a systematic uncertainty, educated from the B^+ decays, is assigned. The SM quark level diagrammatic picture for $\Lambda_b^0 \to pK^-(\eta' \to \pi^+\pi^-\gamma)$ decay is the presence of $u\overline{u}$ pair. Hence, we are expecting a hierarchy of $\pi^+\pi^- > \rho^0 > \eta > \eta'$. The analogous decays in the meson systems are: $B^+ \to \pi^+\pi^-\pi^+$, $B^+ \to \rho^0\pi^+$, $B^+ \to \eta\pi^+$, $B^+ \to \eta'\pi^+$, and shows that very hierarchy. We will assign a systematic uncertainty by considering the change in the result of the introduction of this shape with a ratio of 1:20 as indicated by the B^+ hierarchy.

- A systematic uncertainty will also be assigned for the difference of the kinematics of the charmless decays and the control modes.

5.11.2 Cross-checks

There are two main studies which must be performed for a sanity check of the results after the unblinding of the results:

- The comparison of the results obtained for the independent samples obtained with each of the magnet polarities.

- The comparison of the results obtained for the two categories of L0 trigger requirements: Trigger Independent of Signal (TIS) candidates and Trigger On Signal (TOS) candidates.

5.12 Concluding remarks

This document describes the search for *CP*-violating asymmetries in 4-body fully charged decays of the neutral b-baryons, Λ_b^0 or Ξ_b^0, proceeding through charmless quark transitions $b \to u$ and FCNC quark transitions $b \to s, d$.

The *CP* violation in baryons remains unobserved up to date. In these multibody decays of b-baryons, the interference pattern is expected to be rich of resonance structures, in particular in the low mass two-body baryon resonances (Λ^{*0}, N^{*0} and Δ series). They come likely in association with two-body non-baryonic resonances (i.e. $\pi\pi$, $K\pi$ and K^+K^- invariant mass spectra). The weak interaction induced *CP* asymmetries might hence receive significant enhancement from the phase differences coming from these strongly interacting resonances and makes these decays a favorable terrain for the first observation of *CP* violation in baryon decays.

There are seven decays of interest, namely $\Lambda_b^0 \to p\pi^-\pi^+\pi^-$, $\Lambda_b^0 \to pK^-\pi^+\pi^-$, $\Lambda_b^0 \to pK^-K^+\pi^-$, $\Lambda_b^0 \to pK^-K^+K^-$, $\Xi_b^0 \to pK^-\pi^+\pi^-$, $\Xi_b^0 \to pK^-\pi^+K^-$ and $\Xi_b^0 \to pK^-K^+K^-$, which are reconstructed and selected consistently with common selection tools. A simultaneous mass fitter has been designed to measure their yields and charge conjugate counterparts. A simple counting experiment can measure the direct $\mathcal{A}^{CP}$ up to corrections of instrumental and productions asymmetries. In LHCb, this amounts to correction on the K^+/K^-, π^+/π^- and $p/\overline{p}$ detection asymmetries and b-baryon/$\overline{b}$-baryon production asymmetry. In order to cope with these unknowns, we have chosen to measure the $\Delta\mathcal{A}^{\text{raw}}$ of both Λ_b^0 and Ξ_b^0 charmlessly decaying to fully-charged four-body final states with respect to charmed decays having the same unpaired final tracks, such as $\Lambda_b^0 \to (\Lambda_c^+ \to p\pi^-\pi^+)\pi^-$, $\Lambda_b^0 \to (\Lambda_c^+ \to pK^-\pi^+)\pi^-$ and $\Xi_b^0 \to (\Xi_c^+ \to pK\pi)\pi$. These decays are fitted simultaneously with the charmless spectra.

A particular care has been taken to understand the background sources which can induce *CP* asymmetries distinct from the ones we are aiming at measuring. They are coming from charmless B mesons decays and are controlled from a data-driven technique in the simultaneous fit of the signal and control channels spectra.

The global behaviour of the fit is found satisfactory and we did not find any sign of an overlooked background. The control channels are unblinded and raw asymmetries are found consistent among the years of data taking and compatible with zero.

$$\begin{aligned}
\mathcal{A}^{\rm raw}(\Lambda_b^0 \to (\Lambda_c^+ \to p\pi\pi)\pi, 2011) &= 0.030 \pm 0.029 \\
\mathcal{A}^{\rm raw}(\Lambda_b^0 \to (\Lambda_c^+ \to pK\pi)\pi, 2011) &= 0.018 \pm 0.009 \\
\mathcal{A}^{\rm raw}(\Xi_b^0 \to (\Xi_c^+ \to pK\pi)\pi, 2011) &= 0.019 \pm 0.081 \\
\mathcal{A}^{\rm raw}(\Lambda_b^0 \to (\Lambda_c^+ \to p\pi\pi)\pi, 2012) &= 0.000 \pm 0.019 \\
\mathcal{A}^{\rm raw}(\Lambda_b^0 \to (\Lambda_c^+ \to pK\pi)\pi, 2012) &= 0.011 \pm 0.005 \\
\mathcal{A}^{\rm raw}(\Xi_b^0 \to (\Xi_c^+ \to pK\pi)\pi, 2012) &= -0.003 \pm 0.052
\end{aligned}$$

The evaluation of the systematic uncertainties must proceed after the unblinding. However, a discussion of their sources is given in this document and the methods for their determination (mostly based on pseudo-experiments) have been commissioned.

This analysis document gathers the selection of the decay modes of interest, the simultaneous fit and the blinding strategies, the mass fit model and the study of the fit biases with pseudo-experiments, and eventually the blind fit results and sensitivities.

Chapter 6

Unblinded fit results and interpretation

Contents

After careful scrutiny of the possible background contributions, the simultaneous fit were reran with the signal mass regions and *CP* observables unblinded. The fit results are presented in Section 6.1. Section 6.2 presents the statistical significance of the signals modes. Cross-checks are also performed for sanity checks of the results after unblinding and these are presented in Section 6.4. Finally, Section 6.5 summarizes and interprets the results.

6.1 Fit results

As a reminder, we performed three measurements of $\Delta\mathcal{A}^{CP}$ in different regions of the phase space. The first measurement, whose results are presented in Section 6.1.1, considers the events in the full phase space, hence no invariant mass cut to any combination of the daughter particles is applied. The second measurement involves $\Delta\mathcal{A}^{CP}$ determination in the phase space region where the invariant mass of $p\pi$ or pK is less than 2 GeV/c^2. The results are presented in Section 6.1.2. Lastly, $\Delta\mathcal{A}^{CP}$ measurements are performed in the phase space region where the $p\pi$ or pK is less than 2 GeV/c and invariant mass of the pair of the two other tracks is less than $\sim$1.6 GeV/c^2. The results of the latter measurement are discussed in Section 6.1.3. Table 5.25 in Chapter 5.10 lists the phase space cuts applied. The fit results of the charmed modes are the same as what has been presented in Section 5.10 of Chapter 5.

6.1.1 Full phase space

Figures 6.1 and 6.2 show the fit results of the simultaneous fit obtained using the 2011 data, while Figures 6.3 and 6.4 are for the 2012 data. All events in the phase space are considered. The yields are also reported in Table 6.1, while the *CP* observables are summarized in Table 6.2. The measured yields of $\Xi_b^0 \to pKKK$ using the 2012 data are negative and hence the $\Delta\mathcal{A}^{CP}$ measurement for this mode is not relevant.

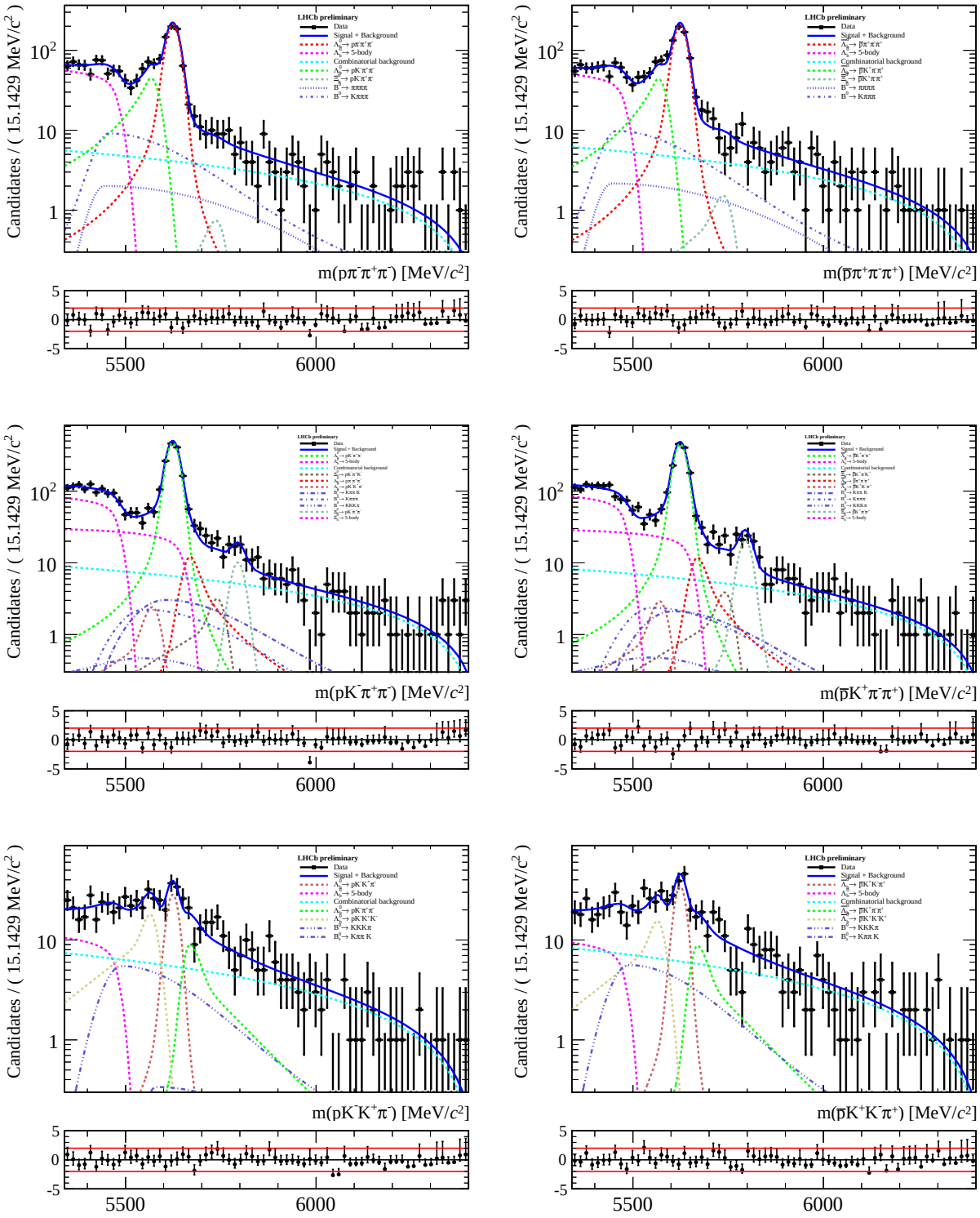

Figure 6.1: Unblinded fit results for the [from top to bottom] $X_b^0 \to p\pi\pi\pi$, $X_b^0 \to pK\pi\pi$ and $X_b^0 \to pKK\pi$ spectra using the full phase space data of 2011. Plots in the left-column are for the spectra with X_b^0 and on the right-column for the spectra with $\overline{X}_b^0$.

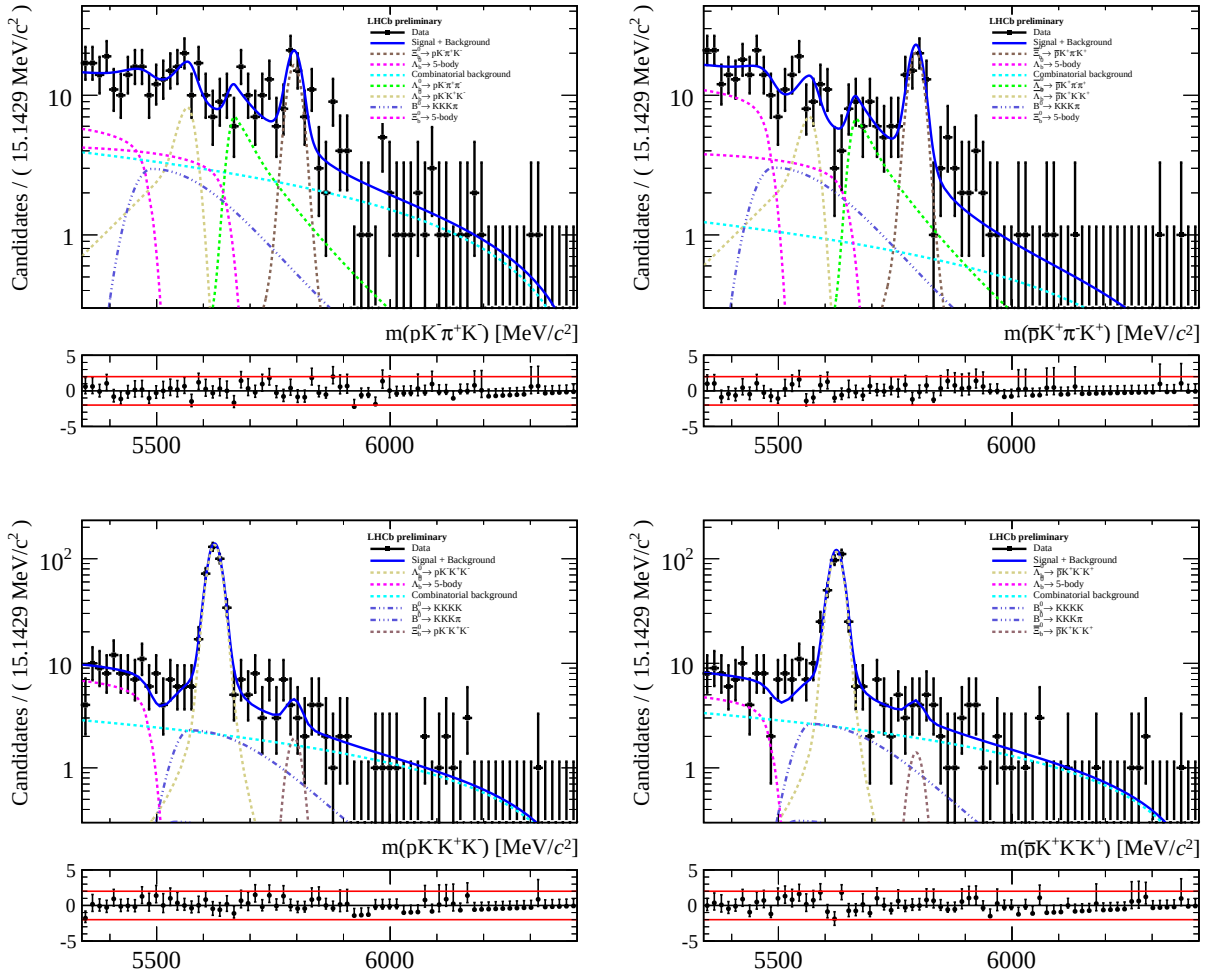

Figure 6.2: Unblinded fit results for the [top] $X_b^0 \to pK\pi K$ and [bottom] $X_b^0 \to pKKK$ spectra using the full phase space data of 2011. Plots in the left-column are for the spectra with X_b^0 and on the right-column for the spectra with $\overline{X}_b^0$.

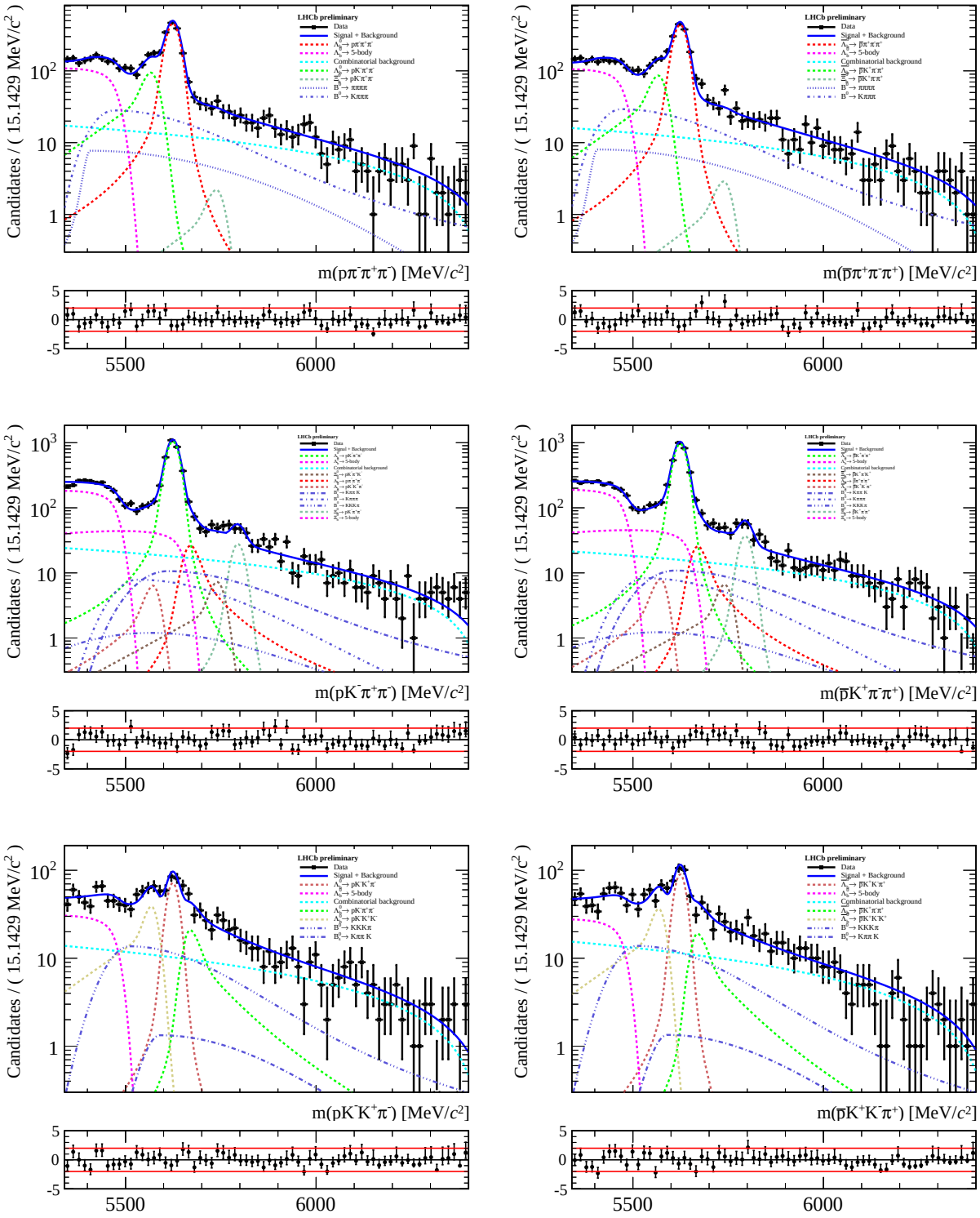

Figure 6.3: Unblinded fit results for the [from top to bottom] $X_b^0 \to p\pi\pi\pi$, $X_b^0 \to pK\pi\pi$ and $X_b^0 \to pKK\pi$ spectra using the full phase space data of 2012. Plots in the left-column are for the spectra with X_b^0 and on the right-column for the spectra with $\overline{X}_b^0$.

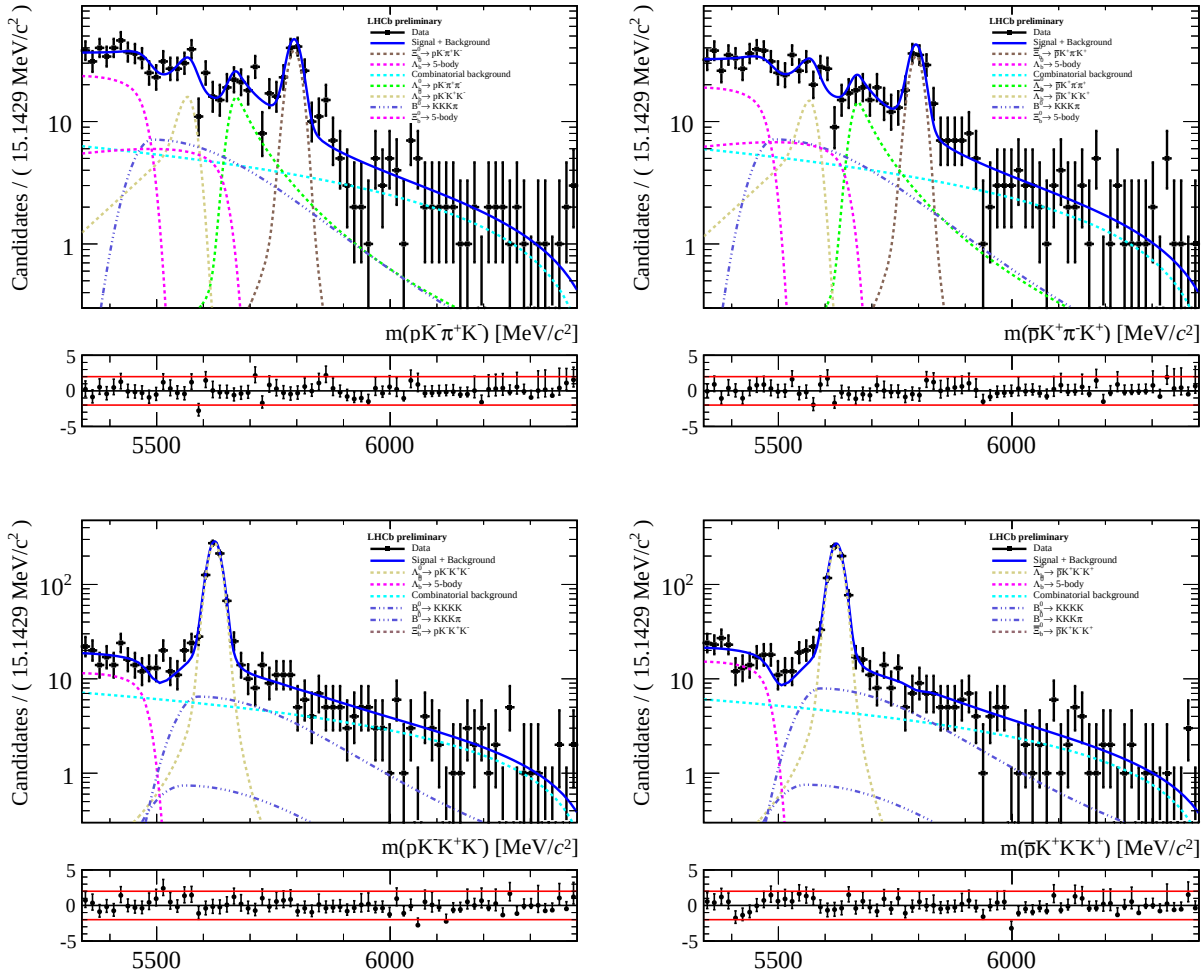

Figure 6.4: Unblinded fit results for the [top] $X_b^0 \to pK\pi K$ and [bottom] $X_b^0 \to pKKK$ spectra using the full phase space data of 2012. Plots in the left-column are for the spectra with X_b^0 and on the right-column for the spectra with $\overline{X}_b^0$.

Table 6.1: Measured yields of the charmless and charmed modes of the simultaneous fit to the full phase space data of 2011 and 2012.

Yield parameter (in Λ_b^0/Ξ_b^0 spectra)	Value	Yield parameter (in $\overline{\Lambda}_b^0/\overline{\Xi}_b^0$ spectra)	Value
Yields for 2011 spectra:			
$\mathcal{N}$ (2011 Signal $\Lambda_b^0 \to p\pi\pi\pi$)	647.405 ± 28.715	$\bar{\mathcal{N}}$	633.736 ± 28.692
$\mathcal{N}$ (2011 Signal $\Lambda_b^0 \to pK\pi\pi$)	1367.015 ± 41.500	$\bar{\mathcal{N}}$	1328.267 ± 40.608
$\mathcal{N}$ (2011 Signal $\Lambda_b^0 \to pKK\pi$)	77.325 ± 12.116	$\bar{\mathcal{N}}$	93.560 ± 12.972
$\mathcal{N}$ (2011 Signal $\Lambda_b^0 \to pKKK$)	350.028 ± 18.995	$\bar{\mathcal{N}}$	301.476 ± 18.100
$\mathcal{N}$ (2011 Signal $\Xi_b^0 \to pK\pi\pi$)	30.958 ± 9.656	$\bar{\mathcal{N}}$	62.927 ± 11.270
$\mathcal{N}$ (2011 Signal $\Xi_b^0 \to pK\pi K$)	47.393 ± 8.857	$\bar{\mathcal{N}}$	58.333 ± 9.024
$\mathcal{N}$ (2011 Signal $\Xi_b^0 \to pKKK$)	5.081 ± 4.311	$\bar{\mathcal{N}}$	3.739 ± 4.337
Yields for 2012 spectra:			
$\mathcal{N}$ (2012 Signal $\Lambda_b^0 \to p\pi\pi\pi$)	1419.699 ± 43.680	$\bar{\mathcal{N}}$	1373.019 ± 43.378
$\mathcal{N}$ (2012 Signal $\Lambda_b^0 \to pK\pi\pi$)	3035.045 ± 61.749	$\bar{\mathcal{N}}$	2779.812 ± 59.614
$\mathcal{N}$ (2012 Signal $\Lambda_b^0 \to pKK\pi$)	195.430 ± 19.268	$\bar{\mathcal{N}}$	245.689 ± 20.629
$\mathcal{N}$ (2012 Signal $\Lambda_b^0 \to pKKK$)	692.925 ± 26.986	$\bar{\mathcal{N}}$	652.178 ± 26.447
$\mathcal{N}$ (2012 Signal $\Xi_b^0 \to pK\pi\pi$)	84.267 ± 16.309	$\bar{\mathcal{N}}$	110.855 ± 17.266
$\mathcal{N}$ (2012 Signal $\Xi_b^0 \to pK\pi K$)	109.408 ± 13.078	$\bar{\mathcal{N}}$	99.013 ± 12.591
$\mathcal{N}$ (2012 Signal $\Xi_b^0 \to pKKK$)	-0.146 ± 5.848	$\bar{\mathcal{N}}$	-1.576 ± 5.551

All signals for particles and antiparticles decays are established but the decay $\Xi_b^0 \to pKKK$. The significance of the most suppressed modes will be discussed in the section 6.2.

Table 6.2: The *CP* asymmetry observables obtained from the unblinded results of the fit to the full phase space data.

CP asymmetry observable	Value
Observables for 2011 spectra:	
$\mathcal{A}^{\text{raw}}$ ($\Lambda_b^0 \to p\pi\pi\pi$)	0.011 ± 0.031
$\mathcal{A}^{\text{raw}}$ ($\Lambda_b^0 \to pK\pi\pi$)	0.014 ± 0.021
$\mathcal{A}^{\text{raw}}$ ($\Lambda_b^0 \to pKK\pi$)	-0.095 ± 0.104
$\mathcal{A}^{\text{raw}}$ ($\Lambda_b^0 \to pKKK$)	0.075 ± 0.040
$\mathcal{A}^{\text{raw}}$ ($\Xi_b^0 \to pK\pi\pi$)	-0.341 ± 0.160
$\mathcal{A}^{\text{raw}}$ ($\Xi_b^0 \to pK\pi K$)	-0.103 ± 0.121
$\mathcal{A}^{\text{raw}}$ ($\Xi_b^0 \to pKKK$)	0.152 ± 0.924
$\Delta\mathcal{A}^{CP} = \mathcal{A}^{\text{raw}}$ ($\Lambda_b^0 \to p\pi\pi\pi$) - $\mathcal{A}^{\text{raw}}$ ($\Lambda_b^0 \to (\Lambda_c^+ \to p\pi\pi)\pi$)	-0.019 ± 0.043
$\Delta\mathcal{A}^{CP} = \mathcal{A}^{\text{raw}}$ ($\Lambda_b^0 \to pK\pi\pi$) - $\mathcal{A}^{\text{raw}}$ ($\Lambda_b^0 \to (\Lambda_c^+ \to pK\pi)\pi$)	-0.003 ± 0.023
$\Delta\mathcal{A}^{CP} = \mathcal{A}^{\text{raw}}$ ($\Lambda_b^0 \to pKK\pi$) - $\mathcal{A}^{\text{raw}}$ ($\Lambda_b^0 \to (\Lambda_c^+ \to p\pi\pi)\pi$)	-0.125 ± 0.108
$\Delta\mathcal{A}^{CP} = \mathcal{A}^{\text{raw}}$ ($\Lambda_b^0 \to pKKK$) - $\mathcal{A}^{\text{raw}}$ ($\Lambda_b^0 \to (\Lambda_c^+ \to pK\pi)\pi$)	0.057 ± 0.041
$\Delta\mathcal{A}^{CP} = \mathcal{A}^{\text{raw}}$ ($\Xi_b^0 \to pK\pi\pi$) - $\mathcal{A}^{\text{raw}}$ ($\Xi_b^0 \to (\Xi_c^+ \to pK\pi)\pi$)	-0.360 ± 0.180
$\Delta\mathcal{A}^{CP} = \mathcal{A}^{\text{raw}}$ ($\Xi_b^0 \to pK\pi K$) - $\mathcal{A}^{\text{raw}}$ ($\Xi_b^0 \to (\Xi_c^+ \to pK\pi)\pi$)	-0.123 ± 0.145
$\Delta\mathcal{A}^{CP} = \mathcal{A}^{\text{raw}}$ ($\Xi_b^0 \to pKKK$) - $\mathcal{A}^{\text{raw}}$ ($\Xi_b^0 \to (\Xi_c^+ \to pK\pi)\pi$)	0.133 ± 0.927
Observables for 2012 spectra:	
$\mathcal{A}^{\text{raw}}$ ($\Lambda_b^0 \to p\pi\pi\pi$)	0.017 ± 0.022
$\mathcal{A}^{\text{raw}}$ ($\Lambda_b^0 \to pK\pi\pi$)	0.044 ± 0.014
$\mathcal{A}^{\text{raw}}$ ($\Lambda_b^0 \to pKK\pi$)	-0.114 ± 0.064
$\mathcal{A}^{\text{raw}}$ ($\Lambda_b^0 \to pKKK$)	0.030 ± 0.028
$\mathcal{A}^{\text{raw}}$ ($\Xi_b^0 \to pK\pi\pi$)	-0.136 ± 0.122
$\mathcal{A}^{\text{raw}}$ ($\Xi_b^0 \to pK\pi K$)	0.050 ± 0.087
$\Delta\mathcal{A}^{CP} = \mathcal{A}^{\text{raw}}$ ($\Lambda_b^0 \to p\pi\pi\pi$) - $\mathcal{A}^{\text{raw}}$ ($\Lambda_b^0 \to (\Lambda_c^+ \to p\pi\pi)\pi$)	0.016 ± 0.029
$\Delta\mathcal{A}^{CP} = \mathcal{A}^{\text{raw}}$ ($\Lambda_b^0 \to pK\pi\pi$) - $\mathcal{A}^{\text{raw}}$ ($\Lambda_b^0 \to (\Lambda_c^+ \to pK\pi)\pi$)	0.033 ± 0.015
$\Delta\mathcal{A}^{CP} = \mathcal{A}^{\text{raw}}$ ($\Lambda_b^0 \to pKK\pi$) - $\mathcal{A}^{\text{raw}}$ ($\Lambda_b^0 \to (\Lambda_c^+ \to p\pi\pi)\pi$)	-0.114 ± 0.066
$\Delta\mathcal{A}^{CP} = \mathcal{A}^{\text{raw}}$ ($\Lambda_b^0 \to pKKK$) - $\mathcal{A}^{\text{raw}}$ ($\Lambda_b^0 \to (\Lambda_c^+ \to pK\pi)\pi$)	0.019 ± 0.029
$\Delta\mathcal{A}^{CP} = \mathcal{A}^{\text{raw}}$ ($\Xi_b^0 \to pK\pi\pi$) - $\mathcal{A}^{\text{raw}}$ ($\Xi_b^0 \to (\Xi_c^+ \to pK\pi)\pi$)	-0.133 ± 0.133
$\Delta\mathcal{A}^{CP} = \mathcal{A}^{\text{raw}}$ ($\Xi_b^0 \to pK\pi K$) - $\mathcal{A}^{\text{raw}}$ ($\Xi_b^0 \to (\Xi_c^+ \to pK\pi)\pi$)	0.053 ± 0.102

6.1.2 Low invariant mass region of ph

The second measurement intends to measure the $\Delta\mathcal{A}^{CP}$ in the phase space region of low invariant mass of $p\pi$ or pK pair. The unblinded fit results of the simultaneous fit are shown in Figures 6.5 and 6.6 for the 2011 data, while Figures 6.7 and 6.8 are for the 2012 data. The extracted yields are summarized in Table 6.3 and the measured CP observables are listed in Table 6.4. Again, the measured yields of $\Xi_b^0 \to pKKK$ using the 2012 data are negative and hence the CP measurements for this mode is not relevant.

Table 6.3: Measured yields of the charmless and charmed modes of the simultaneous fit to the 2011 and 2012 data with $m_{ph} < 2\,\mathrm{GeV}/c^2$ phase space cut in the charmless modes.

Yield parameter (in Λ_b^0/Ξ_b^0 spectra)	Value	Yield parameter (in $\overline{\Lambda}_b^0/\overline{\Xi}_b^0$ spectra)	Value
Yields for 2011 spectra:			
$\mathcal{N}$ (2011 Signal $\Lambda_b^0 \to p\pi\pi\pi$)	443.649 ± 23.685	$\bar{\mathcal{N}}$	428.466 ± 23.513
$\mathcal{N}$ (2011 Signal $\Lambda_b^0 \to pK\pi\pi$)	1036.629 ± 36.180	$\bar{\mathcal{N}}$	962.794 ± 34.593
$\mathcal{N}$ (2011 Signal $\Lambda_b^0 \to pKK\pi$)	46.776 ± 10.049	$\bar{\mathcal{N}}$	66.424 ± 10.884
$\mathcal{N}$ (2011 Signal $\Lambda_b^0 \to pKKK$)	272.994 ± 16.931	$\bar{\mathcal{N}}$	243.941 ± 16.095
$\mathcal{N}$ (2011 Signal $\Xi_b^0 \to pK\pi\pi$)	25.208 ± 7.929	$\bar{\mathcal{N}}$	54.335 ± 10.117
$\mathcal{N}$ (2011 Signal $\Xi_b^0 \to pK\pi K$)	42.731 ± 7.999	$\bar{\mathcal{N}}$	44.840 ± 7.696
$\mathcal{N}$ (2011 Signal $\Xi_b^0 \to pKKK$)	0.039 ± 2.808	$\bar{\mathcal{N}}$	1.546 ± 3.431
Yields for 2012 spectra:			
$\mathcal{N}$ (2012 Signal $\Lambda_b^0 \to p\pi\pi\pi$)	990.035 ± 36.451	$\bar{\mathcal{N}}$	941.771 ± 36.010
$\mathcal{N}$ (2012 Signal $\Lambda_b^0 \to pK\pi\pi$)	2346.842 ± 54.180	$\bar{\mathcal{N}}$	2089.912 ± 51.570
$\mathcal{N}$ (2012 Signal $\Lambda_b^0 \to pKK\pi$)	123.768 ± 15.584	$\bar{\mathcal{N}}$	168.315 ± 16.976
$\mathcal{N}$ (2012 Signal $\Lambda_b^0 \to pKKK$)	553.507 ± 23.756	$\bar{\mathcal{N}}$	497.805 ± 22.723
$\mathcal{N}$ (2012 Signal $\Xi_b^0 \to pK\pi\pi$)	76.604 ± 14.261	$\bar{\mathcal{N}}$	87.245 ± 14.432
$\mathcal{N}$ (2012 Signal $\Xi_b^0 \to pK\pi K$)	112.801 ± 12.573	$\bar{\mathcal{N}}$	84.318 ± 11.167
$\mathcal{N}$ (2012 Signal $\Xi_b^0 \to pKKK$)	-2.251 ± 4.313	$\bar{\mathcal{N}}$	-2.460 ± 4.074

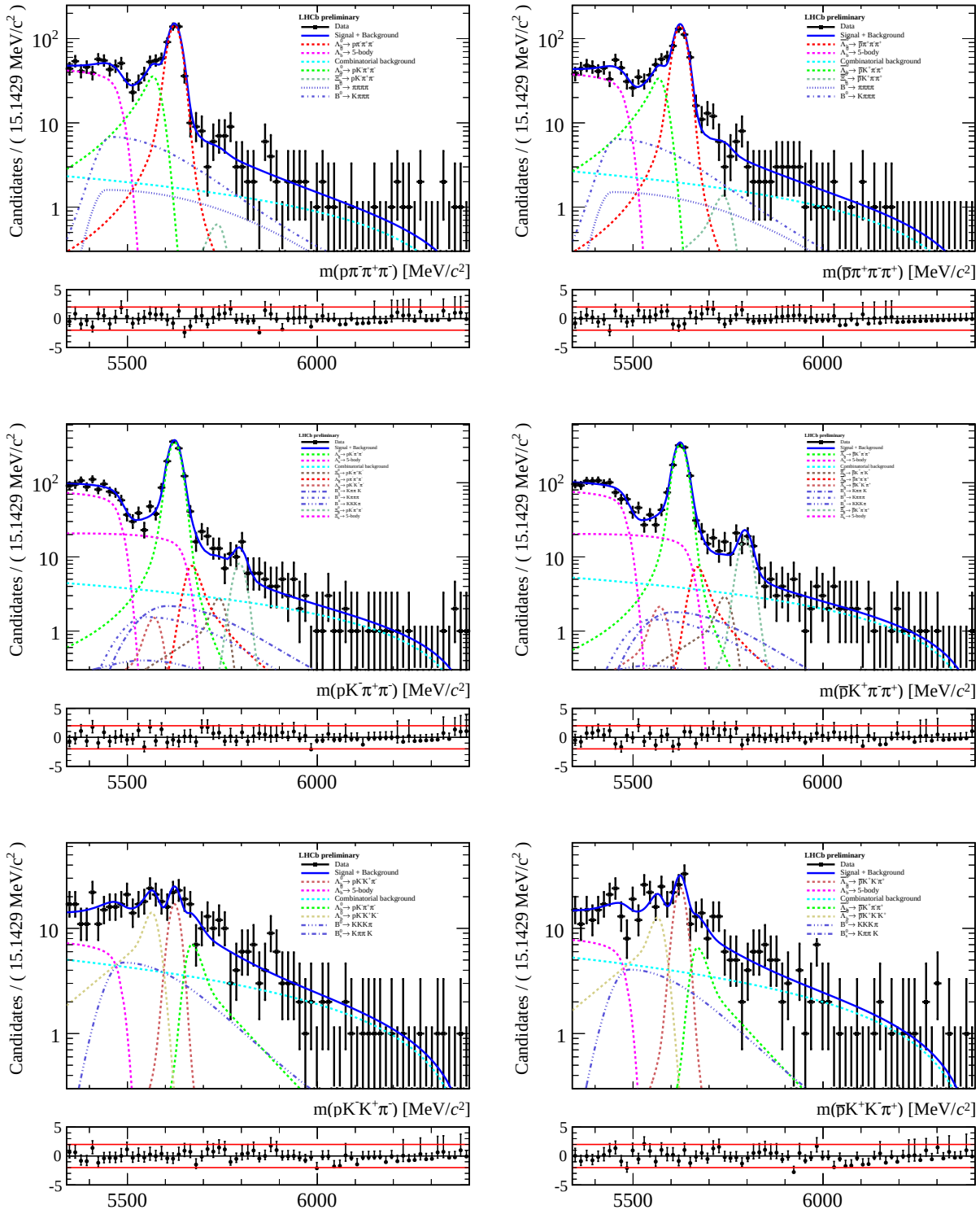

Figure 6.5: Unblinded fit results for the [from top to bottom] $X_b^0 \to p\pi\pi\pi$, $X_b^0 \to pK\pi\pi$ and $X_b^0 \to pKK\pi$ spectra using the 2011 data with $m_{ph} < 2$ GeV/c^2 phase space cut. Plots in the left-column are for the spectra with X_b^0 and on the right-column for the spectra with $\overline{X}{}_b^0$.

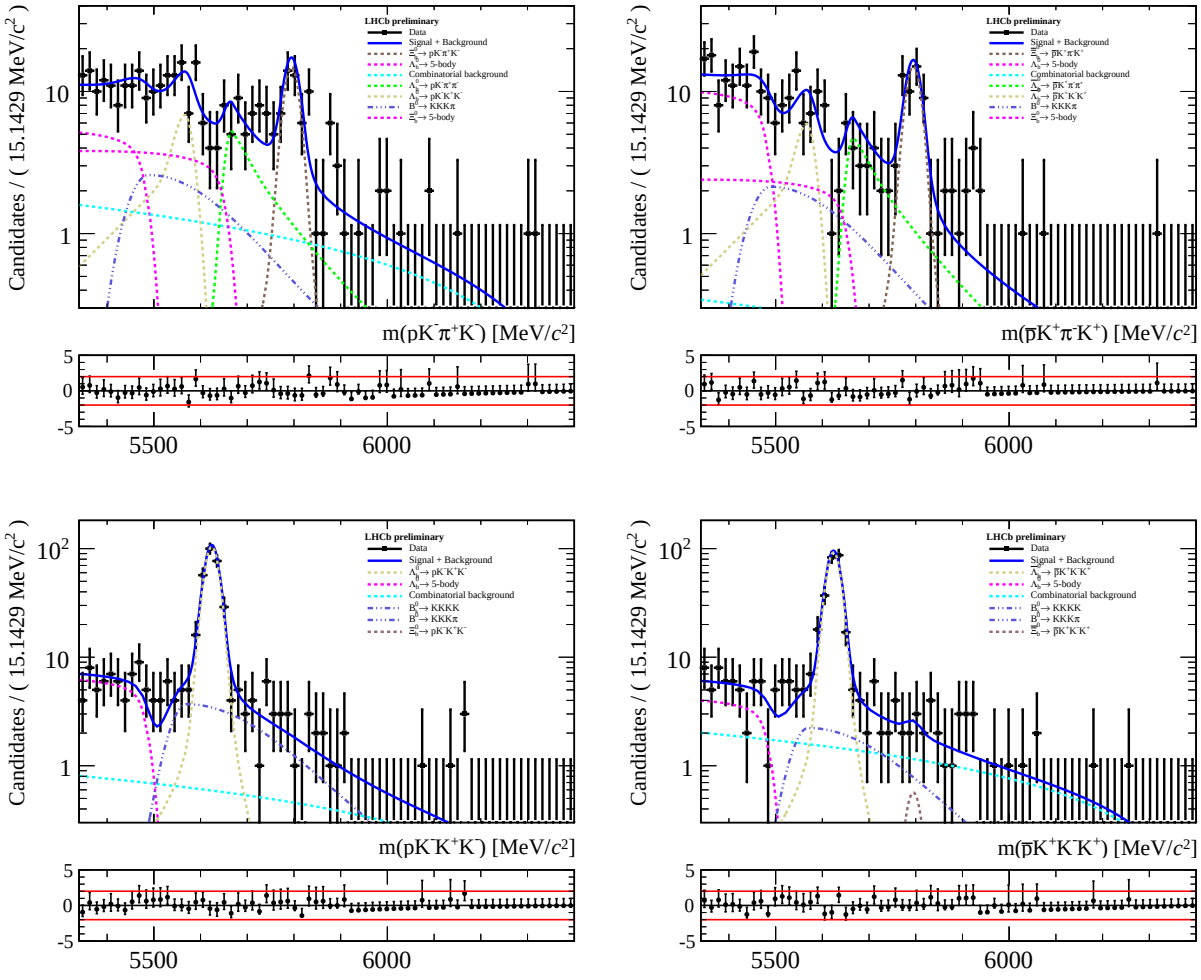

Figure 6.6: Unblinded fit results for the [top] $X_b^0 \to pK\pi K$ and [bottom] $X_b^0 \to pKKK$ spectra using the 2011 data with $m_{ph} < 2$ GeV/c^2 phase space cut. Plots in the left-column are for the spectra with X_b^0 and on the right-column for the spectra with $\overline{X}_b^0$.

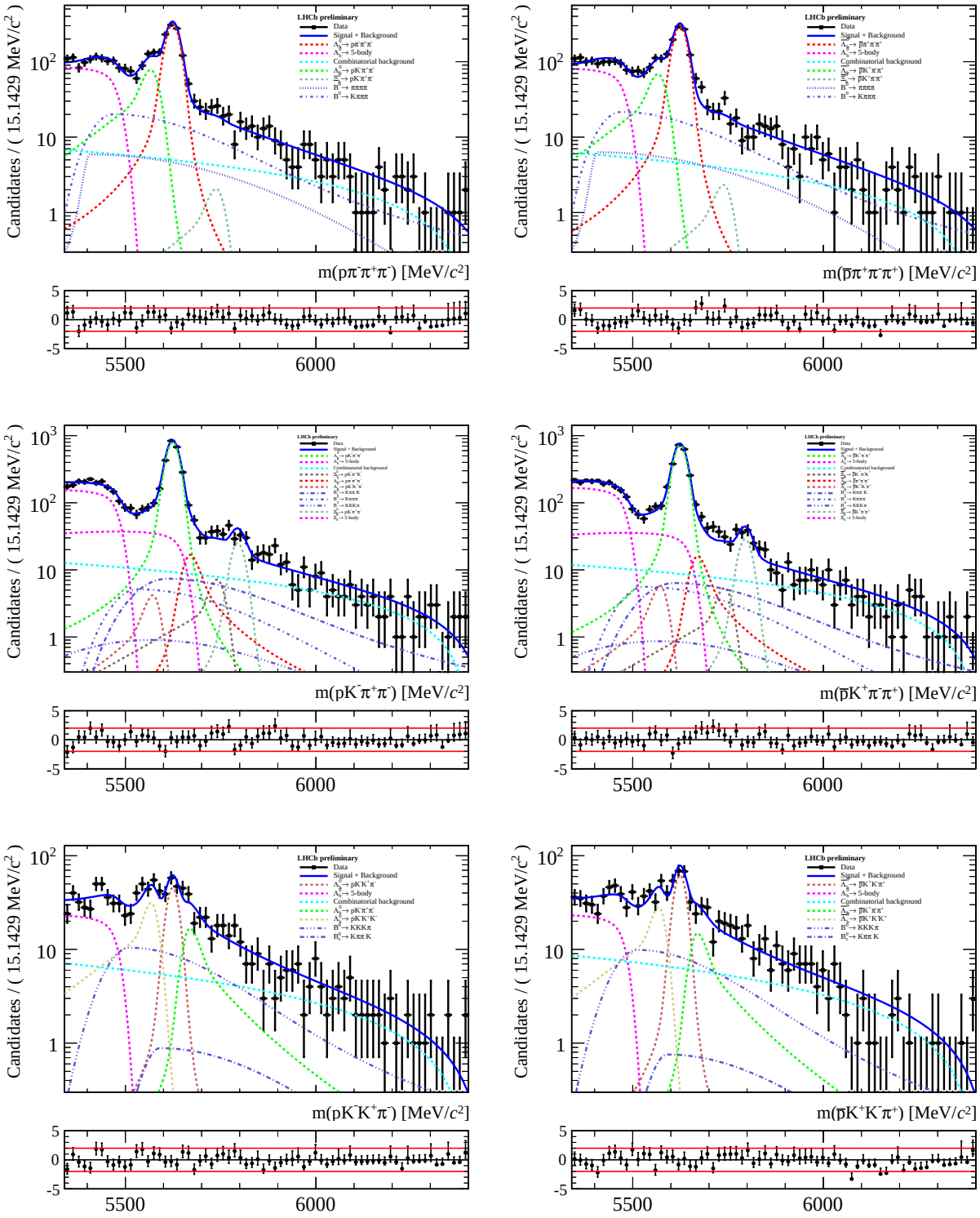

Figure 6.7: Unblinded fit results for the [from top to bottom] $X_b^0 \to p\pi\pi\pi$, $X_b^0 \to pK\pi\pi$ and $X_b^0 \to pKK\pi$ spectra using the 2012 data with $m_{ph} < 2$ GeV/c^2 phase space cut. Plots in the left-column are for the spectra with X_b^0 and on the right-column for the spectra with $\overline{X}_b^0$.

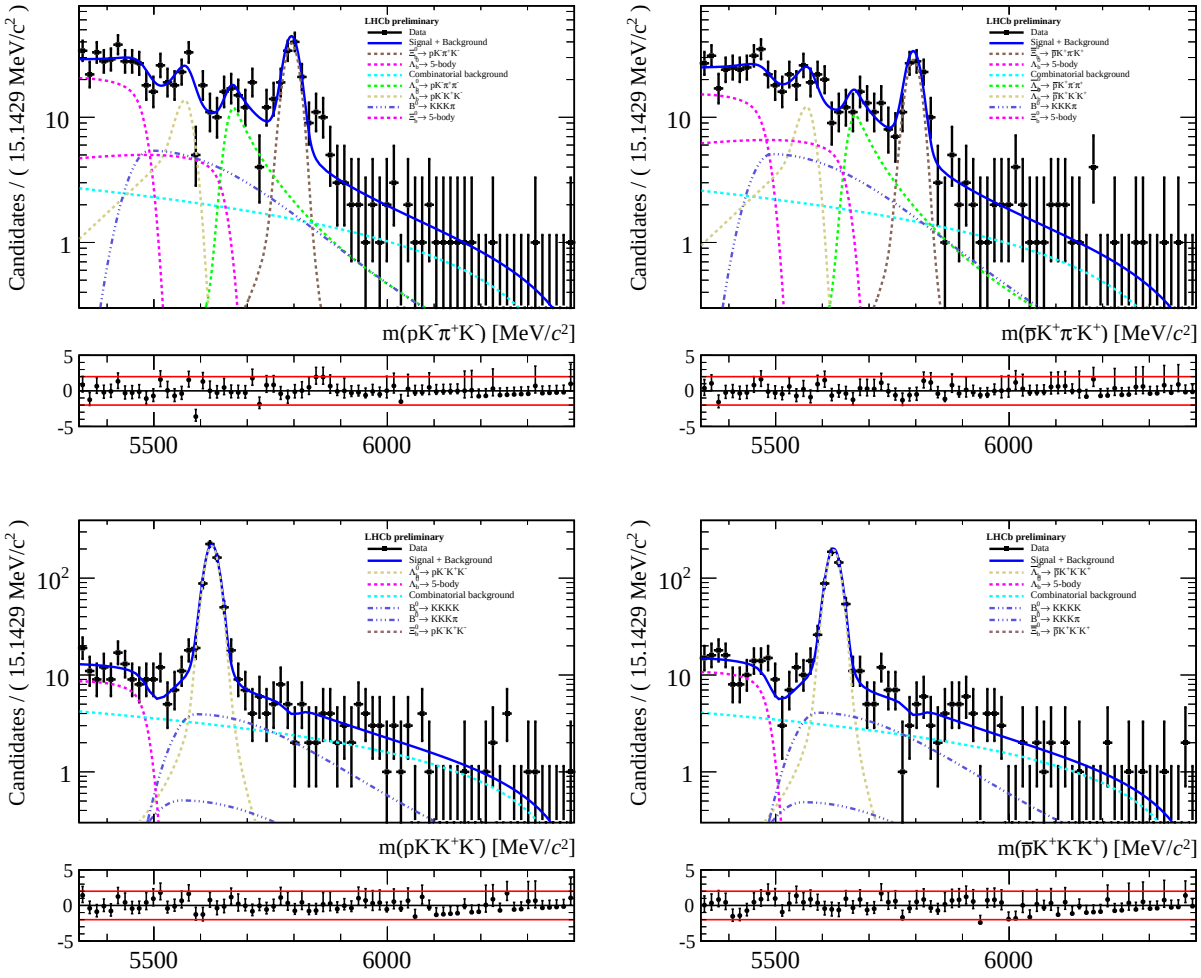

Figure 6.8: Unblinded fit results for the [top] $X_b^0 \to pK\pi K$ and [bottom] $X_b^0 \to pKKK$ spectra using the 2012 data with $m_{ph} < 2$ GeV/c^2 phase space cut. Plots in the left-column are for the spectra with X_b^0 and on the right-column for the spectra with $\overline{X}_b^0$.

Table 6.4: The *CP* asymmetry observables obtained from the unblinded results of the fit to the data with $m_{ph} < 2$ GeV/c^2 phase space cut in the charmless spectra.

CP asymmetry observable	Value
Observables for 2011 spectra:	
$\mathcal{A}^{\rm raw}$ ($\Lambda_b^0 \to p\pi\pi\pi$)	0.017 ± 0.038
$\mathcal{A}^{\rm raw}$ ($\Lambda_b^0 \to pK\pi\pi$)	0.037 ± 0.024
$\mathcal{A}^{\rm raw}$ ($\Lambda_b^0 \to pKK\pi$)	-0.174 ± 0.132
$\mathcal{A}^{\rm raw}$ ($\Lambda_b^0 \to pKKK$)	0.056 ± 0.045
$\mathcal{A}^{\rm raw}$ ($\Xi_b^0 \to pK\pi\pi$)	-0.366 ± 0.160
$\mathcal{A}^{\rm raw}$ ($\Xi_b^0 \to pK\pi K$)	-0.024 ± 0.128
$\Delta\mathcal{A}^{CP} = \mathcal{A}^{\rm raw}$ ($\Lambda_b^0 \to p\pi\pi\pi$) - $\mathcal{A}^{\rm raw}$ ($\Lambda_b^0 \to (\Lambda_c^+ \to p\pi\pi)\pi$)	-0.012 ± 0.048
$\Delta\mathcal{A}^{CP} = \mathcal{A}^{\rm raw}$ ($\Lambda_b^0 \to pK\pi\pi$) - $\mathcal{A}^{\rm raw}$ ($\Lambda_b^0 \to (\Lambda_c^+ \to pK\pi)\pi$)	0.019 ± 0.026
$\Delta\mathcal{A}^{CP} = \mathcal{A}^{\rm raw}$ ($\Lambda_b^0 \to pKK\pi$) - $\mathcal{A}^{\rm raw}$ ($\Lambda_b^0 \to (\Lambda_c^+ \to p\pi\pi)\pi$)	-0.203 ± 0.135
$\Delta\mathcal{A}^{CP} = \mathcal{A}^{\rm raw}$ ($\Lambda_b^0 \to pKKK$) - $\mathcal{A}^{\rm raw}$ ($\Lambda_b^0 \to (\Lambda_c^+ \to pK\pi)\pi$)	0.039 ± 0.046
$\Delta\mathcal{A}^{CP} = \mathcal{A}^{\rm raw}$ ($\Xi_b^0 \to pK\pi\pi$) - $\mathcal{A}^{\rm raw}$ ($\Xi_b^0 \to (\Xi_c^+ \to pK\pi)\pi$)	-0.385 ± 0.179
$\Delta\mathcal{A}^{CP} = \mathcal{A}^{\rm raw}$ ($\Xi_b^0 \to pK\pi K$) - $\mathcal{A}^{\rm raw}$ ($\Xi_b^0 \to (\Xi_c^+ \to pK\pi)\pi$)	-0.043 ± 0.151
Observables for 2012 spectra:	
$\mathcal{A}^{\rm raw}$ ($\Lambda_b^0 \to p\pi\pi\pi$)	0.025 ± 0.026
$\mathcal{A}^{\rm raw}$ ($\Lambda_b^0 \to pK\pi\pi$)	0.058 ± 0.016
$\mathcal{A}^{\rm raw}$ ($\Lambda_b^0 \to pKK\pi$)	-0.153 ± 0.079
$\mathcal{A}^{\rm raw}$ ($\Lambda_b^0 \to pKKK$)	0.053 ± 0.031
$\mathcal{A}^{\rm raw}$ ($\Xi_b^0 \to pK\pi\pi$)	-0.065 ± 0.124
$\mathcal{A}^{\rm raw}$ ($\Xi_b^0 \to pK\pi K$)	0.144 ± 0.085
$\Delta\mathcal{A}^{CP} = \mathcal{A}^{\rm raw}$ ($\Lambda_b^0 \to p\pi\pi\pi$) - $\mathcal{A}^{\rm raw}$ ($\Lambda_b^0 \to (\Lambda_c^+ \to p\pi\pi)\pi$)	0.025 ± 0.032
$\Delta\mathcal{A}^{CP} = \mathcal{A}^{\rm raw}$ ($\Lambda_b^0 \to pK\pi\pi$) - $\mathcal{A}^{\rm raw}$ ($\Lambda_b^0 \to (\Lambda_c^+ \to pK\pi)\pi$)	0.047 ± 0.017
$\Delta\mathcal{A}^{CP} = \mathcal{A}^{\rm raw}$ ($\Lambda_b^0 \to pKK\pi$) - $\mathcal{A}^{\rm raw}$ ($\Lambda_b^0 \to (\Lambda_c^+ \to p\pi\pi)\pi$)	-0.153 ± 0.081
$\Delta\mathcal{A}^{CP} = \mathcal{A}^{\rm raw}$ ($\Lambda_b^0 \to pKKK$) - $\mathcal{A}^{\rm raw}$ ($\Lambda_b^0 \to (\Lambda_c^+ \to pK\pi)\pi$)	0.042 ± 0.032
$\Delta\mathcal{A}^{CP} = \mathcal{A}^{\rm raw}$ ($\Xi_b^0 \to pK\pi\pi$) - $\mathcal{A}^{\rm raw}$ ($\Xi_b^0 \to (\Xi_c^+ \to pK\pi)\pi$)	-0.062 ± 0.135
$\Delta\mathcal{A}^{CP} = \mathcal{A}^{\rm raw}$ ($\Xi_b^0 \to pK\pi K$) - $\mathcal{A}^{\rm raw}$ ($\Xi_b^0 \to (\Xi_c^+ \to pK\pi)\pi$)	0.147 ± 0.100

6.1.3 Low invariant mass region of ph and $h'h''$

The third measurement intends to measure the $\Delta\mathcal{A}^{CP}$ in the phase space region of low invariant mass of $p\pi$ or pK pair and simultaneously having a low invariant mass on the pairing of the other two tracks, *i.e.* the mesonic resonance. The unblinded fit results of the simultaneous fit are shown in Figures 6.9 and 6.10 for the 2011 data, while Figures 6.11 and 6.12 are for the 2012 data. The extracted yields are summarized in Table 6.5 and the measured CP observables are listed in Table 6.6.

Table 6.5: Measured yields of the charmless and charmed modes of the simultaneous fit to the 2011 and 2012 data with $m_{ph} < 2\,\text{GeV}/c^2$ and $m_{h'h''} < \sim 1.65$ GeV/c^2 phase space cuts in the charmless modes.

Yield parameter (in Λ_b^0/Ξ_b^0 spectra)	Value	Yield parameter (in $\overline{\Lambda}_b^0/\overline{\Xi}_b^0$ spectra)	Value
Yields for 2011 spectra:			
$\mathcal{N}$ (2011 Signal $\Lambda_b^0 \to p\pi\pi\pi$)	140.385 ± 13.340	$\bar{\mathcal{N}}$	124.187 ± 12.493
$\mathcal{N}$ (2011 Signal $\Lambda_b^0 \to pK\pi\pi$)	711.650 ± 28.578	$\bar{\mathcal{N}}$	633.825 ± 27.174
$\mathcal{N}$ (2011 Signal $\Lambda_b^0 \to pKK\pi$)	34.057 ± 7.272	$\bar{\mathcal{N}}$	28.178 ± 6.727
$\mathcal{N}$ (2011 Signal $\Lambda_b^0 \to pKKK$)	205.967 ± 12.870	$\bar{\mathcal{N}}$	170.059 ± 12.052
$\mathcal{N}$ (2011 Signal $\Xi_b^0 \to pK\pi\pi$)	4.918 ± 3.593	$\bar{\mathcal{N}}$	20.659 ± 6.159
$\mathcal{N}$ (2011 Signal $\Xi_b^0 \to pK\pi K$)	17.726 ± 5.341	$\bar{\mathcal{N}}$	21.761 ± 5.434
$\mathcal{N}$ (2011 Signal $\Xi_b^0 \to pKKK$)	0.828 ± 1.846	$\bar{\mathcal{N}}$	1.606 ± 2.406
Yields for 2012 spectra:			
$\mathcal{N}$ (2012 Signal $\Lambda_b^0 \to p\pi\pi\pi$)	319.737 ± 20.659	$\bar{\mathcal{N}}$	278.243 ± 19.834
$\mathcal{N}$ (2012 Signal $\Lambda_b^0 \to pK\pi\pi$)	1487.826 ± 41.113	$\bar{\mathcal{N}}$	1333.901 ± 38.905
$\mathcal{N}$ (2012 Signal $\Lambda_b^0 \to pKK\pi$)	73.311 ± 10.721	$\bar{\mathcal{N}}$	95.711 ± 12.029
$\mathcal{N}$ (2012 Signal $\Lambda_b^0 \to pKKK$)	386.097 ± 18.116	$\bar{\mathcal{N}}$	325.933 ± 16.991
$\mathcal{N}$ (2012 Signal $\Xi_b^0 \to pK\pi\pi$)	27.084 ± 7.623	$\bar{\mathcal{N}}$	23.143 ± 7.815
$\mathcal{N}$ (2012 Signal $\Xi_b^0 \to pK\pi K$)	50.804 ± 8.269	$\bar{\mathcal{N}}$	44.114 ± 7.840
$\mathcal{N}$ (2012 Signal $\Xi_b^0 \to pKKK$)	-0.707 ± 3.038	$\bar{\mathcal{N}}$	-0.265 ± 2.754

6.2 Statistical signal significance

We calculate the approximate statistical significance of some of the signal modes using Wilks' theorem [113] in order to determine how many standard deviations away the alternative hypothesis (the nominal fit) is from the null hypothesis of zero yields. The charmless modes $\Lambda_b^0 \to p\pi\pi\pi$, $\Lambda_b^0 \to pK\pi\pi$ and $\Lambda_b^0 \to pKKK$ are unambiguously observed as can be seen in Figures presented in Section 6.1.1. Hence, their corresponding statistical significances are no longer determined.

Separate fits are performed for the $\Lambda_b^0 \to pKK\pi$, $\Xi_b^0 \to pK\pi\pi$, $\Xi_b^0 \to pK\pi K$ and $\Xi_b^0 \to pKKK$ charmless signal modes with yields fixed to zero for both 2011 and 2012 spectra. For these modes, the logarithm of the likelihood ratio $\ln(\mathcal{L}(Y_{\text{Null}})/\mathcal{L}(Y_{\text{Max.}}))$ is obtained, where $\mathcal{L}(Y_{\text{Null}})$ is the likelihood where the signal yields are fixed to zero, while $\mathcal{L}(Y_{\text{Max.}})$ is the likelihood of the nominal fit where the yields are freely floated.

As the size of the sample approaches to infinity, the distribution of the $-2\Delta\ln\mathcal{L}$ approaches a χ^2 distribution with number of degrees-of-freedom equal to the difference in dimensionality of $\mathcal{L}(Y_{\text{Null}})$ and $\mathcal{L}(Y_{\text{Max.}})$. In principle, this is approximately equal to four in this analysis corresponding to the yield parameters of the four spectra. Hence, the probability is calculated assuming a χ^2 distribution with four degrees-of-freedom, and then the

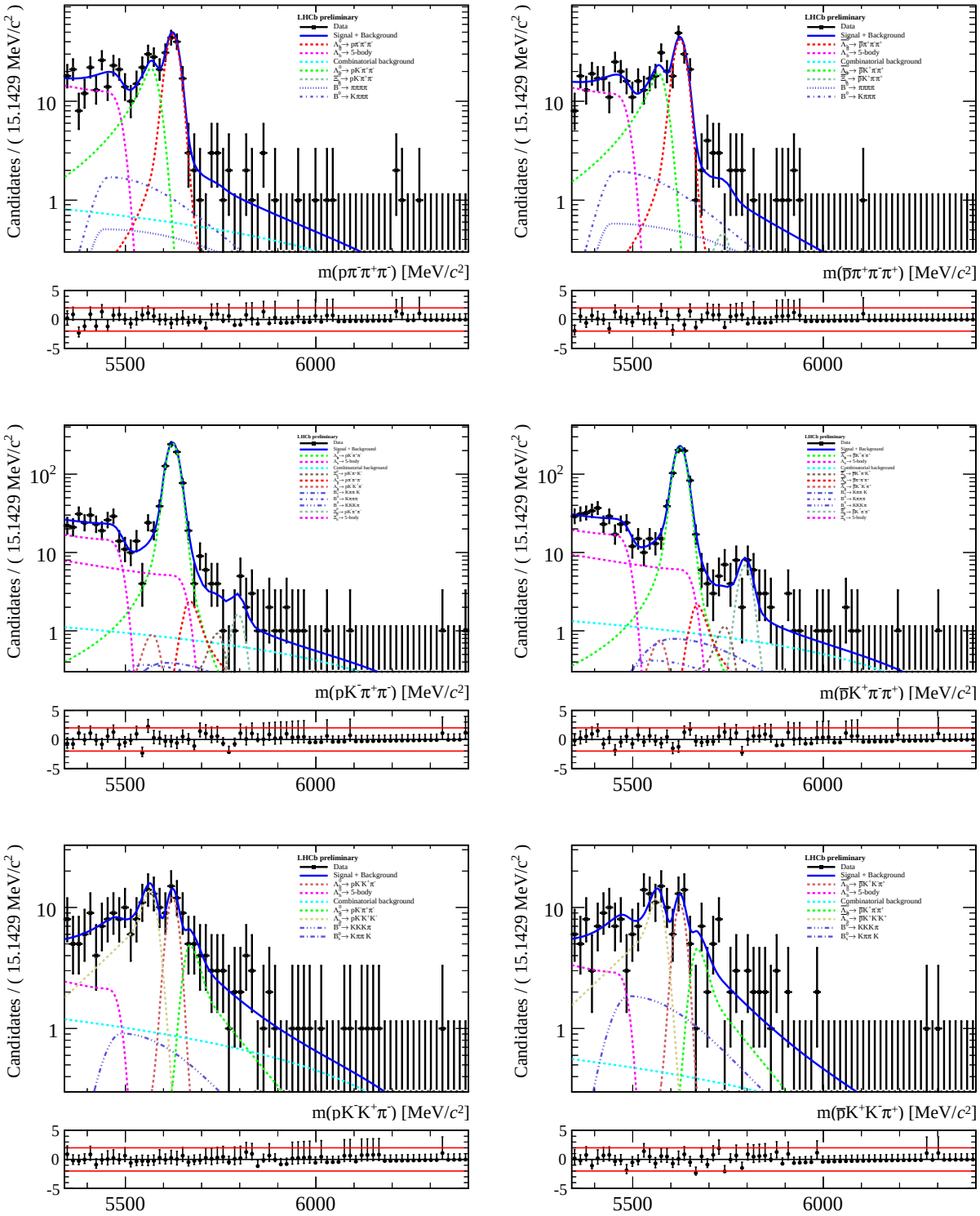

Figure 6.9: Unblinded fit results for the [from top to bottom] $X_b^0 \to p\pi\pi\pi$, $X_b^0 \to pK\pi\pi$ and $X_b^0 \to pKK\pi$ spectra using the 2011 data with $m_{ph} < 2$ GeV/c^2 and $m_{h'h''} < \sim$1.65 GeV/c^2 phase space cuts. Plots in the left-column are for the spectra with X_b^0 and on the right-column for the spectra with $\overline{X}_b^0$.

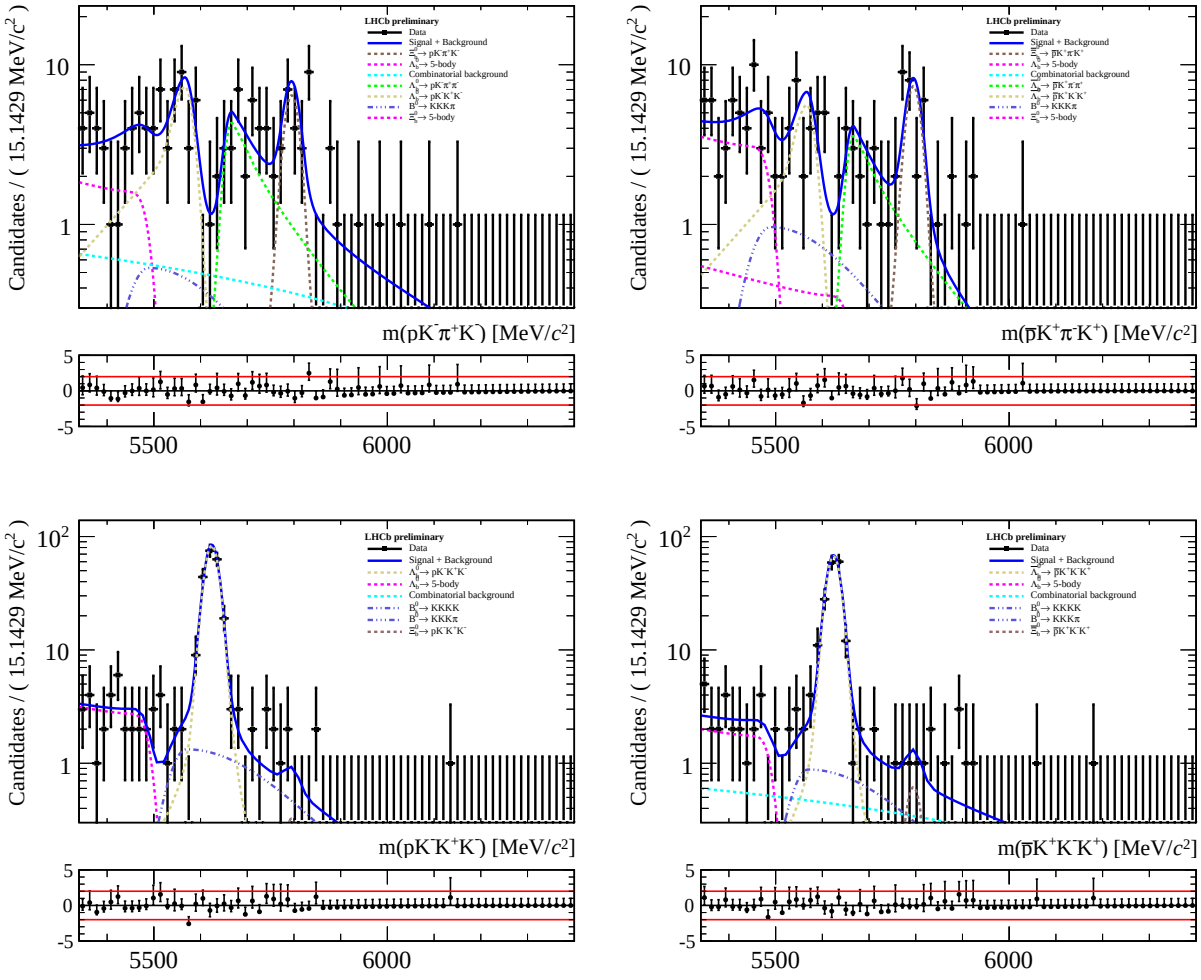

Figure 6.10: Unblinded fit results for the [top] $X_b^0 \to pK\pi K$ and [bottom] $X_b^0 \to pKKK$ spectra using the 2011 data with $m_{ph} < 2$ GeV/c^2 and $m_{h'h''} < \sim$1.65 GeV/c^2 phase space cuts. Plots in the left-column are for the spectra with X_b^0 and on the right-column for the spectra with $\overline{X}{}_b^0$.

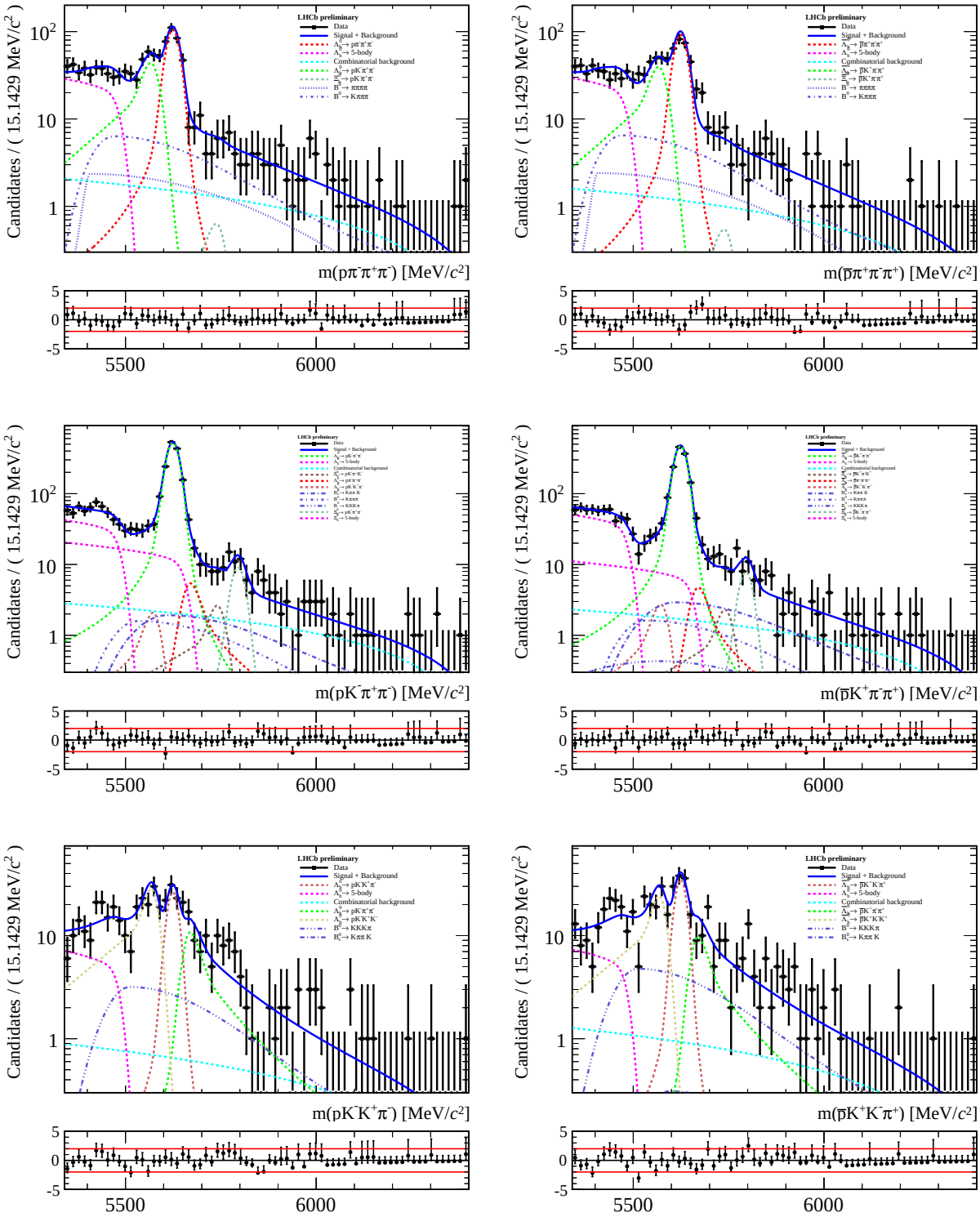

Figure 6.11: Unblinded fit results for the [from top to bottom] $X_b^0 \to p\pi\pi\pi$, $X_b^0 \to pK\pi\pi$ and $X_b^0 \to pKK\pi$ spectra using the 2012 data with $m_{ph} < 2$ GeV/c^2 and $m_{h'h''} < \sim$1.65 GeV/c^2 phase space cuts. Plots in the left-column are for the spectra with X_b^0 and on the right-column for the spectra with $\overline{X}_b^0$.

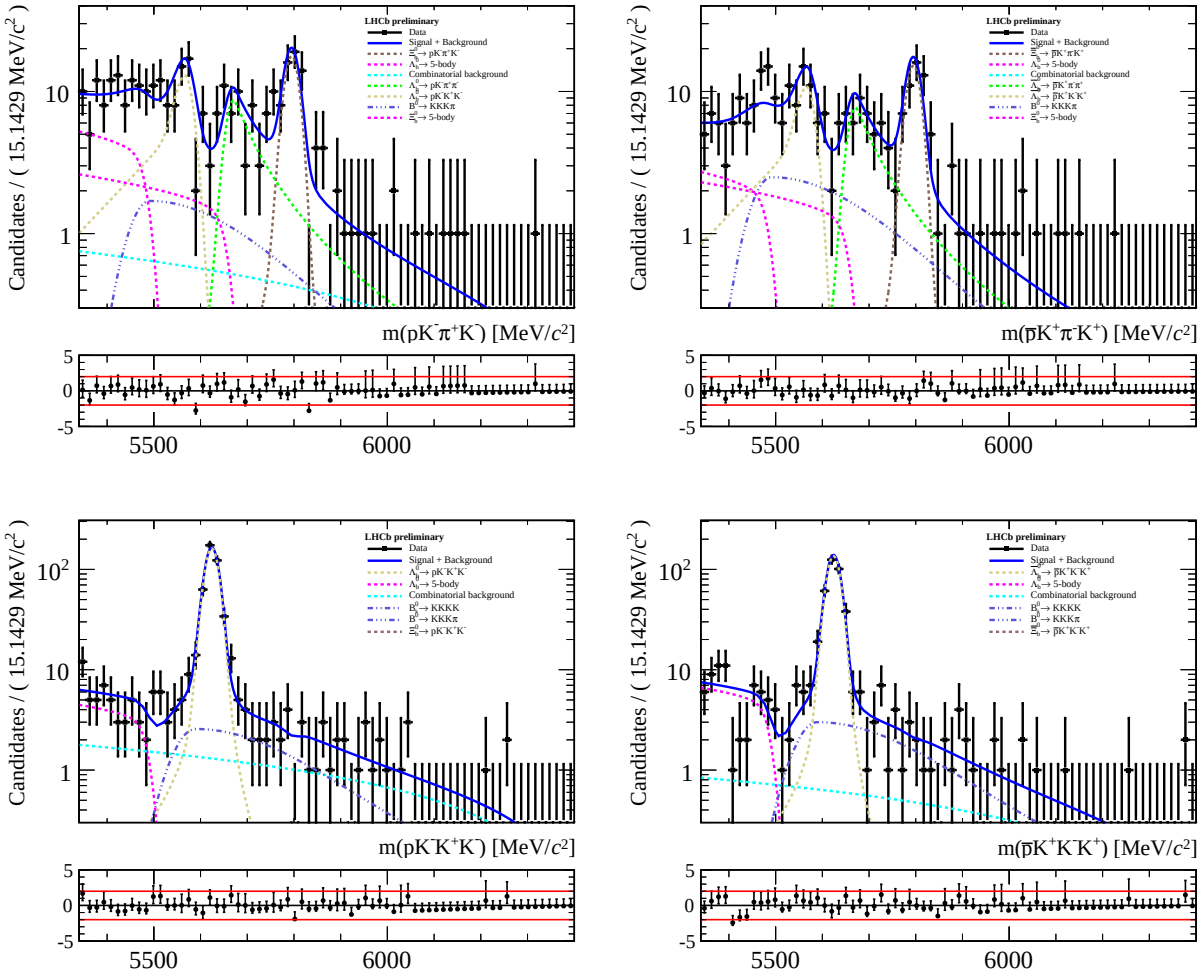

Figure 6.12: Unblinded fit results for the [top] $X_b^0 \to pK\pi K$ and [bottom] $X_b^0 \to pKKK$ spectra using the 2012 data with $m_{ph} < 2$ GeV/c^2 and $m_{h'h''} <\sim 1.65$ GeV/c^2 phase space cuts. Plots in the left-column are for the spectra with X_b^0 and on the right-column for the spectra with $\overline{X}{}_b^0$.

Table 6.6: The *CP* asymmetry observables obtained from the unblinded results of the fit to the data with $m_{ph} < 2$ GeV/c^2 and $m_{h'h''} < \sim 1.65$ GeV/c^2 phase space cuts in the charmless spectra.

CP asymmetry observable	Value
Observables for 2011 spectra:	
$\mathcal{A}^{\rm raw}$ ($\Lambda_b^0 \to p\pi\pi\pi$)	0.061 ± 0.069
$\mathcal{A}^{\rm raw}$ ($\Lambda_b^0 \to pK\pi\pi$)	0.058 ± 0.029
$\mathcal{A}^{\rm raw}$ ($\Lambda_b^0 \to pKK\pi$)	0.094 ± 0.161
$\mathcal{A}^{\rm raw}$ ($\Lambda_b^0 \to pKKK$)	0.095 ± 0.047
$\mathcal{A}^{\rm raw}$ ($\Xi_b^0 \to pK\pi\pi$)	-0.615 ± 0.251
$\mathcal{A}^{\rm raw}$ ($\Xi_b^0 \to pK\pi K$)	-0.102 ± 0.197
$\Delta\mathcal{A}^{CP} = \mathcal{A}^{\rm raw}$ ($\Lambda_b^0 \to p\pi\pi\pi$) - $\mathcal{A}^{\rm raw}$ ($\Lambda_b^0 \to (\Lambda_c^+ \to p\pi\pi)\pi$)	0.031 ± 0.075
$\Delta\mathcal{A}^{CP} = \mathcal{A}^{\rm raw}$ ($\Lambda_b^0 \to pK\pi\pi$) - $\mathcal{A}^{\rm raw}$ ($\Lambda_b^0 \to (\Lambda_c^+ \to pK\pi)\pi$)	0.040 ± 0.030
$\Delta\mathcal{A}^{CP} = \mathcal{A}^{\rm raw}$ ($\Lambda_b^0 \to pKK\pi$) - $\mathcal{A}^{\rm raw}$ ($\Lambda_b^0 \to (\Lambda_c^+ \to p\pi\pi)\pi$)	0.065 ± 0.163
$\Delta\mathcal{A}^{CP} = \mathcal{A}^{\rm raw}$ ($\Lambda_b^0 \to pKKK$) - $\mathcal{A}^{\rm raw}$ ($\Lambda_b^0 \to (\Lambda_c^+ \to pK\pi)\pi$)	0.078 ± 0.048
$\Delta\mathcal{A}^{CP} = \mathcal{A}^{\rm raw}$ ($\Xi_b^0 \to pK\pi\pi$) - $\mathcal{A}^{\rm raw}$ ($\Xi_b^0 \to (\Xi_c^+ \to pK\pi)\pi$)	-0.635 ± 0.264
$\Delta\mathcal{A}^{CP} = \mathcal{A}^{\rm raw}$ ($\Xi_b^0 \to pK\pi K$) - $\mathcal{A}^{\rm raw}$ ($\Xi_b^0 \to (\Xi_c^+ \to pK\pi)\pi$)	-0.122 ± 0.213
Observables for 2012 spectra:	
$\mathcal{A}^{\rm raw}$ ($\Lambda_b^0 \to p\pi\pi\pi$)	0.069 ± 0.048
$\mathcal{A}^{\rm raw}$ ($\Lambda_b^0 \to pK\pi\pi$)	0.055 ± 0.020
$\mathcal{A}^{\rm raw}$ ($\Lambda_b^0 \to pKK\pi$)	-0.133 ± 0.095
$\mathcal{A}^{\rm raw}$ ($\Lambda_b^0 \to pKKK$)	0.084 ± 0.035
$\mathcal{A}^{\rm raw}$ ($\Xi_b^0 \to pK\pi\pi$)	0.078 ± 0.223
$\mathcal{A}^{\rm raw}$ ($\Xi_b^0 \to pK\pi K$)	0.070 ± 0.121
$\Delta\mathcal{A}^{CP} = \mathcal{A}^{\rm raw}$ ($\Lambda_b^0 \to p\pi\pi\pi$) - $\mathcal{A}^{\rm raw}$ ($\Lambda_b^0 \to (\Lambda_c^+ \to p\pi\pi)\pi$)	0.069 ± 0.051
$\Delta\mathcal{A}^{CP} = \mathcal{A}^{\rm raw}$ ($\Lambda_b^0 \to pK\pi\pi$) - $\mathcal{A}^{\rm raw}$ ($\Lambda_b^0 \to (\Lambda_c^+ \to pK\pi)\pi$)	0.043 ± 0.020
$\Delta\mathcal{A}^{CP} = \mathcal{A}^{\rm raw}$ ($\Lambda_b^0 \to pKK\pi$) - $\mathcal{A}^{\rm raw}$ ($\Lambda_b^0 \to (\Lambda_c^+ \to p\pi\pi)\pi$)	-0.133 ± 0.097
$\Delta\mathcal{A}^{CP} = \mathcal{A}^{\rm raw}$ ($\Lambda_b^0 \to pKKK$) - $\mathcal{A}^{\rm raw}$ ($\Lambda_b^0 \to (\Lambda_c^+ \to pK\pi)\pi$)	0.073 ± 0.035
$\Delta\mathcal{A}^{CP} = \mathcal{A}^{\rm raw}$ ($\Xi_b^0 \to pK\pi\pi$) - $\mathcal{A}^{\rm raw}$ ($\Xi_b^0 \to (\Xi_c^+ \to pK\pi)\pi$)	0.081 ± 0.229
$\Delta\mathcal{A}^{CP} = \mathcal{A}^{\rm raw}$ ($\Xi_b^0 \to pK\pi K$) - $\mathcal{A}^{\rm raw}$ ($\Xi_b^0 \to (\Xi_c^+ \to pK\pi)\pi$)	0.073 ± 0.132

probability is expressed in terms of number of standard deviations of a unit Gaussian. We are using the TMath::NormQuantile() routine of ROOT toolkit to calculate the number of standard deviations given the probability. However, due to numerical precision limit, only the result of $\Xi_b^0 \to pKKK$ has been calculated this way. For large values of $-2\Delta\ln\mathcal{L}$, the probability in terms of number of standard deviations of unit Gaussian is approximately equal to $\sqrt{-2\Delta\ln\mathcal{L}}$. For the other three modes, we used this approach.

Table 6.7 summarizes the measured statistical significance of the four modes. The $\Lambda_b^0 \to pKK\pi$, $\Xi_b^0 \to pK\pi\pi$ and $\Xi_b^0 \to pK\pi K$ are observed with more than 5 standard deviations of statistical significance from the null hypothesis, while we found that $\Xi_b^0 \to pKKK$ is compatible with no signal at 0.2 standard deviations.

6.3 Determination of fit biases

In order to check for possible fit biases linked to the global fit strategy, pseudo-experiments are generated using the nominal fit results. The central values and uncertainties of the fit

Table 6.7: Statistical significances of $\Lambda_b^0 \to pKK\pi$, $\Xi_b^0 \to pK\pi\pi$, $\Xi_b^0 \to pK\pi K$ and $\Xi_b^0 \to pKKK$ calculated using Wilks' theorem.

Charmless mode	Statistical siginificance (in σ)
$\Lambda_b^0 \to pKK\pi$	24.2
$\Xi_b^0 \to pK\pi\pi$	12.4
$\Xi_b^0 \to pK\pi K$	19.7
$\Xi_b^0 \to pKKK$	0.2

parameters of the model are obtained from the nominal fit to data using the full phase space sample. In each pseudo-experiment, MC data are produced in accordance to the measured uncertainties of the fit parameters and its correlations. Around 600 independent MC pseudo-experiments are produced and fitted back with the same model. The pull distributions of the $\Delta\mathcal{A}^{CP}$s, fitted with a Gaussian function, are shown in Figures 6.13 and 6.14. As summarized in Table 6.8, the pull distributions of the $\Delta\mathcal{A}^{CP}$ quantities are well-described by a unit Gaussian and no biases were observed. Also gathered in Table 6.8 are the results of the Gaussian fit to the pull distributions of the $\mathcal{A}^{\text{raw}}$ quantities. We observed no biases as well on these observables.

Table 6.8: Summary of the Gaussian means and widths of the pull distributions of the $\mathcal{A}^{\text{raw}}$ and $\Delta\mathcal{A}^{CP}$ measurements.

Observable	2011		2012	
	μ	σ	μ	σ
$\mathcal{A}^{\text{raw}}$ $(\Lambda_b^0 \to p\pi\pi\pi)$	0.067±0.040	1.010±0.028	-0.008±0.038	0.960±0.027
$\mathcal{A}^{\text{raw}}$ $(\Lambda_b^0 \to pK\pi\pi)$	-0.004±0.039	0.984±0.027	-0.038±0.038	0.969±0.027
$\mathcal{A}^{\text{raw}}$ $(\Lambda_b^0 \to pKK\pi)$	0.060±0.038	0.956±0.027	-0.007±0.040	1.014±0.028
$\mathcal{A}^{\text{raw}}$ $(\Lambda_b^0 \to pKKK)$	0.033±0.039	0.994±0.028	-0.012±0.038	0.964±0.027
$\mathcal{A}^{\text{raw}}$ $(\Xi_b^0 \to pK\pi\pi)$	0.001±0.037	0.940±0.026	-0.038±0.040	1.007±0.028
$\mathcal{A}^{\text{raw}}$ $(\Xi_b^0 \to pK\pi K)$	0.025±0.040	1.011±0.028	0.037±0.040	1.014±0.028
$\mathcal{A}^{\text{raw}}$ $(\Lambda_b^0 \to (\Lambda_c^+ \to p\pi\pi)\pi)$	0.026±0.039	0.981±0.027	0.026±0.041	1.029±0.029
$\mathcal{A}^{\text{raw}}$ $(\Lambda_b^0 \to (\Lambda_c^+ \to pK\pi)\pi)$	-0.064±0.041	1.036±0.029	-0.013±0.040	1.006±0.028
$\mathcal{A}^{\text{raw}}$ $(\Xi_b^0 \to (\Xi_c^+ \to pK\pi)\pi)$	-0.045±0.040	1.013±0.028	-0.056±0.040	1.010±0.028
$\Delta\mathcal{A}^{CP}$ $(\Lambda_b^0 \to p\pi\pi\pi)$	0.032±0.041	1.032±0.029	-0.023±0.039	0.989±0.028
$\Delta\mathcal{A}^{CP}$ $(\Lambda_b^0 \to pK\pi\pi)$	0.020±0.038	0.972±0.027	-0.031±0.038	0.957±0.027
$\Delta\mathcal{A}^{CP}$ $(\Lambda_b^0 \to pKK\pi)$	0.051±0.037	0.948±0.027	-0.014±0.040	1.019±0.028
$\Delta\mathcal{A}^{CP}$ $(\Lambda_b^0 \to pKKK)$	0.046±0.039	0.994±0.028	-0.010±0.038	0.953±0.027
$\Delta\mathcal{A}^{CP}$ $(\Xi_b^0 \to pK\pi\pi)$	0.021±0.039	0.975±0.027	-0.015±0.041	1.027±0.029
$\Delta\mathcal{A}^{CP}$ $(\Xi_b^0 \to pK\pi K)$	0.043±0.040	1.012±0.028	0.059±0.039	0.976±0.027

6.4 Cross-checks

Cross-checks are sanity checks in order to examine whether there is a dependence of the results to different subcategories of data. No systematic uncertainty will be assigned in the discrepancy, if there are any, but rather have to be investigated and corrected. Since the 2011 and 2012 data are separated in the nominal fit, the cross-check on the different data taking

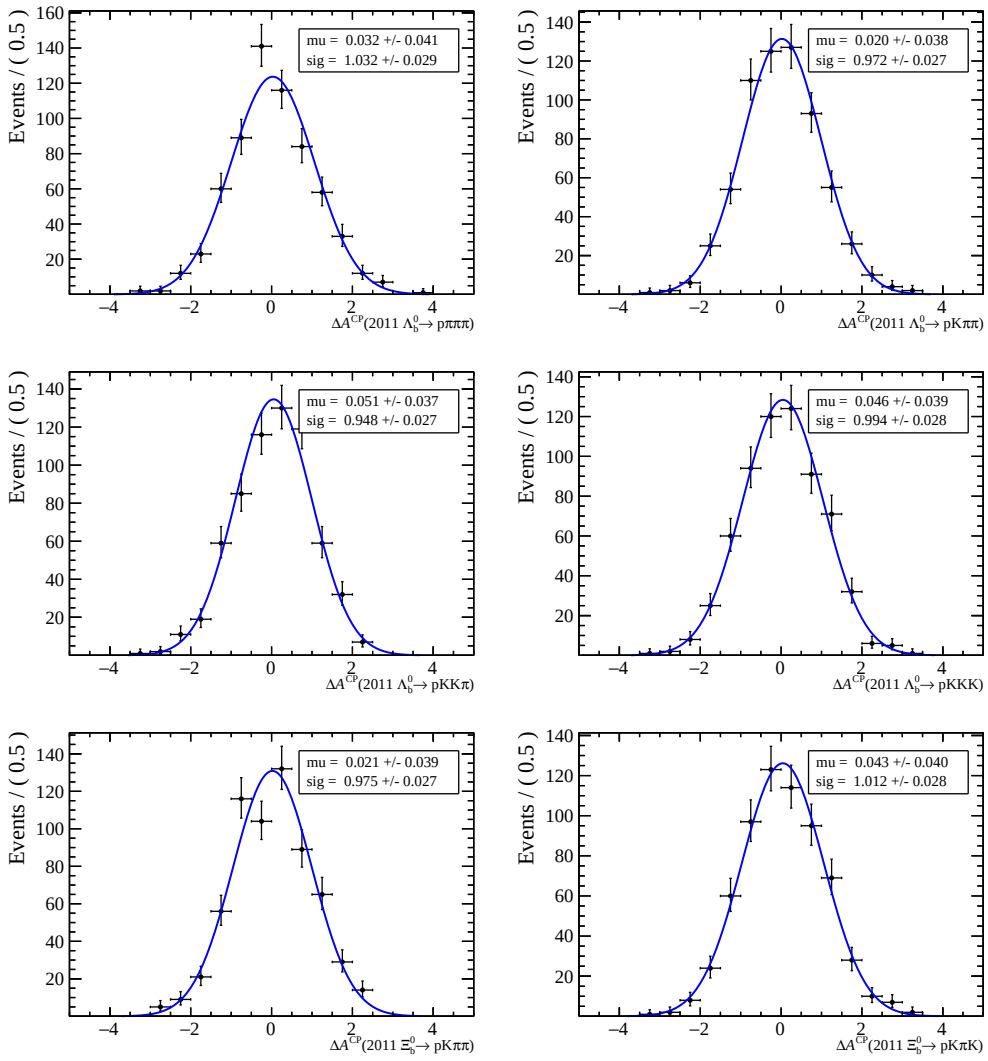

Figure 6.13: Pull distributions of the 2011 $\Delta\mathcal{A}^{CP}$ measurements obtained using about 600 MC-generated pseudo-experiments.

periods comes directly from the fit results. As listed in Section 5.11, we also performed cross-check based on the polarity of the LHCb magnet when the data were taken, and also based on whether one of the daughter tracks of the X_b^0 candidate has triggered the L0 or not. We performed the cross-checks using the full phase data, where we have enough events to allow for further splitting into different categories.

In the cross-check in terms of magnetic polarity, a new simultaneous fit was performed by splitting further the 2011 and 2012 data into two subcategories called MagUp and MagDown (referring to the direction of the magnetic field). We note that in 2011, slightly more data were taken using the MagDown configuration than MagUp, while in 2012 the two data splittings are relatively equal. Although a simultaneous fit has been performed, the signal cross-feed factors, the B physics cross-spectra constraints, the Gaussianly-constrained ratios of signal widths, the combinatorial slopes and the ARGUS parameters are set to be independent for the two subcategories. Since the yield of the dominant B physics background in each spectrum is constrained using estimates in the RHSB, then there is a need for recalculation of these numbers. The new numbers for the constraints are estimated by scaling the old constraints according to the fraction of events categorized as MagDown (or MagUp) w.r.t. to the combined data.

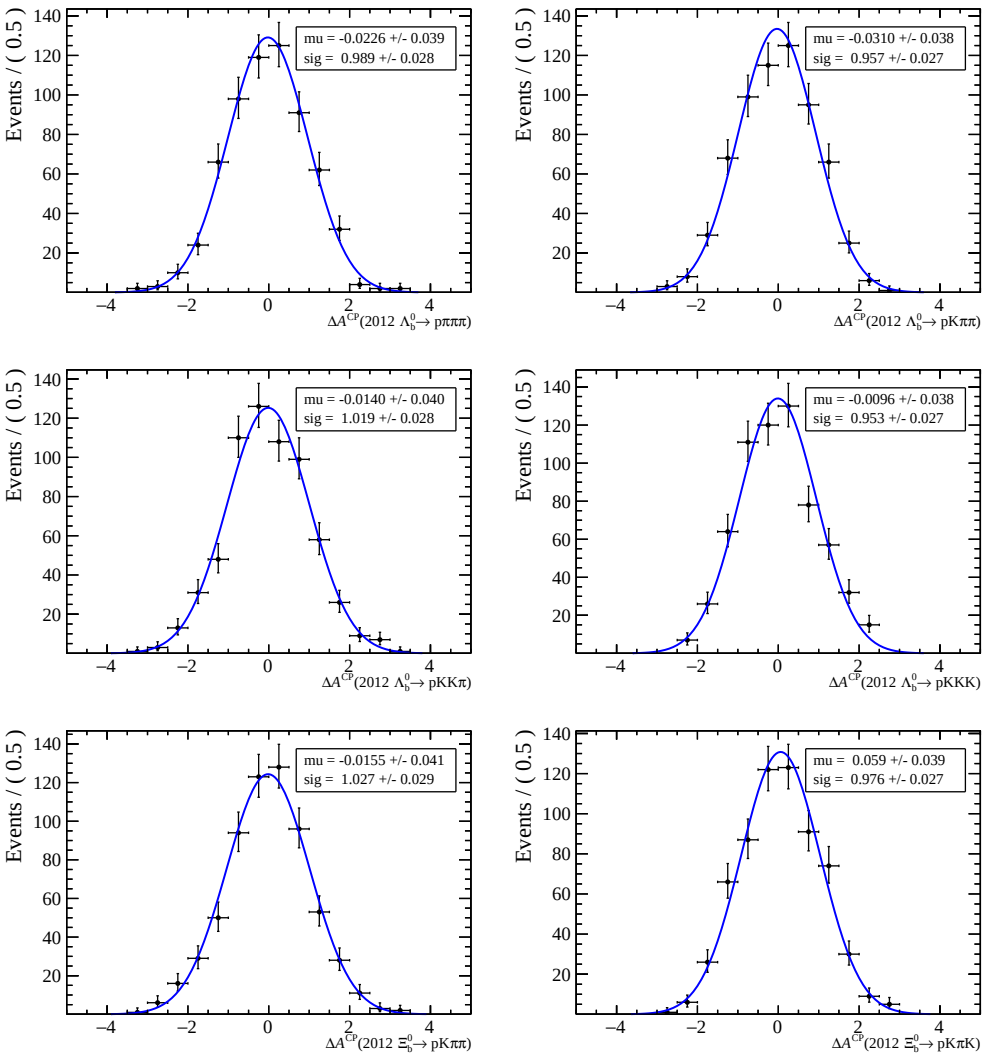

Figure 6.14: Pull distributions of the 2012 $\Delta\mathcal{A}^{CP}$ measurements obtained using about 600 MC-generated pseudo-experiments.

The cross-checks based on the L0 trigger categories are also obtained by simultaneously fitting all the split subcategories. The two subcategories are called L0 Triggered-On-Signal (TOS) events and L0 Triggered-Independent-of-Signal (TIS). As the name suggests, events that are triggered by one of the daughter particles of the X_b^0 candidate are called L0 TOS events, while events triggered by neither of the daughter particles are called L0 TIS events. Like in the case of magnet polarity splitting, the signal cross-feed factors, the B physics cross-spectra constraints, the Gaussianly-constrained ratios of signal widths, the combinatorial slopes and the ARGUS parameters are set to be independent for the two subcategories. Also, the new numbers for the B physics yield constraints are estimated by scaling the old constraints according to the fraction of events categorized as L0 TOS (or L0 TIS) w.r.t. to the combined data.

Shown in Figures 6.15 and 6.16 are the cross-checks on the $\Delta\mathcal{A}^{CP}$ measurements on the different subcategories. Note the different scales of the y-axis. The first two points in the plots, which are found to be compatible within 1.50σ, are the measurements obtained from the nominal fit to the full phase space data. The said two points are then averaged, weighted by their corresponding uncertainties. The calculated average values and the uncertainties are written in each plot and are drawn as blue lines and light blue bands. The $\Delta\mathcal{A}^{CP}$ values of

the subcategories are found be compatible within 2σ from this band. Shown at the bottom on each plot are the compatibilities of the two consecutive points, which are (aside from the first two points) the magnet polarity splitting and L0 trigger category splitting in each year. They are found to be compatible within about 2σ except for the $\Xi_b^0 \to pK\pi\pi$ magnet polarity splitting of 2011 data. However, this discrepancy could be a statistical fluctuation due to limited statistics for this mode.

6.5 Interpretation of results

This section should start with a word of caution. The unblinding of the spectra and results of this analysis happened very recently and the necessary systematics studies onto the $\Delta\mathcal{A}^{CP}$ measurements are not yet completed. The results provided here are hence given with their statistical uncertainty only. However, the analysis strategy was devised such that most of the systematic uncertainties related to the knowledge of backgrounds and signal cross-feeds are suppressed to a first approximation (actually embodied into the statistical uncertainty). On a similar note, it has been shown that the observed fit biases will induce a negligible systematic uncertainty. The remaining systematic uncertainty estimates have still to be worked out and the full understanding of the results should proceed from there. We will hence limit our interpretation to the following series of careful remarks:

- Six out of the seven decay modes searched for in this work have been observed, simultaneously for particle and antiparticle. Only the decay $\Xi_b^0 \to pKKK$ escaped the observation. On a general basis, the invariant mass fits are excellent and the establishment of the signal decays is unambiguous.

- The cross-checks performed on the consistency of the $\Delta\mathcal{A}^{CP}$ measurements by switching the magnet polarity or splitting the trigger streams do not indicate any signs of an experimental problem whatsoever. The obtained consistency satisfies the requirements which were set *a priori* before the unblinding.

- The proton/antiproton asymmetries in the combinatorial backgrounds are measured at the percent level and found to be consistent with zero. That result indicates that no experimental bias is unattended. The asymmetries for the B decays are also found vanishing, inline with former experimental results.

- On the contrary, $\Delta\mathcal{A}^{CP}$ asymmetries in the dominant charmless decays $\Lambda_b^0 \to pK\pi\pi$ and $\Lambda_b^0 \to pKKK$ are interestingly found to simultaneously depart from zero by more than 2.5σ in the low invariant mass region of the phase space as displayed in Table 6.9. A naive estimate of the simultaneous departure from the hypothesis of CP symmetry places the significance of the effect at more than three standard deviations, although a thorough estimate of both the total significance of the result is in order. This observation cries for a dedicated scrutiny of the Phase Space.

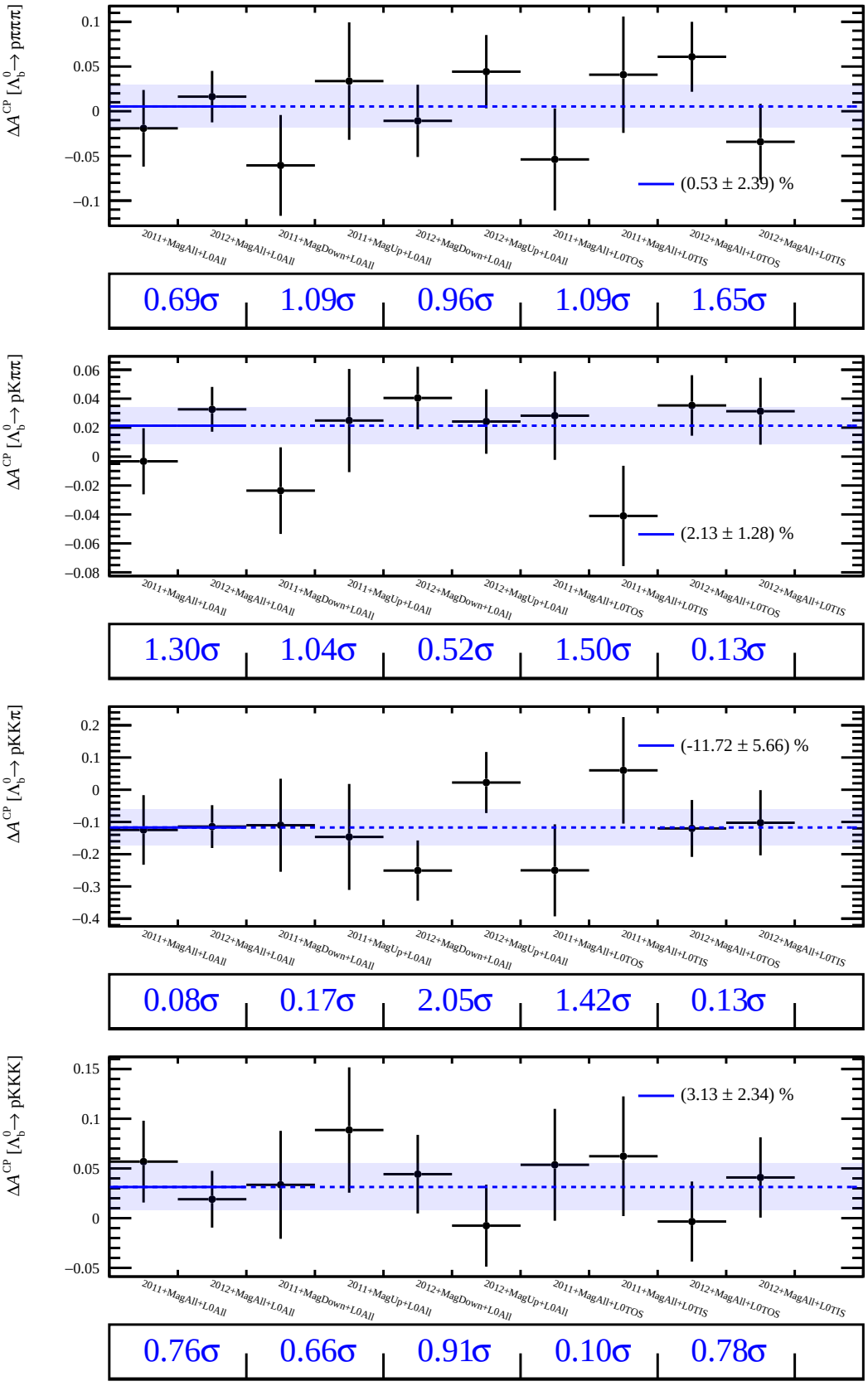

Figure 6.15: Cross-checks on the $\Delta\mathcal{A}^{CP}$ observables of the Λ_b^0 charmless decay modes on different subcategories.

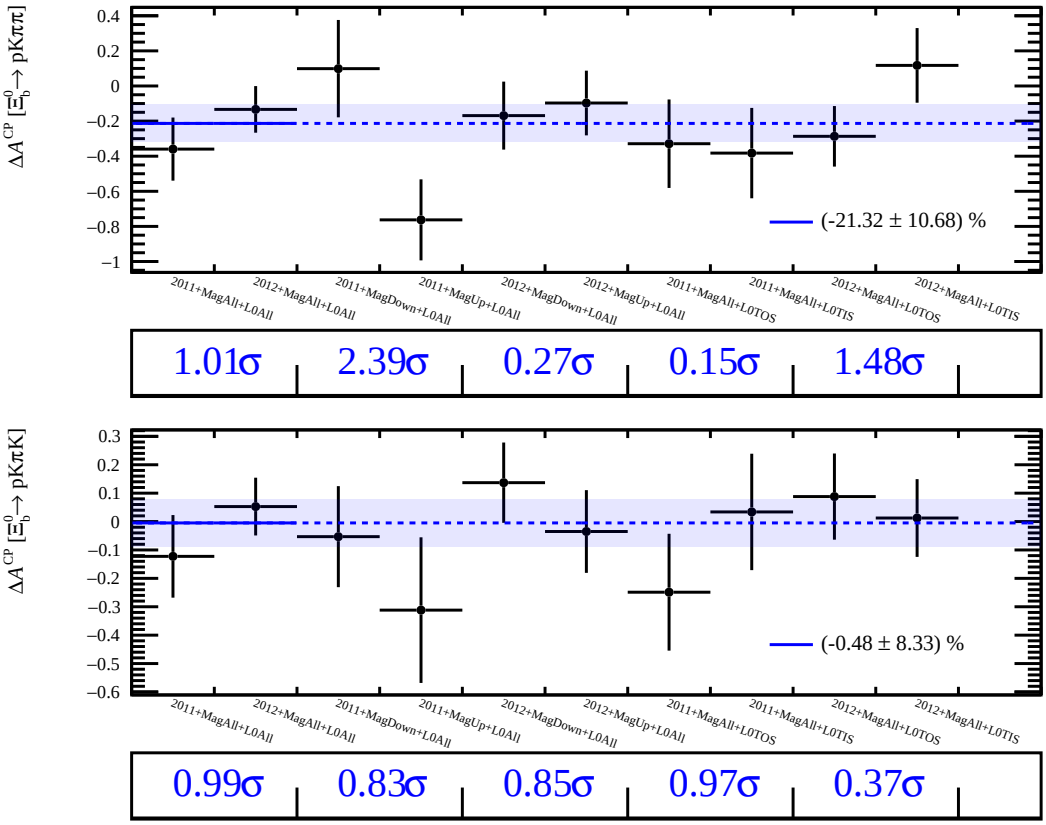

Figure 6.16: Cross-checks on the $\Delta\mathcal{A}^{CP}$ observables of the Ξ_b^0 charmless decay modes on different subcategories.

Table 6.9: Summary of the $\Delta\mathcal{A}^{CP}$ measurements combining the 2011 and 2012 results.

$\Delta\mathcal{A}^{CP}$ observable	Combined results					
	Full phase space		Low m_{ph}		Low m_{ph} & $m_{h'h''}$	
	Measurement	σ_{dev}	Measurement	σ_{dev}	Measurement	σ_{dev}
$\Delta\mathcal{A}^{CP}$ $(\Lambda_b^0 \to p\pi\pi\pi)$	0.006 ± 0.024	0.25σ	0.014 ± 0.027	0.51σ	0.058 ± 0.042	1.38σ
$\Delta\mathcal{A}^{CP}$ $(\Lambda_b^0 \to pK\pi\pi)$	0.021 ± 0.013	1.61σ	0.038 ± 0.014	2.71σ	0.043 ± 0.017	2.52σ
$\Delta\mathcal{A}^{CP}$ $(\Lambda_b^0 \to pKK\pi)$	-0.118 ± 0.056	2.10σ	-0.167 ± 0.069	2.42σ	-0.080 ± 0.083	0.96σ
$\Delta\mathcal{A}^{CP}$ $(\Lambda_b^0 \to pKKK)$	0.032 ± 0.023	1.39σ	0.041 ± 0.026	1.57σ	0.075 ± 0.028	2.67σ
$\Delta\mathcal{A}^{CP}$ $(\Xi_b^0 \to pK\pi\pi)$	-0.206 ± 0.106	1.94σ	-0.167 ± 0.108	1.54σ	-0.160 ± 0.176	0.91σ
$\Delta\mathcal{A}^{CP}$ $(\Xi_b^0 \to pK\pi K)$	-0.005 ± 0.083	0.06σ	0.089 ± 0.083	1.07σ	0.016 ± 0.111	0.14σ

Chapter 7

Summary and conclusions

The results presented in this thesis can be divided into three parts: (1) Ageing and calibration studies of the Pre-shower subdetector of LHCb have been performed; (2) Two-sided limits on the branching fraction of $B_s^0 \to K_S^0 K^+ K^-$ were provided using modified Feldman-Cousins inference using the 2011 data of LHCb; and (3) $\Delta\mathcal{A}^{CP}$ measurements on the four-body fully charged charmless decays of Λ_b^0 and Ξ_b^0 are performed using the full Run I data of LHCb.

The *a posteriori* check in the calibration status of the PS showed that at the end of 2011 data taking campaign, the calibration met the 10% absolute precision requirement. Hence, this result justified the decision of using the same set of numeric gains for the 2012 campaign. At the end of 2012, the absolute precision has slightly degraded to about 12%. The main purpose of the study was to quantify the ageing during the Run I data taking. It has been shown that the PS detector has a typical maximum ageing of 10%. This level of ageing does not require corrective action so far.

As presented in Chapter 4, the number of $B_s^0 \to K_S^0 K^+ K^-$ candidate events obtained was not enough to claim a discovery and subsequently measure the central value of the branching fraction. Instead, two-sided limits were provided using a modified Feldman-Cousins inference. Two separate measurements, based on the reconstructed K_S^0 category, were conducted and eventually combined into the following result:

$$\mathcal{B}(B_s^0 \to K_S^0 K^+ K^-) \quad \epsilon \quad [0.2, 3.4] \times 10^{-6} \quad \text{at } 90\% \text{ C.L.} . \tag{7.1}$$

The data used in this analysis correspond to about $\int \mathcal{L} = 1$ fb^{-1} collected data during the 2011 data taking. As a prospect, an ongoing analysis of the $B_{d,s}^0 \to K_S^0 h^+ h^-$ (h being a π or a K) decay modes is currently conducted in LHCb using the full Run I data.

The main analysis discussed in this thesis is the search for *CP* violation in the charmless decays of Λ_b^0 and Ξ_b^0 baryons. *CP* violation in baryon decays has not been observed to date and its first observation constitutes a physics objective of the LHCb experiment. The choice of the charmless modes conducted in this analysis is driven by the possibility of having a rich interference pattern in the baryonic intermediate resonances in addition to the mesonic resonances, possibly enhancing the particle/antiparticle decay rate asymmetry due to the *CP*-violating weak phase. Three measurements were conducted by looking in the different phase space regions, which are: (1) In the full phase space; (2) In the low invariant mass of baryonic resonance; and (3) In the low invariant mass of baryonic resonance and simultaneously low invariant mass of mesonic resonance (constructed from the other two particles). In order to cancel the production and detection asymmetries, the raw asymmetries of the charmless signal decays are compared to those measured in control channels where the *CP* violation are expected to be small to form the observables $\Delta\mathcal{A}^{CP}$. The first stage of the analysis strategy employs a blind analysis of both the signal region in the mass spectra

and the $\Delta\mathcal{A}^{CP}$ central values. This is in order to understand the different background contributions and avoid subconscious bias in the design of the analysis. The unblinded fit results and $\Delta\mathcal{A}^{CP}$ measurements are eventually presented in Chapter 6. A word of caution has to be taken as the results are given with statistical uncertainty only since the unblinding happened very recently. Some systematics, *e.g.* knowledge on backgrounds and signal cross-feeds, are however included in the fit model as external Gaussian constraints, and hence injected into the statistical uncertainty given by the fit results. Alongside, it has been shown that the observed fit biases will induce a negligible systematic uncertainty.

The results show that the $\Delta\mathcal{A}^{CP}$ measurements are compatible with zero for most of the modes under study, except for the dominant decays $\Lambda_b^0 \to pK\pi\pi$ and $\Lambda_b^0 \to pK^-K^+K^-$, where it departs from zero by more than 2.5σ when looked at the low invariant mass region of the phase space. Naively, these simultaneous departures estimate to about 3σ standard deviations from zero, and consequently cries for a dedicated scrutiny of $\Delta\mathcal{A}^{CP}$ in the phase space. In addition to the *CP* measurements, the seven charmless decay modes were all previously not seen by prior experiments. As discussed in Section 6.2, except for the $\Xi_b^0 \to pKKK$ mode, the said modes are observed unambiguously. In the near future, now that the six decay modes are established, measurements of the branching fractions will follow.

Albeit not presented in the main text, but rather in Appendix B, it is worth mentioning that a reconstruction technique dubbed "partial reconstruction technique"[a] has also been explored and developed. The idea involves reconstructing decays that proceeds through a narrow intermediate resonance and then one of the daughter particles coming from this resonance is missing. This missing particle could be any particle, but mostly neutral particles as they are difficult to reconstruct in LHCb. It has been shown that there is enough constraints to reconstruct the decay thanks to the excellent vertexing of LHCb. Particularly, the technique is commissioned on real data events to search for the well-established decay $B_s^0 \to J/\psi(\mu^+\mu^-)\eta'(\eta\pi^+\pi^-)$, where η is the missing particle. A perspective of application of this technique concerns the not yet achieved measurement of the proton/antiproton detection efficiency difference, which can be an invaluable input for further measurements of *CP* violation in *b*-baryon decays.

[a]Not to be confused with partially reconstructed backgrounds, although in both cases, one or more of the daughter tracks are not reconstructed.

Appendix A

Appendix for Chapter 5

A.1 Delta $\mathcal{A}^{\text{raw}}$

The asymmetry directly measurable from a simple counting experiment is called the raw assymetry $\mathcal{A}^{\text{raw}}$. The general form of raw asymmetry is defined as,

$$\mathcal{A}^{\text{raw}} = \frac{\epsilon\Gamma P - \bar{\epsilon}\bar{\Gamma}\bar{P}}{\epsilon\Gamma P + \bar{\epsilon}\bar{\Gamma}\bar{P}} \tag{A.1}$$

where it is driven by at least three main sources of asymmetries, namely the asymmetry on the decay rates Γ, the asymmetry of the detection efficiencies ϵ of the final tracks, and the asymmetry on the production P. These are given by the following equations:

$$\mathcal{A}^{CP} = \frac{\Gamma(X_b^0 \to f) - \bar{\Gamma}(\overline{X}_b^0 \to \bar{f})}{\Gamma(X_b^0 \to f) + \bar{\Gamma}(\overline{X}_b^0 \to \bar{f})}, \tag{A.2}$$

$$\mathcal{A}^{\text{D}} = \frac{\epsilon(h) - \bar{\epsilon}(\bar{h})}{\epsilon(h) + \bar{\epsilon}(\bar{h})}, \tag{A.3}$$

$$\mathcal{A}^{\text{P}} = \frac{P(X_b^0) - \bar{P}(\overline{X}_b^0)}{P(X_b^0) + \bar{P}(\overline{X}_b^0)} \ . \tag{A.4}$$

Expressing Equation A.1 in terms of the asymmetries in Equations A.2, A.3 and A.4 it can be shown that,

$$\mathcal{A}^{\text{raw}} = \frac{\mathcal{A}^{CP} + \mathcal{A}^{\text{P}} + \mathcal{A}^{\text{D}} + \mathcal{A}^{CP}\mathcal{A}^{\text{P}}\mathcal{A}^{\text{D}}}{1 + \mathcal{A}^{CP}\mathcal{A}^{\text{P}} + \mathcal{A}^{CP}\mathcal{A}^{\text{D}} + \mathcal{A}^{\text{P}}\mathcal{A}^{\text{D}}} \ . \tag{A.5}$$

In this analysis, we define pairs of raw asymmetries, *e.g.* raw asymmetry of the charmless modes and raw asymmetry of the charmed control modes. The two asymmetries are then subtracted to define the $\Delta\mathcal{A}^{\text{raw}}$, where we assumed that there is no CP violation in the charmed control modes. Hence, the $\Delta\mathcal{A}^{\text{raw}}$ is defined as,

$$\Delta\mathcal{A}^{\text{raw}} = \frac{\mathcal{A}^{\text{P}} + \mathcal{A}^{\text{D}}}{1 + \mathcal{A}^{\text{P}}\mathcal{A}^{\text{D}}} - \frac{\mathcal{A}^{CP}_{\text{noC}} + \mathcal{A}^{\text{P}} + \mathcal{A}^{\text{D}} + \mathcal{A}^{CP}_{\text{noC}}\mathcal{A}^{\text{P}}\mathcal{A}^{\text{D}}}{1 + \mathcal{A}^{CP}_{\text{noC}}\mathcal{A}^{\text{P}} + \mathcal{A}^{CP}_{\text{noC}}\mathcal{A}^{\text{D}} + \mathcal{A}^{\text{P}}\mathcal{A}^{\text{D}}} \ , \tag{A.6}$$

where $\mathcal{A}^{CP}_{\text{noC}}$ is the asymmetry of the charmless decay and where we assume (up to corrections of kinematic difference) that the production asymmetry and detection asymmetry are the same for the charmless and charmed modes. We take note that in the case of vanishing $\mathcal{A}^{CP}_{\text{noC}}$, the $\Delta\mathcal{A}^{\text{raw}}$ equates to zero.

A.2 PID K/π (Mis)identification Maps

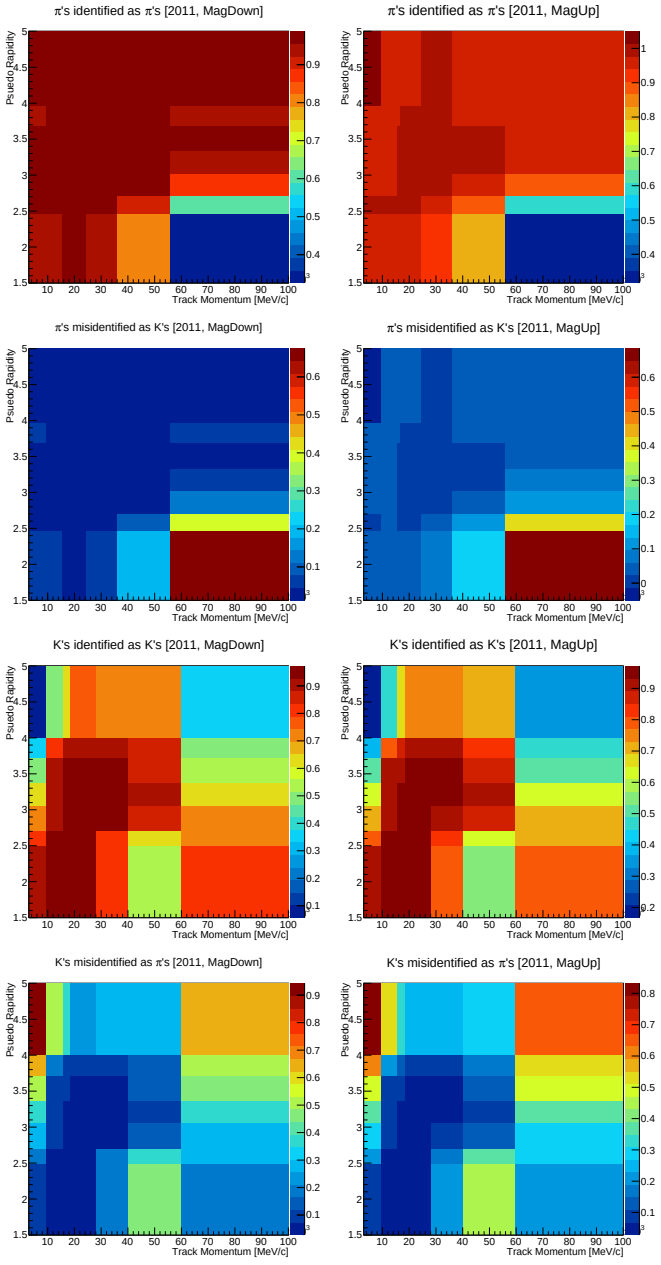

Figure A.1: Efficiency maps of [first-row] pions identified as pions, [second-row] pions misidentified as kaons, [third-row] kaons identified as kaons, and [fourth-row] kaons misidentified as pions for the optimal $\text{PID}_{K\pi}$ cut (0.55,0.55) obtained using the 2011 [first-column] MagDown and [second-column] Mag-Up calibration data.

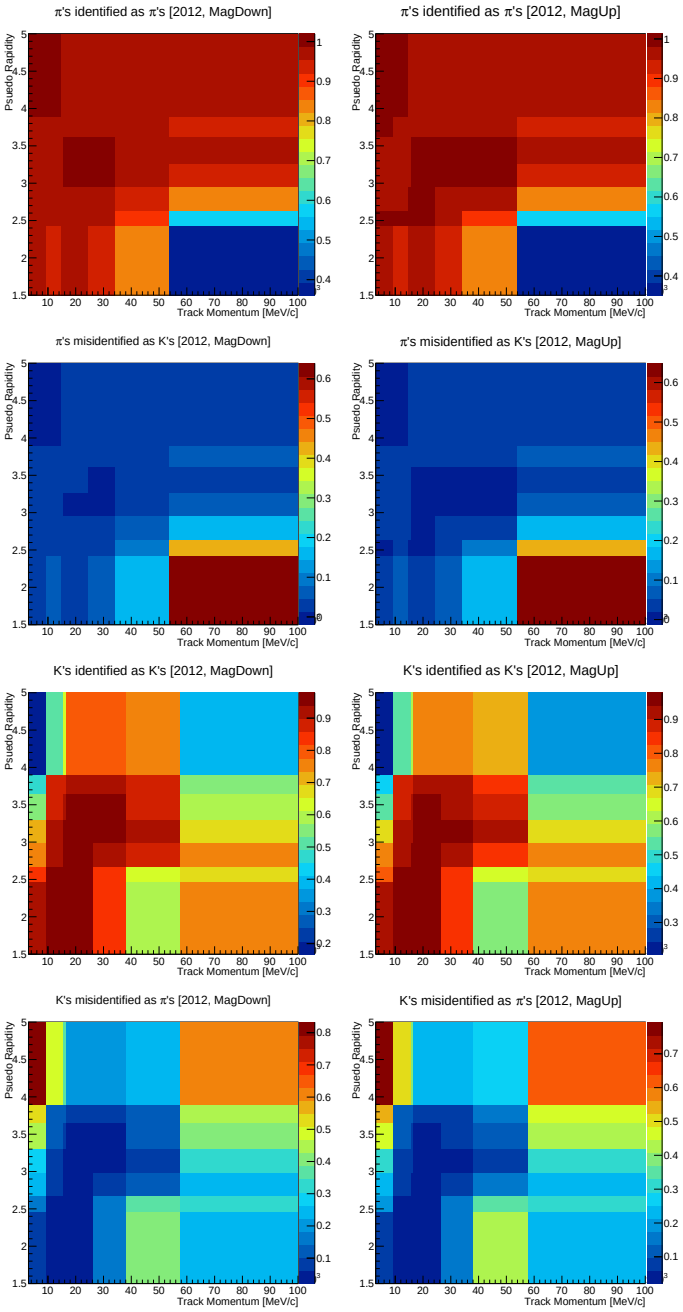

Figure A.2: Efficiency maps of [first-row] pions identified as pions, [second-row] pions misidentified as kaons, [third-row] kaons identified as kaons, and [fourth-row] kaons misidentified as pions for the optimal $\text{PID}_{K\pi}$ cut (0.55,0.55) obtained using the 2012 [first-column] MagDown and [second-column] Mag-Up calibration data.

A.3 PID p (Mis)identification Maps

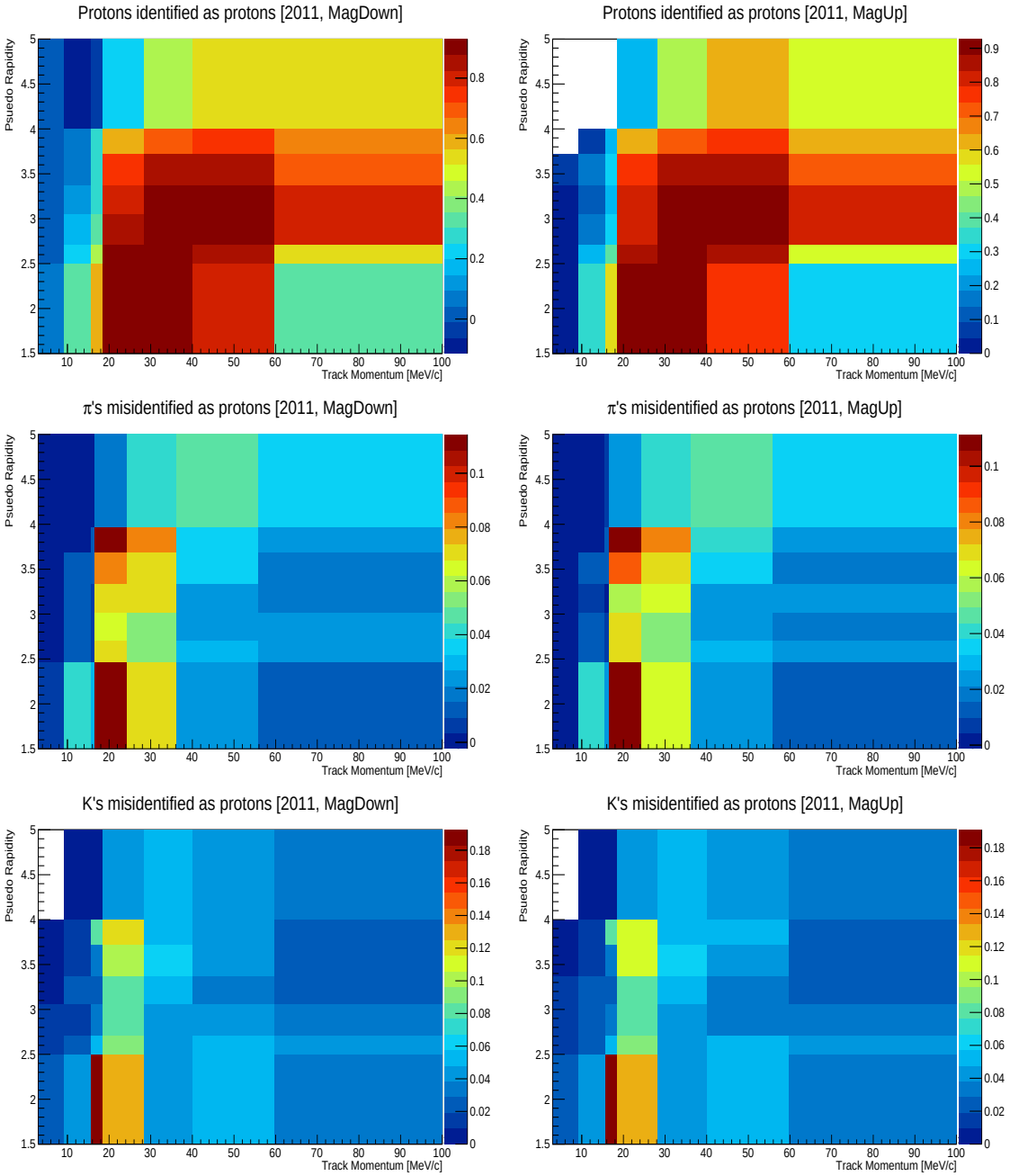

Figure A.3: Efficiency maps of [first-row] protons identified as protons, [second-row] pions misidentified as protons, and [third-row] kaons misidentified as protons for the proton ProbNN$p > 0.50$ cut obtained using the 2011 [first-column] MagDown and [second-column] Mag-Up calibration data.

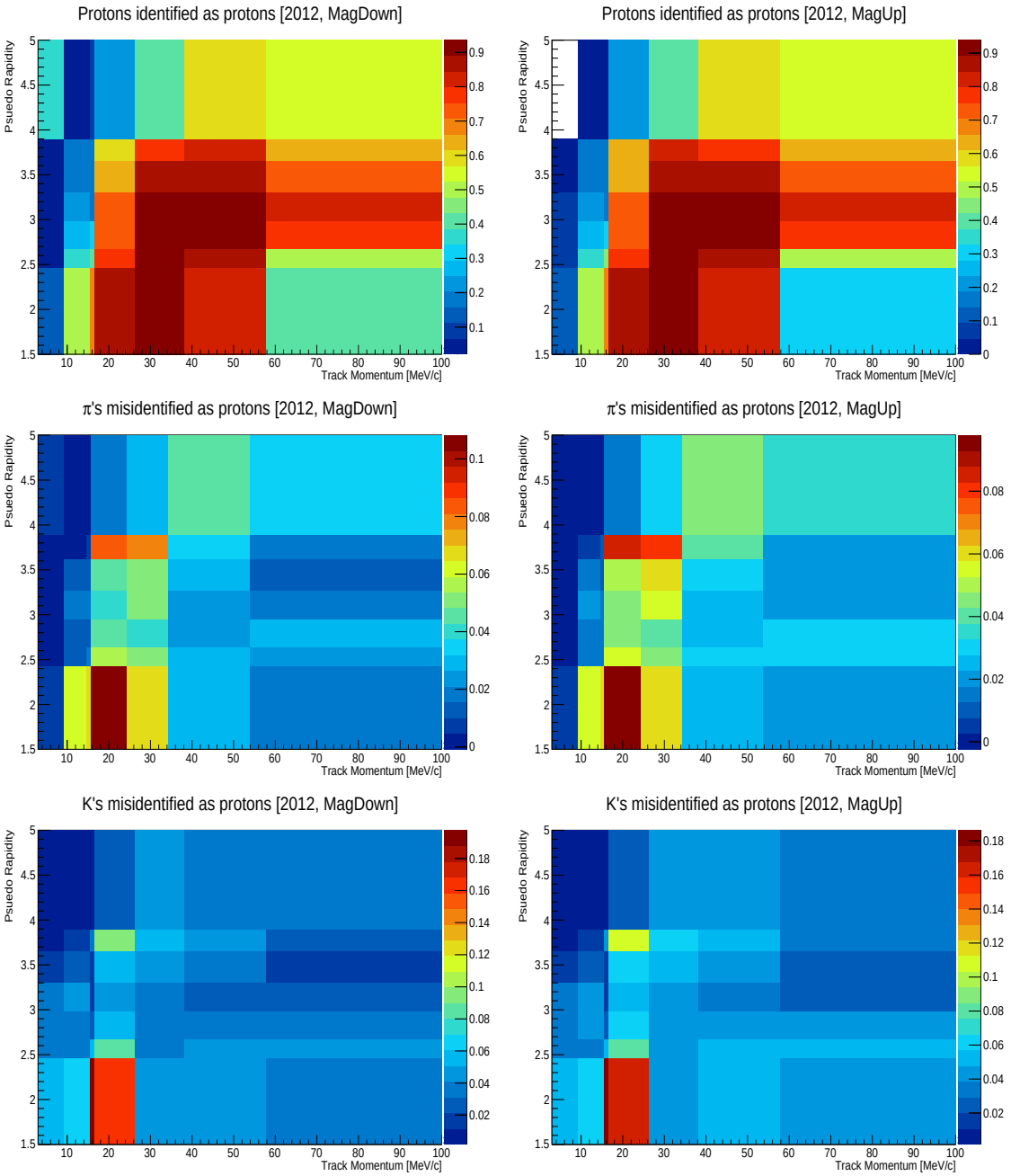

Figure A.4: Efficiency maps of [first-row] protons identified as protons, [second-row] pions misidentified as protons, and [third-row] kaons misidentified as protons for the proton ProbNN$p > 0.50$ cut obtained using the 2012 [first-column] MagDown and [second-column] Mag-Up calibration data.

A.4 PID K/π Figure of Merits

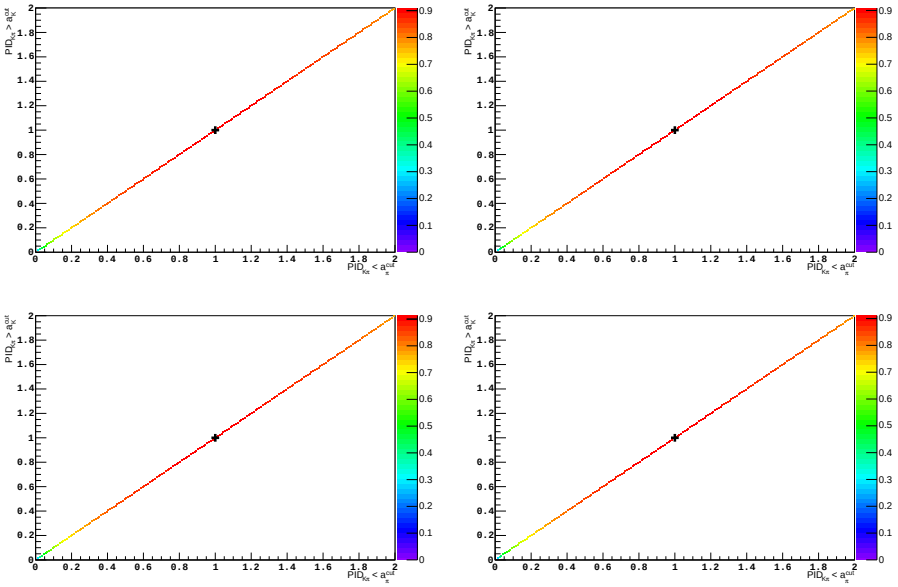

Figure A.5: Figure of merits of $\text{PID}_{K\pi}$ optimization of $\Lambda_b^0 \to p\pi^-\pi^+\pi^-$ for [top-left] 2011 MagDown, [top-right] 2011 MagUp, [bottom-left] 2012 MagDown and [bottom-right] 2012 MagUp.

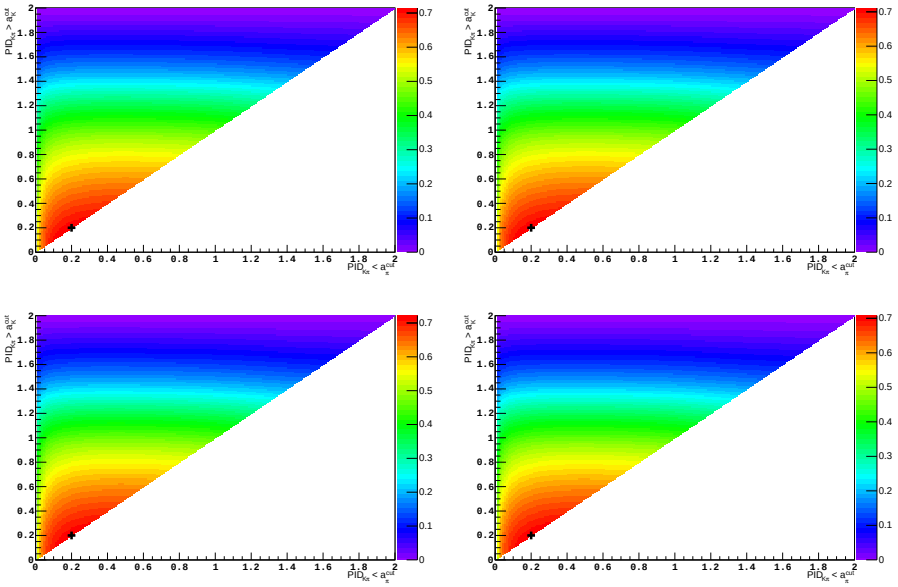

Figure A.6: Figure of merits of $\text{PID}_{K\pi}$ optimization of $\Lambda_b^0 \to pK^-K^+\pi^-$ for [top-left] 2011 MagDown, [top-right] 2011 MagUp, [bottom-left] 2012 MagDown and [bottom-right] 2012 MagUp.

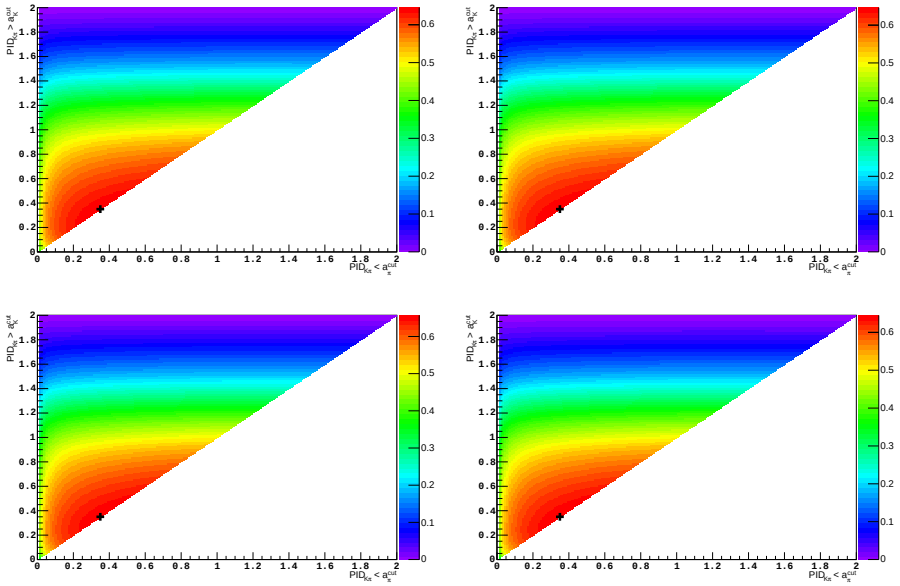

Figure A.7: Figure of merits of $\text{PID}_{K\pi}$ optimization of $\Xi_b^0 \to pK^-\pi^+K^-$ for [top-left] 2011 MagDown, [top-right] 2011 MagUp, [bottom-left] 2012 MagDown and [bottom-right] 2012 MagUp.

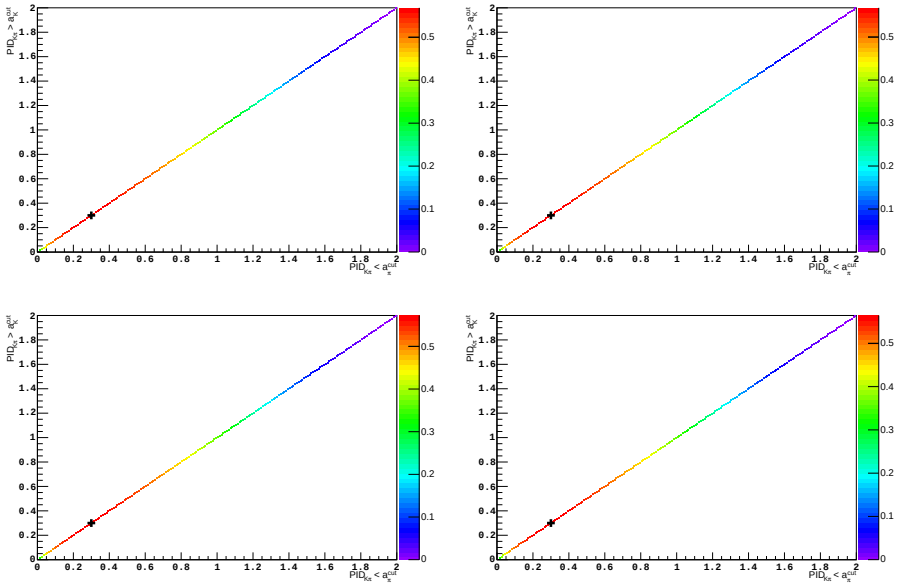

Figure A.8: Figure of merits of $\text{PID}_{K\pi}$ optimization of $\Xi_b^0 \to pK^-K^+K^-$ for [top-left] 2011 MagDown, [top-right] 2011 MagUp, [bottom-left] 2012 MagDown and [bottom-right] 2012 MagUp.

A.5 Signal and Cross-Feed PID K/π Efficiencies

Table A.1: The list signal and cross-feed efficiencies for the ($a_\pi^{\rm cut}$, $a_K^{\rm cut}$) = (0.55, 0.55) on each spectrum. The calibration samples used to obtain these efficiencies come from 2011 data. Only the central values are shown.

Signal decay	Efficiency (in %)		Cross-Feed decay	Efficiency (in %)	
	MagDown	MagUp		MagDown	MagUp
$\Lambda_b^0 \to p\pi^-\pi^+\pi^-$	0.896	0.894	$\Lambda_b^0 \to pK^-\pi^+\pi^-$	0.131	0.131
			$\Xi_b^0 \to pK^-\pi^+\pi^-$	0.131	0.135
			$\Lambda_b^0 \to pK^-K^+\pi^-$	0.020	0.020
			$\Xi_b^0 \to pK^-\pi^+K^-$	0.021	0.021
			$\Lambda_b^0 \to pK^-K^+K^-$	0.003	0.003
			$\Xi_b^0 \to pK^-K^+K^-$	0.003	0.003
$\Xi_b^0 \to pK^-\pi^+\pi^-$	0.796	0.797	$\Lambda_b^0 \to p\pi^-\pi^+\pi^-$	0.038	0.038
			$\Lambda_b^0 \to pK^-K^+\pi^-$	0.128	0.130
			$\Xi_b^0 \to pK^-\pi^+K^-$	0.165	0.164
$\Lambda_b^0 \to pK^-\pi^+\pi^-$	0.797	0.792	$\Lambda_b^0 \to pK^-K^+K^-$	0.027	0.026
			$\Xi_b^0 \to pK^-K^+K^-$	0.026	0.027
$\Lambda_b^0 \to pK^-K^+\pi^-$	0.706	0.703	$\Lambda_b^0 \to p\pi^-\pi^+\pi^-$	0.001	0.001
			$\Lambda_b^0 \to pK^-\pi^+\pi^-$	0.030	0.030
			$\Xi_b^0 \to pK^-\pi^+\pi^-$	0.031	0.031
			$\Xi_b^0 \to pK^-\pi^+K^-$	0.006	0.006
			$\Lambda_b^0 \to pK^-K^+K^-$	0.135	0.131
			$\Xi_b^0 \to pK^-K^+K^-$	0.132	0.134
$\Xi_b^0 \to pK^-\pi^+K^-$	0.702	0.703	$\Lambda_b^0 \to p\pi^-\pi^+\pi^-$	0.001	0.001
			$\Lambda_b^0 \to pK^-\pi^+\pi^-$	0.028	0.028
			$\Xi_b^0 \to pK^-\pi^+\pi^-$	0.028	0.029
			$\Lambda_b^0 \to pK^-K^+\pi^-$	0.004	0.004
			$\Lambda_b^0 \to pK^-K^+K^-$	0.101	0.101
			$\Xi_b^0 \to pK^-K^+K^-$	0.102	0.103
$\Xi_b^0 \to pK^-K^+K^-$	0.641	0.637	$\Lambda_b^0 \to p\pi^-\pi^+\pi^-$	0.00007	0.00008
			$\Lambda_b^0 \to pK^-\pi^+\pi^-$	0.001	0.001
			$\Xi_b^0 \to pK^-\pi^+\pi^-$	0.001	0.001
$\Lambda_b^0 \to pK^-K^+K^-$	0.638	0.638	$\Lambda_b^0 \to pK^-K^+\pi^-$	0.026	0.026
			$\Xi_b^0 \to pK^-\pi^+K^-$	0.027	0.026

Table A.2: The list signal and cross-feed efficiencies for the $(a_\pi^{\text{cut}},\ a_K^{\text{cut}}) = (0.55,\ 0.55)$ on each spectrum. The calibration samples used to obtain these efficiencies come from 2012 data. Only the central values are shown.

Signal decay	Efficiency (in %)		Cross-Feed decay	Efficiency (in %)	
	MagDown	MagUp		MagDown	MagUp
$\Lambda_b^0 \to p\pi^-\pi^+\pi^-$	0.901	0.896	$\Lambda_b^0 \to pK^-\pi^+\pi^-$	0.127	0.130
			$\Xi_b^0 \to pK^-\pi^+\pi^-$	0.130	0.131
			$\Lambda_b^0 \to pK^-K^+\pi^-$	0.019	0.020
			$\Xi_b^0 \to pK^-\pi^+K^-$	0.020	0.021
			$\Lambda_b^0 \to pK^-K^+K^-$	0.004	0.004
			$\Xi_b^0 \to pK^-K^+K^-$	0.004	0.004
$\Xi_b^0 \to pK^-\pi^+\pi^-$	0.801	0.796	$\Lambda_b^0 \to p\pi^-\pi^+\pi^-$	0.037	0.039
			$\Lambda_b^0 \to pK^-K^+\pi^-$	0.128	0.131
			$\Xi_b^0 \to pK^-\pi^+K^-$	0.157	0.161
$\Lambda_b^0 \to pK^-\pi^+\pi^-$	0.805	0.798	$\Lambda_b^0 \to pK^-K^+K^-$	0.026	0.026
			$\Xi_b^0 \to pK^-K^+K^-$	0.027	0.027
$\Lambda_b^0 \to pK^-K^+\pi^-$	0.717	0.706	$\Lambda_b^0 \to p\pi^-\pi^+\pi^-$	0.002	0.002
			$\Lambda_b^0 \to pK^-\pi^+\pi^-$	0.029	0.031
			$\Xi_b^0 \to pK^-\pi^+\pi^-$	0.030	0.032
			$\Xi_b^0 \to pK^-\pi^+K^-$	0.006	0.006
			$\Lambda_b^0 \to pK^-K^+K^-$	0.129	0.130
			$\Xi_b^0 \to pK^-K^+K^-$	0.129	0.131
$\Xi_b^0 \to pK^-\pi^+K^-$	0.713	0.705	$\Lambda_b^0 \to p\pi^-\pi^+\pi^-$	0.001	0.001
			$\Lambda_b^0 \to pK^-\pi^+\pi^-$	0.027	0.029
			$\Xi_b^0 \to pK^-\pi^+\pi^-$	0.028	0.030
			$\Lambda_b^0 \to pK^-K^+\pi^-$	0.004	0.005
			$\Lambda_b^0 \to pK^-K^+K^-$	0.101	0.101
			$\Xi_b^0 \to pK^-K^+K^-$	0.103	0.103
$\Xi_b^0 \to pK^-K^+K^-$	0.648	0.641	$\Lambda_b^0 \to p\pi^-\pi^+\pi^-$	0.00005	0.00006
			$\Lambda_b^0 \to pK^-\pi^+\pi^-$	0.001	0.001
			$\Xi_b^0 \to pK^-\pi^+\pi^-$	0.001	0.001
$\Lambda_b^0 \to pK^-K^+K^-$	0.647	0.642	$\Lambda_b^0 \to pK^-K^+\pi^-$	0.025	0.027
			$\Xi_b^0 \to pK^-\pi^+K^-$	0.027	0.028

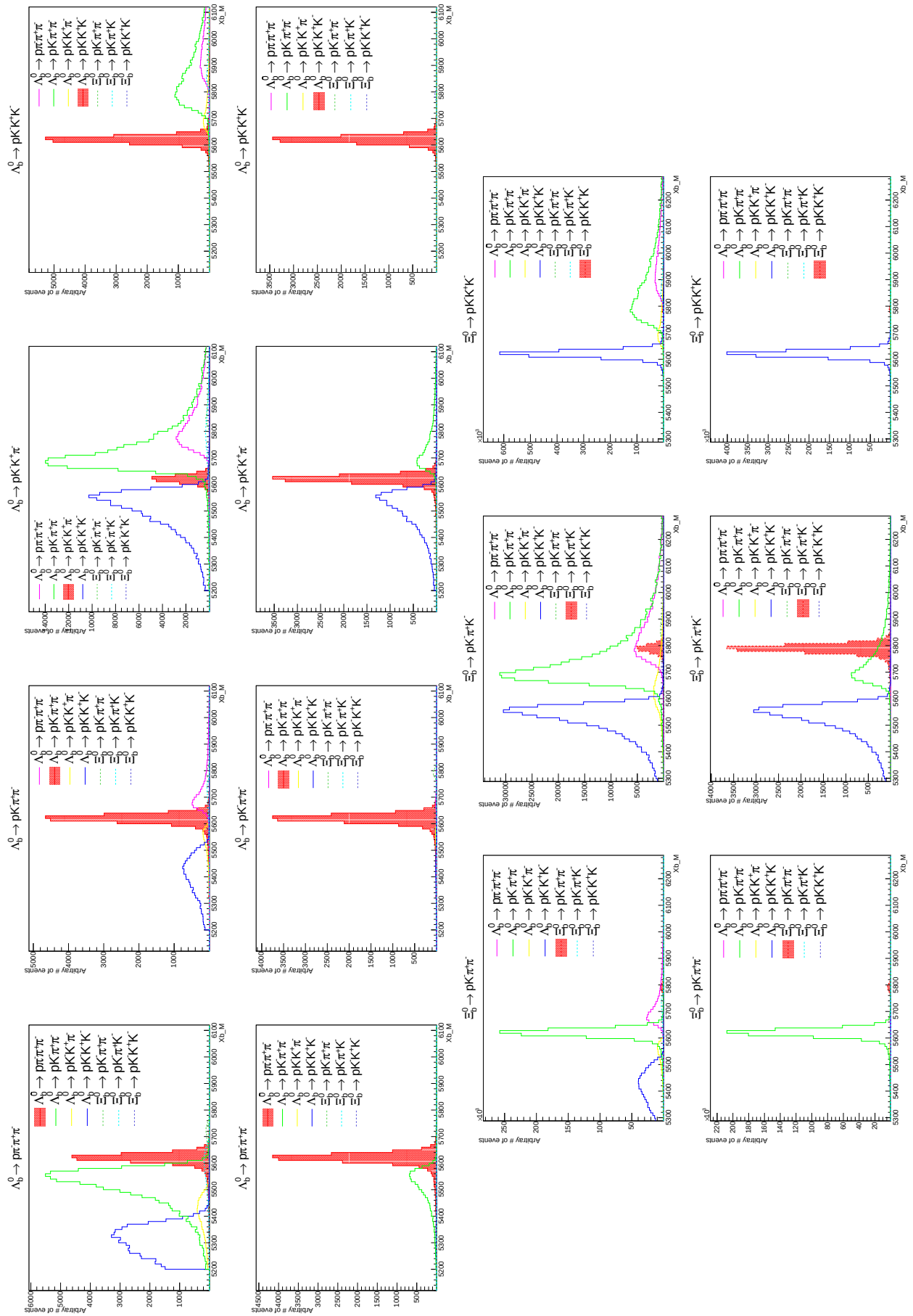

Figure A.9: Illustration of the expected relative yields [1st & 3rd rows] before and [2nd & 4th rows] after the PID$_{K\pi}$ cut using the 2012 MagDown MC samples and the PID weights obtained from the PIDCalibTool. In each spectrum, signal events are colored in red, while the rest are cross-feeds.

A.6 Distribution of variables used in the BDT training

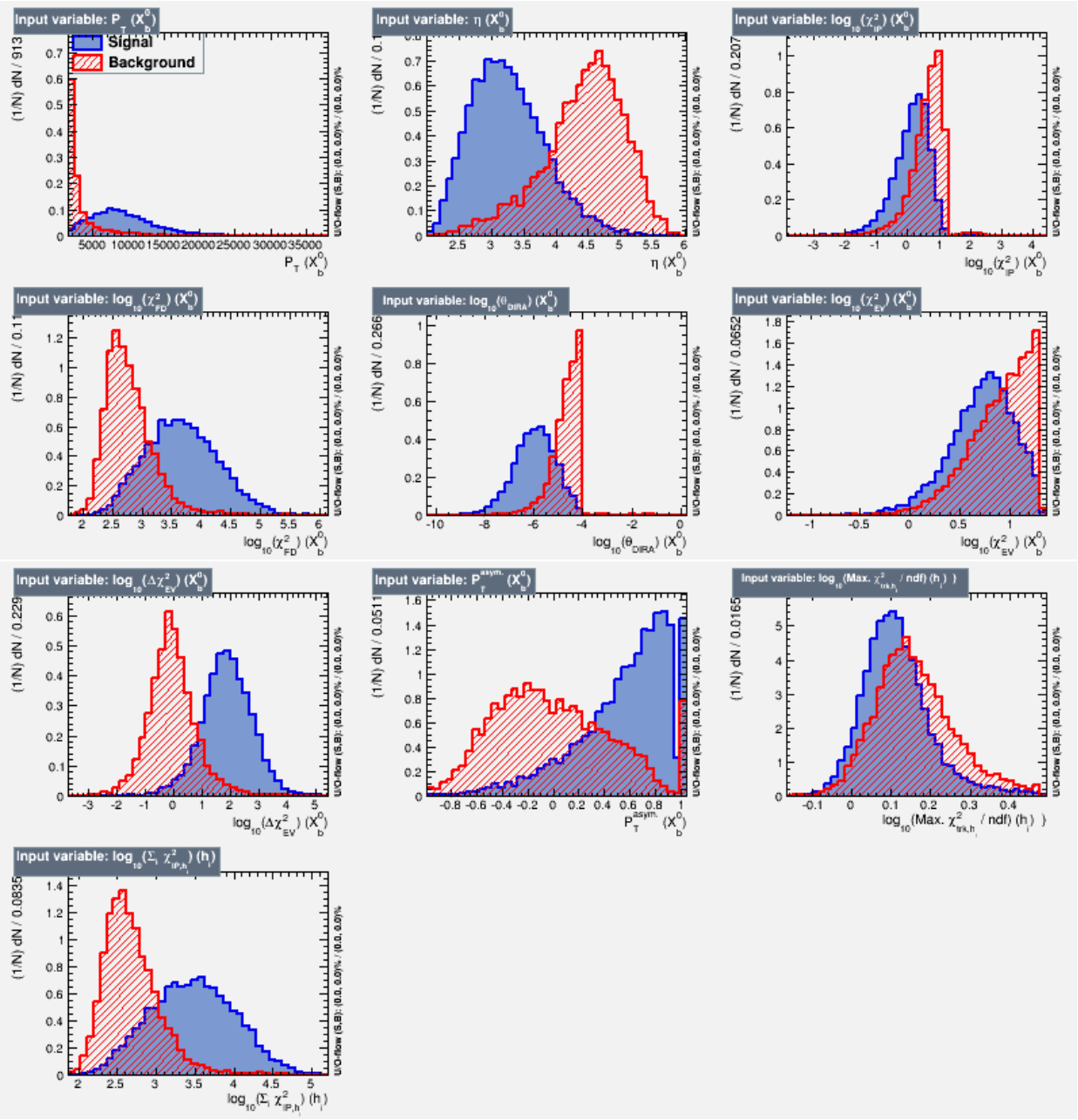

Figure A.10: Distribution of variables used in the training of BDT_2 for 2011, superimposing RHSB background events (in Red) and MC-generated signal events (in Blue).

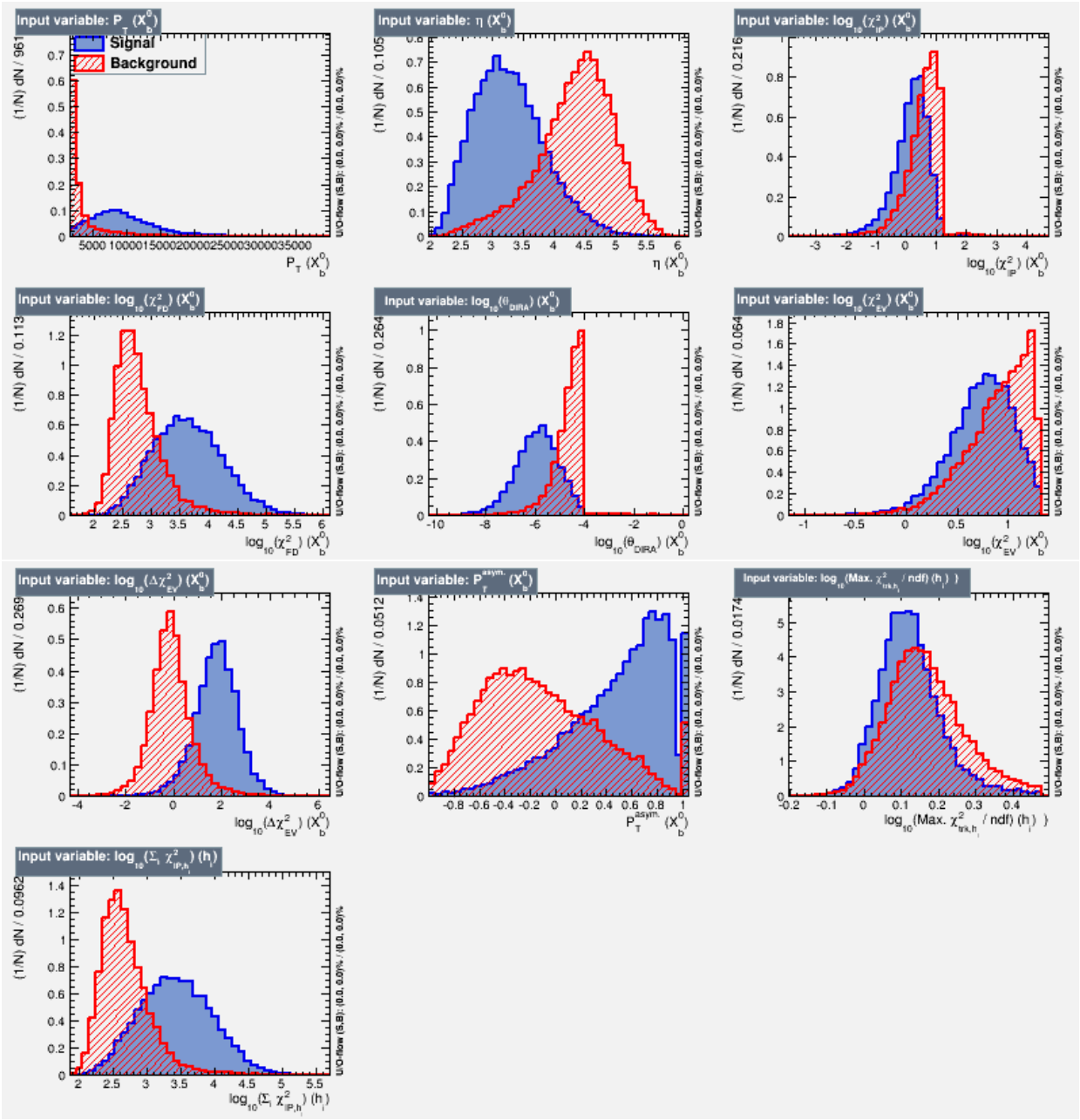

Figure A.11: Distribution of variables used in the training of BDT_1 for 2012, superimposing RHSB background events (in Red) and MC-generated signal events (in Blue).

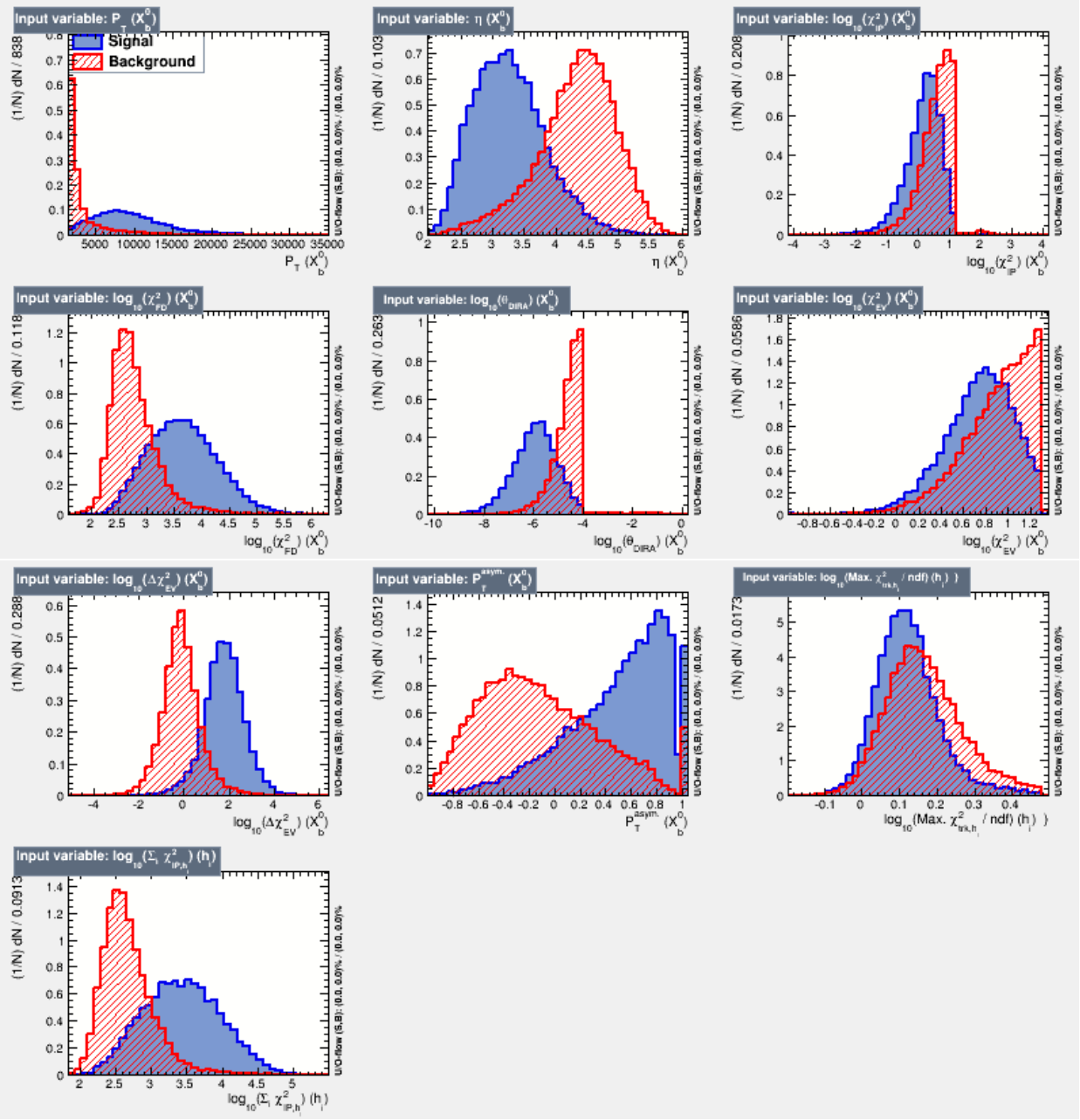

Figure A.12: Distribution of variables used in the training of BDT_2 for 2012, superimposing RHSB background events (in Red) and MC-generated signal events (in Blue).

A.7 Correlations of the variables used in the BDT training

Figure A.13: Linear correlation of variables used in the training of BDT_2 for 2011 (top); BDT_1 for 2012 (middle); and BDT_2 for 2012 (bottom). The plots on the left column are for the signals and on the right-column are for the background events.

A.8 Comparison of some variables of signal modes

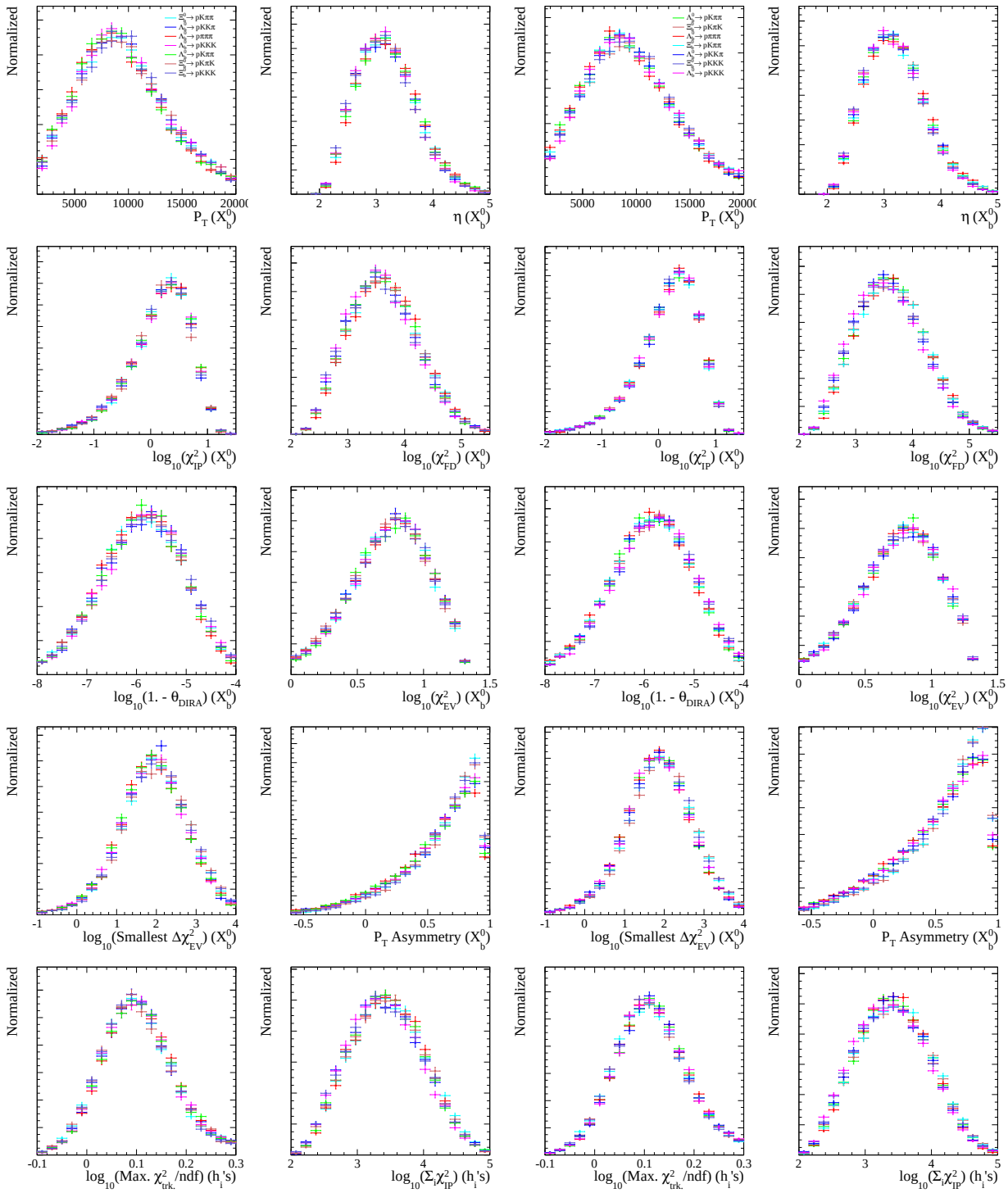

Figure A.14: Comparison of the MC-calculated variables of the seven signal modes using (1st & 2nd columns) 2011 and (3rd & 4th) 2012 MC-generated events.

A.9 B physics backgrounds from RHSB events

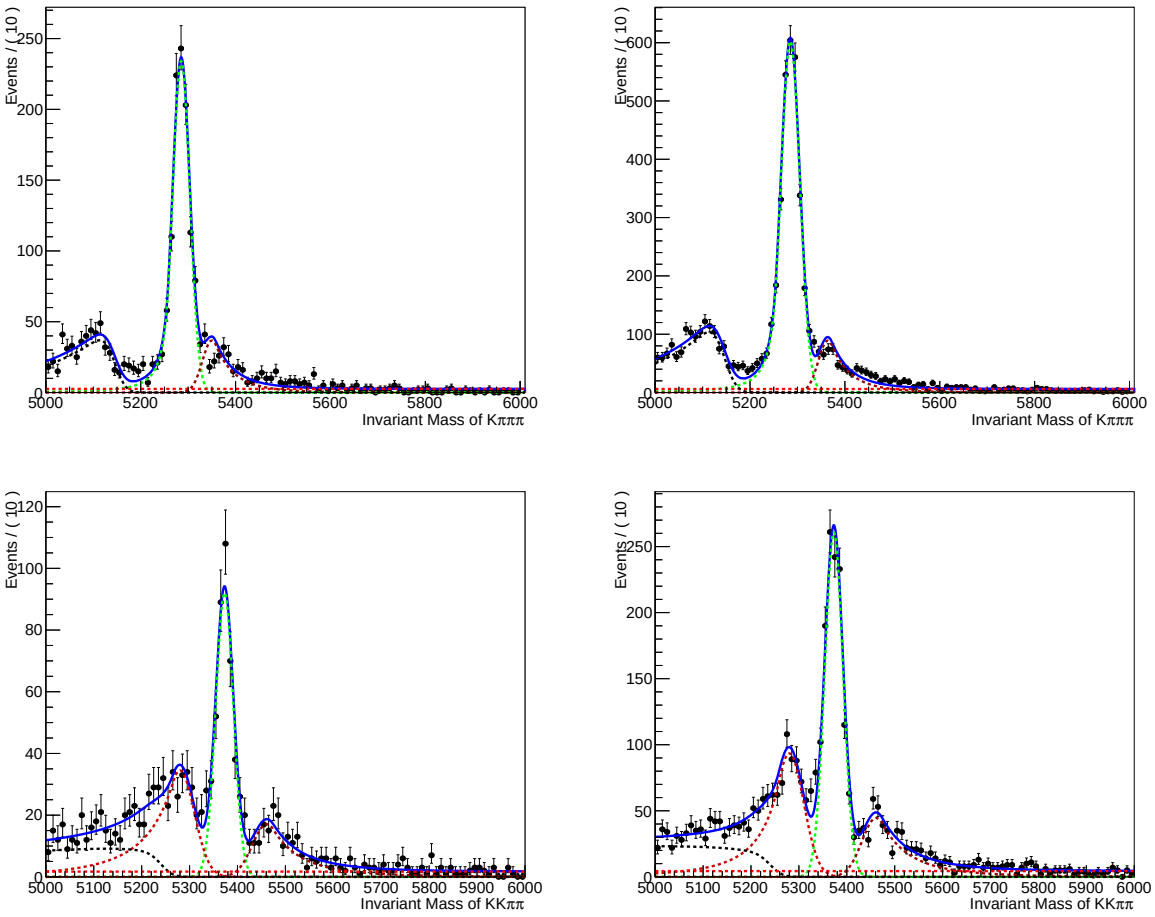

Figure A.15: RHSB events of 2011 & 2012 $X_b^0 \to p\pi\pi\pi$ and $X_b^0 \to pK\pi\pi$ spectra reconstructed as $K\pi\pi\pi$ and $KK\pi\pi$, respectively, with a milder proton PID cut of ProbNN$p > 0.30$.

A.10 Pull study on the B physics yields

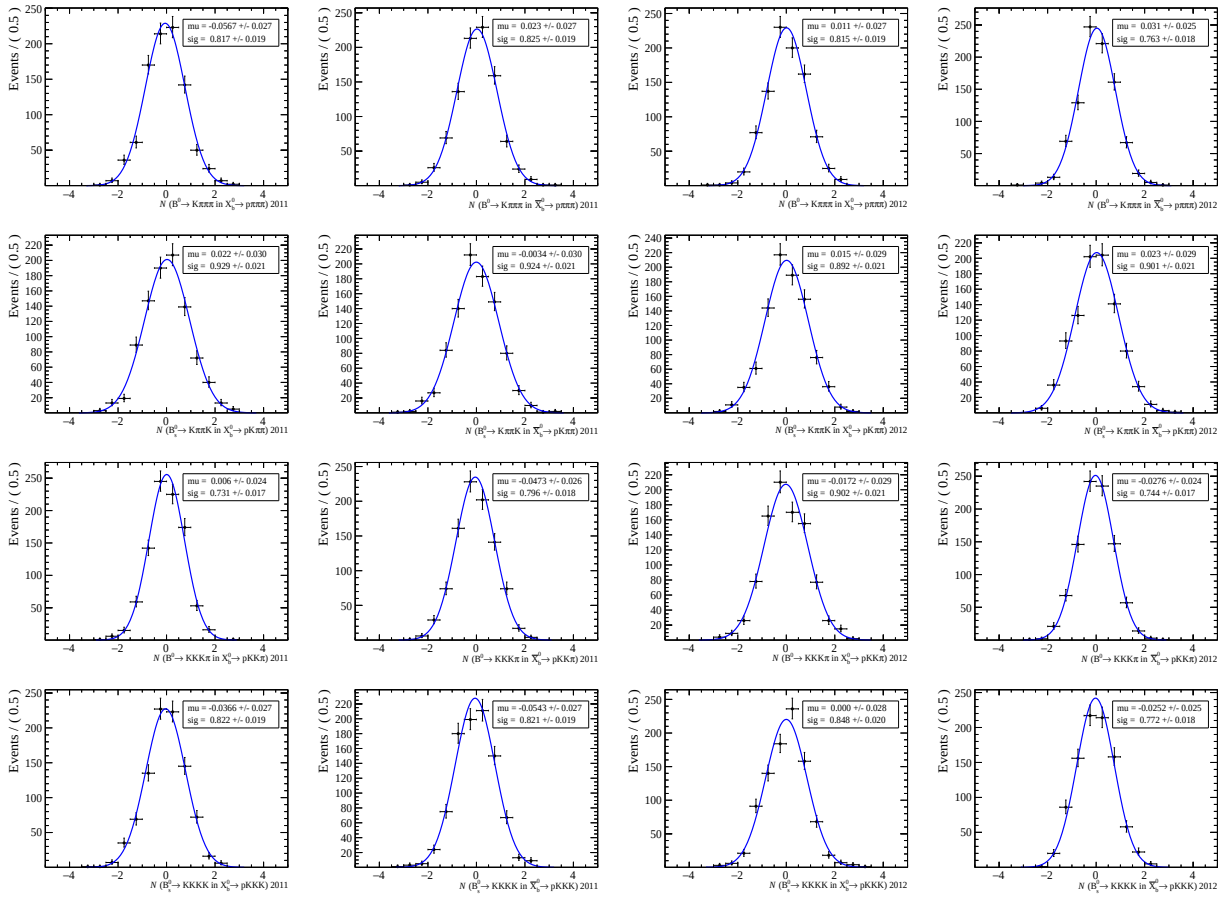

Figure A.16: Pulls of the (left-column) 2011 and (right-column) 2012 B physics yields obtained using about 1000 toys. See Table A.3 for the summary of the Gaussian means and widths.

Table A.3: Summary of the Gaussian means and widths of the pull distribution of the yields of the B physics backgrounds.

Yield parameter	2011		2012	
	μ	σ	μ	σ
$\mathcal{N}$ (CF $B^0 \to K\pi\pi\pi$ in $p\pi\pi\pi$)	-0.057±0.027	0.817±0.019	0.011±0.027	0.815±0.019
$\overline{\mathcal{N}}$ (CF $B^0 \to K\pi\pi\pi$ in $p\pi\pi\pi$)	0.023±0.027	0.825±0.019	0.031±0.025	0.763±0.018
$\mathcal{N}$ (CF $B_s^0 \to K\pi\pi K$ in $pK\pi\pi$)	0.022±0.030	0.929±0.021	0.015±0.029	0.892±0.021
$\overline{\mathcal{N}}$ (CF $B_s^0 \to K\pi\pi K$ in $pK\pi\pi$)	-0.003±0.030	0.924±0.021	0.023±0.029	0.901±0.021
$\mathcal{N}$ (CF $B^0 \to KKK\pi$ in $pKK\pi$)	0.006±0.024	0.731±0.017	-0.017±0.029	0.902±0.021
$\overline{\mathcal{N}}$ (CF $B^0 \to KKK\pi$ in $pKK\pi$)	-0.047±0.026	0.796±0.018	-0.028±0.024	0.744±0.017
$\mathcal{N}$ (CF $B_s^0 \to KKKK$ in $pKKK$)	-0.037±0.027	0.822±0.019	0.000±0.028	0.848±0.020
$\overline{\mathcal{N}}$ (CF $B_s^0 \to KKKK$ in $pKKK$)	-0.054±0.027	0.821±0.019	-0.025±0.025	0.772±0.018

A.11 B physics from RHSB with low mass cut on ph

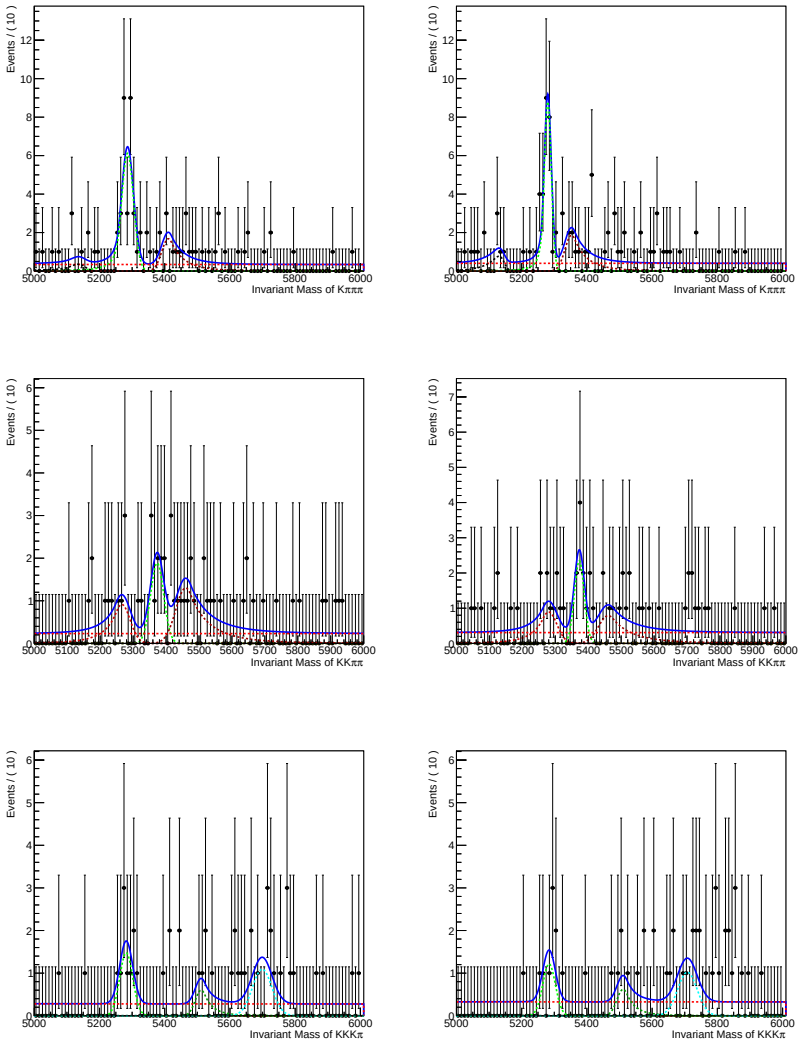

Figure A.17: Invariant mass spectra of 2011 RHSB events from [from top to bottom] $X_b^0 \to p\pi\pi\pi$ as $B^0 \to K\pi\pi\pi$, $X_b^0 \to pK\pi\pi$ as $B_s^0 \to K\pi\pi K$ and $X_b^0 \to pKK\pi$ as $B^0 \to KKK\pi$ (left-column) with p and (right-column) $\overline{p}$ separated. A phase space cut of $m_{ph} < 2$ GeV/c^2 is also applied.

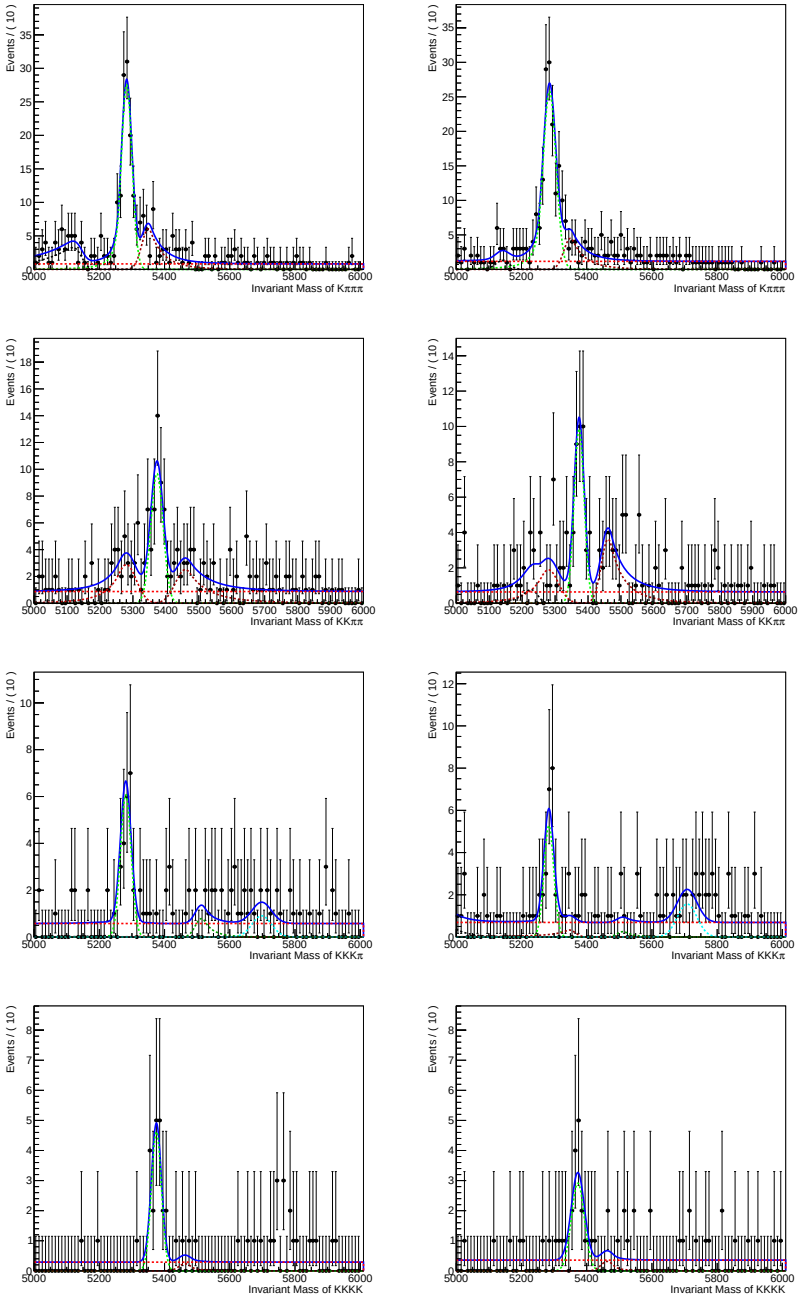

Figure A.18: Invariant mass spectra of 2012 RHSB events from [from top to bottom] $X_b^0 \to p\pi\pi\pi$ as $B^0 \to K\pi\pi\pi$, $X_b^0 \to pK\pi\pi$ as $B_s^0 \to K\pi\pi K$, $X_b^0 \to pKK\pi$ as $B^0 \to KKK\pi$ and $X_b^0 \to pKKK$ as $B_s^0 \to KKKK$ (left-column) with p and (right-column) $\overline{p}$ separated. A phase space cut of $m_{ph} < 2$ GeV/c^2 is also applied.

A.12 B physics from RHSB with low mass cut on ph and $h'h''$

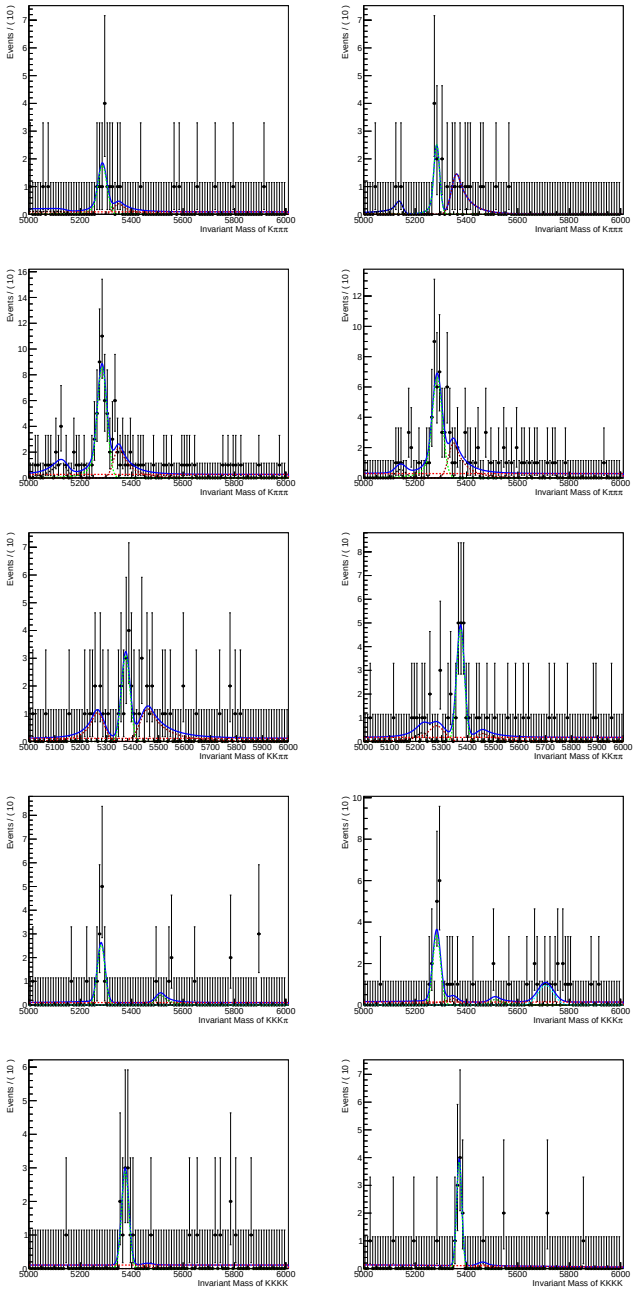

Figure A.19: Invariant mass spectra of RHSB events from [from top to bottom] 2011 $X_b^0 \to p\pi\pi\pi$ as $B^0 \to K\pi\pi\pi$, 2012 $X_b^0 \to p\pi\pi\pi$ as $B^0 \to K\pi\pi\pi$, 2012 $X_b^0 \to pK\pi\pi$ as $B_s^0 \to K\pi\pi K$, 2012 $X_b^0 \to pKK\pi$ as $B^0 \to KKK\pi$ and 2012 $X_b^0 \to pKKK$ as $B_s^0 \to KKKK$ (left-column) with p and (right-column) $\overline{p}$ separated. Phase space cuts of $m_{ph} < 2$ GeV/c^2 and $m_{h'h''} < \sim$1.65 GeV/c^2 are also applied.

A.13 Control spectra fits: Low mass cut on ph in charmless spectra

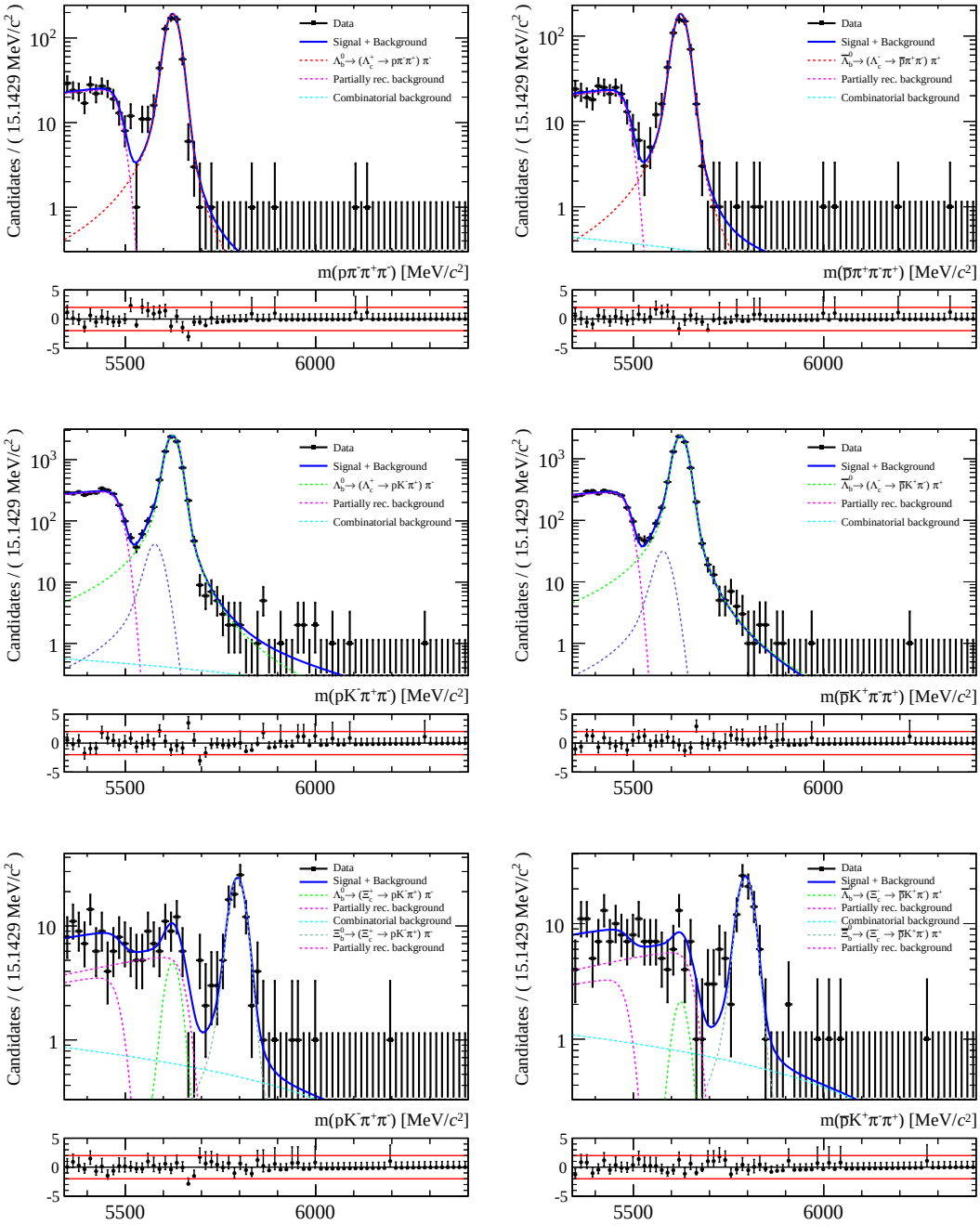

Figure A.20: Fit results for the [from top to bottom] $X_b^0 \to (\Lambda_c^+ \to p\pi\pi)\pi$, $X_b^0 \to (\Lambda_c^+ \to pK\pi)\pi$ and $X_b^0 \to (\Xi_c^+ \to pK\pi)\pi$ spectra using the 2011 data with $m_{ph} < 2$ GeV/c^2 phase space cut on the charmless spectra. Plots in the left-column are for the spectra with X_b^0 and on the right-column for the spectra with $\overline{X}_b^0$.

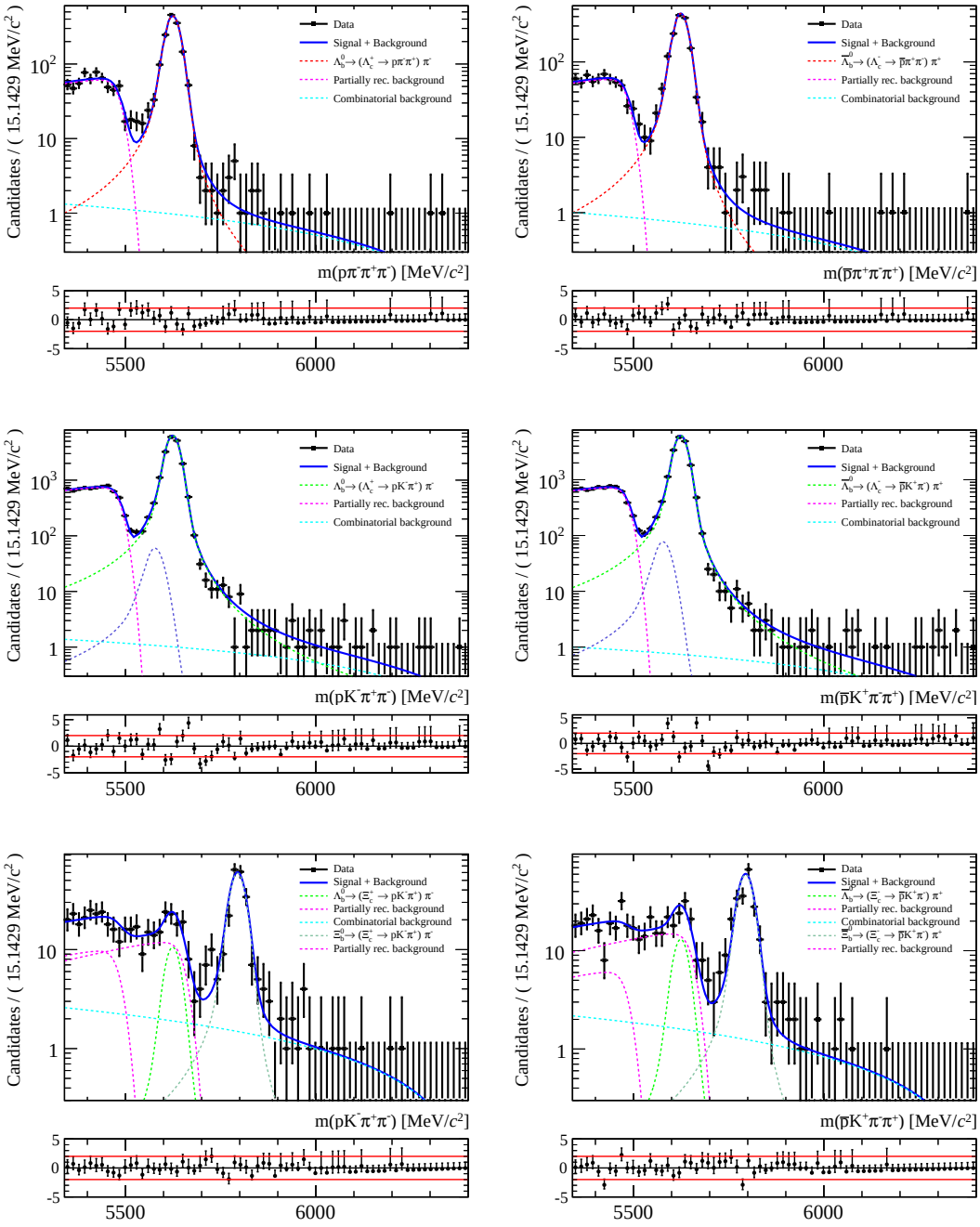

Figure A.21: Fit results for the [from top to bottom] $X_b^0 \to (\Lambda_c^+ \to p\pi\pi)\pi$, $X_b^0 \to (\Lambda_c^+ \to pK\pi)\pi$ and $X_b^0 \to (\Xi_c^+ \to pK\pi)\pi$ spectra using the 2012 data with $m_{ph} < 2$ GeV/c^2 phase space cut on the charmless spectra. Plots in the left-column are for the spectra with X_b^0 and on the right-column for the spectra with $\overline{X}_b^0$.

A.14 Fit parameters: Low mass cut on ph in charmless spectra

Table A.4: Floating parameters of the simultaneous fit to the 2011 and 2012 data with $m_{ph} < 2\,\mathrm{GeV}/c^2$ phase space cut in the charmless modes.

Floating parameter (in Λ_b^0/Ξ_b^0 spectra)	Value	Floating parameter (in $\overline{\Lambda}_b^0/\overline{\Xi}_b^0$ spectra)	Value
μ (Λ_b^0)	5624.057 ± 0.080		
μ (Ξ_b^0) - μ (Λ_b^0)	170.340 ± 0.606		
2012 σ_{core} (Signal $\Lambda_b^0 \to pK\pi\pi$) [ref]	17.182 ± 0.203		
$\mathcal{N}$ ($B^0 \to \pi\pi\pi\pi$ in $p\pi\pi\pi$) / $\mathcal{N}$ ($B^0 \to K\pi\pi\pi$ in $p\pi\pi\pi$)	0.361 ± 0.041		← shared
Parameters for 2011 spectra :			
$\mathcal{N}$ (2011 Signal $\Lambda_b^0 \to p\pi\pi\pi$)	X.XXX ± X.XXX	$\bar{\mathcal{N}}$	X.XXX ± X.XXX
$\mathcal{N}$ (2011 Signal $\Lambda_b^0 \to pK\pi\pi$)	X.XXX ± X.XXX	$\bar{\mathcal{N}}$	X.XXX ± X.XXX
$\mathcal{N}$ (2011 Signal $\Lambda_b^0 \to pKK\pi$)	X.XXX ± X.XXX	$\bar{\mathcal{N}}$	X.XXX ± X.XXX
$\mathcal{N}$ (2011 Signal $\Lambda_b^0 \to pKKK$)	X.XXX ± X.XXX	$\bar{\mathcal{N}}$	X.XXX ± X.XXX
$\mathcal{N}$ (2011 Signal $\Xi_b^0 \to pK\pi K$)	X.XXX ± X.XXX	$\bar{\mathcal{N}}$	X.XXX ± X.XXX
$\mathcal{N}$ (2011 Signal $\Xi_b^0 \to pK\pi\pi$)	X.XXX ± X.XXX	$\bar{\mathcal{N}}$	X.XXX ± X.XXX
$\mathcal{N}$ (2011 Signal $\Xi_b^0 \to pKKK$)	X.XXX ± X.XXX	$\bar{\mathcal{N}}$	X.XXX ± X.XXX
$\mathcal{N}$ (2011 Signal $\Lambda_b^0 \to (\Lambda_c^+ \to p\pi\pi)\pi$)	629.189 ± 25.477	$\bar{\mathcal{N}}$	592.813 ± 24.811
$\mathcal{N}$ (2011 Signal $\Lambda_b^0 \to (\Lambda_c^+ \to pK\pi)\pi$)	7568.570 ± 93.043	$\bar{\mathcal{N}}$	7306.158 ± 91.268
$\mathcal{N}$ (2011 Signal $\Xi_b^0 \to (\Xi_c^+ \to pK\pi)\pi$)	93.305 ± 10.729	$\bar{\mathcal{N}}$	89.844 ± 10.693
$\mathcal{N}$ (2011 Signal $\Lambda_b^0 \to (\Xi_c^+ \to pK\pi)\pi$)	17.029 ± 8.920	$\bar{\mathcal{N}}$	7.568 ± 7.929
$\mathcal{N}$ (2011 Combinatorics in $p\pi\pi\pi$)	98.267 ± 26.735	$\bar{\mathcal{N}}$	110.927 ± 29.027
$\mathcal{N}$ (2011 Combinatorics in $pK\pi\pi$)	204.164 ± 33.029	$\bar{\mathcal{N}}$	236.662 ± 34.187
$\mathcal{N}$ (2011 Combinatorics in $pKK\pi$)	192.867 ± 30.138	$\bar{\mathcal{N}}$	202.415 ± 29.580
$\mathcal{N}$ (2011 Combinatorics in $pKKK$)	65.142 ± 16.067	$\bar{\mathcal{N}}$	89.619 ± 17.789
$\mathcal{N}$ (2011 Combinatorics in $pK\pi K$)	55.573 ± 18.836	$\bar{\mathcal{N}}$	8.313 ± 12.679
$\mathcal{N}$ (2011 Combinatorics in $(\Lambda_c^+ \to p\pi\pi)\pi$)	8.572 ± 5.606	$\bar{\mathcal{N}}$	14.805 ± 6.972

$\mathcal{N}$ (2011 Combinatorics in $(\Lambda_c^+ \to pK\pi)\pi$)	18.851 ± 11.729	$\bar{\mathcal{N}}$	-2.762 ± 9.360
$\mathcal{N}$ (2011 Combinatorics in $(\Xi_c^+ \to pK\pi)\pi$)	28.984 ± 13.195	$\bar{\mathcal{N}}$	36.678 ± 14.228
$\mathcal{N}$ (2011 CF $B^0 \to K\pi\pi\pi$ in $p\pi\pi\pi$)	156.816 ± 18.704	$\bar{\mathcal{N}}$	165.125 ± 17.840
$\mathcal{N}$ (2011 CF $B_s^0 \to K\pi\pi K$ in $pK\pi\pi$)	48.851 ± 12.537	$\bar{\mathcal{N}}$	45.059 ± 13.581
$\mathcal{N}$ (2011 CF $B^0 \to KKK\pi$ in $pKK\pi$)	111.976 ± 18.013	$\bar{\mathcal{N}}$	102.123 ± 17.864
$\mathcal{N}$ (2011 CF $B_s^0 \to KKKK$ in $pKKK$)	20.429 ± 7.636	$\bar{\mathcal{N}}$	25.090 ± 8.808
$\mathcal{N}$ (2011 PR from $\Lambda_b^0 \to$ 5-body in $p\pi\pi\pi$)	393.251 ± 24.341	$\bar{\mathcal{N}}$	331.499 ± 22.826
$\mathcal{N}$ (2011 PR from $\Lambda_b^0 \to$ 5-body in $pK\pi\pi$)	668.947 ± 49.398	$\bar{\mathcal{N}}$	684.267 ± 50.156
$\mathcal{N}$ (2011 PR from $\Xi_b^0 \to$ 5-body in $pK\pi\pi$)	389.040 ± 60.342	$\bar{\mathcal{N}}$	394.462 ± 60.878
$\mathcal{N}$ (2011 PR from $\Lambda_b^0 \to$ 5-body in $pKK\pi$)	69.426 ± 14.463	$\bar{\mathcal{N}}$	78.433 ± 14.651
$\mathcal{N}$ (2011 PR from $\Lambda_b^0 \to$ 5-body in $pKKK$)	48.541 ± 9.508	$\bar{\mathcal{N}}$	34.166 ± 9.160
$\mathcal{N}$ (2011 PR from $\Lambda_b^0 \to$ 5-body in $pK\pi K$)	51.515 ± 16.680	$\bar{\mathcal{N}}$	90.452 ± 16.198
$\mathcal{N}$ (2011 PR from $\Xi_b^0 \to$ 5-body in $pK\pi K$)	63.485 ± 25.781	$\bar{\mathcal{N}}$	50.422 ± 22.176
$\mathcal{N}$ (2011 PR from $\Lambda_b^0 \to$ 5-body in $(\Lambda_c^+ \to p\pi\pi)\pi$)	229.244 ± 15.722	$\bar{\mathcal{N}}$	211.387 ± 15.192
$\mathcal{N}$ (2011 PR from $\Lambda_b^0 \to$ 5-body in $(\Lambda_c^+ \to pK\pi)\pi$)	2805.905 ± 54.474	$\bar{\mathcal{N}}$	2661.935 ± 52.966
$\mathcal{N}$ (2011 PR from $\Lambda_b^0 \to$ 5-body in $(\Xi_c^+ \to pK\pi)\pi$)	33.203 ± 13.558	$\bar{\mathcal{N}}$	30.837 ± 13.762
$\mathcal{N}$ (2011 PR from $\Xi_b^0 \to$ 5-body in $(\Xi_c^+ \to pK\pi)\pi$)	98.481 ± 20.925	$\bar{\mathcal{N}}$	104.072 ± 21.379
2011 c (Combinatorics in charmless decays)	-1.012 ± 0.017		← shared
2011 c (Combinatorics in charmed decays)	-1.081 ± 0.079		← shared
2011 p (PR from Λ_b^0/Ξ_b^0 + 5-body in charmless spectra)	0.186 ± 0.117		← shared
2011 s (PR from Λ_b^0/Ξ_b^0 + 5-body in charmless spectra)	-0.857 ± 4.726		← shared
2011 p (PR from Λ_b^0 + 5-body in $(\Lambda_c^+ \to pK\pi)\pi$)	0.092 ± 0.050		← shared
2011 s (PR from Λ_b^0 + 5-body in $(\Lambda_c^+ \to pK\pi)\pi$)	-5.233 ± 2.647		← shared
$r = (2011\ \sigma_{\text{core}}\ \Lambda_b^0 \to p\pi\pi\pi)/(\sigma_{\text{ref}})$	1.047 ± 0.017		← shared
$r = (2011\ \sigma_{\text{core}}\ \Lambda_b^0 \to pK\pi\pi)/(\sigma_{\text{ref}})$	1.001 ± 0.015		← shared
$r = (2011\ \sigma_{\text{core}}\ \Lambda_b^0 \to pKK\pi)/(\sigma_{\text{ref}})$	0.965 ± 0.018		← shared
$r = (2011\ \sigma_{\text{core}}\ \Lambda_b^0 \to pKKK)/(\sigma_{\text{ref}})$	0.909 ± 0.015		← shared
$r = (2011\ \sigma_{\text{core}}\ \Xi_b^0 \to pK\pi\pi)/(\sigma_{\text{ref}})$	1.033 ± 0.018		← shared
$r = (2011\ \sigma_{\text{core}}\ \Xi_b^0 \to pK\pi K)/(\sigma_{\text{ref}})$	0.991 ± 0.018		← shared

$r = (2011\ \sigma_{\text{core}}\ \Xi_b^0 \to pKKK)/(\sigma_{\text{ref}})$	0.935 ± 0.016		$\leftarrow$ shared
2011 σ_{core} (Signal $\Lambda_b^0 \to (\Lambda_c^+ \to p\pi\pi)\pi$)	18.285 ± 0.499		$\leftarrow$ shared
2011 σ_{core} (Signal $\Lambda_b^0 \to (\Lambda_c^+ \to pK\pi)\pi$)	17.158 ± 0.144		$\leftarrow$ shared
2011 σ_{core} (Signal $\Lambda_b^0 \to (\Xi_c^+ \to pK\pi)\pi$)	20.115 ± 2.024		$\leftarrow$ shared
$f = (2011\ \mathcal{N}$ (CF $\Lambda_b^0 \to p\pi\pi\pi$ in $pK\pi\pi)/(\ \mathcal{N}$ (as Signal))	0.045 ± 0.001		$\leftarrow$ shared
$f = (2011\ \mathcal{N}$ (CF $\Lambda_b^0 \to pK\pi\pi$ in $pKK\pi)/(\ \mathcal{N}$ (as Signal))	0.043 ± 0.001		$\leftarrow$ shared
$f = (2011\ \mathcal{N}$ (CF $\Lambda_b^0 \to pK\pi\pi$ in $p\pi\pi\pi)/(\ \mathcal{N}$ (as Signal))	0.144 ± 0.002		$\leftarrow$ shared
$f = (2011\ \mathcal{N}$ (CF $\Lambda_b^0 \to pK\pi\pi$ in $pK\pi K)/(\ \mathcal{N}$ (as Signal))	0.037 ± 0.001		$\leftarrow$ shared
$f = (2011\ \mathcal{N}$ (CF $\Lambda_b^0 \to pKK\pi$ in $pK\pi\pi)/(\ \mathcal{N}$ (as Signal))	0.170 ± 0.003		$\leftarrow$ shared
$f = (2011\ \mathcal{N}$ (CF $\Lambda_b^0 \to pKKK$ in $pKK\pi)/(\ \mathcal{N}$ (as Signal))	0.173 ± 0.002		$\leftarrow$ shared
$f = (2011\ \mathcal{N}$ (CF $\Lambda_b^0 \to pKKK$ in $pK\pi K)/(\ \mathcal{N}$ (as Signal))	0.144 ± 0.002		$\leftarrow$ shared
$f = (2011\ \mathcal{N}$ (CF $\Xi_b^0 \to pK\pi\pi$ in $p\pi\pi\pi)/(\ \mathcal{N}$ (as Signal))	0.165 ± 0.002		$\leftarrow$ shared
$f = (2011\ \mathcal{N}$ (CF $\Xi_b^0 \to pK\pi K$ in $pK\pi\pi)/(\ \mathcal{N}$ (as Signal))	0.206 ± 0.003		$\leftarrow$ shared
$f = (2011\ \mathcal{N}$ ($B^0 \to K\pi\pi\pi$ in $pK\pi\pi)/(\ \mathcal{N}$ (in Ref.))	0.262 ± 0.009		$\leftarrow$ shared
$f = (2011\ \mathcal{N}$ ($B^0 \to KKK\pi$ in $pKKK)/(\ \mathcal{N}$ (in Ref.))	0.057 ± 0.003		$\leftarrow$ shared
$f = (2011\ \mathcal{N}$ ($B^0 \to KKK\pi$ in $pK\pi\pi)/(\ \mathcal{N}$ (in Ref.))	0.135 ± 0.003		$\leftarrow$ shared
$f = (2011\ \mathcal{N}$ ($B^0 \to KKK\pi$ in $pK\pi K)/(\ \mathcal{N}$ (in Ref.))	0.486 ± 0.012		$\leftarrow$ shared
$f = (2011\ \mathcal{N}$ ($B_s^0 \to K\pi\pi K$ in $pKK\pi)/(\ \mathcal{N}$ (in Ref.))	0.099 ± 0.006		$\leftarrow$ shared
Parameters for 2012 spectra :			
$\mathcal{N}$ (2012 Signal $\Lambda_b^0 \to p\pi\pi\pi$)	X.XXX $\pm$ X.XXX	$\bar{\mathcal{N}}$	X.XXX $\pm$ X.XXX
$\mathcal{N}$ (2012 Signal $\Lambda_b^0 \to pK\pi\pi$)	X.XXX $\pm$ X.XXX	$\bar{\mathcal{N}}$	X.XXX $\pm$ X.XXX
$\mathcal{N}$ (2012 Signal $\Lambda_b^0 \to pKK\pi$)	X.XXX $\pm$ X.XXX	$\bar{\mathcal{N}}$	X.XXX $\pm$ X.XXX
$\mathcal{N}$ (2012 Signal $\Lambda_b^0 \to pKKK$)	X.XXX $\pm$ X.XXX	$\bar{\mathcal{N}}$	X.XXX $\pm$ X.XXX
$\mathcal{N}$ (2012 Signal $\Xi_b^0 \to pK\pi K$)	X.XXX $\pm$ X.XXX	$\bar{\mathcal{N}}$	X.XXX $\pm$ X.XXX
$\mathcal{N}$ (2012 Signal $\Xi_b^0 \to pK\pi\pi$)	X.XXX $\pm$ X.XXX	$\bar{\mathcal{N}}$	X.XXX $\pm$ X.XXX
$\mathcal{N}$ (2012 Signal $\Xi_b^0 \to pKKK$)	X.XXX $\pm$ X.XXX	$\bar{\mathcal{N}}$	X.XXX $\pm$ X.XXX
$\mathcal{N}$ (2012 Signal $\Lambda_b^0 \to (\Lambda_c^+ \to p\pi\pi)\pi$)	1480.754 ± 39.420	$\bar{\mathcal{N}}$	1479.558 ± 39.280
$\mathcal{N}$ (2012 Signal $\Lambda_b^0 \to (\Lambda_c^+ \to pK\pi)\pi$)	19088.482 ± 147.521	$\bar{\mathcal{N}}$	18663.632 ± 146.137

$\mathcal{N}$ (2012 Signal $\Xi_b^0 \to (\Xi_c^+ \to pK\pi)\pi$)	215.108 ± 16.148	$\bar{\mathcal{N}}$	216.413 ± 16.257
$\mathcal{N}$ (2012 Signal $\Lambda_b^0 \to (\Xi_c^+ \to pK\pi)\pi$)	38.369 ± 13.774	$\bar{\mathcal{N}}$	47.371 ± 15.010
$\mathcal{N}$ (2012 Combinatorics in $p\pi\pi\pi$)	247.295 ± 59.423	$\bar{\mathcal{N}}$	229.334 ± 60.145
$\mathcal{N}$ (2012 Combinatorics in $pK\pi\pi$)	566.493 ± 63.899	$\bar{\mathcal{N}}$	509.259 ± 62.780
$\mathcal{N}$ (2012 Combinatorics in $pKK\pi$)	329.196 ± 47.009	$\bar{\mathcal{N}}$	311.058 ± 48.417
$\mathcal{N}$ (2012 Combinatorics in $pKKK$)	168.420 ± 29.601	$\bar{\mathcal{N}}$	155.358 ± 30.858
$\mathcal{N}$ (2012 Combinatorics in $pK\pi K$)	116.596 ± 29.085	$\bar{\mathcal{N}}$	78.393 ± 25.096
$\mathcal{N}$ (2012 Combinatorics in $(\Lambda_c^+ \to p\pi\pi)\pi$)	46.673 ± 12.674	$\bar{\mathcal{N}}$	35.570 ± 11.224
$\mathcal{N}$ (2012 Combinatorics in $(\Lambda_c^+ \to pK\pi)\pi$)	48.681 ± 16.977	$\bar{\mathcal{N}}$	35.443 ± 15.960
$\mathcal{N}$ (2012 Combinatorics in $(\Xi_c^+ \to pK\pi)\pi$)	91.434 ± 20.291	$\bar{\mathcal{N}}$	76.717 ± 19.969
$\mathcal{N}$ (2012 CF $B^0 \to K\pi\pi\pi$ in $p\pi\pi\pi$)	604.102 ± 37.662	$\bar{\mathcal{N}}$	634.687 ± 38.982
$\mathcal{N}$ (2012 CF $B_s^0 \to K\pi\pi K$ in $pK\pi\pi$)	211.049 ± 28.182	$\bar{\mathcal{N}}$	212.314 ± 27.370
$\mathcal{N}$ (2012 CF $B^0 \to KKK\pi$ in $pKK\pi$)	274.802 ± 30.945	$\bar{\mathcal{N}}$	310.243 ± 32.125
$\mathcal{N}$ (2012 CF $B_s^0 \to KKKK$ in $pKKK$)	84.291 ± 19.489	$\bar{\mathcal{N}}$	89.890 ± 18.990
$\mathcal{N}$ (2012 PR from $\Lambda_b^0 \to$ 5-body in $p\pi\pi\pi$)	786.416 ± 36.207	$\bar{\mathcal{N}}$	787.665 ± 35.973
$\mathcal{N}$ (2012 PR from $\Lambda_b^0 \to$ 5-body in $pK\pi\pi$)	1393.548 ± 69.809	$\bar{\mathcal{N}}$	1498.379 ± 69.153
$\mathcal{N}$ (2012 PR from $\Xi_b^0 \to$ 5-body in $pK\pi\pi$)	735.014 ± 87.672	$\bar{\mathcal{N}}$	698.886 ± 86.375
$\mathcal{N}$ (2012 PR from $\Lambda_b^0 \to$ 5-body in $pKK\pi$)	214.210 ± 22.095	$\bar{\mathcal{N}}$	229.688 ± 22.666
$\mathcal{N}$ (2012 PR from $\Lambda_b^0 \to$ 5-body in $pKKK$)	73.347 ± 13.729	$\bar{\mathcal{N}}$	97.956 ± 14.887
$\mathcal{N}$ (2012 PR from $\Lambda_b^0 \to$ 5-body in $pK\pi K$)	178.567 ± 24.594	$\bar{\mathcal{N}}$	140.275 ± 24.245
$\mathcal{N}$ (2012 PR from $\Xi_b^0 \to$ 5-body in $pK\pi K$)	111.223 ± 35.710	$\bar{\mathcal{N}}$	133.661 ± 35.586
$\mathcal{N}$ (2012 PR from $\Lambda_b^0 \to$ 5-body in $(\Lambda_c^+ \to p\pi\pi)\pi$)	573.581 ± 25.103	$\bar{\mathcal{N}}$	550.878 ± 24.474
$\mathcal{N}$ (2012 PR from $\Lambda_b^0 \to$ 5-body in $(\Lambda_c^+ \to pK\pi)\pi$)	6867.941 ± 85.154	$\bar{\mathcal{N}}$	6676.346 ± 83.921
$\mathcal{N}$ (2012 PR from $\Lambda_b^0 \to$ 5-body in $(\Xi_c^+ \to pK\pi)\pi$)	90.995 ± 20.468	$\bar{\mathcal{N}}$	56.791 ± 21.323
$\mathcal{N}$ (2012 PR from $\Xi_b^0 \to$ 5-body in $(\Xi_c^+ \to pK\pi)\pi$)	214.099 ± 31.615	$\bar{\mathcal{N}}$	268.715 ± 34.455
2012 c (Combinatorics in charmless decays)	-1.002 ± 0.019		← shared
2012 c (Combinatorics in charmed decays)	-0.984 ± 0.057		← shared
2012 p (PR from Λ_b^0/Ξ_b^0 + 5-body in charmless spectra)	0.227 ± 0.082		← shared
2012 s (PR from Λ_b^0/Ξ_b^0 + 5-body in charmless spectra)	-2.150 ± 3.338		← shared

2012 p (PR from Λ_b^0 + 5-body in $(\Lambda_c^+ \to pK\pi)\pi$)	0.120 ± 0.032	← shared
2012 s (PR from Λ_b^0 + 5-body in $(\Lambda_c^+ \to pK\pi)\pi$)	-6.651 ± 1.709	← shared
$r = (2012\ \sigma_{\text{core}}\ \Lambda_b^0 \to p\pi\pi\pi)/(\sigma_{\text{ref}})$	1.075 ± 0.015	← shared
$r = (2012\ \sigma_{\text{core}}\ \Lambda_b^0 \to pKK\pi)/(\sigma_{\text{ref}})$	0.967 ± 0.015	← shared
$r = (2012\ \sigma_{\text{core}}\ \Lambda_b^0 \to pKKK)/(\sigma_{\text{ref}})$	0.885 ± 0.012	← shared
$r = (2012\ \sigma_{\text{core}}\ \Xi_b^0 \to pK\pi\pi)/(\sigma_{\text{ref}})$	1.045 ± 0.017	← shared
$r = (2012\ \sigma_{\text{core}}\ \Xi_b^0 \to pK\pi K)/(\sigma_{\text{ref}})$	0.994 ± 0.015	← shared
$r = (2012\ \sigma_{\text{core}}\ \Xi_b^0 \to pKKK)/(\sigma_{\text{ref}})$	0.930 ± 0.014	← shared
2012 σ_{core} (Signal $\Lambda_b^0 \to (\Lambda_c^+ \to p\pi\pi)\pi$)	18.930 ± 0.344	← shared
2012 σ_{core} (Signal $\Lambda_b^0 \to (\Lambda_c^+ \to pK\pi)\pi$)	16.979 ± 0.090	← shared
2012 σ_{core} (Signal $\Lambda_b^0 \to (\Xi_c^+ \to pK\pi)\pi$)	20.426 ± 1.208	← shared
$f = (2012\ \mathcal{N}\ (\text{CF}\ \Lambda_b^0 \to p\pi\pi\pi\ \text{in}\ pK\pi\pi)/(\ \mathcal{N}\ (\text{as Signal}))$	0.044 ± 0.001	← shared
$f = (2012\ \mathcal{N}\ (\text{CF}\ \Lambda_b^0 \to pK\pi\pi\ \text{in}\ pKK\pi)/(\ \mathcal{N}\ (\text{as Signal}))$	0.044 ± 0.001	← shared
$f = (2012\ \mathcal{N}\ (\text{CF}\ \Lambda_b^0 \to pK\pi\pi\ \text{in}\ p\pi\pi\pi)/(\ \mathcal{N}\ (\text{as Signal}))$	0.144 ± 0.002	← shared
$f = (2012\ \mathcal{N}\ (\text{CF}\ \Lambda_b^0 \to pK\pi\pi\ \text{in}\ pK\pi K)/(\ \mathcal{N}\ (\text{as Signal}))$	0.035 ± 0.001	← shared
$f = (2012\ \mathcal{N}\ (\text{CF}\ \Lambda_b^0 \to pKK\pi\ \text{in}\ pK\pi\pi)/(\ \mathcal{N}\ (\text{as Signal}))$	0.165 ± 0.002	← shared
$f = (2012\ \mathcal{N}\ (\text{CF}\ \Lambda_b^0 \to pKKK\ \text{in}\ pKK\pi)/(\ \mathcal{N}\ (\text{as Signal}))$	0.169 ± 0.002	← shared
$f = (2012\ \mathcal{N}\ (\text{CF}\ \Lambda_b^0 \to pKKK\ \text{in}\ pK\pi K)/(\ \mathcal{N}\ (\text{as Signal}))$	0.139 ± 0.002	← shared
$f = (2012\ \mathcal{N}\ (\text{CF}\ \Xi_b^0 \to pK\pi\pi\ \text{in}\ p\pi\pi\pi)/(\ \mathcal{N}\ (\text{as Signal}))$	0.165 ± 0.002	← shared
$f = (2012\ \mathcal{N}\ (\text{CF}\ \Xi_b^0 \to pK\pi K\ \text{in}\ pK\pi\pi)/(\ \mathcal{N}\ (\text{as Signal}))$	0.192 ± 0.002	← shared
$f = (2012\ \mathcal{N}\ (B^0 \to K\pi\pi\pi\ \text{in}\ pK\pi\pi)/(\ \mathcal{N}\ (\text{in Ref.}))$	0.260 ± 0.006	← shared
$f = (2012\ \mathcal{N}\ (B^0 \to KKK\pi\ \text{in}\ pKKK)/(\ \mathcal{N}\ (\text{in Ref.}))$	0.050 ± 0.002	← shared
$f = (2012\ \mathcal{N}\ (B^0 \to KKK\pi\ \text{in}\ pK\pi\pi)/(\ \mathcal{N}\ (\text{in Ref.}))$	0.140 ± 0.002	← shared
$f = (2012\ \mathcal{N}\ (B^0 \to KKK\pi\ \text{in}\ pK\pi K)/(\ \mathcal{N}\ (\text{in Ref.}))$	0.470 ± 0.008	← shared
$f = (2012\ \mathcal{N}\ (B_s^0 \to K\pi\pi K\ \text{in}\ pKK\pi)/(\ \mathcal{N}\ (\text{in Ref.}))$	0.104 ± 0.004	← shared

A.15 Control spectra fits: Low mass cut on ph and $h'h''$ in charmless spectra

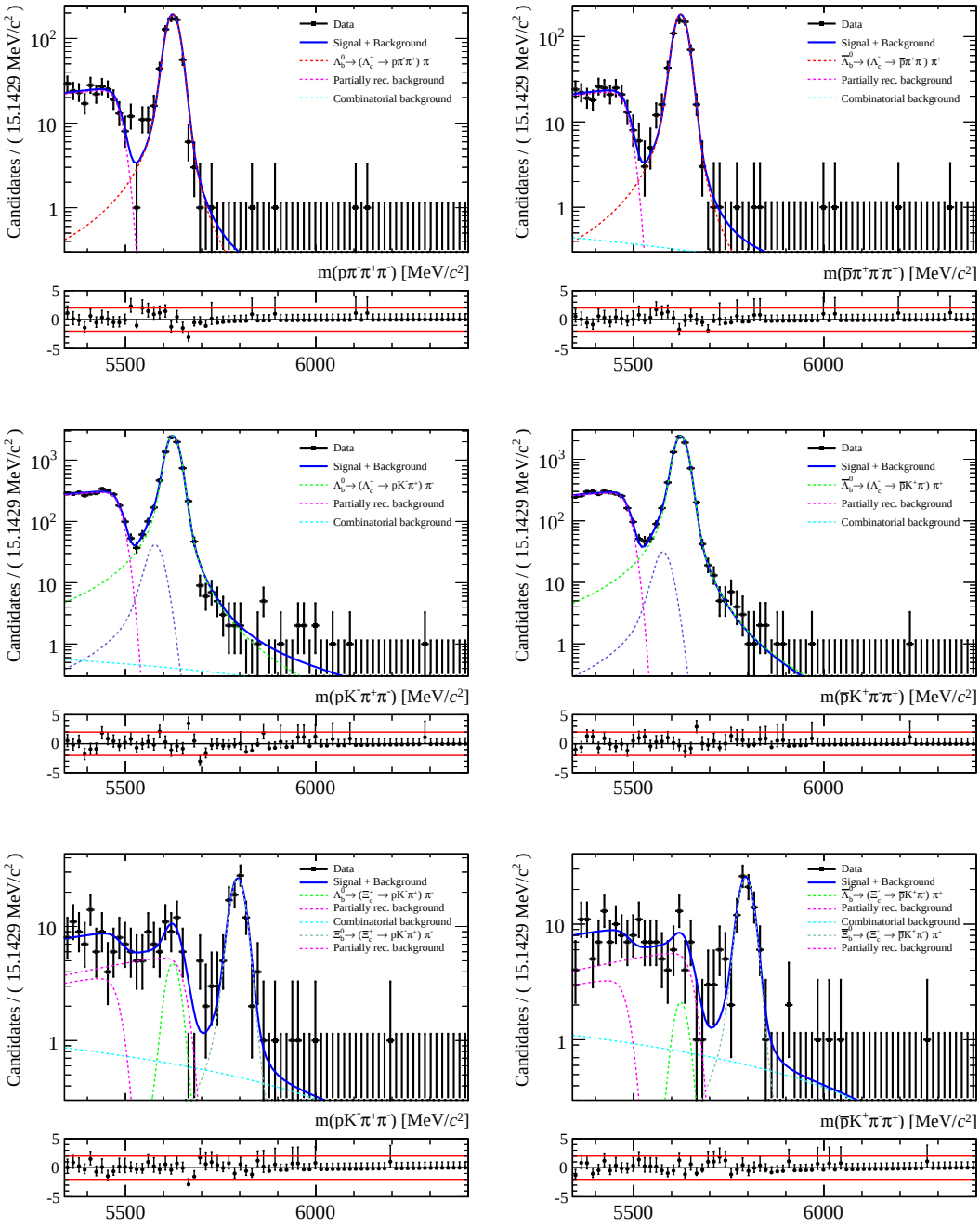

Figure A.22: Fit results for the [from top to bottom] $X_b^0 \to (\Lambda_c^+ \to p\pi\pi)\pi$, $X_b^0 \to (\Lambda_c^+ \to pK\pi)\pi$ and $X_b^0 \to (\Xi_c^+ \to pK\pi)\pi$ spectra using the 2011 data with $m_{ph} < 2$ GeV/c^2 and $m_{h'h''} < \sim$1.65 GeV/c^2 phase space cuts on the charmless spectra. Plots in the left-column are for the spectra with X_b^0 and on the right-column for the spectra with $\overline{X}_b^0$.

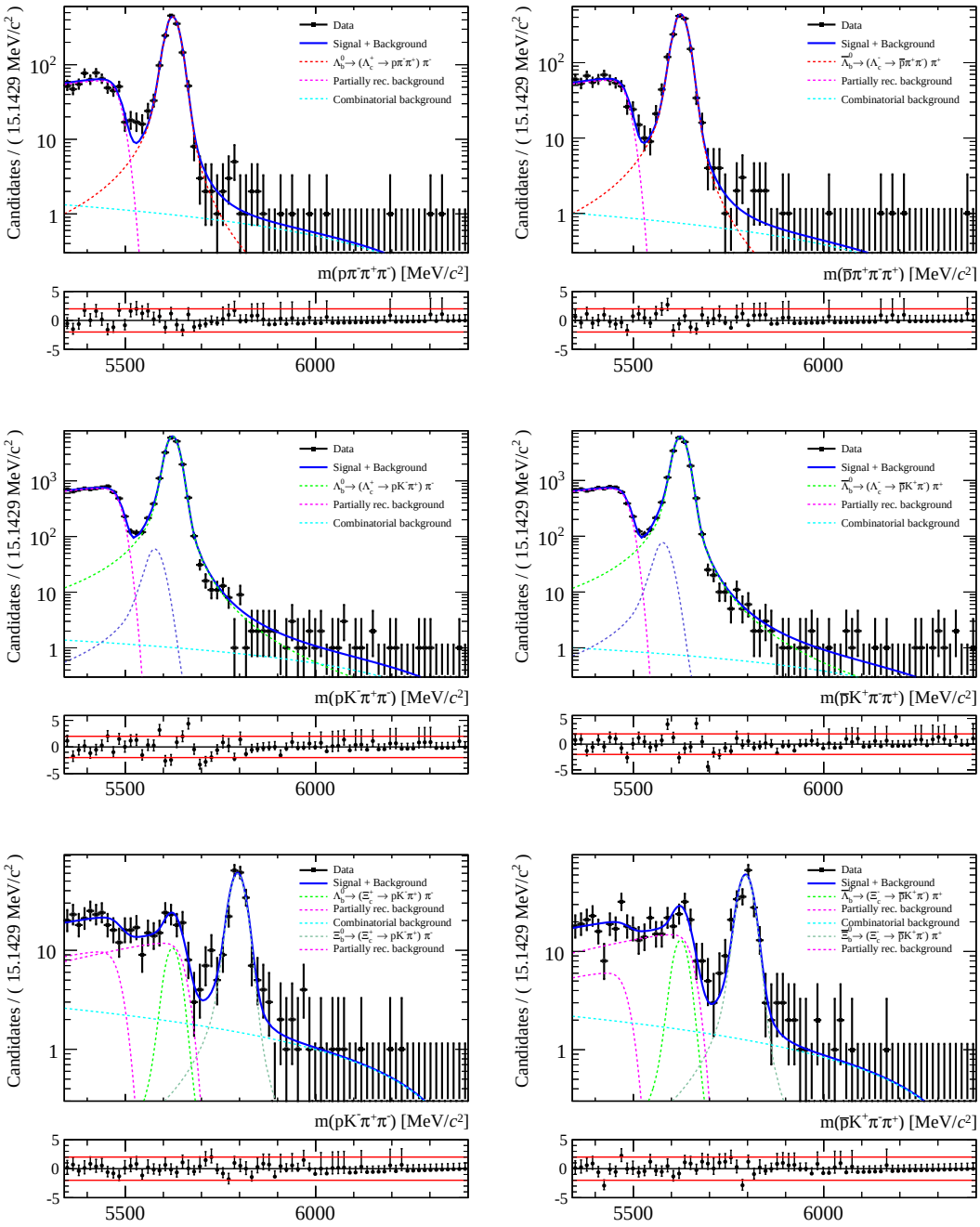

Figure A.23: Fit results for the [from top to bottom] $X_b^0 \to (\Lambda_c^+ \to p\pi\pi)\pi$, $X_b^0 \to (\Lambda_c^+ \to pK\pi)\pi$ and $X_b^0 \to (\Xi_c^+ \to pK\pi)\pi$ spectra using the 2012 data with $m_{ph} < 2$ GeV/c^2 and $m_{h'h''} < \sim$1.65 GeV/c^2 phase space cuts on the charmless spectra. Plots in the left-column are for the spectra with X_b^0 and on the right-column for the spectra with $\overline{X}_b^0$.

A.16 Fit parameters: Low mass cut on ph and $h'h''$ in charmless spectra

Table A.5: Floating parameters of the simultaneous fit to the 2011 and 2012 data with $m_{ph} < 2\,\text{GeV}/c^2$ and $m_{h'h''} < \sim 1.65\ \text{GeV}/c^2$ phase space cuts in the charmless modes.

Floating parameter (in Λ_b^0/Ξ_b^0 spectra)	Value	Floating parameter (in $\overline{\Lambda}_b^0/\overline{\Xi}_b^0$ spectra)	Value
Parameters shared 2011 and 2012 :			
μ (Λ_b^0)	5624.057 ± 0.080		
μ (Ξ_b^0) - μ (Λ_b^0)	170.340 ± 0.606		
2012 σ_{core} (Signal $\Lambda_b^0 \to pK\pi\pi$) [ref]	17.182 ± 0.203		
$\mathcal{N}$ ($B^0 \to \pi\pi\pi\pi$ in $p\pi\pi\pi$) / $\mathcal{N}$ ($B^0 \to K\pi\pi\pi$ in $p\pi\pi\pi$)	0.361 ± 0.041		← shared
Parameters for 2011 spectra :			
$\mathcal{N}$ (2011 Signal $\Lambda_b^0 \to p\pi\pi\pi$)	X.XXX ± X.XXX	$\bar{\mathcal{N}}$	X.XXX ± X.XXX
$\mathcal{N}$ (2011 Signal $\Lambda_b^0 \to pK\pi\pi$)	X.XXX ± X.XXX	$\bar{\mathcal{N}}$	X.XXX ± X.XXX
$\mathcal{N}$ (2011 Signal $\Lambda_b^0 \to pKK\pi$)	X.XXX ± X.XXX	$\bar{\mathcal{N}}$	X.XXX ± X.XXX
$\mathcal{N}$ (2011 Signal $\Lambda_b^0 \to pKKK$)	X.XXX ± X.XXX	$\bar{\mathcal{N}}$	X.XXX ± X.XXX
$\mathcal{N}$ (2011 Signal $\Xi_b^0 \to pK\pi K$)	X.XXX ± X.XXX	$\bar{\mathcal{N}}$	X.XXX ± X.XXX
$\mathcal{N}$ (2011 Signal $\Xi_b^0 \to pK\pi\pi$)	X.XXX ± X.XXX	$\bar{\mathcal{N}}$	X.XXX ± X.XXX
$\mathcal{N}$ (2011 Signal $\Xi_b^0 \to pKKK$)	X.XXX ± X.XXX	$\bar{\mathcal{N}}$	X.XXX ± X.XXX
$\mathcal{N}$ (2011 Signal $\Lambda_b^0 \to (\Lambda_c^+ \to p\pi\pi)\pi$)	629.186 ± 25.479	$\bar{\mathcal{N}}$	592.813 ± 24.813
$\mathcal{N}$ (2011 Signal $\Lambda_b^0 \to (\Lambda_c^+ \to pK\pi)\pi$)	7568.968 ± 93.052	$\bar{\mathcal{N}}$	7306.532 ± 91.274
$\mathcal{N}$ (2011 Signal $\Xi_b^0 \to (\Xi_c^+ \to pK\pi)\pi$)	93.247 ± 10.737	$\bar{\mathcal{N}}$	89.742 ± 10.697
$\mathcal{N}$ (2011 Signal $\Lambda_b^0 \to (\Xi_c^+ \to pK\pi)\pi$)	16.994 ± 8.970	$\bar{\mathcal{N}}$	7.546 ± 7.978
$\mathcal{N}$ (2011 Combinatorics in $p\pi\pi\pi$)	25.885 ± 13.232	$\bar{\mathcal{N}}$	3.741 ± 13.487
$\mathcal{N}$ (2011 Combinatorics in $pK\pi\pi$)	49.297 ± 15.963	$\bar{\mathcal{N}}$	57.396 ± 16.700
$\mathcal{N}$ (2011 Combinatorics in $pKK\pi$)	55.545 ± 15.162	$\bar{\mathcal{N}}$	36.016 ± 15.581
$\mathcal{N}$ (2011 Combinatorics in $pKKK$)	13.854 ± 8.163	$\bar{\mathcal{N}}$	21.482 ± 8.403

$\mathcal{N}$ (2011 Combinatorics in $pK\pi K$)	16.534 ± 10.857	$\bar{\mathcal{N}}$	-6.672 ± 144.343
$\mathcal{N}$ (2011 Combinatorics in $(\Lambda_c^+ \to p\pi\pi)\pi$)	8.572 ± 5.608	$\bar{\mathcal{N}}$	14.803 ± 6.974
$\mathcal{N}$ (2011 Combinatorics in $(\Lambda_c^+ \to pK\pi)\pi$)	18.861 ± 11.732	$\bar{\mathcal{N}}$	-2.765 ± 9.372
$\mathcal{N}$ (2011 Combinatorics in $(\Xi_c^+ \to pK\pi)\pi$)	29.086 ± 13.246	$\bar{\mathcal{N}}$	36.885 ± 14.279
$\mathcal{N}$ (2011 CF $B^0 \to K\pi\pi\pi$ in $p\pi\pi\pi$)	36.252 ± 9.068	$\bar{\mathcal{N}}$	45.766 ± 8.710
$\mathcal{N}$ (2011 CF $B_s^0 \to K\pi\pi K$ in $pK\pi\pi$)	11.732 ± 3.420	$\bar{\mathcal{N}}$	11.021 ± 2.447
$\mathcal{N}$ (2011 CF $B^0 \to KKK\pi$ in $pKK\pi$)	16.645 ± 4.555	$\bar{\mathcal{N}}$	32.486 ± 7.066
$\mathcal{N}$ (2011 CF $B_s^0 \to KKKK$ in $pKKK$)	9.324 ± 2.755	$\bar{\mathcal{N}}$	8.311 ± 2.576
$\mathcal{N}$ (2011 PR from $\Lambda_b^0 \to$ 5-body in $p\pi\pi\pi$)	141.246 ± 14.591	$\bar{\mathcal{N}}$	132.177 ± 13.985
$\mathcal{N}$ (2011 PR from $\Lambda_b^0 \to$ 5-body in $pK\pi\pi$)	158.034 ± 27.935	$\bar{\mathcal{N}}$	166.786 ± 29.842
$\mathcal{N}$ (2011 PR from $\Xi_b^0 \to$ 5-body in $pK\pi\pi$)	129.912 ± 39.461	$\bar{\mathcal{N}}$	170.963 ± 41.667
$\mathcal{N}$ (2011 PR from $\Lambda_b^0 \to$ 5-body in $pKK\pi$)	33.151 ± 9.641	$\bar{\mathcal{N}}$	41.770 ± 9.523
$\mathcal{N}$ (2011 PR from $\Lambda_b^0 \to$ 5-body in $pKKK$)	25.475 ± 6.197	$\bar{\mathcal{N}}$	17.915 ± 5.545
$\mathcal{N}$ (2011 PR from $\Lambda_b^0 \to$ 5-body in $pK\pi K$)	18.733 ± 6.933	$\bar{\mathcal{N}}$	32.579 ± 10.677
$\mathcal{N}$ (2011 PR from $\Xi_b^0 \to$ 5-body in $pK\pi K$)	0.000 ± 15.832	$\bar{\mathcal{N}}$	11.178 ± 15.906
$\mathcal{N}$ (2011 PR from $\Lambda_b^0 \to$ 5-body in $(\Lambda_c^+ \to p\pi\pi)\pi$)	229.243 ± 15.722	$\bar{\mathcal{N}}$	211.386 ± 15.193
$\mathcal{N}$ (2011 PR from $\Lambda_b^0 \to$ 5-body in $(\Lambda_c^+ \to pK\pi)\pi$)	2805.934 ± 54.475	$\bar{\mathcal{N}}$	2661.967 ± 52.967
$\mathcal{N}$ (2011 PR from $\Lambda_b^0 \to$ 5-body in $(\Xi_c^+ \to pK\pi)\pi$)	33.177 ± 13.652	$\bar{\mathcal{N}}$	30.819 ± 13.851
$\mathcal{N}$ (2011 PR from $\Xi_b^0 \to$ 5-body in $(\Xi_c^+ \to pK\pi)\pi$)	98.495 ± 21.122	$\bar{\mathcal{N}}$	104.009 ± 21.591
2011 c (Combinatorics in charmless decays)	-1.016 ± 0.037		← shared
2011 c (Combinatorics in charmed decays)	-1.081 ± 0.078		← shared
2011 p (PR from Λ_b^0/Ξ_b^0 + 5-body in charmless spectra)	-0.176 ± 0.054		← shared
2011 s (PR from Λ_b^0/Ξ_b^0 + 5-body in charmless spectra)	9.990 ± 22.958		← shared
2011 p (PR from Λ_b^0 + 5-body in $(\Lambda_c^+ \to pK\pi)\pi$)	0.091 ± 0.050		← shared
2011 s (PR from Λ_b^0 + 5-body in $(\Lambda_c^+ \to pK\pi)\pi$)	-5.204 ± 2.656		← shared
$r = (2011\ \sigma_{\text{core}}\ \Lambda_b^0 \to p\pi\pi\pi)/(\sigma_{\text{ref}})$	1.050 ± 0.018		← shared
$r = (2011\ \sigma_{\text{core}}\ \Lambda_b^0 \to pK\pi\pi)/(\sigma_{\text{ref}})$	0.998 ± 0.016		← shared
$r = (2011\ \sigma_{\text{core}}\ \Lambda_b^0 \to pKK\pi)/(\sigma_{\text{ref}})$	0.963 ± 0.018		← shared
$r = (2011\ \sigma_{\text{core}}\ \Lambda_b^0 \to pKKK)/(\sigma_{\text{ref}})$	0.910 ± 0.015		← shared

$r = (2011\ \sigma_{\text{core}}\ \Xi_b^0 \to pK\pi\pi)/(\sigma_{\text{ref}})$	1.032 ± 0.018	$\leftarrow$ shared
$r = (2011\ \sigma_{\text{core}}\ \Xi_b^0 \to pK\pi K)/(\sigma_{\text{ref}})$	0.993 ± 0.018	$\leftarrow$ shared
$r = (2011\ \sigma_{\text{core}}\ \Xi_b^0 \to pKKK)/(\sigma_{\text{ref}})$	0.937 ± 0.016	$\leftarrow$ shared
$2011\ \sigma_{\text{core}}$ (Signal $\Lambda_b^0 \to (\Lambda_c^+ \to p\pi\pi)\pi$)	18.285 ± 0.499	$\leftarrow$ shared
$2011\ \sigma_{\text{core}}$ (Signal $\Lambda_b^0 \to (\Lambda_c^+ \to pK\pi)\pi$)	17.159 ± 0.145	$\leftarrow$ shared
$2011\ \sigma_{\text{core}}$ (Signal $\Lambda_b^0 \to (\Xi_c^+ \to pK\pi)\pi$)	20.095 ± 2.020	$\leftarrow$ shared
$f = (2011\ \mathcal{N}$ (CF $\Lambda_b^0 \to p\pi\pi\pi$ in $pK\pi\pi)/(\ \mathcal{N}$ (as Signal))	0.045 ± 0.001	$\leftarrow$ shared
$f = (2011\ \mathcal{N}$ (CF $\Lambda_b^0 \to pK\pi\pi$ in $pKK\pi)/(\ \mathcal{N}$ (as Signal))	0.046 ± 0.001	$\leftarrow$ shared
$f = (2011\ \mathcal{N}$ (CF $\Lambda_b^0 \to pK\pi\pi$ in $p\pi\pi\pi)/(\ \mathcal{N}$ (as Signal))	0.126 ± 0.002	$\leftarrow$ shared
$f = (2011\ \mathcal{N}$ (CF $\Lambda_b^0 \to pK\pi\pi$ in $pK\pi K)/(\ \mathcal{N}$ (as Signal))	0.045 ± 0.001	$\leftarrow$ shared
$f = (2011\ \mathcal{N}$ (CF $\Lambda_b^0 \to pKK\pi$ in $pK\pi\pi)/(\ \mathcal{N}$ (as Signal))	0.139 ± 0.003	$\leftarrow$ shared
$f = (2011\ \mathcal{N}$ (CF $\Lambda_b^0 \to pKKK$ in $pKK\pi)/(\ \mathcal{N}$ (as Signal))	0.240 ± 0.004	$\leftarrow$ shared
$f = (2011\ \mathcal{N}$ (CF $\Lambda_b^0 \to pKKK$ in $pK\pi K)/(\ \mathcal{N}$ (as Signal))	0.204 ± 0.004	$\leftarrow$ shared
$f = (2011\ \mathcal{N}$ (CF $\Xi_b^0 \to pK\pi\pi$ in $p\pi\pi\pi)/(\ \mathcal{N}$ (as Signal))	0.143 ± 0.002	$\leftarrow$ shared
$f = (2011\ \mathcal{N}$ (CF $\Xi_b^0 \to pK\pi K$ in $pK\pi\pi)/(\ \mathcal{N}$ (as Signal))	0.164 ± 0.003	$\leftarrow$ shared
$f = (2011\ \mathcal{N}$ ($B^0 \to K\pi\pi\pi$ in $pK\pi\pi)/(\ \mathcal{N}$ (in Ref.))	0.253 ± 0.009	$\leftarrow$ shared
$f = (2011\ \mathcal{N}$ ($B^0 \to KKK\pi$ in $pKKK)/(\ \mathcal{N}$ (in Ref.))	0.055 ± 0.003	$\leftarrow$ shared
$f = (2011\ \mathcal{N}$ ($B^0 \to KKK\pi$ in $pK\pi\pi)/(\ \mathcal{N}$ (in Ref.))	0.135 ± 0.003	$\leftarrow$ shared
$f = (2011\ \mathcal{N}$ ($B^0 \to KKK\pi$ in $pK\pi K)/(\ \mathcal{N}$ (in Ref.))	0.486 ± 0.012	$\leftarrow$ shared
$f = (2011\ \mathcal{N}$ ($B_s^0 \to K\pi\pi K$ in $pKK\pi)/(\ \mathcal{N}$ (in Ref.))	0.094 ± 0.006	$\leftarrow$ shared

Parameters for 2012 spectra :			
$\mathcal{N}$ (2012 Signal $\Lambda_b^0 \to p\pi\pi\pi$)	X.XXX $\pm$ X.XXX	$\bar{\mathcal{N}}$	X.XXX $\pm$ X.XXX
$\mathcal{N}$ (2012 Signal $\Lambda_b^0 \to pK\pi\pi$)	X.XXX $\pm$ X.XXX	$\bar{\mathcal{N}}$	X.XXX $\pm$ X.XXX
$\mathcal{N}$ (2012 Signal $\Lambda_b^0 \to pKK\pi$)	X.XXX $\pm$ X.XXX	$\bar{\mathcal{N}}$	X.XXX $\pm$ X.XXX
$\mathcal{N}$ (2012 Signal $\Lambda_b^0 \to pKKK$)	X.XXX $\pm$ X.XXX	$\bar{\mathcal{N}}$	X.XXX $\pm$ X.XXX
$\mathcal{N}$ (2012 Signal $\Xi_b^0 \to pK\pi K$)	X.XXX $\pm$ X.XXX	$\bar{\mathcal{N}}$	X.XXX $\pm$ X.XXX
$\mathcal{N}$ (2012 Signal $\Xi_b^0 \to pK\pi\pi$)	X.XXX $\pm$ X.XXX	$\bar{\mathcal{N}}$	X.XXX $\pm$ X.XXX
$\mathcal{N}$ (2012 Signal $\Xi_b^0 \to pKKK$)	X.XXX $\pm$ X.XXX	$\bar{\mathcal{N}}$	X.XXX $\pm$ X.XXX

$\mathcal{N}$ (2012 Signal $\Lambda_b^0 \to (\Lambda_c^+ \to p\pi\pi)\pi$)	1480.742 ± 39.423	$\bar{\mathcal{N}}$	1479.554 ± 39.282
$\mathcal{N}$ (2012 Signal $\Lambda_b^0 \to (\Lambda_c^+ \to pK\pi)\pi$)	19089.503 ± 147.537	$\bar{\mathcal{N}}$	18664.701 ± 146.163
$\mathcal{N}$ (2012 Signal $\Xi_b^0 \to (\Xi_c^+ \to pK\pi)\pi$)	214.938 ± 16.149	$\bar{\mathcal{N}}$	216.151 ± 16.271
$\mathcal{N}$ (2012 Signal $\Lambda_b^0 \to (\Xi_c^+ \to pK\pi)\pi$)	38.119 ± 13.812	$\bar{\mathcal{N}}$	47.039 ± 15.034
$\mathcal{N}$ (2012 Combinatorics in $p\pi\pi\pi$)	65.801 ± 32.934	$\bar{\mathcal{N}}$	43.509 ± 34.494
$\mathcal{N}$ (2012 Combinatorics in $pK\pi\pi$)	102.554 ± 31.808	$\bar{\mathcal{N}}$	91.621 ± 33.343
$\mathcal{N}$ (2012 Combinatorics in $pKK\pi$)	44.565 ± 24.581	$\bar{\mathcal{N}}$	40.707 ± 27.988
$\mathcal{N}$ (2012 Combinatorics in $pKKK$)	60.549 ± 20.090	$\bar{\mathcal{N}}$	27.490 ± 18.890
$\mathcal{N}$ (2012 Combinatorics in $pK\pi K$)	27.418 ± 17.253	$\bar{\mathcal{N}}$	-3.025 ± 13.861
$\mathcal{N}$ (2012 Combinatorics in $(\Lambda_c^+ \to p\pi\pi)\pi$)	46.695 ± 12.677	$\bar{\mathcal{N}}$	35.581 ± 11.225
$\mathcal{N}$ (2012 Combinatorics in $(\Lambda_c^+ \to pK\pi)\pi$)	48.695 ± 16.985	$\bar{\mathcal{N}}$	35.412 ± 15.986
$\mathcal{N}$ (2012 Combinatorics in $(\Xi_c^+ \to pK\pi)\pi$)	91.751 ± 20.340	$\bar{\mathcal{N}}$	77.213 ± 20.089
$\mathcal{N}$ (2012 CF $B^0 \to K\pi\pi\pi$ in $p\pi\pi\pi$)	166.699 ± 20.618	$\bar{\mathcal{N}}$	180.645 ± 19.646
$\mathcal{N}$ (2012 CF $B_s^0 \to K\pi\pi K$ in $pK\pi\pi$)	59.989 ± 16.704	$\bar{\mathcal{N}}$	89.781 ± 17.127
$\mathcal{N}$ (2012 CF $B^0 \to KKK\pi$ in $pKK\pi$)	101.065 ± 18.748	$\bar{\mathcal{N}}$	149.119 ± 22.238
$\mathcal{N}$ (2012 CF $B_s^0 \to KKKK$ in $pKKK$)	46.895 ± 13.770	$\bar{\mathcal{N}}$	56.176 ± 12.830
$\mathcal{N}$ (2012 PR from $\Lambda_b^0 \to$ 5-body in $p\pi\pi\pi$)	259.523 ± 20.856	$\bar{\mathcal{N}}$	263.325 ± 20.800
$\mathcal{N}$ (2012 PR from $\Lambda_b^0 \to$ 5-body in $pK\pi\pi$)	365.604 ± 48.465	$\bar{\mathcal{N}}$	442.733 ± 39.907
$\mathcal{N}$ (2012 PR from $\Xi_b^0 \to$ 5-body in $pK\pi\pi$)	321.839 ± 61.401	$\bar{\mathcal{N}}$	141.023 ± 52.809
$\mathcal{N}$ (2012 PR from $\Lambda_b^0 \to$ 5-body in $pKK\pi$)	78.684 ± 13.178	$\bar{\mathcal{N}}$	82.751 ± 13.603
$\mathcal{N}$ (2012 PR from $\Lambda_b^0 \to$ 5-body in $pKKK$)	35.764 ± 9.219	$\bar{\mathcal{N}}$	54.318 ± 9.625
$\mathcal{N}$ (2012 PR from $\Lambda_b^0 \to$ 5-body in $pK\pi K$)	44.950 ± 17.324	$\bar{\mathcal{N}}$	37.514 ± 15.915
$\mathcal{N}$ (2012 PR from $\Xi_b^0 \to$ 5-body in $pK\pi K$)	34.929 ± 26.089	$\bar{\mathcal{N}}$	13.567 ± 24.343
$\mathcal{N}$ (2012 PR from $\Lambda_b^0 \to$ 5-body in $(\Lambda_c^+ \to p\pi\pi)\pi$)	573.563 ± 25.104	$\bar{\mathcal{N}}$	550.866 ± 24.474
$\mathcal{N}$ (2012 PR from $\Lambda_b^0 \to$ 5-body in $(\Lambda_c^+ \to pK\pi)\pi$)	6867.951 ± 85.154	$\bar{\mathcal{N}}$	6676.374 ± 83.922
$\mathcal{N}$ (2012 PR from $\Lambda_b^0 \to$ 5-body in $(\Xi_c^+ \to pK\pi)\pi$)	90.920 ± 20.530	$\bar{\mathcal{N}}$	56.728 ± 21.379
$\mathcal{N}$ (2012 PR from $\Xi_b^0 \to$ 5-body in $(\Xi_c^+ \to pK\pi)\pi$)	214.275 ± 31.777	$\bar{\mathcal{N}}$	268.868 ± 34.605
2012 c (Combinatorics in charmless decays)	-1.004 ± 0.000		← shared
2012 c (Combinatorics in charmed decays)	-0.984 ± 0.056		← shared

2012 p (PR from Λ_b^0/Ξ_b^0 + 5-body in charmless spectra)	0.016 ± 0.122	← shared
2012 s (PR from Λ_b^0/Ξ_b^0 + 5-body in charmless spectra)	6.354 ± 4.893	← shared
2012 p (PR from Λ_b^0 + 5-body in $(\Lambda_c^+ \to pK\pi)\pi$)	0.121 ± 0.032	← shared
2012 s (PR from Λ_b^0 + 5-body in $(\Lambda_c^+ \to pK\pi)\pi$)	-6.659 ± 1.712	← shared
$r = (2012\ \sigma_{\text{core}}\ \Lambda_b^0 \to p\pi\pi\pi)/(\sigma_{\text{ref}})$	1.069 ± 0.015	← shared
$r = (2012\ \sigma_{\text{core}}\ \Lambda_b^0 \to pKK\pi)/(\sigma_{\text{ref}})$	0.962 ± 0.015	← shared
$r = (2012\ \sigma_{\text{core}}\ \Lambda_b^0 \to pKKK)/(\sigma_{\text{ref}})$	0.894 ± 0.013	← shared
$r = (2012\ \sigma_{\text{core}}\ \Xi_b^0 \to pK\pi\pi)/(\sigma_{\text{ref}})$	1.040 ± 0.017	← shared
$r = (2012\ \sigma_{\text{core}}\ \Xi_b^0 \to pK\pi K)/(\sigma_{\text{ref}})$	0.992 ± 0.015	← shared
$r = (2012\ \sigma_{\text{core}}\ \Xi_b^0 \to pKKK)/(\sigma_{\text{ref}})$	0.929 ± 0.014	← shared
2012 σ_{core} (Signal $\Lambda_b^0 \to (\Lambda_c^+ \to p\pi\pi)\pi$)	18.930 ± 0.344	← shared
2012 σ_{core} (Signal $\Lambda_b^0 \to (\Lambda_c^+ \to pK\pi)\pi$)	16.980 ± 0.091	← shared
2012 σ_{core} (Signal $\Lambda_b^0 \to (\Xi_c^+ \to pK\pi)\pi$)	20.357 ± 1.208	← shared
$f = (2012\ \mathcal{N}\ (\text{CF}\ \Lambda_b^0 \to p\pi\pi\pi\ \text{in}\ pK\pi\pi)/(\ \mathcal{N}\ (\text{as Signal}))$	0.044 ± 0.001	← shared
$f = (2012\ \mathcal{N}\ (\text{CF}\ \Lambda_b^0 \to pK\pi\pi\ \text{in}\ pKK\pi)/(\ \mathcal{N}\ (\text{as Signal}))$	0.047 ± 0.001	← shared
$f = (2012\ \mathcal{N}\ (\text{CF}\ \Lambda_b^0 \to pK\pi\pi\ \text{in}\ p\pi\pi\pi)/(\ \mathcal{N}\ (\text{as Signal}))$	0.127 ± 0.002	← shared
$f = (2012\ \mathcal{N}\ (\text{CF}\ \Lambda_b^0 \to pK\pi\pi\ \text{in}\ pK\pi K)/(\ \mathcal{N}\ (\text{as Signal}))$	0.042 ± 0.001	← shared
$f = (2012\ \mathcal{N}\ (\text{CF}\ \Lambda_b^0 \to pKK\pi\ \text{in}\ pK\pi\pi)/(\ \mathcal{N}\ (\text{as Signal}))$	0.137 ± 0.002	← shared
$f = (2012\ \mathcal{N}\ (\text{CF}\ \Lambda_b^0 \to pKKK\ \text{in}\ pKK\pi)/(\ \mathcal{N}\ (\text{as Signal}))$	0.237 ± 0.003	← shared
$f = (2012\ \mathcal{N}\ (\text{CF}\ \Lambda_b^0 \to pKKK\ \text{in}\ pK\pi K)/(\ \mathcal{N}\ (\text{as Signal}))$	0.198 ± 0.003	← shared
$f = (2012\ \mathcal{N}\ (\text{CF}\ \Xi_b^0 \to pK\pi\pi\ \text{in}\ p\pi\pi\pi)/(\ \mathcal{N}\ (\text{as Signal}))$	0.141 ± 0.002	← shared
$f = (2012\ \mathcal{N}\ (\text{CF}\ \Xi_b^0 \to pK\pi K\ \text{in}\ pK\pi\pi)/(\ \mathcal{N}\ (\text{as Signal}))$	0.152 ± 0.002	← shared
$f = (2012\ \mathcal{N}\ (B^0 \to K\pi\pi\pi\ \text{in}\ pK\pi\pi)/(\ \mathcal{N}\ (\text{in Ref.}))$	0.255 ± 0.006	← shared
$f = (2012\ \mathcal{N}\ (B^0 \to KKK\pi\ \text{in}\ pKKK)/(\ \mathcal{N}\ (\text{in Ref.}))$	0.049 ± 0.002	← shared
$f = (2012\ \mathcal{N}\ (B^0 \to KKK\pi\ \text{in}\ pK\pi\pi)/(\ \mathcal{N}\ (\text{in Ref.}))$	0.140 ± 0.002	← shared
$f = (2012\ \mathcal{N}\ (B^0 \to KKK\pi\ \text{in}\ pK\pi K)/(\ \mathcal{N}\ (\text{in Ref.}))$	0.470 ± 0.008	← shared
$f = (2012\ \mathcal{N}\ (B_s^0 \to K\pi\pi K\ \text{in}\ pKK\pi)/(\ \mathcal{N}\ (\text{in Ref.}))$	0.096 ± 0.004	← shared

A.17 Correlation of signal yields and ARGUS parameters

Table A.6: Correlation of the signal yields and the ARGUS slope and power.

Yield parameter	Correlation (in %)			
	2011		2012	
	power	slope	power	slope
2011 Signal yields:				
$\mathcal{N}$ (Signal $\Lambda_b^0 \to p\pi\pi\pi$)	-1.256	0.452	-0.287	0.157
$\overline{\mathcal{N}}$ (Signal $\Lambda_b^0 \to p\pi\pi\pi$)	-1.306	0.507	-0.312	0.164
$\mathcal{N}$ (Signal $\Lambda_b^0 \to pK\pi\pi$)	-1.709	3.649	-0.202	0.119
$\overline{\mathcal{N}}$ (Signal $\Lambda_b^0 \to pK\pi\pi$)	-1.218	3.039	-0.189	0.105
$\mathcal{N}$ (Signal $\Lambda_b^0 \to pKK\pi$)	-2.527	1.894	-0.129	0.084
$\overline{\mathcal{N}}$ (Signal $\Lambda_b^0 \to pKK\pi$)	-2.018	1.390	-0.149	0.098
$\mathcal{N}$ (Signal $\Lambda_b^0 \to pKKK$)	0.055	-0.141	-0.083	0.052
$\overline{\mathcal{N}}$ (Signal $\Lambda_b^0 \to pKKK$)	-0.460	0.225	-0.122	0.082
$\mathcal{N}$ (Signal $\Xi_b^0 \to pK\pi\pi$)	0.689	-0.317	0.087	-0.024
$\overline{\mathcal{N}}$ (Signal $\Xi_b^0 \to pK\pi\pi$)	0.727	-0.451	0.114	-0.048
$\mathcal{N}$ (Signal $\Xi_b^0 \to pK\pi K$)	-0.643	0.519	-0.101	0.076
$\overline{\mathcal{N}}$ (Signal $\Xi_b^0 \to pK\pi K$)	-0.337	0.231	-0.052	0.026
$\mathcal{N}$ (Signal $\Xi_b^0 \to pKKK$)	1.159	-0.709	-0.002	0.052
$\overline{\mathcal{N}}$ (Signal $\Xi_b^0 \to pKKK$)	0.792	-0.612	0.097	-0.069
$\mathcal{N}$ (Signal $\Lambda_b^0 \to (\Lambda_c^+ \to p\pi\pi)\pi$)	0.003	0.003	0.001	0.001
$\overline{\mathcal{N}}$ (Signal $\Lambda_b^0 \to (\Lambda_c^+ \to p\pi\pi)\pi$)	-0.002	0.006	0.001	0.000
$\mathcal{N}$ (Signal $\Lambda_b^0 \to (\Lambda_c^+ \to pK\pi)\pi$)	-0.204	0.157	-0.318	0.244
$\overline{\mathcal{N}}$ (Signal $\Lambda_b^0 \to (\Lambda_c^+ \to pK\pi)\pi$)	-0.191	0.146	-0.328	0.252
2012 Signal yields:				
$\mathcal{N}$ (Signal $\Lambda_b^0 \to p\pi\pi\pi$)	-0.292	0.164	-1.513	0.582
$\overline{\mathcal{N}}$ (Signal $\Lambda_b^0 \to p\pi\pi\pi$)	-0.288	0.159	-1.665	0.672
$\mathcal{N}$ (Signal $\Lambda_b^0 \to pK\pi\pi$)	-0.308	0.176	-2.946	3.791
$\overline{\mathcal{N}}$ (Signal $\Lambda_b^0 \to pK\pi\pi$)	-0.313	0.177	-2.689	3.863
$\mathcal{N}$ (Signal $\Lambda_b^0 \to pKK\pi$)	-0.133	0.079	-2.568	1.759
$\overline{\mathcal{N}}$ (Signal $\Lambda_b^0 \to pKK\pi$)	-0.146	0.091	-2.678	1.917
$\mathcal{N}$ (Signal $\Lambda_b^0 \to pKKK$)	-0.079	0.047	-0.442	0.334
$\overline{\mathcal{N}}$ (Signal $\Lambda_b^0 \to pKKK$)	-0.079	0.050	-0.549	0.396
$\mathcal{N}$ (Signal $\Xi_b^0 \to pK\pi\pi$)	0.082	-0.011	0.584	-0.311
$\overline{\mathcal{N}}$ (Signal $\Xi_b^0 \to pK\pi\pi$)	0.114	-0.032	1.003	-0.614
$\mathcal{N}$ (Signal $\Xi_b^0 \to pK\pi K$)	-0.086	0.057	-0.485	0.303
$\overline{\mathcal{N}}$ (Signal $\Xi_b^0 \to pK\pi K$)	-0.078	0.059	-0.249	0.141
$\mathcal{N}$ (Signal $\Xi_b^0 \to pKKK$)	-0.008	0.033	0.657	-0.504
$\overline{\mathcal{N}}$ (Signal $\Xi_b^0 \to pKKK$)	0.056	-0.061	1.156	-0.994
$\mathcal{N}$ (Signal $\Lambda_b^0 \to (\Lambda_c^+ \to p\pi\pi)\pi$)	0.006	-0.003	-0.022	0.030
$\overline{\mathcal{N}}$ (Signal $\Lambda_b^0 \to (\Lambda_c^+ \to p\pi\pi)\pi$)	0.002	-0.001	-0.012	0.019
$\mathcal{N}$ (Signal $\Lambda_b^0 \to (\Lambda_c^+ \to pK\pi)\pi$)	-0.307	0.232	-0.475	0.359
$\overline{\mathcal{N}}$ (Signal $\Lambda_b^0 \to (\Lambda_c^+ \to pK\pi)\pi$)	-0.292	0.220	-0.480	0.359

Appendix B

Partial reconstruction of decays involving a resonance in the decay chain

B.1 Introduction

Statistics required by the LHCb physics case might be limited in certain cases by either the detector geometry/acceptance or the low reconstruction efficiency of some particle species (e.g. neutrals including V^0's). In particular, the reconstruction of several neutrals plagues those analysis willing to study these final states. In this analysis, we discuss a rather different approach by not reconstructing one of the decay products – from hereon referred to as partial reconstruction. The partial reconstruction is possible in some decays due to the additional constraint which is the direction of the b-hadron decay.

The basic idea of the partial reconstruction is to reconstruct the momentum and mass of the b-hadron by reconstructing all the charged tracks of the decay products and not reconstructing a final neutral decay product. The non-detected or missing particle can then be determined by decay kinematics, with the aid of topological information. Consider the hadronic decay of B^0 to $J/\psi(\mu^+\mu^-)\eta'(\pi^+\pi^+X)$ shown in Figure B.1. Since the J/ψ and η' decay via electric and strong interactions, the tracks (2 muons and 2 pions) will form a unique decay vertex, which determines the flight direction of b-flavoured hadron. Somewhat similar studies in LHCb were conducted in Ref. [114] and Ref. [115].

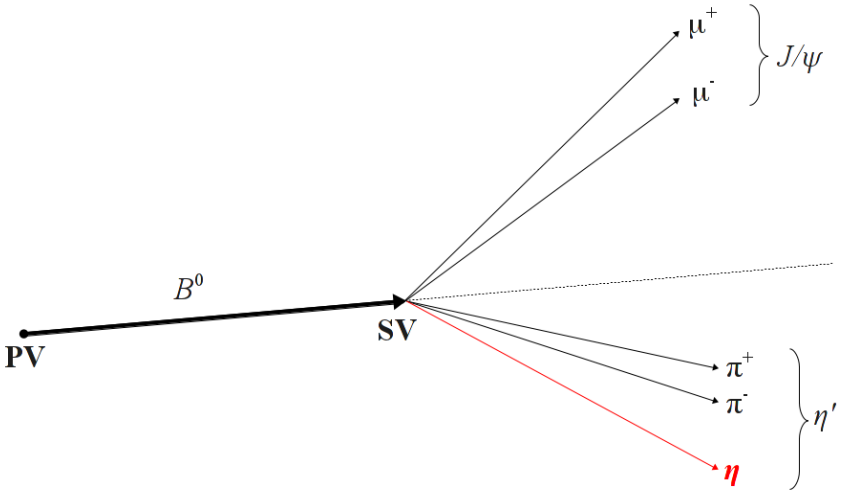

Figure B.1: Illustration of $B^0 \longrightarrow J/\psi(\mu^+\mu^-)\eta'(\pi^+\pi^-X)$ decay, where X can be a photon or η meson. The X particle is not detected and can be reconstructed using decay kinematics.

B.1.1 Partial reconstruction: Equations and procedure

Referring to Figure B.1, the four-vector energy-momentum of B^0 can be obtained even without detecting the X particle if the decay is sufficiently constrained. Counting the number of degrees of freedom, we have a total of 7 which are the three vector components of the momentum of B^0, the invariant mass of B^0, and the three vector components of the missing particle. The first four constraints come from the four vector momentum conservation in the $B^0 \longrightarrow J/\psi(\mu^+\mu^-)\eta'(\pi^+\pi^-X)$ decay,

$$\sqrt{p_B^2 + m_B^2} = \sqrt{p_{J/\psi}^2 + m_{J/\psi}^2} + \sqrt{p_{2\pi}^2 + m_{2\pi}^2} + \sqrt{p_X^2 + m_X^2} \ , \tag{B.1}$$

$$\vec{p}_B = \vec{p}_{J/\psi} + \vec{p}_{2\pi} + \vec{p}_X \ , \tag{B.2}$$

where $\vec{p}_B$, $\vec{p}_{J/\psi}$, $\vec{p}_{2\pi}$ and $\vec{p}_X$ are the three-vector momenta of B^0 meson, J/ψ meson, $\pi^+\pi^-$ mesons from the η' meson decay and X as the missing particle of the η' meson decay, respectively; while m_B, $m_{J/\psi}$, $m_{2\pi}$ and m_X are the corresponding invariant masses, respectively.

The charged tracks due to the pions will form a common secondary vertex (SV)[a] and such provide additional two constraints,

$$\vec{p}_B = \vec{p}^{\,\parallel}_{J/\psi} + \vec{p}^{\,\parallel}_{2\pi} + \vec{p}^{\,\parallel}_X \ , \tag{B.3}$$

$$\vec{0} = \vec{p}^{\,\perp}_{J/\psi} + \vec{p}^{\,\perp}_{2\pi} + \vec{p}^{\,\perp}_X \ , \tag{B.4}$$

where $\vec{p}^{\,\parallel}_{J/\psi}$, $\vec{p}^{\,\parallel}_{2\pi}$ and $\vec{p}^{\,\parallel}_X$ are the vector components of $\vec{p}_{J/\psi}$, $\vec{p}_{2\pi}$ and $\vec{p}_X$, respectively, that are parrallel (or antiparallel) to the direction of $\vec{p}_B$; while the $\vec{p}^{\,\perp}_{J/\psi}$, $\vec{p}^{\,\perp}_{2\pi}$ and $\vec{p}^{\,\perp}_X$ are the corresponding vector components that are perpendicular to the direction of $\vec{p}_B$.

The last additional constraint can be obtained by considering that the decay of B^0 should be constrainted by η' mass $m_{\eta'}$, hence by using the conservation of four vector momentum in the $B^0 \longrightarrow J/\psi\eta'$ decay,

$$m_B^2 = m_{J/\psi}^2 + m_{\eta'}^2 + 2(E_{J/\psi}E_{\eta'} - \vec{p}_{J/\psi} \cdot \vec{p}_{\eta'}) \ , \tag{B.5}$$

where $E_{J/\psi} = \sqrt{p_{J/\psi}^2 + m_{J/\psi}^2}$ and $E_{\eta'} = E_{2\pi} + E_X = \sqrt{p_{2\pi}^2 + m_{2\pi}^2} + \sqrt{p_X^2 + m_X^2}$ are the energies of J/ψ and η', respectively; while $\vec{p}_{J/\psi}$ and $\vec{p}_{\eta'} = \vec{p}_{2\pi} + \vec{p}_X$ are the corresponding three vector momenta.

We have a total of 7 constraints given by Equations B.1 - B.5 for the 7 degrees and hence the problem is well-contrained to be solvable. Solving for the $\vec{p}^{\,\parallel}_X$ results to,

$$\vec{p}^{\,\parallel}_X = (A \pm \sqrt{B})\hat{p}_B \ , \tag{B.6}$$

where,

$$A = \frac{\left[m_\Delta^2 - 2\vec{p}^{\,\perp}_{2\pi} \cdot \left(\vec{p}^{\,\perp}_{2\pi} + \vec{p}^{\,\perp}_{J/\psi}\right)\right] p^{\parallel}_{2\pi}}{2\left(p^{\perp 2}_{2\pi} + m^2_{2\pi}\right)} \ , \tag{B.7}$$

$$B = \left\{ \frac{\left[m_\Delta^2 - 2\vec{p}^{\,\perp}_{2\pi} \cdot \left(\vec{p}^{\,\perp}_{2\pi} + \vec{p}^{\,\perp}_{J/\psi}\right)\right]^2}{2\left(p^{\perp 2}_{2\pi} + m^2_{2\pi}\right)^2} - \frac{m_X^2 + \left(\vec{p}^{\,\perp}_{J/\psi} + \vec{p}^{\,\perp}_{2\pi}\right)^2}{p^{\perp 2}_{2\pi} + m^2_{2\pi}} \right\} E^2_{2\pi} \ , \tag{B.8}$$

[a] Both J/ψ and η' mesons decay quickly resulting in decay vertices overlapping with the decay vertex of the B^0 meson that can not be resolved by the LHCb VELO.

where $\hat{p}_B$ is a unit vector pointing in the direction of $\vec{p}_B$, m^2_Δ is equal to $m^2_{\eta'} - m^2_{2\pi} - m^2_X$, and $E^2_{2\pi}$ is equal to $p^2_{2\pi} + m^2_{2\pi} = p^{\parallel 2}_{2\pi} + p^{\perp 2}_{2\pi} + m^2_{2\pi}$.

Equation B.6[b] is expressed in terms of quantities that can be measured by the LHCb detector with masses $m_{\eta'}$, $m_{\pi^\pm}$ and m_X constrained to their nominal values. This can then be substituted to Equation B.2 to obtain $\vec{p}_B$ and then finally solve for m_B from Equation B.1.

B.1.2 Application of partial reconstruction

The partial reconstruction method outlined in the previous Subsection can also be applied to other decay channels where one of the final decay particles is difficult to reconstruct. The accuracy of this method is dependent on the accuracy of the measurement of the secondary vertex and hence it is expected that the efficiency of this method will improve with increasing number of charged tracks that are used to determine the secondary vertex. The same argument is also true for the primary vertex. Some decay channels that partial reconstruction may be utilized are,

$$B^\pm \longrightarrow K^\pm\eta' \tag{B.9}$$
$$B^0 \longrightarrow K^0_S\eta' \tag{B.10}$$
$$B^0_s \longrightarrow J/\psi\eta', \omega, \phi, \eta \tag{B.11}$$
$$B^0_s \longrightarrow \phi\eta', \omega, \eta \tag{B.12}$$
$$\tag{B.13}$$

where η' is searched for as $\pi^+\pi^-\{\gamma, \eta\}$, η is searched for as $\pi^+\pi^-\pi^0$, and ω and ϕ are searched for as $\pi^+\pi^-\pi^0$. This reconstruction technique might be of value when we want to measure the branching fractions of these decays. But another possible application of partial reconstruction is in the determination of the asymmetry in detection efficiency. For example, the decay of B^0 to $J/\psi(p\bar{p})X$, where X are charged tracks can be used to measure the detection efficiency on p and $\bar{p}$. The idea is to reconstruct only either p or $\bar{p}$ and the charged tracks and then count the number of events. One thing to note here is that since the missing particle is charged, then it will leave hits in VELO detector, giving a hint on which of the two solutions is likely the correct one. This additional information is expected to shrink the mass resolution. Of course this can be extended to detection efficiency asymmetry on K^+ and K^-. Some decay channels that partial partial reconstruction can be used to measure detection efficiency asymmetry are,

$$B^0 \longrightarrow J/\psi(p\bar{p})K^+\pi^- \tag{B.14}$$
$$B^0 \longrightarrow \eta_c(p\bar{p})K^*(892)^0 \tag{B.15}$$
$$B^0 \longrightarrow \psi(2S)(p\bar{p})K^+\pi^- \tag{B.16}$$
$$\tag{B.17}$$

B.2 Commissioning the partial reconstruction in $B^0 \to K^0_S(\pi^+\pi^-)K^\pm\pi^\mp$

We test the partial reconstruction procedure by using the decay channel $B^0 \to K^0_S(\pi^+\pi^-)K^\pm\pi^\mp$ considering the π^- from the K^0_S decay as the missing particle. In this decay channel, the $K^\pm$

[b] A more detailed derivation of Equation B.6 can be found at the Appendix.

and $\pi^{\mp}$ tracks determine the decay vertex position, while the K^0_S flies to a significant distance from the b-hadron decay vertex before decaying to $\pi^+\pi^-$[c]. In this exercise, we use Monte Carlo events[d] in which the K^0_S decays outside the Vertex Locator (VELO) hence dubbed as K^0_S Down-Down (DD), in contrast to K^0_S Long-Long (LL) in which the K^0_S decays inside the VELO and hence provide additional constraint. A total of 62991 MC matched events are used. We are starting the study from a MC-truth based simulation and add up elements of reconstruction step by step to understand the origins and dependencies of the precision of the method.

B.2.1 Reconstruction of $\vec{p}_X$

As shown in Equation B.6, there are two possible solutions for $p^{\parallel}_X$ momentum, resulting to a two-fold ambiguity of the direction and magnitude of the missing π^-. We first try the partial reconstruction by choosing the solution of $p^{\parallel}_X$ which is closer to the true direction of $p^{\parallel}_X$ – hereafter referred as cheated partial reconstruction. This is in anticipation that we could find a procedure that can distinguish which of the two solutions is more probable[e]. Moreover, we choose the true direction of $\vec{p}_{B^0}$ in this first trial. As shown in Figure B.2, with its corresponding pull distribution, the momentum of the missing particle seems to be well determined with a resolution of $\sim$10%[f].

The ratio of terms A and $\sqrt{B}$ of Equation B.6 is shown in Figure B.3(left). The term $\sqrt{B}$ is always less than the A. The term B, as shown in Figure B.3(right), however can sometimes be negative. This is due to the resolution of the reconstruction of the visible charged tracks[g].

It is also possible to have two entries per event candidate by including the two possible solutions in the mass spectrum instead of randomly choosing which one of the two. The mass spectrum of this procedure and the random choice procedure will be relatively the same but the signal significance of this procedure will be $\sqrt{2}$ higher. For the time being, to compare with the weighted approach, we use a random choice. We take note also that an optimal solution might be to enter the two solutions when they differ by more than the resolution and use a random choice when not.

B.2.2 Reconstruction of B^0 Mass

Knowing the four-vector energy-momentum of the missing particle, the mass of the B^0 meson can then be reconstructed using Equation B.5. We investigate this partial reconstruction method by starting with the true direction of $\vec{p}_B$, true momenta of $K^{\pm}\pi^{\mp}$ mesons and cheated partial reconstruction[h]. This will then be slowly degraded: (a) by choosing the wrong solution of Equation B.6; (b) by random choice of the two solutions of Equation B.6; (c) by cheated partial reconstruction with MC true primary vertex but reconstructed secondary vertex; (d) by cheated partial reconstruction with both primary vertex and secondary vertex reconstructed; and (e) by random choice of the two solutions of Equation B.6 with both

[c] This mode was basically considered for convenience since this was used for another study [10.1007/JHEP10(2013)143].

[d] These events are fully reconstructed events.

[e] Such procedures are described in Section B.3.3.

[f] Unfortunately, the MC sample does not contain tuples for the true direction of the pions from the K^0_S decay. It is expected that this resolution will improve if true momenta of the pions are known.

[g] Conversely, background candidates will often have a B parameter negative. It is hence an intrinsic selection discriminant.

[h] Cheated in the sense that we choose the solution of Equation B.6 that is closer to the true value.

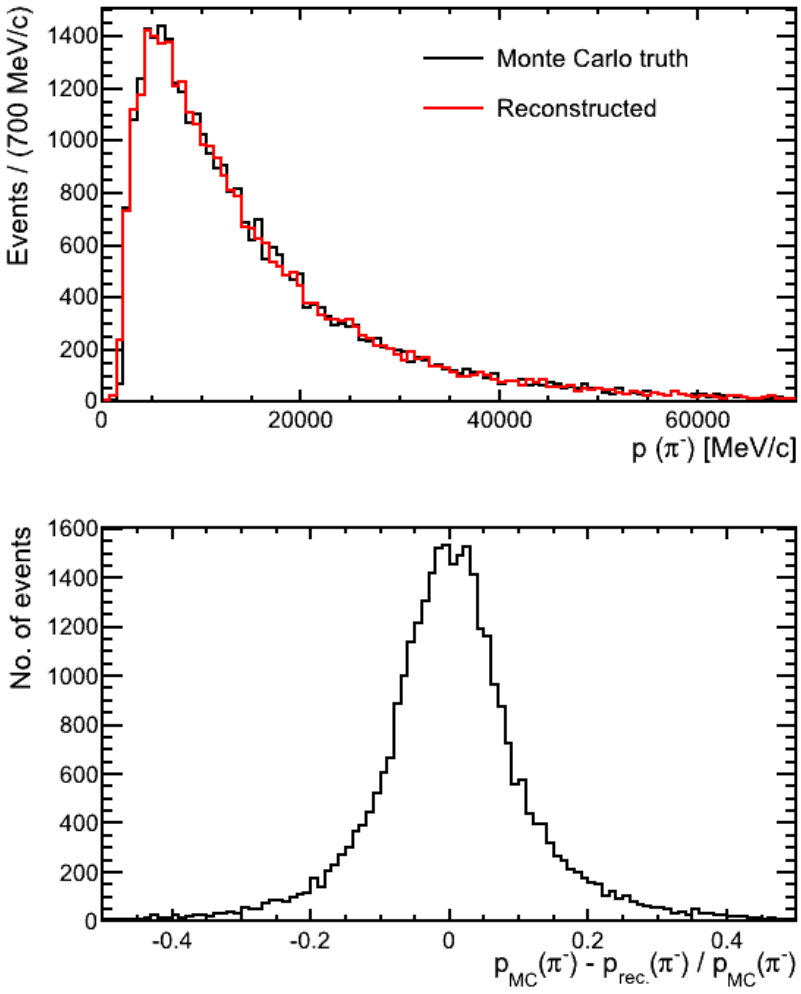

Figure B.2: (top) Superimposed histograms of the magnitude of the momentum of the missing particle as determined from Monte Carlo and reconstruction using decay kinematics. (bottom) The corresponding pull on per a event basis.

primary vertex and secondary vertex reconstructed. These cases are summarized in Table B.1. For each case, we fit the mass distribution with three Gaussian functions, taking note of the resolution of the best Gaussian as this will be compared for the different cases to be studied in the next Subsections.

Case 1

In this case, we use the true direction of $\vec{p}_B$, true[i] momenta of the visible daughter particles and also employ the cheated partial reconstruction algorithm. This can be considered as the asymptotical case, in which the partial reconstruction algorithm can not do better than this asymptotical case. To model the reconstructed mass distribution, we choose to follow a qualitative approach by fitting it with the most adequate sum of Gaussian functions. As can be seen in Figure B.4, the reconstructed m_B distribution can be well-modelled by three Gaussian functions. We take note of the resolution of the first Gaussian which is equal to $\sim$23 MeV/c^2, with a corresponding efficiency of $\sim$53% (28756/54381), as the asymptotical resolution that can be obtained by this partial reconstruction algorithm for the $B^0 \longrightarrow$

[i]Except for the momentum of the accompanying π^+ from the K^0_S due to technical reasons.

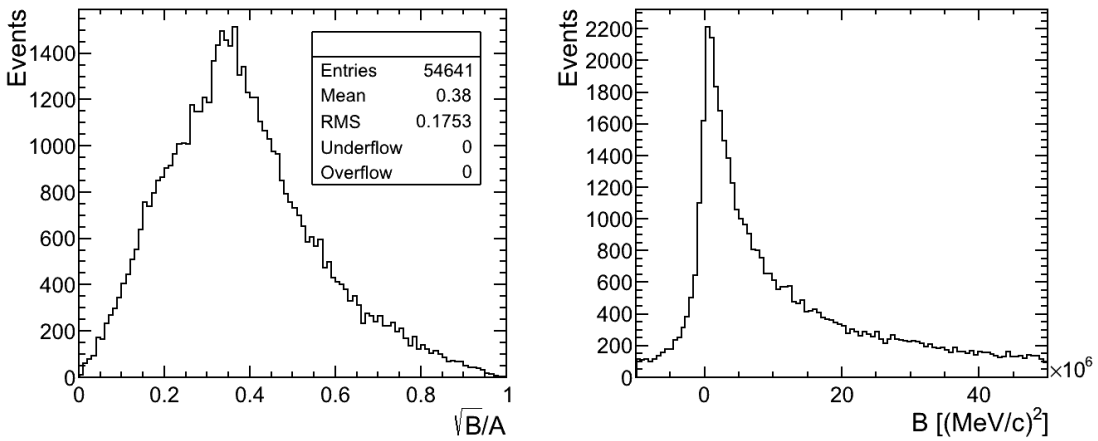

Figure B.3: (left) The ratio of terms A and $\sqrt{B}$ of Equation B.6. Only 54641 out of 62991 (∼87%) events have $B \geq 0$. (right) Distribution of term B showing some negative values.

Table B.1: Several cases for degrading m_B resolution obtained from partial reconstruction.

Case	Choice of $\vec{p}_X^{\parallel}$	Choice of PV	Choice of SV
Case 1	Good Choice (Cheated)	True PV	True SV
Case 2	Wrong Choice	True PV	True SV
Case 3	Random Choice	True PV	True SV
Case 4	Good Choice (Cheated)	True PV	Rec. SV
Case 5	Good Choice (Cheated)	Rec. PV	Rec. SV
Case 6	Random Choice	Rec. PV	Rec. SV

$K_S^0(\pi^+\pi^-)K^\pm\pi^\mp$ Down-Down.

We look for variables that can discriminate the events for the three Gaussian functions in Figure B.4. As such, we divided the mass range in Figure B.4 into 5 regions, as summarized in Table B.2. Events in regions 1 and 5 are associated to Gaussian 3 (worst resolution), events in regions 2 and 4 are associated to Gaussian 2 (moderate resolution), while events in region 3 are associated to Gaussian 1 (best resolution).

The transverse momentum of the π^+ meson[j] from the K_S^0 decay, shows a small discriminating power as shown in Figure B.5. It appears that events with low p_T of π^+ (from the K_S^0 decay) is statistically responsible for the Gaussian function with worst resolution, while events with high p_T of π^+ are on average more prominent for the Gaussian function with best resolution.

[j]The MC true momentum of π^+ (from the K_S^0 decay) was not used in Case 1, the reconstructed momenta of π^+ was used instead.

Table B.2: Division of the mass range in Figure B.4 into 5 regions.

Region No.	Range of m_B	Associated to
Region 1	5000 MeV/c^2 $< m_B <$ 5175 MeV/c^2	Gaussian 3
Region 2	5175 MeV/c^2 $< m_B <$ 5240 MeV/c^2	Gaussian 2
Region 3	5240 MeV/c^2 $< m_B <$ 5325 MeV/c^2	Gaussian 1
Region 4	5325 MeV/c^2 $< m_B <$ 5390 MeV/c^2	Gaussian 2
Region 5	5390 MeV/c^2 $< m_B <$ 5600 MeV/c^2	Gaussian 3

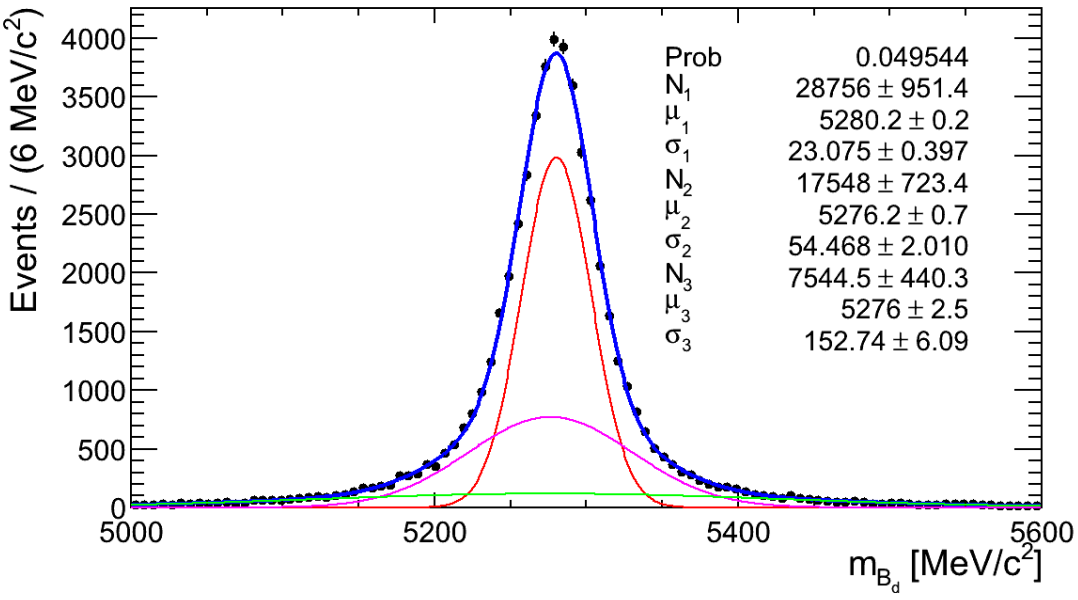

Figure B.4: B^0 invariant mass distribution as obtained using cheated partial reconstruction method using the true $\vec{p}_B$ direction and true momenta of visible daughter particles.

Case 2: Impact of wrong choice

The configuration of case 2 is the same with case 1, except that instead of taking the good choice of $\vec{p}^{\parallel}_X$ from Equation B.6 we take the wrong choice. This will give us the extent of the degradation of the m_B resolution due to wrong choice of the $\vec{p}^{\parallel}_X$ solution. As shown in Figure B.6, the resolution of Gaussian 1 degrades from ∼23 MeV/c^2 to ∼57 MeV/c^2, with a corresponding efficiency of ∼0.0751 (4083.7/54381).

Case 3: Random choice of combinations

Case 3 is the same as with case 1 or case 2, except that the choice of $\vec{p}^{\parallel}_X$ from Equation B.6 is completely random. As can be seen in Figure B.7, the resolution of Gaussian 1 is basically unchanged with respect to the Gaussian 1 of case 1 (σ_1 = ∼23 MeV/c^2). The efficiency is, as expected, twice lower compared to case 1, with only ∼25%.

Case 4: Impact of SV reconstruction

Here, we again utilized the cheated partial algorithm using MC truth primary vertex location but reconstructed secondary vertex. Figure B.8 shows the reconstructed m_B distribution in this configuration, with resolution of Gaussian 1 equal to ∼76 MeV/c^2. The corresponding efficiency is ∼30%. The resolution of Gaussian 1 can be related to the resolution $\sigma_{Rec.}$ due to the reconstruction and the resolution σ_{SV} due to the introduction of reconstructed secondary vertex, as described by this equation,

$$\sigma^2 = \sigma^2_{Rec.} + \sigma^2_{SV} \ . \tag{B.18}$$

Here we suppose that the resolution is due in an uncorrelated way to the addition of kinematical reconstruction and the SV resolutions. $\sigma^2_{Rec.}$ is ∼22 MeV/c^2 as already obtained in case 3, and henceforth using Equation B.18, σ_{SV} is equal to ∼73 MeV/c^2. Despite the crude approximations, we already identified one of the major sources of experimental uncertainties in the mass reconstruction.

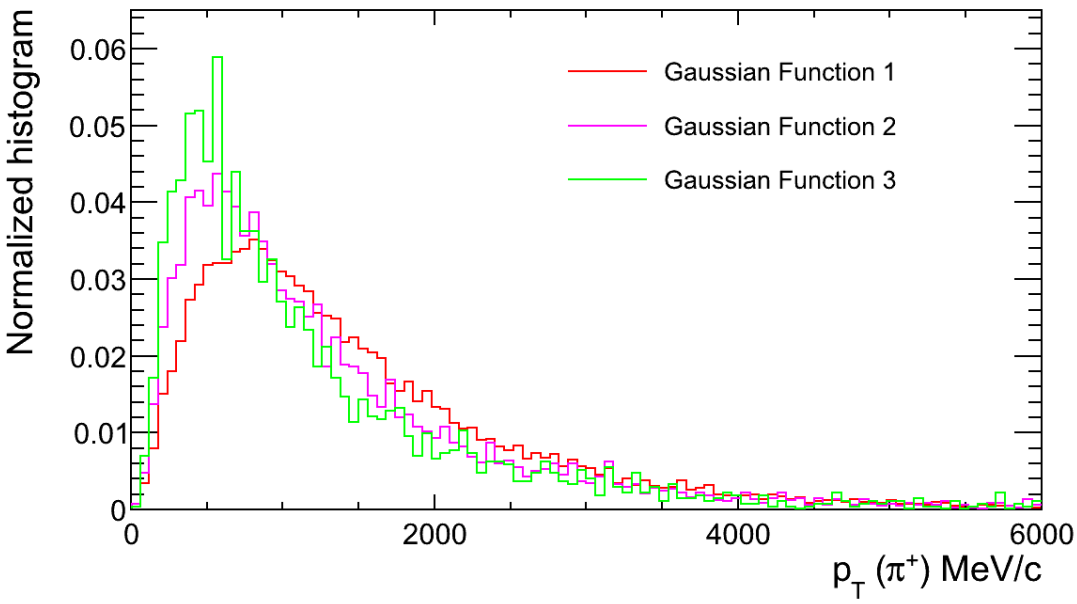

Figure B.5: The tranverse momentum of π^+ from K^0_S decay for the three categories of Gaussian functions.

Case 5: Impact of PV reconstruction

Still employing the cheated partial reconstruction algorithm, we now introduce the reconstructed primary vertex and secondary vertex in case 5. As shown in Figure B.9, the resolution of Gaussian 1 is equal to ∼89 MeV/c^2, with an efficiency of ∼26%. Since here we introduce the reconstructed primary vertex and reconstructed secondary vertex, then the resolution of Gaussian 1 is related to the resolution due to partial reconstruction algorithm, to the resolution due to the introduction of reconstructed primary vertex and to the resolution due to the introduction of reconstructed secondary vertex, as given by,

$$\sigma^2 = \sigma^2_{Rec.} + \sigma^2_{SV} + \sigma^2_{PV} \ . \tag{B.19}$$

$\sigma_{Rec.}$ and σ_{SV} have already been obtained in case 3 and case 4, respectively. Using Equation B.19, we infer σ_{PV} is ∼46 MeV/c^2.

Case 6: Full implementation

Case 6 is the full implementation of the partial reconstruction algorithm. Here, we use the reconstructed primary and secondary vertices, and utilize a random choice of $\vec{p}^{\,\parallel}_X$. The result is shown in Figure B.10. The resolution of Gaussian 1 is 90.74 MeV/c^2, with corresponding efficiency of ∼0.1470 (5887.4/40044).

The whole mass range in Figure B.10 is again divided into 5 regions: Region 1 (4000 - 4890 MeV/c^2), Region 2 (4890 - 5150 MeV/c^2), Region 3 (5150 - 5400 MeV/c^2), Region 4 (5400 - 5610 MeV/c^2) and Region 5 (5610 - 6600 MeV/c^2). By splitting the variables (topological and kinematical) according to the above-mentioned regions, it was possible to identify two main variables distinguishing statistically the badly-reconstructed events from the nicely-reconstructed events. These are the flight distance χ^2 of B^0, and the transverse χ^2 of the end vertex of B^0, as shown in Figure B.11. We then apply a square-cut on the two variables and found out that indeed the reconstructed B^0 mass resolution improves by increasing the cut values on the said variables, as shown in Figure B.12.

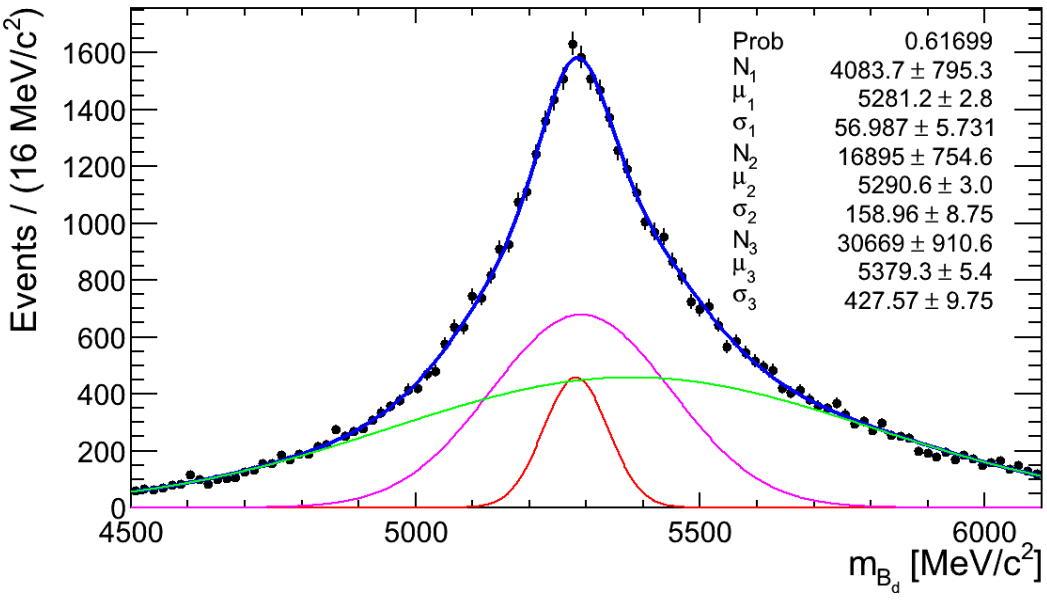

Figure B.6: B^0 invariant mass distribution as obtained using partial reconstruction method using the true $\vec{p}_B$ direction and true momenta of visible daughter particles, but with wrong choice of $\vec{p}_X^{\parallel}$.

B.2.3 Summary

We have shown in this study that the partial reconstruction technique might be a useful technique in some decays where there are enough number of constraints to apply it. Since the energy-momentum relation is a quadratic equation, we obtained two possible solutions for the decay. One can consider to randomly choose between these two solutions as what we did in this chapter, or find a clever way of statistically choosing the better solution, as what we hope to do in the next chapter.

We found out also that the introduction of the reconstructed vertices degrades the B^0 mass resolution. This is not a surprise knowing that the partial reconstruction technique depends on how one can precisely measure the direction of the b-flavoured hadron. Since there are only few tracks used to reconstruct the secondary vertex, hence this has more impact compared to the reconstruction of the primary vertex.

Knowing that the technique depends on the precise measurement of the flight direction of B^0, we have shown that one can improve the reconstructed B^0 mass resolution by cutting hard on the transverse end vertex χ^2 and the flight distance χ^2 as well. There are of course other non-linearly correlated variables that can be used to further remove badly reconstructed events, and this will be studied in the next Section.

B.3 MC studies on $B^0 \to J/\psi(\mu^+\mu^-)\eta'(\eta\pi^+\pi^-)$

We also test the partial reconstruction procedure by using the decay channel $B^0 \longrightarrow J/\psi(\mu^+\mu^-)\eta'(\eta\pi^+\pi^-)$ considering the η from the η' decay as the missing particle. It is actually thought that in reason of the relatively high mass of the missing particle, physical backgrounds from $J/\psi\pi^+\pi^-X$ are suppressed. This decay mode is very suppressed and is only used here for convenience in view of commissioning the method for $B_s^0 \longrightarrow J/\psi\eta'$. In this decay channel, the J/ψ and the two pion tracks from η' decay determine the decay

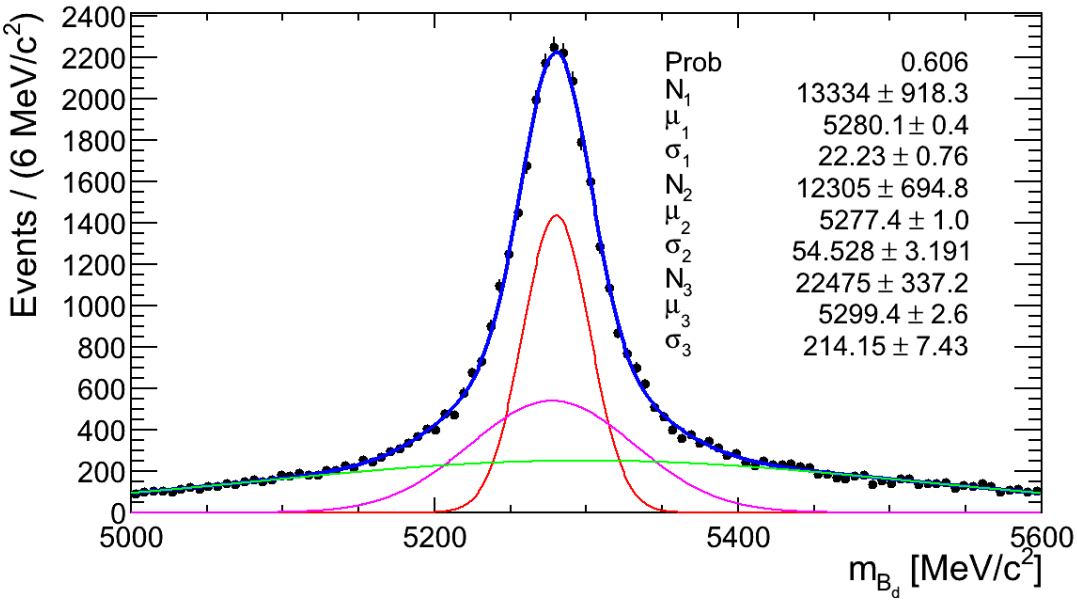

Figure B.7: B^0 invariant mass distribution as obtained using partial reconstruction method using the true $\vec{p}_B$ direction and true momenta of visible daughter particles, but with random choice of $\vec{p}_X^{\parallel}$.

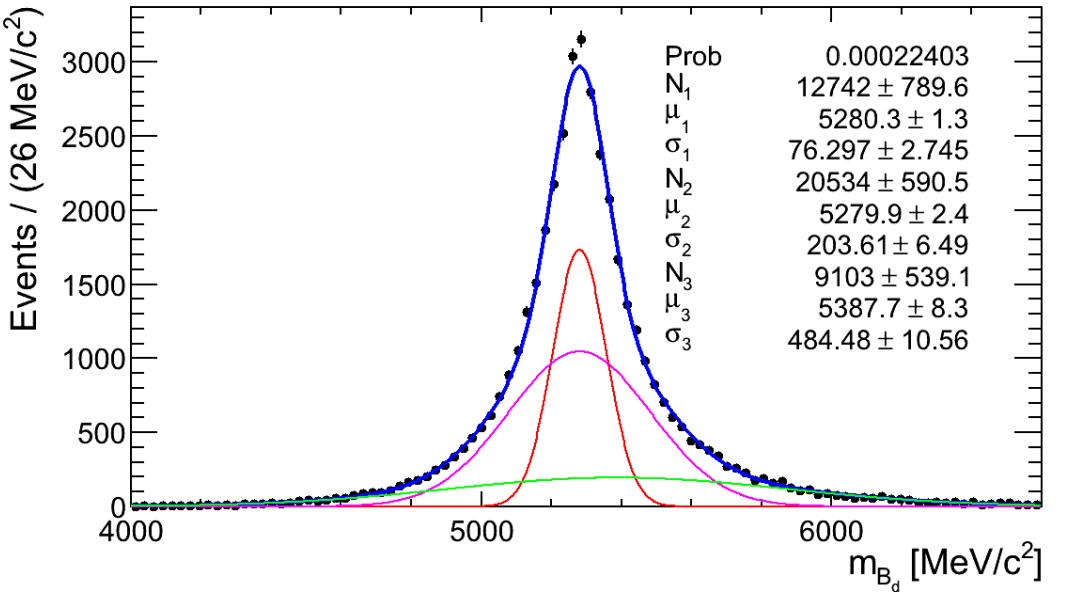

Figure B.8: B^0 invariant mass distribution as obtained using cheated partial reconstruction method using the MC truth primary vertex but reconstructed secondary vertex.

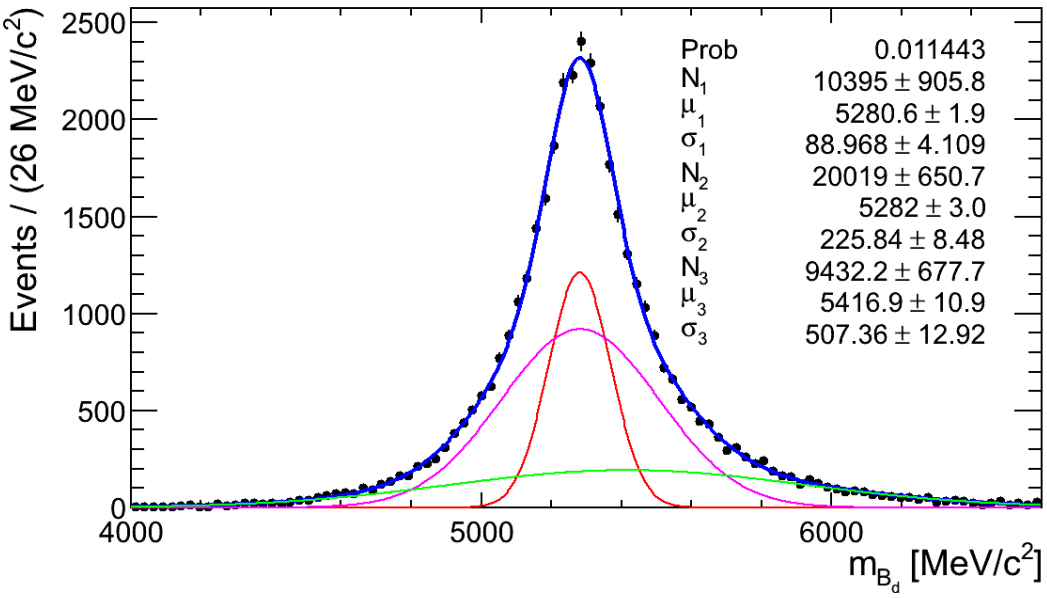

Figure B.9: B^0 invariant mass distribution as obtained using cheated partial reconstruction method but reconstructed primary vertex and secondary vertex.

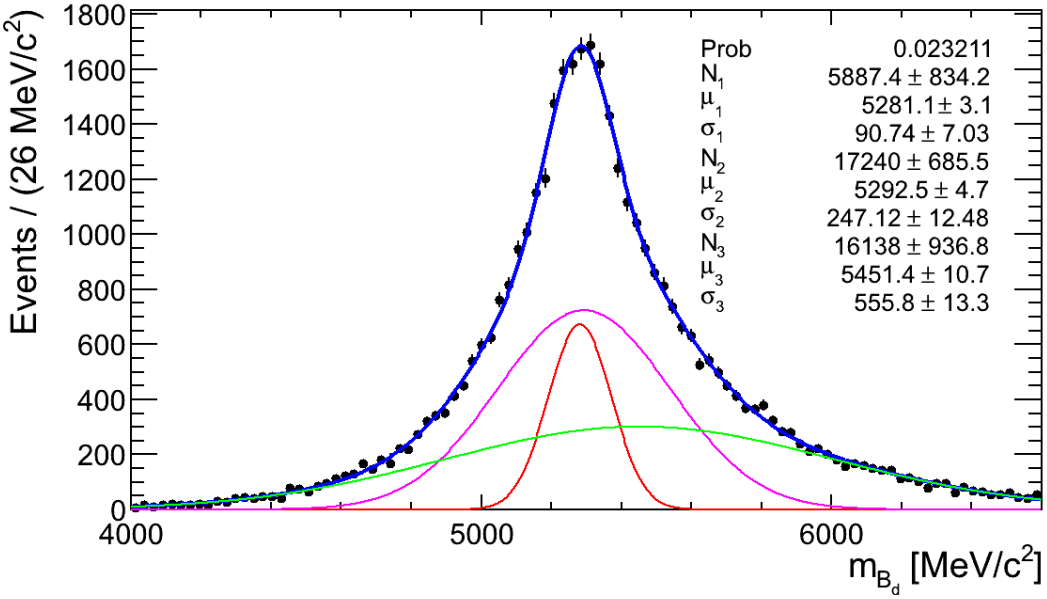

Figure B.10: B^0 invariant mass distribution as obtained using partial reconstruction method with reconstructed primary vertex and secondary vertex.

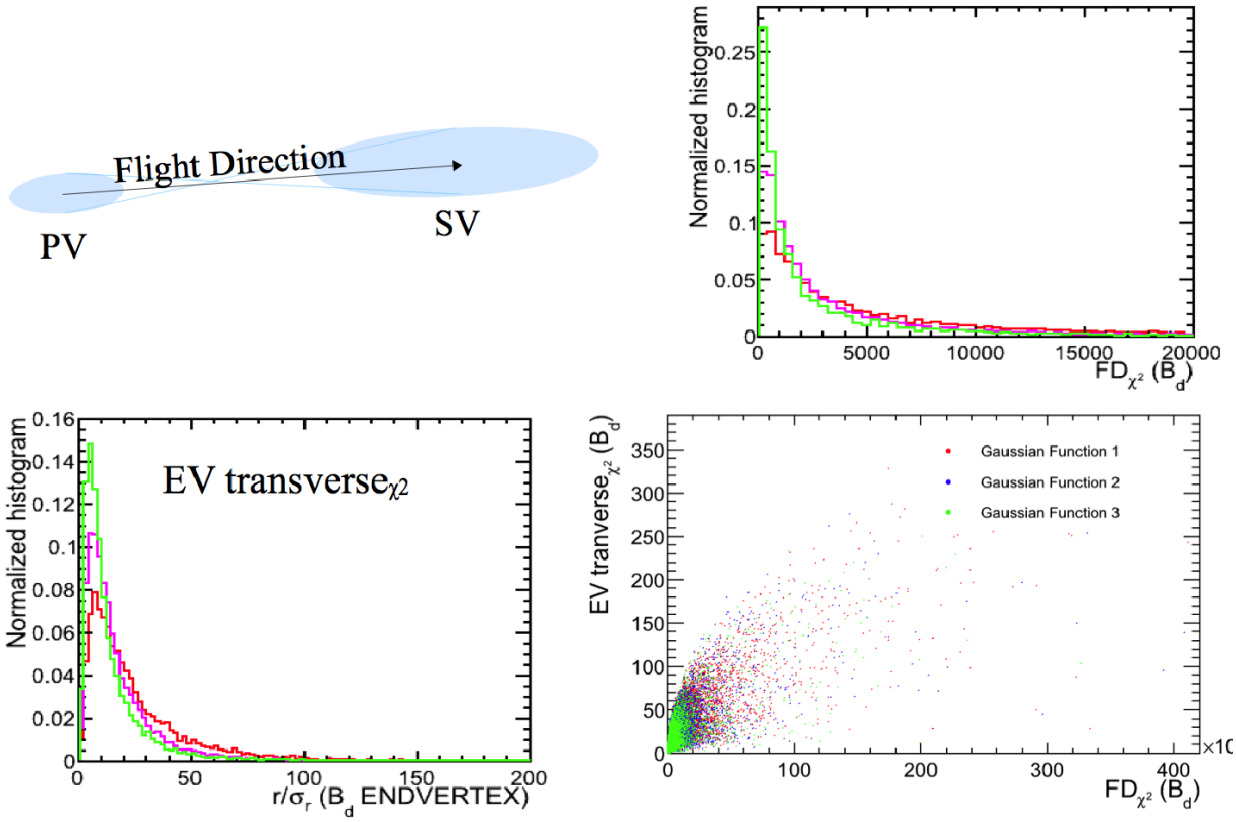

Figure B.11: Two discriminating variables for case 6 for the three Gaussian functions: (top-left) Illustration of how the end vertex and the flight distance plays a significant role in the estimation of the true B^0 flight direction; (top-right) The flight-distance χ^2 of B^0 for the three categories; (bottom-left) The end vertex transverse χ^2 of B^0 for the three categories; (bottom-right) The correlation of the flight-distance χ^2 and end vertex transverse χ^2 of B^0.

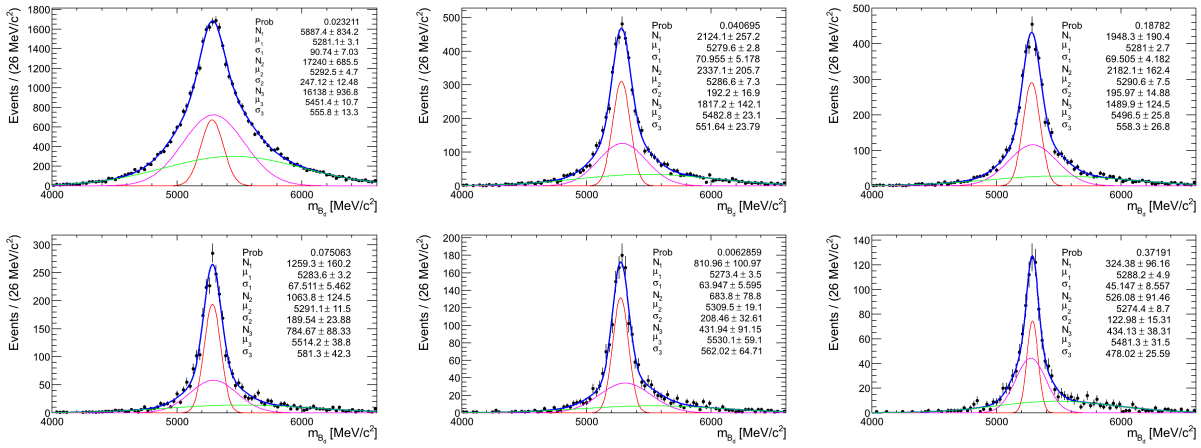

Figure B.12: B^0 mass distribution with increasing cut on (top) the transverse end vertex χ^2 and (bottom) the flight distance χ^2. (Top-left) Without any cut; (top-center) with a cut of $\chi^2_{EV} > 10$ and $\chi^2_{FD} > 10$K; (top-right) with a cut of $\chi^2_{EV} > 20$ and $\chi^2_{FD} > 10$K. (Bottom-left) With a cut of $\chi^2_{EV} > 50$ and $\chi^2_{FD} > 10$K; (bottom-center) with a cut of $\chi^2_{EV} > 50$ and $\chi^2_{FD} > 20$K; (bottom-right) with a cut of $\chi^2_{EV} > 50$ and $\chi^2_{FD} > 30$K.

vertex position. In this exercise, we use Monte Carlo events[k] in which only the final charged particles (μ^+ & μ^- from the J/ψ decay and π^+ & π^- from the η' decay) are MC matched. A total of 105408 MC matched events, both MagUp & MagDown are used. These events will be used to address two questions in the partial reconstruction technique: (1) Can we get a statistically clever way of choosing the good solutions? (2) Can we improve the resolutions by selecting efficiently the best reconstructed events?

B.3.1 Selection of $B^0 \to J/\psi(\mu^+\mu^-)\eta'(\eta\pi^+\pi^-)$ Events

We use the MC generated events based on event type number 11144413, simulated using simulation condition sim-20121025-vc-m{d,u}100 and detector condition dddb-20120831. These generated events have tight generator cuts, as summarized in Table B.3[l]. The J/ψ is forced to decay to $\mu^+\mu^-$ with indefinite number of radiative photons modelled using PHOTOS package, while η' is forced to decay to $\eta\pi^+\pi^-$ and the η is forced to decay to $\gamma\gamma$.

Table B.3: Generator level cuts used in event type 11144413.

Particle	Cut
η'	(GPT > 2.25 * GeV)
$[\mu^+]$cc	(GPT > 500 * MeV) & (GP > 6 * GeV) & inAcc
$[\pi^+]$cc	(GPT > 100 * MeV) & inAcc
$J/\psi(1S)$	(GPT > 500 * MeV) & in_range (1.8 , GY , 4.5)
g	(0 < GPZ) & (150 * MeV < GPT) & inEcalX & inEcalY
inAcc	in_range (0.005 , GTHETA , 0.400)
inEcalX	abs (GPX / GPZ) < 4.5 / 12.5
inEcalY	abs (GPY / GPZ) < 3.5 / 12.5

The selection of $B^0 \to J/\psi(\mu^+\mu^-)\eta'(\eta\pi^+\pi^-)$ events is summarized in Table B.4. The J/ψ candidates are taken from the Phys/StdMassConstrainedJpsi2MuMu/Particles container with additional mass cut of ADMASS('J/psi(1S)') < 80.0*MeV. The η are selected from the Phys/StdLooseResolvedEta/Particles container, while the pions are taken from the container located at Phys/StdLoosePions/Particles. An event filter is also applied to retain only events with fewer than 250 Long tracks.

Table B.4: Selection of $B^0 \longrightarrow J/\psi(\mu^+\mu^-)\eta'(\eta\pi^+\pi^-)$ events.

Particle	Cut
$J/\psi(1S)$	$(\lvert m_{rec} - m_{J/\psi}\rvert < 80.0$ MeV)
η	$(\lvert m_{rec} - m_{\eta}\rvert < 50.0$ MeV)
$[\pi^+]$cc	$(\chi^2_{trk}/\text{ndof} < 4.0)$ & $(P^{ghost}_{trk} < 0.5)$
η'	$(\lvert m_{rec} - m_{\eta'}\rvert < 105.0$ MeV) & $(\chi^2_{vtx} < 10.0)$
B^0	$(4000.0$ MeV $< m_{rec} < 6200.0$ MeV) & $(\chi^2_{vtx} < 10.0)$ & $(\chi^2_{FD} > 50.0)$

B.3.2 Reconstruction of B^0 mass using full truth

A smaller sample of 18859 events, which the η from η' decay are also MC matched, is used to check the validity of the partial reconstruction code. Using the true momentum direction

[k] These events are fully reconstructed events.

[l] See the original dkfile at $DECFILESROOT/dkfiles/Bd_Jpsietap,mm,etapipi=TightCut.dec.

of the B^0 meson, true momenta of the pions and true momentum of J/ψ and also utilizing the cheated partial reconstruction technique, the reconstructed B^0 mass is shown in Figure B.13. Most of the events has a reconstructed B^0 mass at 5279.6 MeV/c^2, with few events at [5276.0 MeV/c^2, 5283.0 MeV/c^2]. This resolution is physics and basically comes from the natural width of η.

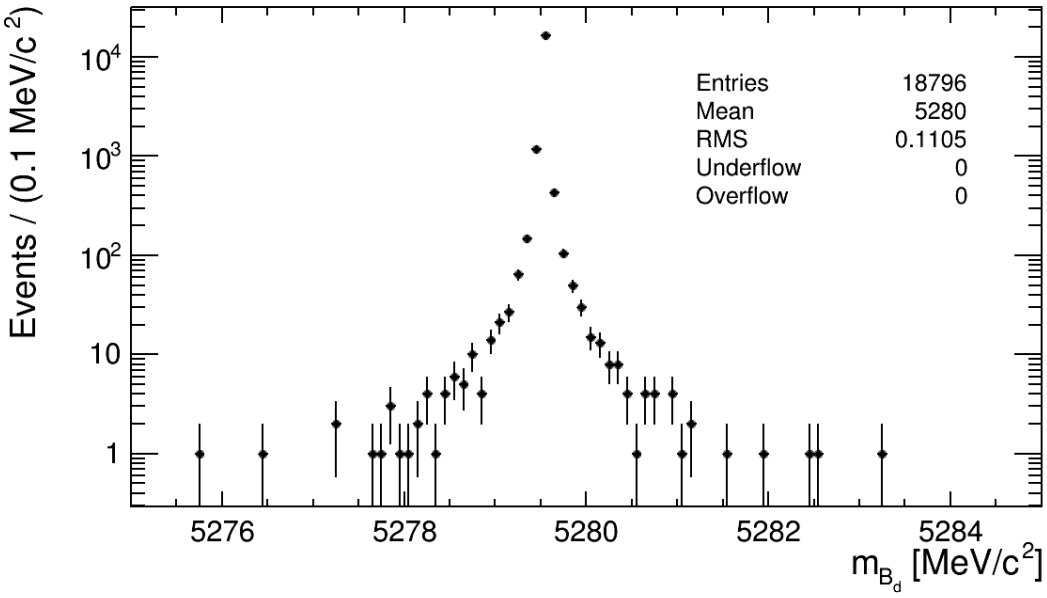

Figure B.13: B^0 invariant mass distribution as obtained using full truth and cheated partial reconstruction technique.

B.3.3 Reconstruction of B^0 mass

We apply the partial reconstruction technique to reconstruct the mass of B^0 for different situations. The first case is the full implementation of partial reconstruction – that is all the charged tracks are reconstructed, the primary and secondary vertices are also reconstructed, and the choice of $\vec{p}_X^{\parallel}$ solution is completely random. On the second case, instead of choosing randomly, the two possible solutions are included in the B^0 mass distribution. On the third case, the two possible solutions are included in the B^0 mass reconstruction but weighted according to each reconstructed proper decay time. The fourth case is of the same concept as the former case, the two possible solutions are weighted according to its corresponding reconstructed momentum. On the fifth case, we combine the two weighting procedure – that is the two possible solutions are weighted based on its corresponding reconstructed proper time and momentum. The three weighting procedures have two entries in the B^0 mass spectrum but the total weight is set to 1. The weighting procedures discussed above are summarized in Table B.5.

The mass difference of the two solutions can be as large as ~500 MeV/c^2 as shown in Figure B.14(left), but most of the events has a mass difference of about zero for the two solutions. Furthermore, the $\sqrt{B}$ term[m] is, on average, minimum at the correct B^0 mass, which means that the mass difference for the two solutions is small in that region (See Figure B.14(right)). Away from the correct B^0 mass, the $\sqrt{B}$ term increases and consequently increases also the mass difference.

[m] The $\sqrt{B}$ term is the term in the equation $p_X^{\parallel} = A \pm \sqrt{B}$.

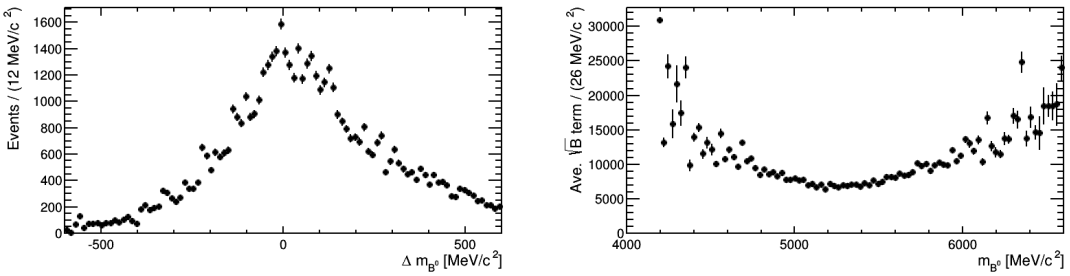

Figure B.14: (left) The mass difference for the two possible solutions. (right) Average $\sqrt{B}$ term as a function of correct B^0 mass.

Table B.5: Different techniques of choosing or weighting the two possible solutions of $\vec{p}_X^{\,\parallel}$.

Case	Remarks
Case 1	Random choice of $\vec{p}_X^{\,\parallel}$
Case 2	Two entries per event
Case 3	Weighting the two solutions of $\vec{p}_X^{\,\parallel}$ according to its corresponding proper time
Case 4	Weighting the two solutions of $\vec{p}_X^{\,\parallel}$ according to its corresponding momentum
Case 5	Weighting the two solutions of $\vec{p}_X^{\,\parallel}$ according to its corresponding proper time and momentum combined

Just like in the case of the $B^0 \to K^0_S(\pi^+\pi^-)K^\pm\pi^\mp$, the quantity B in Equation B.6 can be negative. As shown in Figure B.15, only 60483 out of 105408 has $B > 0$, which is ∼57.38% of the MC matched sample. Events with $B < 0$ are excluded in the subsequent analysis. For events with $B \geq 0$, the quantity $\sqrt{B}$ is always less than the quantity A, as shown on the same Figure and hence $\sqrt{B}$ can be interpreted as a correction to A.

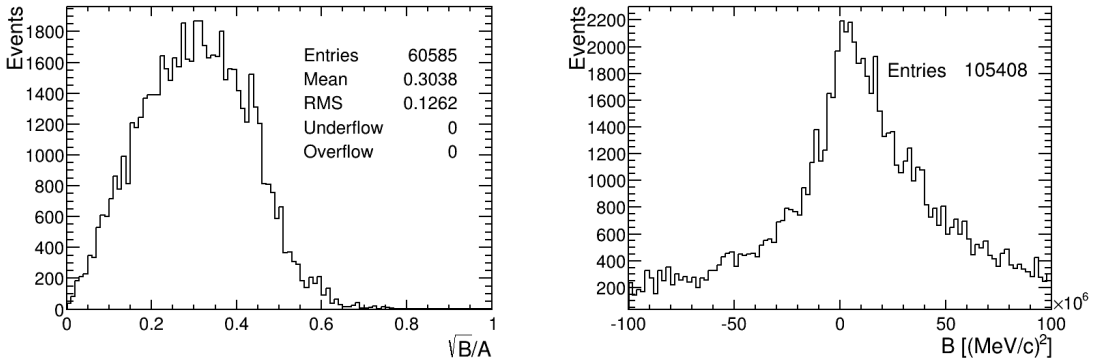

Figure B.15: (left) The ratio of terms A and $\sqrt{B}$ of Equation B.6. Only 60483 out of 105408 (∼57.38%) events have $B \geq 0$. (right) Distribution of term B resulting to both positive and negative values.

Random Choice

The B^0 mass spectrum is shown in Figure B.16(left) for the case where we choose randomly from the two possible solutions of $\vec{p}_X^{\,\parallel}$. Just in the case of $B^0 \longrightarrow K^0_S(\pi^+\pi^-)K^\pm\pi^\mp$, we fit

the B^0 mass spectrum with three Gaussian functions and we take note of the resolution and efficiency of the Gaussian with best resolution. In this case, the best Gaussian has a resolution of ∼87 MeV/c^2 with a corresponding efficiency of ∼29%.

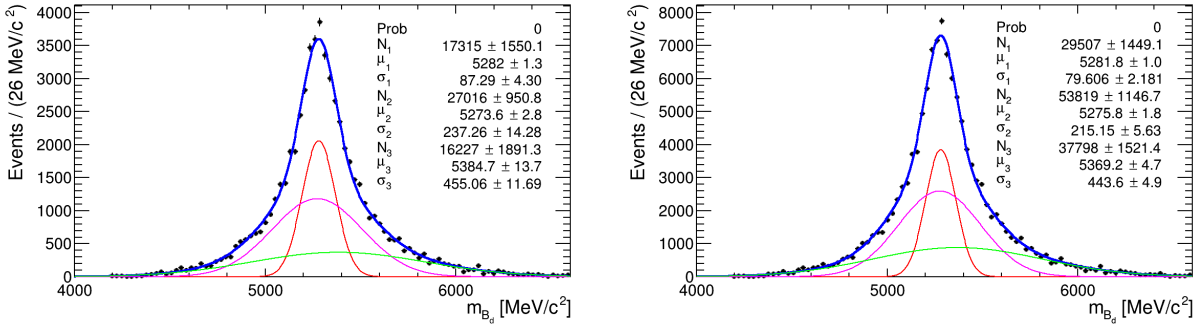

Figure B.16: B^0 invariant mass distribution as obtained using reconstructed vertices and reconstructed tracks. (Left) Random choice of $\vec{p}_X^{\parallel}$. (Right) Two entries per event.

Two entries per event

Instead of choosing randomly, the two possible solutions are included in the B^0 mass spectrum both with weights equal to 1. As shown in Figure B.16(right), it does not differ significantly from the random choice. Although the resolution of best Gaussian is ∼80 MeV/c^2, the corresponding efficiency is 14%, which is lower compared to the random choice. However, this has an advantage. If we assume that the signal and background events will increase by a factor of 2, then the signal signifance $S/\sqrt{S+B}$ will be a factor $\sqrt{2}$ larger than the random choice.

Proper time weighting

The idea of weighting the two possible solutions of $\vec{p}_X^{\parallel}$ according to its corresponding proper time is that the probability of a particle decaying as a function of time is given by an exponential function. The smaller the proper time, the higher the probability of decaying. Hence, the two possible solutions of $\vec{p}_X^{\parallel}$ is weighted according to this. The first possible solution of $\vec{p}_X^{\parallel}$ will result to a proper decay time of B^0, say t_1, while the other solution will result to a proper time decay of say t_2. The weight given to the first solution is $w_1 = e^{-t_1/\tau}/(e^{-t_1/\tau}+e^{-t_2/\tau})$, while the weight given to the second solution is $w_2 = e^{-t_2/\tau}/(e^{-t_1/\tau}+e^{-t_2/\tau})$, where $\tau = 1.530$ ps is the proper mean lifetime of the B^0 meson. Summing up the two weights should of course amount to 1. Therefore, although there are two entries in the B^0 mass spectrum for every $B^0 \longrightarrow J/\psi(\mu^+\mu^-)\eta'(\eta\pi^+\pi^-)$ decay candidate, the total weight is still equal to 1.

As shown in Figure B.17, the best Gaussian has a resolution of ∼81 MeV/c^2, which is better than what was obtained in the random choice procedure, but with smaller efficiency of ∼25%[n]. The superimposition of the total PDF obtained in random choice (in gray curve) and the total PDF obtained in this weighting procedure (in blue curve) is shown in Figure B.17(left).

[n] Cautiously interpreting the results of our qualitative approach, it seems that this weighting procedure improves the resolution as expected but only marginally as shown in Figure B.17.

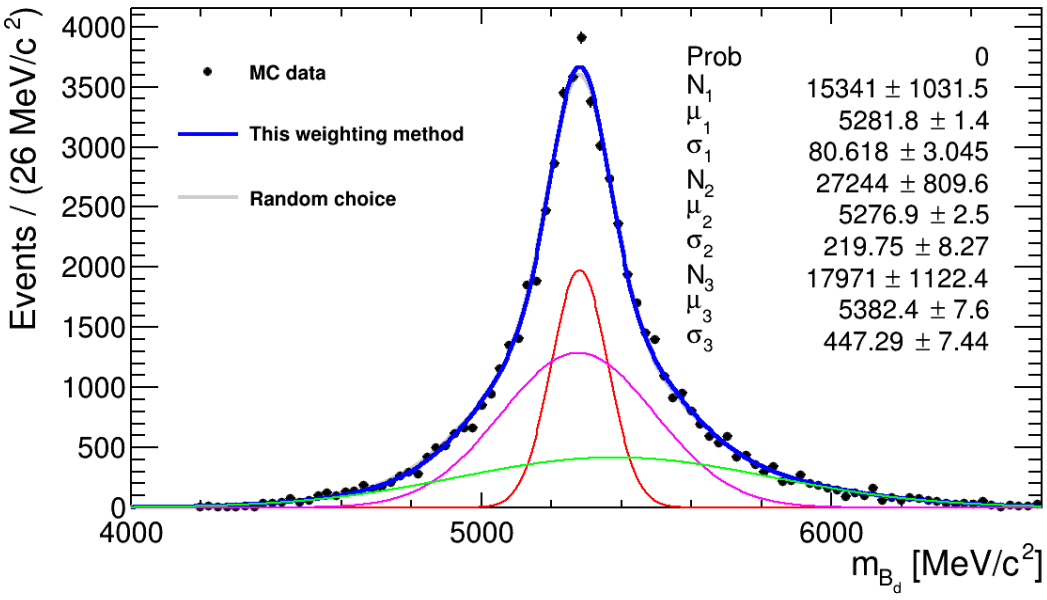

Figure B.17: B^0 invariant mass distribution as obtained using reconstructed vertices, reconstructed tracks and weighted choice of $\vec{p}_X^{\parallel}$ based on its corresponding proper time.

Momentum weighting

In the momentum weighting procedure, a prior probability density function (or histogram) is needed. This can be obtained from the distribution of p_{B^0} on MC matched events, as shown in Figure B.18. Using the same procedure as in the proper time weighting, the first possible solution of $\vec{p}_X^{\parallel}$ will result to a momentum of B^0, say p_1 with corresponding probability P_1, and while the other solution will result to a momentum of say p_2 with corresponding probability P_2. The weight given to the first solution is $w_1 = P_1/(P_1 + P_2)$, while the weight given to the second solution is $w_2 = P_2/(P_1 + P_2)$. Again, although there are two entries in B^0 mass spectrum for every $B^0 \longrightarrow J/\psi(\mu^+\mu^-)\eta'(\eta\pi^+\pi^-)$ decay candidate, the total weight is still equal to 1.

As shown in Figure B.19, the best Gaussian has a resolution of ∼78 MeV/c^2, with an efficiency of ∼24%. Although it improves the resolution with respect to the random choice, the effect is again marginal.

Proper time and momentum weighting

In this case, the two weighting procedures are combined. The first possible solution of $\vec{p}_X^{\parallel}$ will result to a proper time and momentum of B^0, say t_1 (with a corresponding probability $T_1 = e^{-t_1/\tau}$) and p_1 (with corresponding probability P_1), respectively. The other possible solution will result to proper time and momentum of B^0, say t_2 (with a corresponding probability $T_2 = e^{-t_2/\tau}$) and p_2 (with corresponding probability P_2), respectively. The weight given to the first possible solution is $w_1 = (T_1P_1)/(T_1P_1 + T_2P_2)$, while the weight given to the second possible solution is $w_2 = (T_2P_2)/(T_1P_1 + T_2P_2)$. The resulting B^0 mass spectrum for this weighting procedure is as well disappointing as shown in Figure B.20. It happens that the two solutions are very close in lifetime and momentum.

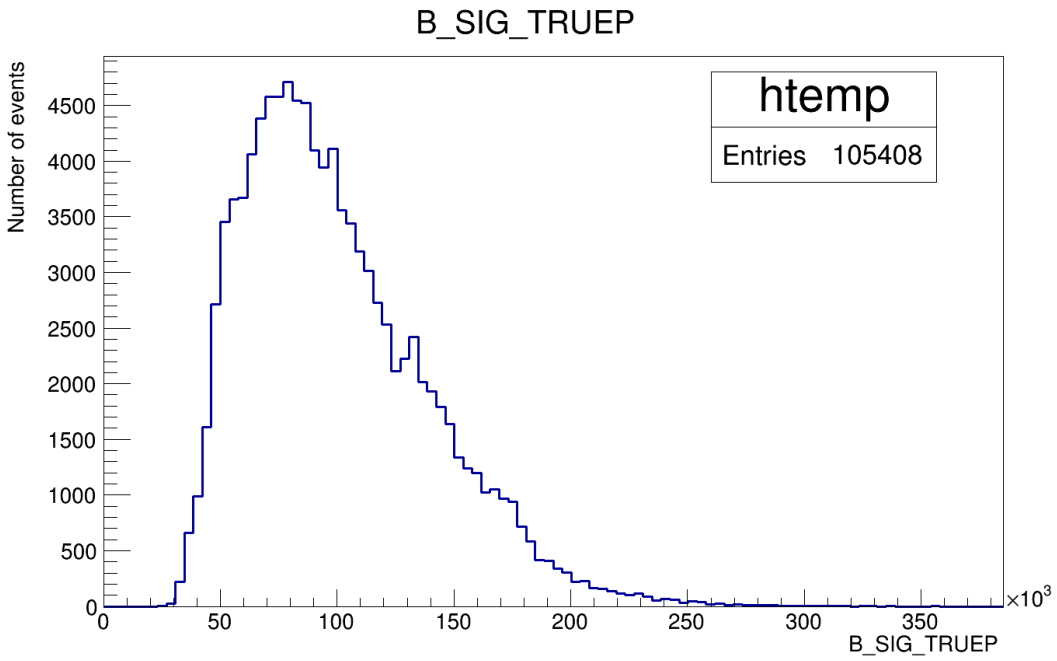

Figure B.18: B^0 Momentum distribution of MC matched events.

Summary on the weighting techniques

Using the three different weighting techniques, we did not find significant improvements w.r.t. the random choice procedure. The weighting technique based on momentum requires a prior momentum distribution, which in this case was obtained from Monte Carlo. Henceforth, this technique relies on the good agreement of data and Monte Carlo. The weighting procedure based on proper time is however well-motivated by physics and must therefore be used in data. Although the improvement is insignificant in the decay mode of $B^0 \to J/\psi\eta'(\pi^+\pi^-\eta)$ that we tested, the introduction of this technique can not be worse than the random choice. One thing to note however is how this procedure will affect the background shape. This can be checked on the data by applying a reverse weighting (put more weight on the wrong solution) and look how the background shape is affected (See Section B.4.5).

B.3.4 Discriminating variables

As already shown in the case of $B^0 \to K^0_S(\pi^+\pi^-)K^\pm\pi^\mp$, there are two variables that can categorize the events resulting to Gaussian with worst resolution and events resulting to Gaussian with best resolution. We found out that the significance of the impact parameter of J/ψ and of the $\pi^\pm$ can also discriminate the said categories, as well as the number of tracks used to create the primary vertex. Using *sPlotting* technique, the reconstructed B^0 mass is considered as the discriminating variable. This allows us to plot sWeighted B^0 flight distance χ^2, B^0 transverse end vertex χ^2 and $J/\psi(1S)$ impact parameter χ^2, $\pi^\pm$ impact parameter χ^2 and number of tracks in the PV of B^0 (although small), as shown in Figure B.21. It has been checked that these variables are, to first order, uncorrelated with the B^0 mass within each category.

The distributions shown in Figure B.21 are then used to train Boosted Decision Trees (BDTs). We consider the sWeighted events corresponding to the Gaussian with best resolution and moderate resolution as the signal, and the events corresponding to the Gaussian

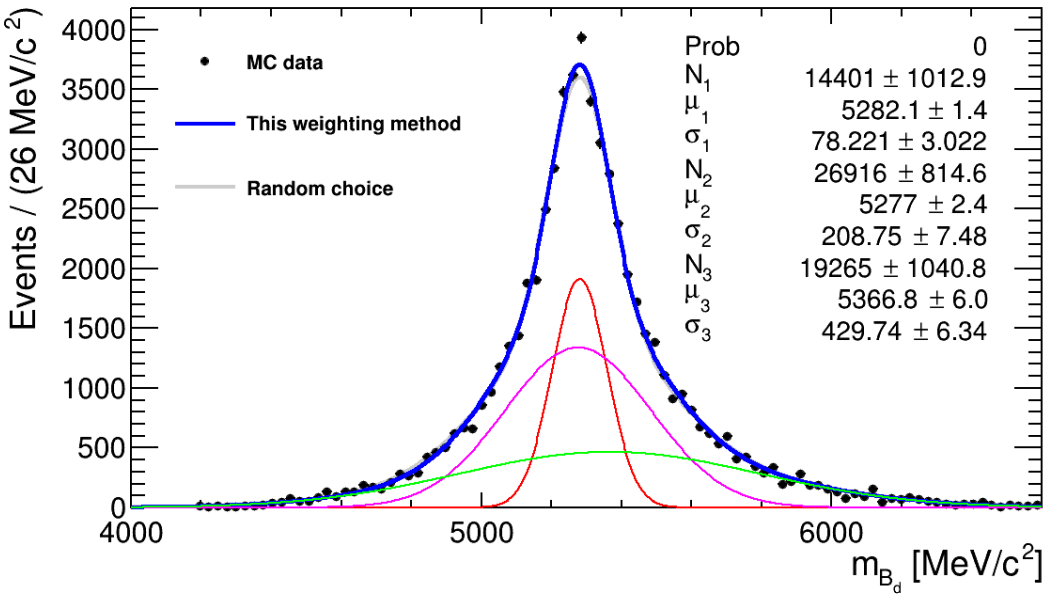

Figure B.19: B^0 invariant mass distribution as obtained using reconstructed vertices, reconstructed tracks and weighted choice of $\vec{p}_X^{\,\parallel}$ based on its corresponding momentum.

with worst resolution as the background[o]. To avoid bias, we design two BDTs – namely BDT1 and BDT2, where half of the events are used to train BDT1, and the other half is used to train BDT2. The events used to train BDT1 are used as test events for BDT2, and vice versa. In this way, the whole sample is the training sample, as well as the test sample.

The histograms of the variable distributions and the linear correlation plots for the two BDTs are provided for in Figures B.22 and Figure B.23, respectively. The BDT discriminant response histogram for the two BDTs are shown in Figure B.24 (top). In order not to bias the analysis, a final single BDT output is provided as the sum of BDT1 and BDT2. This is shown in Figure B.24 (bottom). The double structure of the signal events shown in the BDT response is a reflection of the additional intermediate Gaussian (the Gaussian with moderate resolution). We however believe that these events will contribute a significant part of the signal statistics in the end and must be considered as legitimate signal events.

To find the optimal BDT cut, we use the signal significance $S/\sqrt{S+B}$. The number of signal events S and the number of background events B are obtained by refitting the B^0 mass distribution for every applied BDT cut. Here, the number of events at the best-resolution Gaussian is considered as S, while the number of events at the worst-resolution Gaussian is considered as B. To avoid fluctuation due to instability of the fit and to have a sensible comparison in between BDT cuts, we fixed the resolution of best Gaussian equal to 75.0 MeV/c^2 and let free the other parameters. The resulting Figure of Merit is shown in Figure B.25, where ∼0.08 is shown to be the optimal cut maximizing the signal significance. Looking at the BDT response plot, at ∼0.08 BDT cut, all the background events are all killed. This is also shown in the B^0 mass distribution in Figure B.26, where we apply a BDT cut equal to 0.08 and fixed the resolution of Gaussian 1 equal to 75.0 MeV/c^2.

[o]Although the events in the worst-resolution Gaussian are signal events, we assume that the characteristic of these events represents real background events.

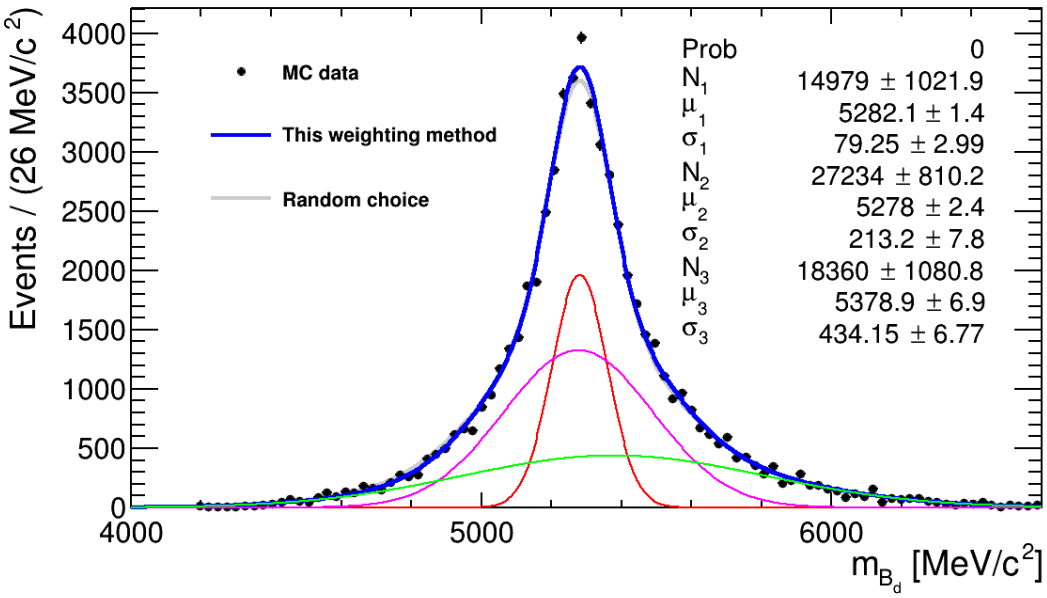

Figure B.20: B^0 invariant mass distribution as obtained using reconstructed vertices, reconstructed tracks and weighted choice of $\vec{p}_X^{\parallel}$ based on its corresponding proper time and momentum combined.

B.3.5 Summary

We have developed a BDT that can select events that will have a good reconstructed B^0 mass resolution. This BDT is based mainly on variables that can select the most relevant vertexing performance. With regards to the weighting methods, we did not find a satisfactory way to choose statistically the good solution. The two solutions for this specific final state are too close for obvious criteria on lifetime and momentum. But as already mentioned in 3.3.6, the weighting method based on proper time is well-motivated by physics and hence can not be worse than the random choice. Should this technique may of some interest for LHCb users, we will provide the choice between the different weighting methods.

B.4 MC Studies on $B_s^0 \to J/\psi(\mu^+\mu^-)\eta'(\eta\pi^+\pi^-)$ and search on real data

Physics-wise, the decay of B_s^0 into a CP eigenstate $J/\psi\eta'$ is one of the easiest way to access the mixing-induced phase of the $B_s^0 - \bar{B}_s^0$ system through a time-dependent analysis. As far as the partial reconstruction technique is concerned, it was thought that this final state with η as the missed particle was relevant. Mostly because of the presence of two neutral particles in the final state, both resulting to a low explicit full reconstruction efficiency.

Searching for the decay mode $B_s^0 \to J/\psi(\mu^+\mu^-)\eta'(\eta\pi^+\pi^-)$, we apply the partial reconstruction technique in this decay using MC-generated events based on event type number 13344402, simulated using condition Sim08-20130503-1-vc-m{d,u}100 and detector condition Sim08-20130503-1. The J/ψ is forced to decay to $\mu^+\mu^-$ with indefinite number of radiative photons as modelled using the PHOTOS package, while η' is forced to decay to either $\eta\pi^+\pi^-$ or $\rho(\pi^+\pi^-)\gamma$[p]. In order to evaluate the real efficiency, the η can decay to any mode and only the μ^+ and μ^- are required to be in the LHCb acceptance angle.

[p]This decay will be used to evaluate background events where the event is mis-assigned as $B_s^0 \to J/\psi(\mu^+\mu^-)\eta'(\eta\pi^+\pi^-)$.

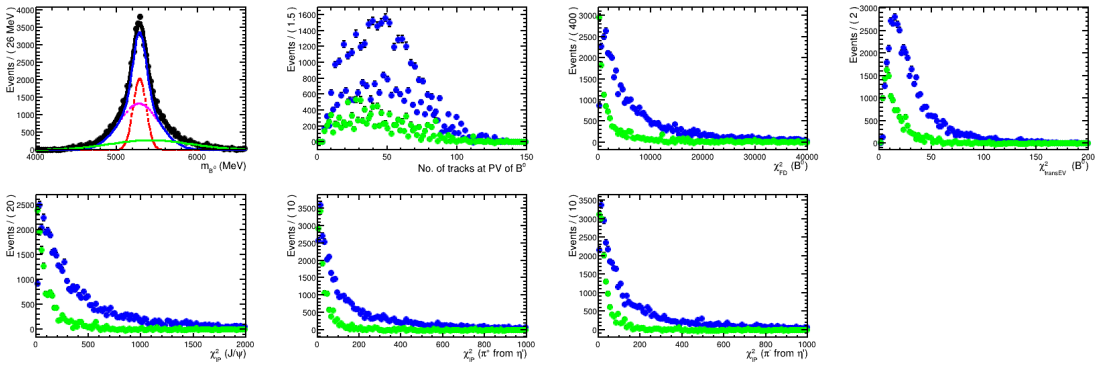

Figure B.21: (From left-to-right, top-to-bottom) Reconstructed B^0 mass using partial reconstruction technique fitted with three Gaussian functions; sWeighted number of tracks used to create PV of B^0; sWeighted B^0 flight distance χ^2; sWeighted B^0 transverse end vertex χ^2; sWeighted $J/\psi(1S)$ impact parameter χ^2; sWeighted π^+ impact parameter χ^2; and sWeighted π^- impact parameter χ^2. Blue events are signal-like, while green are background-like events.

B.4.1 Selection of $B_s^0 \longrightarrow J/\psi(\mu^+\mu^-)\eta'(\eta\pi^+\pi^-)$ events

The selection of $B_s^0 \longrightarrow J/\psi(\mu^+\mu^-)\eta'(\eta\pi^+\pi^-)$ events is summarized in Table B.6. The J/ψ candidates are taken from Phys/StdMassConstrainedJpsi2MuMu/Particles container, while the $\pi^+\pi^-$ candidates are taken from the Phys/StdLoosePions/Particles.

Table B.6: Selection of $B_s^0 \longrightarrow J/\psi(\mu^+\mu^-)\eta'(\eta\pi^+\pi^-)$ candidate events.

Particle	Cut
$J/\psi(1S)$	$(\lvert m_{rec} - m_{J/\psi}\rvert < 80.0$ MeV)
$[\mu^+]$cc	$(\chi^2_{trk}/\text{ndof} < 4.0)$ & $(P^{ghost}_{trk} < 0.5)$
$[\pi^+]$cc	$(\chi^2_{trk}/\text{ndof} < 4.0)$ & $(P^{ghost}_{trk} < 0.5)$
B_s^0	$(4000.0$ MeV $< m_{rec} < 6200.0$ MeV) & $(\chi^2_{vtx} < 10.0)$ & $(\chi^2_{FD} > 50.0)$

B.4.2 Reconstruction of B_s^0 mass

Using the partial reconstruction technique discussed in section 1.1, the reconstructed mass of B_s^0 is shown in Figure B.27. Since none of the weighting techniques in the previous chapter improves the resolution of the mass distribution, random choice of the $p_X^{\parallel}$ is used here. A total of 19036 MC-matched events[q] but only 9500 events are reconstructible. As shown in Figure B.27, the resolution of the narrow Gaussian is $\sim$47 MeV/c^2, with $\sim$12% efficiency.

We apply another weighting technique by considering the reconstructed mass difference of the two possible solutions of $p_X^{\parallel}$. Shown in Figure B.28 is the probability of $p_X^{\parallel} = A + \sqrt{B}$ as the correct solution as a function of mass difference: (left) if the average of the two possible reconstructed mass is less than 5366.77 MeV/c^2; (right) if the average of the two possible reconstructed mass is greater than 5366.77 MeV/c^2. The two probability distribution functions shown in Figure B.28 are then used to assign weights to the two possible solutions, and hence for every $B_s^0 \to J/\psi(\mu^+\mu^-)\eta'(\eta\pi^+\pi^-)$ candidate event, there are two entries in the mass distribution, but the total weight is 1. Shown in Figure B.29 is an improvement on the mass resolution as well as reducing the asymmetry of the distribution after the above-discussed weighting method is applied. However, we do not yet know how this weighting

[q] Since η is missing, only the charged tracks are MC-matched.

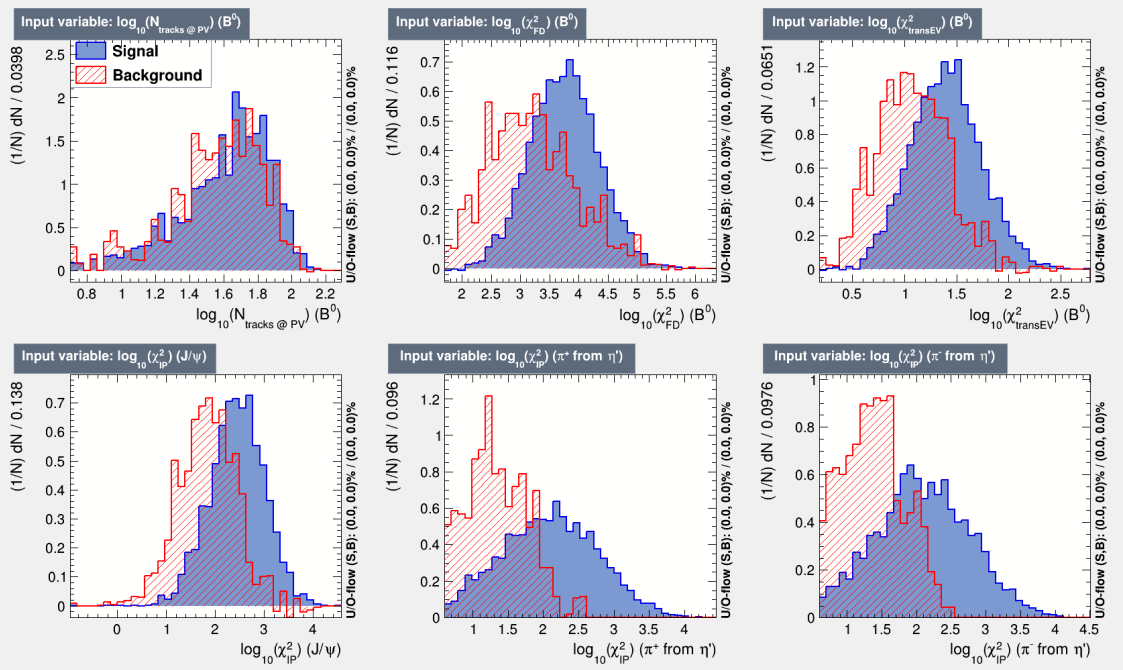

Figure B.22: Distribution of variables used for the training of BDT1. (The same plot can be observed for BDT2).

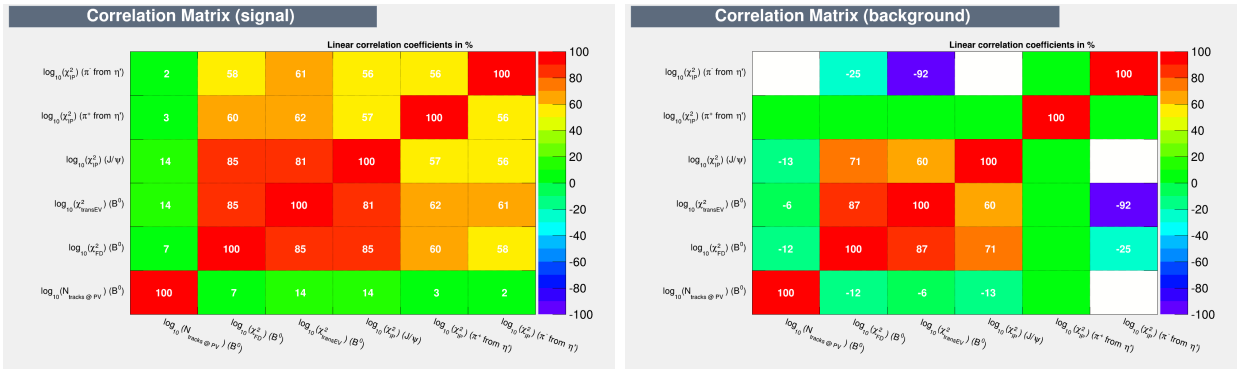

Figure B.23: (Linear correlation matrix of the variables of signal events (left) and background events (right) for BDT1. (The same plot can be observed for BDT2).

method will affect the background events, whether it will bias the distribution or maintain its structure. It has yet to be checked on real background events and for that this weighting technique has not yet been considered so far.

B.4.3 Physical background events

Several decays, which might mimic the decay that we are searching, are listed in Table B.7. Some of these decays are still under investigation, while the others are studied and discussed in the subsections that follow.

$B_s^0 \to J/\psi(\mu^+\mu^-)\eta'(\rho(\pi^+\pi^-)\gamma)$

Since only the charged tracks are reconstructed, it is possible that $\eta'(\rho(\pi^+\pi^-)\gamma)$ events are mis-assigned as $\eta'(\eta\pi^+\pi^-)$. Out of 13019 MC-matched events of $B_s^0 \longrightarrow J/\psi(\mu^+\mu^-)\eta'(\rho(\pi^+\pi^-)\gamma)$,

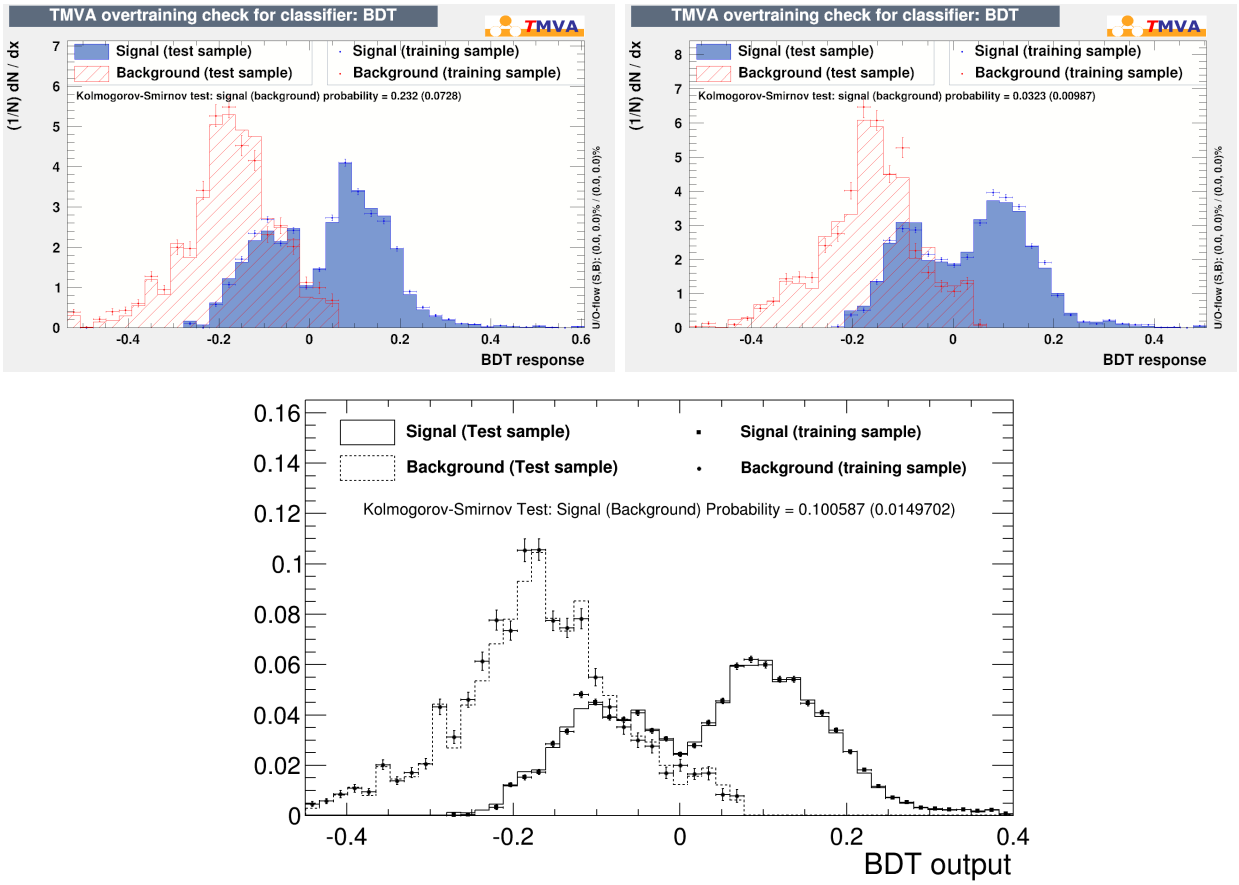

Figure B.24: (Top) Training and test response for BDT1 (left) and for BDT2 (right). (Bottom) Final BDT output as a combination of BDT1 and BDT2.

only 3 events (∼0.023%) are reconstructible[r], since the kinematics of the two pions is different enough from $\eta' \longrightarrow \eta\pi^+\pi^-$.

$B_s^0 \to J/\psi(\mu^+\mu^-)\phi(K^+K^-)$

If the two kaons are misidentified as pions, then the decay $\phi(K^+K^-)$ will be mis-assigned as $\eta'(\eta\pi^+\pi^-)$. Only 326 events are reconstructible out of 40035 (∼0.08%) irrelevant of any PID cut and they peak around 6600 MeV/c^2.

$B_s^0 \to J/\psi(\mu^+\mu^-)\phi(\pi^+\pi^-\pi^0)$

Since the selection only requires the presence of two pions and J/ψ, this decay mode will be mis-assigned as $\eta'(\eta\pi^+\pi^-)$. Out of 7328 MC-matched events, only 85 events (∼1.15%) are reconstructible, although this peaks at the nominal B_s^0 mass. The main reason for this low reconstruction efficiency is the difference in the kinematics compared to the searched decay channel. The searched missing particle η is significantly heavier compared to π^0.

$B^0 \to J/\psi(\mu^+\mu^-)\eta(\pi^+\pi^-\pi^0)$

The branching fraction of $B^0 \to J/\psi\eta(\pi^+\pi^-\pi^0)$ is about the same as that of $B^0 \to J/\psi\eta'(\pi^+\pi^-\eta)$. Using MC data, we applied partial reconstruction on these events with the hypothesis that

[r] Reconstructible in the sense that the B factor in $p_X^{\parallel} = A + \sqrt{B}$ is positive.

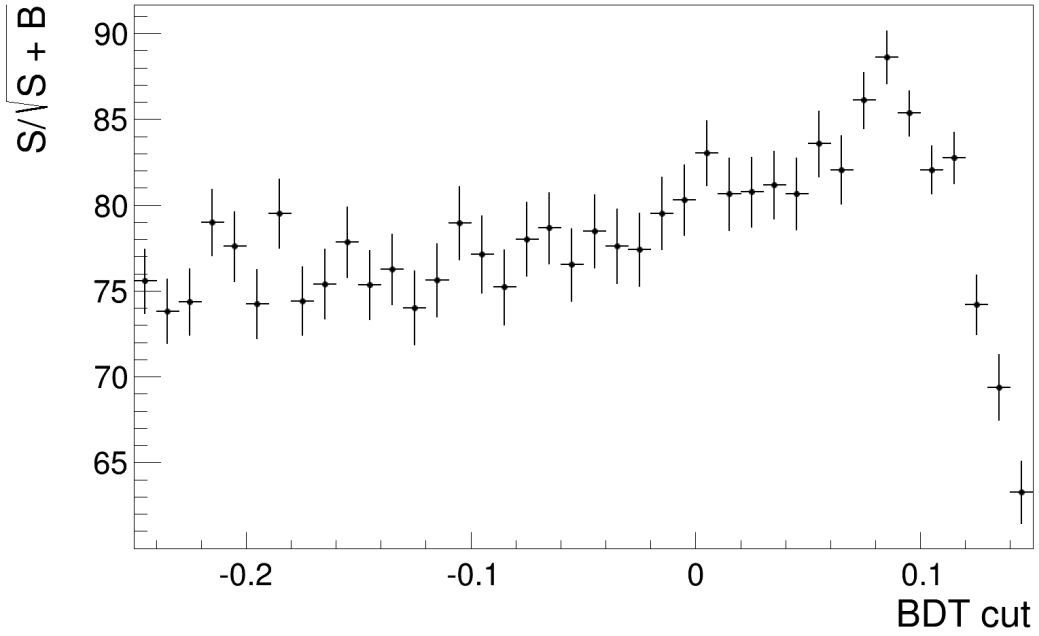

Figure B.25: Signal significance $S/\sqrt{S+B}$ as a function of BDT cut.

these are $J/\psi\eta'(\pi^+\pi^-\eta)$ events. We fitted the distribution with a Gaussian function and a second-order polynomial to have an idea on the peak location and resolution of this background shape. Although the absolute efficiency of this decay mode w.r.t. partial reconstruction technique is not yet known since these MC events are generated with different cuts, these background events would peak at ∼5500 MeV/c^2 with a resolution of ∼175 MeV/c^2, as shown in Figure B.30(left). This is about 150 MeV/c^2 away from the B_s^0 peak. These has to be modelled when fitting the mass distribution of candidate events. Given the mutual cross-feed of $J/\psi\eta$ and $J/\psi\eta'$ channels, the extraction of the branching ratios in these two channels will proceed through a common fit of the two mass distributions with a signal and cross-feed pdf given by the MC.

$B^0 \longrightarrow J/\psi(\mu^+\mu^-)\omega(\pi^+\pi^-\pi^0)$

We applied partial reconstruction technique on $B^0 \to J/\psi\omega(\pi^+\pi^-\pi^0)$ MC generated events. Again, we fit the distribution with a Gaussian and second-order polynomial. As can be seen in Figure B.30(right), these events peak at ∼5400 MeV/c^2 with a resolution of ∼110 MeV/c^2. They hence will populate the signal region and should be modelled. The relative branching fraction and the small efficiency make these background events negligible with respect to the $J/\psi\eta$.

Combinatorial $B^0_{(s)} \to J/\psi h^+h'^-$ events

One has to pay attention of $B^0_{(s)}$ decays into charged-only mode where a wrong PID assignment of charged particle can mimic the decay mode that we are searching. For example, a decay of B^0 to $J/\psi K\pi$ where the kaon is mis-assigned as a pion can be reconstructed as $J/\psi\pi^+\pi^-$ + missing neutral. Luckily, there are two complementary ways to get rid of these harmful decays. First, by applying a good PID cut on the pions. Second, by requesting that the $\chi^2_{\rm IP}$ of B^0 w.r.t. to its own primary vertex (where this $\chi^2_{\rm IP}$ is obtained using the charged tracks only) is > 10 for example, since this variable is sharply peaked at 0 for such decays.

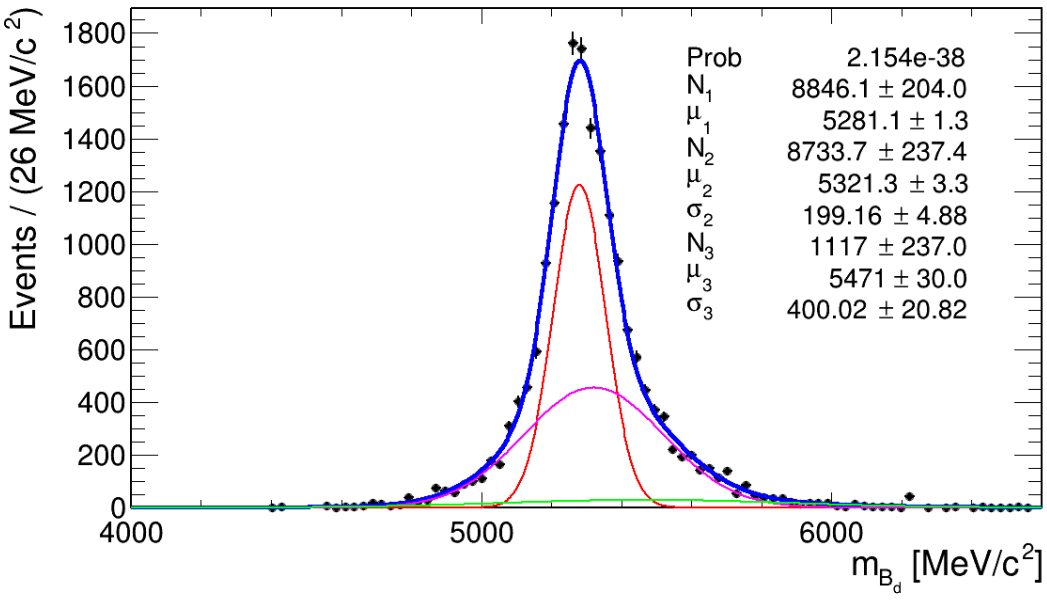

Figure B.26: B^0 invariant mass distribution with BDT cut equal to 0.08. The resolution of Gaussian 1 is fixed to 75.0 MeV/c^2.

The second requirement will also remove most of the $J/\psi\pi^+\pi^-$ events. See for example Figure B.31 for a typical χ^2_{IP} distribution of such decays.

B.4.4 Signal cross-feeds: $\pi^+\pi^-$ from η

In the decay of $B_s^0 \longrightarrow J/\psi\eta'(\pi^+\pi^-\eta)$, the η can decay to $\pi^+\pi^-\{\pi^0,\gamma\}$. The branching fraction of $\eta \longrightarrow \pi^+\pi^-\{\pi^0,\gamma\}$ is 27.34% and hence the charged pions may be mis-assigned as the two pions that come from the η'. Out of 2623 MC-matched events, 1060 events (∼40.41%) are reconstructible peaking the nominal B_s^0 mass as shown in Figure B.32(a). It is also possible that only one pion that comes from η is mis-assigned as the pion that comes from η'. 2857 events (∼51.47%) are reconstructible out of 5551 MC-matched events, as shown in Figure B.32(b). These events are definitely signal events. Although the candidates from the mis-assignment of pions from η peak at the correct B_s^0 mass, the corresponding mass resolution is very degraded and hence distort the signal shape.

B.4.5 Partial reconstruction on the dimuon stream

We applied the selection of $X^0 \longrightarrow J/\psi(\mu^+\mu^-)\pi^+\pi^-$ described in Section B.3, to the dimuon stream of 2012 LHCb real data. The data corresponds to $\int \mathcal{L}dt = 2.08/\text{fb}$ integrated luminousity. A total of 33 655 274 initial candidate events are selected for both MagUp and MagDown configuration. To reduce the data, additional cuts are applied as summarized in Table B.8. For reconstructible signal events, the two following conditions must be satisfied: $A > 0$ and $\sqrt{B} \leq A$. We impose these two requirements to reduce the background contamination. The last cut is applied to remove dimuons not coming from the J/ψ. The $|m^{rec}_{J/\psi} - 3096.916|$ MeV/c^2 $\leq$ 48 MeV/c^2 cut corresponds to the 3σ resolution of the J/ψ mass distribution in the LHCb dimuon stream. The said cuts retain only 168 897 of the selected $X^0 \longrightarrow J/\psi(\mu^+\mu^-)\pi^+\pi^-$ candidate events.

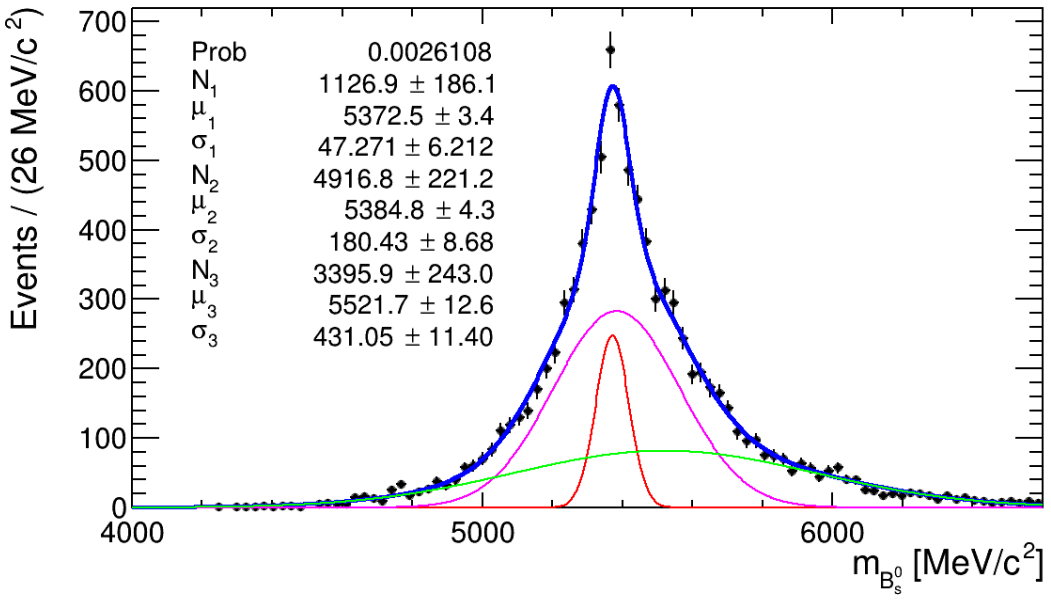

Figure B.27: B_s^0 invariant mass distribution as obtained using reconstructed vertices, reconstructed tracks and random choice of $\vec{p}_X^{\parallel}$.

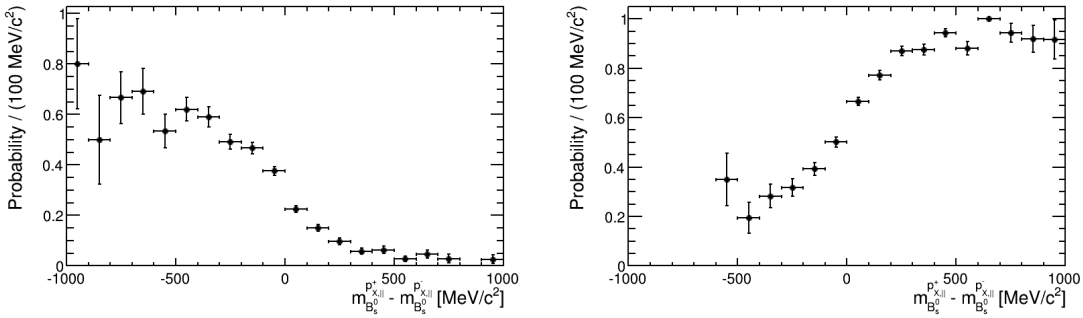

Figure B.28: Probability of $p_{\parallel}^X = A + \sqrt{B}$ as the correct solution as a function of mass difference $m_{rec}^{p_{X,\parallel}^+} - m_{rec}^{p_{X,\parallel}^-}$ if: (left) $(m_{rec}^{p_{X,\parallel}^+} + m_{rec}^{p_{X,\parallel}^-})/2 < 5366.77$ MeV/c^2; (right) $(m_{rec}^{p_{X,\parallel}^+} + m_{rec}^{p_{X,\parallel}^-})/2 > 5366.77$ MeV/c^2.

Removal of combinatorial backgrounds

To further remove combinatorial backgrounds, two Boosted Decision Trees (hereafter referred as BDT_1 and BDT_2) are designed. The background events used to train the BDTs come from the side band of the J/ψ mass distribution, where 50 MeV/$c^2 \leq |m_{J/\psi}^{rec} - 3096.916| \leq$ 80 MeV/c^2, while signal events are the MC-matched signal events. About 3300 signal events and ∼5300 are used to train and test the two BDTs.

The histograms of the variable distributions and the linear correlations plots for BDT_1 are provided for in Figure B.33 and Figure B.34, respectively. The same can be found for BDT_2. The non-linearity of the correlations in between variables justifies to employ the BDT technique. Although some of the variables are highly linearly correlated, the difference of the correlations in between signal and background for a given variable opted us to include these in the BDT. Table B.9 lists the importance of these variables in the two BDTs. The most discriminative variables are the topological variables, which are the χ^2_{transEV} (X^0), χ^2_{FD} (X^0), χ^2_{IP} (J/ψ) and $N_{\text{tracks@PV}}$ (X^0). Note that these variables were used also in the training

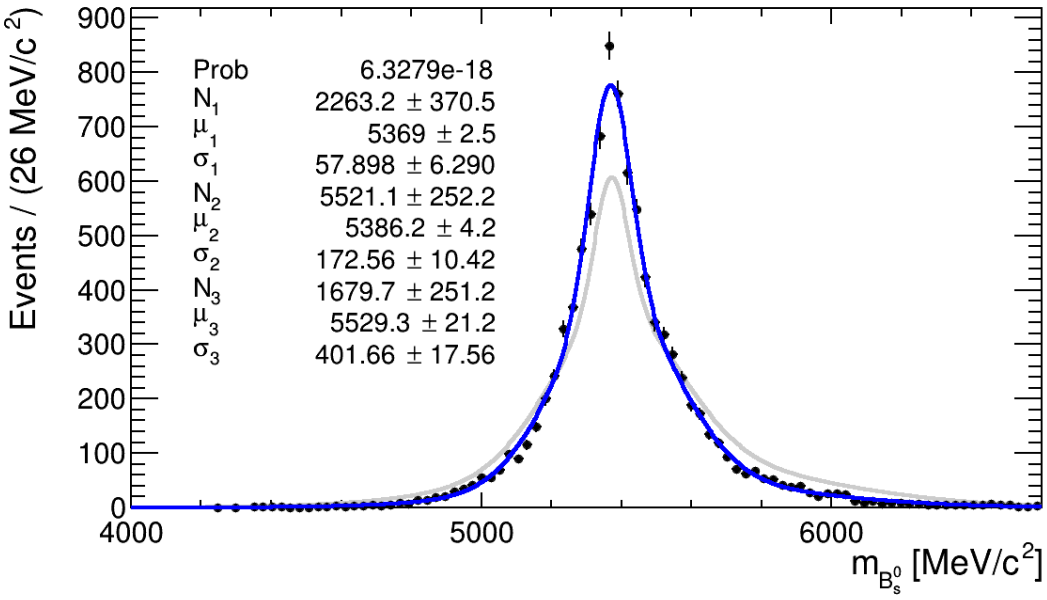

Figure B.29: B_s^0 invariant mass distribution as obtained using reconstructed vertices, reconstructed tracks and weighted choice of $\vec{p}_X^{\,\parallel}$.

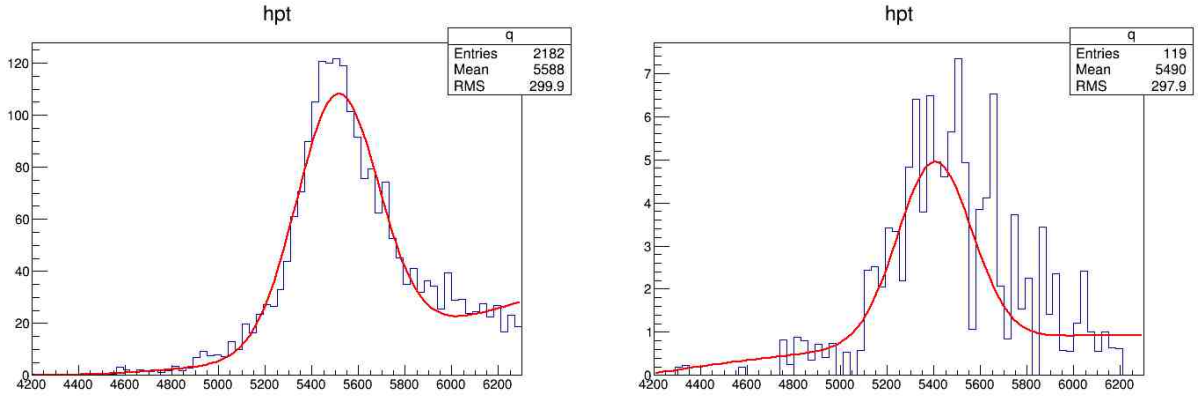

Figure B.30: X^0 mass distribution for (left) $B^0 \to J/\psi\eta(\pi^+\pi^-\pi^0)$ events reconstructed as $J/\psi\eta'(\pi^+\pi^-\eta)$ and (right) $B^0 \to J/\psi\omega(\pi^+\pi^-\pi^0)$ events reconstructed as $J/\psi\eta'(\pi^+\pi^-\eta)$.

of the BDT discussed in section B.3.4 to reject badly reconstructed events. The range of some of the variables covers only few orders of magnitude and hence the logarithm of their values are used instead.

Two types Boosted Decision Trees are added into the data. The first BDT is designed to reject combinatorial backgrounds (hereafter referred as BDTx). This is the BDT presented in this section. The second BDT is designed to reject badly[s] reconstructed events. This is the BDT discussed in section B.3.4 – hereafter referred as BDTy. Applying a BDTx ≥ 0.10 and BDTy ≥ 0.10 cuts on the real dimuon data stream results in Figure B.35[t]. With all these cuts applied, including the two BDTs, we expected ∼1200 events with a signal resolution of ∼88 MeV/c^2. (See Appendix B.6.4 for the efficiencies and expected number of events). By eye inspection, we see that the possible signal peak corresponds to what we expect. To

[s] These are events with reconstructed mass far from the nominal mass of X^0.

[t] This figure was obtained using the weighting method based on proper time. The other weighting methods will be discussed in the next subsection.

Table B.7: Possible sources of background events with its corresponding branching fraction.

Decay	$\mathcal{B}$	$\mathcal{B}/\mathcal{B}_{J/\psi\eta'}$
$B_s^0 \longrightarrow J/\psi(\mu^+\mu^-)\eta'(\pi^+\pi^-\eta)$ [ref.]	$\sim 9.5\times10^{-6}$	~ 1.0
$B^0 \longrightarrow J/\psi(\mu^+\mu^-)K^*(892)^0$	$\sim 7.1\times10^{-5}$	~ 7.5
$B^0 \longrightarrow J/\psi(\mu^+\mu^-)\eta(\pi^+\pi^-\{\pi^0,\gamma\})$	$\sim 8.3\times10^{-6}$	~ 0.9
$B^0 \longrightarrow J/\psi(\mu^+\mu^-)\omega(\pi^+\pi^-\pi^0)$	$< 1.4\times10^{-5}$	< 1.5
$B^0 \longrightarrow J/\psi(\mu^+\mu^-)K^0\pi^+\pi^-$	$\sim 5.9\times10^{-5}$	~ 6.2
$B_s^0 \longrightarrow J/\psi(\mu^+\mu^-)\phi(K^+K^-)$	$\sim 3.2\times10^{-5}$	~ 3.4
$B_s^0 \longrightarrow J/\psi(\mu^+\mu^-)\phi(\pi^+\pi^-\pi^0)$	$\sim 9.9\times10^{-6}$	~ 1.0
$B_s^0 \longrightarrow J/\psi(\mu^+\mu^-)\eta'(\rho(\pi^+\pi^-)\gamma)$	$\sim 6.4\times10^{-6}$	~ 0.7
$B_s^0 \longrightarrow J/\psi(\mu^+\mu^-)K^*(892)^0$	$\sim 5.3\times10^{-6}$	~ 0.6
$B^+ \longrightarrow J/\psi(\mu^+\mu^-)K^+\pi^+\pi^-$	$\sim 4.8\times10^{-5}$	~ 5.1
$B^+ \longrightarrow J/\psi(\mu^+\mu^-)\eta(\pi^+\pi^-\{\pi^0,\gamma\})K^+$	$\sim 1.7\times10^{-6}$	~ 0.2
$B^+ \longrightarrow J/\psi(\mu^+\mu^-)\eta'(\pi^+\pi^-\{\eta,\gamma\})K^+$	$< 3.8\times10^{-6}$	< 0.4
$B^+ \longrightarrow J/\psi(\mu^+\mu^-)\phi(\pi^+\pi^-\pi^0)K^+$	$\sim 4.7\times10^{-7}$	~ 0.05
$B^+ \longrightarrow J/\psi(\mu^+\mu^-)\omega(\pi^+\pi^-\pi^0)K^+$	$\sim 1.7\times10^{-5}$	~ 1.8

Table B.8: Sanity cuts to further reject background events.

Cut	Efficiency on MC signal events
$B \geq 0$	0.501996
$A \geq 0$	0.501996
$A \geq \sqrt{B}$	0.501996
$\lvert m^{rec}_{J/\psi} - 3096.916\rvert$ MeV/c^2 $\leq 48.$ MeV/c^2	0.986441
Combined cut	0.495593

further reduce possible contamination of kaons misidentified as pions, we applied a tight cut on the PID of the two pion tracks. Applying $\mathrm{DLL}_{K\pi} \leq -5$ and $\mathrm{DLL}_{p\pi} \leq 10$ cuts on the two pion candidates results in Figure B.36.

We apply an additional cut of χ^2_{IP} $(X^0_{\mathrm{4tracks}}) > 10$ to further remove $J/\psi(\mu^+\mu^-)h^+h'^-$ events, since this variable is highly-peaked at 0 for these type of events. Only 6 out of 1195 were removed after applying the cut, which means that the BDT and the PID cuts has effectively removed these events already. We take note that the χ^2_{IP} (X^0_{4tracks}) variable is included in the BDTx. We also checked whether $\psi(2S) \rightarrow J/\psi\pi^+\pi^-$ is a potential background. As shown in Figure B.37, we did not find a peak at the nominal mass of $\psi(2S)$ and hence we conclude that these events were already removed.

We also applied partial reconstruction technique to a MC sample of $B^0/B^+_u \rightarrow J/\psi X$ inclusive events whether these will contribute to the signal region in the search for $B^0_s \rightarrow J/\psi\eta'(\pi\pi\eta)$. As summarized in Appendix B.6.5, the said events do not contribute to the signal peak region[u]; while looking at the MC sample of $B^0_s \rightarrow J/\psi X$ inclusive events, (by eye inspection) the number of events in the peaking region is consistent with what we expect as the signal events.

[u]The cuts used are not exactly the same as the ones used in the data, i.e. no BDT cuts, due to technicalities, but the cuts are chosen to be as close as possible.

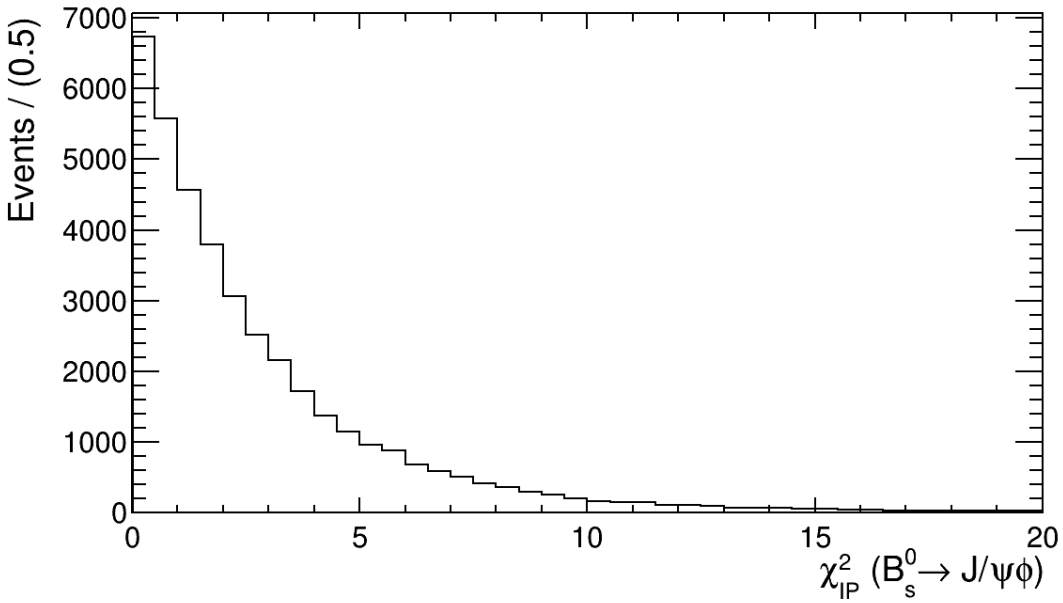

Figure B.31: $\chi^2_{\rm IP}$ distribution of MC-matched $B_s^0 \longrightarrow J/\psi(\mu^+\mu^-)\phi(K^+K^-)$.

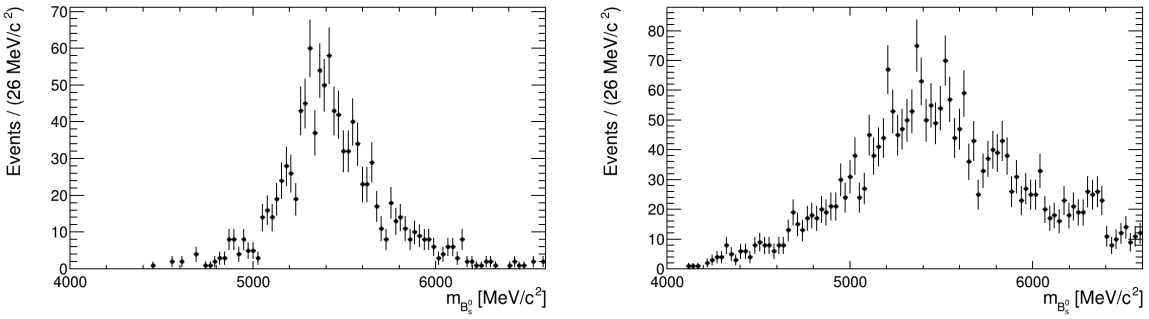

Figure B.32: Pions from η mis-assigned as pions from η'.

$B^0_{(s)}$ mass distribution using different weighting methods

In Section B.3.3, we observed that the three different weighting methods do not significantly change the X^0 mass distribution. Those weighting methods are based on reconstructed proper time, reconstructed momentum and combination of both. We check how these weighting methods affect the X^0 mass distribution on the real data after all the cuts applied. Shown in Figure B.38 are the X^0 mass distribution [top-left] using two entries per candidate event, [top-right] using proper time as basis for weighting, [bottom-left] using the momentum as basis for weighting and [bottom-right] using both proper time & momentum as basis. We did not find a significant change in the distribution for the three weighting methods.

Although we have studied in the previous section the effects of the weighting techniques on the signal events, we did not know how will these affect the background shape. To check how the weighting affects the distribution, the reconstructed mass distributions are weighted in reverse. We do this reverse weighting by putting more weight on the events which are less likely to be the correct solution. From the distributions shown in the Figure B.38, we did not find significant change on the background events and hence we conclude that the weighting procedures do not bias the background shape.

Table B.9: BDT variable importance ranking [0,1] for BDT_1 and BDT_2.

Variable	Importance	
	BDT_1	BDT_2
X^0 $\log_{10}(\chi^2_{\text{transEV}})$	0.138	0.1646
X^0 $\log_{10}(\chi^2_{\text{FD}})$	0.1207	0.1006
J/ψ $\log_{10}(\chi^2_{\text{IP}})$	0.1093	0.1325
X^0 $\log_{10}(N_{\text{tracks}})$ @ PV	0.1006	0.06877
π^- $\log_{10}(\chi^2_{\text{IP}})$	0.08325	0.09256
π^+ $\log_{10}(\chi^2_{\text{IP}})$	0.07885	0.1014
J/ψ $\log_{10}(P_{\text{T}})$	0.06274	0.04316
X^0 $\log_{10}(P_{\text{T}})$	0.05998	0.05152
X^0 $\log_{10}(\eta)$	0.05378	0.04719
X^0 $\log_{10}(\chi^2_{\text{EV}})$	0.05270	0.05280
π^+ $\log_{10}(P_{\text{T}})$	0.04835	0.03449
X^0 $\log_{10}(\chi^2_{\text{IP}})$	0.04768	0.06923
π^- $\log_{10}(P_{\text{T}})$	0.04412	0.04111

B.5 Conclusions

We discussed in this document a novel technique to reconstruct a certain class of b-hadron decay in the absence of the explicit reconstruction of one of its decay products. The missing momentum is constrained by the knowledge of the b-hadron direction from the reconstructions of the primary and secondary vertices of the candidate and the presence of a narrow intermediate resonance in the decay chain, up to a two-fold ambiguity.

The technique has been commissioned for the sake of simplicity with a well established final state $B^0_s \to J/\psi\eta'(\eta' \to \pi^+\pi^-\eta)$, where the η is the missing particle. It is mandatory to envisage simultaneously the similar final states but one particle which can feed in the spectrum of the reconstruction hypothesis. It happens that the only relevant cross-feed for the mode of interest is coming from the decay $B^0_s \to J/\psi\eta(\eta \to \pi^+\pi^-\pi^0)$ where the π^0 is not reconstructed. Conversely, it has been shown possible to reconstruct this decay.

Two multivariate discriminators have been built in order to first select the candidates with vertexing properties adequate for partial reconstruction and second to reject combinatorial backgrounds. The typical performance in term of reconstructed mass resolution for the modes scrutinized in this study is of the order of 60 MeV/c^2. Although a mass model for partially reconstructed background and signal candidates has to be be provided to draw quantitative conclusions, we estimated that the gain in statistics w.r.t. a full reconstruction of $B^0_s \to J/\psi\eta'(\to \pi^+\pi^-\eta)$ can reach a factor of $\mathcal{O}(10)$. More modes were considered with intermediate resonances such as $\phi \to \pi^+\pi^-(\pi^0)$ or $\eta' \to \pi^+\pi^-(\gamma)$ but happened to be drowned by cross-feeds of similar final states or physical backgrounds.

The two-fold ambiguity for the momentum solutions mentioned above has been studied along different weighting of the solutions. The weighting techniques proposed in this document show a marginal improvement in terms of resolution with respect to considering the two solutions. It is worth to note however that this result is most likely dependent upon the decay mode to be reconstructed.

Let us conclude this note by sketching few perspectives of application of this partial reconstruction method to physics studies. This is certainly not exhausting the whole possible applications of the method. In the scope of the charmless $b-$hadron decays, the obvious candidates are $B^0_s \to \phi\eta', \phi\eta, \eta'\eta, \eta'\eta', \eta\eta$. These modes are penguin-dominated transitions

and analogously to $B_s^0 \to \phi\phi$ allows to access the weak mixing phase of the B_s^0 meson, without the need of an angular analysis since the final states are pure CP eigenstates. On the same note, but addressing the weak mixing phase of the B^0 meson, another candidate of interest is $B^0 \to \eta' K_S^0$. Another field of application is the search for exotic charmonia states, for which one of the most promising final state involves $B^\pm \to Y(\to \psi\omega)K^\pm$, where $\omega \to \pi\pi(\pi^0)$. Eventually, we will apply this partial reconstruction technique in order to select unbiased samples of protons and antiprotons from $J/\psi \to p\bar{p}$ issued in the class of decays $B \to J/\psi hh'(h)$ where h can be either a pion or kaon and either the p or the $\bar{p}$ is not reconstructed. Whether the statistics of the sample will allow it, the absolute $p/\bar{p}$ reconstruction efficiency difference can be computed and serves as the necessary input for studies of CP violation in b-baryon decays.

Should there be an interest in using or developing this method within the LHCb collaboration, we would be happy to share and release this tool of partial reconstruction.

B.6 Appendix

B.6.1 Partial reconstruction in $B_s^0 \to J/\psi(\mu^+\mu^-)\phi(\pi^+\pi^-\pi^0)$

For the sake of completeness, we are reporting in this appendix the challenging reconstruction of $B_s^0 \to J/\psi(\mu^+\mu^-)\phi(\pi^+\pi^-\pi^0)$, where a much larger physical background is expected in contrast to $B_s^0 \to J/\psi\eta'$, $J/\psi\eta$. Searching for the decay mode $B_s^0 \to J/\psi(\mu^+\mu^-)\phi(\pi^+\pi^-\pi^0)$, we apply partial reconstruction technique on the same real data sample used in the search for $B_s^0 \to J/\psi(\mu^+\mu^-)\eta'(\eta\pi^+\pi^-)$ (See discussion in Section B.4.5). Henceforth, we replace the mass of the missing particle as the nominal mass of π^0 and the intermediate mass as the nominal mass of $\phi(1020)$. The visible branching fraction of $B_s^0 \to J/\psi(\mu^+\mu^-)\phi(\pi^+\pi^-\pi^0)$ is about the same as $B_s^0 \to J/\psi(\mu^+\mu^-)\eta'(\eta\pi^+\pi^-)$. Hence it might be possible to reconstruct the said decay using partial reconstruction technique. The result is shown in Figure B.39. One should take note that no BDT cut is applied yet here.

However, it is possible that kaons are misidentified as pions and still produces a peak at the B_s^0 nominal mass. Considering that there are decays involving $J/\psi(\mu^+\mu^-)K^\pm\pi^\mp$, which branching fractions are larger than that of $B_s^0 \to J/\psi(\mu^+\mu^-)\phi(\pi^+\pi^-\pi^0)$, we put additional PID cuts to make sure that we are considering only pions. This is summarized in Table B.10. After applying the PID cuts, the peak disappears as shown in Figure B.40(left). Although the visible branching fraction of $B_s^0 \to J/\psi\phi(\pi^+\pi^-\pi^0)$ is about the same as $B_s^0 \to J/\psi\eta'(\eta\pi^+\pi^-)$, it is possible that the former is contaminated by more background events. What we have shown here is that $J/\psi(\mu^+\mu^-)K^\pm\pi^\mp X$ is present in the B_s^0 peak. One can also notice a peak at around 5100 MeV/c^2, which becomes more visible when we applied the same BDT cut as what we applied in the search for $J/\psi\eta'$ in Section B.4. See Figure B.40(right). This peak might be from $J/\psi K\pi\pi$ events, an hypothesis that is still under investigation.

Table B.10: PID cuts applied to retain only pions. $\mathrm{DLL}_{K\pi}$ is the logarithm of the likelihood ratio of the kaon and pion hypotheses, and the $\mathrm{DLL}_{p\pi}$ is the logarithm of the likelihood ratio of the proton and pion hypotheses.

Particle	PID cut
$\pi^\pm$	$\mathrm{DLL}_{K\pi} < -5$
$\pi^\pm$	$\mathrm{DLL}_{p\pi} < 10$

B.6.2 Decay kinematics of $B^0 \to J/\psi(\mu^+\mu^-)\eta'(\pi^+\pi^-\eta)$

Referring to Figure B.41, the four vector momentum of B^0 can be obtained even without detecting the missing particle X since the decay is well constrained. As presented in Section B.1.1, there are seven constraints for the 7 degrees of freedom and hence the problem is solvable. The first four constraints come from the four vector momentum conservation in the $B^0 \longrightarrow J/\psi(\pi^+\pi^-)\eta'(\pi^+\pi^- X)$ decay. Using obvious notations, these are given by,

$$\sqrt{p_B^2 + m_B^2} = \sqrt{p_{J/\psi}^2 + m_{J/\psi}^2} + \sqrt{p_{2\pi}^2 + m_{2\pi}^2} + \sqrt{p_X^2 + m_X^2} \tag{B.20}$$

$$\vec{p}_B = \vec{p}_{J/\psi} + \vec{p}_{2\pi} + \vec{p}_X \tag{B.21}$$

If we resolve the vector components of the momenta of the daughter particles in the direction parallel to B^0 (denoted by $\|$) and in the direction perpendicular to B^0 (denoted by $\perp$), then the momentum conservation gives us,

$$\vec{p}_B = \vec{p}^{\,\|}_{J/\psi} + \vec{p}^{\,\|}_{2\pi} + \vec{p}^{\,\|}_X \tag{B.22}$$

$$\vec{0} = \vec{p}^{\,\perp}_{J/\psi} + \vec{p}^{\,\perp}_{2\pi} + \vec{p}^{\,\perp}_X \tag{B.23}$$

Squaring both sides of Equation B.20,

$$\begin{aligned} p_B^2 + m_B^2 = &\left[\sqrt{p_{J/\psi}^2 + m_{J/\psi}^2} + \sqrt{p_{2\pi}^2 + m_{2\pi}^2}\right]^2 \\ &+ 2\left[\sqrt{p_{J/\psi}^2 + m_{J/\psi}^2} + \sqrt{p_{2\pi}^2 + m_{2\pi}^2}\right] \cdot \left[\sqrt{p_X^2 + m_X^2}\right] \\ &+ p_X^2 + m_X^2 \end{aligned} \tag{B.24}$$

$$\begin{aligned} p_B^2 + m_B^2 = &\, p_{J/\psi}^2 + m_{J/\psi}^2 + p_{2\pi}^2 + m_{2\pi}^2 + 2\sqrt{\left(p_{J/\psi}^2 + m_{J/\psi}^2\right)\left(p_{2\pi}^2 + m_{2\pi}^2\right)} \\ &+ 2\left[\sqrt{p_{J/\psi}^2 + m_{J/\psi}^2} + \sqrt{p_{2\pi}^2 + m_{2\pi}^2}\right] \cdot \left[\sqrt{p_X^2 + m_X^2}\right] \\ &+ p_X^2 + m_X^2 \end{aligned} \tag{B.25}$$

From Equation B.22, we perform a scalar product with itself on both sides of the equation resulting to,

$$p_B^2 = p_{J/\psi}^{\|2} + p_{2\pi}^{\|2} + p_X^{\|2} + 2\vec{p}^{\,\|}_{J/\psi} \cdot \vec{p}^{\,\|}_{2\pi} + 2\vec{p}^{\,\|}_{J/\psi} \cdot \vec{p}^{\,\|}_X + 2\vec{p}^{\,\|}_{2\pi} \cdot \vec{p}^{\,\|}_X \tag{B.26}$$

Substituting Equation B.26 to Equation B.25, knowing that $p_X^2 = p_X^{\|2} + p_X^{\perp 2}$, $p_X^{\perp 2} = p_{J/\psi}^{\perp 2} + p_{2\pi}^{\perp 2} + 2\vec{p}_{J/\psi} \cdot \vec{p}^{\,\perp}_{2\pi}$ (from Equation B.23), $p_{J/\psi}^2 = p_{J/\psi}^{\|2} + p_{J/\psi}^{\perp 2}$, $p_{2\pi}^2 = p_{2\pi}^{\|2} + p_{2\pi}^{\perp 2}$ and cancelling out some terms, we got,

$$\begin{aligned} \left(m_B^2 - m_{J/\psi}^2 - m_{2\pi}^2 - m_X^2\right) + 2\Big[&\left(\vec{p}^{\,\|}_{J/\psi} \cdot \vec{p}^{\,\perp}_{2\pi} + \vec{p}^{\,\|}_{J/\psi} \cdot \vec{p}^{\,\perp}_X + \vec{p}^{\,\|}_{2\pi} \cdot \vec{p}^{\,\perp}_X\right) \\ &- \left(p_{J/\psi}^{\perp 2} + p_{2\pi}^{\perp 2} + \vec{p}^{\,\perp}_{J/\psi} \cdot \vec{p}^{\,\perp}_{2\pi}\right)\Big] \\ &= 2E_{J/\psi}E_{2\pi} + 2\left(E_{J/\psi} + E_{2\pi}\right)E_X \end{aligned} \tag{B.27}$$

where $E_{J/\psi} = \sqrt{p_{J/\psi}^2 + m_{J/\psi}^2}$, $E_{2\pi} = \sqrt{p_{2\pi}^2 + m_{2\pi}^2}$ and $E_X = \sqrt{p_X^2 + m_X^2}$.

The last additional constraint can be obtained by considering that the decay of B^0 should be constrainted by η' mass $m_{\eta'}$, hence by using the conservation of four vector momentum in the $B^0 \longrightarrow J/\psi\eta'$ decay,

$$m_B^2 = m_{J/\psi}^2 + m_{\eta'}^2 + 2(E_{J/\psi}E_{\eta'} - \vec{p}_{J/\psi} \cdot \vec{p}_{\eta'}) \tag{B.28}$$

where $E_{\eta'} = E_{2\pi} + E_X = \sqrt{p_{2\pi}^2 + m_{2\pi}^2} + \sqrt{p_X^2 + m_X^2}$ and $\vec{p}_{\eta'} = \vec{p}_{2\pi} + \vec{p}_X$ are the energy and three vector momenta of η', respectively.

Substituting Equation B.28 to Equation B.27 and cancelling out some terms to simplify the equation, we got,

$$\left[m_{\eta'}^2 - m_{2\pi}^2 - m_X^2 - 2\vec{p}_{2\pi}^{\perp} \cdot \left(\vec{p}_{2\pi}^{\perp} + \vec{p}_{J/\psi}^{\perp}\right)\right] + 2\vec{p}_{2\pi}^{\parallel} \cdot \vec{p}_X^{\parallel} = 2E_{2\pi}E_X \tag{B.29}$$

Knowing that $E_{2\pi} = \sqrt{p_{2\pi}^2 + m_{2\pi}^2}$ and $E_X = \sqrt{p_X^2 + m_X^2}$, we square both sides of Equation B.29 and substituting $p_X^2 = p_X^{\parallel 2} + p_X^{\perp 2}$ and $p_X^{\perp 2} = p_{J/\psi}^{\perp 2} + p_{2\pi}^{\perp 2} + 2\vec{p}_{J/\psi} \cdot \vec{p}_{2\pi}^{\perp}$ (from Equation B.23), we have,

$$\begin{aligned}
&\left[m_\Delta^2 - 2\vec{p}_{2\pi}^{\perp} \cdot \left(\vec{p}_{2\pi}^{\perp} + \vec{p}_{J/\psi}^{\perp}\right)\right]^2 \\
&\quad + 4\left[m_\Delta^2 - 2\vec{p}_{2\pi}^{\perp} \cdot \left(\vec{p}_{2\pi}^{\perp} + \vec{p}_{J/\psi}^{\perp}\right)\right] \vec{p}_{2\pi}^{\parallel} \cdot \vec{p}_X^{\parallel} \\
&\quad + 4p_{2\pi}^{\parallel 2} p_X^{\parallel 2} \\
&\quad = 4\left(p_{2\pi}^{\parallel 2} + p_{2\pi}^{\perp 2} + m_{2\pi}^2\right)\left(p_X^{\parallel 2} + p_{J/\psi}^{\perp 2} + p_{2\pi}^{\perp 2} + 2\vec{p}_{J/\psi}^{\perp} \cdot \vec{p}_{2\pi}^{\perp} + m_X^2\right)
\end{aligned} \tag{B.30}$$

where,

$$m_\Delta^2 = m_{\eta'}^2 - m_{2\pi}^2 - m_X^2 \tag{B.31}$$

Rearranging Equation B.30,

$$\begin{aligned}
0 &= 4\left(p_{2\pi}^{\perp 2} + m_{2\pi}^2\right) p_X^{\parallel 2} \\
&\quad - 4\left[m_\Delta^2 - 2\vec{p}_{2\pi}^{\perp} \cdot \left(\vec{p}_{2\pi}^{\perp} + \vec{p}_{J/\psi}^{\perp}\right)\right] p_{2\pi}^{\parallel} p_X^{\parallel} \\
&\quad + \left\{4\left(p_{2\pi}^2 + m_{2\pi}^2\right)\left[m_X^2 + \left(\vec{p}_{J/\psi}^{\perp} + \vec{p}_{2\pi}^{\perp}\right)^2\right] - \left[m_\Delta^2 - 2\vec{p}_{2\pi}^{\perp} \cdot \left(\vec{p}_{2\pi}^{\perp} + \vec{p}_{J/\psi}^{\perp}\right)\right]^2\right\}
\end{aligned} \tag{B.32}$$

The only unknown quantity in Equation B.32 is the $p_X^{\parallel}$. Equation B.32 is quadratic w.r.t. $p_X^{\parallel}$, which is the component of the momentum vector of the missing particle X in the flight direction of the B^0 meson. Solving this equation using the quadratic equation, yields,

$$p_X^{\parallel} = A \pm \sqrt{B} \tag{B.33}$$

where,

$$A = \frac{\left[m_\Delta^2 - 2\vec{p}_{2\pi}^{\perp} \cdot \left(\vec{p}_{2\pi}^{\perp} + \vec{p}_{J/\psi}^{\perp}\right)\right] p_{2\pi}^{\parallel}}{2\left(p_{2\pi}^{\perp 2} + m_{2\pi}^2\right)} \tag{B.34}$$

$$B = \frac{\left[m_\Delta^2 - 2\vec{p}_{2\pi}^{\perp} \cdot \left(\vec{p}_{2\pi}^{\perp} + \vec{p}_{J/\psi}^{\perp}\right)\right]^2 E_{2\pi}^2}{4\left(p_{2\pi}^{\perp 2} + m_{2\pi}^2\right)^2} - \frac{\left[m_X^2 + \left(\vec{p}_{2\pi}^{\perp} + \vec{p}_{J/\psi}^{\perp}\right)^2\right] E_{2\pi}^2}{\left(p_{2\pi}^{\perp 2} + m_{2\pi}^2\right)} \tag{B.35}$$

where,

$$m_\Delta^2 = m_{\eta'}^2 - m_{2\pi}^2 - m_X^2 \tag{B.36}$$

$$E_{2\pi}^2 = p_{2\pi}^2 + m_{2\pi}^2 \tag{B.37}$$

$$p_{2\pi}^2 = (\vec{p}_{\pi^+} + \vec{p}_{\pi^-})^2 = p_{\pi^+}^2 + p_{\pi^-}^2 + 2\vec{p}_{\pi^+} \cdot \vec{p}_{\pi^-} \tag{B.38}$$

$$m_{2\pi}^2 = \sqrt{p_{\pi^+}^2 + m_{\pi^+}^2} + \sqrt{p_{\pi^-}^2 + m_{\pi^-}^2} - p_{2\pi}^2 \tag{B.39}$$

B.6.3 Parallel and perpendicular components of the momentum vectors of the visible particles

If $\vec{d}$ is the displacement vector from the primary vertex (PV) to the secondary vertex (SV) of X^0 meson, then,

$$\vec{p}^{\parallel}_{J/\psi} = \frac{\vec{p}_{J/\psi}\cdot\vec{d}}{d}\hat{d} = \frac{\vec{p}_{J/\psi}\cdot\vec{d}}{d}\left(\frac{\vec{d}}{d}\right) = \frac{\vec{p}_{J/\psi}\cdot\vec{d}}{d^2}\left(d_x\hat{i}+d_y\hat{j}+d_z\hat{k}\right) \tag{B.40}$$

$$\vec{p}^{\parallel}_{J/\psi} = \frac{\vec{p}_{J/\psi}\cdot\vec{d}}{d^2}d_x\hat{i} + \frac{\vec{p}_{J/\psi}\cdot\vec{d}}{d^2}d_y\hat{j} + \frac{\vec{p}_{J/\psi}\cdot\vec{d}}{d^2}d_z\hat{k} \tag{B.41}$$

then,

$$\vec{p}^{\perp}_{J/\psi} = \vec{p}_{J/\psi} - \vec{p}^{\parallel}_{J/\psi} \tag{B.42}$$

We do the same for the $\vec{p}^{\parallel}_{2\pi}$ and $\vec{p}^{\perp}_{2\pi}$, where,

$$\vec{p}^{\parallel}_{2\pi} = \frac{\vec{p}_{2\pi}\cdot\vec{d}}{d^2}d_x\hat{i} + \frac{\vec{p}_{2\pi}\cdot\vec{d}}{d^2}d_y\hat{j} + \frac{\vec{p}_{2\pi}\cdot\vec{d}}{d^2}d_z\hat{k} \tag{B.43}$$

$$\vec{p}^{\perp}_{2\pi} = \vec{p}_{2\pi} - \vec{p}^{\parallel}_{2\pi} \tag{B.44}$$

For the missing particle X, then,

$$\vec{p}^{\perp}_{X} = -\left(\vec{p}^{\perp}_{J/\psi} + \vec{p}^{\perp}_{2\pi}\right) \tag{B.45}$$

$$\vec{p}^{\parallel}_{X} = p^{\parallel}_{X}\hat{d} = \frac{\vec{p}_{2\pi}\cdot\vec{d}}{d^2}d_x\hat{i} + \frac{\vec{p}_{2\pi}\cdot\vec{d}}{d^2}d_y\hat{j} + \frac{\vec{p}_{2\pi}\cdot\vec{d}}{d^2}d_z\hat{k} \tag{B.46}$$

$$\vec{p}_{X} = \vec{p}^{\parallel}_{X} + \vec{p}^{\perp}_{X} \tag{B.47}$$

B.6.4 Efficiencies and expected number of events

We want to compare the event yield that can be obtained using partial reconstruction technique versus the 79 events that were obtained by the explicit full reconstruction [116]. Hence, the efficiency splitting is necessary. We do this by looking at MC events where only the J/ψ is required to be in acceptance. The corresponding efficiency of each cut is shown in Table B.11. With these cuts, the expected signal distribution is shown in Figure B.42.

Table B.11: Efficiencies corresponding to each cut.

Cut	Efficiency
Acceptance	$\epsilon_{\text{acc}} = 0.25$
Trigger	$\epsilon_{\text{trig}} = 0.90$
Reconstruction	$\epsilon_{\text{rec}} = 0.07564$
Stripping	$\epsilon_{\text{strip}} = 0.7976$
Bfactor ≥ 0	$\epsilon_{\text{B}_{\text{factor}}} = 0.501996$
$\lvert m^{rec}_{J/\psi} - 3096.916\rvert$ MeV/c^2 $\leq 48.$ MeV/c^2	$\epsilon_{\text{m}_{J/\psi}} = 0.986441$
BDTx ≥ 0.10	$\epsilon_{\text{BDTx}} = 0.168889$
BDTy ≥ 0.10	$\epsilon_{\text{BDTy}} = 0.298079$
Combined	$\epsilon_{\text{total}} = 1.28637 \times 10^{-3}$

Given the efficiencies summarized in Table B.11, we calculate the expected number of signal events $N_{\rm sig}$ using the following equation,

$$N_{\rm sig} = L \cdot \sigma_{b\bar{b}} \cdot 2 f_{B_s^0} \cdot \mathcal{B}_{B_s^0 \longrightarrow J/\psi(\mu^+\mu^-)\eta'(\eta\pi^+\pi^-)} \cdot \epsilon_{\rm total} \simeq 1212 \tag{B.48}$$

where $L = \int \mathcal{L} dt = 2.08/\text{fb}$ is the integrated luminousity for the 2012 LHCb data, $\sigma_{b\bar{b}} = 291.6\mu\text{b}$ is the production cross-section of $b\bar{b}$-pairs in the 2012 LHCb data, $f_{B_s^0} = 0.105$ is the hadronization fraction of a $b(\bar{b})$ into a B_s^0 ($\bar{B}_s^0$) meson, and $\mathcal{B}_{B_s^0 \to J/\psi(\mu^+\mu^-)\eta'(\eta\pi^+\pi^-)} = \mathcal{B}_{B_s^0 \to J/\psi\eta'} \times \mathcal{B}_{J/\psi \to \mu^+\mu^-} \times \mathcal{B}_{\eta, \to \eta\pi^+\pi^-} = 9.522394 \times 10^{-6}$ is the visible fraction of $B_s^0 \to J/\psi(\mu^+\mu^-)\eta'(\eta\pi^+\pi^-)$. The result of the partial reconstruction technique gives more expected event yield but with lower signal to background ratio compared to the explicit full reconstruction.

B.6.5 MC $B^0/B_u^+ \to J/\psi X$ inclusive events

We have applied partial reconstruction technique, under the reconstruction hypothesis $B_s^0 \to J/\psi\eta'(\pi^+\pi^-\eta)$, to the inclusive $B^0/B_u^+ \to J/\psi X$ Monte-Carlo data sample. This sample contains 10 millions of such events, with the muons from the J/ψ decay in the acceptance. The size of this sample is approximately a factor five smaller than the actual data sample considered in our analysis. The B_s^0 mass candidates reconstructed using a set of cuts similar to the actual ones applied in the data are displayed Figure B.43(left). These events do not peak in the signal region of $J/\psi\eta'$.

The very same MC sample has been analysed with partial reconstruction under the hypothesis $B_s^0 \to J/\psi\phi(\pi^+\pi^-\pi^0)$. In contrast to the former case, the mass distribution shown on Figure B.43(right) exhibits a peak around 5100 MeV/c^2. Among the physics processes which could account for this excess, the most appealing explanation is coming from $B^{(0,\pm)} \to J/\psi K, K_S^0\pi\pi$ decays, as discussed in Appendix B.6.1. Further investigation is however required to sort out the origin of the peak.

B.6.6 MC $B_s^0 \to J/\psi X$ inclusive events

We have in addition applied partial reconstruction technique, along the same hypothesis, to the analogous inclusive $B_s^0 \to J/\psi X$ Monte-Carlo data sample of 10 million events. Because of the hadronisation fraction of the b quark into B_s^0 meson, this sample corresponds approximately to the total number of data events analysed to reconstruct $B_s^0 \to J/\psi\eta'(\pi^+\pi^-\eta)$. This sample includes in natural proportions the signal we are searching for. Shown in Figure B.44 is the mass distribution obtained by the partial reconstruction method ($B_s^0 \to J/\psi\eta'(\pi^+\pi^-\eta)$) on this sample. We convincingly observe a peaking structure at the nominal B_s^0 mass (about 5300 - 5400 MeV/c^2). By eye inspection, the number of reconstructed events in the data is consistent with the number of MC reconstructed candidates which are seen in the peak.

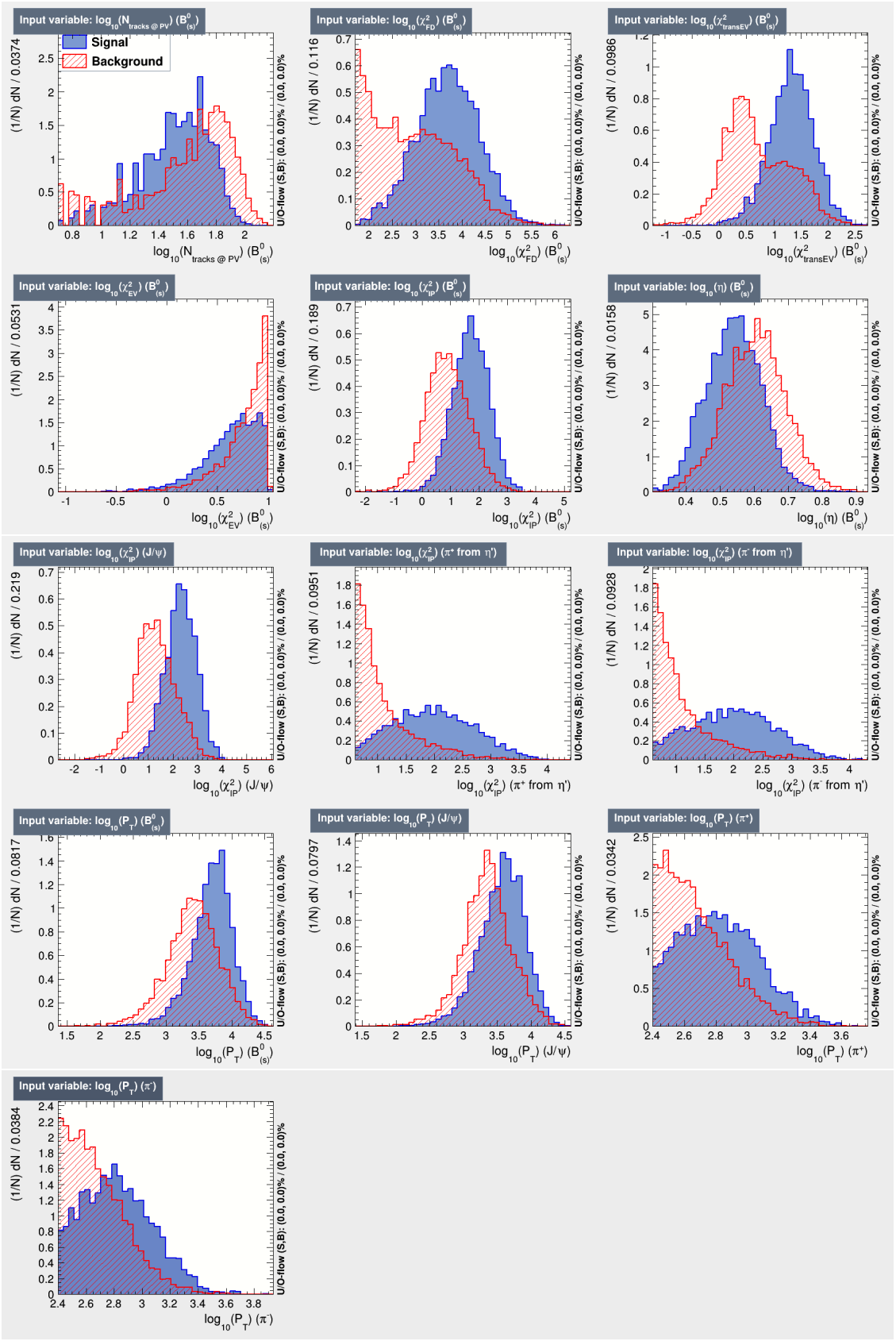

Figure B.33: Distribution of variables used for the training of BDT_1. The same plot can be observed for BDT_2.

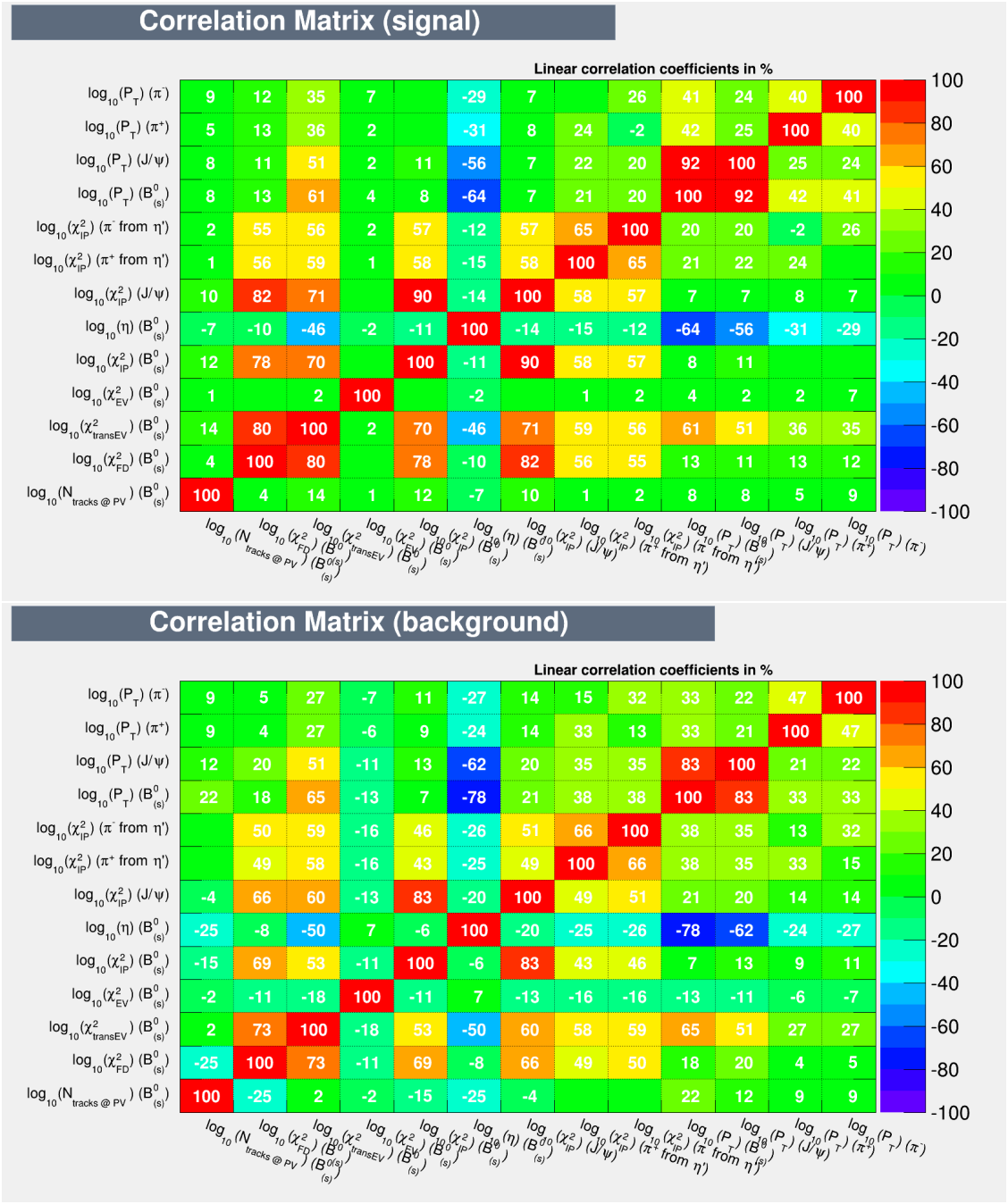

Figure B.34: Linear correlation matrix of the variables of signal events (left) and background events (right) for BDT_1. The same plot can be observed for BDT_2.

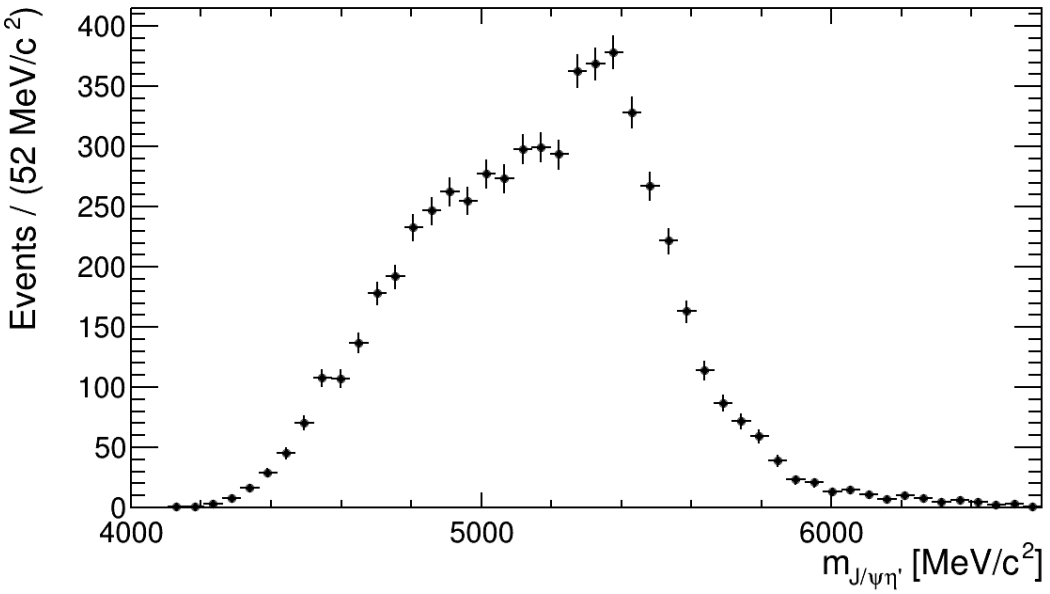

Figure B.35: X^0 mass distribution as reconstructed using partial reconstruction technique on real data searching for the decay $B_s^0 \longrightarrow J/\psi(\mu^+\mu^-)\eta'(\eta\pi^+\pi^-)$. Random choice method was used to obtain these plots, the weighted spectrum is shown in Figure B.38.

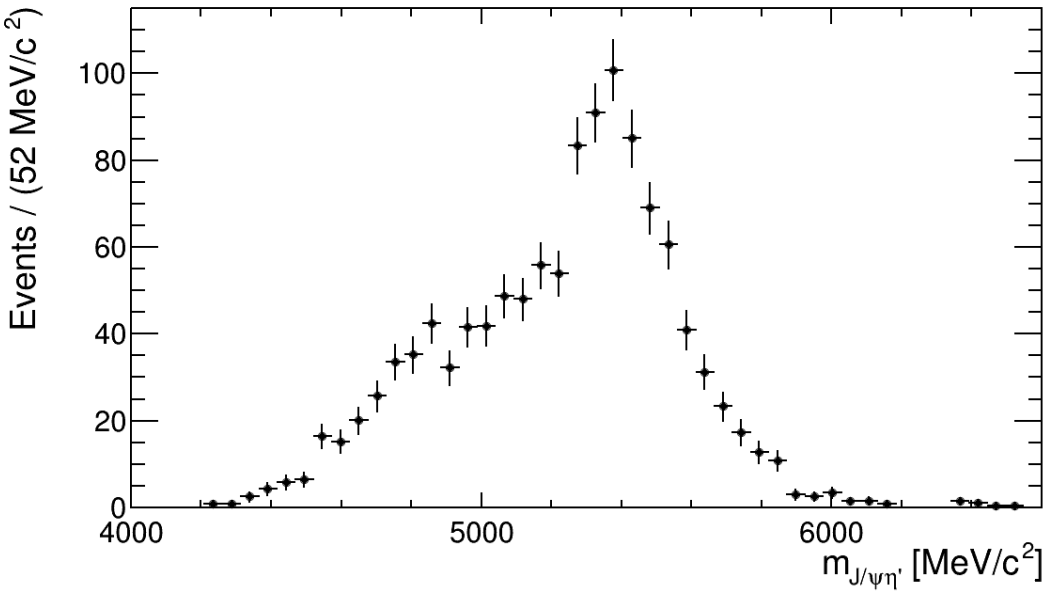

Figure B.36: X^0 mass distribution as reconstructed using partial reconstruction technique on real data searching for the decay $B_s^0 \longrightarrow J/\psi(\mu^+\mu^-)\eta'(\eta\pi^+\pi^-)$ with $\mathrm{PID}_K \leq -5$ and $\mathrm{PID}_p \leq 10$ on the two pions.

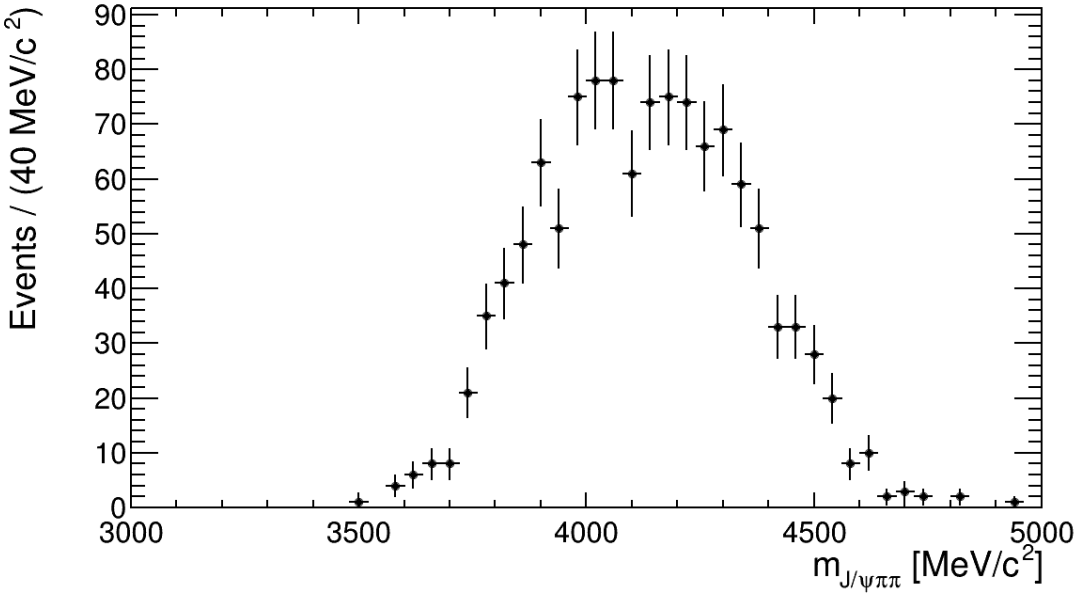

Figure B.37: Reconstructed $J/\psi\pi\pi$ mass distribution after applying all the cuts including $\text{PID}_K \leq -5$ and $\text{PID}_p \leq 10$ cuts on the two pions.

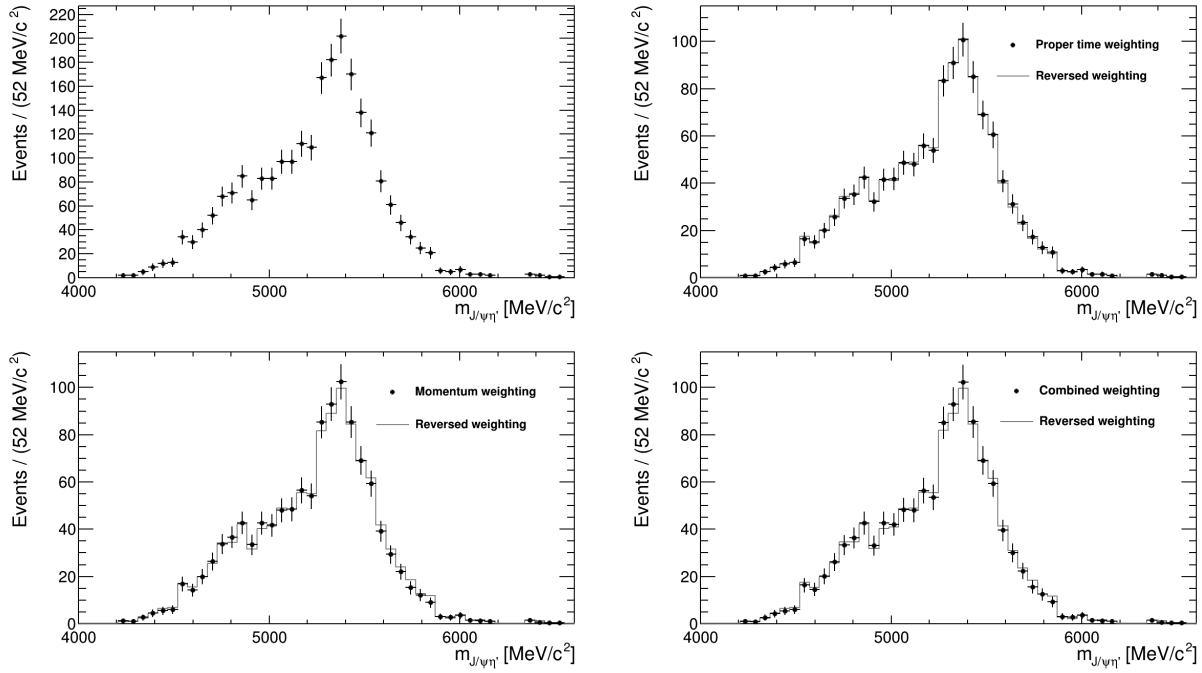

Figure B.38: X^0 mass distribution (top-left) using two entries per candidate event; (top-right) using proper time as basis for weighting; (bottom-left) using momentum as basis; and (bottom-right) using proper time & momentum as basis.

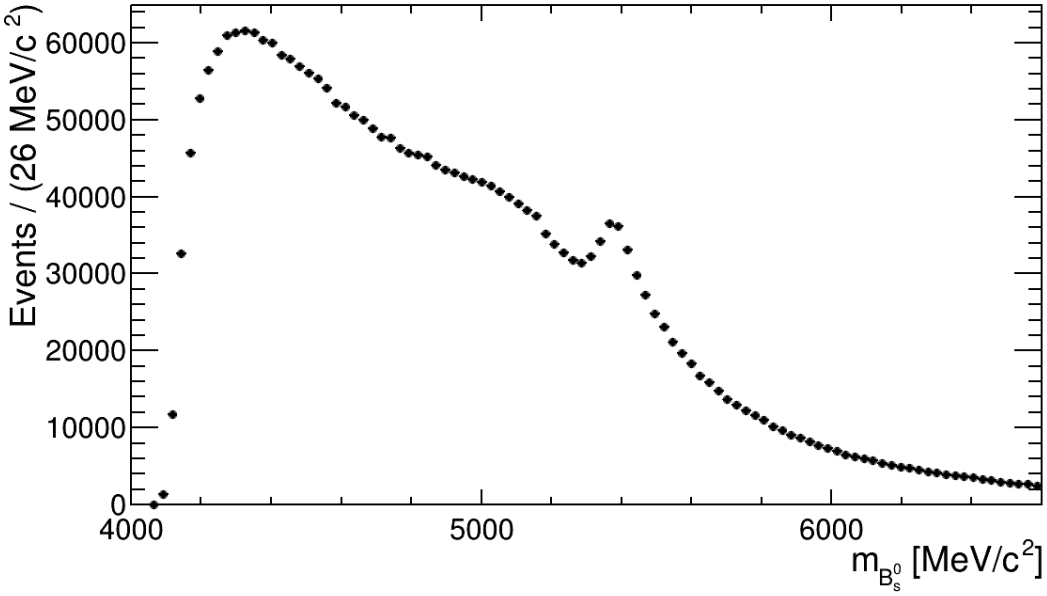

Figure B.39: $J/\psi\phi$ mass distribution as reconstructed using partial reconstruction technique on real data searching for the decay $B_s^0 \to J/\psi(\mu^+\mu^-)\phi(\pi^+\pi^-\pi^0)$ with no PID cuts.

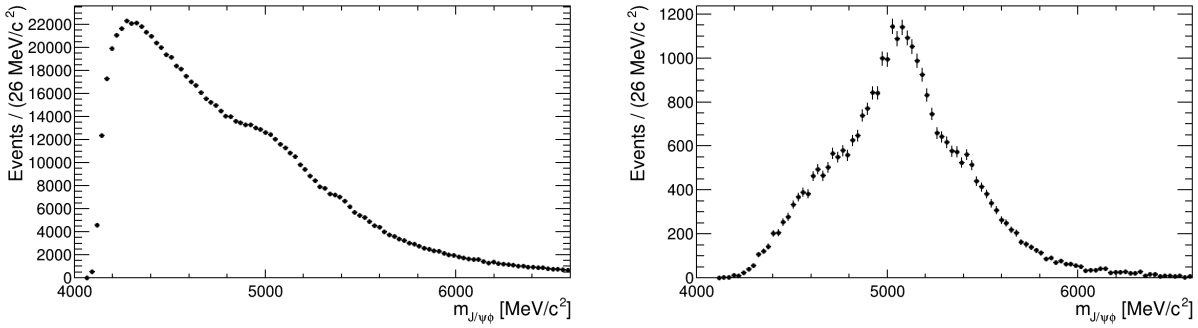

Figure B.40: (Left) $J/\psi\phi$ mass distribution as reconstructed using partial reconstruction technique on real data searching for the decay $B_s^0 \to J/\psi(\mu^+\mu^-)\phi(\pi^+\pi^-\pi^0)$ with PID cuts; and (Right) with additional BDT cuts.

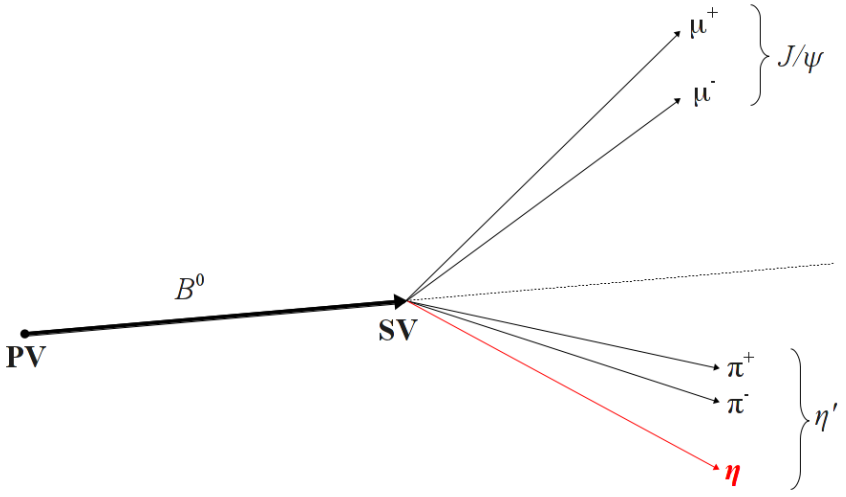

Figure B.41: Illustration of $B^0 \longrightarrow J/\psi(\pi^+\pi^-)\eta'(\pi^+\pi^- X)$ decay, where X can be a photon or η meson. The X particle is not detected and can be reconstructed using decay kinematics.

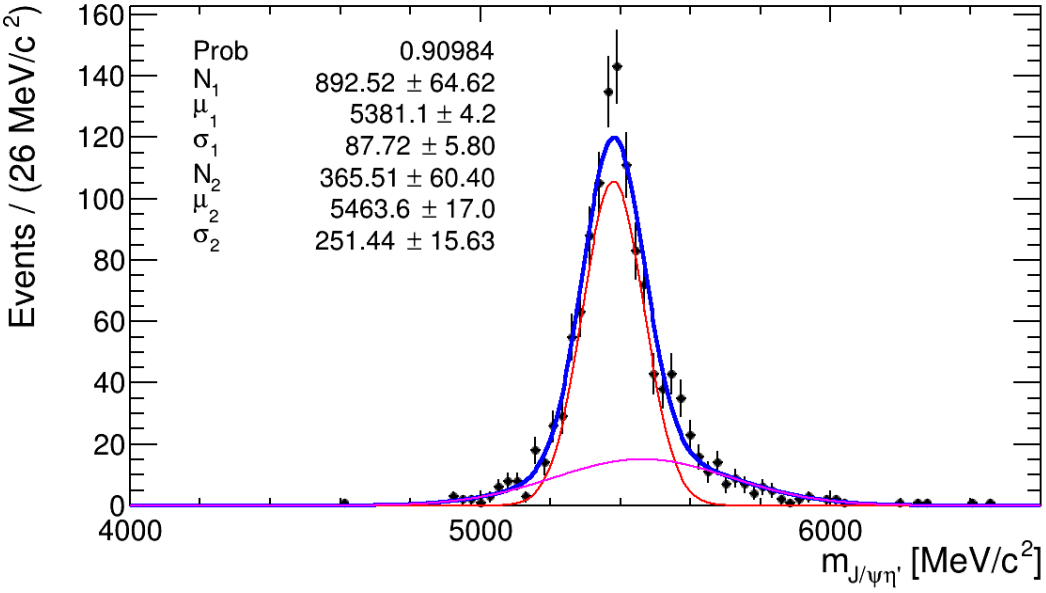

Figure B.42: Expected signal event distribution after applying all the cuts.

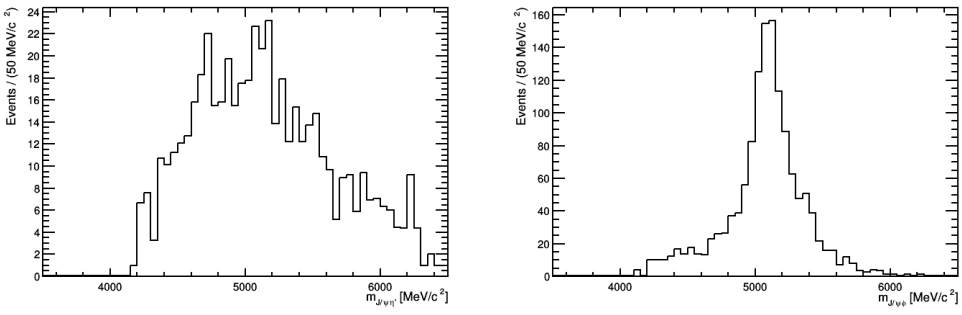

Figure B.43: X^0 mass distribution as reconstructed using partial reconstruction technique using $B^0/B_u^+ \to J/\psi X$ inclusive MC events searching for [left] $B_s^0 \to J/\psi\eta'(\pi^+\pi^-\eta)$ and [right] $B_s^0 \to J/\psi\phi(\pi^+\pi^-\pi^0)$.

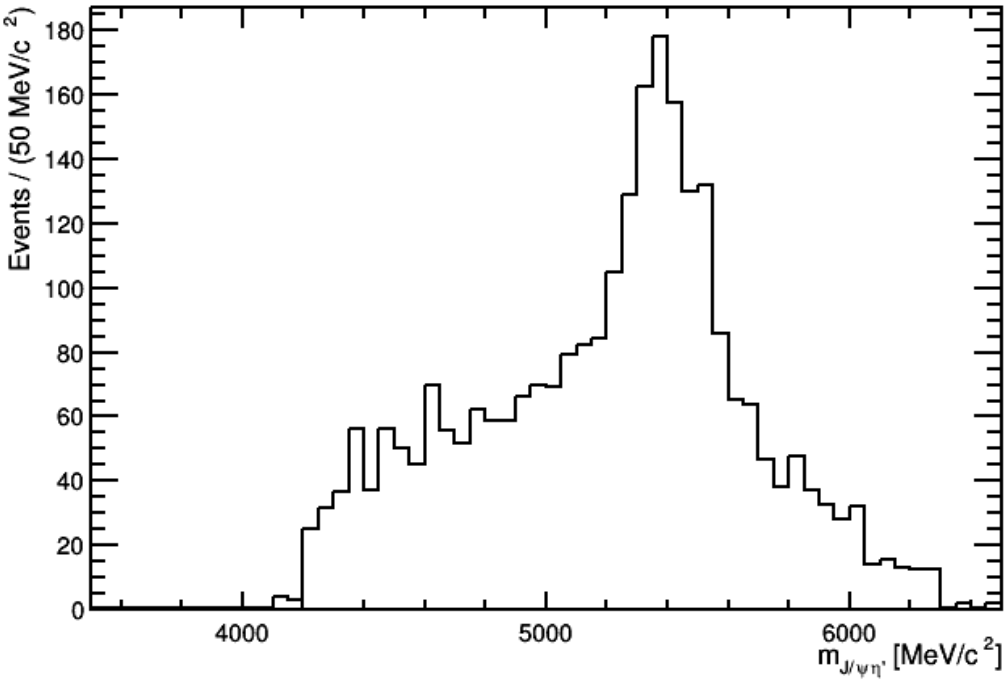

Figure B.44: X^0 mass distribution as reconstructed using partial reconstruction technique using $B_s^0 \to J/\psi X$ inclusive MC events searching for $B_s^0 \to J/\psi\eta'(\pi^+\pi^-\eta)$.

Bibliography

[1] J. H. Christenson *et al.*, *Evidence for the* 2π *Decay of the* K_2^0 *Meson*, Phys. Rev. Lett. **13** (1964) 138.

[2] BABAR Collaboration, B. Aubert *et al.*, *Observation of CP Violation in the* B^0 *Meson System*, Phys. Rev. Lett. **87** (2001) 091801.

[3] BABAR Collaboration, P. del Amo Sanchez *et al.*, *Measurement of* CP *observables in* $B^\pm \to D_{CP}K^\pm$ *decays and constraints on the CKM angle* γ, Phys. Rev. D **82** (2010) 072004.

[4] BABAR Collaboration, B. Aubert *et al.*, *Direct* CP *Violating Asymmetry in* $B^0 \to K^+\pi^-$ *Decays*, Phys. Rev. Lett. **93** (2004) 131801.

[5] Belle Collaboration, K. Abe *et al.*, *Observation of Large CP Violation in the Neutral B Meson System*, Phys. Rev. Lett. **87** (2001) 091802.

[6] Belle Collaboration, Y. Chao *et al.*, *Evidence for Direct* CP *Violation in* $B^0 \to K^+\pi^-$*Decays*, Phys. Rev. Lett. **93** (2004) 191802.

[7] Belle Collaboration, A. Poluektov *et al.*, *Evidence for direct* CP *violation in the decay* $B^\pm \to D^{(*)}K^\pm$, $D \to K_S^0\pi^+\pi^-$ *and measurement of the CKM phase* ϕ_3, Phys. Rev. D **81** (2010) 112002.

[8] LHCb collaboration, R. Aaij *et al.*, *Observation of* CP *violation in* $B^\pm \to DK^\pm$ *decays*, Phys. Lett. **B712** (2012) 203, Erratum ibid. **B713** (2012) 351, arXiv:1203.3662.

[9] LHCb collaboration, R. Aaij *et al.*, *First observation of* CP *violation in the decays of* B_s^0 *mesons*, Phys. Rev. Lett. **110** (2013) 221601, arXiv:1304.6173.

[10] M. Kobayashi and T. Maskawa, *CP-Violation in the Renormalizable Theory of Weak Interaction*, Prog. Theor. Phys. **49** (1973) 652.

[11] J. Charles *et al.*, *Predictions of selected flavour observables within the Standard Model*, Phys. Rev. **D84** (2011) 033005, arXiv:1106.4041.

[12] A. Bevan *et al.*, *Standard Model updates and new physics analysis with the Unitarity Triangle fit*, Nucl. Phys. Proc. Suppl. **241-242** (2013) 89.

[13] CDF collaboration, T. Aaltonen *et al.*, *Measurements of Direct CP-Violating Asymmetries in Charmless Decays of Bottom Baryons*, Phys. Rev. Lett. **113** (2014) 242001.

[14] LHCb collaboration, R. Aaij *et al.*, *Searches for* Λ_b^0 *and* Ξ_b^0 *decays to* $K_S^0 p\pi^-$ *and* $K_S^0 pK^-$ *final states with first observation of the* $\Lambda_b^0 \to K_S^0 p\pi^-$ *decay*, JHEP **04** (2014) 087, arXiv:1402.0770.

[15] LHCb collaboration, R. Aaij *et al.*, *Observation of the $\Lambda_b^0 \to J/\psi p\pi^-$ decay*, JHEP **07** (2014) 103, arXiv:1406.0755.

[16] LHCb collaboration, R. Aaij *et al.*, *Study of $B^0_{(s)} \to K^0_S h^+ h'^-$ decays with first observation of $B^0_s \to K^0_S K^\pm \pi^\mp$ and $B^0_s \to K^0_S \pi^+ \pi^-$*, JHEP **10** (2013) 143, arXiv:1307.7648.

[17] Particle Data Group, K. A. Olive *et al.*, *Review of particle physics*, Chin. Phys. **C38** (2014) 090001.

[18] ATLAS Collaboration and CMS Collaboration, G. Aad *et al.*, *Combined Measurement of the Higgs Boson Mass in pp Collisions at $\sqrt{s} = 7$ and 8 TeV with the ATLAS and CMS Experiments*, Phys. Rev. Lett. **114** (2015) 191803.

[19] CMS Collaboration, V. Khachatryan *et al.*, *Constraints on the spin-parity and anomalous HVV couplings of the Higgs boson in proton collisions at 7 and 8 TeV*, Phys. Rev. D **92** (2015) 012004.

[20] ATLAS collaboration, G. Aad *et al.*, *Study of the spin and parity of the Higgs boson in diboson decays with the ATLAS detector*, arXiv:1506.05669, submitted to EPJC.

[21] F. Englert and R. Brout, *Broken Symmetry and the Mass of Gauge Vector Mesons*, Phys. Rev. Lett. **13** (1964) 321.

[22] P. W. Higgs, *Broken symmetries, massless particles and gauge fields*, Phys. Lett. **12** (1964) 132.

[23] P. W. Higgs, *Broken Symmetries and the Masses of Gauge Bosons*, Phys. Rev. Lett. **13** (1964) 508.

[24] G. S. Guralnik, C. R. Hagen, and T. W. B. Kibble, *Global Conservation Laws and Massless Particles*, Phys. Rev. Lett. **13** (1964) 585.

[25] P. W. Higgs, *Spontaneous Symmetry Breakdown without Massless Bosons*, Phys. Rev. **145** (1966) 1156.

[26] T. W. B. Kibble, *Symmetry breaking in nonAbelian gauge theories*, Phys. Rev. **155** (1967) 1554.

[27] ATLAS Collaboration, G. Aad *et al.*, *Observation of a new particle in the search for the Standard Model Higgs boson with the ATLAS detector at the LHC*, Phys. Lett. **B716** (2012) 1, arXiv:1207.7214.

[28] CMS Collaboration, S. Chatrchyan *et al.*, *Observation of a new boson at a mass of 125 GeV with the CMS experiment at the LHC*, Phys. Lett. **B716** (2012) 30, arXiv:1207.7235.

[29] S. L. Glashow, *Partial Symmetries of Weak Interactions*, Nucl. Phys. **22** (1961) 579.

[30] S. Weinberg, *A Model of Leptons*, Phys. Rev. Lett. **19** (1967) 1264.

[31] A. Salam, *Weak and Electromagnetic Interactions*, Conf. Proc. **C680519** (1968) 367.

[32] S. L. Glashow, J. Iliopoulos, and L. Maiani, *Weak Interactions with Lepton-Hadron Symmetry*, Phys. Rev. **D2** (1970) 1285.

[33] N. Cabibbo, *Unitary Symmetry and Leptonic Decays*, Phys. Rev. Lett. **10** (1963) 531.

[34] C. S. Wu *et al.*, *Experimental Test of Parity Conservation in Beta Decay*, Phys. Rev. **105** (1957) 1413.

[35] R. L. Garwin, L. M. Lederman, and M. Weinrich, *Observations of the Failure of Conservation of Parity and Charge Conjugation in Meson Decays: The Magnetic Moment of the Free Muon*, Phys. Rev. **105** (1957) 1415.

[36] L. Wolfenstein, *Parametrization of the Kobayashi-Maskawa Matrix*, Phys. Rev. Lett. **51** (1983) 1945.

[37] CKMfitter Group, J. Charles *et al.*, *CP violation and the CKM matrix: Assessing the impact of the asymmetric B factories*, Eur. Phys. J. **C41** (2005) 1, arXiv:hep-ph/0406184.

[38] C. Jarlskog, *Commutator of the Quark Mass Matrices in the Standard Electroweak Model and a Measure of Maximal CP Violation*, Phys. Rev. Lett. **55** (1985) 1039.

[39] NA48, A. Lai *et al.*, *A Precise measurement of the direct CP violation parameter Re(epsilon-prime / epsilon)*, Eur. Phys. J. **C22** (2001) 231, arXiv:hep-ex/0110019.

[40] Heavy Flavor Averaging Group, Y. Amhis *et al.*, *Averages of b-hadron, c-hadron, and τ-lepton properties as of summer 2014*, arXiv:1412.7515, updated results and plots available at http://www.slac.stanford.edu/xorg/hfag/.

[41] LHCb collaboration, R. Aaij *et al.*, *First measurement of time-dependent CP violation in $B_s^0 \to K^+K^-$ decays*, JHEP **10** (2013) 183, arXiv:1308.1428.

[42] J. Charles *et al.*, *Current status of the Standard Model CKM fit and constraints on $\Delta F = 2$ New Physics*, Phys. Rev. **D91** (2015), no. 7 073007, arXiv:1501.05013.

[43] C. Albajar *et al.*, *First observation of the beauty baryon Λ_b in the decay channel $\Lambda_b \to J/\psi\Lambda$ at the CERN proton-antiproton collider*, Physics Letters B **273** (1991), no. 4 540.

[44] LHCb collaboration, R. Aaij *et al.*, *Observation of two new Ξ_b^- baryon resonances*, Phys. Rev. Lett. **114** (2015) 062004, arXiv:1411.4849.

[45] CDF, T. Aaltonen *et al.*, *Observation of the Ξ_b^0 Baryon*, Phys. Rev. Lett. **107** (2011) 102001, arXiv:1107.4015.

[46] LHCb collaboration, R. Aaij *et al.*, *Study of beauty hadron decays into pairs of charm hadrons*, Phys. Rev. Lett. **112** (2014) 202001, arXiv:1403.3606.

[47] LHCb collaboration, R. Aaij *et al.*, *Precision measurement of the ratio of the Λ_b^0 to $\bar{B}^0$ lifetimes*, Phys. Lett. **B734** (2014) 122, arXiv:1402.6242.

[48] LHCb collaboration, R. Aaij *et al.*, *Precision measurement of the mass and lifetime of the Ξ_b^0 baryon*, Phys. Rev. Lett. **113** (2014) 032001, arXiv:1405.7223.

[49] LHC Study Group, T. S. Pettersson and P. Lefèvre, *The Large Hadron Collider: conceptual design*, Tech. Rep. CERN-AC-95-05-LHC, CERN, Geneva, Oct, 1995.

[50] L. Evans and P. Bryant, *LHC Machine*, JINST **3** (2008) S08001.

[51] O. S. Brüning *et al.*, *LHC Design Report*, CERN, Geneva, 2004. https://cds.cern.ch/record/782076.

[52] E. Halkiadakis, *Introduction to the LHC Experiments*, in *Physics of the large and the small, TASI 09, proceedings of the Theoretical Advanced Study Institute in Elementary Particle Physics, Boulder, Colorado, USA, 1-26 June 2009*, pp. 489–518, 2011. arXiv:1004.5564. doi: 10.1142/9789814327183_0009.

[53] ATLAS Collaboration, W. W. Armstrong *et al.*, *ATLAS: Technical proposal for a general-purpose pp experiment at the Large Hadron Collider at CERN*, LHC Tech. Proposal, 1994. https://cds.cern.ch/record/290968.

[54] ATLAS Collaboration, A. Airapetian *et al.*, *ATLAS: Detector and physics performance technical design report. Volume 1*, Technical Design Report ATLAS, CERN, Geneva, 1999. https://cds.cern.ch/record/391176.

[55] ATLAS, G. Aad *et al.*, *The ATLAS Experiment at the CERN Large Hadron Collider*, JINST **3** (2008) S08003.

[56] CMS Collaboration, *Technical proposal*, LHC Tech. Proposal, CERN, Geneva, 1994. https://cds.cern.ch/record/290969.

[57] CMS, S. Chatrchyan *et al.*, *The CMS experiment at the CERN LHC*, JINST **3** (2008) S08004.

[58] ALICE Collaboration, *ALICE: Technical proposal for a Large Ion collider Experiment at the CERN LHC*, LHC Tech. Proposal, CERN, Geneva, 1995. https://cds.cern.ch/record/293391.

[59] ALICE Collaboration, *The forward muon spectrometer of ALICE: addendum to the technical proposal for a Large Ion Collider experiment at the CERN LHC*, LHC Tech. Proposal, CERN, Geneva, 1996. https://cds.cern.ch/record/314011.

[60] ALICE, K. Aamodt *et al.*, *The ALICE experiment at the CERN LHC*, JINST **3** (2008) S08002.

[61] LHCb Collaboration, *LHCb : Technical Proposal*, Tech. Proposal, CERN, Geneva, 1998. https://cds.cern.ch/record/622031.

[62] LHCb collaboration, A. A. Alves Jr. *et al.*, *The LHCb detector at the LHC*, JINST **3** (2008) S08005.

[63] TOTEM Collaboration, W. Kienzle *et al.*, *TOTEM, Total Cross Section, Elastic Scattering and Diffraction Dissociation at the LHC: Technical Proposal*, Tech. Rep. CERN-LHCC-99-007. LHCC-P-5, CERN, Geneva, Mar, 1999.

[64] TOTEM Collaboration, V. Berardi *et al.*, *Total cross-section, elastic scattering and diffraction dissociation at the Large Hadron Collider at CERN: TOTEM Technical Design Report*, Technical Design Report TOTEM, CERN, Geneva, 2004.

[65] TOTEM, G. Anelli *et al.*, *The TOTEM experiment at the CERN Large Hadron Collider*, JINST **3** (2008) S08007.

[66] LHCf Collaboration, O. Adriani *et al.*, *Technnical Proposal for the CERN LHCf Experiment: Measurement of Photons and Neutral Pions in the Very Forward Region of LHC*, Tech. Rep. CERN-LHCC-2005-032. LHCC-P-007, CERN, Geneva, Sep, 2005. revised version submitted on 2005-10-04 11:34:56.

[67] LHCf Collaboration, O. Adriani *et al.*, *LHCf experiment: Technical Design Report*, Technical Design Report LHCf, CERN, Geneva, 2006.

[68] LHCf, O. Adriani *et al.*, *The LHCf detector at the CERN Large Hadron Collider*, JINST **3** (2008) S08006.

[69] MoEDAL Collaboration, J. Pinfold *et al.*, *Technical Design Report of the MoEDAL Experiment*, Tech. Rep. CERN-LHCC-2009-006. MoEDAL-TDR-001, CERN, Geneva, Jun, 2009.

[70] J. L. Pinfold, *The MoEDAL Experiment at the LHC*, in *Proceedings, 13th ICATPP Conference on Astroparticle, Particle, Space Physics and Detectors for Physics Applications (ICATPP 2011)*, pp. 515–524, 2012. doi: 10.1142/9789814405072_0076.

[71] MoEDAL, V. A. Mitsou, *The physics case for the MoEDAL experiment at LHC*, EPJ Web Conf. **95** (2015) 04042, arXiv:1411.7651.

[72] LHCb, R. Aaij *et al.*, *LHCb Detector Performance*, Int. J. Mod. Phys. **A30** (2015), no. 07 1530022, arXiv:1412.6352.

[73] E. Norrbin and R. Vogt, *Bottom production asymmetries at the LHC*, in *Fifth Workshop on electronics for LHC experiments, Snowmass, CO, USA, 20-24 Sep 1999: Proceedings*, 2000. arXiv:hep-ph/0003056.

[74] E. Norrbin and T. Sjostrand, *Production and hadronization of heavy quarks*, Eur. Phys. J. **C17** (2000) 137, arXiv:hep-ph/0005110.

[75] LHCb, CMS, V. Khachatryan *et al.*, *Observation of the rare $B_s^0 \to \mu^+\mu^-$ decay from the combined analysis of CMS and LHCb data*, Nature **522** (2015) 68, arXiv:1411.4413.

[76] A. D. Sakharov, *Violation of CP Invariance, c Asymmetry, and Baryon Asymmetry of the Universe*, Pisma Zh. Eksp. Teor. Fiz. **5** (1967) 32, [Usp. Fiz. Nauk161,61(1991)].

[77] LHCb collaboration, *LHCb VELO (VErtex LOcator): Technical Design Report*, CERN-LHCC-2001-011. LHCb-TDR-005.

[78] R. Aaij *et al.*, *Performance of the LHCb Vertex Locator*, JINST **9** (2014) 09007, arXiv:1405.7808.

[79] LHCb VELO Group, H. L. Snoek, *The LHCb VELO: Performance and radiation damage*, Nucl. Instrum. Meth. **A765** (2014) 35.

[80] LHCb collaboration, *LHCb magnet: Technical Design Report*, CERN-LHCC-2000-007. LHCb-TDR-001.

[81] LHCb collaboration, *LHCb inner tracker: Technical Design Report*, CERN-LHCC-2002-029. LHCb-TDR-008.

[82] LHCb collaboration, *LHCb outer tracker: Technical Design Report*, CERN-LHCC-2001-024. LHCb-TDR-006.

[83] LHCb Outer Tracker Group, R. Arink *et al.*, *Performance of the LHCb Outer Tracker*, JINST **9** (2014), no. 01 P01002, arXiv:1311.3893.

[84] LHCb collaboration, *LHCb calorimeters: Technical Design Report*, CERN-LHCC-2000-036. LHCb-TDR-002.

[85] E. Guschin and S. V. Laptev, *Monte-carlo study of LHCb preshower*, .

[86] S. Barsuk *et al.*, *Design and construction of electromagnetic calorimeter for LHCb experiment*, .

[87] R. Djeliadine, O. Iouchtchenko, and V. F. Obraztsov, *LHCb hadron trigger and Hcal cell size and length optimization*, .

[88] LHCb, *LHCb muon system technical design report*, .

[89] LHCb collaboration, *LHCb trigger system: Technical Design Report*, CERN-LHCC-2003-031. LHCb-TDR-010.

[90] T. Head, *The LHCb trigger system*, JINST **9** (2014) C09015.

[91] V. Gligorov, C. Thomas, and M. Williams, *The HLT inclusive B triggers*, .

[92] S. Monteil, *Mesures de précision électrofaibles*, Habilitation à diriger des recherches, Université Blaise Pascal - Clermont-Ferrand II, France, Dec, 2009, https://tel.archives-ouvertes.fr/tel-00561855.

[93] K. G. Sobczak, *Study of charmless three-body decays of neutral B mesons with the LHCb spectrometer*, PhD thesis, Université Blaise Pascal - Clermont-Ferrand II, France, Dec, 2011, https://tel.archives-ouvertes.fr/tel-00686906.

[94] L. Landau, *On the energy loss of fast particles by ionization*, J. Phys. (USSR) **8** (1944) 201.

[95] P. Huet and E. Sather, *Electroweak baryogenesis and standard model CP violation*, Phys. Rev. **D51** (1995) 379, arXiv:hep-ph/9404302.

[96] M. Ciuchini, M. Pierini, and L. Silvestrini, *New bounds on the CKM matrix from $B \to K\pi\pi$ Dalitz plot analyses*, Phys. Rev. **D74** (2006) 051301, arXiv:hep-ph/0601233.

[97] M. Ciuchini, M. Pierini, and L. Silvestrini, *Hunting the CKM weak phase with time-integrated Dalitz analyses of $B_s^0 \to KK\pi$ and $B_s^0 \to K\pi\pi$ decays*, Phys. Lett. **B645** (2007) 201, arXiv:hep-ph/0602207.

[98] M. Gronau, D. Pirjol, A. Soni, and J. Zupan, *Improved method for CKM constraints in charmless three-body B and B_s^0 decays*, Phys. Rev. **D75** (2007) 014002, arXiv:hep-ph/0608243.

[99] M. Gronau, D. Pirjol, A. Soni, and J. Zupan, *Constraint on $\bar{\rho}, \bar{\eta}$ from $B \to K^*\pi$*, Phys. Rev. **D77** (2008) 057504, arXiv:0712.3751.

[100] I. Bediaga, G. Guerrer, and J. M. de Miranda, *Extracting the quark mixing phase γ from $B^\pm \to K^\pm\pi^+\pi^-$, $B^0 \to K_S\pi^+\pi^-$, and $\bar{B}^0 \to K_S\pi^+\pi^-$*, Phys. Rev. **D76** (2007) 073011, arXiv:hep-ph/0608268.

[101] LHCb collaboration, *Branching fraction measurements of $B^0_{d,s}$ decays to $K^0_S hh'$ final states, including first observation of $B^0_s \to K_S K\pi$*, LHCb-CONF-2012-023.

[102] Belle, J. Dalseno *et al.*, *Time-dependent Dalitz Plot Measurement of CP Parameters in B0 —> K0(s) pi+ pi- Decays*, Phys. Rev. **D79** (2009) 072004, arXiv:0811.3665.

[103] BaBar, B. Aubert *et al.*, *Time-dependent amplitude analysis of B0 —> K0(S) pi+ pi-*, Phys. Rev. **D80** (2009) 112001, arXiv:0905.3615.

[104] G. J. Feldman and R. D. Cousins, *A Unified approach to the classical statistical analysis of small signals*, Phys. Rev. **D57** (1998) 3873, arXiv:physics/9711021.

[105] Heavy Flavor Averaging Group, Y. Amhis *et al.*, *Averages of B-Hadron, C-Hadron, and tau-lepton properties as of early 2012*, arXiv:1207.1158.

[106] Particle Data Group, J. Beringer *et al.*, *Review of particle physics*, Phys. Rev. **D86** (2012) 010001, and 2013 partial update for the 2014 edition.

[107] LHCb collaboration, R. Aaij *et al.*, *Measurement of the $D^\pm$ production asymmetry in 7 TeV pp collisions*, Phys. Lett. **B718** (2013) 902, arXiv:1210.4112.

[108] LHCb collaboration, R. Aaij *et al.*, *Measurement of the fragmentation fraction ratio f_s/f_d and its dependence on B meson kinematics*, JHEP **04** (2013) 001, arXiv:1301.5286.

[109] A. Hoecker *et al.*, *TMVA - Toolkit for Multivariate Data Analysis*, arXiv:physics/0703039v5.

[110] G. Punzi, *Sensitivity of searches for new signals and its optimization*, in *Statistical Problems in Particle Physics, Astrophysics, and Cosmology* (L. Lyons, R. Mount, and R. Reitmeyer, eds.), p. 79, 2003. arXiv:physics/0308063.

[111] CDF Statistics Committee, L. Demortier and L. Lyons, *Everything you always wanted to know about pulls*, CDF Public Note 5776 (2012).

[112] T. M. Karbach and M. Schlupp, *Constraints on Yield Parameters in Extended Maximum Likelihood Fits*, arXiv:1210.7141.

[113] S. S. Wilks, *The Large-Sample Distribution of the Likelihood Ratio for Testing Composite Hypotheses*, Annals Math. Statist. **9** (1938), no. 1 60.

[114] A. Chuinard and F. Blanc, *Branching fractions and charge asymmetry in $B^+ \to \eta' K^+$ decays at LHCb*, http://lphe.epfl.ch/publications/diplomas/ac.masters.pdf.

[115] S. Stone, Z. Xing, and L. Zhang, *Partial reconstruction of $b \to$ charm + $\pi^+\pi^-\pi^-$ and $B^0_s \to D^+_s D^-_s$ decays*, LHCb-INT-2013-001.

[116] LHCb collaboration, R. Aaij *et al.*, *Evidence for the decay $B^0 \to J/\psi\omega$ and measurement of the relative branching fractions of B^0_s meson decays to $J/\psi\eta$ and $J/\psi\eta'$*, Nuclear Physics B **867** (2013), no. 3 547, arXiv:1210.2631.